Maturation of prefrontal circuitry in relationship to behavioral abilities

DISSERTATION

with the aim of achieving a doctoral degree
at the Faculty of Mathematics, Informatics and Natural Sciences
Department of Biology
University of Hamburg

Submitted by
Jastyn Anne Pöpplau

2021
Hamburg, Germany

This work has been performed at the Institute of Developmental Neurophysiology at the University Medical Center Hamburg-Eppendorf.
Director: Prof. Dr. Ileana L. Hanganu-Opatz

First evaluator: Prof. Dr. Ileana L. Hanganu-Opatz

Institute of Developmental Neurophysiology
Center for Molecular Neurobiology (ZMNH)
University Medical Center Hamburg-Eppendorf (UKE)

Second evaluator: Prof. Dr. Thomas G. Oertner

Institute for Synaptic Physiology
Center for Molecular Neurobiology (ZMNH)
University Medical Center Hamburg-Eppendorf (UKE)

Third evaluator: Prof. Dr. Marlene Bartos

Institute of Physiology
University of Freiburg

Day of disputation: 02.12.2021

Contents

Acknowledgments

This work could not have been realized without the support and guidance of numerous people. Thanks to all of them for this unforgettable and enriching journey.

First and foremost, I wish to express my deepest gratitude to my supervisor Prof. Dr. Ileana L. Hanganu-Opatz for giving me the opportunity to perform this work in her institute and for her continuous and most helpful advice and support. I am grateful to her for encouraging my scientific career development by promoting my participation at conferences, workshops, and meetings. This gave me confidence and fostered my presentation skills and scientific thinking. Further, I would like to thank her for giving me the freedom to develop and pursue my own research interests.

Many thanks also go to my co-supervisor Prof. Dr. Thomas G. Oertner for his most helpful feedback and his support attending workshops and the FENS Winter School.

I would like to thank all former and current members of the Hanganu-Opatz lab for practical guidance and lively discussions, helping me to see things from a different perspective. I share many lasting memories and achievements with them. In particular, I would like to thank Dr. Sebastian Bitzenhofer and Dr. Mattia Chini for their patience in answering my questions and teaching me during my early stages. They were the best tutors a Ph.D. student can imagine, providing honest criticism accompanied with helpful suggestions.

Special thanks also go to Annette Marquardt, Achim Dahlmann and Peggy Putthoff for their excellent technical assistance and support. For technical support outside the lab, I am most thankful to Torsten Renz and Fritz Kutschera for helping me to implement my challenging ideas and building new constructions.

Further, I would like to thank all co-authors involved in the studies presented here for the amazing and fruitful teamwork. It was a great experience to work with so many people of different backgrounds.

I would like to thank my friends for all the refreshing moments we had together. Their company helped me to relax from my to-do list.

I am very grateful to my family for letting me explore my own direction in life while staying next to my side.

Finally, I want to thank my person of calm. Thank you deeply Thore for always taking away my fears and helping me to focus again.

Declaration on oath / Eidesstattliche Versicherung

Declaration on oath

I hereby declare, on oath, that I, Jastyn A. Pöpplau, have written the present dissertation by my own and have not used other than the acknowledged resources and aids.

Sincerely,

Jastyn A. Pöpplau

City and date	Signature

Eidesstattliche Versicherung

Hiermit erkläre ich, Jastyn A. Pöpplau, an Eides statt, dass ich die vorliegende Dissertationsschrift selbst verfasst und keine anderen als die angegebenen Quellen und Hilfsmittel benutzt habe.

Mit freundlichen Grüßen,

Jastyn A. Pöpplau

Ort, Datum	Unterschrift

Summary

Network oscillations orchestrate neuronal communication and information flow. They represent a commonly observed characteristic of the cerebral cortex and arise from synchronized activity of neuronal ensembles. In the adult prefrontal cortex oscillatory activity within gamma frequency ranges has been attributed to underlie cognitive processing. Consistent with this, the defining features of prefrontal gamma oscillations are compromised in mental disorders and associated with symptomatic behavioral disabilities, in particular, within the cognitive domain. Immature forms of coordinated rhythmic activity in the prefrontal cortex emerge early in life. Yet, with a missing link to their adult equivalent. Specifically, the cellular mechanisms and developmental dynamics of their convergence to mature oscillatory gamma activity as well as the causal impact of early (dys)functional maturation for later cognitive abilities are unknown. In light of the developmental etiology of mental disorders, these unidentified mechanisms embody key aspects with a pressing need to be addressed.

This thesis aims to approach these knowledge gaps by using the mouse as a model system in combination with the application and improvement of diverse techniques, ranging from *in vivo* electrophysiology to morphological investigations. Starting with the detailed dissection of the anesthetic effects in the developing and adult brain, we demonstrate age-, area-, and agent-dependent consequences of anesthesia on brain activity. In the early postnatal brain, anesthesia exerts a differential action compared to the more mature brain. Besides an overall dampening of activity under anesthesia, the frequency structure of neuronal oscillations is maintained regardless of the recorded brain region or used anesthetic agent. This is contrary to the adult brain, where anesthesia favors slow oscillations but reduces the magnitude of faster ones. Still, with a unique activity signature of distinct anesthetics. With respect to the revealed confounding effects of anesthesia, specifically when aiming investigations across development, these studies fostered the methodological development of non-anesthetized head-fixed electrophysiological recordings in immature mice. Bolstered with this advanced methodology, we identify pyramidal neurons in the superficial layers of the prelimbic subdivision of the medial prefrontal cortex as key players in shaping the developmental dynamics of prefrontal gamma oscillations. In line with previous reports, this specific population entrains local circuits in fast oscillatory rhythms already during early postnatal ages. Yet, with increasing frequency and amplitude throughout development, reaching classical gamma frequency ranges at juvenile age. This process relates to the timeline of the progressive embedding of parvalbumin-expressing fast-spiking interneurons into developing prefrontal circuits. Notably, this particular interneuronal population is central for generating gamma oscillations in the adult cortex via fast inhibitory feedback on excitatory neurons.

Even when associated with mature prefrontal gamma oscillations, it remains an open question whether early coordinated activity actively contributes to the subsequent development of prefrontal circuitry and adult behavior. We systematically addressed this question by using two approaches. First, by employing a mouse model mimicking the developmental and multifactorial etiology of mental disorders, we report that under pathological conditions early prefrontal activity is already disturbed during the first postnatal week. Reduced strength and disorganized patterns of oscillatory activity relate to severe structural and functional abnormalities of pyramidal neurons, particularly, in the superficial layers. Moreover, these early dysfunctionalities are predictive for later

emerging cognitive deficits. Next, we causally proved the functional engagement of early prefrontal activity in shaping cortical network refinement by transiently augmenting neonatal coordinated activity via optogenetic stimulation of pyramidal neurons in the superficial layers. This mild manipulation resulted in reversible structural changes of the stimulated neuronal population but was accompanied by permanent circuit dysfunctions. Increased interneuronal feedback of parvalbumin-expressing fast-spiking interneurons tilted the excitation/inhibition balance towards inhibition. This, in turn, resulted in weaker synchronization of population activity within gamma frequency ranges and ultimately in social and cognitive disabilities at adult age.

In their whole, these compelling findings support early coordinated activity as a driver of physiological but also pathophysiological maturation of prefrontal circuitry and finally adult prefrontal-dependent behavioral abilities. Moreover, these results highlight prefrontal pyramidal neurons in the superficial layers as key elements for (dys)functional circuit formation and consequently as a sensitive substrate for subtle developmental disturbances. The results presented here shine new light on unknown developmental mechanisms and offer extended experimental strategies. Furthermore, they serve as a foundation for subsequent research, potentially enabling the future identification of early biomarkers and therapeutic targets concerning mental diseases.

Zusammenfassung

Netzwerk-Oszillationen orchestrieren die neuronale Kommunikation und Informationsverarbeitung. Sie repräsentieren ein verbreitetes Phänomen im zerebralen Kortex und werden durch die synchronisierte Aktivität von neuronalen Ensembles induziert. Im adulten präfrontalen Kortex wird speziell oszillatorischer Aktivität im Gamma-Frequenzbereich zugeschrieben, der Entstehung von kognitiven Prozessen zugrunde zu liegen. In diesbezüglichem Zusammenhang sind die Merkmale dieser Gamma-Oszillationen in psychiatrischen Erkrankungen kompromittiert und assoziiert mit symptomatischen Verhaltenseinschränkungen, insbesondere in kognitiven Bereichen. Unreife Formen koordinierter, rhythmischer Gehirnaktivität im präfrontalen Kortex entstehen zwar früh im Leben, jedoch ist ein direkter Bezug zum adulten Gegenstück bisher nicht etabliert. Genauer ausgedrückt, die zellulären Mechanismen und entwicklungsbedingten Dynamiken wie diese frühen Formen zu reifen oszillatorischen Mustern konvertieren, als auch ein kausaler Zusammenhang zwischen früher dysfunktionaler und funktionaler Reifung mit adulter kognitiver Leistung, ist unbekannt. In Anbetracht der entwicklungsbedingten Ätiologie von psychiatrischen Erkrankungen, verkörpern diese unidentifizierten Mechanismen dringen zu adressierende Schlüsselaspekte.

Diese hier vorgelegte Arbeit hat das Ziel diese Wissenslücken anzugehen. Hierfür wird die Maus als Modelsystem genutzt und kombiniert mit der Nutzung und Fortentwicklung von diversen Methoden, reichend von *in vivo* elektrophysiologischen Ableitungen, bis hin zu morphologischen Untersuchungen. Angefangen mit einer detaillierten Zergliederung von Anästhesie induzierten Effekten auf das sich in der Entwicklung befindende und adulte Gehirn, zeigen wir hier alters-, areal- und agens-bedingte anästhetische Konsequenzen für die Gehirnaktivität auf. Im frühen postnatalen Gehirn übt Anästhesie eine differentielle Wirkung im Vergleich zum Adultem aus. Zwar führt diese zu einer umfassenden Dämpfung der Aktivität, jedoch ist die Frequenzstruktur nicht affektiert, ungeachtet von der gemessenen Gehirnregion oder den genutzten anästhetischen Agenzien. Dies steht im Gegensatz zum adulten Gehirn, in welchem Anästhesie die Stärke von langsamen Oszillationen erhöht und von schnellen erniedrigt, allerdings mit einer spezifischen Aktivitätssignatur für das jeweilige anästhetische Agens. In Anbetracht dieser differenziellen Wirkung von Anästhesie auf unreife Gehirnaktivität, induzierten diese Studien die Entwicklung von methodischen Techniken, welche elektrophysiologische Ableitungen ohne Anästhesie in kopffixierten jungen Tieren ermöglichen. Mittels der Unterstützung dieses methodischen Fortschritts, konnten Pyramidalneurone in der äußeren Schicht im prelimbischen Areal des präfrontalen Kortexes als Schlüsselelemente für die entwicklungsbedingte Formation von Gamma-Oszillationen identifiziert werden. Im Einklang mit vorherigen Veröffentlichungen ist diese spezifische Neuronenpopulation in der Lage, schnelle oszillatorische Rhythmen zu induzieren und dies bereits während der frühen postnatalen Phase. Darauf aufbauend erweitern wir das Bild und zeigen auf, dass sich mit fortschreitendem Alter die Stärke dieser frühen Oszillationen erhöht und sich die Frequenz beschleunigt, bis klassische Gamma-Frequenzbereiche im jugendlichen Alter erreicht werden. Dieser Prozess steht zeitlich in Relation zu der zunehmenden Einbettung von Parvalbumin-exprimierenden, schnellfeuernden Interneuronen in präfrontale Schaltkreise, welche im adulten Kortex beschrieben sind, die Generation von Gamma-Oszillationen durch schnelle Feedbackhemmung zu vermitteln.

Wie aufgezeigt, ist frühe koordinierte Aktivität zwar zu dem Entstehungsprozess reifer Gamma-Oszillationen assoziiert, jedoch bleibt die Frage offen, ob diese auch aktiv zur darauffolgenden Entwicklung von präfrontalen Schaltkreisen und damit zur Entstehung von adulten Verhaltensfähigkeiten mit beiträgt. Unter der Nutzung zweier Herangehensweisen wurde diese Frage systematisch adressiert. Zuerst wurde ein Mausmodell genutzt, welches die entwicklungsbedingte und multifaktorielle Ätiologie von psychiatrischen Erkrankungen widerspiegelt. Unter pathologischen Bedingungen in diesem Model, ist die präfrontale Gehirnaktivität bereits während der ersten postnatalen Woche beeinträchtigt. Die reduzierte Stärke und Koordination der oszillatorischen Aktivität steht insbesondere in Verbindung zu den erheblichen strukturellen und funktionalen Abnormalitäten von Pyramidalneuronen spezifisch in der äußeren Schicht. Des Weiteren sind diese frühen Dysfunktionalitäten prognostisch für später entstehende kognitive Defizite. Im nächsten Schritt prüften wir die kausale Rolle von früher präfrontaler Aktivität für die Formatierung kortikaler Schaltkreise, mittels einer transienten Erhöhung von neonataler, koordinierter Aktivität durch optogenetische Stimulation von Pyramidalneuronen in der äußeren Schicht. Diese leichte Manipulation führte zu reversiblen strukturellen Veränderungen in der stimulierten neuronalen Population, war aber verbunden mit permanenten Schaltkreisdysfunktionen. Das erhöhte Feedback von Parvalbumin-exprimierenden, schnellfeuernden Interneuronen resultierte in einer Schieflage der Balance zwischen Erregung und Hemmung in Richtung zu erhöhter Hemmung. Dies wiederum führte zu einer abgeschwächten Synchronisation von neuronaler Populationsaktivität im Gamma-Frequenzbereich und letzten Endes zu sozialen und kognitiven Verhaltenseinschränkungen im adulten Alter.

In ihrer Summe bestärken diese Ergebnisse die Annahme, dass frühe koordinierte Aktivität einen substanziellen Beitrag zur physiologischen, als auch pathophysiologischen Reifung von präfrontalen Schaltkreisen und somit auch für adulte Verhaltensfähigkeiten, spezifisch im kognitiven Bereich, hat. Darüber hinaus heben diese Ergebnisse präfrontale Pyramidalneurone in der äußeren Schicht als Schlüsselelemente für die (dys)funktionale Schaltkreisformation und dementsprechend als sensitive Zellpopulation für Veränderungen während der Entwicklung hervor. Diese hier präsentierenten Befunde und methodischen Fortschritte scheinen neues Licht auf bisher unbekannte entwicklungsbedingte Mechanismen und erweitern bisherige experimentelle Strategien. Daher stellen sie eine nützliche Grundlage für weiterführende Forschung dar, welche potenziell zu der zukünftigen Identifikation von frühen Biomarkern und therapeutischen Strategien zur Diagnose und Behandlung von psychiatrischen Erkrankungen führen wird.

Abbreviations

5HT3aR	5-hydroxytryptamine 3a receptor
ACC	Anterior cingulate cortex
AMPA	α-amino-3-hydroxy-5-methyl-4-isoxazolepropionic acid
BiPOLES	Bidirectional pair of opsins for light-induced excitation and silencing
CA1	*Cornu ammonis* 1
CGE	Caudal ganglionic eminence
ChR2	Channelrhodopsin-2
DISC1	Disrupted-In-Schizophrenia 1
E	Embryonic age
E/I	Excitation/inhibition
EEG	Electroencephalographic
EPSC	Excitatory postsynaptic current
ES	Early stimulated
FBI	Feedback inhibition
FF	Flat-cleaved optical fiber
FFI	Feed-forward inhibition
FS	Fast-spiking
GABA	γ-aminobutyric acid
GE	Genetic-environmental
HP	Hippocampus
IPSC	Inhibitory postsynaptic current
IUE	*In utero* electroporation
KCC2	Potassium-chloride cotransporter 2
Keta/Xyl	Ketamine/xylazine
Layer 2/3	Superficial layers
Layer 5/6	Deep layers
LFP	Local field potential
MD	Mediodorsal nucleus
MGE	Medial ganglionic eminence
MMF	Medetomidine/midazolam/fentanyl
MUA	Multi-unit activity
P	Postnatal day
PFC	Prefrontal cortex
PL	Prelimbic
PV	Parvalbumin
PYR	Pyramidal neuron
RS	Regular-spiking
SOM	Somatostatin
SP	Subplate
SUA	Single-unit activity
TF	Tapered optical fiber
VIP	Vasoactive intestinal polypeptide

1. Introduction

1.1. The mammalian neocortex: Homology across dimensions

1.1.1. Neocortical evolution and architecture

From an evolutionary point of view the neocortex is the youngest part of the cerebral cortex and unique to the mammalian species. It received its prefix "neo" in the 19th century based on the assumption to be the last cortical area evolved from an olfactory-dominated cerebral hemisphere. This might not hold true according to subsequent studies investigating the origin of the neocortex in the following century. Therefore, the classical term isocortex might be a more phylogenetic neutral descriptor (Fuster, 2001; Northcutt and Kaas, 1995). However, during the developmental course of evolution the outermost parts of the mammalian cerebral cortex underwent enormous architectural changes, thus validating the term neocortex as reasonable. The unique nature of the mammalian neocortex becomes clear by comparing homologous areas of other vertebrates, such as reptiles. The dorsal cortex of reptiles consists of a single thin layer of mainly pyramidal neurons (PYRs) intermingled with a few interneurons. On the other hand, even early mammals possessed a neuronal aggregate of six contiguous layers with a distinct composition of PYRs and interneurons, a unique feature of the neocortex (Kaas, 2011). In early mammals, brain size differed little between species with a similar number of neocortical areas. During the following period of neocortical expansion these areas increased in size and new areas were added. These areas were first defined in the early 20th century by their histological architecture and suggested to represent a patchwork of functional subunits. This view largely lasts until today but with greater knowledge about the specific connections, modular functions, and gene expression profiles each area possesses. However, the boundaries are still not well understood and functional, anatomical, and transcriptomic specifications are overlapping between areas as well as within the same area. This might have led to the great number of subdivisions comprising of around 200 defined areas in primates today (Northcutt and Kaas, 1995; Yamamori and Rockland, 2006).

The process of neocortical expansion reached the highest stage in humans, where the neocortex makes up around 80 % of the brain mass and resulted in an about ten times larger brain than it would be predicted by the body mass (Azevedo et al., 2009). Not only the increasing number of neurons accounts for this enlargement but also increasing neuronal size and subcortical white matter. For instance, other primates compared to humans have been found to possess a proportional equal number of neurons but of different scales. Moreover, even neurons within the same primate brain show an increasing neuronal size, branching complexity, and spine number from posterior to more anterior regions (Azevedo et al., 2009; Douglas and Martin, 2004; Harris and Shepherd, 2015). Furthermore, while great variations across mammalian species are found in neocortical surface area (up to hundreds of times), the cortical thickness varies only a little between two to five times (Florio and Huttner, 2014; Kaas, 2011). These points suggest that, besides an increased number and size of area subunits, the basic patterns of structure and function might be conserved throughout the neocortex and mammalian species. This idea of a serial homology has been supported by neuro-physiological and -anatomical studies. Central to these findings is the characterization of the canonical cortical microcircuit that shares similar cellular compositions, connection patterns, and computational concepts to process varying information (Douglas and

Martin, 2004; Harris and Shepherd, 2015). This serial homology across cortical areas and mammalian species is an important notion for translational research. It enhances the significance of investigations of easier accessible species than humans, such as rodents, the main explored species in this thesis.

1.1.2. The logic of neocortical circuits

Besides quantitative differences, the neocortex of all mammals consists of two main classes of neurons. These classes are comprised of glutamatergic excitatory neurons, which make up around 80 % of all cortical neurons and γ-aminobutyric acid (GABA)ergic interneurons corresponding to the remaining 20 % (Florio and Huttner, 2014). Each main class can be further subdivided into several classes depending on their morphology, connectivity, laminar location, physiological phenotype, or molecular expression profile. The characteristic distribution across the cortex and connection profile of certain neuron classes give rise to the six-layered structure and show largely similar patterns across the neocortex. Each neuron type integrates into a specific local and long-range network supported by glial cells and blood vessels to form a coordinated functional circuit (Florio and Huttner, 2014; Harris and Shepherd, 2015). The canonical microcircuit follows a layered hierarchy from superficial (layer 2/3) to deep (layer 5/6) layers and has been well described for sensory cortices. Excitatory input from the thalamus arrives in the main input layer 4 by innervating multiple cell types. Layer 4 excitatory neurons project to layer 2/3 from where the signal is propagated to the main output layer 5/6 (Douglas and Martin, 2004; Harris and Mrsic-Flogel, 2013; Harris and Shepherd, 2015). This simplified circuit scheme provided a better understanding of the functional implications of the mainly anatomically defined canonical microcircuit. However, it omits area and species variations and thus a substantial amount of additional input/output connections. Further, by interfering connectivity only from excitatory neurons it ignores local and long-range connectivity of interneurons. Thereby it even completely neglects layer 1 from the circuit, which consists mainly of interneurons and the apical dendrites of excitatory neurons (Douglas and Martin, 2004; Felleman and Van Essen, 1991). This simplification of diversity becomes clear by disaggregating the main neuron classes in more detail.

Excitatory neurons can be subdivided into three main classes according to their axonal spread and projection targets, comprising intratelencephalic, corticothalamic, and pyramidal tract neurons. Intratelencephalic neurons are present in layers 2 to 6 and are a diverse class with various projection targets. Among many other targets within the cerebrum, intratelencephalic neurons are the only class projecting to the contralateral hemisphere. Pyramidal tract neurons are large PYRs located in layer 5b with primary subcortical destinations. Corticothalamic neurons are present in layer 6 and project mainly to the ipsilateral thalamus. Whereas in layer 5/6 classes are intermingled, intratelencephalic neurons are the only ones found in layer 2/3. The basic principles of laminar distribution and asymmetric connection patterns of excitatory neuron classes show a high similarity across areas, favoring the principle of a conserved serial organization (Anastasiades and Carter, 2021; Harris and Shepherd, 2015). Interneurons, despite their lower proportion in cortical circuits and their commonality to release the inhibitory neurotransmitter GABA on their postsynaptic target, display a diverse neuronal class with heterogeneous phenotypes. Consequently, attempts to classify them according to pure morphological features have failed in the neocortex (Hangya et al., 2014; Tremblay et al., 2016). A breakthrough was the use of molecular markers which promoted

the identification of three main subclasses that exist across species. Parvalbumin (PV)-expressing neurons comprise approximately 40 % and somatostatin (SOM)- as well as 5-hydroxytryptamine 3a receptor (5HT3aR)-expressing neurons around 30 % of the main interneuron classes, respectively. These classes show largely non-overlapping expression profiles and can be further subdivided by shared morphological or electrophysiological features or by additional co-expression markers. PV interneurons for example, can be further classified into fast-spiking (FS) neurons displaying mainly a basket cell morphology. However, with deeper levels of classification the overlap between classes increases. Nonetheless, especially the 5HT3aR-expressing group can be more reliably subdivided into vasoactive intestinal polypeptide (VIP)-expressing and non-VIP-expressing neurons. Non-VIP interneurons are enriched in layer 1, whereas VIP interneurons are more abundant in layer 2/3. On the other hand, PV and SOM interneurons populate primarily layer 5/6. While this is true for the most part, nearly all classes can be found with a lower proportion in any layer and show area-dependent variability in their laminar distribution. The majority of connections among excitatory neurons within the same area are rather weak and corresponding connectivity rates are approximately in the range of only 10 to 20 %. In contrast, much higher connectivity rates have been found between excitatory neurons and interneurons. This underpins the non-autonomous interactions among the main neuron classes and leads to the formation of various circuit motifs that give rise to the generation of cortical rhythms (Harris and Shepherd, 2015; Tremblay et al., 2016).

1.1.3. Cortical circuit motifs and rhythm generation

Certain interneuron classes show preferential patterns in their postsynaptic neuronal target. PV-expressing neurons innervate mainly the soma or axon initial segment of excitatory neurons and provide fast and powerful inhibition, enabling them to regulate overall activity levels. They form recurrent loops with excitatory neurons by providing feedback inhibition (FBI) but also forwarding local and long-range input via feed-forward inhibition (FFI). SOM interneurons mainly target the dendrites of excitatory neurons, leading to a more focal and localized inhibition to gate synaptic inputs. They are primarily implicated to constitute FBI and less prominently FFI circuit motifs. On the other hand, VIP interneurons target mainly other interneurons with a preference for PV- and SOM-expressing ones. Thus, VIP interneurons are in a well-suited position to generate disinhibition by preserving excitatory cells from the inhibitory action of other interneurons. Excitatory neurons can activate certain inhibitory circuit motifs and thereby influence the activity among themselves (Hangya et al., 2014; Harris and Shepherd, 2015; Jang et al., 2020). These canonical inhibitory circuit motifs give rise to synchronized network activity, an energy-efficient mechanism of information transfer (Buzsaki and Draguhn, 2004; Womelsdorf et al., 2014).

Timed inhibitory control synchronizes the spiking of excitatory neurons, grouping them into assemblies. This is mediated by rhythmic inhibitory postsynaptic currents (IPSCs) that induce hyperpolarizing membrane potentials in excitatory neurons. Received IPSCs, in turn, lead to alternating windows of reduced and enhanced excitability, causing rhythmic excitatory potentials in target neurons via excitatory postsynaptic currents (EPSCs) (Buzsaki and Draguhn, 2004; Buzsaki et al., 2013). Such synaptic transmissions, but also other sources of transmembrane currents, induce voltage fluctuations in the extracellular medium. These fluctuations can be monitored with electroencephalogram (EEG), electrocorticogram or local field potential (LFP)

recordings with higher invasiveness according to this order (Buzsaki et al., 2012). By using such methods, electrophysiological recordings revealed that cortical circuits resonate in specific frequency bands, ranging from infraslow up to ultrafast oscillations and thereby spanning four orders of magnitude. These network oscillations are often correlated between areas. While slow rhythms tend to originate from functional networks spanning a large volume and sometimes are even a brain-wide phenomenon, fast oscillations are more correlated to local synchronized network activity (Buzsaki and Draguhn, 2004; Buzsaki and Wang, 2012; Wang, 2010). This might be mainly owed to the high energetic demands of fast oscillations (Kann, 2011) and solved by cross-frequency coupling, a brain-wide feature of network oscillations (Buzsaki and Watson, 2012). To ensure coupling and information transfer between distant brain regions the amplitude of fast oscillations is often modulated by the phase of slower ones (Buzsaki and Wang, 2012; Sirota et al., 2008). However, also gamma oscillations can travel directly between areas, either via FFI by long-range projecting interneurons, targeting mainly inhibitory interneurons in the target region or via fast conducting excitatory projection neurons to exert direct control of downstream circuits (Buzsaki et al., 2013; Melzer and Monyer, 2020). While the causal functional consequences of oscillations are still a matter of debate, they reflect at least certain behavioral states in an area-specific manner and thereby reveal insights into how the brain operates (Doelling and Assaneo, 2021; Sohal, 2016). Moreover, certain inhibitory circuit motifs are linked to specific frequency bands (Womelsdorf et al., 2014). Whereas PV interneuron mediated FBI of excitatory neurons resonates in beta and gamma frequencies (Cardin et al., 2009), SOM interneuron mediated disynaptic FFI of excitatory neurons tends to resonate in slower theta and beta frequencies (Berger et al., 2010). Even if multiple factors, such as the mediating interneuron type, laminar origin, and kinetics of synaptic currents are contributing to the resulting frequency range, it underpins the close relationship between oscillations and neuronal activity (Womelsdorf et al., 2014).

A remarkable feature of oscillations is their size-invariant occurrence. All characteristic features are preserved across mammalian species. These features include the frequency-dependent hierarchy of oscillation, showing an almost linear decrease of log power with increasing log frequency. Moreover, virtually all known oscillatory patterns have been observed in any investigated mammalian species and specific frequency bands are linked to comparable behavioral states (Buzsaki et al., 2013). Especially, cortical gamma oscillations are augmented during cognitive tasks (Fitzgibbon et al., 2004) and have been linked to working memory load in humans (Howard et al., 2003) as well as in mice (Yamamoto et al., 2014). Subtle inter-species variation in timing and some structural differences might mainly relate to time preservation issues. For instance, slow oscillations propagate faster in humans (Massimini et al., 2004) than in rats (Luczak et al., 2007). Perhaps this ensures a functional communication of distant brain areas within similar time windows throughout brain size and might correlate with increased white matter, axonal size, and myelination to enable faster conductance (Buzsaki et al., 2013; Wang et al., 2008). Overall, the mammalian neocortex shows a significant homology in serial microcircuit organization and effective local and global communication, pointing in the direction of similar mechanisms underlying cortical functions and dysfunctions across species.

1.1.4. The neocortex and its frontal lobe

Located in the anterior pole of the neocortex situates the prefrontal cortex (PFC). The PFC represents the highest level of cortical hierarchy by being the latest phylogenetically as well as ontogenetically developed region of the neocortex and is considered to be the hub of cognitive processing (Fuster, 2001; Miller and Cohen, 2001). Early structural definitions declared the PFC as being a granular frontal cortex, by possessing a granular layer 4, that receives projections of the mediodorsal nucleus (MD) of the thalamus. However, even the traditionally included areas contained agranular or poorly developed granular regions and such definitions mainly hold true for the PFC of primates. Furthermore, it turned out that the MD projects not exclusively to frontal regions and additional thalamic nuclei connect with the PFC, thus the connectivity-based definition lacks precision (Carlen, 2017; Preuss, 1995; Preuss and Wise, 2021; Uylings et al., 2003).

In today's view, the PFC encompasses a great number of subregions with varying definitions of interspecies homologs across studies, debating the utility of translational rodent research (Carlen, 2017; Laubach et al., 2018; Le Merre et al., 2021; Preuss, 1995; Uylings et al., 2003; van Heukelum et al., 2020). Rodents possess fewer frontal areas than primates and all lack the granular layer 4 in most rodent species. The MD projection cortex of rodents roughly corresponds to the anterior cingulate cortex (ACC) in primates. This structural homolog encompasses the subdivisions cingulate, prelimbic (PL), and infralimbic cortex in the medial PFC of rodents and corresponds to areas 24, 32, and 25 in primates, respectively. This thesis centers its attention mainly on the rodent medial PFC with a key focus on the PL. Originally, at the beginning of the 20th century, the ACC belonged not to the PFC because it is agranular and located at the border between neocortex and allocortex and therefore considered as a limbic or paralimbic region (Carlen, 2017; Laubach et al., 2018; Preuss and Wise, 2021; van Heukelum et al., 2020). Nonetheless, some more recent studies include the ACC as a subregion of the primate PFC by discovering its importance during cognitive tasks, a functional aspect mainly attributed to the dorsolateral PFC (Arnsten and Rubia, 2012; Bush et al., 2000; Bush et al., 2002; Duan et al., 2021). This underpins the error-proneness of early attempts to interfere function purely from structure and trying to map specific functions to certain regions by neglecting complementing ones. This represents a challenging approach especially for association cortices, such as the PFC (Fuster, 2001; Keeler and Robbins, 2011; Le Merre et al., 2021). Therefore, the identification of functional homologs might be the more fruitful approach for interspecies translation since rodents can hold similar functions in architecturally different regions. In humans, the PFC is implicated in a wide range of cognitive functions, all dedicated to formulate a suited goal and to generate an appropriate output in a constantly changing environment (Miller, 2000). This includes multi-faceted processes, such as attention, working memory, decision making, emotional, and social behavior as well as speech production and reasoning (Fuster, 2001, 2015; Keeler and Robbins, 2011). While especially the latter might reach its highest and most complex stage in humans, certain aspects of cognition can be also found in rodents, as all mammals have common needs and have to adapt their behavior accordingly (Brown and Bowman, 2002; Carlen, 2017; Chini and Hanganu-Opatz, 2021; Le Merre et al., 2021).

The rodent medial PFC shows a similar dorsal-ventral gradient in cognitive functioning as the primate PFC. With more dorsal regions underlying decision making and attention to ventral regions supporting emotions and motivation (Anastasiades and Carter, 2021; Arnsten and Rubia,

2012). The underlying architecture and processes supporting these functions and their compartmentation can be well investigated in rodents, favored by the development of diverse molecular and genetic tools. Even if still in progress, recent research identified unique wiring rules and microcircuit structures in the medial PFC when compared to sensory areas, potentially enabling its unique computational processes. The medial PFC receives diverse projections from nearly all neocortical areas but also other areas, such as thalamus, basolateral amygdala, hippocampus (HP) and claustrum project to the medial PFC. Most of the direct connections are reciprocal. Thus, the medial PFC is well-positioned to exert top-down control by computing diverse information to instruct a suited output. Despite the lack of a granular layer 4, the medial PFC follows a similar layered hierarchy as described for sensory areas. Thalamic inputs arrive in medial PFC in all layers with strong projections from MD to layer 2/3. Layer 2/3 in medial PFC shows relatively strong interconnections and forwards the amplified inputs to layer 5/6, the main output layer (Anastasiades and Carter, 2021). One of the few unidirectional monosynaptic connections emerges from the hippocampal *cornu ammonis* 1 (CA1) area and the adjacent subiculum and reaches the medial PFC mainly in the ventral portion in layer 5/6 with few fibers in layer 2/3 (Ferino et al., 1987; Jay and Witter, 1991). This innervation gradient might also correspond to the relatively sharp border of layer 2/3 compactness found between dorsal and ventral PL (Van De Werd et al., 2010). However, while these studies mainly focused on excitatory projection neurons, the picture might be more complex by including long-range projecting interneurons. Recently, a subset of medial PFC interneurons, which project monosynaptically to inhibitory hippocampal microcircuits, has been identified, suggesting a richer diversity of medial PFC connections than currently described (Malik et al., 2021). Many incoming projections target inhibitory circuit motifs in medial PFC, that show similarities but also differ in their cellular composition from sensory areas. For example, the PL of the medial PFC possesses fewer PV but more SOM and non-VIP 5HT3aR interneurons (Anastasiades and Carter, 2021). Strikingly, the proportional input from PV to SOM interneurons is similar to those mediated by VIP interneurons, which are thought to be the main disinhibitory elements in sensory cortices (Ahrlund-Richter et al., 2019). This synopsis highlights only a fraction of the unique architecture of the medial PFC circuitry but offers a concept of its matchless computational possibilities.

1.1.5. Prefrontal associated dysfunctions and their etiology

On the downside of prefrontal mediated functions are cognitive dysfunctions, resulting in disorders affecting the mental health. Mental disorders are a diverse class of diseases but share a common trait of affected cognitive functions, substantially compromising the quality of life and leading to significant healthcare costs and economic burdens (Brandon and Sawa, 2011; Greenberg et al., 2015; Horvath and Mirnics, 2009; Millan et al., 2012). Even after decades of research, patients suffer from a non-curative predominantly symptom-based treatment with many off-target effects leading to adverse drug reactions (Millan et al., 2012; Millan et al., 2016; Zhu, 2020). While the exact classification of mental disorders is still a matter of debate (Stein et al., 2020), most of them share a developmental etiology with their onset during childhood or adolescence (Solmi et al., 2021) and are caused by genetic and environmental factors interfering with normal brain maturation (Feigenson et al., 2014; Horvath and Mirnics, 2009; Schubert et al., 2015).

To identify prognostic molecular biomarkers, more than 900 protein-coding genes and additional non-coding elements have been linked with increased susceptibility (Parenti et al., 2020). However, an increased genetic risk leads not indispensably to disease onset. Only around one-third of high-risk patients convert, supporting a multifactorial nature of mental disorders (Millan et al., 2016; Spencer-Smith and Anderson, 2009). Moreover, the identified risk genes are not predictive for a certain disease. Many diseases show a high degree of genetic overlap, potentially leading to the substantial comorbidity among them with shared behavioral endophenotypes, in particular, within the cognitive domain (Brainstorm et al., 2018; Parenti et al., 2020). In addition, diverse risk genes might trigger common cascades of lasting alterations and therefore might not suffice as curative targets at later stages (Millan et al., 2012). This is underpinned by the circumstance that most of these risk genes are strongly expressed during development (Marin, 2016). These issues point at different diseases being caused by overlapping pathophysiological processes induced by diverse and disruptive gene-environment interactions during development. The identification of such processes can foster the development of causative treatments as well as the discovery of more suitable biomarkers. Due to ethical reasons, the early origin of misguided processes cannot be investigated in humans. Moreover, human studies cannot control for confounding effects such as medication and lifestyle. While rodents lack the complexity of human cognitive functions, they are accessible at human fetal stages and studies in rodents can control for environmental and genetic conditions (Chini and Hanganu-Opatz, 2021; Horvath and Mirnics, 2009), the latter even with area and cell-type specificity (Niwa et al., 2010; Rao and Wilkinson, 2006).

A convergence across human and rodent findings are the common alterations in PFC circuitry. Cognitive functions develop relatively late in life compared to sensory and motor performances. This is associated with the protracted development of the PFC which reaches its full maturity not before adolescence. The PFC shows the longest period of maturation, regarding myelination, synaptogenesis, and pruning criteria (Chini and Hanganu-Opatz, 2021; Delevich et al., 2018; Fuster, 2001). This prolonged maturation is signed by periods of increased plasticity with non-linear changes in structural remodeling and skill achievements (Klune et al., 2021), which match suggested vulnerable timepoints for pathological development in humans (Spencer-Smith and Anderson, 2009). Rodent studies further confirm that interfering at specific timepoints with normal prefrontal development increases the vulnerability for impaired cognitive functioning (Rubino et al., 2015; Shao et al., 2013; Xu et al., 2019; Yang et al., 2015). In line with this, we found that a transient increase of prefrontal activity during the second postnatal week leads to lasting alterations in prefrontal circuitry and disturbed working memory and social interaction at young adult age, whereas stimulations applied five days later had only minor effects (Bitzenhofer et al., 2021). In humans, several mental disorders are further linked to structural and functional abnormalities especially within prefrontal regions, such as reduced volume, dendritic complexity, and spine density as well as altered patterns of activity (Glantz and Lewis, 2000; Hare and Duman, 2020; Konopaske et al., 2014; Meyer-Lindenberg, 2010). These findings have been replicated in many rodent models of disease, including our own findings (Chini et al., 2020; Martinez-Cerdeno, 2017; Winship et al., 2019).

While many additional aspects point to a predominant role of the PFC in underlying the origin and symptoms of mental disorders, it has to be considered that the PFC acts not in an isolated manner. Its functioning is strongly dependent on the quality of information it receives as

well as on how sent instructions are processed in downstream regions (Spencer-Smith and Anderson, 2009). Nonetheless, whereby the PFC is associated with the whole spectrum of cognitive dysfunctions, certain circuits have been found to underlie specific aspects (Meyer-Lindenberg, 2010). The prefrontal-amygdala circuit is primarily associated with altered social cognition and emotional regulation (Brunet-Gouet and Decety, 2006; Gangopadhyay et al., 2021; Rasetti et al., 2009). On the other hand, the prefrontal-hippocampal circuit is important for context guided memory (Place et al., 2016) and altered synchrony as well as connectivity results in poor working and recognition memory abilities as well as in impaired goal-directed learning (Adams et al., 2020; Godsil et al., 2013; Hartung et al., 2016; Sigurdsson et al., 2010). These two examples are only a brief extract of the numerous and complex circuitry implicated in impaired cognitive functioning. Among other parameters, the diversity of affected brain regions hampers a direct identification of a common origin in humans. Given the substantial similarities of interspecies findings, rodents are highly instrumental to identify key processes during (dys)functional development.

1.2. Neocortical ontogeny

1.2.1. Neuronal differentiation and structural lamination

The development of the cerebral cortex is a temporally and spatially tight controlled program of dependent and overlapping phases. This process extends from neurulation at early prenatal until relatively late postnatal stages where circuit refinement processes complete. These sequential milestones are remarkably similar in rodents and to what is known in humans (Chini and Hanganu-Opatz, 2021; Lim et al., 2018). As soon as the neural tube has formed progenitor cells in the dorsal neuroepithelium start to proliferate. Excitatory neurons are generated through asymmetric cell division of early arising radial glia cells into immature neurons and additional radial glia progenitor cells. Radial glia cells elongate to the outer pial surface to build a scaffold for young migrating neurons (Marin and Rubenstein, 2003). The earliest generation of postmitotic neurons migrates to the pial surface to build the preplate. Subsequently generated excitatory neurons in the ventricular zone, which comprise mainly PYRs, migrate radially to form the cortical plate by splitting the preplate into the outer marginal zone (later layer 1) and subjacent subplate (SP) (Kirischuk et al., 2017). The marginal zone and SP contain transient instructive populations of pioneer neurons, which die almost completely through apoptosis after the cortical maturation has finished. Cajal-Retzius neurons in the marginal zone are important for cortical pattering by secreting reelin to guide radial migrating PYRs (Luhmann et al., 2020; Molnar et al., 2020). The SP contains a diverse population of neurons with remarkably mature morphological and transcriptomic profiles already at embryonic stages and assists cortical circuit construction in many ways (Ghezzi et al., 2021; Hoerder-Suabedissen and Molnar, 2015). SP neurons enable functional column segregation by forming a relay station of thalamocortical connections. This important transient circuit plays a major role in orchestrating the early forms of cortical activity (Hanganu et al., 2001, 2002; Luhmann et al., 2009).

PYRs innervate the growing cortical plate in a so-called inside-out fashion by migrating through the already formed layers, resulting in a birthdate-dependent laminar gradient from layers 6 to 2 (Kirischuk et al., 2017; Molnar and Clowry, 2012). Recent molecular investigations point in the direction that the diversity of PYRs emerges postmitotically during lamina allocation and is less

determined by the dividing progenitor pool (Di Bella et al., 2021). On the other hand, interneuron diversity is thought to rely on the temporal and spatial specification of progenitor cells but needs postmitotic cues to unfold. In contrast to PYRs, interneurons are generated in the subpallium with major progenitor pools in the medial ganglionic eminence (MGE) and caudal ganglionic eminence (CGE). The MGE primarily gives rise to later PV- and SOM-expressing interneurons, whereas interneurons divided from CGE mainly correspond to the 5HT3aR-expressing family. Postmitotic interneurons migrate tangentially to the developing cortex mainly via an upper or lower route to innervate the marginal zone or ventricular zone, respectively. Interneurons start to migrate earlier than PYRs but reach their destination with a relatively long delay at a timepoint when PYRs already have started to form a layered structure. Once arrived, interneurons switch from tangential to radial migration to sort into certain layers. This process of interneuronal sorting is guided by cues released from PYRs and occurs in a comparable birthdate-dependent inside-out fashion (Lim et al., 2018). However, mainly MGE derived interneurons display this gradient. CGE derived interneurons start to proliferate later than interneurons from MGE and populate to 75 % layers 1 to 3 regardless of their birthdate (Miyoshi and Fishell, 2011).

After reaching their destinations cortical neurons start to establish synaptic connections. This is primarily controlled by intrinsic genetic programs, such as the upregulation of potassium-chloride cotransporter 2 (KCC2) that co-occurs with migration termination and the emergence of network activity (Hanganu-Opatz et al., 2021; Miyoshi and Fishell, 2011). Even so, subtype-specific functional properties and molecular expression profiles also play important roles in guiding the spatial distribution of initial synaptic contacts (Favuzzi et al., 2019; Kepecs and Fishell, 2014). Many of these formatting circuits are transient and are refined within the first and second postnatal week in rodents. Cortical neurons are generated in higher numbers than later persist until adulthood. PYRs undergo a reduction of 12 % within the first postnatal days, followed by interneurons, which undergo a more intensive reduction of 30 % (Wong et al., 2018). The timing of this neuronal pruning is of high relevance. A delayed normalization of interneuronal numbers results in long-lasting behavioral consequences (Magno et al., 2021). The tendency to undergo apoptotic death is determined by intrinsic factors when reaching a mature state. Nonetheless, especially interneuronal pruning has been shown to occur in an activity-dependent manner, determined by the strength of circuit integration (Denaxa et al., 2018; Lim et al., 2018). Decreased GABAergic input onto PYRs as well as increased excitatory input from PYRs to interneurons increases the survival rate of interneurons, indicating activity as a pro-survival factor (Duan et al., 2020; Wong et al., 2018). These and other synergetic interactions of structural formation and emergence of electrical activity suggest early patterns of activity as an important readout and mediator of key developmental processes.

1.2.2. Emergence of network activity and state dependency

To enable coordinated network activity, even between distant brain regions, the patchwork of immature neurons has to interconnect in a functional manner. Whereas initial contacts are mainly determined by intrinsic genetic factors, the refinement of early plastic synapses depends greatly on activity-dependent mechanisms (Hanganu-Opatz, 2010). In rodents, the first small-scale electrical events in the developing cortical plate emerge shortly before birth (Corlew et al., 2004). Around birth, these electrical events occupy larger territories and show already coordinated

patterns of population activity. They occur spontaneously and originate in the posterior cerebral cortex and spread out to the whole cortex towards the anterior pole with a sparse rate of around two per one minute (Cirelli and Tononi, 2015; Kirischuk et al., 2017). This discontinuity is a hallmark of early brain activity. Long periods of brain-wide silence, present in the form of an isoelectric recording trace, are interrupted by bursts of activity capturing many areas and occurring sometimes even brain-wide. With age, coordinated oscillatory events of low frequency become more abundant and are complemented with faster frequency bursts. In the rodent literature, these spontaneous events have been termed spindle bursts, due to their characteristic pattern in LFP recordings. Alike patterns have been identified during development across distant species, sharing a similar temporal structure and spatial distribution despite the use of different recording methods (Chini and Hanganu-Opatz, 2021; Kirischuk et al., 2017). For instance, in humans these patterns have been termed delta brushes and can be observed in EEG recordings of preterm infants and correspond in their developmental stage to early postnatal stages in rodents (Khazipov and Luhmann, 2006; Kidokoro, 2021; Workman et al., 2013). Several reasons account for the sparsity of early activity, such as immature neuronal properties, few synaptic contacts, and weak thalamocortical connectivity. Nonetheless, early bursts of activity are already present before sensory pathways are mature and emerge without experience, suggesting an intrinsic generation. They arise correlated to events originating in the immature sensory periphery, such as retinal waves or spontaneous muscle twitches, but are also generated in the immature thalamocortical circuit (Cirelli and Tononi, 2015; Hanganu-Opatz, 2010; Martini et al., 2021). The SP is an important amplifier of early activity and its ablation leads largely to the elimination of spindle bursts (Luhmann et al., 2009; Tolner et al., 2012). On the other hand, blocking of retinal waves reduces but does not completely prevent the occurrence of spindle bursts in visual cortex (Hanganu et al., 2006). Similarly, sensory deprivation reduces the occurrence of spontaneous events in somatosensory cortex but affects mainly local events, whereas global events coupled between motor and sensory areas are largely untouched (Cross et al., 2021). These revealing findings suggest the presence of different underlying mechanisms in generating the early forms of cortical activity.

A shared feature of early spontaneous events is their dissociation from behavior. They occur during any state, during wakefulness as well as within active and quiet sleeping periods (Cirelli and Tononi, 2015). This contrasts with adult brain activity, which is strongly modulated by the behavioral state and shows distinct oscillatory patterns during sleep, such as sleep spindles and slow-wave activity with characteristic up and down states (Neckelmann and Ursin, 1993; Niethard et al., 2018). We observed a similar divergence between adult and developing activity with respect to anesthesia-induced effects. In mice aged between postnatal day (P) 8 and 10 anesthesia enhances the signal discontinuity in a dose-dependent manner regardless of the used anesthetic agent or recorded brain area. Besides this global decrease in LFP power, active events showed the same spectral distribution as pre-anesthesia periods. This phenomenon was also present in human infants aged 0 to 2 months. On the contrary, in juvenile mice and human infants older than 4 months anesthesia reduces the power of fast but enhances slow oscillations (Chini et al., 2019). In the adult brain, our investigations of anesthetic effects on hippocampal network activity further showed agent- and area-specific actions of anesthesia (Yang et al., 2021). Consequently, these age-dependent effects of anesthesia have to be considered when investigating developmental changes of network activity.

1.2.3. Cellular mechanism of developing prefrontal activity

Besides growing knowledge of mechanisms underlying the development of network activity in the cerebral cortex, little is known about the circumstances in the PFC. Lower areas of the cortical hierarchy are primarily associated with specific sensory and motor functions, making them shapeable during investigations of their developmental role. The unique microcircuit structure, connectivity, and complex integrative functions of the PFC complicate its functional comprehension (Fuster, 2001). Considering the key role of the PFC in mental disorders and their etiology, a better understanding of the development of prefrontal activity is required. By addressing this knowledge gap, most of the presented studies in this thesis focus on cellular elements in the mouse medial PFC and their role during functional and abnormal prefrontal development as well as on technical challenges of their investigation. They follow the stream of previous investigations and enrich the current knowledge.

The emergence of prefrontal activity follows a similar timeline to what has been described for sensory cortices but is delayed in comparison to HP (Brockmann et al., 2011). In sensory cortices, activity becomes continuous shortly before eye-opening and appearance of an active sleep/wake cycle, starting at P10 and completing at around P13 (Cirelli and Tononi, 2015; Golshani et al., 2009; Rochefort et al., 2009; Shen and Colonnese, 2016). Specifically, in the medial PFC activity starts to occur with around 10 % of active periods at P2/3 and converges to continuous activity at P11/12. This is accompanied by an exponential increase in firing rates and LFP power (Chini et al., 2021). One of the main drivers of the maturation of prefrontal activity is the HP. Already at neonatal age, the medial PFC receives direct projections from the intermediate/ventral CA1 and hippocampal lesions impair the generation of prefrontal spindle bursts (Brockmann et al., 2011). Especially, in the PL spindle bursts with nested beta/low-gamma episodes are time-locked to discontinuous hippocampal theta bursts and can be induced by optogenetic stimulation of HP confined to 8 Hz (Ahlbeck et al., 2018; Brockmann et al., 2011). The cellular substrate for the local generation of these early beta/low-gamma oscillations in the PL was identified with layer-specific optogenetic stimulations of channelrhodopsin-2 (ChR2)-expressing PYRs. In mice of 8 to 10 days of age, optogenetic ramp light stimulation, which is a light stimulus of increasing intensity, of layer 2/3 but not layer 5/6 PYRs induces rhythmic LFP activity and synchronized population activity that peaks at around 20 Hz (Bitzenhofer et al., 2017b). The unique ability of layer 2/3 PYRs to generate relatively fast rhythmic activity already at early postnatal ages, suggests a functional importance of this particular subpopulation. Here, we establish a link between early and adult gamma oscillations in the medial PFC by recording mice from P5 to 40. Pronounced spontaneous prefrontal oscillatory activity within faster frequency ranges emerges towards the end of the second postnatal week. The amplitude and frequency of these spontaneous gamma oscillations increase until around P25 and stabilize afterwards. While initially at around 20 Hz, peak frequency accelerates until reaching 50 Hz, located within the classical gamma-band frequency range (30-80 Hz). Remarkably, layer 2/3 PYR-driven oscillatory activity follows a similar timeline and induces an analogical increase in peak amplitude and frequency over age. This close relationship between spontaneous and layer 2/3 PYR-evoked activity, indicates layer 2/3 PYRs as a substantial driver of prefrontal gamma oscillations throughout development (Bitzenhofer et al., 2020).

The early functional role of layer 2/3 PYRs is further supported by our investigations of a mouse model of mental disorders. This model mimics the dual genetic-environmental (GE) etiology of such disorders by combining the disruption of the Disrupted-In-Schizophrenia 1 (DISC1) gene with a maternal immune activation. In GE mice layer 2/3 PYRs are the key substrate of reduced and disorganized prefrontal beta/low-gamma activity. Their decreased firing rates and abnormal timing relate to a sparsification of their dendritic complexity and spine density during the second postnatal week and might underlie emerging cognitive deficits during pre-juvenile age (Chini et al., 2020). These findings highlight the close relationship between early prefrontal activity and dysfunctional maturation of prefrontal circuitry and behavior. However, a key question that emerges is whether early activity simply reflects (patho)physiological maturation or actively contributes to it. To address this question, we focused on layer 2/3 PYRs, due to their functional role already during early development. We demonstrate that an elevation of layer 2/3 induced activity from P7 to 11 causes long-lasting alterations in the interneuronal feedback and shifts the excitation/inhibition (E/I) balance towards increased inhibition. This, in turn, results in weaker synchronization of population activity within gamma-band frequencies and ultimately in cognitive and social disabilities at adult age (Bitzenhofer et al., 2021). Thus, altered early prefrontal activity as a result of diverse disturbances might trigger a cascade of consequences resulting in similar cognitive deficits across mental diseases. This emphasizes the importance of research dedicated to identifying the early cellular mechanisms of disease pathology.

1.3. Objectives and thesis overview

The overarching aim of this thesis is the identification of cellular mechanisms contributing to the (dys)functional maturation of prefrontal circuitry in relation to behavioral abilities. In order to do so, the mouse is used as a model system in combination with the application and improvement of a wide range of techniques ranging from in vivo electrophysiological recordings and optogenetics up to morphological investigations. A partial body of this work dissects anesthesia-induced effects on network activity at different developmental stages. In light of the revealed confounding and age-specific effects of anesthesia, these studies fostered the establishment of non-anesthetized electrophysiological recordings in developing mice, reflecting the strong methodological focus of this thesis.

Chapter 2.1 joins this focus by using optogenetic electrophysiological *in vivo* recordings of neonatal mice for a comparative analysis of optoelectrodes with flat-cleaved optical fibers (FFs) and tapered optical fibers (TFs), the latter engineered to restrict the light delivery spatially to the neuronal population of interest. **Chapter 2.2** investigates the effects of anesthesia in neonatal and juvenile mice in diverse brain regions and relates the findings to EEG recordings of human infants to develop a prediction algorithm for anesthetic depth in the immature brain. **Chapter 2.3** deepens the understanding of anesthesia-mediated effects in the adult CA1 area of HP by focusing on immediate network activity signatures and long-term consequences for synaptic connectivity and memory consolidation of three distinct anesthetic agents and relates the findings to natural sleep. **Chapter 2.4** explores the age-dependent changes of prefrontal gamma activity and demonstrates the underlying mechanism of frequency acceleration by using optogenetic stimulation of layer 2/3 PYRs in non- and anesthetized mice aged from P5 to 40. **Chapter 2.5** identifies layer 2/3 PYRs as the early substrate of prefrontal dysfunctions in the dual-hit GE mouse model of mental disorders and resolves reported deficits with pharmacological inhibition of inflammatory microglia response. **Chapter 2.6** follows the stream of evidence and proves the causal role of layer 2/3 PYR mediated early prefrontal activity in shaping adult cognitive and social abilities by incorporating a vast array of techniques including electrophysiological recordings in young non-anesthetized mice combined with behavioral assessments.

2. Included articles

2.1. Article I

The full article can be found at the end of this thesis. Please refer to the manuscript for additional information and detailed description of the methods and results.

2.1.1. Tapered Fibers Combined With a Multi-Electrode Array for Optogenetics in Mouse Medial Prefrontal Cortex

Leonardo Sileo*, Sebastian H. Bitzenhofer*, Barbara Spagnolo*, **Jastyn A. Pöpplau***, Tobias Holzhammer, Marco Pisanello, Filippo Pisano, Elisa Bellistri, Emanuela Maglie, Massimo De Vittorio, Patrick Ruther, Ileana L. Hanganu-Opatz[+] and Ferruccio Pisanello[+]

*These authors have contributed equally to this work as first authors
[+]These authors have contributed equally to this work as last authors

Frontiers in Neuroscience 2018; DOI: https://doi.org/10.3389/fnins.2018.00771

2.1.2. Abstract – article I

Optogenetics offers many advantages in terms of cell-type specificity, allowing to investigate functional connectivity between different brain areas at high spatial and neural population selectivity. In order to obtain simultaneous optical control and electrical readout of neural activity, devices called "optrodes" are employed. They are typically composed of a linear array of microelectrodes integrated on a slender probe shafts combined with flat-cleaved optical fibers (FF) placed above the recording sites. However, due to tissue absorption and scattering, light delivered by the FF unevenly illuminates the region of interest. This issue is of particular relevance when cellular populations are disposed along the dorso-ventral axis, such as in medial prefrontal cortex (mPFC) where cortical layers are aligned vertically. The study presented here aims at using tapered optical fibers (TFs) in combination with a 16-electrode neural probe to better access neural populations distributed along the dorso-ventral axis in the mPFC of newborn mice, restricting light delivery over a specific portion of the cortical layer of interest. Half of the TF surface is coated with a reflecting metal blocking the light to enable light delivery from one side of the probe's shaft only, with the probe base being designed to host the fiber without interfering with the wire-bonds that connect the recording sites to a printed circuit board. Monte-Carlo simulations have been implemented to define the relative TF-probe position and to identify the light intensity distribution above the recording sites. *In vivo* recordings indicate that simultaneous optical stimulation and electrical readout of neural activity in the mPFC benefit from the use of the engineered TF-based optrode in terms of a more uniform light distribution along the dorso-ventral axis and the possibility of restricting light delivery to a subset of electrical recording sites of interest.

2.1.3. Personal contribution – article I

I, Jastyn A. Pöpplau, contributed with the following to article I:

- Software modifications and setup constructions for TF measurements.
- *In utero* electroporation (IUE) at embryonic age (E) 15.5 to express ChR2 in layer 2/3 PYRs.
- Electrophysiological, extracellular *in vivo* recordings in medial PFC of neonatal mice combined with optogenetic stimulations using FFs and TFs, respectively.
- Histological confirmation of electrode and optical fiber position.
- Analysis of electrophysiological recordings together with Sebastian H. Bitzenhofer.
- Design of *in vivo* figures in Adobe Illustrator together with Sebastian H. Bitzenhofer.
- Taking part in data interpretation.
- Assisting in writing the first draft.
- Reviewing and editing the manuscript.

Hamburg, ...

Date Jastyn A. Pöpplau Ileana L. Hanganu-Opatz

2.2. Article II

The full article can be found at the end of this thesis. Please refer to the manuscript for additional information and detailed description of the methods and results.

2.2.1. Neural Correlates of Anesthesia in Newborn Mice and Humans

Mattia Chini, Sabine Gretenkord, Johanna K. Kostka, **Jastyn A. Pöpplau**, Laura Cornelissen, Charles B. Berde, Ileana L. Hanganu-Opatz[+] and Sebastian H. Bitzenhofer[+]

[+]These authors have contributed equally to this work as last authors

Frontiers in Neural Circuits 2019; DOI: https://doi.org/10.3389/fncir.2019.00038

2.2.2. Abstract – article II

Monitoring the hypnotic component of anesthesia during surgeries is critical to prevent intraoperative awareness and reduce adverse side effects. For this purpose, electroencephalographic (EEG) methods complementing measures of autonomic functions and behavioral responses are in use in clinical practice. However, in human neonates and infants existing methods may be unreliable and the correlation between brain activity and anesthetic depth is still poorly understood. Here, we characterized the effects of different anesthetics on brain activity in neonatal mice and developed machine learning approaches to identify electrophysiological features predicting inspired or end-tidal anesthetic concentration as a proxy for anesthetic depth. We show that similar features from EEG recordings can be applied to predict anesthetic concentration in neonatal mice and humans. These results might support a novel strategy to monitor anesthetic depth in human newborns.

2.2.3. Personal contribution – article II

I, Jastyn A. Pöpplau, contributed with the following to article II:

- Head-post implantation and accustoming implanted mice to run under head-fixed conditions on a spinning-disc.

- Electrophysiological, extracellular *in vivo* recordings in medial PFC of non-anesthetized juvenile mice and subsequent urethane anesthesia induction.

- Formal analysis of electrophysiological recordings of juvenile mice.

- Reviewing and editing the manuscript.

Hamburg, ...

Date Jastyn A. Pöpplau Ileana L. Hanganu-Opatz

2.3. Article III

The full article can be found at the end of this thesis. Please refer to the manuscript for additional information and detailed description of the methods and results.

2.3.1. Anesthetics fragment hippocampal network activity, alter spine dynamics, and affect memory consolidation

Wei Yang*, Mattia Chini*, **Jastyn A. Pöpplau**, Andrey Formozov, Alexander Dieter, Patrick Piechocinski, Cynthia Rais, Fabio Morellini, Olaf Sporns, Ileana L. Hanganu-Opatz and J. Simon Wiegert

*These authors have contributed equally to this work as first authors

PLOS Biology 2021; DOI: https://doi.org/10.1371/journal.pbio.3001146

2.3.2. Abstract – article III

General anesthesia is characterized by reversible loss of consciousness accompanied by transient amnesia. Yet, long-term memory impairment is an undesirable side effect. How different types of general anesthetics (GAs) affect the hippocampus, a brain region central to memory formation and consolidation, is poorly understood. Using extracellular recordings, chronic 2-photon imaging, and behavioral analysis, we monitor the effects of isoflurane (Iso), medetomidine/midazolam/fentanyl (MMF), and ketamine/xylazine (Keta/Xyl) on network activity and structural spine dynamics in the hippocampal CA1 area of adult mice. GAs robustly reduced spiking activity, decorrelated cellular ensembles, albeit with distinct activity signatures, and altered spine dynamics. CA1 network activity under all 3 anesthetics was different to natural sleep. Iso anesthesia most closely resembled unperturbed activity during wakefulness and sleep, and network alterations recovered more readily than with Keta/Xyl and MMF. Correspondingly, memory consolidation was impaired after exposure to Keta/Xyl and MMF, but not Iso. Thus, different anesthetics distinctly alter hippocampal network dynamics, synaptic connectivity, and memory consolidation, with implications for GA strategy appraisal in animal research and clinical settings.

2.3.3. Personal contribution – article III

I, Jastyn A. Pöpplau, contributed with the following to article III:

- Head-post implantation and accustoming implanted mice to move under head-fixed conditions in a mobile home cage.

- Electrophysiological, extracellular *in vivo* recordings in HP of non-anesthetized adult mice and subsequent medetomidine/midazolam/fentanyl (MMF), ketamine/xylazine (Keta/Xyl), or isoflurane anesthesia induction.

- Electrophysiological, extracellular *in vivo* recordings in HP of adult mice during wakefulness and natural sleep combined with neck muscle electromyography and pupil measurements.

- Histological confirmation of electrode position and image acquisition.

- Single-unit clustering using Klusta.

- Analysis of electrophysiological recordings. 1/f slope analysis and sleep scorings were performed by Mattia Chini.

- Conceptualization of electrophysiological experiments including software development and hardware construction.

- Taking part in data interpretation and design of figures in Adobe Illustrator.

- Assisting in writing the first draft.

- Reviewing and editing the manuscript.

Hamburg, ...

Date Jastyn A. Pöpplau Ileana L. Hanganu-Opatz

2.4. Article IV

The full article can be found at the end of this thesis. Please refer to the manuscript for additional information and detailed description of the methods and results.

2.4.1. Gamma activity accelerates during prefrontal development

Sebastian H. Bitzenhofer, **Jastyn A. Pöpplau** and Ileana L. Hanganu-Opatz

eLife 2020; DOI: https://doi.org/10.7554/eLife.56795

2.4.2. Abstract – article IV

Gamma oscillations are a prominent activity pattern in the cerebral cortex. While gamma rhythms have been extensively studied in the adult prefrontal cortex in the context of cognitive (dys)functions, little is known about their development. We addressed this issue by using extracellular recordings and optogenetic stimulations in mice across postnatal development. We show that fast rhythmic activity in the prefrontal cortex becomes prominent during the second postnatal week. While initially at about 15 Hz, fast oscillatory activity progressively accelerates with age and stabilizes within gamma frequency range (30–80 Hz) during the fourth postnatal week. Activation of layer 2/3 pyramidal neurons drives fast oscillations throughout development, yet the acceleration of their frequency follows similar temporal dynamics as the maturation of fast-spiking interneurons. These findings uncover the development of prefrontal gamma activity and provide a framework to examine the origin of abnormal gamma activity in neurodevelopmental disorders.

2.4.3. Personal contribution – article IV

I, Jastyn A. Pöpplau, contributed with the following to article IV:

- IUE at E15.5 to express ChR2 in layer 2/3 PYRs together with Sebastian H. Bitzenhofer.
- Head-post implantation and accustoming implanted mice to run under head-fixed conditions on a spinning-disc.
- Electrophysiological, extracellular *in vivo* recordings in medial PFC of non-anesthetized juvenile mice combined with optogenetic stimulations.
- Electrophysiological, extracellular *in vivo* recordings in PFC of urethane-anesthetized neonatal and juvenile mice combined with optogenetic stimulations together with Sebastian H. Bitzenhofer.
- Histological confirmation of electrode position, immunohistochemical staining, image acquisition, and cell quantification together with Annette Marquardt.
- Formal analysis of electrophysiological recordings.
- Design of figures in Adobe Illustrator together with Sebastian H. Bitzenhofer.
- Assisting in project conceptualization and writing the first draft.
- Reviewing and editing the manuscript.

Hamburg, ...

Date Jastyn A. Pöpplau Ileana L. Hanganu-Opatz

2.5. Article V

The full article can be found at the end of this thesis. Please refer to the manuscript for additional information and detailed description of the methods and results.

2.5.1. Resolving and Rescuing Developmental Miswiring in a Mouse Model of Cognitive Impairment

Mattia Chini, **Jastyn A. Pöpplau**, Christoph Lindemann, Laura Carol-Perdiguer, Marilena Hnida, Victoria Oberländer, Xiaxia Xu, Joachim Ahlbeck, Sebastian H. Bitzenhofer, Christoph Mulert and Ileana L. Hanganu-Opatz

Neuron 2020; DOI: https://doi.org/10.1016/j.neuron.2019.09.042

2.5.2. Abstract – article V

Cognitive deficits, core features of mental illness, largely result from dysfunction of prefrontal networks. This dysfunction emerges during early development, before a detectable behavioral readout, yet the cellular elements controlling the abnormal maturation are still unknown. Here, we address this open question by combining *in vivo* electrophysiology, optogenetics, neuroanatomy, and behavioral assays during development in mice mimicking the dual genetic-environmental etiology of psychiatric disorders. We report that pyramidal neurons in superficial layers of the prefrontal cortex are key elements causing disorganized oscillatory entrainment of local circuits in beta-gamma frequencies. Their abnormal firing rate and timing relate to sparser dendritic arborization and lower spine density. Administration of minocycline during the first postnatal week, potentially acting via microglial cells, rescues the neuronal deficits and restores pre-juvenile cognitive abilities. Elucidation of the cellular substrate of developmental miswiring causing later cognitive deficits opens new perspectives for identification of neurobiological targets amenable to therapies.

2.5.3. Personal contribution – article V

I, Jastyn A. Pöpplau, contributed with the following to article V:

- Histological brain slice preparation and immunohistochemistry.
- Confocal image acquisition.
- Morphological image analysis. Namely, Sholl analysis, spine quantification, cell density quantification, and assessment of microglia morphology. Assessment of microglia morphology was performed together with Mattia Chini and Marilena Hnida.
- Formal analysis of morphological investigations.
- Design of figures in Adobe Illustrator together with Mattia Chini.
- Taking part in data interpretation.
- Reviewing and editing the manuscript.

Hamburg, ...

Date Jastyn A. Pöpplau Ileana L. Hanganu-Opatz

2.6. Article VI

The full article can be found at the end of this thesis. Please refer to the manuscript for additional information and detailed description of the methods and results.

2.6.1. A transient developmental increase in prefrontal activity alters network maturation and causes cognitive dysfunction in adult mice

Sebastian H. Bitzenhofer*, **Jastyn A. Pöpplau***, Mattia Chini, Annette Marquardt and Ileana L. Hanganu-Opatz

*These authors have contributed equally to this work as first authors

Neuron 2021; DOI: https://doi.org/10.1016/j.neuron.2021.02.011

2.6.2. Abstract – article VI

Disturbed neuronal activity in neuropsychiatric pathologies emerges during development and might cause multifold neuronal dysfunction by interfering with apoptosis, dendritic growth, and synapse formation. However, how altered electrical activity early in life affects neuronal function and behavior in adults is unknown. Here, we address this question by transiently increasing the coordinated activity of layer 2/3 pyramidal neurons in the medial prefrontal cortex of neonatal mice and monitoring long-term functional and behavioral consequences. We show that increased activity during early development causes premature maturation of pyramidal neurons and affects interneuronal density. Consequently, altered inhibitory feedback by fast-spiking interneurons and excitation/inhibition imbalance in prefrontal circuits of young adults result in weaker evoked synchronization of gamma frequency. These structural and functional changes ultimately lead to poorer mnemonic and social abilities. Thus, prefrontal activity during early development actively controls the cognitive performance of adults and might be critical for cognitive symptoms in neuropsychiatric diseases.

2.6.3. Personal contribution – article VI

I, Jastyn A. Pöpplau, contributed with the following to article VI:

- IUE at E15.5 to express ChR2 in layer 2/3 PYRs in mice used for non-anesthetized *in vivo* recordings as well as for *in vitro* recordings and young adult behavioral assessments.

- Viral injections in medial PFC of mice used for *in vitro* recordings or photo-tagging experiments.

- *In vivo* light dose titration tests at neonatal and pre-juvenile age for transcranial stimulations.

- Chronic stimulation of neonatal and pre-juvenile mice used for non-anesthetized *in vivo* recordings as well as for *in vitro* recordings and young adult behavioral assessments.

- Behavioral assessments of chronically stimulated mice at young adult age. Behavioral assessments of pre-juvenile mice were conducted together with Sebastian H. Bitzenhofer.

- Software development and hardware construction for non-anesthetized *in vivo* recordings.

- Electrophysiological, extracellular *in vivo* recordings in medial PFC and HP of non-anesthetized young adult mice combined with optogenetic stimulations or behavioral assessments.

- Histological confirmation of electrode position, immunohistochemical staining, image acquisition, and cell quantification together with Annette Marquardt.

- Confocal image acquisition, Sholl analysis and spine density quantification of layer 2/3 PYRs.

- Analysis of electrophysiological recordings of non-anesthetized mice, single-unit clustering using Klusta, and statistical analysis.

- Design of figures in Adobe Illustrator together with Sebastian H. Bitzenhofer.

- Taking part in project conceptualization and data interpretation.

- Writing the first draft together with Sebastian H. Bitzenhofer, reviewing and editing the manuscript.

Hamburg, ...

Date Jastyn A. Pöpplau Ileana L. Hanganu-Opatz

3. Discussion

3.1. Methodological implications

3.1.1. Combination of extracellular recordings with optogenetic manipulation

Electrophysiological, extracellular recordings and optogenetic manipulations and, in particular, their combination are two key techniques used in this thesis. The development of optogenetics advanced the field of neuroscience significantly in causally probing circuit connectivity and function (Lee et al., 2020). Previously used techniques, including electrical stimulation and pharmacological manipulation, lacked the high temporal, spatial, and cell-type-specific resolution of optogenetics, hampering a precise dissection of neuronal circuits (Deisseroth, 2011; Yizhar et al., 2011). The rapidly growing toolbox of optogenetics includes diverse tools for activation or silencing of neuronal activity (Bernstein and Boyden, 2011) and more recently an improved bidirectional tool for combinatory manipulations within the same population of interest (BiPOLES: Bidirectional pair of opsins for light-induced excitation and silencing) (Vierock et al., 2021). Besides the great advantages of optogenetic manipulations, their use offers many pitfalls. This might lead to misinterpretation of results, especially when aiming for optogenetically mediated silencing or compartment-specific manipulations (Li et al., 2019; Moore et al., 2018; Wiegert and Oertner, 2016; Yizhar et al., 2011). Confirming such risks, recently a study reported opposite outcomes when probing behavior upon manipulation of the same neuronal population with two different ChR2 variants (Baleisyte et al., 2021). Thus, the optogenetic tool of choice has to be selected carefully, according to the intended circuit manipulation and by considering the tool's characteristics, such as kinetics and light requirements, as well as the targeting strategy used for opsin expression (Yizhar et al., 2011).

Here, we probed the acute effects of optogenetic manipulations with simultaneous measurements of extracellular, and in a few cases intracellular, electrophysiological activity. IUE at E15.5 was primarily used to achieve cell-type specificity and enables targeting of 20 to 30 % of layer 2/3 PYRs in medial PFC, according to previously established protocols (Bitzenhofer et al., 2017a; Bitzenhofer et al., 2017b). We observed stable expression densities until P40, the maximum age of our investigations. Thus, confirming IUE as a suitable method to study the same neuronal population throughout development (Bitzenhofer et al., 2021). The opsin of choice for *in vivo* experiments, a double mutant form (E123T/T159C) of ChR2 (Berndt et al., 2011), was selected to achieve similar network effects upon stimulation of layer 2/3 PYRs at neonatal age as previously reported. Accordingly, ChR2 was expressed under the control of the ubiquitous cytomegalovirus enhancer fused to chicken beta-actin promoter, leading to expression in the whole cell (Bitzenhofer et al., 2017a; Bitzenhofer et al., 2017b). In consequence, illumination of layer 2/3 PYRs reaches not only the soma but also light-sensitive dendritic compartments and intermingled axons. Therefore, action potential generation might be differentially influenced by triggering additional dendritic or axonal processes. (Messier et al., 2018; Shemesh et al., 2017; Spruston, 2008). Hence, it remains to be investigated if the chosen methodological strategy contributed to our observations and if alternative targeting strategies restricted to somatic compartments would yield identical outcomes.

The applied stimulation intensities for extracellular optogenetic *in vivo* recordings were similarly adjusted as in Bitzenhofer et al., 2017b to trigger spiking in response to more than 25 % of 3 ms long light pulses at 16 Hz. This resulted in equivalent used light power, shown to induce minimal heating effects (Bitzenhofer et al., 2017b). In the case of transcranial stimulations, in order to generate early stimulated (ES) mice, light-dose (power and duration) titration experiments with an extracranially placed stimulation fiber and an inserted recording electrode were performed to determine sufficient light intensities for chronic stimulations. The chosen 30 mW laser output power was confirmed to correspond to 10 mW applied for intracranial stimulations with optoelectrodes by light attenuation measurements of tissue adhesive and skull (Bitzenhofer et al., 2021).

To control for photoelectrical artifacts, evoked mainly in consequence of abrupt changes in light intensity that are potentially caused by photons hitting the recording sites (Mikulovic et al., 2016), we employed in most cases within animal control light stimulations. Yellow light (594 nm) control stimulation with equal light intensities induced similar photoelectrical effects as blue light stimulation (473 nm) in PBS but induced no spiking activity in ChR2-expressing mice. However, both wavelengths induced light on and off artifacts in LFP traces filtered for 1 to 100 Hz (Sileo et al., 2018). Therefore, we restricted our LFP analysis mainly to the two centered seconds of 3 s long ramp stimulations. This strategy revealed no significant changes in LFP activity during control light stimulation but clear effects upon blue light stimulations (Bitzenhofer et al., 2021; Bitzenhofer et al., 2020). To identify triggered action potentials of neurons nearby the recording site, multi-unit activity (MUA), defined as fast activity in the frequency range of 500 to 9000 Hz, can be analyzed (Sileo et al., 2018). Yet, light-induced fast signal deflections can interfere with action potential detection (Mikulovic et al., 2016). MUA can be sorted into single-unit activity (SUA) by using clustering algorithms mainly based on the extracellular waveform shape of an action potential in the signal (Rossant et al., 2016). Despite some drawbacks of SUA clustering, such as a bias towards high firing units (Sakata and Harris, 2009), it enables a distinction of action potentials, also named spikes, and background noise and attributes single spike clusters to one neuron (Rossant et al., 2016). Our SUA analysis confirmed the absence of triggered spikes upon control light stimulation but clear spiking in response to blue light (Bitzenhofer et al., 2021; Bitzenhofer et al., 2020). Taken together, yellow light control stimulations can be used to distinguish light artifacts from induced activity during optogenetic experiments using ChR2 and can help to identify suitable light intensities for stimulations as well as analytical strategies. This within animal control for light stimulation side-effects might be an alternative to transfecting additional mice with an opsin-free construct for control. A strategy that was also used in an article presented in this thesis, which led to comparable results (Chini et al., 2020).

In one experiment presented in this thesis, BiPOLES was used to probe the consequences of activating or silencing PV interneurons in ES and control mice by using *in vitro* whole-cell patch-clamp recordings of non-transfected PYRs surrounded by ChR2-expressing PYRs in layer 2/3 of medial PFC. Blue light stimulation simultaneously activated layer 2/3 PYRs and silenced PV interneurons. Controversially, in control mice the ratio of EPSCs to IPSCs in non-transfected layer 2/3 PYRs showed a shift towards inhibition in comparison to equivalent experiments without silencing PV interneurons (Bitzenhofer et al., 2021). A similar striking effect of optogenetic silencing of PV interneurons has been observed previously and attributed to a paradoxical increase

of interneuron firing. This increase is potentially mediated by an excitation-induced overweight of optogenetically induced silencing, which consequently leads to rebound excitation of PV interneurons. However, in this study silencing of PV interneurons increased both EPSCs and IPSCs in PYRs, leaving the ratio nearly unaffected (Moore et al., 2018). Our settings differ in several lines from the ones of these observations, such as the used opsin for silencing, brain area and consequently underlying connectivity, and, in particular, the simultaneous activation of a subset of layer 2/3 PYRs. Therefore, the underlying mechanisms of the shift towards increased inhibition are not univocally clear. Paradoxical effects of optogenetic stimulation might account for our observation but also other disinhibitory circuit effects might play a role (see chapter 3.2). Nonetheless, this incidental side observation underpins the tight interactions of circuit elements and encourages cautious data interpretation when using optogenetics.

To obtain a simultaneous *in vivo* read-out of electrical activity and spatially related optical control, optoelectrodes are commonly utilized. These tools need to meet several requirements, extending from minimization of photoelectrical artifacts and invasiveness to uniform illumination of the region of interest. The selection of a tool of choice is therefore not trivial and depends on the experimental settings (Pisanello et al., 2016). Here, we validated the suitability of a novel optoelectrode with an optical TF for acute *in vivo* recordings in comparison to classically used optoelectrodes with optical FFs. FF devices consist of a microelectrode united with an optical fiber ending above the most superficial recording site. Consequently, this design results in an inhomogeneous light power distribution. Highest power values are achieved for the most top recording sites and decrease towards lower sites, spanning several orders of magnitude. The design employed here, on the other hand, comprises a microelectrode in parallel to a TF, the latter with decreasing diameter towards the tip. The TF emits light directed towards the microelectrode, resulting in a more uniform light power distribution across the recording sites. *In vivo* recordings of ChR2-expressing layer 2/3 PYRs in neonatal mice confirmed a more homogenous neuronal activation profile, reduced photoelectrical artifacts, and minimized tissue damage of TFs with respect to FFs (Sileo et al., 2018). Even so, we refrained from the use of TFs in subsequent experiments. The reasoning for this was the technical challenge to place optical fiber and electrode shank consistently in parallel, indispensable for a reliable comparison between experiments and groups. However, this study confirmed the in vivo suitability of TFs and most likely encouraged the subsequent development of combined implants using the TF technology (Pisano et al., 2019). A valuable tool, especially to reach deep brain structures with minimal invasiveness.

3.1.2. Anesthetic effects in the immature and adult brain

General anesthesia is an induced state for surgical purposes, mediated by injected or inhaled drugs acting on the central nervous system. These anesthetic agents induce changes in the behavioral state including temporal loss of consciousness, accompanied by immobility, analgesia, and amnesia. Ideally, such changes should be restricted to the surgical procedure and reversible without lasting side-effects (Franks, 2008; Rudolph and Antkowiak, 2004).

Here, we dissected the induced consequences of three commonly applied anesthetics, isoflurane, MMF, and Keta/Xyl, for hippocampal functioning in adult mice (Yang et al., 2021). The HP is central to the effects of anesthesia, given the prominent action of general anesthesia on

the memory system (Zurek et al., 2014). All three general anesthetics induced specific network activity signatures and were distinct from natural sleep. A shared feature of all anesthetics was their reduction of neuronal firing rates and a proportional dominance of LFP power below 5 Hz, leading to a shift in E/I balance towards inhibition. However, the temporal profile, recovery rate, and effect strength differed markedly and thus, also affected their lasting actions. The anesthetic agents which impacted the network activity most, had also the most severe effects on spine dynamics and memory formation. Overall, besides inducing a similar physiological state by mediating unconsciousness, the investigated agents differed strongly in their acute and long-term consequences. Further, the actions on HP might be distinct from other brain regions. All three anesthetics fragmented and decorrelated hippocampal activity, present among different readouts and levels of analysis (Yang et al., 2021). This is different from what has been reported in cortical regions, where correlations between neuronal ensembles during spontaneous activity were found to be increased under anesthesia (Goltstein et al., 2015). Thus, these opposing findings suggest brain region-specific actions of anesthetic agents in the adult brain. Besides a potential relevance for medical purposes, this detailed dissection of commonly used anesthetics might help to guide the choice of the anesthetic agent and augments the awareness of potential interferences with achieved results in basic neuroscience.

In rodent research, general anesthesia is used during surgeries but also to reduce the stress level for the animal and to minimize motion artifacts during head-fixed measurements. In addition to the already mentioned anesthetic agents, isoflurane, MMF, Keta/Xyl, urethane is commonly used during non-survival experiments. An advantage of urethane is that it induces a behavioral unconsciousness that closely mimics natural sleep patterns in electrophysiological recordings and induces sleep-like breathing rhythms (Clement et al., 2008; Pagliardini et al., 2013). Furthermore, urethane has only moderate effects on excitatory or inhibitory synaptic signal transmission by acting not predominantly on a specific channel as a target. It exerts its actions mainly through the potentiation of resting potassium conductance, leading to a retained hyperpolarized state in neurons (Hara and Harris, 2002; Sceniak and Maciver, 2006). In contrast, most other general anesthetics, with exception of ketamine, increase inhibitory currents, due to an agonistic action on $GABA_A$ receptors (Franks, 2008; Rudolph and Antkowiak, 2004). Along with $GABA_A$ receptors as a common target the list for additional actions of certain anesthetics is long. For example, isoflurane is suggested to additionally exert an antagonistic action on α-amino-3-hydroxy-5-methyl-4-isoxazolepropionic acid (AMPA) receptors and a slight inhibitory effect on N-methyl-D-aspartate receptors (Rudolph and Antkowiak, 2004). Moreover, isoflurane inhibits presynaptic glutamate transmitter release (Wu et al., 2004). The different and diverse molecular targets of general anesthetics affect brain function in many ways. Besides their inhibitory action on excitatory arousal pathways, their disruption of thalamic activity is thought to be the major source of slow oscillations and loss of consciousness under anesthesia but also during natural sleep. During waking corticothalamic neurons prevent the thalamus to enter a synchronized oscillatory state via tonic excitation. Anesthesia acts directly on cortical and subcortical neurons, probably interfering with the feedback loop between cortex and thalamus (Bhattacharya et al., 2021; Franks, 2008; Rudolph and Antkowiak, 2004). The unique oscillatory profiles, inter- and long-range connectivity, and cellular composition of distinct brain regions most likely contribute to the region and agent-specific actions of anesthesia in the adult brain (Mashour and Avidan, 2017; Paasonen et al., 2018; Yang et al., 2021).

Most of the effective agents used in the adult brain lead to an inadequate anesthetic depth and high mortality rate in young animals (Danneman and Mandrell, 1997). Inhaled anesthetics, such as isoflurane and urethane for non-survival experiments, have been mainly used for investigations of the developing brain in rodents with tolerable side-effects (Chini et al., 2019; Danneman and Mandrell, 1997; Shumkova et al., 2021). The presence of the high similarity of discontinuous patterns of activity across different brain regions at early postnatal ages (Ben-Ari, 2001; Brockmann et al., 2011; Chini et al., 2021; Hanganu et al., 2006; Khazipov et al., 2004; Rochefort et al., 2009), suggests a differential action of anesthesia in the immature brain. Here, we addressed the influence of anesthesia on early brain activity in mice and human infants. This not only leads to a translational value of this study but also identifies considerable aspects of methodological issues for explorations of brain activity throughout development. As for human infants, the anesthesia-modulated activity of neonatal mice has a number of unique properties, distinct from activity in the adult brain with respect to anesthesia. Electrophysiological recordings of several brain regions, HP, PFC, lateral entorhinal cortex, and olfactory bulb, in mice aged from P8 to 10 revealed that urethane anesthesia augments the proportion of silent periods, leading to an overall dampening of LFP power and decrease of spiking activity. Nonetheless, active periods were only marginally affected. In all recorded areas, firing rates as well as spectral properties of LFP power were almost identical during active periods compared to pre-anesthesia periods. The reduction in overall activity did not convey a perturbation of E/I balance, signal complexity, and functional long-range synchrony between areas. Despite different molecular targets than urethane, isoflurane had an analogical effect on brain activity with a dose-dependent enhancement of silent periods. Just like in neonatal mice, EEG recordings of human infants of 0 to 2 months of age showed an anesthesia-mediated dampening of activity without imposing a specific frequency range. This is in stark contrast to recordings performed in juvenile mice, where anesthesia increased the power of slow oscillations below 4 Hz but decreased the power of faster ones, resembling the emergence of alpha oscillations during anesthesia in human babies older than 4 months (Chini et al., 2019). This is in line with previous reports, identifying a non-frequency specific suppression of spontaneous activity by P7 but clear induced high-amplitude low-frequency oscillations by P14 in the somatosensory cortex under isoflurane anesthesia (Chang et al., 2016). Taken together, in the early postnatal brain anesthesia seems to exert a different action compared to the more mature brain by maintaining the frequency structure of neuronal oscillations regardless of the recorded brain region or used anesthetic agent.

Frequency-specific effects of anesthesia seem to emerge around P12, co-occurring with the switch from discontinuous to continuous activity and unfolding of an active sleep-wake cycle (Ackman et al., 2014; Cirelli and Tononi, 2015; Shen and Colonnese, 2016). Until P14, active and quiet sleep is the most prominent state of rodents with frequent switches between states and only short bouts of wakefulness. States become more persistent by P10 and reach adult-like cycling by P14 (Cirelli and Tononi, 2015; Rensing et al., 2018). This high sleep pressure might correlate to recent findings, identifying increased intracellular chloride concentrations in cortical interneurons as being responsible for the promotion of tiredness (Alfonsa et al., 2021). Chloride concentrations in immature neurons are increased compared to mature ones, due to functionally low expressed levels of KCC2. Functional upregulation of KCC2 and mediated chloride extrusion rises steeply until the end of the second postnatal week (Virtanen et al., 2021). By following a similar timeline, the lowering of intracellular chloride concentration might therefore contribute to the reduction in

sleep pressure. However, many other developmental milestones bundle at the border of the end of the second postnatal week.

By P10, massive growth aspects of the brain are completed (Cirelli and Tononi, 2015) and are followed by a narrow burst of neovascularization, leading to an improved oxygen supply of cellular elements (Coelho-Santos et al., 2021). The adult neuromodulatory system has a significant role in mediating the sleep-wake cycle by controlling the arousal system (Eban-Rothschild et al., 2018; Lee and Dan, 2012). Adult-like noradrenergic and cholinergic innervations of the neocortex are found to emerge during the beginning of the third postnatal week, in line with the onset of mature sleep-wake cycling (Janiesch et al., 2011; Latsari et al., 2002). The coincidence of the emergence of slow oscillations during sleep and under anesthesia by P12 has been suggested to rely on increased short- and long-range connectivity and, in particular, on a more mature recurrent corticothalamic network (Ackman et al., 2014; Sitdikova et al., 2014). In line with this, mature arborizations of direct projections from cortex to thalamus have been found to emerge at the end of the second postnatal week (Frassoni et al., 1995). However, the thalamus already has an impact on the generation of cortical activity at early postnatal ages. Apart from events triggered by the sensory periphery, early bursts of spontaneous cortical activity are proposed to be mainly generated in the corticothalamic circuit. With age, this is complemented by an increased intracortical generation of activity, especially within faster frequency ranges (Minlebaev et al., 2011). Related to this, isoflurane suppresses mainly spontaneous activity but only marginally triggered events at P7 but suppresses both at P14 (Chang et al., 2016). Hence the assumption, that anesthesia has a particular effect on the immature corticothalamic loop, which contributes accompanied with low intercortical connectivity to the unique effects of anesthesia at early postnatal ages. Furthermore, a key role for the structural guidance and establishment of functional connectivity between the thalamus and cortex is played by the SP (Grant et al., 2012). The SP presents an early link between ingrowing thalamic fibers and the developing cortex. After establishment, connectivity is rearranged and SP neurons undergo apoptotic death until most of them are eliminated by P14 (Hoerder-Suabedissen and Molnar, 2015; Luhmann et al., 2018). Collectively, the numerous developmental milestones achieved around the end of the second postnatal week most likely jointly contribute to the growing association of brain activity and behavioral state as well as to region- and agent-specific effects of anesthesia. These unequal impacts of anesthetics have to be considered when interpreting data gathered across progressing maturation. Therefore, developmental investigations should ideally be enriched with measurements in the non-anesthetized state.

3.1.3. Non-anesthetized head-fixed extracellular recordings in developing mice

Non-anesthetized electrophysiological recordings can be performed under head-fixed conditions. An acute surgery mainly under isoflurane anesthesia for the implantation of bars for the head fixation and application of local anesthesia at the cutting edges along the skin, is followed by a recovery period. Afterwards mice can be fixated in the recording setup for electrode insertion and subsequent measurements (Bitzenhofer et al., 2021; Bitzenhofer et al., 2020; Chini et al., 2019; Chini et al., 2020). This procedure is especially successful in young mice with limited behavioral abilities and sleep as the predominant state (Rensing et al., 2018). The comfort of the mouse pup can be enhanced by keeping it on a heating blanket with 37°C to maintain the body temperature

and additional cotton fibers surrounding the pup can be used to imitate a nest (Hanganu et al., 2006). This workflow works reliably during the first 12 days after birth (Bitzenhofer et al., 2021; Bitzenhofer et al., 2020; Chini et al., 2021). However, with increasing waking periods and body movement not only the signal quality impairs but also the well-being of the animal. Head fixation of non-anesthetized rodents with emerged behavioral abilities can even elevate the urge to move by letting them perceive this restricted condition as threatening (Schwarz et al., 2010). To reduce the stress and discomfort as well as noise-inducing movements, restrainers are commonly used. Restrainers are narrow plastic tubes or stable blankets, which enclose the body of the animal tied and immobilizing it. Even if claimed to be calming for the animal, such procedure requires long training periods that are often combined with food or water restriction (Guo et al., 2014; Li et al., 2018; Schwarz et al., 2010). These time-extended protocols might be suitable for adult animals but would exceed time windows of interest for developmental research. Moreover, food as well as water restriction leads to significant weight loss (Goltstein et al., 2018). This would interfere with the required increase in weight during normal development, leading to altered brain maturation and consequently to unphysiological results (Berardino et al., 2020; Oliverio et al., 1975). Two other possibilities of non-anesthetized measurements are either the combination of head fixation with a moveable ground or chronic implantation of recording devices. The latter enables measurements in freely-moving mice, able to express almost completely their natural behavioral repertoire. Unfortunately, even lightweight implants of new generations weigh around 2 to 3 g. By including the additional weight of head-stage and cement, essential for attachment and chronic stability, one ends up with at least 3.5 g (Freedman et al., 2016; Voigts et al., 2020). This would account for a substantial portion of the body weight by considering the youngest age of mice employed for non-anesthetized recordings in some of the studies presented here with around 7 to 8 g at P18 on the day of surgery (Bitzenhofer et al., 2021; Wei et al., 2017).

Consequently, the method of choice we implemented here was the head fixation on a moveable ground combined with acute insertion of extracellular recording electrodes. We adjusted common protocols for head-post implantation in several lines. The chosen adapters for head fixation were the lightest models, weighting around 1 g. Due to the fragile skull at young ages, we refrained from the frequent practice of etching the skull. To ensure adhesion of the cement, we instead drilled fine lines on the skull's surface to increase its roughness. The craniotomy, above the area of interest, was protected with a custom-made 3D-printed synthetic window, specifically designed to match the curvature of the skull and experimental needs during later electrode insertion (Bitzenhofer et al., 2021; Bitzenhofer et al., 2020; Chini et al., 2019). These and other technical improvements led to high stability of the implant. Further observations confirmed a permanent and steady position from P15 until the end of investigations at P60 without inducing adverse tissue reactions, weight loss, or affecting major growth parameters of the brain (Pöpplau and Hanganu-Opatz, unpublished data). This was particularly challenging since mice gain weight steeply and grow immensely in size. These parameters change not only during the first two weeks but also from the beginning of the third until the fourth week of life, with an increase of more than three times in weight and with two times in body, tail, and head length. Furthermore, during the same time, the craniofacial skeleton undergoes significant extension in anterior-posterior, transverse, and less pronounced in vertical growth directions (Vora et al., 2015; Wang et al., 2016; Wei et al., 2017). Hence, the established protocol enables chronic non-anesthetized measurements across development without an interference of typical growth.

The mice recovered well from surgical head-post implantation within a few hours. They adapted fast to head-fixed conditions, enabling the first electrophysiological recordings already five days after surgery. As movable ground a custom-made spinning-disc was utilized (Bitzenhofer et al., 2021; Bitzenhofer et al., 2020; Chini et al., 2019). The spinning-disc was designed to meet the needs of the young and light-weight mice. It consisted of light carbon fiber-based material supported by embedded radial ball-bearings to reduce the push resistance and consequently the force required to move the disc. The ball-bearings were covered with silicone to lower the noise levels, emerging during running periods. To reduce the stress level of the mouse, the fixation position was shielded with two-sided walls along the curved disc shape. Monitoring of the animal's position and speed was achieved by a rotary encoder at the central axis of the spinning-disc (Figure 1).

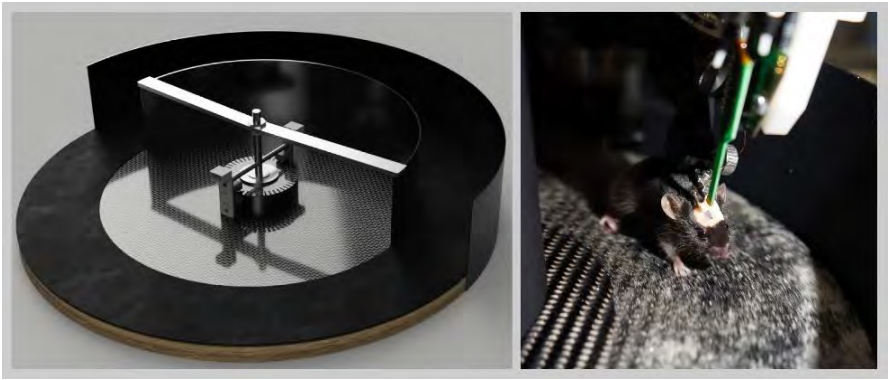

Figure 1. Establishment of chronic head-fixed recordings in developing mice using a custom-made spinning-disc setup. Left, schematic of spinning-disc setup design. Right, photograph of a P23 mouse during head-fixed recording on implemented spinning-disc setup.

An additional commercial setup, consisting of an air-floated platform to enable spatial movements, led to an equal amount of time need for training the mice and was used in some of the studies presented here (Bitzenhofer et al., 2021; Yang et al., 2021). Thus, both setups fulfilled the requirements for immature mice.

The methodological approach described above, permitted a comparison of electrophysiological activity measured in urethane anesthetized and non-anesthetized mice at different ages. In line with our previous observations in P8 to 10 mice (Chini et al., 2019), baseline activity, i.e. before using any stimulus, recorded at P11/12 showed under urethane anesthesia a reduced peak strength of fast frequencies above 12 Hz in comparison to recordings without anesthesia (Bitzenhofer et al., 2019). At older ages, the difference in peak strength between states increased, reaching two times higher values at pre-juvenile (P23-25) and three times higher values at young adult age (P38-40) in non-anesthetized mice compared to anesthetized ones. Notably, this increase in peak strength observed between pre-juvenile and young adult age in non-anesthetized mice was not present under anesthesia. However, the peak where the most prominent amplitude occurred settled in similar frequency ranges during baseline activity in anesthetized as well as in non-anesthetized mice. This changed during acute blue light ramp stimulation of layer 2/3 PYRs. Both states reached a similar increase in the effect magnitude but peak frequencies were significantly faster in non-anesthetized mice than in anesthetized ones, accumulating at 60 Hz or 50 Hz, respectively (Bitzenhofer et al., 2019). The dampening action of urethane anesthesia might account for these observations. Whereas urethane anesthesia has only minor effects on synaptic transmissions, it depresses the intrinsic excitability of neurons, leading to reduced firing rates (Hara and Harris, 2002; Sceniak and Maciver, 2006). Apart from these dissimilarities, the state of the mice did not affect the comparison between experimental groups. Independent cohorts of anesthetized

and non-anesthetized mice showed nearly identical group differences (Bitzenhofer et al., 2021). A considerable aspect of the non-anesthetized state is the non-perturbed perception of sensory inputs. This might lead to side-effects especially during optogenetic manipulations, caused by visual inputs through incomplete light shielding. Nonetheless, we observed no differences between states at pre-juvenile and young adult age during yellow light control stimulations (Bitzenhofer et al., 2019). Altogether, the enrichment of experiments with non-anesthetized recordings secured the reliability of our findings. Considering the markable differences in the non-anesthetized state between pre-juvenile and young adult prefrontal activity, and the lack of these under anesthesia, the former condition might be the more fruitful one for investigations of basic developmental changes of activity, at least in the medial PFC.

3.1.4. Translational considerations of rodent research

Translational unpredictable failures, i.e. low animal-to-human translational success rates, and the notion of an incomplete capturing of exquisitely human-associated factors, led to the questioning of the usefulness of rodent research (Kola and Landis, 2004; Leenaars et al., 2019; Wong and Josselyn, 2016). One specific reason for this debate might be the charge of the use of inadequate animal models, capturing not the full disease spectrum observed in humans with mental disorders. Indeed, many rodent studies focus on isolated variants despite the certainty that mono-genetic or -factorial forms of mental disorders are rather the exception than the norm (Feigenson et al., 2014; Parenti et al., 2020). However, homologues mutations in mice and humans have been found to induce similar prefrontal-dependent deficits (Bertero et al., 2018). Moreover, the controlled conditions of laboratory rodents offer unique possibilities. Risk factors can be investigated in isolation but also in combination as well as their timing during development by using so-called dual-hit models. This enables a dissected understanding of contributing factors (Hartung et al., 2016; Khan and Powell, 2018; Parenti et al., 2020). In Chini et al., 2020 we followed this developmental and multifactorial etiology by investigating the dual-hit GE mouse model and identified several abnormalities. These abnormalities are also individually linked to mono-hit factors. However, only in their combination they can capture the entire scope of deficits that result in behavioral disabilities (Chini et al., 2020; Hartung et al., 2016).

Another reason for questioning the translatability of rodent research might be the lack of inherently human behavioral repertoires. The key for this issue could potentially be not to model certain diseases as a whole, but to focus on specific behavioral endophenotypes. This could enable a direct link between origin and cause, which is not yet possible in humans (Keeler and Robbins, 2011; Schubert et al., 2015). This thesis focuses mainly on aspects of cognition and, in particular, on working and recognition memory, executive functions and social cognition. We studied the performance during learning and used the natural explorative tendency of mice, leading to faster learning rates and more willing participation than forced tasks paired with punishment (Keeler and Robbins, 2011; Rosenberg et al., 2021). A battery of behavioral tests was employed at diverse developmental stages (Bitzenhofer et al., 2021; Chini et al., 2020). Object recognition tasks are especially suitable for young mice since they have a spontaneous nature. These tasks require no learning or reward for motivation, the latter being not possible to achieve before mice are weaned from the mother. Object recognition can be tested shortly after full maturation of sensory and motor abilities as early as P16 (Le Roy et al., 2001). Recognition tasks require the functional

communication between PFC and HP but different task designs have weighted dependencies. On the one hand, recency recognition tasks are more PFC dependent, whereas, on the other hand, location recognition tasks are more HP dependent (Barker and Warburton, 2011; Keeler and Robbins, 2011). Such tasks are also used in human patients and find their counterparts in visually guided touch screen versions. Nonetheless, rodents might also use other senses during these tasks, limiting absolute translatability. Further, the degree of exploration is dependent on the salience of the object for the mouse (Keeler and Robbins, 2011; Wallace et al., 2015). The salience can be enhanced by testing social cognition by monitoring the interaction with another mouse, familiar or novel, over an object. This in turn has been shown to rely most prominently on the prefrontal-amygdala circuit in humans as well as in mice (Bicks et al., 2015; Gangopadhyay et al., 2021). In Bitzenhofer et al., 2021 the dissection of different behavioral paradigms underpinned our hypothesis that in ES mice deficits are mainly localized in the PFC, resulting in disturbed interactions of dependent pathways (Bitzenhofer et al., 2021).

In older mice, rewarded working and reference memory tasks extending over several trials and days can be used. As commonly implemented in rodents, we employed here an 8-arm radial maze test with four baited arms and a delayed non-match-to-sample task in a Y-maze (Bitzenhofer et al., 2021). In particular, the delayed non-match-to-sample task has almost analogues counterparts in task design in humans and increasing the delay has been shown to raise the error rate across mammalian species. This task involves specifically the dorsolateral PFC in humans and non-human primates (Wallace et al., 2015). In line with this, activity in the medial PFC of rodents has been shown to underlie working memory abilities (Le Merre et al., 2021). This further confirms that rodents can hold comparable functions in anatomically different structures. Overall, rodents can match human behavior in some remarkable and important aspects (Keeler and Robbins, 2011). However, in the end different disciplines most likely have to accept that the mouse behavioral repertoire is not like the one of humans. While the former presents a failure on cognitive level, the latter in the utility for molecular and cellular investigations of disease origin. This acceptance can foster the identification of convergences across interspecies findings, revealing common principles (Horvath and Mirnics, 2009).

3.2. Mechanisms of gamma acceleration during prefrontal development

Early activity within fast frequency ranges can be detected early in the medial PFC of rodents. Starting at the end of the first postnatal week in rats, bouts of beta/low-gamma frequency oscillations occur superimposed on slow theta-alpha bursts during transient active periods. These events are prominent prefrontal network activity patterns and have been termed nested gamma spindle bursts (Brockmann et al., 2011). Even when ranging within relatively fast frequencies, the features of these early forms of gamma oscillations markedly differ from their adult counterpart in several aspects, such as rhythmicity, frequency, duration, and occurrence. In the adult brain, gamma oscillations settle between 30-80 Hz and have been proposed to increase information processing. They are correlated to a number of operations ranging from perception to cognition (Bosman et al., 2014; Buzsaki and Wang, 2012; Cardin, 2016; Sohal, 2016). Consistent with this, compromised spectral and temporal structure as well as altered strength of gamma oscillations is suggested to underlie cognitive disabilities in rodents and humans (Bitzenhofer et al., 2021; Cho et al., 2015; Minzenberg et al., 2010; Uhlhaas and Singer, 2010; Yamamoto et al., 2018). Gamma oscillations

can be detected in almost any brain area with region-specific mechanisms, revealing insights into local motifs of circuit operations (Cardin, 2016; Womelsdorf et al., 2014). Nonetheless, their rhythmogenesis is commonly associated to precisely timed and coordinated interactions of excitatory and inhibitory neurons. In particular, inhibition of the perisomatic region of PYRs is essential for the generation of gamma oscillations (Buzsaki and Wang, 2012; Cardin, 2016). Already during the first postnatal week, the bouts of beta/low-gamma oscillations in the medial PFC rely on glutamatergic drive of PYRs onto interneurons (Bitzenhofer et al., 2015). Thus, despite their unique appearance, distinct from adult gamma oscillations, they seem to share common principles. If and how the early forms of gamma oscillations converge with adult patterns is unknown. This knowledge gap is of particular interest since we and others have demonstrated that abnormal patterns of fast activity in mouse models of mental disorders arise already during early development (Chini et al., 2020; Richter et al., 2019).

In Bitzenhofer et al., 2020, we elucidated the mechanisms of the development of prefrontal activity with a specific focus on fast frequency ranges by using extracellular recordings combined with optogenetic manipulation in the PL of the medial PFC of mice aged from P5 to 40. We found that in mice fast frequency activity above 12 Hz can be detected at the beginning of the second postnatal week. Distinct peaks in the power spectrum emerge at around P12 (Bitzenhofer et al., 2020), coinciding with the switch to continuous activity in medial PFC (Chini et al., 2021). These spectral peaks are initially at around 20 Hz and increase in amplitude and frequency until P25. Afterwards they stabilize within the classical gamma frequency range at 50 to 60 Hz (Bitzenhofer et al., 2020). Following the stream of previous investigations, identifying prefrontal layer 2/3 PYRs as contributors to early fast frequency activity (Bitzenhofer et al., 2017b), we similarly applied ramp light stimulation to ChR2-expressing layer 2/3 PYRs (Bitzenhofer et al., 2020). Ramp stimulation permitted the exploration of rhythms arising from intrinsic network generation throughout development without forcing a determined frequency (Adesnik and Scanziani, 2010; Bitzenhofer et al., 2017b). Layer 2/3 PYR-induced gamma oscillations followed similar dynamics in frequency and amplitude development, indicating a substantial contribution of layer 2/3 PYRs to the maturation of endogenous gamma oscillations. Until around P15, neurons mainly increased their firing in response to ramp stimulation. However, with progressing age the number of activated neurons was balanced with a similar number of inactivated ones (Bitzenhofer et al., 2020). This is consistent with previous findings, identifying a surrounding suppression of firing upon stimulation of layer 2/3 PYRs (Adesnik and Scanziani, 2010). A similar early lack of co-tuning of inhibition with increasing excitation until around P25 has been observed previously during sensory stimulation in the auditory cortex (Dorrn et al., 2010). Further, modeling work suggests that this developmental shift enables a more precise spike timing (Jia et al., 2021), essential for gamma rhythmogenesis. In line with these and our results, increasing inhibition has been found to modulate the frequency of gamma oscillations by balancing excitation (Atallah and Scanziani, 2009). Thus, a developmental shift towards increased inhibition most likely supports the observed acceleration in gamma frequency.

In order to establish a link and to reveal the contributions of interneurons to this developmental process, we attempted to distinguish these neuronal subpopulations according to their SUA waveform shape (Bitzenhofer et al., 2020). This approach is commonly used to categorize regular-spiking (RS) and FS neurons, the latter representing putative PV-expressing

interneurons (Mitchell et al., 2007; Niell and Stryker, 2008). Indeed, we confirmed through photo-tagging of ChR2 transfected PV-expressing interneurons that in our setting in mice older than P23 nearly 85 % of tagged units display a FS phenotype (Bitzenhofer et al., 2021). However, using a fixed threshold for fast-spiking criteria is less suitable during early development, due to the immature physiological abilities of PV interneurons. This consequently results in a high overlap of RS and FS waveform features (Bitzenhofer et al., 2020; Miyamae et al., 2017). To overcome this issue, we utilized a waveform-based dimensionality reduction and subsequent clustering approach, resulting in an unbiased detection of FS neurons over age. FS neurons can be detected at the end of the second postnatal week and increase in their proportion until around P25. The extracellular waveform properties, such as trough to peak latency and half-width, shorten with age for RS and most prominently for FS neurons, indicating a shift towards mature physiological abilities. Consistent with this, intracellular measurements of FS interneurons in medial PFC showed that the FS phenotype reaches a mature state not before P21 and shows the slowest progression in layer 2/3 of medial PFC (Miyamae et al., 2017). This is accompanied by a continuous increase of EPSCs and IPSCs in FS interneurons until around P25 and potentially reflects an increment of synaptic connectivity (Miyamae et al., 2017; Okaty et al., 2009). Layer 2/3 PYRs in medial PFC, on the other hand, show the most prominent maturation of dendritic complexity and intracellular properties until around P16 (Kroon et al., 2019). This potentially relates to the rather minor changes in waveform features we found for RS neurons, mainly contributing to PYRs (Bitzenhofer et al., 2020). Nonetheless, especially the frequency of IPSCs in PYRs augments until around P30, causing a shift towards inhibition (Kroon et al., 2019; Virtanen et al., 2018). In line with this, adult-like PV-mediated hyperpolarizing GABAergic inhibition of the axon initial segment of layer 2/3 PYRs in medial PFC emerges not before P30 (Rinetti-Vargas et al., 2017).

In agreement with the sustained maturation of the FS phenotype, we found that PV expression cannot be detected before P11 and is followed by a pronounced upregulation until around P25. On the contrary, SOM expression remains stable over the whole age range from P5 to 40. This developmental progression of PV expression appears to follow a protracted timeline in the medial PFC. In the barrel cortex, PV-expressing cells can be already detected by P10 with a minor not significant upregulation until P20 (Kalemaki et al., 2021). By considering that dendrite targeting SOM interneurons contribute to beta/low-gamma activity (20-40 Hz) (Chen et al., 2017; Hakim et al., 2018; Veit et al., 2017), whereas rhythmic FFI or FBI of the perisomatic region of PYRs by PV interneurons leads to synchronization within faster gamma frequencies (30-80 Hz) (Cardin et al., 2009; Chen et al., 2017), the identified acceleration of gamma frequency might relate to the transition of interneuronal dominance from SOM to PV interneurons (Figure 2). To continue on this line of thought, SOM interneurons might mediate the establishment of connectivity between PYRs and PV interneurons. SOM interneurons originate at an earlier timepoint than PV interneurons and show a premature embedding into cortical circuits with transient connections (Lim et al., 2018; Marques-Smith et al., 2016; Tuncdemir et al., 2016). During the first three postnatal weeks, the strength of cortical synapses between SOM interneurons and PYRs gradually decreases, whereas reciprocal innervations between PV interneurons and PYRs progressively augment (Anastasiades et al., 2016; Guan et al., 2017; Pan et al., 2019). Recent connectomic mapping of the barrel cortex underpinned such a switch of interneuronal synaptic preference. During the first postnatal week cortical GABAergic axons target mainly dendrites, followed by an increasing preference for perisomatic regions, reaching adult-like connectivity at

around P28 (Gour et al., 2021). The integration of PV interneurons into SOM-dominated circuits seems to depend on the functionality of SOM interneurons, since their silencing or early sensory deprivation prevents the emergence of perisomatic motifs and PV mediated FFI (Dard et al., 2021; Tuncdemir et al., 2016). An analogical increase in gamma frequency across development has been identified in the visual cortex and found to depend on visual experience (Chen et al., 2015). Besides the lack of direct sensory input, the onset and acceleration of gamma frequency in medial PFC might also initially depend on the early functional integration of SOM interneurons to mediate the embedding of PV interneurons. Subsequently, synaptic strengthening and development of the FS phenotype most likely contribute to the emergence of mature gamma oscillations. However, it is most likely that other interneurons than SOM and PV are also of early functional importance (Hanganu-Opatz et al., 2021). VIP interneurons for example, even when born at later embryonic ages (Miyoshi and Fishell, 2011), form synaptic contacts already during the first postnatal week (Vagnoni et al., 2020) and their developmental dysfunction is associated with behavioral disabilities at adult age (Batista-Brito et al., 2017).

In the adult cortex, the generation of beta/low-gamma versus faster gamma oscillations is suggested to rely either on direct reciprocal interactions of PV and SOM interneurons or on an indirect disinhibitory control by VIP interneurons (Chen et al., 2017). In the medial PFC, the former might contribute to the generation of 50 to 60 Hz gamma oscillations, regarding the substantial presence of anatomical projections from PV onto SOM interneurons (Ahrlund-Richter et al., 2019). A reciprocal interaction of PV and SOM interneurons might also be an explanation for the increase of IPSCs in neighboring PYRs (as mentioned in chapter 3.1.1.) upon silencing of PV interneurons while stimulating ChR2-expressing layer 2/3 PYRs (Bitzenhofer et al., 2021). Future *in vivo* recordings could verify this assumption by uncovering the generation of beta/slow-gamma oscillations upon such circuit manipulation rather than inducing prominent 50 to 60 Hz oscillations as elicited during pure layer 2/3 PYR stimulation. Moreover, applying this approach over age could prove the potential regime switch from SOM to PV interneurons by causing no consequences for layer 2/3 PYR-induced activity during silencing of PV interneurons at early postnatal ages (Figure 2).

Another contributing factor to the identified process might be the extent of intra- and translaminar connectivity during development. In layer 2/3 of the adult cortex, gamma generation depends on unperturbed intralaminar connectivity. Furthermore, layer 2/3 induced activiy modulates the activity of downstream layers, possibly inducing relevant feedback signals (Adesnik and Scanziani, 2010; Pluta et al., 2019). At the end of the second postnatal week, layer 2/3 PYRs are already functionally interconnected, whereas the opposite is true for layer 5/6. Early translaminar connections, even when anatomically established, are functionally silent by lacking AMPA receptors, which is revised by P16 (Anastasiades and Butt, 2012; Anastasiades et al., 2016). The low interconnectivity of layer 5/6 potentially contributes to the absence of layer 5/6-induced beta/low-gamma activity at early postnatal ages (Bitzenhofer et al., 2017b), since at adult age in the visual cortex gamma activity can be elicited from any layer (Adesnik, 2018). However, given the unique anatomical constellation and connectivity of the medial PFC, that is distinct from sensory areas (Anastasiades and Carter, 2021), the identified process might be uniquely served to layer 2/3 in the medial PFC. Further investigations would be required for a description of similarly occurring courses of development in different prefrontal layers. Lastly, not only layer specificity but also

uniformity of the by IUE targeted population of layer 2/3 PYRs might contribute to our findings, particularly as PYRs emerging from the same progenitor pool show unique transcriptionally defined intra- and translaminar connectivity (Ellender et al., 2019).

Overall, the close relationship of layer 2/3 PYR-induced and spontaneously occurring activity indicates that a substantial portion of the developmental dynamics of gamma oscillation is covered by the integration of this specific subpopulation into prefrontal circuits. Even when potentially not accounting for the full spectrum of mechanisms, the in-depth elucidation of the development of prefrontal gamma oscillations conducted here might lead to a better understanding of the timeline of disease-related dysfunctions.

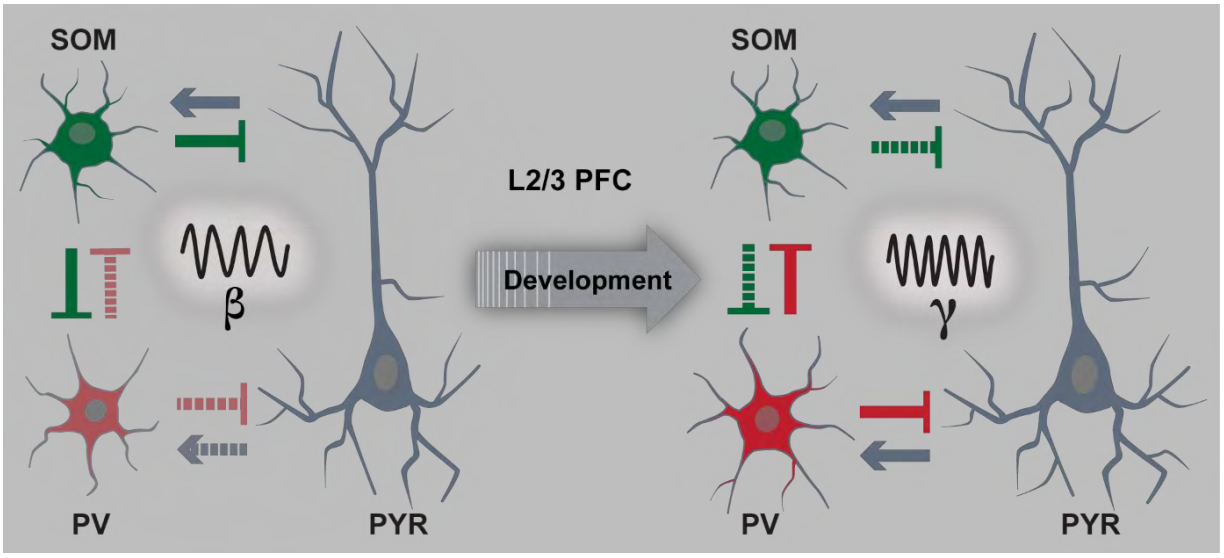

Figure 2. Progressive embedding of PV interneurons into prefrontal circuits relates to developmental frequency acceleration of layer 2/3 pyramidal neuron-induced gamma oscillations. Hypothetical model of early postnatal circuit motifs (left) and adult circuit motifs (right) resonating in beta and gamma frequency range, respectively. Abbreviations: L2/3, layer 2/3; PFC, prefrontal cortex; SOM, somatostatin; PV, parvalbumin; PYR, pyramidal neuron; β, beta; γ, gamma. Figure references (Anastasiades et al., 2016; Bitzenhofer et al., 2020; Chen et al., 2017; Chini et al., 2020; Gour et al., 2021; Guan et al., 2017; Kroon et al., 2019; Miyamae et al., 2017; Okaty et al., 2009; Pan et al., 2019).

3.3. Altered early prefrontal activity: Diverse origins cause shared symptomatology

The early emergence of coordinated activity in the medial PFC (Bitzenhofer et al., 2017b) and its convergence to adult gamma oscillations (Bitzenhofer et al., 2020), which are associated with cognitive functioning (Bosman et al., 2014), suggest a functional role of activity already at premature stages. Consequently, alterations of oscillatory prefrontal activity might already emerge early during the pathological development of mental diseases, prior to the onset of behavioral symptoms. Arguing for this, altered early activity has been identified in the PFC of mouse models of mental disorders (Chini et al., 2020; Hartung et al., 2016; Peixoto et al., 2016; Richter et al., 2019) and has been shown to be of prognostic value for later mental development in preterm infants (Iyer et al., 2015; Tokariev et al., 2019). Yet, the lack of an understanding of the causing substrates prevents the development of effective treatments for mental disorders, especially within the cognitive domain (Marin, 2016).

In Chini et al., 2020, we sought to address this knowledge gap by performing an in-depth dissection of layer and cell type specific prefrontal deficits in the dual-hit GE mouse model at the beginning of the second postnatal week. The results pointed in the direction of layer specific disturbances. Layer 2/3 PYRs in the PL of the medial PFC of GE mice displayed an oversimplified dendritic complexity, accompanied with a severely reduced spine density. On the contrary, structural parameters for PYRs in layer 5/6 were largely normal. These layer 2/3-specific morphological alterations were reflected in extracellular measurements of early prefrontal activity. Restricted to this layer, the power of oscillations as well as SUA was substantially reduced. Optogenetically layer 2/3 PYR-induced activity revealed an inability of this specific population to entrain prefrontal beta/low-gamma oscillations, due to their disorganized and mistimed firing in response to the stimulus (Chini et al., 2020). Following the evidence of a possible involvement of microglia cells in the ontogeny of mental disorders (Howes and McCutcheon, 2017; Neniskyte and Gross, 2017), we identified a hyper-mature microglia network. Overactivated microglia cells caused an over-pruning of glutamatergic synapses in the medial PFC of GE mice. Pharmacological inhibition of the inflammatory microglia cell response was sufficient to regularize the described structural and functional deficits as well as emerging cognitive disabilities during the third postnatal week (Chini et al., 2020). Whereas the GE model, in view of its genetic component, might reflect the pathology present in schizophrenia (Brandon and Sawa, 2011), other risk genes are also in focus of current research. Modifications of these genes are used to generate early models of mental disorders as well, relating to different classes of diseases, such as autism (Peixoto et al., 2016; Richter et al., 2019). In contrast to GE mice, these models have been found to display augmented levels of prefrontal activity at similar early ages. Still, at an older age, the initial alterations seem to converge to analogical behavioral deficits (Abazyan et al., 2010; Chini et al., 2020; Hartung et al., 2016; Peixoto et al., 2016; Richter et al., 2019; Wang et al., 2011). This highlights that altered early prefrontal activity, with a shift in either direction compared to normal development, is predictive for later emerging cognitive deficits.

Yet, it is controversial whether early activity simply mirrors such pathological maturation or actively contributes to it. As discussed above, activity-dependent formations take place during numerous courses of development, including neuronal differentiation, synapse formation, circuit wiring, pruning, and interneuronal survival (Blanquie et al., 2017; Lim et al., 2018; Mizuno et al., 2007; Yasuda et al., 2021). In particular, patterned coordinated forms of early activity are suggested to guide circuit assembling (Kirischuk et al., 2017; Kirkby et al., 2013). To bring the consequences of coordinated early activity for adult cognitive behavior on a causal chain, we developed in Bitzenhofer et al., 2021 an approach for mild manipulation of neonatal oscillations by transiently augmenting activity levels via non-invasive optogenetic transcranial stimulations (Bitzenhofer et al., 2021). We focused for stimulations on layer 2/3 PYRs, due to their ability to mediate coordinated activity, alike spontaneous activity, already during the second postnatal week (Bitzenhofer et al., 2017b; Bitzenhofer et al., 2020). During the time of manipulation from P7 to 11 the migration of cortical neurons has largely finished (Luhmann et al., 2016). Nontheless, the time window is of high relevance for the onset of oscillatory activity in the medial PFC (Bitzenhofer et al., 2020; Chini et al., 2021) and therefore essential for activity-dependent circuit formation (Mizuno et al., 2007; Whitford et al., 2002; Wong et al., 2018). On the behavioral level, transient early stimulations induced long-lasting impairments of prefrontal-dependent cognitive and social abilities. These disturbed behavioral abilities might result from permanent structural and functional changes. In

fact, the increased levels of early activity caused a stimulus outlasting augmentation of beta/low-gamma activity as well as a premature dendritic growth and spine density of layer 2/3 PYRs directly after the stimulation period (Bitzenhofer et al., 2021). These results underpin the close relationship of neuronal activity and structure as well as confirm that activity influences dendritic and synaptic formation. This most likely occurs via activity-dependent regulation of transcriptional gene expression programs and signaling pathways (Fiore et al., 2009; Vaillant et al., 2002; Whitford et al., 2002). On the other hand, at the timepoint when behavioral disabilities emerged, the morphology of layer 2/3 PYRs and spontaneous activity were found to be predominantly normal. This suggests that rather task or input-related activity might be compromised by accounting for disturbed prefrontal processing. Several lines of evidence confirmed this assumption. During social interactions as well as upon acute activation of the medial PFC, either direct by stimulation of layer 2/3 PYRs or indirect via stimulation of the intermediate HP, the power of prefrontal oscillations was substantially reduced, specifically within the gamma frequency range. This in turn was revealed to result from an inability to generate synchronized population activity, accompanied with a shift of E/I balance towards inhibition. Analysis of FS neurons suggested an abnormally high FBI as the cause of E/I imbalance. Confirming this, we identified an upregulation of PV expression in the medial PFC of ES mice and an elevated dendritic complexity of PV interneurons. Furthermore, silencing of PV interneurons was sufficient to restore prefrontal E/I balance (Bitzenhofer et al., 2021). Of note, a similar critical involvement of abnormal PV interneuron function in mediating E/I imbalance as well as altered PV expression levels in the PFC are thought to underlie the cognitive symptoms of mental disorders (Ferguson and Gao, 2018; Lewis et al., 2012). Aside from the missing link to a specific mental disease, due to the lack of an affected genetic risk component, the used approach might relate to preterm birth conditions. Indeed, preterm infants display increased EEG activity especially within frontal regions, which correlates with premature structural growth (Benders et al., 2015; Tokariev et al., 2019) and a subsequently increased risk to develop cognitive deficits (Larroque et al., 2008; Taylor and Clark, 2016).

Taken together the investigations of the GE and ES model jointly confirm that early activity and, in particular, its coordinated forms within beta/low-gamma frequencies, actively contribute to the (dys)functional maturation of prefrontal circuitry and related behaviors. Besides an opposite phenotype, i.e. reduced versus increased activity and structural parameters, early alterations converge to similar behavioral prefrontal-dependent disabilities at older ages (Figure 3) (Bitzenhofer et al., 2021; Chini et al., 2020; Hartung et al., 2016; Lowes and Harris, 2021). Recently the open-access datasets of Bitzenhofer et al., 2021 and Chini et al., 2020 were adopted for deepened analysis (Chini et al., 2021). This study illustrates that in the PFC a shift from early highly synchronized activity to more sparse and decorrelated activity takes place (Chini et al., 2021). These results are in line to what has been described for sensory areas and reflect a PV interneuron mediated transition to more local circuits (Golshani et al., 2009; Modol et al., 2020; Rochefort et al., 2009). This decorrelation of prefrontal population activity is closely associated with a developmental increase of inhibition strength, shifting the E/I balance towards inhibition. Neurons of GE as well as ES mice show a decreased correlation with lower magnitude specifically between layer 2/3 neurons or between chronically stimulated layer 2/3 PYRs in the case of GE and ES mice, respectively. Consequently, decreased correlations result in a similar abnormal tilt of E/I balance towards inhibition in both models (Figure 3) (Chini et al., 2021).

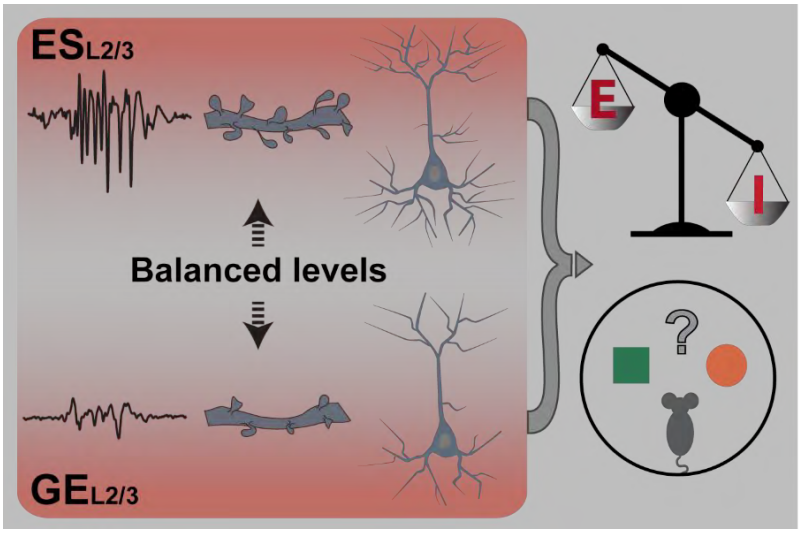

Figure 3. Opposite dysfunctions in prefrontal layer 2/3 pyramidal neurons cause shared alterations in excitation/inhibition balance and cognitive behavior. Summarizing illustration of identified early structural and functional changes in layer 2/3 of the medial prefrontal cortex in ES and GE mice (left) and resulting consequences (right). Abbreviations: L2/3, layer 2/3; ES, early stimulated; GE, genetic-environmental; E, excitation; I, inhibition. Figure references (Bitzenhofer et al., 2021; Chini et al., 2021; Chini et al., 2020).

Another commonality of these models is their shared dysfunctionality in layer 2/3 PYRs, either as the cause of genetic and environmental disturbances or experimentally induced (Figure 3) (Bitzenhofer et al., 2021; Chini et al., 2020). An analogical approach to our ES protocol was recently performed to induce cortex-wide excitation in PYRs from P4 to 14 (Medendorp et al., 2021), resulting in similar alterations as found for ES mice (Bitzenhofer et al., 2021). Of note, identical chronic excitation of certain interneuron populations in this study produced only minor behavioral changes (Medendorp et al., 2021). This indicates PYRs as a vulnerable population for early insults and regarding the specificity of our stimulation protocol, in particular, layer 2/3 PYRs might display this phenotype. In line with this, restricting DISC1 alterations transiently during perinatal development to layer 2/3 PYRs in GE mice is sufficient to reproduce not only early structural and functional deficits but also disturbed cognitive abilities (Chini et al., 2020; Xu et al., 2019). Additionally, overexpression of the complement component 4 protein, encoded by a gene which's alternations are linked to an increased risk for developing schizophrenia (Sekar et al., 2016), results in microglia cell activation. Activated microglia cells, in turn, over-prune synapses of prefrontal layer 2/3 PYRs, which ultimately causes cognitive and social disabilities (Comer et al., 2020; Druart et al., 2021). It is therefore tempting to speculate, that risk gene alterations might increase the susceptibility specifically of layer 2/3 PYRs and make them prone for microglia induced over-pruning, potentially primed and overactivated by a second hit as present in the GE model (Chini et al., 2020; Matcovitch-Natan et al., 2016). Even when not accessible during lifetime, postmortem samples of human patients diagnosed with schizophrenia revealed an increased number of differentially expressed genes and reduced spine density particularly in prefrontal layer 2/3 PYRs (Glantz and Lewis, 2000; Kolluri et al., 2005; Wu et al., 2021). Altogether, several lines of evidence point in the direction of layer 2/3 PYRs as a developmentally sensitive population with respect to mental diseases. However, further studies are needed in order to confirm this hypothesis and might be able to causally link the transcriptomic gene expression profiles of prefrontal layer 2/3 PYRs to their (dys)functions. Such correlations might enable the identification of substrate-specific risk genes with value for future drug targets.

3.4. Critical periods of prefrontal development and future perspectives

Brain development is not linear. The pace of key refinement processes during brain development undergoes fluctuations and peaks during growth spurts (Spencer-Smith and Anderson, 2009). Such phases of rapid development are characterized by heightened plasticity, sensitive for experiences. These so-called critical periods have been well characterized across sensory systems and take place during early postnatal stages in rodents (Hensch, 2005). Multiple streams of evidence lead to believe that critical periods, and, in particular, in the context of cognition occur in the PFC as well. The prefrontal timeline is protracted, reaching the critical period closure after all other cortical areas (Reh et al., 2020; Spencer-Smith and Anderson, 2009).

Two time windows have been suggested for the PFC and associated with an increased vulnerability with respect to mental disorders (Selemon and Zecevic, 2015). The end of pregnancy in humans, corresponding to early postnatal stages in rodents (Workman et al., 2013) and the adolescent period, beginning with the onset of puberty at around P30 in rodents and with around 12 years of age in humans (Juraska and Drzewiecki, 2020). Whereas this thesis identified and discussed mainly the numerous changes occurring during the early phases of prefrontal development, the PFC undergoes major reorganization during the adolescent period as well. Behaviorally adolescence is the time window where mature and, in particular, prefrontal-dependent cognitive skills emerge (Klune et al., 2021; Konstantoudaki et al., 2018; Larsen and Luna, 2018). Milestones in cognitive skill achievement can be correlated to structural and functional changes in the PFC (Goldman-Rakic, 1987; Klune et al., 2021; Spencer-Smith and Anderson, 2009). For instance, some of these changes affect key traits implicated in mental disorders and match in their developmental profile the relatively late onset during youth (Solmi et al., 2021). Prefrontal PYRs undergo an overproduction of spines and dendrites during early adolescence. Subsequently, spine number and dendritic complexity substantially reduce during late adolescence, mediated by transient activation of microglia cells (Delevich et al., 2018; Juraska and Drzewiecki, 2020; Mallya et al., 2019). Synaptic pruning deficits during this time are suggested to prelude the onset of mental disorders (Bian et al., 2015). Moreover, the number of dopaminergic innervations in PFC gradually increases over adolescence. This is accompanied by a peak of dopamine receptor densities, making the adolescent prefrontal circuitry sensitive for dysfunctions within the dopaminergic system (Murray et al., 2017; Walker et al., 2017). In addition and as already mentioned, prefrontal PV interneurons show a prolonged upregulation of PV, paralleling with inhibitory synapse growth and increasing functionality of FS PV interneurons over adolescence (Caballero and Tseng, 2016). Of note, PV expression appears to match the maturity of cortical areas, proposing this population as a hub for critical period timing (Reh et al., 2020).

In view of the hypothesis of two critical periods, the first during early development and the second during adolescence (Selemon and Zecevic, 2015) and combined with the multifactorial etiology of mental disorders (Feigenson et al., 2014; Parenti et al., 2020), it is tempting to speculate that early insults induce lasting changes in prefrontal circuitry. Altered circuitry, in turn, might increase the vulnerability during the subsequent critical period and the risk for the onset of symptoms (Lowes and Harris, 2021). This presumably takes place in an additive manner, with multiple early insults leading to an earlier onset. Supporting this hypothesis, we found the greatest changes in cognitive behavior and prefrontal activity in ES mice during young adulthood, i.e. late

adolescence, and only slight group differences in a few parameters at pre-juvenile age. Moreover, particularly late-maturing FS PV interneurons started to be affected after the pre-juvenile period. In terms of dendritic complexity of layer 2/3 PYRs, we observed a significant increase over age for controls but not for ES mice, most likely provoked by the premature structural growth (Bitzenhofer et al., 2021). Our selected age ranges preclude a statement about the occurrences during early adolescence, where the described structural peak takes place (Delevich et al., 2018). However, it cannot be ruled out that the early overgrowth is followed by a lasting arrested growth, missing required developmental fluctuations and reminiscent to the structural dynamics observed in the brain development of humans with autism (Courchesne, 2004). Furthermore, stimulations applied 5 days later during development were not capable of causing the observed comprehensive alterations and had only minor effects on evoked prefrontal activity (Bitzenhofer et al., 2021). These findings support the early postnatal phase as a sensitive period for disturbances. Yet, it remains to be investigated if similar manipulations during adolescence would bear equal consequences. For instance, altering prefrontal activity or environmental conditions during adolescence, but not adulthood, has been found to impair cognitive functioning and prefrontal activity in a lasting manner (Canetta et al., 2021; Rubino et al., 2015; Shao et al., 2013).

On the contrary, the combination of two early insults in the GE model led to an onset of behavioral symptoms already at young pre-juvenile age, preceded by disturbed prefrontal activity during the first postnatal week (Chini et al., 2020). Mono-hit models, on the other hand, display normal prefrontal activity and only minor behavioral changes at similar early ages (Hartung et al., 2016). Nonetheless, single genetic alterations in the DISC1 gene or its transient knockdown have been found to drive behavioral abnormalities especially in prefrontal-dependent tasks and molecular alterations in PFC with an onset after puberty (Brandon and Sawa, 2011; Niwa et al., 2010). However, it has also been demonstrated that genetic mono-hits induce no or only minor alterations (Abazyan et al., 2010; Brandon and Sawa, 2011). Similarly diverging findings have been reported for maternal immune activation offspring in rodents (Bergdolt and Dunaevsky, 2019; Mueller et al., 2021). Furthermore, human epidemiological studies report an increased but not deterministic risk for developing schizophrenia or autism after exposure to prenatal infections or in consequence to maternal immune dysfunctions (Brown, 2012; Canetta et al., 2014). Thus, the synergetic interaction of an environmental and genetic stressor increases the risk and might lead to an earlier onset. Single-hits still seem to comprise a risk, especially for the subsequent critical period, but potentially with a higher capacity of the immature brain to recover (Spencer-Smith and Anderson, 2009). Blocking the inflammatory response of microglia cells during the first week, but not at slightly later stages, prevented the emergence of behavioral disabilities in GE mice (Chini et al., 2020). To that end, it remains unknown if such interventions during the adolescent period, when the PFC undergoes a second window of plasticity, would unfold a pro-cognitive action for behavioral disabilities as well. In that sense, adolescence might not only be a time window of increased vulnerability but also a second window of opportunity for therapeutic strategies. Therapeutic interventions during adolescence would also be less complicated to achieve than during the perinatal period, particularly in humans (Fuhrmann et al., 2015; Steinberg, 2010). Preventive therapies in adolescent rodent models of mental disorders using drugs but also environmental enrichment and cognitive training, have been shown to impede the emergence of pathological phenotypes in adulthood (Marin, 2016). However, a comprehensive and causal understanding of how structural and functional changes in PFC during adolescence are linked to

the emergence of cognitive abilities and consequently give rise to its vulnerability is missing (Caballero and Tseng, 2016; Klune et al., 2021). Future research dedicated to filling this gap and based on the growing knowledge of early prefrontal development might be able to connect the pieces of the puzzle into a complete picture of the protracted timeline of prefrontal development. Such comprehensive knowledge is indispensable for understanding the mechanisms of disease pathophysiology.

3.5. Concluding remarks

Coordinated rhythmic activity in the adult PFC and, in particular, within the gamma frequency range has been attributed to underlie cognitive processing (Bosman et al., 2014; Cardin, 2016; Sohal, 2016). Moreover, gamma oscillations are compromised in mental disorders and associated with behavioral disabilities, especially within the cognitive domain (Minzenberg et al., 2010; Uhlhaas and Singer, 2010; Yamamoto et al., 2014). This relationship underpins the importance of gamma oscillations for adult functioning. Immature forms of coordinated fast prefrontal activity have been shown to emerge early in life (Bitzenhofer et al., 2017b; Brockmann et al., 2011) but so far with a missing link to their adult equivalent. In other words, the developmental dynamics and the cellular mechanisms throughout the transition to mature gamma activity as well as a causal influence of early (dys)functional maturation to later cognitive abilities are unknown. These unidentified mechanisms represent key aspects with a need to be addressed, specifically in light of the developmental etiology of mental disorders.

This thesis gave important insights into these knowledge gaps by using the mouse as a model system in combination with a wealth of advanced techniques. Starting with a detailed dissection of anesthetic effects in the developing and adult brain, we identified unique traits of age-, area- and agent-dependent consequences of anesthesia on brain activity (Chini et al., 2019; Yang et al., 2021). With respect to the revealed confounding effects of anesthesia, these studies fostered the development of an approach for non-anesthetized electrophysiological recordings in developing mice. This methodological improvement is of high relevance not only for the studies presented here but also for future studies, aiming to elucidate the principles of brain development. Equipped with this advanced methodology, we demonstrate that layer 2/3 PYRs in the PL of the medial PFC are key elements in shaping the dynamic maturation of prefrontal gamma oscillations throughout development (Bitzenhofer et al., 2020). Early disturbances of the physiological profile of this particular subpopulation, either as the cause of genetic and environmental disturbances or experimentally induced, provoked a tilt in the E/I balance towards inhibition and impaired prefrontal-dependent cognitive abilities in a lasting manner (Bitzenhofer et al., 2021; Chini et al., 2021; Chini et al., 2020). Thus, these are compelling arguments supporting early activity as a driver of physiological but also pathological maturation of prefrontal circuitry. On our journey, the uncovered mechanisms inspired us to ask advanced questions. Particularly, these questions focus on the mechanisms governing the acceleration of gamma frequency in medial PFC as well as on the origin of the vulnerability of the adolescent period on the large and of layer 2/3 PYRs on the small scale. Therefore, the results presented here not only shine new light on unknown developmental mechanisms but also serve as a foundation for subsequent research, presumably enabling future identification of early biomarkers of mental diseases and the development of customized therapeutic strategies.

4. References

[1] Abazyan, B., Nomura, J., Kannan, G., Ishizuka, K., Tamashiro, K.L., Nucifora, F., Pogorelov, V., Ladenheim, B., Yang, C., Krasnova, I.N.*, et al.* (2010). Prenatal interaction of mutant DISC1 and immune activation produces adult psychopathology. Biol Psychiatry 68, 1172-1181.

[2] Ackman, J.B., Zeng, H., and Crair, M.C. (2014). Structured dynamics of neural activity across developing neocortex. BioRxiv, 012237.

[3] Adams, R.A., Bush, D., Zheng, F., Meyer, S.S., Kaplan, R., Orfanos, S., Marques, T.R., Howes, O.D., and Burgess, N. (2020). Impaired theta phase coupling underlies frontotemporal dysconnectivity in schizophrenia. Brain 143, 1261-1277.

[4] Adesnik, H. (2018). Layer-specific excitation/inhibition balances during neuronal synchronization in the visual cortex. J Physiol 596, 1639-1657.

[5] Adesnik, H., and Scanziani, M. (2010). Lateral competition for cortical space by layer-specific horizontal circuits. Nature 464, 1155-1160.

[6] Ahlbeck, J., Song, L., Chini, M., Bitzenhofer, S.H., and Hanganu-Opatz, I.L. (2018). Glutamatergic drive along the septo-temporal axis of hippocampus boosts prelimbic oscillations in the neonatal mouse. Elife 7.

[7] Ahrlund-Richter, S., Xuan, Y., van Lunteren, J.A., Kim, H., Ortiz, C., Pollak Dorocic, I., Meletis, K., and Carlen, M. (2019). A whole-brain atlas of monosynaptic input targeting four different cell types in the medial prefrontal cortex of the mouse. Nat Neurosci 22, 657-668.

[8] Alfonsa, H., Brodersen, P., Newey, S.E., Yamagata, T., Panayi, M.C., Bannerman, D.M., Vyazovskiy, V.V., and Akerman, C.J. (2021). Intraneuronal chloride levels encode tiredness in cortex. BioRxiv, 444189.

[9] Anastasiades, P.G., and Butt, S.J. (2012). A role for silent synapses in the development of the pathway from layer 2/3 to 5 pyramidal cells in the neocortex. J Neurosci 32, 13085-13099.

[10] Anastasiades, P.G., and Carter, A.G. (2021). Circuit organization of the rodent medial prefrontal cortex. Trends Neurosci 44, 550-563.

[11] Anastasiades, P.G., Marques-Smith, A., Lyngholm, D., Lickiss, T., Raffiq, S., Katzel, D., Miesenbock, G., and Butt, S.J. (2016). GABAergic interneurons form transient layer-specific circuits in early postnatal neocortex. Nat Commun 7, 10584.

[12] Arnsten, A.F., and Rubia, K. (2012). Neurobiological circuits regulating attention, cognitive control, motivation, and emotion: disruptions in neurodevelopmental psychiatric disorders. J Am Acad Child Adolesc Psychiatry 51, 356-367.

[13] Atallah, B.V., and Scanziani, M. (2009). Instantaneous modulation of gamma oscillation frequency by balancing excitation with inhibition. Neuron 62, 566-577.

[14] Azevedo, F.A., Carvalho, L.R., Grinberg, L.T., Farfel, J.M., Ferretti, R.E., Leite, R.E., Jacob Filho, W., Lent, R., and Herculano-Houzel, S. (2009). Equal numbers of neuronal and

nonneuronal cells make the human brain an isometrically scaled-up primate brain. J Comp Neurol 513, 532-541.

[15] Baleisyte, A., Schneggenburger, R., and Kochubey, O. (2021). Optogenetic stimulation of medial amygdala GABA neurons with kinetically different channelrhodopsin variants yield opposite behavioral outcomes. BioRxiv, 450543.

[16] Barker, G.R., and Warburton, E.C. (2011). When is the hippocampus involved in recognition memory? J Neurosci 31, 10721-10731.

[17] Batista-Brito, R., Vinck, M., Ferguson, K.A., Chang, J.T., Laubender, D., Lur, G., Mossner, J.M., Hernandez, V.G., Ramakrishnan, C., Deisseroth, K.*, et al.* (2017). Developmental Dysfunction of VIP Interneurons Impairs Cortical Circuits. Neuron 95, 884-895 e889.

[18] Ben-Ari, Y. (2001). Developing networks play a similar melody. Trends Neurosci 24, 353-360.

[19] Benders, M.J., Palmu, K., Menache, C., Borradori-Tolsa, C., Lazeyras, F., Sizonenko, S., Dubois, J., Vanhatalo, S., and Huppi, P.S. (2015). Early Brain Activity Relates to Subsequent Brain Growth in Premature Infants. Cereb Cortex 25, 3014-3024.

[20] Berardino, B.G., Ballarini, F., Chertoff, M., Igaz, L.M., and Canepa, E.T. (2020). Nutritional stress timing differentially programs cognitive abilities in young adult male mice. Nutr Neurosci, 1-13.

[21] Bergdolt, L., and Dunaevsky, A. (2019). Brain changes in a maternal immune activation model of neurodevelopmental brain disorders. Prog Neurobiol 175, 1-19.

[22] Berger, T.K., Silberberg, G., Perin, R., and Markram, H. (2010). Brief bursts self-inhibit and correlate the pyramidal network. PLoS Biol 8.

[23] Berndt, A., Schoenenberger, P., Mattis, J., Tye, K.M., Deisseroth, K., Hegemann, P., and Oertner, T.G. (2011). High-efficiency channelrhodopsins for fast neuronal stimulation at low light levels. Proc Natl Acad Sci U S A 108, 7595-7600.

[24] Bernstein, J.G., and Boyden, E.S. (2011). Optogenetic tools for analyzing the neural circuits of behavior. Trends Cogn Sci 15, 592-600.

[25] Bertero, A., Liska, A., Pagani, M., Parolisi, R., Masferrer, M.E., Gritti, M., Pedrazzoli, M., Galbusera, A., Sarica, A., Cerasa, A.*, et al.* (2018). Autism-associated 16p11.2 microdeletion impairs prefrontal functional connectivity in mouse and human. Brain 141, 2055-2065.

[26] Bhattacharya, S., Cauchois, M.B.L., Iglesias, P.A., and Chen, Z.S. (2021). The impact of a closed-loop thalamocortical model on the spatiotemporal dynamics of cortical and thalamic traveling waves. Sci Rep 11, 14359.

[27] Bian, W.J., Miao, W.Y., He, S.J., Qiu, Z., and Yu, X. (2015). Coordinated Spine Pruning and Maturation Mediated by Inter-Spine Competition for Cadherin/Catenin Complexes. Cell 162, 808-822.

[28] Bicks, L.K., Koike, H., Akbarian, S., and Morishita, H. (2015). Prefrontal Cortex and Social Cognition in Mouse and Man. Front Psychol 6, 1805.

[29] Bitzenhofer, S.H., Ahlbeck, J., and Hanganu-Opatz, I.L. (2017a). Methodological Approach for Optogenetic Manipulation of Neonatal Neuronal Networks. Front Cell Neurosci 11, 239.

[30] Bitzenhofer, S.H., Ahlbeck, J., Wolff, A., Wiegert, J.S., Gee, C.E., Oertner, T.G., and Hanganu-Opatz, I.L. (2017b). Layer-specific optogenetic activation of pyramidal neurons causes beta-gamma entrainment of neonatal networks. Nat Commun 8, 14563.

[31] Bitzenhofer, S.H., Popplau, J.A., Chini, M., Marquardt, A., and Hanganu-Opatz, I.L. (2019). Activity-dependent maturation of prefrontal gamma oscillations sculpts cognitive performance. BioRxiv, 558957.

[32] Bitzenhofer, S.H., Popplau, J.A., Chini, M., Marquardt, A., and Hanganu-Opatz, I.L. (2021). A transient developmental increase in prefrontal activity alters network maturation and causes cognitive dysfunction in adult mice. Neuron 109, 1350-1364 e1356.

[33] Bitzenhofer, S.H., Popplau, J.A., and Hanganu-Opatz, I. (2020). Gamma activity accelerates during prefrontal development. Elife 9.

[34] Bitzenhofer, S.H., Sieben, K., Siebert, K.D., Spehr, M., and Hanganu-Opatz, I.L. (2015). Oscillatory activity in developing prefrontal networks results from theta-gamma-modulated synaptic inputs. Cell Rep 11, 486-497.

[35] Blanquie, O., Yang, J.W., Kilb, W., Sharopov, S., Sinning, A., and Luhmann, H.J. (2017). Electrical activity controls area-specific expression of neuronal apoptosis in the mouse developing cerebral cortex. Elife 6.

[36] Bosman, C.A., Lansink, C.S., and Pennartz, C.M. (2014). Functions of gamma-band synchronization in cognition: from single circuits to functional diversity across cortical and subcortical systems. Eur J Neurosci 39, 1982-1999.

[37] Brainstorm, C., Anttila, V., Bulik-Sullivan, B., Finucane, H.K., Walters, R.K., Bras, J., Duncan, L., Escott-Price, V., Falcone, G.J., Gormley, P.*, et al.* (2018). Analysis of shared heritability in common disorders of the brain. Science 360.

[38] Brandon, N.J., and Sawa, A. (2011). Linking neurodevelopmental and synaptic theories of mental illness through DISC1. Nat Rev Neurosci 12, 707-722.

[39] Brockmann, M.D., Poschel, B., Cichon, N., and Hanganu-Opatz, I.L. (2011). Coupled oscillations mediate directed interactions between prefrontal cortex and hippocampus of the neonatal rat. Neuron 71, 332-347.

[40] Brown, A.S. (2012). Epidemiologic studies of exposure to prenatal infection and risk of schizophrenia and autism. Dev Neurobiol 72, 1272-1276.

[41] Brown, V.J., and Bowman, E.M. (2002). Rodent models of prefrontal cortical function. Trends Neurosci 25, 340-343.

[42] Brunet-Gouet, E., and Decety, J. (2006). Social brain dysfunctions in schizophrenia: a review of neuroimaging studies. Psychiatry Res 148, 75-92.

[43] Bush, G., Luu, P., and Posner, M.I. (2000). Cognitive and emotional influences in anterior cingulate cortex. Trends Cogn Sci 4, 215-222.

[44] Bush, G., Vogt, B.A., Holmes, J., Dale, A.M., Greve, D., Jenike, M.A., and Rosen, B.R. (2002). Dorsal anterior cingulate cortex: a role in reward-based decision making. Proc Natl Acad Sci U S A 99, 523-528.

[45] Buzsaki, G., Anastassiou, C.A., and Koch, C. (2012). The origin of extracellular fields and currents--EEG, ECoG, LFP and spikes. Nat Rev Neurosci 13, 407-420.

[46] Buzsaki, G., and Draguhn, A. (2004). Neuronal oscillations in cortical networks. Science 304, 1926-1929.

[47] Buzsaki, G., Logothetis, N., and Singer, W. (2013). Scaling brain size, keeping timing: evolutionary preservation of brain rhythms. Neuron 80, 751-764.

[48] Buzsaki, G., and Wang, X.J. (2012). Mechanisms of gamma oscillations. Annu Rev Neurosci 35, 203-225.

[49] Buzsaki, G., and Watson, B.O. (2012). Brain rhythms and neural syntax: implications for efficient coding of cognitive content and neuropsychiatric disease. Dialogues Clin Neurosci 14, 345-367.

[50] Caballero, A., and Tseng, K.Y. (2016). GABAergic Function as a Limiting Factor for Prefrontal Maturation during Adolescence. Trends Neurosci 39, 441-448.

[51] Canetta, S., Sourander, A., Surcel, H.M., Hinkka-Yli-Salomaki, S., Leiviska, J., Kellendonk, C., McKeague, I.W., and Brown, A.S. (2014). Elevated maternal C-reactive protein and increased risk of schizophrenia in a national birth cohort. Am J Psychiatry 171, 960-968.

[52] Canetta, S.E., Holt, E.S., Benoit, L.J., Teboul, E., Todd Ogden, R., Harris, A.Z., and Kellendonk, C. (2021). Mature parvalbumin interneuron function in prefrontal cortex requires activity during a postnatal sensitive period. BioRxiv, 433943.

[53] Cardin, J.A. (2016). Snapshots of the Brain in Action: Local Circuit Operations through the Lens of gamma Oscillations. J Neurosci 36, 10496-10504.

[54] Cardin, J.A., Carlen, M., Meletis, K., Knoblich, U., Zhang, F., Deisseroth, K., Tsai, L.H., and Moore, C.I. (2009). Driving fast-spiking cells induces gamma rhythm and controls sensory responses. Nature 459, 663-667.

[55] Carlen, M. (2017). What constitutes the prefrontal cortex? Science 358, 478-482.

[56] Chang, P.S., Walker, S.M., and Fitzgerald, M. (2016). Differential Suppression of Spontaneous and Noxious-evoked Somatosensory Cortical Activity by Isoflurane in the Neonatal Rat. Anesthesiology 124, 885-898.

[57] Chen, G., Rasch, M.J., Wang, R., and Zhang, X.H. (2015). Experience-dependent emergence of beta and gamma band oscillations in the primary visual cortex during the critical period. Sci Rep 5, 17847.

[58] Chen, G., Zhang, Y., Li, X., Zhao, X., Ye, Q., Lin, Y., Tao, H.W., Rasch, M.J., and Zhang, X. (2017). Distinct Inhibitory Circuits Orchestrate Cortical beta and gamma Band Oscillations. Neuron 96, 1403-1418 e1406.

[59] Chini, M., Gretenkord, S., Kostka, J.K., Popplau, J.A., Cornelissen, L., Berde, C.B., Hanganu-Opatz, I.L., and Bitzenhofer, S.H. (2019). Neural Correlates of Anesthesia in Newborn Mice and Humans. Front Neural Circuits 13, 38.

[60] Chini, M., and Hanganu-Opatz, I.L. (2021). Prefrontal Cortex Development in Health and Disease: Lessons from Rodents and Humans. Trends Neurosci 44, 227-240.

[61] Chini, M., Pfeffer, T., and Hanganu-Opatz, I.L. (2021). Developmental increase of inhibition drives decorrelation of neural activity. bioRxiv, 451299.

[62] Chini, M., Popplau, J.A., Lindemann, C., Carol-Perdiguer, L., Hnida, M., Oberlander, V., Xu, X., Ahlbeck, J., Bitzenhofer, S.H., Mulert, C., and Hanganu-Opatz, I.L. (2020). Resolving and Rescuing Developmental Miswiring in a Mouse Model of Cognitive Impairment. Neuron 105, 60-74 e67.

[63] Cho, K.K., Hoch, R., Lee, A.T., Patel, T., Rubenstein, J.L., and Sohal, V.S. (2015). Gamma rhythms link prefrontal interneuron dysfunction with cognitive inflexibility in Dlx5/6(+/-) mice. Neuron 85, 1332-1343.

[64] Cirelli, C., and Tononi, G. (2015). Cortical development, electroencephalogram rhythms, and the sleep/wake cycle. Biol Psychiatry 77, 1071-1078.

[65] Clement, E.A., Richard, A., Thwaites, M., Ailon, J., Peters, S., and Dickson, C.T. (2008). Cyclic and sleep-like spontaneous alternations of brain state under urethane anaesthesia. PLoS One 3, e2004.

[66] Coelho-Santos, V., Berthiaume, A.A., Ornelas, S., Stuhlmann, H., and Shih, A.Y. (2021). Imaging the construction of capillary networks in the neonatal mouse brain. Proc Natl Acad Sci U S A 118.

[67] Comer, A.L., Jinadasa, T., Sriram, B., Phadke, R.A., Kretsge, L.N., Nguyen, T.P.H., Antognetti, G., Gilbert, J.P., Lee, J., Newmark, E.R.*, et al.* (2020). Increased expression of schizophrenia-associated gene C4 leads to hypoconnectivity of prefrontal cortex and reduced social interaction. PLoS Biol 18, e3000604.

[68] Corlew, R., Bosma, M.M., and Moody, W.J. (2004). Spontaneous, synchronous electrical activity in neonatal mouse cortical neurones. J Physiol 560, 377-390.

[69] Courchesne, E. (2004). Brain development in autism: early overgrowth followed by premature arrest of growth. Ment Retard Dev Disabil Res Rev 10, 106-111.

[70] Cross, C.M., Mediavilla Santos, L., Whiteley, N., Luyt, K., and Ashby, M.C. (2021). Early functional connectivity in the developing sensorimotor network that is independent of sensory experience. bioRxiv, 448057.

[71] Danneman, P.J., and Mandrell, T.D. (1997). Evaluation of five agents/methods for anesthesia of neonatal rats. Lab Anim Sci 47, 386-395.

[72] Dard, R.F., Leprince, E., Denis, J., Rao-Balappa, S., Lopez, C., Giorgi-Kurz, M., Szwagier, T., Dumont, T., Rouault, H., Minlebaev, M.*, et al.* (2021). The rapid developmental rise of somatic inhibition disengages hippocampal dynamics from self-motion. bioRxiv, 447542.

[73] Deisseroth, K. (2011). Optogenetics. Nat Methods 8, 26-29.

[74] Delevich, K., Thomas, A.W., and Wilbrecht, L. (2018). Adolescence and "Late Blooming" Synapses of the Prefrontal Cortex. Cold Spring Harb Symp Quant Biol 83, 37-43.

[75] Denaxa, M., Neves, G., Rabinowitz, A., Kemlo, S., Liodis, P., Burrone, J., and Pachnis, V. (2018). Modulation of Apoptosis Controls Inhibitory Interneuron Number in the Cortex. Cell Rep 22, 1710-1721.

[76] Di Bella, D.J., Habibi, E., Stickels, R.R., Scalia, G., Brown, J., Yadollahpour, P., Yang, S.M., Abbate, C., Biancalani, T., Macosko, E.Z., *et al.* (2021). Molecular logic of cellular diversification in the mouse cerebral cortex. Nature.

[77] Doelling, K.B., and Assaneo, M.F. (2021). Neural oscillations are a start toward understanding brain activity rather than the end. PLoS Biol 19, e3001234.

[78] Dorrn, A.L., Yuan, K., Barker, A.J., Schreiner, C.E., and Froemke, R.C. (2010). Developmental sensory experience balances cortical excitation and inhibition. Nature 465, 932-936.

[79] Douglas, R.J., and Martin, K.A. (2004). Neuronal circuits of the neocortex. Annu Rev Neurosci 27, 419-451.

[80] Druart, M., Nosten-Bertrand, M., Poll, S., Crux, S., Nebeling, F., Delhaye, C., Dubois, Y., Mittag, M., Leboyer, M., Tamouza, R., *et al.* (2021). Elevated expression of complement C4 in the mouse prefrontal cortex causes schizophrenia-associated phenotypes. Mol Psychiatry.

[81] Duan, L.Y., Horst, N.K., Cranmore, S.A.W., Horiguchi, N., Cardinal, R.N., Roberts, A.C., and Robbins, T.W. (2021). Controlling one's world: identification of sub-regions of primate PFC underlying goal-directed behavior. Neuron.

[82] Duan, Z.R.S., Che, A., Chu, P., Modol, L., Bollmann, Y., Babij, R., Fetcho, R.N., Otsuka, T., Fuccillo, M.V., Liston, C., *et al.* (2020). GABAergic Restriction of Network Dynamics Regulates Interneuron Survival in the Developing Cortex. Neuron 105, 75-92 e75.

[83] Eban-Rothschild, A., Appelbaum, L., and de Lecea, L. (2018). Neuronal Mechanisms for Sleep/Wake Regulation and Modulatory Drive. Neuropsychopharmacology 43, 937-952.

[84] Ellender, T.J., Avery, S.V., Mahfooz, K., Scaber, J., von Klemperer, A., Nixon, S.L., Buchan, M.J., van Rheede, J.J., Gatti, A., Waites, C., *et al.* (2019). Embryonic progenitor pools generate diversity in fine-scale excitatory cortical subnetworks. Nat Commun 10, 5224.

[85] Favuzzi, E., Deogracias, R., Marques-Smith, A., Maeso, P., Jezequel, J., Exposito-Alonso, D., Balia, M., Kroon, T., Hinojosa, A.J., E, F.M., and Rico, B. (2019). Distinct molecular programs regulate synapse specificity in cortical inhibitory circuits. Science 363, 413-417.

[86] Feigenson, K.A., Kusnecov, A.W., and Silverstein, S.M. (2014). Inflammation and the two-hit hypothesis of schizophrenia. Neurosci Biobehav Rev 38, 72-93.

[87] Felleman, D.J., and Van Essen, D.C. (1991). Distributed hierarchical processing in the primate cerebral cortex. Cereb Cortex 1, 1-47.

[88] Ferguson, B.R., and Gao, W.J. (2018). PV Interneurons: Critical Regulators of E/I Balance for Prefrontal Cortex-Dependent Behavior and Psychiatric Disorders. Front Neural Circuits 12, 37.

[89] Ferino, F., Thierry, A.M., and Glowinski, J. (1987). Anatomical and electrophysiological evidence for a direct projection from Ammon's horn to the medial prefrontal cortex in the rat. Exp Brain Res 65, 421-426.

[90] Fiore, R., Khudayberdiev, S., Christensen, M., Siegel, G., Flavell, S.W., Kim, T.K., Greenberg, M.E., and Schratt, G. (2009). Mef2-mediated transcription of the miR379-410 cluster regulates activity-dependent dendritogenesis by fine-tuning Pumilio2 protein levels. EMBO J 28, 697-710.

[91] Fitzgibbon, S.P., Pope, K.J., Mackenzie, L., Clark, C.R., and Willoughby, J.O. (2004). Cognitive tasks augment gamma EEG power. Clin Neurophysiol 115, 1802-1809.

[92] Florio, M., and Huttner, W.B. (2014). Neural progenitors, neurogenesis and the evolution of the neocortex. Development 141, 2182-2194.

[93] Franks, N.P. (2008). General anaesthesia: from molecular targets to neuronal pathways of sleep and arousal. Nat Rev Neurosci 9, 370-386.

[94] Frassoni, C., Arcelli, P., Regondi, M.C., Selvaggio, M., De Biasi, S., and Spreafico, R. (1995). Branching pattern of corticothalamic projections from the somatosensory cortex during postnatal development in the rat. Brain Res Dev Brain Res 90, 111-121.

[95] Freedman, D.S., Schroeder, J.B., Telian, G.I., Zhang, Z., Sunil, S., and Ritt, J.T. (2016). OptoZIF Drive: a 3D printed implant and assembly tool package for neural recording and optical stimulation in freely moving mice. J Neural Eng 13, 066013.

[96] Fuhrmann, D., Knoll, L.J., and Blakemore, S.J. (2015). Adolescence as a Sensitive Period of Brain Development. Trends Cogn Sci 19, 558-566.

[97] Fuster, J.M. (2001). The prefrontal cortex--an update: time is of the essence. Neuron 30, 319-333.

[98] Fuster, J.M. (2015). The Prefrontal Cortex, 5th edn (Boston: Elsevier/AP, Academic Press is an imprint of Elsevier, 444).

[99] Gangopadhyay, P., Chawla, M., Dal Monte, O., and Chang, S.W.C. (2021). Prefrontal-amygdala circuits in social decision-making. Nat Neurosci 24, 5-18.

[100] Ghezzi, F., Marques-Smith, A., Anastasiades, P.G., Lyngholm, D., Vagnoni, C., Rowett, A., Parameswaran, G., Hoerder-Suabedissen, A., Nakagawa, Y., Molnar, Z., and Butt, S.J.B. (2021). Non-canonical role for Lpar1-EGFP subplate neurons in early postnatal mouse somatosensory cortex. Elife 10.

[101] Glantz, L.A., and Lewis, D.A. (2000). Decreased dendritic spine density on prefrontal cortical pyramidal neurons in schizophrenia. Arch Gen Psychiatry 57, 65-73.

[102] Godsil, B.P., Kiss, J.P., Spedding, M., and Jay, T.M. (2013). The hippocampal-prefrontal pathway: the weak link in psychiatric disorders? Eur Neuropsychopharmacol 23, 1165-1181.

[103] Goldman-Rakic, P.S. (1987). Development of cortical circuitry and cognitive function. Child Dev 58, 601-622.

[104] Golshani, P., Goncalves, J.T., Khoshkhoo, S., Mostany, R., Smirnakis, S., and Portera-Cailliau, C. (2009). Internally mediated developmental desynchronization of neocortical network activity. J Neurosci 29, 10890-10899.

[105] Goltstein, P.M., Montijn, J.S., and Pennartz, C.M. (2015). Effects of isoflurane anesthesia on ensemble patterns of Ca2+ activity in mouse v1: reduced direction selectivity independent of increased correlations in cellular activity. PLoS One 10, e0118277.

[106] Goltstein, P.M., Reinert, S., Glas, A., Bonhoeffer, T., and Hubener, M. (2018). Food and water restriction lead to differential learning behaviors in a head-fixed two-choice visual discrimination task for mice. PLoS One 13, e0204066.

[107] Gour, A., Boergens, K.M., Heike, N., Hua, Y., Laserstein, P., Song, K., and Helmstaedter, M. (2021). Postnatal connectomic development of inhibition in mouse barrel cortex. Science 371.

[108] Grant, E., Hoerder-Suabedissen, A., and Molnar, Z. (2012). Development of the corticothalamic projections. Front Neurosci 6, 53.

[109] Greenberg, P.E., Fournier, A.A., Sisitsky, T., Pike, C.T., and Kessler, R.C. (2015). The economic burden of adults with major depressive disorder in the United States (2005 and 2010). J Clin Psychiatry 76, 155-162.

[110] Guan, W., Cao, J.W., Liu, L.Y., Zhao, Z.H., Fu, Y., and Yu, Y.C. (2017). Eye opening differentially modulates inhibitory synaptic transmission in the developing visual cortex. Elife 6.

[111] Guo, Z.V., Hires, S.A., Li, N., O'Connor, D.H., Komiyama, T., Ophir, E., Huber, D., Bonardi, C., Morandell, K., Gutnisky, D.*, et al.* (2014). Procedures for behavioral experiments in head-fixed mice. PLoS One 9, e88678.

[112] Hakim, R., Shamardani, K., and Adesnik, H. (2018). A neural circuit for gamma-band coherence across the retinotopic map in mouse visual cortex. Elife 7.

[113] Hanganu-Opatz, I.L. (2010). Between molecules and experience: role of early patterns of coordinated activity for the development of cortical maps and sensory abilities. Brain Res Rev 64, 160-176.

[114] Hanganu-Opatz, I.L., Butt, S.J.B., Hippenmeyer, S., De Marco Garcia, N.V., Cardin, J.A., Voytek, B., and Muotri, A.R. (2021). The Logic of Developing Neocortical Circuits in Health and Disease. J Neurosci 41, 813-822.

[115] Hanganu, I.L., Ben-Ari, Y., and Khazipov, R. (2006). Retinal waves trigger spindle bursts in the neonatal rat visual cortex. J Neurosci 26, 6728-6736.

[116] Hanganu, I.L., Kilb, W., and Luhmann, H.J. (2001). Spontaneous synaptic activity of subplate neurons in neonatal rat somatosensory cortex. Cereb Cortex 11, 400-410.

[117] Hanganu, I.L., Kilb, W., and Luhmann, H.J. (2002). Functional synaptic projections onto subplate neurons in neonatal rat somatosensory cortex. J Neurosci 22, 7165-7176.

[118] Hangya, B., Pi, H.J., Kvitsiani, D., Ranade, S.P., and Kepecs, A. (2014). From circuit motifs to computations: mapping the behavioral repertoire of cortical interneurons. Curr Opin Neurobiol 26, 117-124.

[119] Hara, K., and Harris, R.A. (2002). The anesthetic mechanism of urethane: the effects on neurotransmitter-gated ion channels. Anesth Analg 94, 313-318, table of contents.

[120] Hare, B.D., and Duman, R.S. (2020). Prefrontal cortex circuits in depression and anxiety: contribution of discrete neuronal populations and target regions. Mol Psychiatry 25, 2742-2758.

[121] Harris, K.D., and Mrsic-Flogel, T.D. (2013). Cortical connectivity and sensory coding. Nature 503, 51-58.

[122] Harris, K.D., and Shepherd, G.M. (2015). The neocortical circuit: themes and variations. Nat Neurosci 18, 170-181.

[123] Hartung, H., Cichon, N., De Feo, V., Riemann, S., Schildt, S., Lindemann, C., Mulert, C., Gogos, J.A., and Hanganu-Opatz, I.L. (2016). From Shortage to Surge: A Developmental Switch in Hippocampal-Prefrontal Coupling in a Gene-Environment Model of Neuropsychiatric Disorders. Cereb Cortex 26, 4265-4281.

[124] Hensch, T.K. (2005). Critical period plasticity in local cortical circuits. Nat Rev Neurosci 6, 877-888.

[125] Hoerder-Suabedissen, A., and Molnar, Z. (2015). Development, evolution and pathology of neocortical subplate neurons. Nat Rev Neurosci 16, 133-146.

[126] Horvath, S., and Mirnics, K. (2009). Breaking the gene barrier in schizophrenia. Nat Med 15, 488-490.

[127] Howard, M.W., Rizzuto, D.S., Caplan, J.B., Madsen, J.R., Lisman, J., Aschenbrenner-Scheibe, R., Schulze-Bonhage, A., and Kahana, M.J. (2003). Gamma oscillations correlate with working memory load in humans. Cereb Cortex 13, 1369-1374.

[128] Howes, O.D., and McCutcheon, R. (2017). Inflammation and the neural diathesis-stress hypothesis of schizophrenia: a reconceptualization. Transl Psychiatry 7, e1024.

[129] Iyer, K.K., Roberts, J.A., Hellstrom-Westas, L., Wikstrom, S., Hansen Pupp, I., Ley, D., Vanhatalo, S., and Breakspear, M. (2015). Cortical burst dynamics predict clinical outcome early in extremely preterm infants. Brain 138, 2206-2218.

[130] Jang, H.J., Chung, H., Rowland, J.M., Richards, B.A., Kohl, M.M., and Kwag, J. (2020). Distinct roles of parvalbumin and somatostatin interneurons in gating the synchronization of spike times in the neocortex. Sci Adv 6, eaay5333.

[131] Janiesch, P.C., Kruger, H.S., Poschel, B., and Hanganu-Opatz, I.L. (2011). Cholinergic control in developing prefrontal-hippocampal networks. J Neurosci 31, 17955-17970.

[132] Jay, T.M., and Witter, M.P. (1991). Distribution of hippocampal CA1 and subicular efferents in the prefrontal cortex of the rat studied by means of anterograde transport of Phaseolus vulgaris-leucoagglutinin. J Comp Neurol 313, 574-586.

[133] Jia, D.W., Ponte Costa, R., and Vogels, T.P. (2021). Developmental depression-facilitation shift controls excitation-inhibition balance. BioRxiv, 431593.

[134] Juraska, J.M., and Drzewiecki, C.M. (2020). Cortical reorganization during adolescence: What the rat can tell us about the cellular basis. Dev Cogn Neurosci 45, 100857.

[135] Kaas, J.H. (2011). Neocortex in early mammals and its subsequent variations. Ann N Y Acad Sci 1225, 28-36.

[136] Kalemaki, K., Xu, X., Velli, A., Christodoulou, O., Denaxa, M., Hanganu-Opatz, I.L., Karagogeos, D., and Sidiropoulou, K. (2021). The developmental changes in intrinsic and synaptic properties of prefrontal neurons enhance local network activity from the second to the third postnatal week in mice. bioRxiv, 913913.

[137] Kann, O. (2011). The energy demand of fast neuronal network oscillations: insights from brain slice preparations. Front Pharmacol 2, 90.

[138] Keeler, J.F., and Robbins, T.W. (2011). Translating cognition from animals to humans. Biochem Pharmacol 81, 1356-1366.

[139] Kepecs, A., and Fishell, G. (2014). Interneuron cell types are fit to function. Nature 505, 318-326.

[140] Khan, A., and Powell, S.B. (2018). Sensorimotor gating deficits in "two-hit" models of schizophrenia risk factors. Schizophr Res 198, 68-83.

[141] Khazipov, R., and Luhmann, H.J. (2006). Early patterns of electrical activity in the developing cerebral cortex of humans and rodents. Trends Neurosci 29, 414-418.

[142] Khazipov, R., Sirota, A., Leinekugel, X., Holmes, G.L., Ben-Ari, Y., and Buzsaki, G. (2004). Early motor activity drives spindle bursts in the developing somatosensory cortex. Nature 432, 758-761.

[143] Kidokoro, H. (2021). Delta brushes are not just a hallmark of EEG in human preterm infants. Pediatr Int 63, 130-136.

[144] Kirischuk, S., Sinning, A., Blanquie, O., Yang, J.W., Luhmann, H.J., and Kilb, W. (2017). Modulation of Neocortical Development by Early Neuronal Activity: Physiology and Pathophysiology. Front Cell Neurosci 11, 379.

[145] Kirkby, L.A., Sack, G.S., Firl, A., and Feller, M.B. (2013). A role for correlated spontaneous activity in the assembly of neural circuits. Neuron 80, 1129-1144.

[146] Klune, C.B., Jin, B., and DeNardo, L.A. (2021). Linking mPFC circuit maturation to the developmental regulation of emotional memory and cognitive flexibility. Elife 10.

[147] Kola, I., and Landis, J. (2004). Can the pharmaceutical industry reduce attrition rates? Nat Rev Drug Discov 3, 711-715.

[148] Kolluri, N., Sun, Z., Sampson, A.R., and Lewis, D.A. (2005). Lamina-specific reductions in dendritic spine density in the prefrontal cortex of subjects with schizophrenia. Am J Psychiatry 162, 1200-1202.

[149] Konopaske, G.T., Lange, N., Coyle, J.T., and Benes, F.M. (2014). Prefrontal cortical dendritic spine pathology in schizophrenia and bipolar disorder. JAMA Psychiatry 71, 1323-1331.

[150] Konstantoudaki, X., Chalkiadaki, K., Vasileiou, E., Kalemaki, K., Karagogeos, D., and Sidiropoulou, K. (2018). Prefrontal cortical-specific differences in behavior and synaptic plasticity between adolescent and adult mice. J Neurophysiol 119, 822-833.

[151] Kroon, T., van Hugte, E., van Linge, L., Mansvelder, H.D., and Meredith, R.M. (2019). Early postnatal development of pyramidal neurons across layers of the mouse medial prefrontal cortex. Sci Rep 9, 5037.

[152] Larroque, B., Ancel, P.Y., Marret, S., Marchand, L., Andre, M., Arnaud, C., Pierrat, V., Roze, J.C., Messer, J., Thiriez, G.*, et al.* (2008). Neurodevelopmental disabilities and special care of 5-year-old children born before 33 weeks of gestation (the EPIPAGE study): a longitudinal cohort study. Lancet 371, 813-820.

[153] Larsen, B., and Luna, B. (2018). Adolescence as a neurobiological critical period for the development of higher-order cognition. Neurosci Biobehav Rev 94, 179-195.

[154] Latsari, M., Dori, I., Antonopoulos, J., Chiotelli, M., and Dinopoulos, A. (2002). Noradrenergic innervation of the developing and mature visual and motor cortex of the rat brain: a light and electron microscopic immunocytochemical analysis. J Comp Neurol 445, 145-158.

[155] Laubach, M., Amarante, L.M., Swanson, K., and White, S.R. (2018). What, If Anything, Is Rodent Prefrontal Cortex? eNeuro 5.

[156] Le Merre, P., Ahrlund-Richter, S., and Carlen, M. (2021). The mouse prefrontal cortex: Unity in diversity. Neuron 109, 1925-1944.

[157] Le Roy, I., Carlier, M., and Roubertoux, P.L. (2001). Sensory and motor development in mice: genes, environment and their interactions. Behav Brain Res 125, 57-64.

[158] Lee, C., Lavoie, A., Liu, J., Chen, S.X., and Liu, B.H. (2020). Light Up the Brain: The Application of Optogenetics in Cell-Type Specific Dissection of Mouse Brain Circuits. Front Neural Circuits 14, 18.

[159] Lee, S.H., and Dan, Y. (2012). Neuromodulation of brain states. Neuron 76, 209-222.

[160] Leenaars, C.H.C., Kouwenaar, C., Stafleu, F.R., Bleich, A., Ritskes-Hoitinga, M., De Vries, R.B.M., and Meijboom, F.L.B. (2019). Animal to human translation: a systematic scoping review of reported concordance rates. J Transl Med 17, 223.

[161] Lewis, D.A., Curley, A.A., Glausier, J.R., and Volk, D.W. (2012). Cortical parvalbumin interneurons and cognitive dysfunction in schizophrenia. Trends Neurosci 35, 57-67.

[162] Li, N., Chen, S., Guo, Z.V., Chen, H., Huo, Y., Inagaki, H.K., Chen, G., Davis, C., Hansel, D., Guo, C., and Svoboda, K. (2019). Spatiotemporal constraints on optogenetic inactivation in cortical circuits. Elife 8.

[163] Li, R., Wang, M., Yao, J., Liang, S., Liao, X., Yang, M., Zhang, J., Yan, J., Jia, H., Chen, X., and Li, X. (2018). Two-Photon Functional Imaging of the Auditory Cortex in Behaving Mice: From Neural Networks to Single Spines. Front Neural Circuits 12, 33.

[164] Lim, L., Mi, D., Llorca, A., and Marin, O. (2018). Development and Functional Diversification of Cortical Interneurons. Neuron 100, 294-313.

[165] Lowes, D.C., and Harris, A.Z. (2021). Early to beta and neuronally precocial makes a mouse have weak gamma and be less social. Neuron 109, 1250-1252.

[166] Luczak, A., Bartho, P., Marguet, S.L., Buzsaki, G., and Harris, K.D. (2007). Sequential structure of neocortical spontaneous activity in vivo. Proc Natl Acad Sci U S A 104, 347-352.

[167] Luhmann, H.J., Kilb, W., and Hanganu-Opatz, I.L. (2009). Subplate cells: amplifiers of neuronal activity in the developing cerebral cortex. Front Neuroanat 3, 19.

[168] Luhmann, H.J., Kilb, W., and Kirischuk, S. (2020). Synapse Development and Maturation, Chapter 22-Cajal–Retzius and subplate cells: transient cortical neurons and circuits with long-term impact, 2 edn (Elsevier/AP, Academic Press is an imprint of Elsevier, 485-500).

[169] Luhmann, H.J., Kirischuk, S., and Kilb, W. (2018). The Superior Function of the Subplate in Early Neocortical Development. Front Neuroanat 12, 97.

[170] Luhmann, H.J., Sinning, A., Yang, J.W., Reyes-Puerta, V., Stuttgen, M.C., Kirischuk, S., and Kilb, W. (2016). Spontaneous Neuronal Activity in Developing Neocortical Networks: From Single Cells to Large-Scale Interactions. Front Neural Circuits 10, 40.

[171] Magno, L., Asgarian, Z., Pendolino, V., Velona, T., Mackintosh, A., Lee, F., Stryjewska, A., Zimmer, C., Guillemot, F., Farrant, M.*, et al.* (2021). Transient developmental imbalance of cortical interneuron subtypes presages long-term changes in behavior. Cell Rep 35, 109249.

[172] Malik, R., Li, Y., Schamiloglu, S., and Sohal, V.S. (2021). Top-down control of hippocampal signal-to-noise by prefrontal long-range inhibition. bioRxiv, 433441.

[173] Mallya, A.P., Wang, H.D., Lee, H.N.R., and Deutch, A.Y. (2019). Microglial Pruning of Synapses in the Prefrontal Cortex During Adolescence. Cereb Cortex 29, 1634-1643.

[174] Marin, O. (2016). Developmental timing and critical windows for the treatment of psychiatric disorders. Nat Med 22, 1229-1238.

[175] Marin, O., and Rubenstein, J.L. (2003). Cell migration in the forebrain. Annu Rev Neurosci 26, 441-483.

[176] Marques-Smith, A., Lyngholm, D., Kaufmann, A.K., Stacey, J.A., Hoerder-Suabedissen, A., Becker, E.B., Wilson, M.C., Molnar, Z., and Butt, S.J. (2016). A Transient Translaminar GABAergic Interneuron Circuit Connects Thalamocortical Recipient Layers in Neonatal Somatosensory Cortex. Neuron 89, 536-549.

[177] Martinez-Cerdeno, V. (2017). Dendrite and spine modifications in autism and related neurodevelopmental disorders in patients and animal models. Dev Neurobiol 77, 393-404.

[178] Martini, F.J., Guillamon-Vivancos, T., Moreno-Juan, V., Valdeolmillos, M., and Lopez-Bendito, G. (2021). Spontaneous activity in developing thalamic and cortical sensory networks. Neuron.

[179] Mashour, G.A., and Avidan, M.S. (2017). Black swans: challenging the relationship of anaesthetic-induced unconsciousness and electroencephalographic oscillations in the frontal cortex. Br J Anaesth 119, 563-565.

[180] Massimini, M., Huber, R., Ferrarelli, F., Hill, S., and Tononi, G. (2004). The sleep slow oscillation as a traveling wave. J Neurosci 24, 6862-6870.

[181] Matcovitch-Natan, O., Winter, D.R., Giladi, A., Vargas Aguilar, S., Spinrad, A., Sarrazin, S., Ben-Yehuda, H., David, E., Zelada Gonzalez, F., Perrin, P.*, et al.* (2016). Microglia development follows a stepwise program to regulate brain homeostasis. Science 353, aad8670.

[182] Medendorp, W.E., Bjorefeldt, A., Crespo, E.L., Prakash, M., Pal, A., Waddell, M.L., Moore, C.I., and Hochgeschwender, U. (2021). Selective postnatal excitation of neocortical pyramidal neurons results in distinctive behavioral and circuit deficits in adulthood. iScience 24, 102157.

[183] Melzer, S., and Monyer, H. (2020). Diversity and function of corticopetal and corticofugal GABAergic projection neurons. Nat Rev Neurosci 21, 499-515.

[184] Messier, J.E., Chen, H., Cai, Z.L., and Xue, M. (2018). Targeting light-gated chloride channels to neuronal somatodendritic domain reduces their excitatory effect in the axon. Elife 7.

[185] Meyer-Lindenberg, A. (2010). From maps to mechanisms through neuroimaging of schizophrenia. Nature 468, 194-202.

[186] Mikulovic, S., Pupe, S., Peixoto, H.M., Do Nascimento, G.C., Kullander, K., Tort, A.B., and Leao, R.N. (2016). On the photovoltaic effect in local field potential recordings. Neurophotonics 3, 015002.

[187] Millan, M.J., Agid, Y., Brune, M., Bullmore, E.T., Carter, C.S., Clayton, N.S., Connor, R., Davis, S., Deakin, B., DeRubeis, R.J.*, et al.* (2012). Cognitive dysfunction in psychiatric disorders: characteristics, causes and the quest for improved therapy. Nat Rev Drug Discov 11, 141-168.

[188] Millan, M.J., Andrieux, A., Bartzokis, G., Cadenhead, K., Dazzan, P., Fusar-Poli, P., Gallinat, J., Giedd, J., Grayson, D.R., Heinrichs, M.*, et al.* (2016). Altering the course of schizophrenia: progress and perspectives. Nat Rev Drug Discov 15, 485-515.

[189] Miller, E.K. (2000). The prefrontal cortex and cognitive control. Nat Rev Neurosci 1, 59-65.

[190] Miller, E.K., and Cohen, J.D. (2001). An integrative theory of prefrontal cortex function. Annu Rev Neurosci 24, 167-202.

[191] Minlebaev, M., Colonnese, M., Tsintsadze, T., Sirota, A., and Khazipov, R. (2011). Early gamma oscillations synchronize developing thalamus and cortex. Science 334, 226-229.

[192] Minzenberg, M.J., Firl, A.J., Yoon, J.H., Gomes, G.C., Reinking, C., and Carter, C.S. (2010). Gamma oscillatory power is impaired during cognitive control independent of medication status in first-episode schizophrenia. Neuropsychopharmacology 35, 2590-2599.

[193] Mitchell, J.F., Sundberg, K.A., and Reynolds, J.H. (2007). Differential attention-dependent response modulation across cell classes in macaque visual area V4. Neuron 55, 131-141.

[194] Miyamae, T., Chen, K., Lewis, D.A., and Gonzalez-Burgos, G. (2017). Distinct Physiological Maturation of Parvalbumin-Positive Neuron Subtypes in Mouse Prefrontal Cortex. J Neurosci 37, 4883-4902.

[195] Miyoshi, G., and Fishell, G. (2011). GABAergic interneuron lineages selectively sort into specific cortical layers during early postnatal development. Cereb Cortex 21, 845-852.

[196] Mizuno, H., Hirano, T., and Tagawa, Y. (2007). Evidence for activity-dependent cortical wiring: formation of interhemispheric connections in neonatal mouse visual cortex requires projection neuron activity. J Neurosci 27, 6760-6770.

[197] Modol, L., Bollmann, Y., Tressard, T., Baude, A., Che, A., Duan, Z.R.S., Babij, R., De Marco Garcia, N.V., and Cossart, R. (2020). Assemblies of Perisomatic GABAergic Neurons in the Developing Barrel Cortex. Neuron 105, 93-105 e104.

[198] Molnar, Z., and Clowry, G. (2012). Cerebral cortical development in rodents and primates. Prog Brain Res 195, 45-70.

[199] Molnar, Z., Luhmann, H.J., and Kanold, P.O. (2020). Transient cortical circuits match spontaneous and sensory-driven activity during development. Science 370.

[200] Moore, A.K., Weible, A.P., Balmer, T.S., Trussell, L.O., and Wehr, M. (2018). Rapid Rebalancing of Excitation and Inhibition by Cortical Circuitry. Neuron 97, 1341-1355 e1346.

[201] Mueller, F.S., Scarborough, J., Schalbetter, S.M., Richetto, J., Kim, E., Couch, A., Yee, Y., Lerch, J.P., Vernon, A.C., Weber-Stadlbauer, U., and Meyer, U. (2021). Behavioral, neuroanatomical, and molecular correlates of resilience and susceptibility to maternal immune activation. Mol Psychiatry 26, 396-410.

[202] Murray, R.M., Bhavsar, V., Tripoli, G., and Howes, O. (2017). 30 Years on: How the Neurodevelopmental Hypothesis of Schizophrenia Morphed Into the Developmental Risk Factor Model of Psychosis. Schizophr Bull 43, 1190-1196.

[203] Neckelmann, D., and Ursin, R. (1993). Sleep stages and EEG power spectrum in relation to acoustical stimulus arousal threshold in the rat. Sleep 16, 467-477.

[204] Neniskyte, U., and Gross, C.T. (2017). Errant gardeners: glial-cell-dependent synaptic pruning and neurodevelopmental disorders. Nat Rev Neurosci 18, 658-670.

[205] Niell, C.M., and Stryker, M.P. (2008). Highly selective receptive fields in mouse visual cortex. J Neurosci 28, 7520-7536.

[206] Niethard, N., Ngo, H.V., Ehrlich, I., and Born, J. (2018). Cortical circuit activity underlying sleep slow oscillations and spindles. Proc Natl Acad Sci U S A 115, E9220-E9229.

[207] Niwa, M., Kamiya, A., Murai, R., Kubo, K., Gruber, A.J., Tomita, K., Lu, L., Tomisato, S., Jaaro-Peled, H., Seshadri, S.*, et al.* (2010). Knockdown of DISC1 by in utero gene transfer disturbs postnatal dopaminergic maturation in the frontal cortex and leads to adult behavioral deficits. Neuron 65, 480-489.

[208] Northcutt, R.G., and Kaas, J.H. (1995). The emergence and evolution of mammalian neocortex. Trends Neurosci 18, 373-379.

[209] Okaty, B.W., Miller, M.N., Sugino, K., Hempel, C.M., and Nelson, S.B. (2009). Transcriptional and electrophysiological maturation of neocortical fast-spiking GABAergic interneurons. J Neurosci 29, 7040-7052.

[210] Oliverio, A., Castellano, C., and Allegra, S.P. (1975). Effects of genetic and nutritional factors on post-natal reflex and behavioral development in the mouse. Exp Aging Res 1, 41-56.

[211] Paasonen, J., Stenroos, P., Salo, R.A., Kiviniemi, V., and Grohn, O. (2018). Functional connectivity under six anesthesia protocols and the awake condition in rat brain. Neuroimage 172, 9-20.

[212] Pagliardini, S., Gosgnach, S., and Dickson, C.T. (2013). Spontaneous sleep-like brain state alternations and breathing characteristics in urethane anesthetized mice. PLoS One 8, e70411.

[213] Pan, N.C., Fang, A., Shen, C., Sun, L., Wu, Q., and Wang, X. (2019). Early Excitatory Activity-Dependent Maturation of Somatostatin Interneurons in Cortical Layer 2/3 of Mice. Cereb Cortex 29, 4107-4118.

[214] Parenti, I., Rabaneda, L.G., Schoen, H., and Novarino, G. (2020). Neurodevelopmental Disorders: From Genetics to Functional Pathways. Trends Neurosci 43, 608-621.

[215] Peixoto, R.T., Wang, W., Croney, D.M., Kozorovitskiy, Y., and Sabatini, B.L. (2016). Early hyperactivity and precocious maturation of corticostriatal circuits in Shank3B(-/-) mice. Nat Neurosci 19, 716-724.

[216] Pisanello, F., Sileo, L., and De Vittorio, M. (2016). Micro- and Nanotechnologies for Optical Neural Interfaces. Front Neurosci 10, 70.

[217] Pisano, F., Pisanello, M., Lee, S.J., Lee, J., Maglie, E., Balena, A., Sileo, L., Spagnolo, B., Bianco, M., Hyun, M.*, et al.* (2019). Depth-resolved fiber photometry with a single tapered optical fiber implant. Nat Methods 16, 1185-1192.

[218] Place, R., Farovik, A., Brockmann, M., and Eichenbaum, H. (2016). Bidirectional prefrontal-hippocampal interactions support context-guided memory. Nat Neurosci 19, 992-994.

[219] Pluta, S.R., Telian, G.I., Naka, A., and Adesnik, H. (2019). Superficial Layers Suppress the Deep Layers to Fine-tune Cortical Coding. J Neurosci 39, 2052-2064.

[220] Preuss, T.M. (1995). Do rats have prefrontal cortex? The rose-woolsey-akert program reconsidered. J Cogn Neurosci 7, 1-24.

[221] Preuss, T.M., and Wise, S.P. (2021). Evolution of prefrontal cortex. Neuropsychopharmacology.

[222] Rao, M.K., and Wilkinson, M.F. (2006). Tissue-specific and cell type-specific RNA interference in vivo. Nat Protoc 1, 1494-1501.

[223] Rasetti, R., Mattay, V.S., Wiedholz, L.M., Kolachana, B.S., Hariri, A.R., Callicott, J.H., Meyer-Lindenberg, A., and Weinberger, D.R. (2009). Evidence that altered amygdala activity in schizophrenia is related to clinical state and not genetic risk. Am J Psychiatry 166, 216-225.

[224] Reh, R.K., Dias, B.G., Nelson, C.A., 3rd, Kaufer, D., Werker, J.F., Kolb, B., Levine, J.D., and Hensch, T.K. (2020). Critical period regulation across multiple timescales. Proc Natl Acad Sci U S A 117, 23242-23251.

[225] Rensing, N., Moy, B., Friedman, J.L., Galindo, R., and Wong, M. (2018). Longitudinal analysis of developmental changes in electroencephalography patterns and sleep-wake states of the neonatal mouse. PLoS One 13, e0207031.

[226] Richter, M., Murtaza, N., Scharrenberg, R., White, S.H., Johanns, O., Walker, S., Yuen, R.K.C., Schwanke, B., Bedurftig, B., Henis, M.*, et al.* (2019). Altered TAOK2 activity causes autism-related neurodevelopmental and cognitive abnormalities through RhoA signaling. Mol Psychiatry 24, 1329-1350.

[227] Rinetti-Vargas, G., Phamluong, K., Ron, D., and Bender, K.J. (2017). Periadolescent Maturation of GABAergic Hyperpolarization at the Axon Initial Segment. Cell Rep 20, 21-29.

[228] Rochefort, N.L., Garaschuk, O., Milos, R.I., Narushima, M., Marandi, N., Pichler, B., Kovalchuk, Y., and Konnerth, A. (2009). Sparsification of neuronal activity in the visual cortex at eye-opening. Proc Natl Acad Sci U S A 106, 15049-15054.

[229] Rosenberg, M., Zhang, T., Perona, P., and Meister, M. (2021). Mice in a labyrinth show rapid learning, sudden insight, and efficient exploration. Elife 10.

[230] Rossant, C., Kadir, S.N., Goodman, D.F.M., Schulman, J., Hunter, M.L.D., Saleem, A.B., Grosmark, A., Belluscio, M., Denfield, G.H., Ecker, A.S.*, et al.* (2016). Spike sorting for large, dense electrode arrays. Nat Neurosci 19, 634-641.

[231] Rubino, T., Prini, P., Piscitelli, F., Zamberletti, E., Trusel, M., Melis, M., Sagheddu, C., Ligresti, A., Tonini, R., Di Marzo, V., and Parolaro, D. (2015). Adolescent exposure to THC in female rats disrupts developmental changes in the prefrontal cortex. Neurobiol Dis 73, 60-69.

[232] Rudolph, U., and Antkowiak, B. (2004). Molecular and neuronal substrates for general anaesthetics. Nat Rev Neurosci 5, 709-720.

[233] Sakata, S., and Harris, K.D. (2009). Laminar structure of spontaneous and sensory-evoked population activity in auditory cortex. Neuron 64, 404-418.

[234] Sceniak, M.P., and Maciver, M.B. (2006). Cellular actions of urethane on rat visual cortical neurons in vitro. J Neurophysiol 95, 3865-3874.

[235] Schubert, D., Martens, G.J., and Kolk, S.M. (2015). Molecular underpinnings of prefrontal cortex development in rodents provide insights into the etiology of neurodevelopmental disorders. Mol Psychiatry 20, 795-809.

[236] Schwarz, C., Hentschke, H., Butovas, S., Haiss, F., Stuttgen, M.C., Gerdjikov, T.V., Bergner, C.G., and Waiblinger, C. (2010). The head-fixed behaving rat--procedures and pitfalls. Somatosens Mot Res 27, 131-148.

[237] Sekar, A., Bialas, A.R., de Rivera, H., Davis, A., Hammond, T.R., Kamitaki, N., Tooley, K., Presumey, J., Baum, M., Van Doren, V.*, et al.* (2016). Schizophrenia risk from complex variation of complement component 4. Nature 530, 177-183.

[238] Selemon, L.D., and Zecevic, N. (2015). Schizophrenia: a tale of two critical periods for prefrontal cortical development. Transl Psychiatry 5, e623.

[239] Shao, F., Han, X., Shao, S., and Wang, W. (2013). Adolescent social isolation influences cognitive function in adult rats. Neural Regen Res 8, 1025-1030.

[240] Shemesh, O.A., Tanese, D., Zampini, V., Linghu, C., Piatkevich, K., Ronzitti, E., Papagiakoumou, E., Boyden, E.S., and Emiliani, V. (2017). Temporally precise single-cell-resolution optogenetics. Nat Neurosci 20, 1796-1806.

[241] Shen, J., and Colonnese, M.T. (2016). Development of Activity in the Mouse Visual Cortex. J Neurosci 36, 12259-12275.

[242] Shumkova, V., Sitdikova, V., Rechapov, I., Leukhin, A., and Minlebaev, M. (2021). Effects of urethane and isoflurane on the sensory evoked response and local blood flow in the early postnatal rat somatosensory cortex. Sci Rep 11, 9567.

[243] Sigurdsson, T., Stark, K.L., Karayiorgou, M., Gogos, J.A., and Gordon, J.A. (2010). Impaired hippocampal-prefrontal synchrony in a genetic mouse model of schizophrenia. Nature 464, 763-767.

[244] Sileo, L., Bitzenhofer, S.H., Spagnolo, B., Popplau, J.A., Holzhammer, T., Pisanello, M., Pisano, F., Bellistri, E., Maglie, E., De Vittorio, M.*, et al.* (2018). Tapered Fibers Combined With a Multi-Electrode Array for Optogenetics in Mouse Medial Prefrontal Cortex. Front Neurosci 12, 771.

[245] Sirota, A., Montgomery, S., Fujisawa, S., Isomura, Y., Zugaro, M., and Buzsaki, G. (2008). Entrainment of neocortical neurons and gamma oscillations by the hippocampal theta rhythm. Neuron 60, 683-697.

[246] Sitdikova, G., Zakharov, A., Janackova, S., Gerasimova, E., Lebedeva, J., Inacio, A.R., Zaynutdinova, D., Minlebaev, M., Holmes, G.L., and Khazipov, R. (2014). Isoflurane suppresses early cortical activity. Ann Clin Transl Neurol 1, 15-26.

[247] Sohal, V.S. (2016). How Close Are We to Understanding What (if Anything) gamma Oscillations Do in Cortical Circuits? J Neurosci 36, 10489-10495.

[248] Solmi, M., Radua, J., Olivola, M., Croce, E., Soardo, L., Salazar de Pablo, G., Il Shin, J., Kirkbride, J.B., Jones, P., Kim, J.H.*, et al.* (2021). Age at onset of mental disorders worldwide: large-scale meta-analysis of 192 epidemiological studies. Mol Psychiatry.

[249] Spencer-Smith, M., and Anderson, V. (2009). Healthy and abnormal development of the prefrontal cortex. Dev Neurorehabil 12, 279-297.

[250] Spruston, N. (2008). Pyramidal neurons: dendritic structure and synaptic integration. Nat Rev Neurosci 9, 206-221.

[251] Stein, D.J., Szatmari, P., Gaebel, W., Berk, M., Vieta, E., Maj, M., de Vries, Y.A., Roest, A.M., de Jonge, P., Maercker, A.*, et al.* (2020). Mental, behavioral and neurodevelopmental disorders in the ICD-11: an international perspective on key changes and controversies. BMC Med 18, 21.

[252] Steinberg, L. (2010). A behavioral scientist looks at the science of adolescent brain development. Brain Cogn 72, 160-164.

[253] Taylor, H.G., and Clark, C.A. (2016). Executive function in children born preterm: Risk factors and implications for outcome. Semin Perinatol 40, 520-529.

[254] Tokariev, A., Stjerna, S., Lano, A., Metsaranta, M., Palva, J.M., and Vanhatalo, S. (2019). Preterm Birth Changes Networks of Newborn Cortical Activity. Cereb Cortex 29, 814-826.

[255] Tolner, E.A., Sheikh, A., Yukin, A.Y., Kaila, K., and Kanold, P.O. (2012). Subplate neurons promote spindle bursts and thalamocortical patterning in the neonatal rat somatosensory cortex. J Neurosci 32, 692-702.

[256] Tremblay, R., Lee, S., and Rudy, B. (2016). GABAergic Interneurons in the Neocortex: From Cellular Properties to Circuits. Neuron 91, 260-292.

[257] Tuncdemir, S.N., Wamsley, B., Stam, F.J., Osakada, F., Goulding, M., Callaway, E.M., Rudy, B., and Fishell, G. (2016). Early Somatostatin Interneuron Connectivity Mediates the Maturation of Deep Layer Cortical Circuits. Neuron 89, 521-535.

[258] Uhlhaas, P.J., and Singer, W. (2010). Abnormal neural oscillations and synchrony in schizophrenia. Nat Rev Neurosci 11, 100-113.

[259] Uylings, H.B., Groenewegen, H.J., and Kolb, B. (2003). Do rats have a prefrontal cortex? Behav Brain Res 146, 3-17.

[260] Vagnoni, C., Baruchin, L.J., Ghezzi, F., Ratti, S., Molnár, Z., and Butt, S.J.B. (2020). Ontogeny of the VIP+ interneuron sensory-motor circuit prior to active whisking. BioRxiv, 182238.

[261] Vaillant, A.R., Zanassi, P., Walsh, G.S., Aumont, A., Alonso, A., and Miller, F.D. (2002). Signaling mechanisms underlying reversible, activity-dependent dendrite formation. Neuron 34, 985-998.

[262] Van De Werd, H.J., Rajkowska, G., Evers, P., and Uylings, H.B. (2010). Cytoarchitectonic and chemoarchitectonic characterization of the prefrontal cortical areas in the mouse. Brain Struct Funct 214, 339-353.

[263] van Heukelum, S., Mars, R.B., Guthrie, M., Buitelaar, J.K., Beckmann, C.F., Tiesinga, P.H.E., Vogt, B.A., Glennon, J.C., and Havenith, M.N. (2020). Where is Cingulate Cortex? A Cross-Species View. Trends Neurosci 43, 285-299.

[264] Veit, J., Hakim, R., Jadi, M.P., Sejnowski, T.J., and Adesnik, H. (2017). Cortical gamma band synchronization through somatostatin interneurons. Nat Neurosci 20, 951-959.

[265] Vierock, J., Rodriguez-Rozada, S., Dieter, A., Pieper, F., Sims, R., Tenedini, F., Bergs, A.C.F., Bendifallah, I., Zhou, F., Zeitzschel, N.*, et al.* (2021). BiPOLES is an optogenetic tool developed for bidirectional dual-color control of neurons. Nat Commun 12, 4527.

[266] Virtanen, M.A., Lacoh, C.M., Fiumelli, H., Kosel, M., Tyagarajan, S., de Roo, M., and Vutskits, L. (2018). Development of inhibitory synaptic inputs on layer 2/3 pyramidal neurons in the rat medial prefrontal cortex. Brain Struct Funct 223, 1999-2012.

[267] Virtanen, M.A., Uvarov, P., Mavrovic, M., Poncer, J.C., and Kaila, K. (2021). The Multifaceted Roles of KCC2 in Cortical Development. Trends Neurosci 44, 378-392.

[268] Voigts, J., Newman, J.P., Wilson, M.A., and Harnett, M.T. (2020). An easy-to-assemble, robust, and lightweight drive implant for chronic tetrode recordings in freely moving animals. J Neural Eng 17, 026044.

[269] Vora, S.R., Camci, E.D., and Cox, T.C. (2015). Postnatal Ontogeny of the Cranial Base and Craniofacial Skeleton in Male C57BL/6J Mice: A Reference Standard for Quantitative Analysis. Front Physiol 6, 417.

[270] Walker, D.M., Bell, M.R., Flores, C., Gulley, J.M., Willing, J., and Paul, M.J. (2017). Adolescence and Reward: Making Sense of Neural and Behavioral Changes Amid the Chaos. J Neurosci 37, 10855-10866.

[271] Wallace, T.L., Ballard, T.M., and Glavis-Bloom, C. (2015). Animal paradigms to assess cognition with translation to humans. Handb Exp Pharmacol 228, 27-57.

[272] Wang, J., Tang, H., Wang, X., Zhang, X., Zhang, C., Zhang, M., Zhao, Y., Zhao, L., and Shen, J. (2016). The structural alteration of gut microbiota in low-birth-weight mice undergoing accelerated postnatal growth. Sci Rep 6, 27780.

[273] Wang, S.S., Shultz, J.R., Burish, M.J., Harrison, K.H., Hof, P.R., Towns, L.C., Wagers, M.W., and Wyatt, K.D. (2008). Functional trade-offs in white matter axonal scaling. J Neurosci 28, 4047-4056.

[274] Wang, X., McCoy, P.A., Rodriguiz, R.M., Pan, Y., Je, H.S., Roberts, A.C., Kim, C.J., Berrios, J., Colvin, J.S., Bousquet-Moore, D.*, et al.* (2011). Synaptic dysfunction and abnormal behaviors in mice lacking major isoforms of Shank3. Hum Mol Genet 20, 3093-3108.

[275] Wang, X.J. (2010). Neurophysiological and computational principles of cortical rhythms in cognition. Physiol Rev 90, 1195-1268.

[276] Wei, X., Thomas, N., Hatch, N.E., Hu, M., and Liu, F. (2017). Postnatal Craniofacial Skeletal Development of Female C57BL/6NCrl Mice. Front Physiol 8, 697.

[277] Whitford, K.L., Dijkhuizen, P., Polleux, F., and Ghosh, A. (2002). Molecular control of cortical dendrite development. Annu Rev Neurosci 25, 127-149.

[278] Wiegert, J.S., and Oertner, T.G. (2016). How (not) to silence long-range projections with light. Nat Neurosci 19, 527-528.

[279] Winship, I.R., Dursun, S.M., Baker, G.B., Balista, P.A., Kandratavicius, L., Maia-de-Oliveira, J.P., Hallak, J., and Howland, J.G. (2019). An Overview of Animal Models Related to Schizophrenia. Can J Psychiatry 64, 5-17.

[280] Womelsdorf, T., Valiante, T.A., Sahin, N.T., Miller, K.J., and Tiesinga, P. (2014). Dynamic circuit motifs underlying rhythmic gain control, gating and integration. Nat Neurosci 17, 1031-1039.

[281] Wong, A.H., and Josselyn, S.A. (2016). Caution When Diagnosing Your Mouse With Schizophrenia: The Use and Misuse of Model Animals for Understanding Psychiatric Disorders. Biol Psychiatry 79, 32-38.

[282] Wong, F.K., Bercsenyi, K., Sreenivasan, V., Portales, A., Fernandez-Otero, M., and Marin, O. (2018). Pyramidal cell regulation of interneuron survival sculpts cortical networks. Nature 557, 668-673.

[283] Workman, A.D., Charvet, C.J., Clancy, B., Darlington, R.B., and Finlay, B.L. (2013). Modeling transformations of neurodevelopmental sequences across mammalian species. J Neurosci 33, 7368-7383.

[284] Wu, X., Shukla, R., Alganem, K., Zhang, X., Eby, H.M., Devine, E.A., Depasquale, E., Reigle, J., Simmons, M., Hahn, M.K.*, et al.* (2021). Transcriptional profile of pyramidal neurons in chronic schizophrenia reveals lamina-specific dysfunction of neuronal immunity. Mol Psychiatry.

[285] Wu, X.S., Sun, J.Y., Evers, A.S., Crowder, M., and Wu, L.G. (2004). Isoflurane inhibits transmitter release and the presynaptic action potential. Anesthesiology 100, 663-670.

[286] Xu, X., Chini, M., Bitzenhofer, S.H., and Hanganu-Opatz, I.L. (2019). Transient Knock-Down of Prefrontal DISC1 in Immune-Challenged Mice Causes Abnormal Long-Range Coupling and Cognitive Dysfunction throughout Development. J Neurosci 39, 1222-1235.

[287] Yamamori, T., and Rockland, K.S. (2006). Neocortical areas, layers, connections, and gene expression. Neurosci Res 55, 11-27.

[288] Yamamoto, J., Suh, J., Takeuchi, D., and Tonegawa, S. (2014). Successful execution of working memory linked to synchronized high-frequency gamma oscillations. Cell 157, 845-857.

[289] Yamamoto, T., Sugaya, N., Siegle, G.J., Kumano, H., Shimada, H., Machado, S., Murillo-Rodriguez, E., Rocha, N.B., Nardi, A.E., Takamura, M.*, et al.* (2018). Altered Gamma-Band Activity as a Potential Biomarker for the Recurrence of Major Depressive Disorder. Front Psychiatry 9, 691.

[290] Yang, W., Chini, M., Popplau, J.A., Formozov, A., Dieter, A., Piechocinski, P., Rais, C., Morellini, F., Sporns, O., Hanganu-Opatz, I.L., and Wiegert, J.S. (2021). Anesthetics fragment hippocampal network activity, alter spine dynamics, and affect memory consolidation. PLoS Biol 19, e3001146.

[291] Yang, X.D., Liao, X.M., Uribe-Marino, A., Liu, R., Xie, X.M., Jia, J., Su, Y.A., Li, J.T., Schmidt, M.V., Wang, X.D., and Si, T.M. (2015). Stress during a critical postnatal period induces region-specific structural abnormalities and dysfunction of the prefrontal cortex via CRF1. Neuropsychopharmacology 40, 1203-1215.

[292] Yasuda, M., Nagappan-Chettiar, S., Johnson-Venkatesh, E.M., and Umemori, H. (2021). An activity-dependent determinant of synapse elimination in the mammalian brain. Neuron 109, 1333-1349 e1336.

[293] Yizhar, O., Fenno, L.E., Davidson, T.J., Mogri, M., and Deisseroth, K. (2011). Optogenetics in neural systems. Neuron 71, 9-34.

[294] Zhu, T. (2020). Challenges of Psychiatry Drug Development and the Role of Human Pharmacology Models in Early Development-A Drug Developer's Perspective. Front Psychiatry 11, 562660.

[295] Zurek, A.A., Yu, J., Wang, D.S., Haffey, S.C., Bridgwater, E.M., Penna, A., Lecker, I., Lei, G., Chang, T., Salter, E.W., and Orser, B.A. (2014). Sustained increase in alpha5GABAA receptor function impairs memory after anesthesia. J Clin Invest 124, 5437-5441.

5. Reprints of articles

- **Article I**

  Sileo L*, Bitzenhofer SH*, Spagnolo B*, **Pöpplau JA***, Holzhammer T, Pisanello M, et al. (2018) Tapered Fibers Combined With a Multi-Electrode Array for Optogenetics in Mouse Medial Prefrontal Cortex. *Front. Neurosci.* 2018;12:1–10.

  *These authors have contributed equally to this work as first authors

- **Article II**

  Chini M, Gretenkord S, Kostka JK, **Pöpplau JA**, Cornelissen L, Berde CB, et al. (2019) Neural Correlates of Anesthesia in Newborn Mice and Humans. *Front. Neural Circuits.* 13, 38.

- **Article III**

  Yang W*, Chini M*, **Pöpplau JA**, Formozov A, Dieter A, Piechocinski P, et al. (2021) Anesthetics fragment hippocampal network activity, alter spine dynamics, and affect memory consolidation. *PLOS Biology.* 19(4): e3001146.

  *These authors have contributed equally to this work as first authors

- **Article IV**

  Bitzenhofer SH, **Pöpplau JA**, Hanganu-Opatz IL (2020) Gamma activity accelerates during prefrontal development. *eLife.* 9, e56795.

- **Article V**

  Chini M, **Pöpplau JA**, Lindemann C, Carol-Perdiguer L, Hnida M, Oberländer V, et al. (2020) Resolving and Rescuing Developmental Miswiring in a Mouse Model of Cognitive Impairment. *Neuron.* 105(1):60-74.

- **Article VI**

  Bitzenhofer SH*, **Pöpplau JA***, Chini M, Marquardt A, Hanganu-Opatz IL (2021) A transient developmental increase in prefrontal activity alters network maturation and causes cognitive dysfunction in adult mice. *Neuron.* 109(8):1350-1364.e6.

  *These authors have contributed equally to this work as first authors

frontiers in Neuroscience

ORIGINAL RESEARCH
published: 26 October 2018
doi: 10.3389/fnins.2018.00771

Tapered Fibers Combined With a Multi-Electrode Array for Optogenetics in Mouse Medial Prefrontal Cortex

Leonardo Sileo[1†], Sebastian H. Bitzenhofer[2†], Barbara Spagnolo[1†], Jastyn A. Pöpplau[2†], Tobias Holzhammer[3,4], Marco Pisanello[1], Filippo Pisano[1], Elisa Bellistri[1], Emanuela Maglie[1,5], Massimo De Vittorio[1,5], Patrick Ruther[3,6‡], Ileana L. Hanganu-Opatz[2‡] and Ferruccio Pisanello[1‡]*

[1] Istituto Italiano di Tecnologia, Center for Biomolecular Nanotechnologies, Arnesano, Italy, [2] Developmental Neurophysiology, Institute of Neuroanatomy, University Medical Center Hamburg-Eppendorf, Hamburg, Germany, [3] Department of Microsystems Engineering (IMTEK), University of Freiburg, Freiburg im Breisgau, Germany, [4] ATLAS Neuroengineering bvba, Leuven, Belgium, [5] Dipartimento di Ingegneria dell'Innovazione, Universitá del Salento, Lecce, Italy, [6] Cluster of Excellence BrainLinks-BrainTools, University of Freiburg, Freiburg im Breisgau, Germany

OPEN ACCESS

Edited by:
Mikhail Lebedev,
Duke University, United States

Reviewed by:
Sotiris Masmanidis,
University of California, Los Angeles, United States
Kuan Hong Wang,
National Institute of Mental Health (NIMH), United States

***Correspondence:**
Ferruccio Pisanello
ferruccio.pisanello@iit.it

[†]These authors have contributed equally to this work as first authors

[‡]These authors have contributed equally to this work as last authors

Specialty section:
This article was submitted to Neural Technology, a section of the journal Frontiers in Neuroscience

Received: 31 July 2018
Accepted: 04 October 2018
Published: 26 October 2018

Citation:
Sileo L, Bitzenhofer SH, Spagnolo B, Pöpplau JA, Holzhammer T, Pisanello M, Pisano F, Bellistri E, Maglie E, De Vittorio M, Ruther P, Hanganu-Opatz IL and Pisanello F (2018) Tapered Fibers Combined With a Multi-Electrode Array for Optogenetics in Mouse Medial Prefrontal Cortex. Front. Neurosci. 12:771. doi: 10.3389/fnins.2018.00771

Optogenetics offers many advantages in terms of cell-type specificity, allowing to investigate functional connectivity between different brain areas at high spatial and neural population selectivity. In order to obtain simultaneous optical control and electrical readout of neural activity, devices called "optrodes" are employed. They are typically composed of a linear array of microelectrodes integrated on a slender probe shafts combined with flat-cleaved optical fibers (FF) placed above the recording sites. However, due to tissue absorption and scattering, light delivered by the FF unevenly illuminates the region of interest. This issue is of particular relevance when cellular populations are disposed along the dorso-ventral axis, such as in medial prefrontal cortex (mPFC) where cortical layers are aligned vertically. The study presented here aims at using tapered optical fibers (TFs) in combination with a 16-electrode neural probe to better access neural populations distributed along the dorso-ventral axis in the mPFC of newborn mice, restricting light delivery over a specific portion of the cortical layer of interest. Half of the TF surface is coated with a reflecting metal blocking the light to enable light delivery from one side of the probe's shaft only, with the probe base being designed to host the fiber without interfering with the wire-bonds that connect the recording sites to a printed circuit board. Monte-Carlo simulations have been implemented to define the relative TF-probe position and to identify the light intensity distribution above the recording sites. *In vivo* recordings indicate that simultaneous optical stimulation and electrical readout of neural activity in the mPFC benefit from the use of the engineered TF-based optrode in terms of a more uniform light distribution along the dorso-ventral axis and the possibility of restricting light delivery to a subset of electrical recording sites of interest.

Keywords: optogenetics, optrode, optical fibers, medial prefrontal cortex, tapered fibers

INTRODUCTION

With the increasing use of optogenetics to investigate functional connectivity in the mouse brain, the development of implantable devices for the simultaneous optical control and electrical monitoring of neural activity has been a major research focus in recent years (Grosenick et al., 2015; Cho et al., 2016; Pisanello et al., 2016). In their earlier implementation, these opto-electrodes (optrodes) were composed of a single light source and a single recording electrode (Gradinaru et al., 2007). More than 10 years of development have allowed obtaining different configurations, in which multiple optical stimulation channels can be accompanied with multi electrode arrays (MEA), providing multi-point optical control and electrical readout of neural activity. This can be obtained with several technologies, including μLEDs realized on one substrate comprising multiple recording sites (Wu et al., 2015) or on separate substrates (Ayub et al., 2016, 2017), flexible electronics (Kim et al., 2013; Goßler et al., 2014) or solid state waveguides (Segev et al., 2016; Schwaerzle et al., 2017; Lanzio et al., 2018) potentially providing multiple diffraction gratings for the outcoupling of light (Lanzio et al., 2018).

Although these technologies have the potential to help neuroscientists to better match stimulation and recording patterns with the anatomy of the brain region of interest, devices commonly used in neuroscience labs are still based on flat-cleaved optical fibers (FF) placed above linear arrays of electrodes for extracellular recording (Neuronexus, 2015; Atlas Neurotechnologies, 2017; Cambrige Neurotechnologies, 2017). However, this widely used approach encounters important limitations when the cellular population of interest is distributed along the dorso-ventral direction. Indeed, light emitted above the recording sites undergoes tissue attenuation and scattering. This results in a highly inhomogeneous distribution of power density, that can span several orders of magnitudes along the recording sites if they are positioned along more than 1 mm (Yizhar et al., 2011; Stujenske et al., 2015; Schmid et al., 2016). This fact is illustrated in **Figure 1A** with a Monte-Carlo simulation indicating the power density in brain tissue generated by an optical fiber with a numerical aperture NA = 0.22 and a core size of 100 μm, emitting light above a linear array of 16 electrodes. As indicated by the iso-power density lines, one obtains a decrease in optical power by about two orders of magnitude from the top most recording site to the bottom one. The above-mentioned technologies based in microsystems engineering can help in challenging this issue by placing multiple emitters very close to the individual recording sites. However, these discrete sets of light delivery points face different pitfalls, such as a potential tissue heating induced by Joule's effects for μLEDs, limited outcoupling efficiencies of diffraction gratings and the high commercialization costs to make these probes available to neuroscience labs. In this scenario, tapered optical fibers (TFs) (Pisanello et al., 2014, 2017) represent on the other hand a valid alternative to these approaches, allowing to tailor the light delivery pattern to the anatomy of the functional region of interest (Pisanello et al., 2018; Pisano et al., 2018). This is possible by exploiting two main features of these devices: (i) the narrowing waveguide allows to exploit mode division demultiplexing to deliver light gradually along a specific segment of the taper (Pisanello et al., 2018); indeed, as the taper narrows, the number of guided modes supported by the waveguide decreases, with modes not allowed to propagate toward the tip being outcoupled around the taper, and (ii) the possibility of using metal coatings to mask emission and to direct light to specific sites and directions (Pisano et al., 2018).

In this work we describe the engineering of an optrode based on a TF placed besides a 16-electrodes silicon-based neural probe following the Michigan style. The tapered fiber is designed to deliver light to the tissue above a subset of recording sites by exploiting a gold coating deposited on one half of the taper. Monte-Carlo simulations are implemented to define the relative TF-shank placement to obtain a fairly uniform power density in the tissue above the selected electrodes. The geometrical assembly is specifically thought to deliver light on (and to record signal from) pyramidal neurons in layers 2/3 of the prelimbic (PL) region of the medial prefrontal cortex (mPFC), in which Channelrhodopsin (ChR2) was selectively expressed by means of *in utero* electroporation (IUE). Extracellular electrophysiology data in mice at postnatal day (P) 8–10 confirm that the device can be used to monitor both local field potentials and single unit action potentials, with the TF design allowing for a more uniform illumination above the chosen subset of recording sites.

RESULTS

Optrode Design and Fabrication

The optrode presented in this work has been designed with the goal of engineering light delivery in the mPFC of rodents. Area- and layer-specific stimulation in prefrontal networks is critical to understand the origin and significance of neuronal activity patterns. Layer-specific optogenetic stimulation in the mPFC can be achieved by layer-specific expression of ChR2 by IUE (**Figure 1C**) (Bitzenhofer et al., 2017a,b). However, the restriction of transfection to specific subdivisions of the mPFC is difficult to achieve with *in utero* electroporation, but critical to study prefrontal function due to different or even opposing functions of dorsal and ventral subdivisions of the mPFC (Hardung et al., 2017). The alternative approach to restrict stimulation is to limit the area of illumination in transfected tissue. However, most commercially available optrodes are often based on linear array of electrodes for extracellular recording combined with a FF placed above the probe shank, as illustrated in **Figure 1A**. This configuration results in a highly inhomogeneous illumination of neurons directly facing the recording sites, as quantified by the displayed iso-power density lines, obtained with the Monte-Carlo method published by Stujenske et al. (2015) to assess the power density distribution along the electrode carrying probe shank.

To overcome this limitation and to obtain a more uniform light intensity across specific recording sites, we engineered an optrode design consisting of a silicon-based probe in combination with a TF emitting light from one side of the silicon shank (**Figure 1B**). The optical design of the TF is optimized

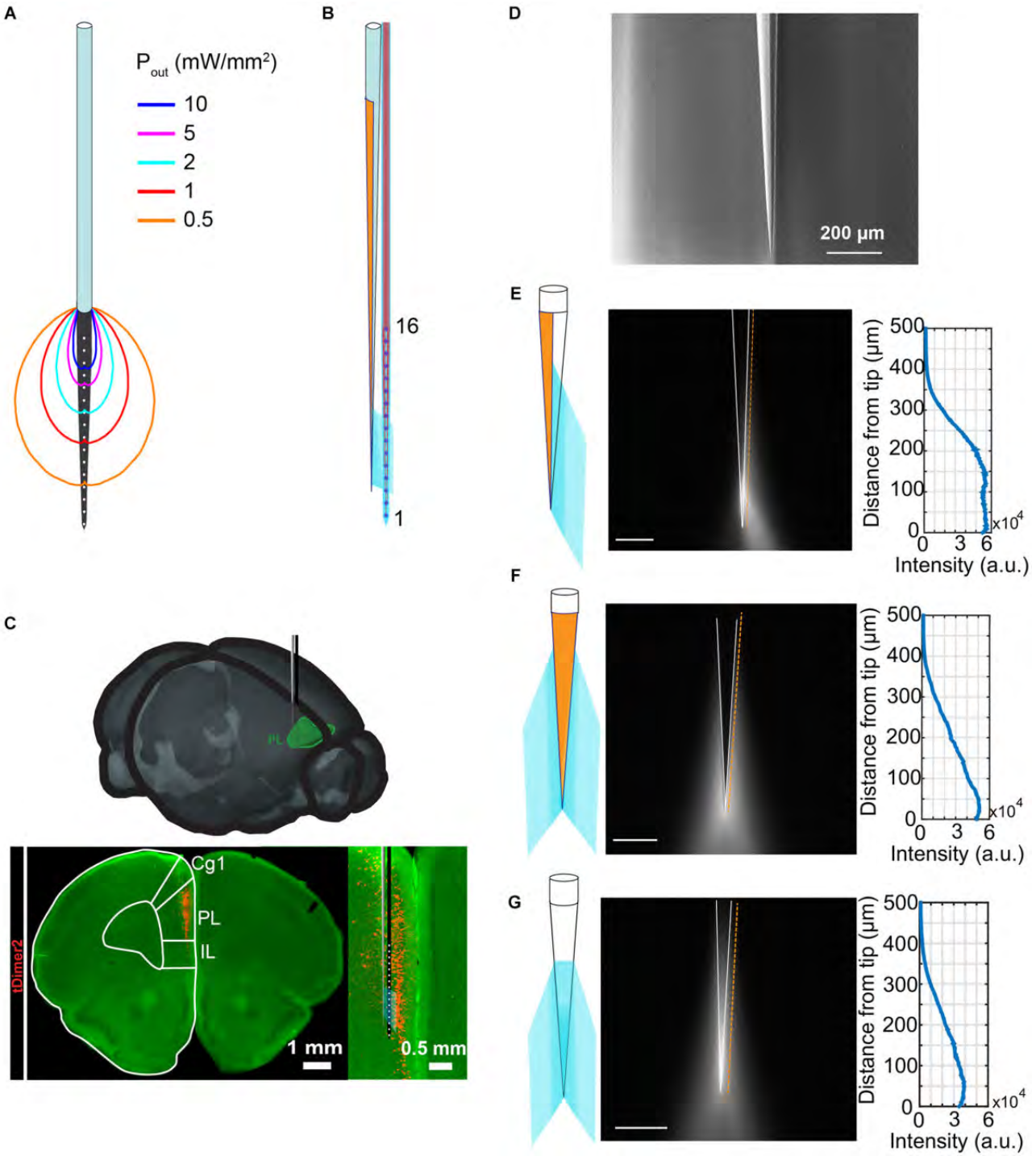

FIGURE 1 | Tailoring light delivery to a subregion of mPFC. **(A)** Representation of a commercially available optrode (A1 × 16-3mm-100-703-OA16LP, light fiber terminates 200 µm from the top recording site) and power density distribution iso-lines obtained with Monte-Carlo simulations for a total power of 1 mW delivered to the tissue. **(B)** Schematic representation of the optrode designed in this work, consisting of a half-metallized TF beside a multielectrode array. **(C)** Schematic overview of recording setup of the prelimbic subdivision of the mPFC. Digital photomontage reconstructing the position of the designed opto-electrode in the PL of a P9 mouse after IUE with ChR2(ET/TC) and tDimer2 (red) at embryonic age (E)15.5. Inset, optical light fiber (gray) and electrode shank (black) including the position of the recording sites (white) over the prelimbic depth are displayed at higher magnification. **(D)** Typical scanning electron microscope image of the realized TF. **(E–G)** Emission properties of the realized TF (side view) in a cartoon (left) and with the TF submerged in fluorescein:PBS droplet (center). Half of the taper is coated with ∼5 nm of Cr and ∼200 nm of Au. The graph (right) shows the emission profile acquired along the orange line in the center panel (scale bars represent 100 µm).

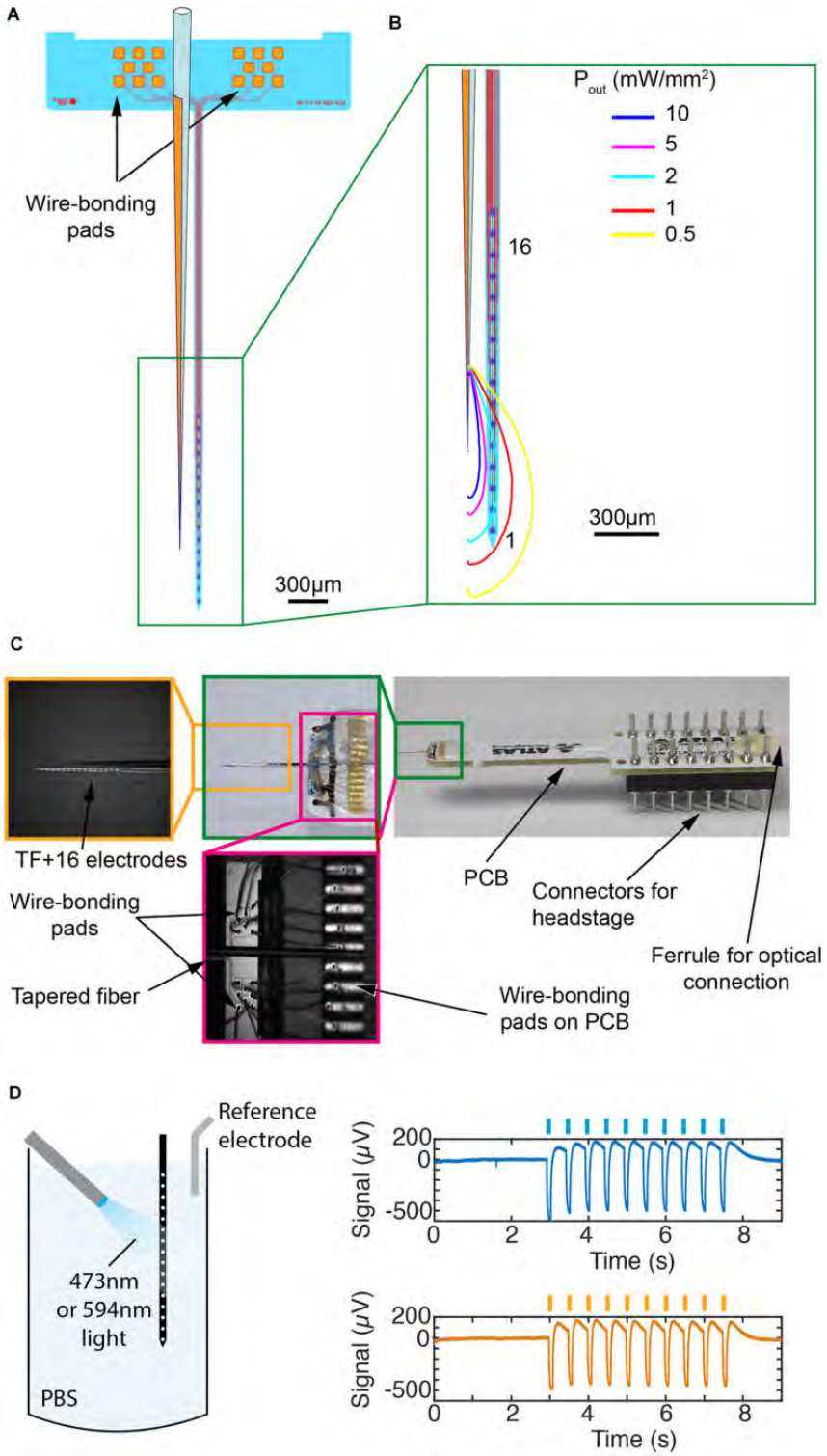

FIGURE 2 | Engineering of the TF-based optrode. **(A)** Layout of the silicon-based probe array with 16 IrO_x recording sites (diameter 35 µm) arranged at a pitch of 100 µm along a 4-mm-long probe shank and two groups of bonding pads arranged on the probe base (2.5 mm × 0.58 mm). Fiber position is also reported. **(B)** Monte-Carlo simulations of power density distribution iso-lines generated by the realized TF and overlapped with a sketch of the microelectrodes array. **(C)** Final optrode assembly on a PCB (right side) with enlarged view of the wire bonds on the probe base and PCB (center) and the tip region indicating the electrodes and TF (left). **(D)** Test of photoelectric effect induced by blue or yellow light in PBS. An optical fiber was placed 900 µm in front of the shank and delivers 200-ms-long pulses of 10 mW at wavelengths of 473 or 594 nm. The two graphs on the right show photoelectric effects generated by both wavelengths (the non-filtered signal is shown). Peak-to-peak amplitudes are 687 µV ± 13 µV and 624 µV ± 8 µV (mean ± std, n = 10) for the 473 and 594 nm lasers, respectively.

with the aim of providing a relatively uniform light intensity only in a region above selected recording sites along the probe shank. Further, the light emission geometry matches the dorso-ventral extension of the neural population of interest. Among the available TFs configurations (Pisano et al., 2018), we chose an optical fiber with core/cladding diameters of 105 μm/125 μm and a numerical aperture of NA = 0.22. The TF was realized by the heat-and-pull technique, resulting in a taper angle Ψ of ∼4°, which has already been shown to provide a tissue illumination over an extent of ∼400 μm (Pisanello et al., 2018). To deliver light only toward the shank, half of the taper is coated with a 200-nm-thick, thermally evaporated gold layer. A typical output of the fabrication process is shown in the scanning electron microscope image in **Figure 1D**, while the light delivery behavior of a TF with these geometrical characteristics is illustrated in **Figures 1E–G** for three different angular views, with the TF submerged in a fluorescent liquid. By virtue of the metal reflectivity, light delivery is confined to about 180° around the waveguide.

The neural probe applied here (see probe layout in **Figure 2A**) comprises a slender, tapered probe shaft with a maximum width of 75 μm at the probe base. The shaft carries 16 recording sites with a diameter of 35 μm arranged at a center-to-center distance of 100 μm. The probe shaft is connected to a rectangular probe base (2.5 mm × 0.58 mm) on which two groups of eight contact pads (80 μm × 80 μm) are arranged, interfacing the individual recording sites. The probe metallization is made of a layer stack of titanium/gold/titanium with the electrode metallization being realized by reactive sputter deposition and lift-off of iridium oxide. Probe shaft and base have a thickness of 50 μm and are realized using standard micro-electromechanical systems (MEMS) technologies combined with the etching before grinding (EBG) approach (Herwik et al., 2011).

To estimate light delivery properties in scattering tissue and to define the relative TF-shank placement, a modified Monte-Carlo algorithm was implemented to take into account light emission along a tapered waveguide. This approach allows to estimate light distribution around the taper and to engineer the relative position between the TF and the probe shank. **Figure 2B** shows iso-power density lines for a TF which is placed at ∼150 μm beside the shank emitting a total optical power of 1 mW. Tissue above the electrodes #1 through #6 receive a relatively uniform power density of about 2 mW/mm^2. Recording sites #8 to #16 receive an optical power density < 0.5 mW/mm^2, with a steep decrease across electrode #7. This represents a key difference between the TF-based optrode design and the commercially available system shown in **Figure 1A**, in which tissue above electrodes from #7 to #16 receive a power density above 2 mW/mm^2, but in a highly inhomogeneous way.

In order to position the TF within the above-mentioned distance relative to the probe shank, the electrical contact pads on the probe base interfacing the recording sites on the shank are laid out as depicted in **Figure 2A**, i.e., the two groups of eight pads are positioned off-center on the probe base with respect to the probe shaft position. This allows for wire bonding the pads to a printed circuit board (PCB) while the optical fiber is positioned in-between the two groups of contact pads. The resulting optrode is shown in **Figure 2C**, assembled by using two computer-controlled micromanipulators to obtain a precise relative positioning and axial alignment between TF, probe shank and PCB. Once in place, the TF is adhesively fixed to the probe base using UV curable epoxy glue, which at the same time mechanically protects the wire bonds between the pads on the probe base pads and PCB. The optical microscopy image in **Figure 2C** illustrates the highly parallel alignment between TF and probe shank expected to minimize tissue damage during optrode insertion into the brain.

Optical Control and Electrical Readout of Neuronal Activity in the mPFC of Neonatal Mice

Light fibers on commercially available optrodes typically end above the top recording sites, i.e., the electrode positioned closest to the probe base. With this configuration light can be easily restricted to local patches of cortex at the surface of the brain, such as somatosensory or motor cortices. The mPFC is located at the midline of the forebrain with vertically oriented layers. With the available optrodes it is hard to restrict the inhomogeneous illumination of cortical patches to prefrontal subdivisions, especially for small sized neonatal mouse brains. In order to evaluate whether the TF-based optrode engineered in this work overcomes these limitations, we compared it to a commercially available FF-based optrode (NeuroNexus, A1 × 16-3 mm-100-703-OA16LP, light fiber terminates 200 μm from the top recording site, **Figure 1A**) by using *in vivo* optogenetics in neonatal mice. For extracellular recordings the optrodes were inserted (2.4 mm) into the mPFC to reach ChR2-expressing pyramidal neurons in layers 2/3 of the prelimbic subdivision in mice at the age of (P) 8–10 (**Figure 1C**). Laser power for light delivery was adjusted to trigger neuronal spiking in response to $>$ 20% of 3 ms-long light pulses at 16 Hz. Typical single channel local field potentials (LFPs, right column) and multi-unit activity (MUA, middle column), defined as activity in the frequency band from 500–9000 Hz, are displayed in **Figures 3A–D** for FF and TF optrodes, respectively. TF and FF induced neural activity was compared in response to blue light pulses (473 nm, total output power ∼1 mW, **Figures 3A,C**). Blue light pulses evoked comparable LFP and MUA for light delivery with TF and FF at the recording sites close to the fiber output, with the TF optrode eliciting neural activity on about 7 recordings sites starting from the tip, as expected from the Monte-Carlo simulations shown in **Figure 2B**. To characterize light artifacts of the probes and to distinguish them from induced activity in the same position where light-triggered activity is measured, yellow light pulses (594 nm, **Figures 3B,D**) that do not activate ChR2 were used. *Ex vivo* recordings of photoelectric effects with pulsed light of 473 and 594 nm induced similar light artifacts (**Figure 2D**). To evaluate the evoked responses over multiple animals, a modulation index was defined as $(x_{\text{stim}} - x_{\text{pre}})/(x_{\text{stim}} + x_{\text{pre}})$, where x_{stim} is the median amplitude of the

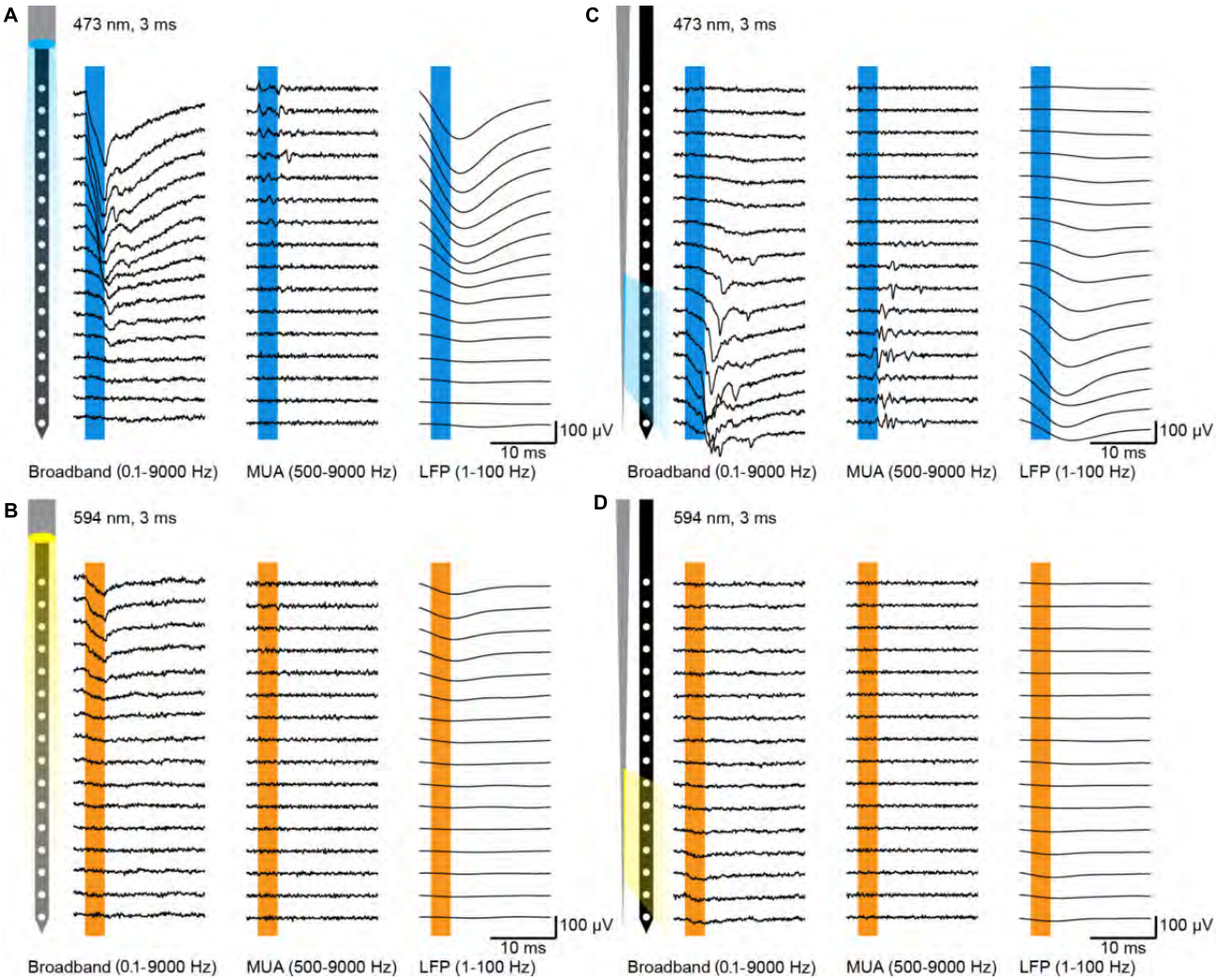

FIGURE 3 | Typical electrophysiology recordings with FF- and TF-based optrodes. **(A)** Characteristic extracellular multi-site recording of light-induced activity (3 ms pulse, 473 nm) with illumination from the top in the mPFC of a neonatal mouse expressing ChR2(ET/TC) in layer 2/3 pyramidal neurons transfected by IUE. **(B)** Same as A for stimulation with yellow light (3 ms pulse, 594 nm) to trigger pure light artifact. **(C,D)** Same as A,B for illumination from the side with a TF.

broadband signal, LFP or MUA in response to the light pulse and x_{pre} is the median signal amplitude before the pulse. Results of this analysis are reported in **Figure 4**. For both LFP and MUA channels, top illumination with FF evoked strong activity at the topmost recording sites with waning modulation toward the shaft's tip, whereas illumination with TF triggered activity mainly in the illuminated recording sites, as shown in **Figures 4A,C**, respectively. Compared to FF, TF-based optrodes illuminate a subset of recording sites more homogenously resulting in more evenly distributed activity. Light artifacts recorded with yellow light stimulation were present in the frequency band of LFP, but not in MUA for TF and FF, as shown by the single channel data in **Figures 3B,D** and multiple animal averages in **Figures 4B,D**. Thus, TFs provide sufficient light output to trigger comparable activity in mPFC of neonatal mice as FF, with TF allowing for a more homogenous illumination of local cortical patches.

DISCUSSION AND CONCLUSION

In this work we propose an optrode design thought to better distribute light on cellular populations distributed in the dorso-ventral direction and to restrict illumination to subregions of the mPFC. It is based on a half-coated TF placed beside a 16-electrode silicon-based neural probe, whose relative position allows for delivering light to brain tissue addressed by a subset of the 16 recording sites. The system was tested on neonatal mice expressing ChR2 in layers 2/3 pyramidal neurons in the mPFC, distributed dorso-ventrally over ∼2 mm, as shown in **Figure 1C**. To reduce the invasiveness of the optrode, also because of the mice's young age at the time of the experiment, we chose to work with the smallest-available TF (NA = 0.22, core/cladding diameters 105 µm/125 µm, taper angle $\Psi \approx 4°$, sub-micrometer tip). FF commonly used to reach this region,

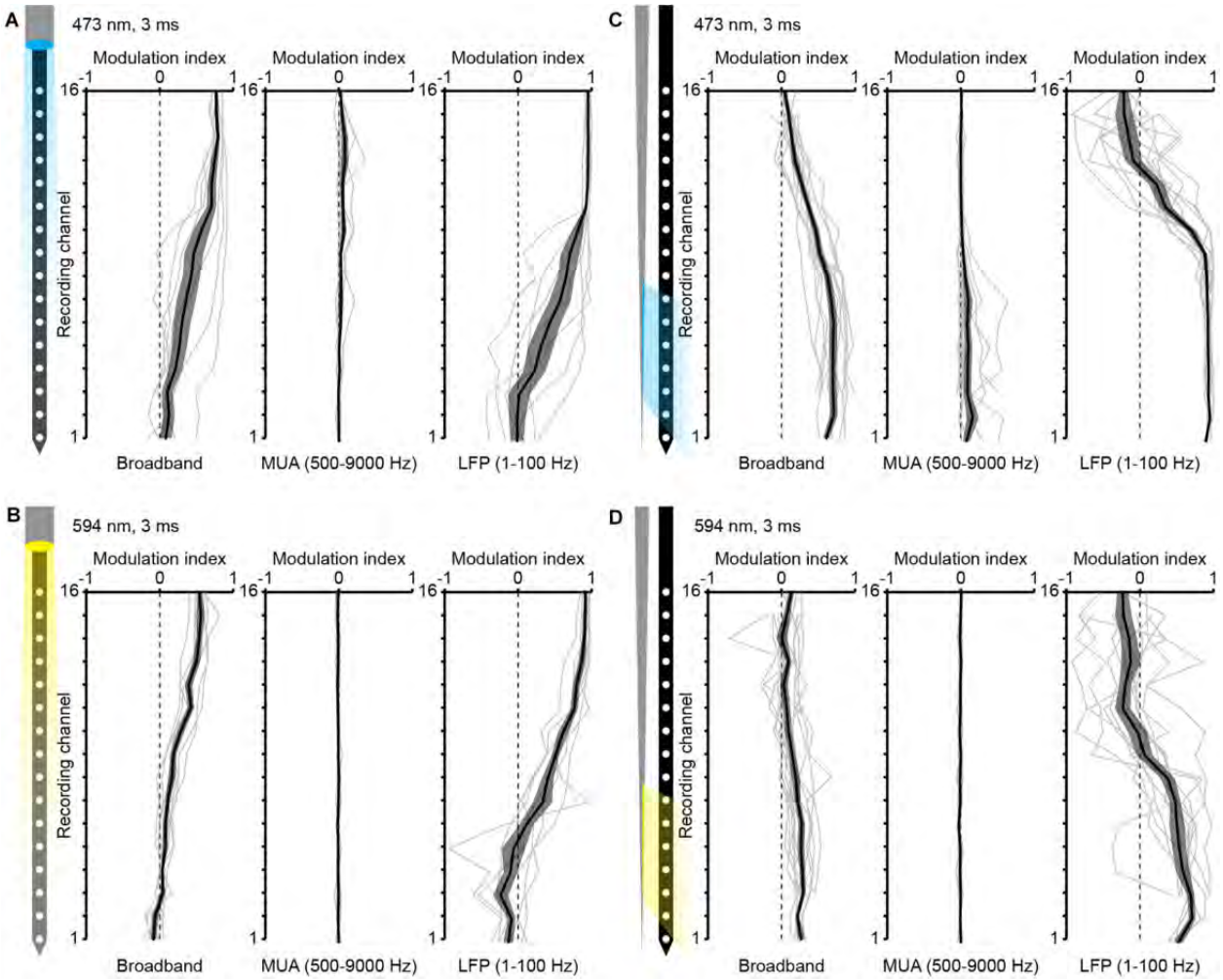

FIGURE 4 | *In vivo* experiments over multiple animals. **(A)** Quantification of the modulation index over recording sites for illumination with blue light pulses (3 ms, 473 nm) with a commercial optrode with illumination from the top (n = 7 mice). **(B)** Same as A for illumination from the side with a TF (n = 12 mice). **(C)** Same as A with yellow light (3 ms, 596 nm) to estimate photoelectric response. **(D)** Same as C to estimate photoelectric response of TF-based optrodes.

have diameters of 125 μm causing increased tissue damage. They generate light-stimulated activity over ∼7 recording sites (**Figure 3A**) with a highly inhomogeneous power density, ranging from 20 mW/mm^2 to 2 mW/mm^2, exponentially decreasing as the distance from facet increases (**Figure 1A**). Moreover, the geometrical configuration of FF-based optrodes has an intrinsic limitation related to fiber positioning: electrodes close to the shaft's tip interfacing with the less-damaged tissue can hardly be reached with a high-enough optical power density, unless light power delivered to the fiber is increased by two orders of magnitude (Schmid et al., 2016). Instead, placing a side-emitting TF beside the neural probe allows to direct light on the tissue above the selected recording sites. Although the data reported here are shown for illumination of recording sites close to the shank's tip, the TF/probe design enables using any subset of adjacent recording sites by changing the relative position of the TF along the probe shaft. To define the set of illuminated recording sites, a Monte-Carlo simulation approach was implemented, allowing to identify the geometrical distribution of photons and the above-threshold region prior to the experiment. This, coupled with the possibility to engineer light delivery geometries by tailoring the taper angle (Pisanello et al., 2018) or using micro and nano fabrication approaches to structure the fiber taper (Pisanello et al., 2014, 2015; Pisano et al., 2018; Rizzo et al., 2018), let us envision that the TF-based optrode configuration can be extended to several experimental designs.

The activation of cells adjacent to specific subsets of recordings sites can be obtained also by other technologies, including optrodes based on μLEDs and solid-state waveguides. However, these approaches are based on different technological platforms that require complex fabrication processes, highly increasing the costs and time to bring them to market. Our design is instead based on a well-established combination between optical fibers and silicon-based neural probes following the Michigan style, and it requires only a few process steps to be modified: (i) layout of the

wire-bonding pads on the probe base and (ii) precise alignment and assembly of the TF relative to the probe shaft.

TF-based optrodes provide a better control of neuronal activity, due to homogenous illumination of several recording sites induced by the highly different distribution of light typically seen for FF-based optrodes. They also improve spatial restriction of illumination to local patches of vertically oriented cortical areas. The ability to homogenously illuminate locally restricted patches in vertically oriented cortices, such as the mPFC, allows to investigate functions and interactions of prefrontal subdivisions, such as the prelimbic and infralimbic PFC throughout development. Overall, the optrode configuration proposed in this work allows for a better access to dorso-ventrally distributed neuronal populations, improving light delivery uniformity and to choose the position and the number of the recording sites to be illuminated.

MATERIALS AND METHODS

Realization of the Multi-Electrodes Probe

The silicon-based electrode array, as illustrated in **Figure 2A** with the respective mask layout, is realized using the etching before grinding (EBG) technology detailed elsewhere (Herwik et al., 2011). It applies 4-inch silicon (Si) wafers which are covered on their front side with a stress-compensated 1-μm-thick layer stack of silicon-oxide (SiO_x) and silicon nitride (Si_xN_y) realized by plasma enhanced chemical vapor deposition (PEVCD). Next, the probe metallization which interfaces the recording sites with the contact pads via 1.5-μm-wide metal tracks is deposited and patterned using sputter deposition of titanium (Ti, 30 nm), gold (Au, 250 nm) and Ti (30 nm) and lift-off applying an image reversal resist, respectively. The metallization is covered by another, stress-compensated PECVD stack of Si_xO/Si_xN_x (total thickness 1.5 μm). This layer stack is patterned using reactive ion etching (RIE) in combination with a positive photoresist serving as the masking layer to electrically access the contact pads (80 × 80 μm^2) on the probe base and the recording sites through respective vias (diameter 5 μm). This etch step removes as well the upper Ti layer exposing the Au of the probe metallization. Next, the electrode metallization (diameter 35 μm) is deposited by sputter deposition and reactive sputter deposition of iridium (Ir, 100 nm) and iridium oxide (IrO_x, 200 nm), respectively. The Ir/IrO_x layer stack is patterned using lift-off as well. Subsequently, we pattern the dielectric PECVD layer stacks (total thickness 2.5 μm) using RIE followed by deep reactive ion etching (DRIE) of the bulk silicon substrate to generate trenches (width 40 μm) defining to probe shape. These trenches are etched to a depth t_{etch} exceeding the intended probe shaft thickness t_{shaft} by 20 μm. Finally, the silicon wafer is ground from the rear using a commercial grinding process by DISCO Hi-TEC Europe GmbH (Kirchheim, Germany) to a thickness of 50 μm by which the probes are automatically released. Once peeled from an adhesive tape used during wafer grinding, the probes are ready for assembly. For this, probes are adhesively fixed onto a PCB and wire bonded using gold wires with a diameter of 25.4 μm.

Tapered Fibers Fabrication and Assembly With the Neural Probe

Tapered fibers were obtained from OptogeniX[1] with a taper angle of $\psi \approx 4°$ and a numerical aperture of NA = 0.22 (core/cladding diameters 105/125 μm) (Pisanello et al., 2018). A 5-nm-thick Cr layer and a 200-nm-thick gold layer were deposited along the taper using evaporation which blocks ca. 180° of the TF from light emission. In order to ensure a correct deposition of the layers also close to the tip of the TF, the fiber was slightly tilted toward the crucibles during evaporation. After metal deposition, the obtained fibers were connectorized with a ceramic ferrule (diameter 1.25 mm) resulting in an overall fiber length that matches with the neural probe-PCB assembly (**Figure 2C**). Optical properties of the waveguide were tested in a PBS:fluorescein bath and emission profiles were determined by recording the fluorescence counts on a line parallel to the taper edge (**Figures 1E–G**).

The as prepared TF is fixed on a micromanipulator (Scientifica) and placed in parallel to the probe shank at a distance of ∼100 μm aligning the TF tip with the fifth electrode. The non-tapered fiber section is positioned in the space between the two groups of probe base bonding pads and fixed with UV curable epoxy glue.

Monte-Carlo Simulations

Monte-Carlo simulations were implemented in Matlab to estimate the power density distribution generated by flat-flat cleaved fibers (**Figure 1A**) or TFs (**Figure 2B**). In the case of FFs, the method proposed by Stujenske et al. (2015) was used to model an optical fiber with NA = 0.22 and core/cladding diameters of 105/125 μm, emitting a total power of 1 mW. In the case of metal-coated TFs, the code described in Stujenske et al. (2015) was modified in order to account for light emission from the conical surface of the taper. This was implemented by modifying the initial conditions of emitted photons in terms of emission position and output angles. Photon emission probability along the taper was estimated from the direct measurement of the light emission profile (see measurement in **Figure 1E**), while output angles were obtained by ray tracing simulations (Pisanello et al., 2018). Around the taper axis, photons emission probability was considered uniform in the angular range 0° to 180° and zero from 180° to 360°, to simulate the presence of the metal layer. Scattering was simulated in a domain of size 3 mm × 3 mm, discretized with a mesh of 5 μm × 5 μm. The matrix resulting from the simulation represents a spatial distribution of photons, weighted in intensity according to the energy left in a steady state (Stujenske et al., 2015). To draw the iso-power density lines in **Figures 1A** and **2B**, a 2-dimensional filter and a threshold were applied according to the examined power density volume. Output power was set to 1 mW and the Henyey–Greenstain scattering model was used at λ = 473 nm, with absorption

[1] www.optogenix.com

coefficient $a = 0.37\ mm^{-1}$, scattering coefficient $s = 11\ mm^{-1}$ and anisotropy parameter $g = 0.89$.

In utero Electroporation

All experiments were performed in compliance with the German laws and the guidelines of the European Community for the use of animals in research and were approved by the local ethical committee (Behörde für Gesundheit und Verbraucherschutz/Lebensmittelsicherheit und Veterinärwesen) (132/12, N18/015). Timed-pregnant C57Bl/6J mice were housed individually in breeding cages at a 12 h light/12 h dark cycle and fed *ad libitum*. Vaginal plug detection was defined embryonic day (E) 0.5, while birth was assigned as postnatal day (P) 0. Additional wet food supplemented with 2–4 drops Metacam (0.5 mg/ml, Boehringer-Ingelheim, Germany) was given from 1 day before until 2 days after surgery. At E15.5 pregnant mice were injected subcutaneously with buprenorphine (0.05 mg/kg body weight) 30 min before surgery. Surgery was performed under isoflurane anesthesia (induction: 5%, maintenance: 3.5%) on a heating blanket, eyes were covered with eye ointment, and toe pinch reflex and breathing were monitored throughout the surgery. Uterine horns were exposed and moistened with warm sterile PBS. 0.75–1.25 µl solution containing 1.25 µg/µl DNA pAAV-CAG-ChR2(E123T/T159C)-2A-tDimer2 and 0.1% fast green dye were injected in the right lateral ventricle of each embryo using pulled borosilicate glass capillaries. Each embryo was placed between the electroporation tweezer-type paddles (5 mm diameter, Protech, TX, United States) oriented at a 20° leftward angle from the midline and a 10° angle downward from anterior to posterior to transfect neural precursor cells of layer 2/3 medial prefrontal pyramidal cells. Five electrode pulses (35 V, 50 ms, 950 ms interval) were applied with an electroporator (CU21EX, BEX, Japan). Uterine horns were placed back into the abdominal cavity after electroporation and abdominal muscles and skin were sutured.

In vivo Tests

Multi-site extracellular recordings were performed in the mPFC of P8-10 mice. Mice were injected i.p. with urethane (1 mg/g body weight; Sigma-Aldrich, MO, United States) prior to surgery. Under isoflurane anesthesia (induction: 5%, maintenance: 2.5%) the head was fixed into a stereotaxic apparatus using two plastic bars mounted on the nasal and occipital bones with dental cement. The bone above the PFC (0.5 mm anterior to bregma, 0.1 mm right to the midline for layer 2/3) was carefully removed by drilling a hole of < 0.5 mm in diameter. After a 10–20 min recovery period on a heating blanket, linear multi-site optrodes with a flat-cleaved light fiber attached ending 200 µm above the first recording site (NeuroNexus, MI, United States), or linear multi-site neural probes with a tapered light fiber attached were inserted 2.4 mm deep into the mPFC perpendicular to the skull surface. A silver wire in the cerebellum served as ground and reference electrode. Extracellular signals were band-pass filtered (0.1–9000 Hz) and digitized (32 kHz) with a multi-channel extracellular amplifier (Digital Lynx SX, Neuralynx, Bozeman, MO, United States) and the Cheetah acquisition software (Neuralynx, Bozeman, MO, United States). Pulsed light stimulations were performed with an arduino uno (Arduino, Italy) controlled laser (473 nm/594 nm, Omicron, Austria). Recording signals were band pass filtered to isolate local field potential (LFP, 1–100 Hz) and multi-unit activity (MUA, 500–9000 Hz) using a third-order Butterworth filter forward and backward to preserve phase information. To reduce signal contamination by photoelectric effects, 10-ms-long time windows starting 1 ms after the end of the light pulse were analyzed.

DATA AVAILABILITY STATEMENT

The datasets for this study are available upon request to the authors.

AUTHOR CONTRIBUTIONS

All authors listed have made a substantial, direct and intellectual contribution to the work, and approved it for publication.

FUNDING

FiP, BS, FeP, EB, and EM acknowledge funding from the European Research Council under the European Union's Horizon 2020 research and innovation program (#677683). MDV acknowledge funding from the European Research Council under the European Union's Horizon 2020 research and innovation program (#692943). SB, JP, and IH-O acknowledge funding from the European Research Council under the European Union's Horizon 2020 research and innovation program (#681577) and from the German Research Foundation [SFB 936 (B5) and SPP 1665 (Ha4466/12-1)]. LS, MP, and MDV are funded by the US National Institutes of Health (U01NS094190). This work was partly supported by BrainLinks-BrainTools, Cluster of Excellence funded by the German Research Foundation (DFG, Grant No. EXC 1086).

REFERENCES

Atlas Neurotechnologies (2017). Available at: http://www.atlasneuro.com/

Ayub, S., Barz, F., Paul, O., and Ruther, P. (2016). "Heterogeneous 3D optrode with variable spatial resolution for optogenetic stimulation and electrophysiological recording," in *Proceedings of the 38th Annual International Conference of the IEEE Engineering in Medicine and Biology Society (EMBC)*, (Piscataway, NJ: IEEE), 1762–1765. doi: 10.1109/EMBC.2016.7591058

Ayub, S., Gentet, L. J., Fiáth, R., Schwaerzle, M., Borel, M., David, F., et al. (2017). Hybrid intracerebral probe with integrated bare LED chips for optogenetic studies. *Biomed. Microdevices* 19:49. doi: 10.1007/s10544-017-0190-3

Bitzenhofer, S. H., Ahlbeck, J., and Hanganu-Opatz, I. L. (2017a). Methodological approach for optogenetic manipulation of neonatal neuronal networks. *Front. Cell. Neurosci.* 11:239. doi: 10.3389/fncel.2017.00239

Bitzenhofer, S. H., Ahlbeck, J., Wolff, A., Wiegert, J. S., Gee, C. E., Oertner, T. G., et al. (2017b). Layer-specific optogenetic activation of pyramidal neurons

causes beta–gamma entrainment of neonatal networks. *Nat. Commun.* 8:14563. doi: 10.1038/ncomms14563

Cambrige Neurotechnologies (2017). Available at: https://www.cambridgeneurotech.com/

Cho, Y. K., Zheng, G., Augustine, G. J., Hochbaum, D., Cohen, A., Knöpfel, T., et al. (2016). Roadmap on neurophotonics. *J. Opt.* 18:093007. doi: 10.1088/2040-8978/18/9/093007

Goßler, C., Bierbrauer, C., Moser, R., Kunzer, M., Holc, K., Pletschen, W., et al. (2014). GaN-based micro-LED arrays on flexible substrates for optical cochlear implants. *J. Phys. D Appl. Phys.* 47:205401. doi: 10.1088/0022-3727/47/20/205401

Gradinaru, V., Thompson, K. R., Zhang, F., Mogri, M., Kay, K., Schneider, M. B., et al. (2007). Targeting and readout strategies for fast optical neural control in vitro and in vivo. *J. Neurosci.* 27, 14231–14238. doi: 10.1523/JNEUROSCI.3578-07.2007

Grosenick, L., Marshel, J. H., and Deisseroth, K. (2015). Closed-loop and activity-guided optogenetic control. *Neuron* 86, 106–139. doi: 10.1016/J.NEURON.2015.03.034

Hardung, S., Epple, R., Jäckel, Z., Eriksson, D., Uran, C., Senn, V., et al. (2017). A functional gradient in the rodent prefrontal cortex supports behavioral inhibition. *Curr. Biol.* 27, 549–555. doi: 10.1016/j.cub.2016.12.052

Herwik, S., Paul, O., and Ruther, P. (2011). Ultrathin silicon chips of arbitrary shape by etching before grinding. *J. Microelectromech. Syst.* 20, 791–793. doi: 10.1109/JMEMS.2011.2148159

Kim, T., McCall, J. G., Jung, Y. H., Huang, X., Siuda, E. R., Li, Y., et al. (2013). Injectable, cellular-scale optoelectronics with applications for wireless optogenetics. *Science* 340, 211–216. doi: 10.1126/science.1232437

Lanzio, V., West, M., Koshelev, A., Telian, G., Micheletti, P., Lambert, R., et al. (2018). High-density electrical and optical probes for neural readout and light focusing in deep brain tissue. *J. Micro Nanolithogr. MEMS MOEMS* 17:1. doi: 10.1117/1.JMM.17.2.025503

Neuronexus (2015). Available at: http://neuronexus.com/

Pisanello, F., Mandelbaum, G., Pisanello, M., Oldenburg, I. A., Sileo, L., Markowitz, J. E., et al. (2017). Dynamic illumination of spatially restricted or large brain volumes via a single tapered optical fiber. *Nat. Neurosci.* 20, 1180–1188. doi: 10.1038/nn.4591

Pisanello, F., Sileo, L., and De Vittorio, M. (2016). Micro- and nanotechnologies for optical neural interfaces. *Front. Neurosci.* 10:70. doi: 10.3389/fnins.2016.00070

Pisanello, F., Sileo, L., Oldenburg, I. A., Pisanello, M., Martiradonna, L., Assad, J. A., et al. (2014). Multipoint-emitting optical fibers for spatially addressable in vivo optogenetics. *Neuron* 82, 1245–1254. doi: 10.1016/j.neuron.2014.04.041

Pisanello, M., Della Patria, A., Sileo, L., Sabatini, B. L., De Vittorio, M., and Pisanello, F. (2015). Modal demultiplexing properties of tapered and nanostructured optical fibers for in vivo optogenetic control of neural activity. *Biomed. Opt. Express* 6, 4014–4026. doi: 10.1364/BOE.6.004014

Pisanello, M., Pisano, F., Sileo, L., Maglie, E., Bellistri, E., Spagnolo, B., et al. (2018). Tailoring light delivery for optogenetics by modal demultiplexing in tapered optical fibers. *Sci. Rep.* 8:4467. doi: 10.1038/s41598-018-22790-z

Pisano, F., Pisanello, M., Sileo, L., Qualtieri, A., Sabatini, B. L., De Vittorio, M., et al. (2018). Focused ion beam nanomachining of tapered optical fibers for patterned light delivery. *Microelectron. Eng.* 195, 41–49. doi: 10.1016/j.mee.2018.03.023

Rizzo, A., Lemma, E. D., Pisano, F., Pisanello, M., Sileo, L., De Vittorio, M., et al. (2018). Laser micromachining of tapered optical fibers for spatially selective control of neural activity. *Microelectron. Eng.* 192, 88–95. doi: 10.1016/J.MEE.2018.02.010

Schmid, F., Wachsmuth, L., Schwalm, M., Prouvot, P.-H., Jubal, E. R., Fois, C., et al. (2016). Assessing sensory versus optogenetic network activation by combining (o)fMRI with optical $Ca2^{+}$ recordings. *J. Cereb. Blood Flow Metab.* 36, 1885–1900. doi: 10.1177/0271678X15619428

Schwaerzle, M., Paul, O., and Ruther, P. (2017). Compact silicon-based optrode with integrated laser diode chips, SU-8 waveguides and platinum electrodes for optogenetic applications. *J. Micromech. Microeng.* 27:065004. doi: 10.1088/1361-6439/aa6ad4

Segev, E., Reimer, J., Moreaux, L. C., Fowler, T. M., Chi, D., Sacher, W. D., et al. (2016). Patterned photostimulation via visible-wavelength photonic probes for deep brain optogenetics. *Neurophotonics* 4:011002. doi: 10.1117/1.NPh.4.1.011002

Stujenske, J. M., Spellman, T., and Gordon, J. A. (2015). Modeling the spatiotemporal dynamics of light and heat propagation for in vivo optogenetics. *Cell Rep.* 12, 525–534. doi: 10.1016/j.celrep.2015.06.036

Wu, F., Stark, E., Ku, P.-C., Wise, K. D., Buzsáki, G., and Yoon, E. (2015). Monolithically integrated μLEDs on silicon neural probes for high-resolution optogenetic studies in behaving animals. *Neuron* 88, 1136–1148. doi: 10.1016/j.neuron.2015.10.032

Yizhar, O., Fenno, L. E., Davidson, T. J., Mogri, M., and Deisseroth, K. (2011). Optogenetics in neural systems. *Neuron* 71, 9–34. doi: 10.1016/J.NEURON.2011.06.004

Conflict of Interest Statement: TH had an academic [Department of Microsystems Engineering (IMTEK), Albert-Ludwigs-Universität Freiburg, Germany] and company (ATLAS Neuroengineering bvba, Leuven, Belgium) affiliation.

The remaining authors declare that the research was conducted in the absence of any commercial or financial relationships that could be construed as a potential conflict of interest.

frontiers in Neural Circuits

ORIGINAL RESEARCH
published: 22 May 2019
doi: 10.3389/fncir.2019.00038

Neural Correlates of Anesthesia in Newborn Mice and Humans

Mattia Chini[1], *Sabine Gretenkord*[1], *Johanna K. Kostka*[1], *Jastyn A. Pöpplau*[1], *Laura Cornelissen*[2,3], *Charles B. Berde*[2,3], *Ileana L. Hanganu-Opatz*[1*†] *and Sebastian H. Bitzenhofer*[1*†‡]

[1]Developmental Neurophysiology, Institute of Neuroanatomy, University Medical Center Hamburg-Eppendorf, Hamburg, Germany, [2]Department of Anesthesiology, Critical Care and Pain Medicine, Boston Children's Hospital, Boston, MA, United States, [3]Department of Anesthesia, Harvard Medical School, Boston, MA, United States

Monitoring the hypnotic component of anesthesia during surgeries is critical to prevent intraoperative awareness and reduce adverse side effects. For this purpose, electroencephalographic (EEG) methods complementing measures of autonomic functions and behavioral responses are in use in clinical practice. However, in human neonates and infants existing methods may be unreliable and the correlation between brain activity and anesthetic depth is still poorly understood. Here, we characterized the effects of different anesthetics on brain activity in neonatal mice and developed machine learning approaches to identify electrophysiological features predicting inspired or end-tidal anesthetic concentration as a proxy for anesthetic depth. We show that similar features from EEG recordings can be applied to predict anesthetic concentration in neonatal mice and humans. These results might support a novel strategy to monitor anesthetic depth in human newborns.

Keywords: development, anesthesia, LFP, EEG, mouse, human, machine learning, network dynamics

OPEN ACCESS

Edited by:
Tommaso Pizzorusso, University of Florence, Italy

Reviewed by:
Paola Binda, University of Pisa, Italy
Laura Baroncelli, Italian National Research Council (CNR), Italy

***Correspondence:**
Ileana L. Hanganu-Opatz
hangop@zmnh.uni-hamburg.de
Sebastian H. Bitzenhofer
sbitzenhofer@ucsd.edu

†These authors have contributed equally to this work

‡Present address:
Sebastian H. Bitzenhofer, Center for Neural Circuits and Behavior, Department of Neurosciences, University of California, San Diego, La Jolla, CA, United States

Received: *31 January 2019*
Accepted: *03 May 2019*
Published: *22 May 2019*

Citation:
Chini M, Gretenkord S, Kostka JK, Pöpplau JA, Cornelissen L, Berde CB, Hanganu-Opatz IL and Bitzenhofer SH (2019) Neural Correlates of Anesthesia in Newborn Mice and Humans. Front. Neural Circuits 13:38. doi: 10.3389/fncir.2019.00038

INTRODUCTION

Reliable monitoring of anesthesia depth is critical during surgery. It allows for loss of consciousness, analgesia and immobility without incurring the risk of side effects and complications due to anesthetic misdosing. Typically used measures to monitor anesthesia depth are inspired and end-tidal anesthetic concentrations as well as physiologic parameters, including respiratory rate and depth (in the absence of neuromuscular blockade or controlled ventilation), heart rate, blood pressure, and responses to noxious stimuli (Punjasawadwong et al., 2014). These measures all respond to spinal and brainstem reflexes and are not specific for arousal or cortical responses to noxious events.

Anesthesia-induced changes in brain activity can be measured with electroencephalographic (EEG) recordings. Specific algorithms have been developed to predict anesthesia depth in adults (Glass et al., 1997; Prichep et al., 2004; Kreuzer, 2017). The most commonly used of such methods, the Bispectral Index, has been shown to significantly reduce intraoperative awareness, amount of anesthetic used, recovery time and post-anesthesia care unit stay in a recent Cochrane meta-analysis (Punjasawadwong et al., 2014), but see (Kalkman et al., 2011; Hajat et al., 2017). However, evidence of similar benefits in infants and younger children is sparse, as recently shown (Cornelissen et al., 2015, 2017, 2018a). EEG in anesthetized infants changes dramatically depending on postnatal age. Slow oscillations are present from birth on, whereas theta and alpha oscillations

occur 3 months after birth, but lack the frontal dominance typically seen in adults (Davidson et al., 2005; Lo et al., 2009; Hayashi et al., 2012; Cornelissen et al., 2015; Koch et al., 2017).

EEG recordings mainly monitor neocortical activity. Converging evidence from animal and human studies has shown that most anesthetics slow EEG oscillations (Alkire et al., 2008; Chauvette et al., 2011; Purdon et al., 2015). While power at high frequency oscillations is reduced (>40 Hz), power at slower frequencies (<15 Hz) is enhanced (Purdon et al., 2015). The computations underlying proprietary indexes such as the Bispectral index or Narcotrend are thought to take advantage of these phenomena (Kertai et al., 2012). However, in preterm and term neonates for the first weeks of life, EEG during sleep-wake cycles is weakly correlated with behavioral states and shows characteristic bursts or spontaneous activity transients (Milh et al., 2007; O'Toole et al., 2016). Anesthesia-induced theta and alpha oscillations have been reported to emerge around 3–4 months of age, albeit with less frontal predominance than in older children and adults (Cornelissen et al., 2015, 2018a). Moreover, high concentrations/doses of anesthetics have been reported to depress brain activity and enhance signal discontinuity in both human and rodent neonates (Chang et al., 2016; Cornelissen et al., 2017; Stolwijk et al., 2017). However, to our knowledge, a comprehensive algorithmic approach identifying EEG parameters that robustly correlate with anesthetic depth during early postnatal development is still lacking.

Here, we developed a novel strategy to model anesthesia depth by using common electrophysiological features that correlate with inhaled anesthetic concentrations during early development of mice and humans at similar stage of brain development. We performed intracranial electrophysiological recordings to study the temporal and dose-dependent dynamics of brain activity in neonatal mice [postnatal day (P) 8–10] during bolus urethane administration, and during dose-titrated isoflurane general anesthesia, respectively. Dominant local field potential (LFP) features of anesthetic state were identified and used to develop a machine-learning algorithm that distinguishes non-anesthetized from deeply anesthetized states and predicts anesthetic concentration as a proxy for anesthetic depth. Using a similar approach, we used multielectrode EEG recordings to study the dose-dependent dynamics of brain activity in a secondary analysis of a combined new and previously reported data set (Cornelissen et al., 2018a) of human infants 0–6 months of age during induction, maintenance and emergence from general anesthesia (sevoflurane, isoflurane, or desflurane) administered for routine surgical care. Dominant EEG features of anesthetic state were identified and used to develop a machine-learning algorithm to predict end-tidal volume anesthetic concentration (an indirect measure of anesthetic concentration in the brain, and anesthetic depth).

MATERIALS AND METHODS

Animals

All experiments were performed in compliance with the German laws and the guidelines of the European Community for the use of animals in research and were approved by the local ethical committee (G132/12, G17/015, N18/015). Experiments were carried out on C57Bl/6J mice of both sexes. Timed-pregnant mice from the animal facility of the University Medical Center Hamburg-Eppendorf were housed individually at a 12 h light/12 h dark cycle, with *ad libitum* access to water and food. Day of birth was considered P0.

In vivo Electrophysiology in Neonatal Mice

Multisite extracellular recordings were performed in the prefrontal cortex (PFC) and HP, or lateral entorhinal cortex (LEC) and olfactory bulb (OB) of P8–10 mice. Pups were on a heating blanket during the entire procedure. Under isoflurane anesthesia (induction: 5%; maintenance: 2.5%), craniotomies were performed above PFC (0.5 mm anterior to Bregma, 0.1–0.5 mm right to Bregma) and HP (3.5 mm posterior to Bregma, 3.5 mm right to Bregma), or LEC (0 mm anterior to lambda, 6.5 mm right to lambda) and OB (0.5–0.8 mm anterior from the frontonasal suture, 0.5 mm right from internasal suture). Pups were head-fixed into a stereotaxic apparatus using two plastic bars mounted on the nasal and occipital bones with dental cement. Multisite electrodes (NeuroNexus, MI, USA) were inserted into PFC (four-shank, A4x4 recording sites, 100 μm spacing, 2.0 mm deep) and HP (one-shank, A1x16 recording sites, 50 μm spacing, 1.6 mm deep, 20° angle from the vertical plane), or LEC (one-shank, A1x16 recording sites, 100 μm spacing, 2 mm deep, 10° angle from the vertical plane) and OB (one-shank, A1x16 recording sites, 50 μm spacing, 1.4–1.8 mm deep). A silver wire was inserted into the cerebellum and served as ground and reference electrode. Pups were allowed to recover for 30 min prior to recordings. Extracellular signals were band-pass filtered (0.1–9,000 Hz) and digitized (32 kHz) with a multichannel extracellular amplifier (Digital Lynx SX, Neuralynx, Bozeman, MO, USA).

In vivo Electrophysiology in Juvenile Mice

Multisite extracellular recordings were performed in the PFC of P24–39 mice. Under isoflurane anesthesia (induction: 5%; maintenance: 2.5%), a metal head-post (Luigs and Neumann) was attached to the skull with dental cement and 2-mm craniotomies were performed above PFC (0.5–2.0 mm anterior to Bregma, 0.1–0.5 mm right to Bregma) and protected by a customized synthetic window. A silver wire was implanted in the cerebellum as ground and reference electrode. Surgery was performed at least 5 days before recordings. After recovery mice were trained to run on a custom-made spinning-disc. For recordings, craniotomies were uncovered and multisite electrodes (NeuroNexus, MI, USA) were inserted into PFC (one-shank, A1x16 recording sites, 50 μm spacing, 2.0 mm deep). Extracellular signals were band-pass filtered (0.1–9,000 Hz) and digitized (32 kHz) with a multichannel extracellular amplifier (Digital Lynx SX, Neuralynx, Bozeman, MO, USA).

Recordings Under Urethane

Activity was recorded for 15 min without anesthesia before intraperitoneally injecting urethane (1 mg/g body weight; Sigma-Aldrich, St. Louis, MO, USA). Activity was recorded for further 45 min. Animals were transcardially perfused after recordings,

brains were sectioned coronally, and wide field images were acquired to verify recording electrode positions.

Recordings Under Isoflurane

Mouth piece of an isoflurane evaporator (Harvard Apparatus, Holliston, MA, USA) was placed in front of the pups in the recording setup until animals accustomed to it. Activity was recorded for 15 min 0% isoflurane, but with the evaporator running (1.4 l/min). Afterward, isoflurane was added to the airflow and increased every 15 min (1%, 2%, 3%). Animals were transcardially perfused after recordings, brains were sectioned coronally, and wide field images were acquired to verify recording electrode positions.

Electroencephalographic Recordings in Human Neonates and Young Infants

Neonates and infants who were scheduled for an elective surgical procedure were recruited from the pre-operative clinic at Boston Children's Hospital from 12/2012 to 08/2018 (under Institutional Review Board P-3544, with written informed consent obtained from parents/legal guardians). Subjects required surgery below the neck, were clinically stable on the day of study and American Society of Anesthesiologists' physical status I or II. Exclusion criteria were born with congenital malformations or other genetic conditions thought to influence brain development, diagnosed with a neurological or cardiovascular disorder, or born at <32 weeks post-menstrual age. Datasets from previously published work (n = 25; Cornelissen et al., 2018a) and new subjects (n = 10) were included in the analysis. Data are presented from 35 subjects aged 0–6 months.

Anesthetic Management

Each patient received anesthesia induced with sevoflurane (32 subjects), isoflurane (two subjects) or desflurane (one subject) alone or a combination of one of the previous and nitrous oxide. Epochs used for analysis were comprised of sevoflurane, isoflurane or desflurane administration with air and oxygen, titrated to clinical signs; end-tidal anesthetic concentration was adjusted per the anesthetist's impression of clinical need, not a pre-set end-tidal anesthetic concentration.

EEG Recording

EEG data were acquired using an EEG cap (WaveGuard EEG cap, Advanced NeuroTechnology, Netherlands). Thirty-three- or 41-recording electrodes were positioned per the modified international 10/20 electrode placement system. Reference and ground electrodes were located at Fz and AFz respectively. EEG activity from 0.1 to 500 Hz was recorded with an Xltek EEG recording system (EMU40EX, Natus Medical Inc., Canada). Signals were digitized at a sampling rate of 1,024 Hz and a resolution of 16-bit. The EEG recording was started prior to anesthetic induction to capture the loss of consciousness and stopped once the participant reached the Post-Anesthesia Recovery to capture recovery of consciousness. For some infants, the EEG recording was started after anesthetic induction.

Clinical Data Collection

Demographics and clinical information were collected from the electronic medical records and from the in-house Anesthesia Information Management System (AIMS; **Supplementary Table S1**). None of the pathologies causing the need of surgery presented a risk for brain maturation. End-tidal sevoflurane, oxygen, and nitrous oxide concentrations were downloaded from the anesthetic monitoring device (Dräger Apollo, Dräger Medical Inc., Telford, PA, USA) to a recording computer in real-time using ixTrend software (ixcellence, Germany). Signals were recorded at a 1 Hz sampling rate.

Data Analysis

In vivo data were analyzed with custom-written algorithms in the Matlab environment. Data were processed as following: band-pass filtered (500–5,000 Hz) to analyze multi-unit activity (MUA) and band-pass filtered (2–100 Hz) using a third-order Butterworth filter before downsampling to analyze LFP. Filtering procedures were performed in a phase preserving manner.

Multi-Unit Activity

MUA was detected as the peak of negative deflections exceeding five times the standard deviation of the filtered signal and having a prominence larger than half the peak itself. Firing rates were computed by dividing the total number of spikes by the duration of the analyzed time window.

Detection of Oscillatory Activity

Discontinuous active periods were detected with a modified version of a previously developed algorithm for unsupervised analysis of neonatal oscillations (Cichon et al., 2014). Briefly, deflections of the root mean square of band-pass filtered signals (1–100 Hz) exceeding a variance-depending threshold were considered as network oscillations. The threshold was determined by a Gaussian fit to the values ranging from 0 to the global maximum of the root-mean-square histogram. If two oscillations occurred within 200 ms of each other they were considered as one. Only oscillations lasting >1 s were included, and their occurrence, duration and amplitude were computed.

Power Spectral Density

For power spectral density analysis, 1 s-long windows of full signal or network oscillations were concatenated, and the power was calculated using Welch's method with non-overlapping windows.

Imaginary Coherence

The imaginary part of coherence, which is insensitive to volume-conduction-based effects (Nolte et al., 2004), was calculated by taking the absolute value of the imaginary component of the normalized cross-spectrum.

Pairwise Phase Consistency

Pairwise phase consistency (PPC) was computed as previously described (Vinck et al., 2010). Briefly, the phase in the band of interest was extracted using Hilbert transform and the mean of the cosine of the absolute angular distance among all pairs of phases was calculated.

1/f Slope

1/f slope was computed as previously described (Gao et al., 2017). We used robust linear regression (MATLAB function *robustfit*)

to find the best fit over 20–40 Hz frequency range of the power spectral density, in 1-min bins.

Sample Entropy

Sample Entropy was computed using the SampEn function (MATLAB File Exchange) in 1.5 s windows and in 2 Hz frequency bins. Tolerance was set to 0.2 * std (signal), and tau to 1.

EEG Data Analysis

EEG signal was visually inspected to detect and reject channels with low signal to noise ratio and re-referenced to a common average reference. The signal was automatically scored in 5 s epochs, and channels in which signal was significantly contaminated by artifacts (patient handling, surgical electrocautery etc.) were discarded. Epochs were rejected if signal was saturated due to electrocautery, signal exceeded 150 μV, or the median signal across all EEG channels exceeds 30 μV (**Supplementary Figure S5**). Minutes containing more than 10 s of contaminated signal were removed from further analysis. On average 14 $\pm$ 9% (median $\pm$ median absolute deviation) of the signal was discarded. To compute EEG amplitude, we smoothed the absolute value of the signal, using a moving average filter with a window of 1,024 points (1 s). If more than one volatile anesthetic was used, we retained only epochs in which the main anesthetic was used in isolation. Subjects with epidural anesthesia halfway through the surgery (n = 2 subjects), or with less than 20 min of artifact-free signal (n = 5 subjects) were excluded from further analysis.

Feature Engineering

Features to predict anesthetic concentration in neonatal mice were calculated in 1-min bins. LFP power in the 1–100 Hz range in 10 Hz bins, the percentage of active periods, median length and number of oscillations, median and maximum signal amplitude were computed. All features were computed for both PFC and HP and were normalized to their median value in the non-anesthetized 15 min of recordings. Features to predict anesthetic concentration in human infants were also calculated in 1-min bins. The median amplitude of the smoothed EEG signal and the percentage of the EEG envelope that fell into each amplitude quartile was computed. Amplitude quartiles were computed on the entire EEG trace, averaged over channels. All features were calculated for unfiltered signal, and in the 1–50 Hz range in 5 Hz bins, averaged over channels. Features were normalized to their median value in the non-anesthetized portion of the recording, or lowest anesthetic concentration, if no artifact-free minute was available.

Regressors

Machine-learning analyses were performed using Python (Python Software Foundation, NH, USA) in the Spyder (Pierre Raybaut, The Spyder Development Team) development environment. Model training and performance evaluation were carried out using the scikit-learn toolbox. The set was iteratively (n = 100) divided between a training (2/3 of the set) and a cross-validation (1/3) set. Hyper-parameter of the model was tuned on the training set, which was further split using the standard three-fold cross-validation split implemented by the function "GridSearchCV," to which a "pipeline" object was passed. The "pipeline" object was built using the "Pipeline" function, and concatenating quantile transformation of the input features ("Quantile Transformer," tuning the number of quantiles), feature selection ("Select Percentile," using mutual information and tuning the percentage of features to select) and Radial Basis Function (RBF) kernel support-vector classification/regression (tuning the regularization parameters C and epsilon (regression only), and the kernel coefficient gamma). The classifier input was fed to the regressor as an additional feature. Performance assessment was then computed on the cross-validation set. Regressor decision space was reduced and plotted with t-sne. The decision space was approximated by imposing a Voronoi tessellation on the 2d plot, using k-nearest regression on the t-sne coordinates (Migut et al., 2015).

Statistics

Statistical analyses were performed using R Statistical Software (Foundation for Statistical Computing, Austria). Data were tested for significant differences ($^{*}p < 0.05$, $^{**}p < 0.01$ and $^{***}p < 0.001$) using non-parametric one- and two-way repeated-measures ANOVA (ARTool R package) with Bonferroni corrected *post hoc* analysis (emmeans R package). Correlations were computed using Spearman's rank correlation coefficient (rho). No statistical measures were used to estimate the sample size since the effect size was unknown. For the main experimental results, more information about tests used, values and parameters are provided in the supplementary material (**Supplementary Table S2**).

Data Availability

Electrophysiological data for hippocampus and prefrontal cortex mouse recordings, under both urethane and isoflurane condition, is available at the following open-access repository: https://web.gin.g-node.org/mchini/Neural_correlates_of_anesthesia_in_newborn_mice_and_humans.

RESULTS

Anesthesia Affects the Occurrence but Not the Spectral and Temporal Structure of Oscillatory Events in Neonatal Mice

We monitored the impact of anesthesia on immature brain activity in several cortical areas [PFC, hippocampus (HP), and LEC] as well as in a sensory area OB. For this, multi-site extracellular recordings of LFP and MUA were performed from P8 to 10 mice before and for 45 min after induction of anesthesia by intraperitoneal urethane injection (**Figure 1A**), an anesthetic commonly used in rodents (Khazipov et al., 2004; Colonnese and Khazipov, 2010).

The recorded network activity had a highly fragmented structure (defined as discontinuous activity) in all investigated areas (PFC, HP, LEC and OB). The full signal (i.e., entire LFP trace) consisted of transient episodes of oscillatory discharges with mixed frequencies (from here referred to as "active periods"), alternating with periods of relative electrical silence

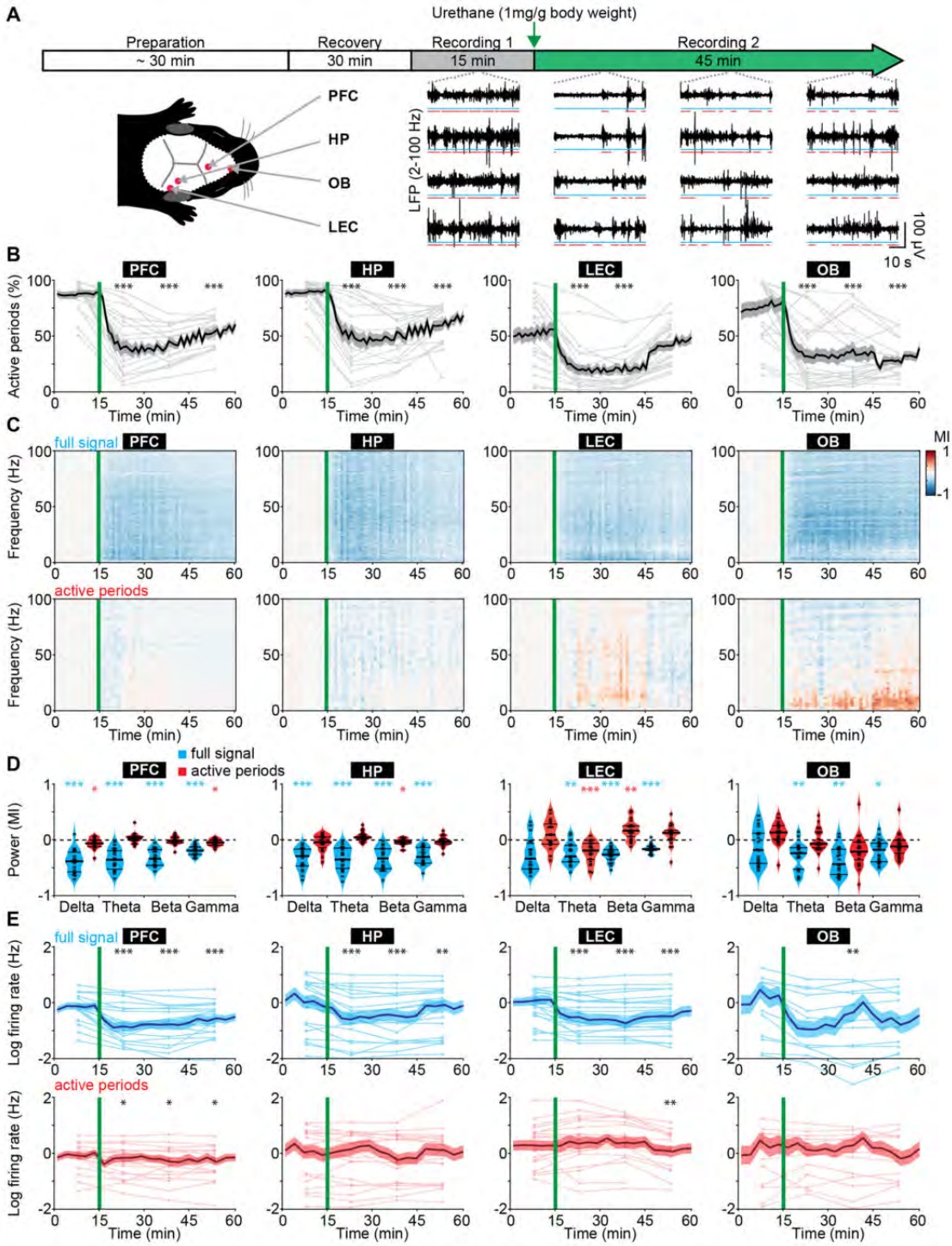

FIGURE 1 | Frequency-unspecific dampening of neuronal activity during urethane anesthesia in neonatal mice. **(A)** Schematic representation of experimental paradigm and recording sites as well as characteristic local field potential (LFP) recordings of discontinuous activity in the prefrontal cortex (PFC), HP, lateral entorhinal cortex (LEC), and olfactory bulb (OB) of neonatal mice (P8–10) during non-anesthetized and urethane-anesthetized state. Time windows of active periods are marked by red lines. **(B)** Line plots displaying the relative occurrence of active periods normalized to total recording time in PFC, HP, OB and LEC before and after urethane injection. **(C)** Color-coded MI of power spectra for full signal (top) and active periods (bottom) recorded in PFC, HP, LEC and OB of neonatal mice before and after urethane injection. **(D)** Violin plots displaying the MI of power in delta (2–4 Hz), theta-alpha (4–12 Hz), beta (12–30 Hz) and gamma (30–100 Hz) frequency bands for full signal (blue) and active periods (red) recorded in the PFC, HP, LEC and OB. **(E)** Line plots displaying multi-unit activity (MUA) rates during full signal (blue) and active periods (red). In **(B,C,E)** green lines correspond to the time point of urethane injection.

and suppressed activity (from here referred to as "silent periods"; **Figure 1A**; Khazipov et al., 2004; Hanganu et al., 2006; Brockmann et al., 2011; Bitzenhofer et al., 2017; Gretenkord et al., 2019). The prevalence of active periods decreased rapidly and robustly over time in all investigated brain areas upon urethane injection (**Figure 1B**). The most prominent reduction was observed 5–15 min after urethane injection. A partial recovery towards baseline levels during the following 30 min was detected in cortical areas, and to a lesser extent in OB (**Figure 1B**). The temporal sequence of events likely reflects the pharmacokinetics of urethane and is line with the previously reported quick onset (few minutes) and long-lasting effects of urethane anesthesia (2–4 h; Huh and Cho, 2013).

The anesthesia-induced reduced occurrence of active periods was reflected in a broadband (1–100 Hz) decrease in oscillatory power shown as modulation index (MI) defined as $(power_{post} - power_{pre})/(power_{post} + power_{pre})$. In contrast, power spectra during active periods were largely unaffected (**Figure 1C**). Of note, for OB, delta and theta power during active periods increased over time after urethane injection and might be related to an observed augmentation of respiration amplitude. Spectral properties of full signal and active periods were quantified for delta (2–4 Hz), theta-alpha (4–12 Hz), beta (12–30 Hz) and gamma (30–100 Hz) frequency bands for the first 15 min post urethane administration, the time window of strongest reduction of active periods. In contrast to the significant reduction of full signal power in all frequency bands, the power during active periods was only marginally affected by anesthesia (**Figure 1D**). Thus, urethane anesthesia affected network activity in the immature rodent brain predominantly by decreasing the amount of active periods without perturbing the frequency structure of active periods. This is in stark contrast with the well-characterized switch from a low-amplitude high-frequency regime to a high-amplitude low-frequency regime of electrical activity that has been reported for the adult rodent and human brain (Voss and Sleigh, 2007; Alkire et al., 2008).

Anesthesia was shown to induce alterations of long-range network interactions in adult rodents (Bettinardi et al., 2015) and humans (Ferrarelli et al., 2010; Lewis et al., 2012; Sarasso et al., 2015). We examined whether similar alterations are present in the immature mouse brain. Simultaneous recordings of HP and PFC, as well as OB and LEC were analyzed to assess the effects of anesthesia on long-range functional coupling. We previously showed that at the end of the first postnatal week hippocampal theta bursts drive the oscillatory entrainment of local circuits in the PFC, whereas discontinuous activity in OB controls the network activity in LEC (Brockmann et al., 2011; Ahlbeck et al., 2018; Gretenkord et al., 2019). Urethane did not modify these interactions. The synchrony within networks quantified by HP-PFC and OB-LEC coherence was similar during baseline (no urethane anesthesia) and in the presence of urethane (**Supplementary Figure S1A**). These data indicate that the core features of long-range functional coupling are retained under anesthesia in neonatal mice.

Anesthesia modified neuronal firing in all investigated areas. Firing rates in PFC, HP, LEC and OB decreased after urethane injection and only partially recovered during the following 45 min (**Figure 1E**). However, firing rates during active periods were only marginally affected. To examine whether the timing of neuronal firing to the phase of oscillatory activity was altered by anesthesia, we calculated PPC, a firing rate-independent measure of spike-LFP phase locking (Vinck et al., 2010). All four brain regions showed similar frequency-resolved phase locking profiles before and after urethane injection (**Supplementary Figures S1B,C**).

Anesthetics have been shown to alter the excitation/inhibition balance in the adult brain through their action on specific ion channels involved in synaptic transmission (Gao et al., 2017). Such alteration is usually monitored by changes in the 1/f slope of power spectral density. Further, signal complexity and information content measured by sample entropy have been correlated with behavioral states of adults, such as consciousness, sleep/wake states and anesthesia (Liang et al., 2015; Liu et al., 2018). For neonatal mice, we observed similar values of 1/f slope and sample entropy before and during urethane anesthesia (**Supplementary Figures S1D–F**), suggesting that urethane does not perturb cortical excitation/inhibition balance and signal complexity at this early age. The findings provide additional evidence to the hypothesis that anesthesia has unique effects on the immature brain.

To add additional evidence for this hypothesis, we extended the time window of investigation and performed extracellular recordings from the PFC of juvenile mice (P24–39). At this age oscillatory activity is continuous, thus a distinction between active and inactive periods is not possible. In contrast to the frequency-unspecific reduction of active periods in neonates, urethane anesthesia increased the oscillatory power in the delta frequency band and suppressed power in beta and gamma frequency bands (**Supplementary Figure S2**), confirming the anesthetic effects in the adult brain (Alkire et al., 2008; Chauvette et al., 2011; Purdon et al., 2015).

Taken together, these results indicate that urethane anesthesia dampened neonatal brain activity mainly by augmenting the discontinuity of network activity, i.e., reducing the proportion of time the brain spent in active periods. However, the active periods were largely unaffected in their temporal structure and firing dynamics. In contrast, urethane anesthesia in older mice led to frequency-specific changes. Thus, urethane anesthesia differently impacts neonatal and adult brain activity in mice.

Suppression of Active Periods Predicts Anesthetic Concentration in Neonatal Mice

To test whether the effects of urethane on neonatal brain activity generalize to other anesthetics, we performed LFP and MUA recordings from HP and PFC of P8–10 mice at increasing doses of isoflurane-induced anesthesia (0, 1, 2 and 3%; 15 min per concentration; **Figure 2A**). Urethane hyperpolarizes neurons by potentiating a resting potassium conductance (Pagliardini et al., 2013), whereas most other anesthetics, such as isoflurane and sevoflurane, mainly act by potentiating $GABA_A$ receptor-mediated transmission (Franks, 2006). Isoflurane reduced the incidence of active periods in a dose-dependent manner (**Figure 2B**). Accordingly, the broadband reduction of LFP power

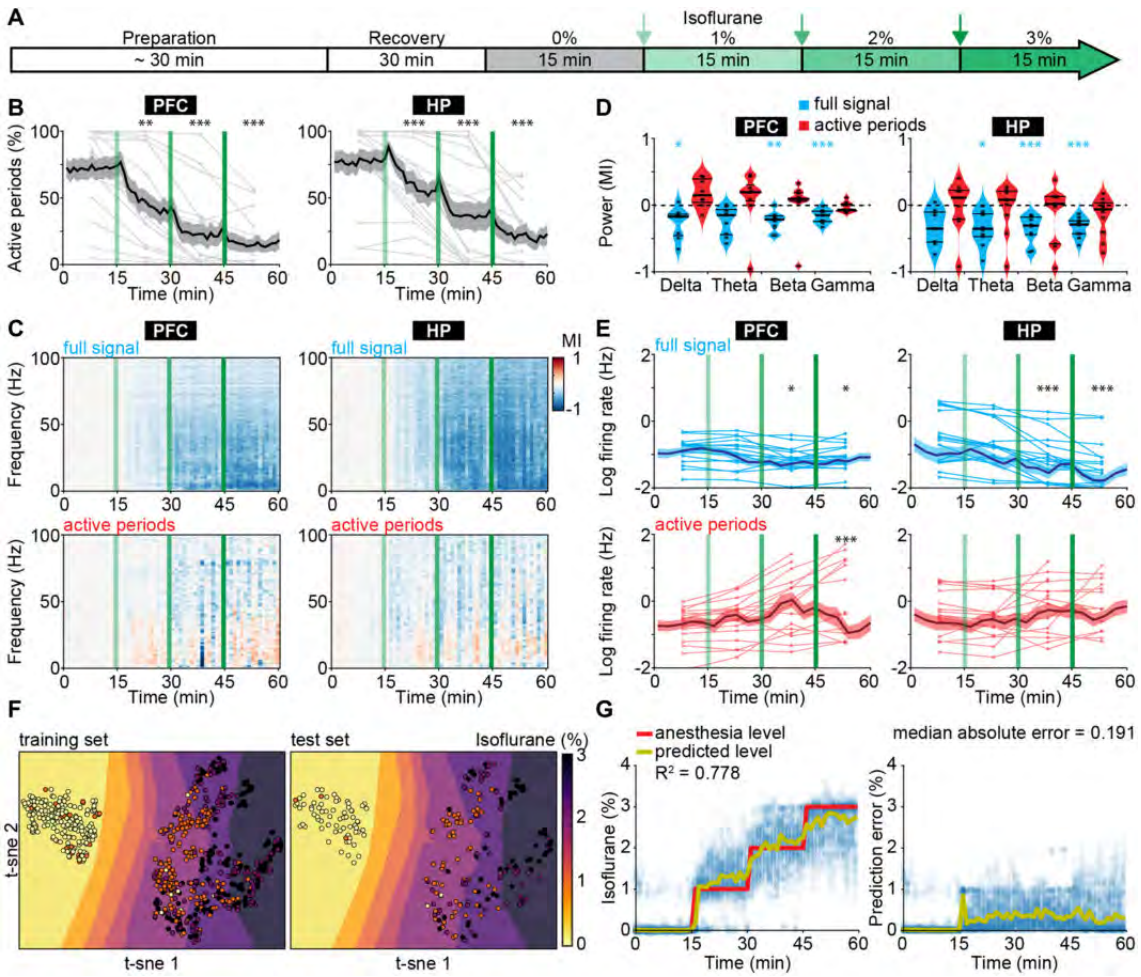

FIGURE 2 | Suppression of active periods in relationship with the depth of isoflurane anesthesia in neonatal mice. **(A)** Schematic representation of experimental protocol for LFP recordings without anesthesia and during increasing levels of isoflurane anesthesia in neonatal mice (P8–10). **(B)** Line plots displaying the relative occurrence of active periods in PFC and HP during increasing levels of isoflurane anesthesia. **(C)** Color-coded MI of power spectra for full signal (top) and active periods (bottom) during increasing levels of isoflurane anesthesia. **(D)** Violin plots displaying the MI of power in delta (2–4 Hz), theta (4–12 Hz), beta (12–30 Hz) and gamma (30–100 Hz) frequency bands for full signal (blue) and active periods (red). **(E)** Line plots displaying MUA firing rates during full signal (blue) and active periods (red). In **(B,C,E)** green lines correspond to the time points of increasing isoflurane anesthesia. **(F)** Visualization of anesthesia depth prediction by t-sne plots. Background color codes for predicted anesthesia depth, while the color of the dots represents the actual anesthesia level in the training (left) and test set (right). **(G)** Scatter plots displaying anesthesia depth predictions with support vector regression (left) and absolute errors between anesthesia depth prediction and actual anesthesia depth (right).

was also dependent on isoflurane concentration (**Figures 2C,D**). Power spectra of active periods remained largely unaffected in the presence of isoflurane, similarly to the urethane effects (**Figures 2C,D**). MUA rates during active periods in PFC and HP were hardly modified in the presence of isoflurane, yet the overall firing decreased corresponding to the reduced occurrence of active periods (**Figure 2E**). Together, these findings identify the suppression of active periods as the main effect of bolus urethane injection and isoflurane anesthesia in the neonatal mouse brain.

The development-specific response of the immature brain to anesthesia might represent the main obstacle when trying to predict anesthesia depth in infants using algorithms based on the mature brain activity of adults. Therefore, we next aimed to use electrophysiological properties specific for anesthetized neonatal mice to predict the concentration of administered isoflurane. We used support vector regression (**Supplementary Figure S3**), with the following input features: median amplitude of broadband LFP, percent of time spent in active periods, and spectral power from 1 to 100 Hz in 10 Hz bins for both hippocampal and prefrontal activity. An additional feature was the output of a support vector classifier that received the same features as for the support vector regression, and that was designed to predict whether the animal was under anesthesia or not. The algorithm accurately predicted anesthesia depth across all levels of isoflurane concentration (**Figures 2F,G**). Estimation of information content of the different features identified the median amplitude of broadband LFP as the most informative feature (**Supplementary Figure S4A**). As the power of active

periods was only marginally affected by anesthesia, this feature mainly mirrors the suppression of active periods. Interestingly, the algorithm was also able to distinguish non-anesthetized from anesthetized recordings from neonatal mice under urethane, even though it had not been exposed to this dataset during training (**Supplementary Figure S4B**).

Thus, features of electrophysiological activity that capture the particularities of immature neuronal networks can predict anesthetic concentration in neonatal mice. The generalization of the classifier to a different anesthetic indicates that it can identify general anesthesia-related features of brain activity in neonatal mice.

Frequency-Unspecific Suppression of Activity in Anesthetized Human Neonates and Young Infants

To test if human neonates and infants, similarly to mice, respond to anesthesia with a broadband decrease of periods of oscillatory activity, we examined EEG recordings from humans aged 0–6 months postnatal age, who received general anesthesia with volatile anesthetics (sevoflurane 32 subjects, isoflurane two subjects, desflurane one subject) for surgery (**Supplementary Table S1**).

In neonatal mice, the median LFP amplitude of broadband activity was identified as the most informative feature to predict anesthetic depth. We, therefore, applied the same data analysis approach to human EEG data (**Supplementary Figure S5**). We found the median amplitude of broadband EEG activity (averaged across all recording electrodes across the scalp) was negatively correlated with end-tidal anesthetic concentration (etAnesthetic) in human neonates from birth until 2 months postnatal age (**Figures 3A,B**). For older human infants, the correlation of the median EEG amplitude with the anesthetic concentration switched to a positive correlation, in agreement with adult human data (Hagihira, 2015). This relationship was even stronger using expected birth age, corrected for conceptional age (**Supplementary Figure S6A**). This switch from negative to positive correlation was also visible in the normalized median EEG amplitude when averaged for age-grouped babies (0–2, 2–4, 4–6 months; **Figure 3C**).

Quantification of median EEG amplitude across frequencies revealed a broadband suppression of EEG activity in human neonates of 0–2 months (**Figure 3D**). In contrast, the relationship between activity amplitude and etAnesthetic indicated frequency-specificity in human infants of 2–4 and 4–6 months, as previously reported (Cornelissen et al., 2017). Frontal activity has been shown to be particularly sensitive to age-varying anesthesia-related effects in human neonates (Cornelissen et al., 2015). Analysis of only frontal electrodes (Fp1, Fp2, F3, F4, F7, F8, Fpz) showed the same age-dependent anesthesia-induced changes as analysis of full scalp electrodes (**Supplementary Figures S6B–D**).

Thus, analogous to what we found in neonatal mice, general anesthesia in human infants younger than 2 months suppressed neuronal population activity, as reported previously (Cornelissen et al., 2015), while at older age anesthesia induced frequency-specific effects.

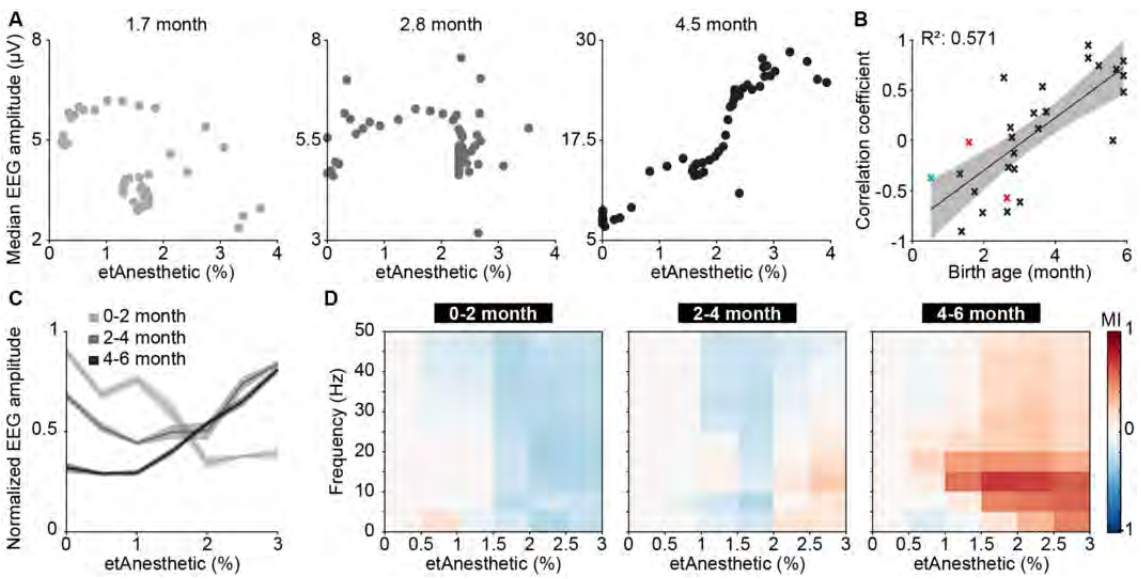

FIGURE 3 | Age-dependent switch from broadband suppression to frequency-specific effects of general anesthesia on electroencephalographic (EEG) activity in human neonates and infants. **(A)** Scatter plots displaying the median EEG amplitude as a function of anesthetic concentration for representative examples of 0–2, 2–4 and 4–6 months of age. **(B)** Scatter plot displaying the correlation coefficient of median EEG amplitude and anesthetic concentration in relation to birth age for sevoflurane (black), isoflurane (red), and desflurane (blue). **(C)** Line plots displaying normalized EEG amplitude as a function of anesthetic concentration. **(D)** Color-coded MI of median EEG amplitudes in different frequency bands as a function of anesthetic concentration for human babies of 0–2 months (left), 2–4 months (middle) and 4–6 months (right).

A Model to Predict End-Tidal Volume of Sevoflurane Anesthesia in Human Neonates and Infants

The correlation of EEG activity with etAnesthetic as well as the similar effects of anesthesia in neonatal mice and in humans from birth to 2 months old, suggests that anesthetic depth in babies might be predicted using similar features to those used in neonatal mice. To test this, we used a machine-learning algorithm with a similar architecture as the one we developed for neonatal mice (**Supplementary Figure S3**). The algorithm was modified to account for the developmental switch from broadband suppression to frequency-specific modulation by training three different regressors using 2 and 4 months as cut-offs. All regressors received the same input features (see "Materials and Methods" section and **Supplementary Figure S5**). Features derived from EEG activity were able to predict etAnesthetic with high accuracy for all age groups (0–2 months R^2 = 0.806, 2–4 months R^2 = 0.688, 4–6 months R^2 = 0.787; **Figures 4A–C**). In line with the frequency-specific alterations observed only in the older age groups, frequency-related features were rated more important for prediction of anesthesia depth in infants of 2–4 and 4–6 months than in neonates of 0–2 months (**Supplementary Figures S7A–C**). Predicting anesthesia depth for all ages with a single classifier considering age as an input feature performed with high accuracy (0–6 months R^2 = 0.689; **Figure 4D**, **Supplementary Figure S7D**). Training the predictor with only 20% of the data and testing it on the remaining 80% resulted in a reduced, but still solid prediction (R^2 = 0.512, median absolute error = 0.209) indicating the robustness of the predictor (**Supplementary Figure S8A**). This result confirms the age-varying effects of anesthesia on the brain and stresses the importance of considering age when developing algorithms aiming to assess anesthetic depth. Predicting anesthesia depth with a reduced number of four EEG channels (F4, P4, F3, P3) or two EEG channels (P4, P3) often used for long-term monitoring yielded similar results (four channels R^2 = 0.713, median absolute error = 0.134; two channels R^2 = 0.671, median absolute error = 0.161; **Supplementary Figures S8B,C**).

Thus, mouse and human neonates show similar changes in network activity in response to anesthesia. These results highlight how neurophysiological activity could be beneficial for future attempts at predicting anesthetic depth in clinical settings.

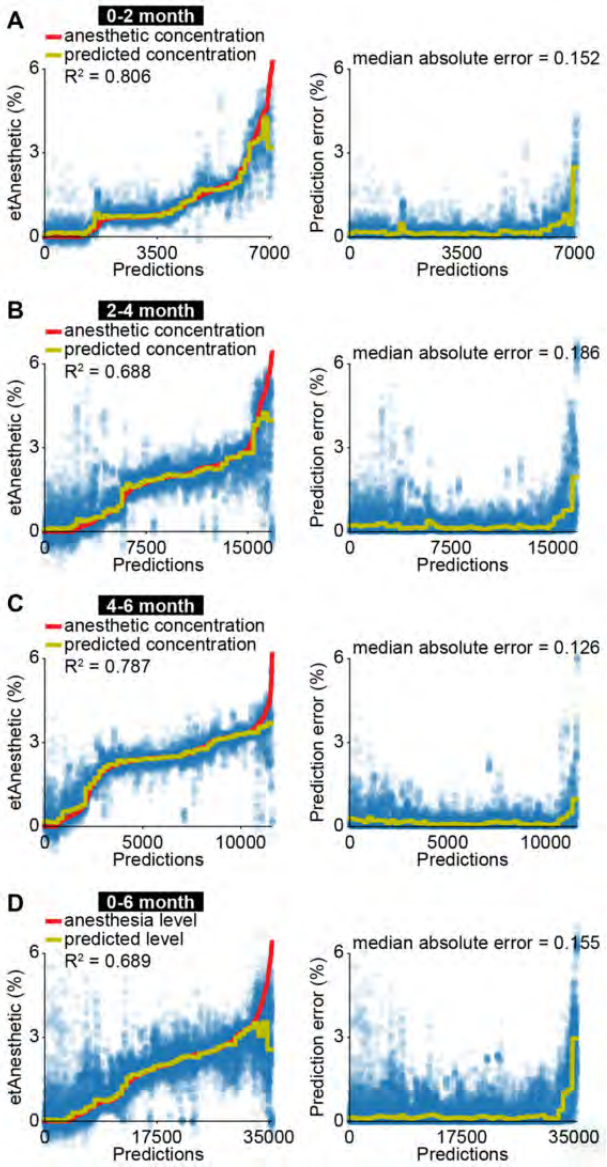

FIGURE 4 | EEG activity is predictive for anesthetic concentration in human infants. **(A)** Scatter plots displaying measured anesthetic concentration and predicted anesthetic concentration of support vector regression for all predictions (left) and absolute difference between measured and predicted anesthetic concentration (right) for human neonates of 0–2 months. **(B)** Same as **(A)** for human infants of 2–4 months. **(C)** Same as **(A)** for human infants of 4–6 months. **(D)** Same as **(A)** for human neonates and infants of 0–6 months.

DISCUSSION

Monitoring brain function during anesthesia is desirable to avoid intraoperative awareness and side effects resulting from unnecessarily high doses of anesthetics. Since consciousness is an elusive concept and cannot be directly measured, EEG features have been used to guide anesthesia delivery during human surgery. Monitoring methods developed for adults perform poorly in human neonates and infants, particularly during the first months of life (Davidson et al., 2005; Hayashi et al., 2012; Poorun et al., 2016; Koch et al., 2017). Age-specific effects of anesthetics on immature brain activity are considered the main reason for such poor performance. Implementation of neonate- and infant-specific anesthesia monitors requires elucidation of distinct anesthesia-induced EEG features during early development. We took advantage of a translational approach to address this open question. We first carried out an in-depth investigation of anesthetic effects on brain activity in neonatal mice, and then applied this knowledge to develop features that would correlate with an anesthetic concentration in human neonates.

In contrast to the continuous EEG signal observed in adults, neonatal EEG around birth is characterized by a highly discontinuous and fragmented temporal organization, with bursts of cerebral activity (active periods) alternating with interburst intervals lacking activity (silent periods; Anderson et al., 1985; Connell et al., 1987; Stockard-Pope et al., 1992; Lamblin et al., 1999; Vecchierini et al., 2003, 2007; Stevenson et al., 2017). Neonatal mice show a similar discontinuous organization of cortical activity (Khazipov et al., 2004; Hanganu et al., 2006; Brockmann et al., 2011). In accordance with the similar organization of early activity patterns in age-matched mouse pups and human infants, we found comparable effects of anesthesia on LFP and EEG signals, respectively.

It is well established that in the adult rodent and human brain most anesthetics favor slow oscillations at the expense of faster ones, thereby slowing the EEG rhythm (Alkire et al., 2008; Chauvette et al., 2011; Purdon et al., 2015). This principle is thought to underlie most algorithms that are clinically used to predict anesthesia depth (Davidson et al., 2005). Indeed, such algorithms perform poorly with anesthetics, such as ketamine, that do not share this mechanism of action (Hans et al., 2005). In line with previous studies (Ackman et al., 2014; Kirmse et al., 2015), we report that both urethane and isoflurane anesthesia affect brain activity in a different way in neonatal mice. Instead of favoring slow oscillations at the expense of faster ones, anesthesia in neonatal mice broadly suppresses activity in a frequency-unspecific manner. The dampening of cortical activity for human infants of 0–2 months suggests a development specific effect of anesthesia on immature brain activity that translates between mice and humans.

In rodents, the switch from activity suppression to frequency-specific modulation of neuronal activity by anesthesia has been reported to occur around P12 (Ackman et al., 2014). This coincides with the emergence of slow oscillations during sleep, suggested to depend on the maturation of thalamocortical networks (Steriade et al., 1993; Ackman et al., 2014). Consistent with our previous studies evaluating EEG properties of this data set, we found that theta and alpha oscillatory activity under anesthesia emerges in humans at around 4 months postnatal age (Cornelissen et al., 2015, 2017, 2018a). Developmental changes in the brain explain the changes in EEG dynamics that occur with postnatal age. In humans, gross brain development occurs in a caudal to rostral direction, with myelination of the medulla, pons, and thalamus starting within the first few postnatal weeks, and frontal cortex myelination starting around 3–4 postnatal months (Brody et al., 1987; Kinney et al., 1988). Regional differences in the rate of synaptogenesis, glucose metabolism and myelination across the cortex occur between subcortical and cortical regions, and between different regions of the cortex during the first 12 postnatal months in human infants (Huttenlocher and Dabholkar, 1997; Tau and Peterson, 2010; Dehorter et al., 2012; Catts et al., 2013; Semple et al., 2013; Murata and Colonnese, 2019). A key role in brain development is played by subplate neurons, the first neurons generated in the cerebral cortex, which guide the formation of thalamocortical connections (Kanold and Luhmann, 2010; Kostović and Judas, 2010). The subplate cells form the first functional connections and relay oscillatory activity in the developing brain (Kanold and Luhmann, 2010). Alpha oscillations in the anesthetized brain are postulated to be produced by thalamocortical circuits, and the gradual emergence of highly powered alpha oscillations at 4-months of age suggests an important developmental milestone has been reached in the processes guided by the subplate neurons. Future studies with a wider age range in mice and humans, including data of human infants studied at preterm, and children in older than 6 months of age, may deepen the understanding of anesthetic effects on brain activity throughout development.

The anesthetics evaluated across species in this study were comparable but not identical in terms of mechanism of action. Moreover, anesthetic management practices used in mice were simplified compared to commonly-used anesthetic practices in the clinic. Multimodal anesthesia requires the use of low-dose anesthetics in combination with analgesic and neuromuscular blocking agents to provide optimal anesthesia and reduce the side effect. These agents act on different drug targets in the nervous system and may have subtle but different effects on brain oscillatory activity (Brown et al., 2018).

In adult human volunteers, the correlation with anesthetic depth and EEG parameters can be performed using verbal reports to establish a threshold for unconsciousness (Purdon et al., 2015). However, in non-verbal populations such as human infants, one must rely on indirect behavioral measures which are more readily performed on emergence rather than induction and incision (Cornelissen et al., 2018b). Future investigations need to include surgical incision and other stimuli into the mouse models to understand with greater granularity the anesthetic titration around the minimal concentrations required to suppress movement, autonomic, and cortical responses to noxious stimuli.

In summary, we report that the suppression of brain activity in mouse and human neonates correlates with anesthetic concentration. The detailed understanding of anesthesia effects on network activity in mice allowed us to identify features and develop a machine-learning algorithm that is able to predict anesthetic concentration from EEG recordings in human neonates. We propose that, after appropriate training, an algorithm based on what we introduce here could learn to associate specific EEG effects with certain anesthetic doses. Eventual mismatches between administered and predicted anesthetic dose would then identify patients that are particularly sensitive/insensitive to an anesthetic, thus helping the anesthetist in administering appropriate levels of anesthetics. By these means, the risk of adverse neurodevelopmental outcome might be mitigated.

ETHICS STATEMENT

All animal experiments were performed in compliance with the German laws and the guidelines of the European Community for the use of animals in research and were approved by the local ethical committee (G132/12, G17/015, N18/015). Human neonates and infants who were scheduled for an elective surgical procedure were recruited from the pre-operative clinic at Boston Children's Hospital from 12/2012 to 08/2018 (under Institutional

Review Board P-3544, with written informed consent obtained from parents/legal guardians).

AUTHOR CONTRIBUTIONS

MC, SB and IH-O designed the experiments. MC, SB, SG, JK, JP, and LC carried out the experiments. MC, SB, SG, JK and JP analyzed the data. MC, SB, LC, CB and IH-O interpreted the data and wrote the article. All authors discussed and commented on the manuscript.

FUNDING

This work was funded by grants from the European Research Council (ERC-2015-CoG 681577 to IH-O), the German Research Foundation (Ha 4466/10-1, SPP 1665, SFB 936 B5 to IH-O) and the International Anesthesia Research Society (to LC). IH-O is a founding member of FENS Kavli Network of Excellence. This manuscript has been released as a Pre-Print at BioRxiv.

ACKNOWLEDGMENTS

We thank P. Putthoff, A. Marquardt, A. Dahlmann, and K. Titze for excellent technical assistance.

SUPPLEMENTARY MATERIAL

The Supplementary Material for this article can be found online at: https://www.frontiersin.org/articles/10.3389/fncir.2019.00038/full#supplementary-material

REFERENCES

Ackman, J. B., Zeng, H., and Crair, M. C. (2014). Structured dynamics of neural activity across developing neocortex. *BioRxiv* [Preprint]. doi: 10.1101/012237

Ahlbeck, J., Song, L., Chini, M., Bitzenhofer, S. H., and Hanganu-Opatz, I. L. (2018). Glutamatergic drive along the septo-temporal axis of hippocampus boosts prelimbic oscillations in the neonatal mouse. *Elife* 7:e33158. doi: 10.7554/eLife.33158

Alkire, M. T., Hudetz, A. G., and Tononi, G. (2008). Consciousness and anesthesia. *Science* 322, 876–880. doi: 10.1126/science.1149213

Anderson, C. M., Torres, F., and Faoro, A. (1985). The EEG of the early premature. *Electroencephalogr. Clin. Neurophysiol.* 60, 95–105. doi: 10.1016/0013-4694(85)90015-X

Bettinardi, R. G., Tort-Colet, N., Ruiz-Mejias, M., Sanchez-Vives, M. V., and Deco, G. (2015). Gradual emergence of spontaneous correlated brain activity during fading of general anesthesia in rats: evidences from fMRI and local field potentials. *Neuroimage* 114, 185–198. doi: 10.1016/j.neuroimage.2015.03.037

Bitzenhofer, S. H., Ahlbeck, J., Wolff, A., Wiegert, J. S., Gee, C. E., Oertner, T. G., et al. (2017). Layer-specific optogenetic activation of pyramidal neurons causes beta-gamma entrainment of neonatal networks. *Nat. Commun.* 8:14563. doi: 10.1038/ncomms14563

Brockmann, M. D., Pöschel, B., Cichon, N., and Hanganu-Opatz, I. L. (2011). Coupled oscillations mediate directed interactions between prefrontal cortex and hippocampus of the neonatal rat. *Neuron* 71, 332–347. doi: 10.1016/j.neuron.2011.05.041

Brody, B. A., Kinney, H. C., Kloman, A. S., and Gilles, F. H. (1987). Sequence of central-nervous-system myelination in human infancy: I. An autopsy study of myelination. *J. Neuropath. Exp. Neurol.* 46, 283–301. doi: 10.1097/00005072-198705000-00005

Brown, E. N., Pavone, K. J., and Naranjo, M. (2018). Multimodal general anesthesia: theory and practice. *Anesth. Analg.* 127, 1246–1258. doi: 10.1213/ANE.0000000000003668

Catts, V. S., Fung, S. J., Long, L. E., Joshi, D., Vercammen, A., Allen, K. M., et al. (2013). Rethinking schizophrenia in the context of normal neurodevelopment. *Front. Cell. Neurosci.* 7:60. doi: 10.3389/fncel.2013.00060

Chang, P. S., Walker, S. M., and Fitzgerald, M. (2016). Differential suppression of spontaneous and noxious-evoked somatosensory cortical activity by isoflurane in the neonatal rat. *Anesthesiology* 124, 885–898. doi: 10.1097/ALN.0000000000001017

Chauvette, S., Crochet, S., Volgushev, M., and Timofeev, I. (2011). Properties of slow oscillation during slow-wave sleep and anesthesia in cats. *J. Neurosci.* 31, 14998–15008. doi: 10.1523/JNEUROSCI.2339-11.2011

Cichon, N. B., Denker, M., Grün, S., and Hanganu-Opatz, I. L. (2014). Unsupervised classification of neocortical activity patterns in neonatal and pre-juvenile rodents. *Front. Neural Circuits* 8:50. doi: 10.3389/fncir.2014.00050

Colonnese, M. T., and Khazipov, R. (2010). "Slow activity transients" in infant rat visual cortex: a spreading synchronous oscillation patterned by retinal waves. *J. Neurosci.* 30, 4325–4337. doi: 10.1523/JNEUROSCI.4995-09.2010

Connell, J. A., Oozeer, R., and Dubowitz, V. (1987). Continuous 4-channel EEG monitoring: a guide to interpretation, with normal values, in preterm infants. *Neuropediatrics* 18, 138–145. doi: 10.1055/s-2008-1052466

Cornelissen, L., Bergin, A. M., Lobo, K., Donado, C., Soul, J. S., and Berde, C. B. (2017). Electroencephalographic discontinuity during sevoflurane anesthesia in infants and children. *Paediatr. Anaesth.* 27, 251–262. doi: 10.1111/pan.13061

Cornelissen, L., Donado, C., Lee, J. M., Liang, N. E., Mills, I., Tou, A., et al. (2018a). Clinical signs and electroencephalographic patterns of emergence from sevoflurane anaesthesia in children: an observational study. *Eur. J. Anaesthesiol.* 35, 49–59. doi: 10.1097/EJA.0000000000000739

Cornelissen, L., Kim, S. E., Lee, J. M., Brown, E. N., Purdon, P. L., and Berde, C. B. (2018b). Electroencephalographic markers of brain development during sevoflurane anaesthesia in children up to 3 years old. *Br. J. Anaesth.* 120, 1274–1286. doi: 10.1016/j.bja.2018.01.037

Cornelissen, L., Kim, S. E., Purdon, P. L., Brown, E. N., and Berde, C. B. (2015). Age-dependent electroencephalogram (EEG) patterns during sevoflurane general anesthesia in infants. *Elife* 4:e06513. doi: 10.7554/eLife.06513

Davidson, A. J., Huang, G. H., Rebmann, C. S., and Ellery, C. (2005). Performance of entropy and bispectral index as measures of anaesthesia effect in children of different ages. *Br. J. Anaesth.* 95, 674–679. doi: 10.1093/bja/aei247

Dehorter, N., Vinay, L., Hammond, C., and Ben-Ari, Y. (2012). Timing of developmental sequences in different brain structures: physiological and pathological implications. *Eur. J. Neurosci.* 35, 1846–1856. doi: 10.1111/j.1460-9568.2012.08152.x

Ferrarelli, F., Massimini, M., Sarasso, S., Casali, A., Riedner, B. A., Angelini, G., et al. (2010). Breakdown in cortical effective connectivity during midazolam-induced loss of consciousness. *Proc. Natl. Acad. Sci. U S A* 107, 2681–2686. doi: 10.1073/pnas.0913008107

Franks, N. P. (2006). Molecular targets underlying general anaesthesia. *Br. J. Pharmacol.* 147, S72–S81. doi: 10.1038/sj.bjp.0706441

Gao, R., Peterson, E. J., and Voytek, B. (2017). Inferring synaptic excitation/inhibition balance from field potentials. *Neuroimage* 158, 70–78. doi: 10.1016/j.neuroimage.2017.06.078

Glass, P. S., Bloom, M., Kearse, L., Rosow, C., Sebel, P., and Manberg, P. (1997). Bispectral analysis measures sedation and memory effects of propofol, midazolam, isoflurane and alfentanil in healthy volunteers. *Anesthesiology* 86, 836–847. doi: 10.1097/00000542-199704000-00014

Gretenkord, S., Kostka, J. K., Hartung, H., Watznauer, K., Fleck, D., Minier-Toribio, A., et al. (2019). Coordinated electrical activity in the olfactory bulb

gates the oscillatory entrainment of entorhinal networks in neonatal mice. *PLoS. Biol.* 17:e2006994. doi: 10.1371/journal.pbio.2006994

Hagihira, S. (2015). Changes in the electroencephalogram during anaesthesia and their physiological basis. *Br. J. Anaesth.* 115, i27–i31. doi: 10.1093/bja/aev212

Hajat, Z., Ahmad, N., and Andrzejowski, J. (2017). The role and limitations of EEG-based depth of anaesthesia monitoring in theatres and intensive care. *Anaesthesia* 72, 38–47. doi: 10.1111/anae.13739

Hanganu, I. L., Ben-Ari, Y., and Khazipov, R. (2006). Retinal waves trigger spindle bursts in the neonatal rat visual cortex. *J. Neurosci.* 26, 6728–6736. doi: 10.1523/JNEUROSCI.0752-06.2006

Hans, P., Dewandre, P. Y., Brichant, J. F., and Bonhomme, V. (2005). Comparative effects of ketamine on bispectral index and spectral entropy of the electroencephalogram under sevoflurane anaesthesia. *Br. J. Anaesth.* 94, 336–340. doi: 10.1093/bja/aei047

Hayashi, K., Shigemi, K., and Sawa, T. (2012). Neonatal electroencephalography shows low sensitivity to anesthesia. *Neurosci. Lett.* 517, 87–91. doi: 10.1016/j.neulet.2012.04.028

Huh, Y., and Cho, J. (2013). Urethane anesthesia depresses activities of thalamocortical neurons and alters its response to nociception in terms of dual firing modes. *Front. Behav. Neurosci.* 7:141. doi: 10.3389/fnbeh.2013.00141

Huttenlocher, P. R., and Dabholkar, A. S. (1997). Regional differences in synaptogenesis in human cerebral cortex. *J. Comp. Neurol.* 387, 167–178. doi: 10.1002/(sici)1096-9861(19971020)387:2<167::aid-cne1>3.0.co;2-z

Kalkman, C. J., Peelen, L. M., and Moons, K. G. (2011). Pick up the pieces: depth of anesthesia and long-term mortality. *Anesthesiology* 114, 485–487. doi: 10.1097/ALN.0b013e31820c2ba2

Kanold, P. O., and Luhmann, H. J. (2010). The subplate and early cortical circuits. *Annu. Rev. Neurosci.* 33, 23–48. doi: 10.1146/annurev-neuro-060909-153244

Kertai, M. D., Whitlock, E. L., and Avidan, M. S. (2012). Brain monitoring with electroencephalography and the electroencephalogram-derived bispectral index during cardiac surgery. *Anesth. Analg.* 114, 533–546. doi: 10.1213/ANE.0b013e31823ee030

Khazipov, R., Sirota, A., Leinekugel, X., Holmes, G. L., Ben-Ari, Y., and Buzsaki, G. (2004). Early motor activity drives spindle bursts in the developing somatosensory cortex. *Nature* 432, 758–761. doi: 10.1038/nature03132

Kinney, H. C., Brody, B. A., Kloman, A. S., and Gilles, F. H. (1988). Sequence of Central Nervous-System Myelination in Human Infancy .2. Patterns of Myelination in Autopsied Infants. *J. Neuropathol. Exp. Neurol.* 47, 217–234. doi: 10.1097/00005072-198805000-00003

Kirmse, K., Kummer, M., Kovalchuk, Y., Witte, O. W., Garaschuk, O., and Holthoff, K. (2015). GABA depolarizes immature neurons and inhibits network activity in the neonatal neocortex *in vivo*. *Nat. Commun.* 6:7750. doi: 10.1038/ncomms8750

Koch, S., Stegherr, A. M., Morgeli, R., Kramer, S., Toubekis, E., Lichtner, G., et al. (2017). Electroencephalogram dynamics in children during different levels of anaesthetic depth. *Clin. Neurophysiol.* 128, 2014–2021. doi: 10.1016/j.clinph.2017.07.417

Kostović, I., and Judas, M. (2010). The development of the subplate and thalamocortical connections in the human foetal brain. *Acta Paediatr.* 99, 1119–1127. doi: 10.1111/j.1651-2227.2010.01811.x

Kreuzer, M. (2017). EEG based monitoring of general anesthesia: taking the next steps. *Front. Comput. Neurosci.* 11:56. doi: 10.3389/fncom.2017.00056

Lamblin, M. D., André, M., Challamel, M. J., Curzi-Dascalova, L., d'Allest, A. M., De Giovanni, E., et al. (1999). Electroencephalography of the premature and term newborn. Maturational aspects and glossary. *Neurophysiol. Clin.* 29, 123–219. doi: 10.1016/S0987-7053(99)80051-3

Lewis, L. D., Weiner, V. S., Mukamel, E. A., Donoghue, J. A., Eskandar, E. N., Madsen, J. R., et al. (2012). Rapid fragmentation of neuronal networks at the onset of propofol-induced unconsciousness. *Proc. Natl. Acad. Sci. U S A* 109, E3377–E3386. doi: 10.1073/pnas.1210907109

Liang, Z., Wang, Y., Sun, X., Li, D., Voss, L. J., Sleigh, J. W., et al. (2015). EEG entropy measures in anesthesia. *Front. Comput. Neurosci.* 9:16. doi: 10.3389/fncom.2015.00016

Liu, Q., Ma, L., Fan, S. Z., Abbod, M. F., and Shieh, J. S. (2018). Sample entropy analysis for the estimating depth of anaesthesia through human EEG signal at different levels of unconsciousness during surgeries. *PeerJ* 6:e4817. doi: 10.7717/peerj.4817

Lo, S. S., Sobol, J. B., Mallavaram, N., Carson, M., Chang, C., Grieve, P. G., et al. (2009). Anesthetic-specific electroencephalographic patterns during emergence from sevoflurane and isoflurane in infants and children. *Paediatr. Anaesth.* 19, 1157–1165. doi: 10.1111/j.1460-9592.2009.03128.x

Migut, M. A., Worring, M., and Veenman, C. J. (2015). Visualizing multi-dimensional decision boundaries in 2D. *Data Min. Knowl. Discov.* 29, 273–295. doi: 10.1007/s10618-013-0342-x

Milh, M., Kaminska, A., Huon, C., Lapillonne, A., Ben-Ari, Y., and Khazipov, R. (2007). Rapid cortical oscillations and early motor activity in premature human neonate. *Cereb. Cortex* 17, 1582–1594. doi: 10.1093/cercor/bhl069

Murata, Y., and Colonnese, M. T. (2019). Thalamic inhibitory circuits and network activity development. *Brain Res.* 1706, 13–23. doi: 10.1016/j.brainres.2018.10.024

Nolte, G., Bai, O., Wheaton, L., Mari, Z., Vorbach, S., and Hallett, M. (2004). Identifying true brain interaction from EEG data using the imaginary part of coherency. *Clin. Neurophysiol.* 115, 2292–2307. doi: 10.1016/j.clinph.2004.04.029

O'Toole, J. M., Boylan, G. B., Vanhatalo, S., and Stevenson, N. J. (2016). Estimating functional brain maturity in very and extremely preterm neonates using automated analysis of the electroencephalogram. *Clin. Neurophysiol.* 127, 2910–2918. doi: 10.1016/j.clinph.2016.02.024

Pagliardini, S., Funk, G. D., and Dickson, C. T. (2013). Breathing and brain state: urethane anesthesia as a model for natural sleep. *Respir. Physiol. Neurobiol.* 188, 324–332. doi: 10.1016/j.resp.2013.05.035

Poorun, R., Hartley, C., Goksan, S., Worley, A., Boyd, S., Cornelissen, L., et al. (2016). Electroencephalography during general anaesthesia differs between term-born and premature-born children. *Clin. Neurophysiol.* 127, 1216–1222. doi: 10.1016/j.clinph.2015.10.041

Prichep, L. S., Gugino, L. D., John, E. R., Chabot, R. J., Howard, B., Merkin, H., et al. (2004). The patient state index as an indicator of the level of hypnosis under general anaesthesia. *Br. J. Anaesth.* 92, 393–399. doi: 10.1093/bja/aeh082

Punjasawadwong, Y., Phongchiewboon, A., and Bunchungmongkol, N. (2014). Bispectral index for improving anaesthetic delivery and postoperative recovery. *Cochrane Database Syst. Rev.* 6:CD003843. doi: 10.1002/14651858.CD003843

Purdon, P. L., Sampson, A., Pavone, K. J., and Brown, E. N. (2015). Clinical electroencephalography for anesthesiologists: Part I: background and basic signatures. *Anesthesiology* 123, 937–960. doi: 10.1097/ALN.0000000000000841

Sarasso, S., Boly, M., Napolitani, M., Gosseries, O., Charland-Verville, V., Casarotto, S., et al. (2015). Consciousness and complexity during unresponsiveness induced by propofol, Xenon and Ketamine. *Curr. Biol.* 25, 3099–3105. doi: 10.1016/j.cub.2015.10.014

Semple, B. D., Blomgren, K., Gimlin, K., Ferriero, D. M., and Noble-Haeusslein, L. J. (2013). Brain development in rodents and humans: identifying benchmarks of maturation and vulnerability to injury across species. *Prog. Neurobiol.* 106–107, 1–16. doi: 10.1016/j.pneurobio.2013.04.001

Steriade, M., Nuñez, A., and Amzica, F. (1993). Intracellular analysis of relations between the slow (<1 Hz) neocortical oscillation and other sleep rhythms of the electroencephalogram. *J. Neurosci.* 13, 3266–3283. doi: 10.1523/jneurosci.13-08-03266.1993

Stevenson, N. J., Oberdorfer, L., Koolen, N., O'Toole, J. M., Werther, T., Klebermass-Schrehof, K., et al. (2017). Functional maturation in preterm infants measured by serial recording of cortical activity. *Sci. Rep.* 7:12969. doi: 10.1038/s41598-017-13537-3

Stockard-Pope, J. E., Werner, S. S., and Bickford, R. G. (1992). *Atlas of Neonatal Electroencephalography*. New York, NY: Raven Press.

Stolwijk, L. J., Weeke, L. C., de Vries, L. S., van Herwaarden, M. Y. A., van der Zee, D. C., van der Werff, D. B. M., et al. (2017). Effect of general anesthesia on neonatal aEEG-A cohort study of patients with non-cardiac

congenital anomalies. *PLoS One* 12:e0183581. doi: 10.1371/journal.pone.0183581

Tau, G. Z., and Peterson, B. S. (2010). Normal development of brain circuits. *Neuropsychopharmacology* 35, 147–168. doi: 10.1038/npp.2009.115

Vecchierini, M. F., André, M., and d'Allest, A. M. (2007). Normal EEG of premature infants born between 24 and 30 weeks gestational age: terminology, definitions and maturation aspects. *Neurophysiol. Clin.* 37, 311–323. doi: 10.1016/j.neucli.2007.10.008

Vecchierini, M. F., d'Allest, A. M., and Verpillat, P. (2003). EEG patterns in 10 extreme premature neonates with normal neurological outcome: qualitative and quantitative data. *Brain Dev.* 25, 330–337. doi: 10.1016/s0387-7604(03)00007-x

Vinck, M., van Wingerden, M., Womelsdorf, T., Fries, P., and Pennartz, C. M. (2010). The pairwise phase consistency: a bias-free measure of rhythmic neuronal synchronization. *Neuroimage* 51, 112–122. doi: 10.1016/j.neuroimage.2010.01.073

Voss, L., and Sleigh, J. (2007). Monitoring consciousness: the current status of EEG-based depth of anaesthesia monitors. *Best Pract. Res. Clin. Anaesthesiol.* 21, 313–325. doi: 10.1016/j.bpa.2007.04.003

Conflict of Interest Statement: The authors declare that the research was conducted in the absence of any commercial or financial relationships that could be construed as a potential conflict of interest.

Supplementary Materials

Neural correlates of anesthesia in newborn mice and humans

Mattia Chini[1], Sabine Gretenkord[1], Johanna K. Kostka[1], Jastyn A. Pöpplau[1], Laura Cornelissen[2,3], Charles B. Berde[2,3], Ileana L. Hanganu-Opatz[1,*] & Sebastian H. Bitzenhofer[1,†*]

[1] Developmental Neurophysiology, Institute of Neuroanatomy, University Medical Center Hamburg-Eppendorf, Hamburg, Germany
[2] Department of Anesthesiology, Critical Care and Pain Medicine, Boston Children's Hospital, Boston, Massachusetts
[3] Department of Anaesthesia, Harvard Medical School, Boston, Massachusetts
[†] Present address: Center for Neural Circuits and Behavior, Department of Neurosciences, University of California, San Diego, La Jolla, CA, USA

* Equal contribution

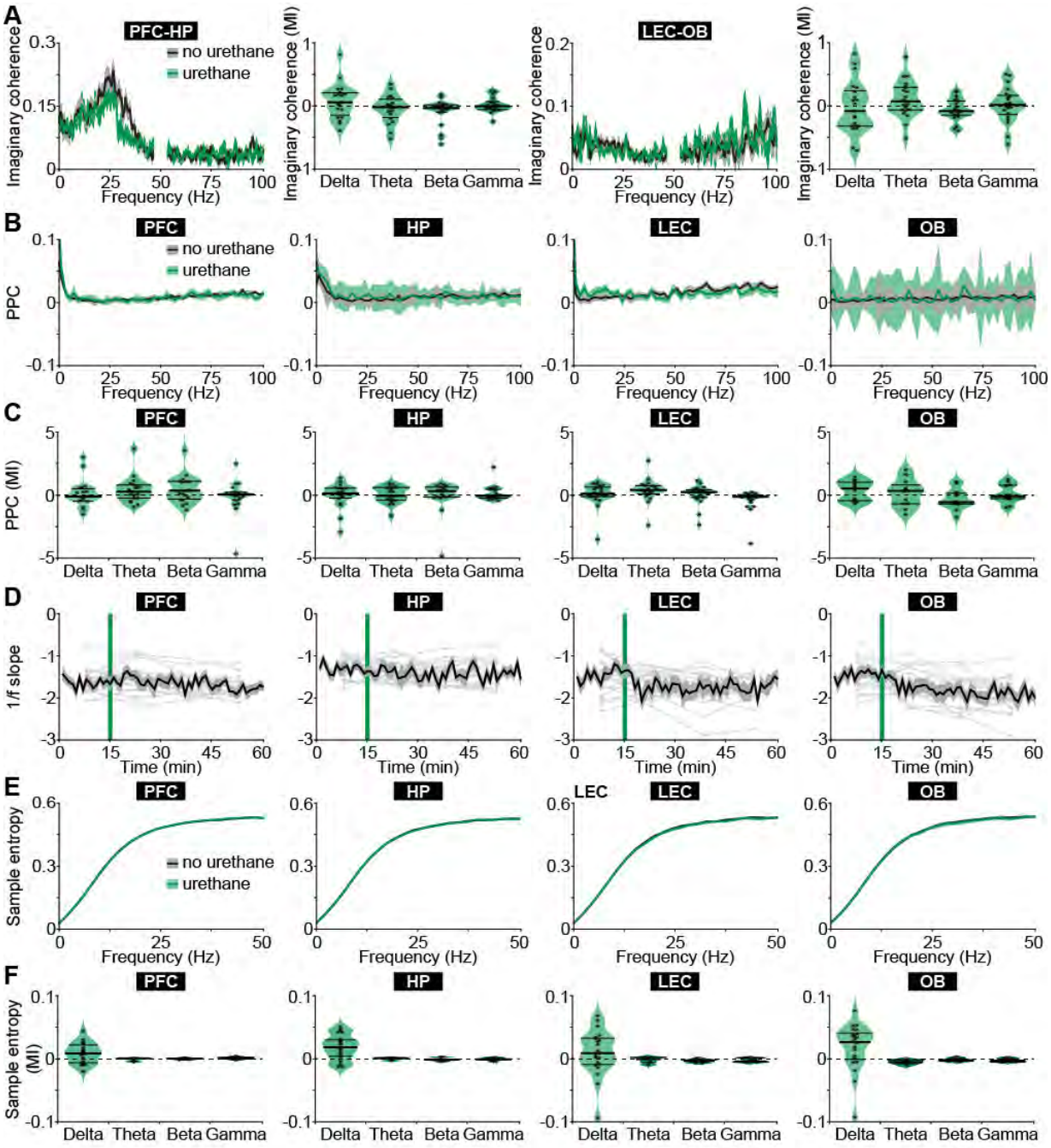

Fig. S1. Urethane anesthesia does not affect spectral features and timing of activity in neonatal mice. (**A**) Line plots displaying the imaginary coherence between PFC-HP and LEC-OB in neonatal mice (P8-10) as a function of frequency before (black) and after (green) urethane injection. Violin plots displaying the MI of the imaginary coherence in delta (2-4 Hz), theta-alpha (4-12 Hz), beta (12-30 Hz) and gamma (30-100 Hz) frequency bands. (**B**) Line plots displaying the PPC of MUA to the oscillatory phase before and after urethane injection. (**C**) Violin plots displaying the MI of PPC in delta, theta, beta and gamma frequency bands. (**D**) Line plots displaying the slope of the 1/f decay for gamma frequencies over time. Green lines mark the time point of urethane injection. (**E**) Line plots displaying the sample entropy as a function of frequency before and after urethane

injection. (**F**) Violin plots displaying the MI of the sample entropy in delta, theta, beta and gamma frequency bands.

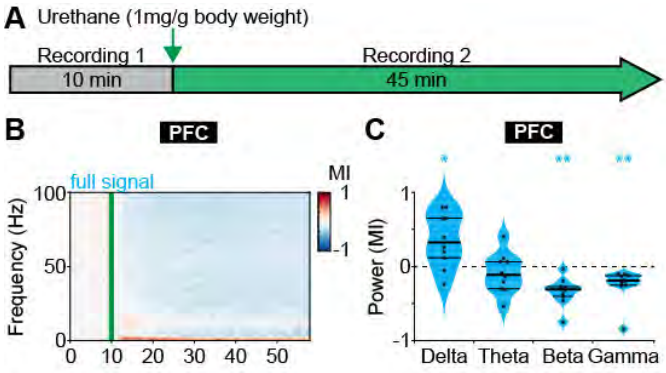

Fig. S2. Frequency-specific effects of urethane anesthesia in juvenile mice. (**A**) Schematic representation of experimental paradigm of LFP recordings in PFC of non-anesthetized and urethane-anesthetized juvenile mice (P24-39). (**B**) Color-coded MI of oscillatory power for full signal before and after urethane injection. Green line corresponds to the time point of urethane injection. (**C**) Violin plots displaying the MI of oscillatory power in delta (2-4 Hz), theta-alpha (4-12 Hz), beta (12-30 Hz) and gamma (30-100 Hz) frequency bands for full signal.

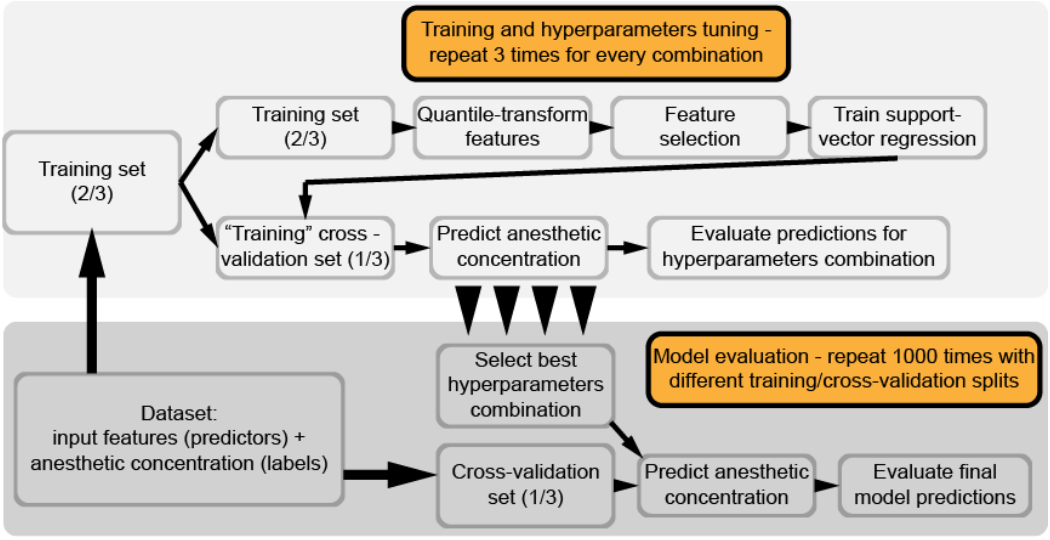

Fig. S3. Machine learning algorithm. Flowchart depicting steps for machine learning algorithm.

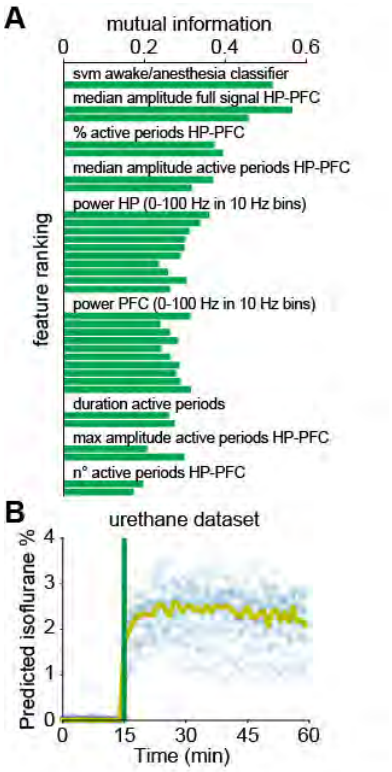

Fig. S4. Median amplitude is most informative for predicting anesthetic concentration in neonatal mice. (**A**) Bar plot displaying the feature ranking for anesthesia depth prediction by mutual information between each feature and anesthesia depth. (**B**) Scatter plot displaying predicted isoflurane concentration using features of LFP recordings from PFC and HP of urethane-anesthetized mice. Green line marks the time point of urethane injection.

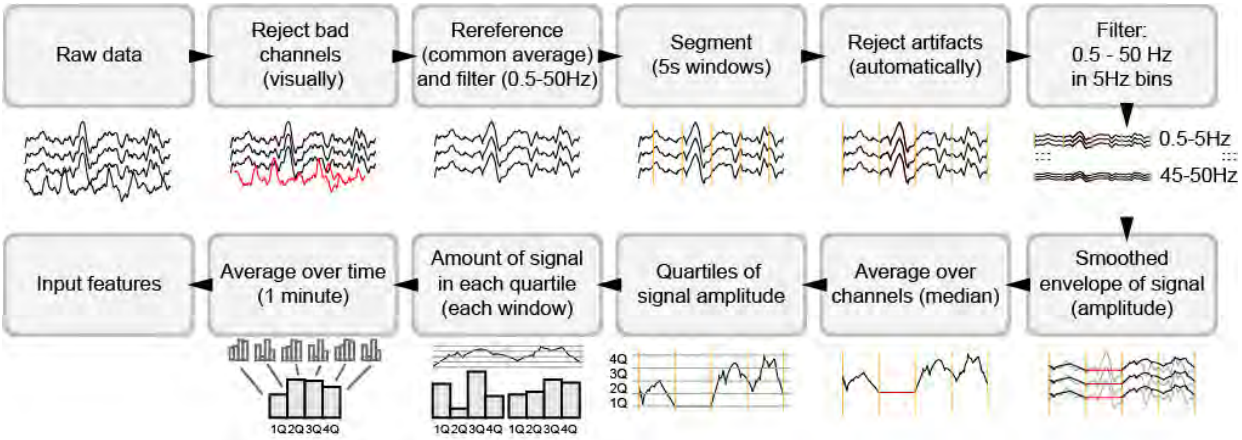

Fig. S5. EEG data processing. Flowchart depicting analysis steps for EEG data processing.

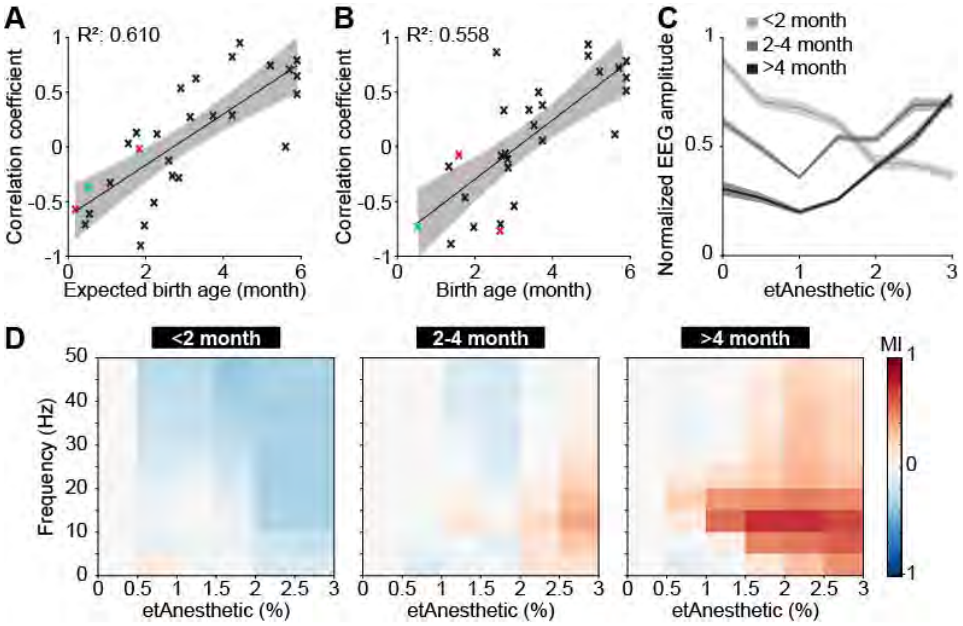

Fig. S6. Age-dependent switch from broadband suppression to frequency-specific effects of general anesthesia on EEG activity for post conceptual age and frontal electrodes. (**A**) Scatter plot displaying the correlation coefficient of median EEG amplitude and anesthetic concentration in relationship to expected birth age for sevoflurane (black), isoflurane (red), and desflurane (blue). (**B**) Scatter plot displaying the correlation coefficient of median EEG amplitude of frontal electrodes and anesthetic concentration in relationship to birth age for sevoflurane (black), isoflurane (red), and desflurane (blue). (**C**) Line plots displaying normalized EEG amplitude of frontal electrodes as a function of anesthetic concentration. (**D**) Color-coded MI of median EEG amplitudes of frontal electrodes in different frequency bands as a function of anesthetic concentration for human babies of 0-2 months (left), 2-4 months (middle) and 4-6 months (right).

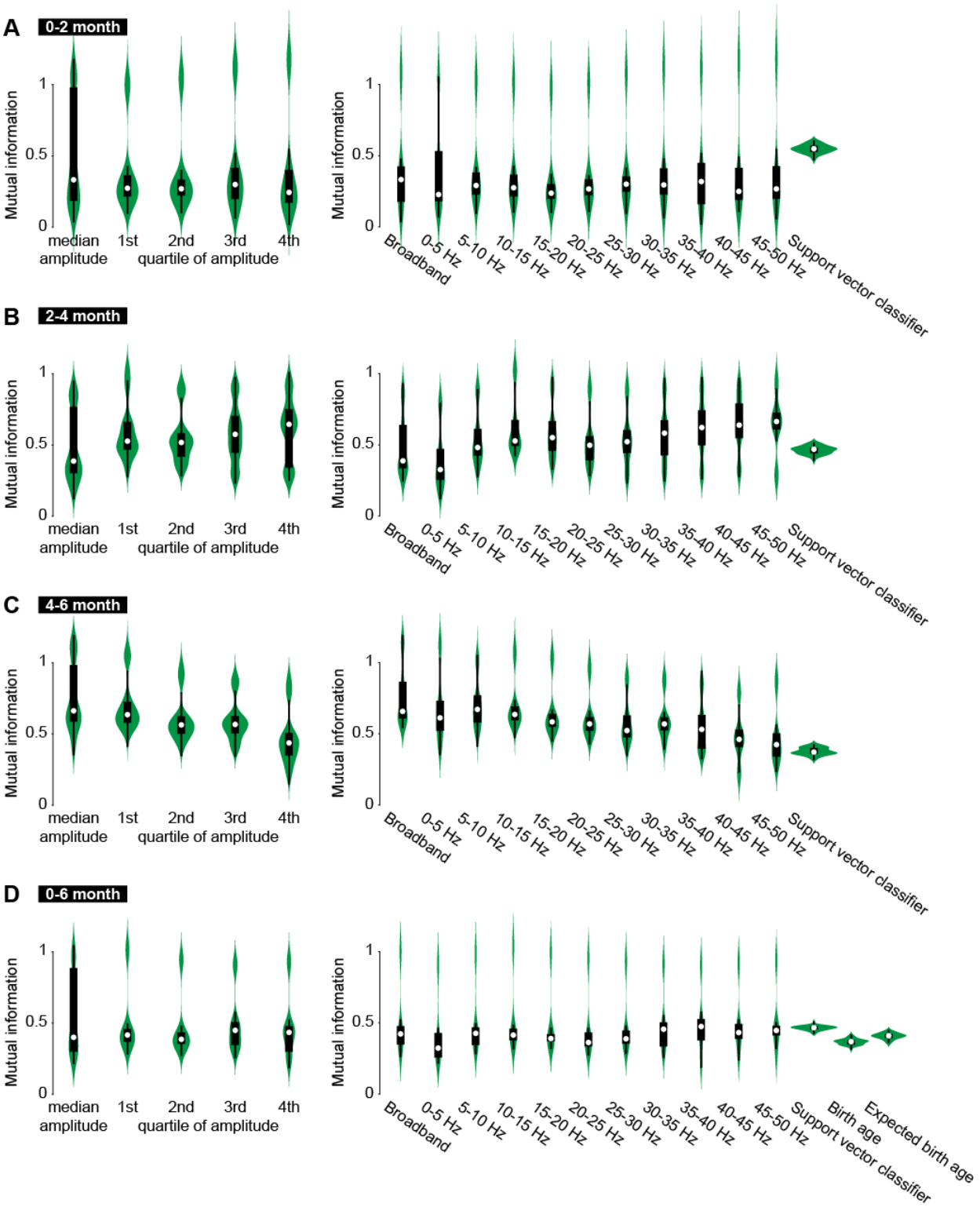

Fig. S7. Features predicting anesthetic concentration from EEG recordings in human infants. (**A**) Violin plots displaying mutual information between each feature and predicted anesthetic concentration for amplitude-related features (left) and frequency-related features (right) for human infants of 0-2 months of age. (**B**) Same as (A) for human

infants of 2-4 months of age. (**C**) Same as (A) for human infants of 4-6 months of age. (**D**) Same as (A) for human infants of 0-6 months of age.

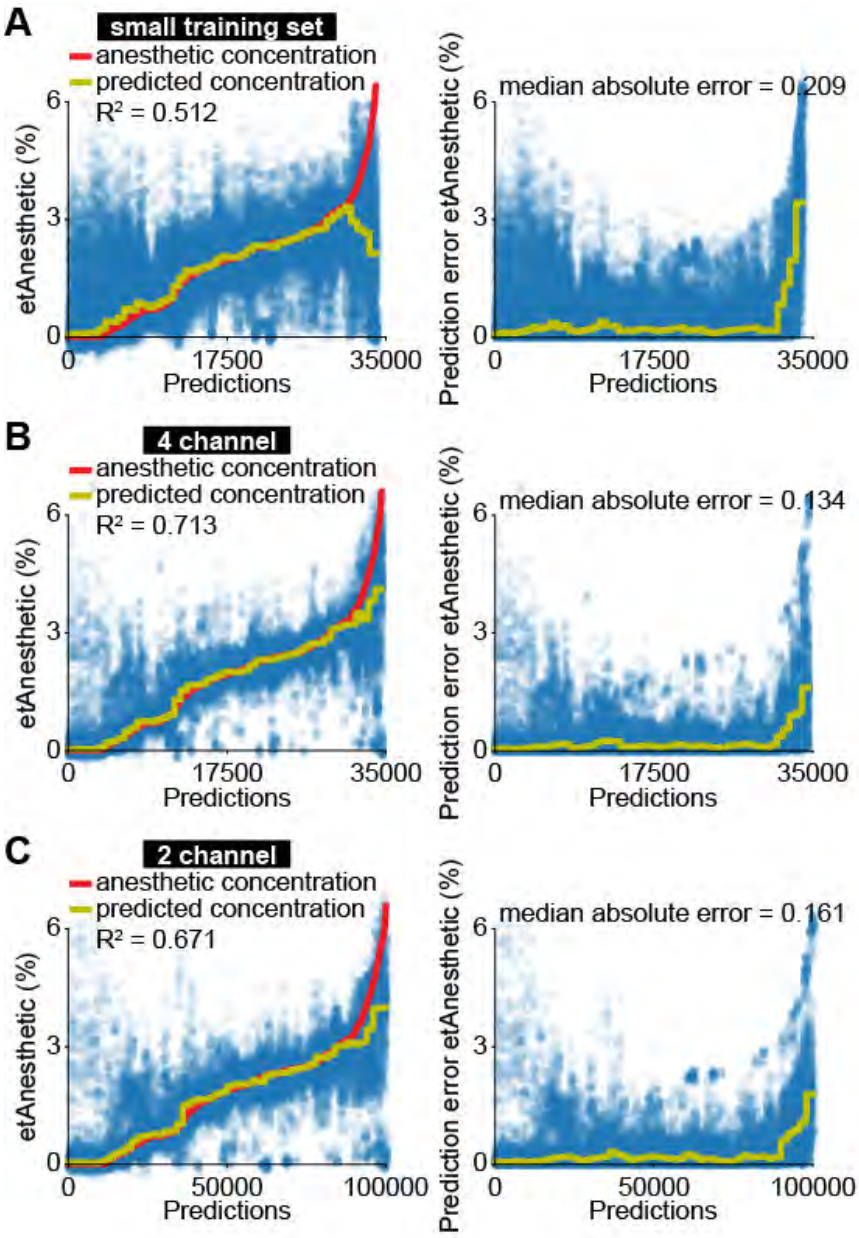

Fig. S8. Reduced data set of EEG activity is still predictive for anesthetic concentration in human infants. (**A**) Scatter plots displaying measured anesthetic concentration and predicted anesthetic concentration of support vector regression for all predictions (left) and absolute difference between measured and predicted anesthetic concentration (right) for a reduced training data set of 20%. (**B**) Scatter plots displaying measured anesthetic concentration and predicted anesthetic concentration of support vector regression for all predictions (left) and absolute difference between measured and predicted anesthetic concentration (right) for reduced EEG data of 4 channels (F4, P4, F3, P3). (**C**) Same as (B) for reduced EEG data of 2 channels (P4, P3).

Tab. S1. Demographic information.

	All Subjects	Age Groups		
	0-6 months	0-2 months	2-4 months	4-6 months
	N=35	n=6	n=19	n=10
Age at birth (weeks; median, IQR)	38.00 [36.64, 39.00]	39.71 [38.25, 40.53]	37.00 [34.00, 39.00]	39.00 [37.44, 39.00]
PNA (months; median, IQR))	3.06 [2.64, 4.42]	1.51 [1.36, 1.73]	2.89 [2.74, 3.52]	5.54 [5.08, 5.91]
Weight (kg, median, IQR)	5.97 [4.89, 7.09]	4.91 [4.80, 5.01]	5.76 [4.89, 6.62]	7.29 [6.42, 8.10]
Male (n, %)	30 (85.7)	5 (83.3)	16 (84.2)	9 (90.0)
Duration of Anesthesia (mins; median, IQR)	114.00 [82.5, 181.00]	190.00 [123.50, 211.50]	114.00 [85.00, 154.00]	89.00 [76.5, 181.75]

ID	Age at birth (weeks)	Postnatal age (months)	Weight (kg)	Sex	Surgery	Duration Anesthesia
1	39,0	0,53	3,7	Female	Anorectoplasty	217
2	38,0	1,35	5,7	Male	Hernia Repair	103
3	41,0	1,41	4,8	Male	Hernia Repair	93
4	40,4	1,61	5,0	Male	Extrophy of Bladder Closure, Spica Cast	185
5	40,6	1,77	4,8	Male	Colostomy Closure	268
6	37,5	1,87	5,0	Male	Hernia Repair, Frenulotomy	195
7	39,0	2,04	5,0	Male	Circumcision	60
8	42,0	2,60	6,0	Male	Hernia Repair	89
9	34,0	2,60	4,8	Male	Hernia Repair	103
10	29.1	2,69	3,3	Male	Hernia Repair, Circumcision	152
11	39,0	2,73	7,2	Male	Hernia Repair, Orchidopexy	187
12	30,3	2,76	3,4	Male	Hernia Repair	149
13	35,4	2,79	4,7	Male	Hernia Repair, Meatoplasty	114
14	34,0	2,83	5,0	Male	Hernia Repair	79
15	39,0	2,89	6,1	Female	Hernia Repair	96
16	37,0	2,89	6,3	Male	Hernia Repair	140
17	39,0	3,02	5,8	Female	Vaginoscopy	156

18	29,0	3,06	4,2	Male	Hernia Repair	185
19	38,0	3,45	6,9	Male	Hernia Repair	72
20	39,0	3,52	7,2	Male	Fistulotomy	58
21	37,0	3,52	6,1	Female	Nephrectomy	170
22	37,0	3,58	5,7	Male	Hernia Repair	118
23	41,0	3,71	5,8	Male	Hernia Repair	102
24	39,0	3,81	7,0	Male	Pyleoplasty	177
25	39,0	3,81	7,6	Male	Fistulotomy	81
26	39,0	4,04	7,4	Male	Hernia Repair	94
27	42,0	4,80	6,3	Female	Hernia Repair	76
28	29,1	5,03	7,8	Male	Hernia Repair	78
29	38,0	5,26	6,3	Male	Hypospadias Repair	22
30	39,0	5,36	8,5	Male	Orchidopexy	76
31	39,1	5,72	7,2	Male	Colostomy Closure	310
32	29,0	5,78	9,1	Male	Fistulotomy	62
33	40,4	5,95	8,2	Male	Hypospadias Repair	189
34	39,0	6,01	6,7	Male	Chordee Release	160
35	30,3	6,05	3,2	Male	Circumcision	84

Tab. S2. Statistics summary.

Figure 1B

Active periods PFC

one-way anova
Analysis of Variance of Aligned Rank Transformed Data

Table Type: Repeated Measures Analysis of Variance Table (Type I)
Model: Repeated Measures (aov)
Response: art(variable)

	Error Df	Df.res	F value	Pr(>F)
1 time anm:t	3	54	59.792	< 2.22e-16 ***

Signif. codes: 0 '***' 0.001 '**' 0.01 '*' 0.05 '.' 0.1 ' ' 1

contrast	estimate	SE	df	t.ratio	p.value
1 - 2	35.000000	3.280084	54	10.670	<.0001
1 - 3	40.105263	3.280084	54	12.227	<.0001

Figure 1B

Active periods HP

one-way anova
Analysis of Variance of Aligned Rank Transformed Data

Table Type: Repeated Measures Analysis of Variance Table (Type I)
Model: Repeated Measures (aov)
Response: art(variable)

	Error Df	Df.res	F value	Pr(>F)
1 time anm:t	3	54	35.13	9.916e-13 ***

Signif. codes: 0 '***' 0.001 '**' 0.01 '*' 0.05 '.' 0.1 ' ' 1

contrast	estimate	SE	df	t.ratio	p.value
1 - 2	31.894737	3.912163	54	8.153	<.0001
1 - 3	36.631579	3.912163	54	9.364	<.0001

Figure 1B

Active periods LEC

one-way anova
Analysis of Variance of Aligned Rank Transformed Data

Table Type: Repeated Measures Analysis of Variance Table (Type I)
Model: Repeated Measures (aov)
Response: art(variable)

	Error Df	Df.res	F value	Pr(>F)
1 time anm:t	3	60	29.392	8.1185e-12 ***

Signif. codes: 0 '***' 0.001 '**' 0.01 '*' 0.05 '.' 0.1 ' ' 1

contrast	estimate	SE	df	t.ratio	p.value
1 - 2	26.285714	3.86664	60	6.798	<.0001
1 - 3	29.142857	3.86664	60	7.537	<.0001

Figure 1B

Active periods OB

one-way anova
Analysis of Variance of Aligned Rank Transformed Data

Table Type: Repeated Measures Analysis of Variance Table (Type I)
Model: Repeated Measures (aov)
Response: art(variable)

	Error Df	Df.res	F value	Pr(>F)
1 time anm:t	3	60	27.283	2.9636e-11 ***

Signif. codes: 0 '***' 0.001 '**' 0.01 '*' 0.05 '.' 0.1 ' ' 1

contrast	estimate	SE	df	t.ratio	p.value
1 - 2	28.4761905	4.2771	60	6.658	<.0001
1 - 3	32.5714286	4.2771	60	7.615	<.0001

1 - 4 29.000000 3.280084 54 8.841 <.0001
2 - 3 5.105263 3.280084 54 1.556 0.4118
2 - 4 -6.000000 3.280084 54 -1.829 0.2711
3 - 4 -11.105263 3.280084 54 -3.386 0.0071

P value adjustment: tukey method for comparing a family of 4 estimates

Figure 1D

Power full signal PFC

two-way anova
Analysis of Variance of Aligned Rank Transformed Data

Table Type: Repeated Measures Analysis of Variance Table (Type I)
Model: Repeated Measures (aov)
Response: art(variable)

	Error Df	Df.res	F value	Pr(>F)
1 cond	anm:c 1	18	69.487	1.3576e-07 ***
2 cond:freq	anm:: 3	54	61.935	< 2.22e-16 ***

Signif. codes: 0 '***' 0.001 '**' 0.01 '*' 0.05 '.' 0.1 ' ' 1

Bonferroni post-hoc comparison

delta	theta	beta	gamma
3.051758e-05	1.525879e-05	1.525879e-05	1.525879e-05

Power active periods PFC

two-way anova
Analysis of Variance of Aligned Rank Transformed Data

Table Type: Repeated Measures Analysis of Variance Table (Type I)
Model: Repeated Measures (aov)
Response: art(variable)

	Error Df	Df.res	F value	Pr(>F)
1 cond	anm:c 1	18	22.274	0.00017099 ***
2 cond:freq	anm:: 3	54	13.800	8.5004e-07 ***

Signif. codes: 0 '***' 0.001 '**' 0.01 '*' 0.05 '.' 0.1 ' ' 1

1 - 4 26.947368 3.912163 54 6.888 <.0001
2 - 3 4.736842 3.912163 54 1.211 0.6228
2 - 4 -4.947368 3.912163 54 -1.265 0.5891
3 - 4 -9.684211 3.912163 54 -2.475 0.0754

P value adjustment: tukey method for comparing a family of 4 estimates

Figure 1D

Power full signal HP

two-way anova
Analysis of Variance of Aligned Rank Transformed Data

Table Type: Repeated Measures Analysis of Variance Table (Type I)
Model: Repeated Measures (aov)
Response: art(variable)

	Error Df	Df.res	F value	Pr(>F)
1 cond	anm:c 1	18	46.382	2.2384e-06 ***
2 cond:freq	anm:: 3	54	48.874	2.0854e-15 ***

Signif. codes: 0 '***' 0.001 '**' 0.01 '*' 0.05 '.' 0.1 ' ' 1

Bonferroni post-hoc comparison

delta	theta	beta	gamma
1.525879e-05	1.525879e-05	1.525879e-05	1.525879e-05

Power active periods HP

two-way anova
Analysis of Variance of Aligned Rank Transformed Data

Table Type: Repeated Measures Analysis of Variance Table (Type I)
Model: Repeated Measures (aov)
Response: art(variable)

	Error Df	Df.res	F value	Pr(>F)
1 cond	anm:c 1	18	13.4602	0.0017565 **
2 cond:freq	anm:: 3	54	4.4602	0.0071739 **

Signif. codes: 0 '***' 0.001 '**' 0.01 '*' 0.05 '.' 0.1 ' ' 1

1 - 4 4.666667 3.86664 60 1.207 0.6249
2 - 3 2.857143 3.86664 60 0.739 0.8810
2 - 4 -21.619048 3.86664 60 -5.591 <.0001
3 - 4 -24.476190 3.86664 60 -6.330 <.0001

P value adjustment: tukey method for comparing a family of 4 estimates

Figure 1D

Power full signal LEC

two-way anova
Analysis of Variance of Aligned Rank Transformed Data

Table Type: Repeated Measures Analysis of Variance Table (Type I)
Model: Repeated Measures (aov)
Response: art(variable)

	Error Df	Df.res	F value	Pr(>F)
1 cond	anm:c 1	20	29.561	2.5383e-05 ***
2 cond:freq	anm:: 3	60	14.028	4.8921e-07 ***

Signif. codes: 0 '***' 0.001 '**' 0.01 '*' 0.05 '.' 0.1 ' ' 1

Bonferroni post-hoc comparison

delta	theta	beta	gamma
0.08628464	4.703522e-03	3.814697e-06	0.0003356934

Power active periods LEC

two-way anova
Analysis of Variance of Aligned Rank Transformed Data

Table Type: Repeated Measures Analysis of Variance Table (Type I)
Model: Repeated Measures (aov)
Response: art(variable)

	Error Df	Df.res	F value	Pr(>F)
1 cond	anm:c 1	20	17.512	0.00045669 ***
2 cond:freq	anm:: 3	60	11.020	7.3369e-06 ***

Signif. codes: 0 '***' 0.001 '**' 0.01 '*' 0.05 '.' 0.1 ' ' 1

1 - 4 32.9523810 4.2771 60 7.704 <.0001
2 - 3 4.0952381 4.2771 60 0.957 0.7739
2 - 4 4.4761905 4.2771 60 1.047 0.7229
3 - 4 0.3809524 4.2771 60 0.089 0.9997

P value adjustment: tukey method for comparing a family of 4 estimates

Figure 1D

Power full signal OB

two-way anova
Analysis of Variance of Aligned Rank Transformed Data

Table Type: Repeated Measures Analysis of Variance Table (Type I)
Model: Repeated Measures (aov)
Response: art(variable)

	Error Df	Df.res	F value	Pr(>F)
1 cond	anm:c 1	20	4.2525	0.052427 .
2 cond:freq	anm:: 3	60	3.6152	0.018139 *

Signif. codes: 0 '***' 0.001 '**' 0.01 '*' 0.05 '.' 0.1 ' ' 1

Bonferroni post-hoc comparison

delta	theta	beta	gamma
1.00000000	2.883911e-03	1.171112e-03	0.0171394348

Power active periods OB

two-way anova
Analysis of Variance of Aligned Rank Transformed Data

Table Type: Repeated Measures Analysis of Variance Table (Type I)
Model: Repeated Measures (aov)
Response: art(variable)

	Error Df	Df.res	F value	Pr(>F)
1 cond	anm:c 1	20	1.3282	0.262711
2 cond:freq	anm:: 3	60	2.5393	0.064904 .

Signif. codes: 0 '***' 0.001 '**' 0.01 '*' 0.05 '.' 0.1 ' ' 1

Bonferroni post-hoc comparison
delta theta beta gamma
2.471924e-02 9.650116e-01 1.000000e+00 2.857971e-02

Figure 1E

Log firing rate full signal PFC
one-way anova
Analysis of Variance of Aligned Rank Transformed Data

Table Type: Repeated Measures Analysis of Variance Table (Type I)
Model: Repeated Measures (aov)
Response: art(variable)

	Error Df	Df.res	F value	Pr(>F)
1 time anm:t	3	54	27.752	5.3925e-11 ***

Signif. codes: 0 '***' 0.001 '**' 0.01 '*' 0.05 '.' 0.1 ' ' 1

contrast	estimate	SE	df	t.ratio	p.value
1 - 2	18.3684211	2.347886	54	7.823	<.0001
1 - 3	18.5263158	2.347886	54	7.891	<.0001
1 - 4	14.1578947	2.347886	54	6.030	<.0001
2 - 3	0.1578947	2.347886	54	0.067	0.9999
2 - 4	-4.2105263	2.347886	54	-1.793	0.2877
3 - 4	-4.3684211	2.347886	54	-1.861	0.2571

P value adjustment: tukey method for comparing a family of 4 estimates

Log firing rate active periods PFC
one-way anova
Analysis of Variance of Aligned Rank Transformed Data

Table Type: Repeated Measures Analysis of Variance Table (Type I)
Model: Repeated Measures (aov)
Response: art(variable)

	Error Df	Df.res	F value	Pr(>F)
1 time anm:t	3	54	4.7319	0.0052906 **

Bonferroni post-hoc comparison
delta theta beta gamma
9.012909e-01 7.232666e-02 4.943848e-02 6.256104e-01

Figure 1E

Log firing rate full signal HP
one-way anova
Analysis of Variance of Aligned Rank Transformed Data

Table Type: Repeated Measures Analysis of Variance Table (Type I)
Model: Repeated Measures (aov)
Response: art(variable)

	Error Df	Df.res	F value	Pr(>F)
1 time anm:t	3	54	13.869	8.0251e-07 ***

Signif. codes: 0 '***' 0.001 '**' 0.01 '*' 0.05 '.' 0.1 ' ' 1

contrast	estimate	SE	df	t.ratio	p.value
1 - 2	9.3684211	1.71104	54	5.475	<.0001
1 - 3	9.7105263	1.71104	54	5.675	<.0001
1 - 4	5.8684211	1.71104	54	3.430	0.0062
2 - 3	0.3421053	1.71104	54	0.200	0.9971
2 - 4	-3.5000000	1.71104	54	-2.046	0.1844
3 - 4	-3.8421053	1.71104	54	-2.245	0.1241

P value adjustment: tukey method for comparing a family of 4 estimates

Log firing rate active periods HP
one-way anova
Analysis of Variance of Aligned Rank Transformed Data

Table Type: Repeated Measures Analysis of Variance Table (Type I)
Model: Repeated Measures (aov)
Response: art(variable)

	Error Df	Df.res	F value	Pr(>F)
1 time anm:t	3	54	1.9002	0.14053

Bonferroni post-hoc comparison
delta theta beta gamma
1.00000000 1.907349e-05 4.703522e-03 0.0862846375

Figure 1E

Log firing rate full signal LEC
one-way anova
Analysis of Variance of Aligned Rank Transformed Data

Table Type: Repeated Measures Analysis of Variance Table (Type I)
Model: Repeated Measures (aov)
Response: art(variable)

	Error Df	Df.res	F value	Pr(>F)
1 time anm:t	3	60	12.998	1.204e-06 ***

Signif. codes: 0 '***' 0.001 '**' 0.01 '*' 0.05 '.' 0.1 ' ' 1

contrast	estimate	SE	df	t.ratio	p.value
1 - 2	1.123810e+01	2.139859	60	5.252	<.0001
1 - 3	1.123810e+01	2.139859	60	5.252	<.0001
1 - 4	1.009524e+01	2.139859	60	4.718	0.0001
2 - 3	1.421085e-14	2.139859	60	0.000	1.0000
2 - 4	-1.142857e+00	2.139859	60	-0.534	0.9504
3 - 4	-1.142857e+00	2.139859	60	-0.534	0.9504

P value adjustment: tukey method for comparing a family of 4 estimates

Log firing rate active periods LEC
one-way anova
Analysis of Variance of Aligned Rank Transformed Data

Table Type: Repeated Measures Analysis of Variance Table (Type I)
Model: Repeated Measures (aov)
Response: art(variable)

	Error Df	Df.res	F value	Pr(>F)
1 time anm:t	3	60	11.826	3.4682e-06 ***

Bonferroni post-hoc comparison
delta theta beta gamma
0.11605835 9.713669e-01 2.840424e-02 0.0862846375

Figure 1E

Log firing rate full signal OB
one-way anova
Analysis of Variance of Aligned Rank Transformed Data

Table Type: Repeated Measures Analysis of Variance Table (Type I)
Model: Repeated Measures (aov)
Response: art(variable)

	Error Df	Df.res	F value	Pr(>F)
1 time anm:t	3	60	5.1927	0.0029577 **

Signif. codes: 0 '***' 0.001 '**' 0.01 '*' 0.05 '.' 0.1 ' ' 1

contrast	estimate	SE	df	t.ratio	p.value
1 - 2	6.3333333	2.434027	60	2.602	0.0551
1 - 3	9.4047619	2.434027	60	3.864	0.0015
1 - 4	5.6904762	2.434027	60	2.338	0.1009
2 - 3	3.0714286	2.434027	60	1.262	0.5905
2 - 4	-0.6428571	2.434027	60	-0.264	0.9935
3 - 4	-3.7142857	2.434027	60	-1.526	0.4286

P value adjustment: tukey method for comparing a family of 4 estimates

Log firing rate active periods OB
one-way anova
Analysis of Variance of Aligned Rank Transformed Data

Table Type: Repeated Measures Analysis of Variance Table (Type I)
Model: Repeated Measures (aov)
Response: art(variable)

	Error Df	Df.res	F value	Pr(>F)
1 time anm:t	3	60	1.0235	0.38868

Signif. codes: 0 '***' 0.001 '**' 0.01 '*' 0.05 '.' 0.1 ' ' 1
contrast estimate SE df t.ratio p.value
1 - 2 7.3684211 2.394314 54 3.077 0.0168
1 - 3 7.7368421 2.394314 54 3.231 0.0110
1 - 4 6.8947368 2.394314 54 2.880 0.0283
2 - 3 0.3684211 2.394314 54 0.154 0.9987
2 - 4 -0.4736842 2.394314 54 -0.198 0.9972
3 - 4 -0.8421053 2.394314 54 -0.352 0.9849

P value adjustment: tukey method for comparing a family of 4 estimates

Figure 2B

Active periods PFC

one-way anova
Analysis of Variance of Aligned Rank Transformed Data

Table Type: Repeated Measures Analysis of Variance Table (Type I)
Model: Repeated Measures (aov)
Response: art(variable)

Error Df Df.res F value Pr(>F)
1 time anm:t 3 48 52.546 3.3847e-15 ***

Signif. codes: 0 '***' 0.001 '**' 0.01 '*' 0.05 '.' 0.1 ' ' 1
contrast estimate SE df t.ratio p.value
1 - 2 10.41176 2.962703 48 3.514 0.0052
1 - 3 21.29412 2.962703 48 7.187 <.0001
1 - 4 35.47059 2.962703 48 11.972 <.0001
2 - 3 10.88235 2.962703 48 3.673 0.0033
2 - 4 25.05882 2.962703 48 8.458 <.0001
3 - 4 14.17647 2.962703 48 4.785 0.0001

P value adjustment: tukey method for comparing a family of 4 estimates

Figure 2D

Power full signal PFC

two-way anova

Signif. codes: 0 '***' 0.001 '**' 0.01 '*' 0.05 '.' 0.1 ' ' 1
contrast estimate SE df t.ratio p.value
1 - 2 2.052632 1.936114 54 1.060 0.7149
1 - 3 3.368421 1.936114 54 1.740 0.3136
1 - 4 4.368421 1.936114 54 2.256 0.1214
2 - 3 1.315789 1.936114 54 0.680 0.9044
2 - 4 2.315789 1.936114 54 1.196 0.6319
3 - 4 1.000000 1.936114 54 0.516 0.9548

P value adjustment: tukey method for comparing a family of 4 estimates

Figure 2B

Active periods HP

one-way anova
Analysis of Variance of Aligned Rank Transformed Data

Table Type: Repeated Measures Analysis of Variance Table (Type I)
Model: Repeated Measures (aov)
Response: art(variable)

Error Df Df.res F value Pr(>F)
1 time anm:t 3 48 59.575 3.2938e-16 ***

Signif. codes: 0 '***' 0.001 '**' 0.01 '*' 0.05 '.' 0.1 ' ' 1
contrast estimate SE df t.ratio p.value
1 - 2 11.235294 2.538526 48 4.426 0.0003
1 - 3 23.382353 2.538526 48 9.211 <.0001
1 - 4 31.617647 2.538526 48 12.455 <.0001
2 - 3 12.147059 2.538526 48 4.785 0.0001
2 - 4 20.382353 2.538526 48 8.029 <.0001
3 - 4 8.235294 2.538526 48 3.244 0.0112

P value adjustment: tukey method for comparing a family of 4 estimate

Figure 2D

Power full signal HP

two-way anova

Signif. codes: 0 '***' 0.001 '**' 0.01 '*' 0.05 '.' 0.1 ' ' 1
contrast estimate SE df t.ratio p.value
1 - 2 -3.761905 2.429108 60 -1.549 0.4155
1 - 3 -4.761905 2.429108 60 -1.960 0.2145
1 - 4 8.238095 2.429108 60 3.391 0.0066
2 - 3 -1.000000 2.429108 60 -0.412 0.9763
2 - 4 12.000000 2.429108 60 4.940 <.0001
3 - 4 13.000000 2.429108 60 5.352 <.0001

P value adjustment: tukey method for comparing a family of 4 estimates

Signif. codes: 0 '***' 0.001 '**' 0.01 '*' 0.05 '.' 0.1 ' ' 1
contrast estimate SE df t.ratio p.value
1 - 2 -3.2380952 2.486221 60 -1.302 0.5650
1 - 3 -2.4285714 2.486221 60 -0.977 0.7631
1 - 4 -4.1428571 2.486221 60 -1.666 0.3503
2 - 3 0.8095238 2.486221 60 0.326 0.9880
2 - 4 -0.9047619 2.486221 60 -0.364 0.9834
3 - 4 -1.7142857 2.486221 60 -0.690 0.9007

P value adjustment: tukey method for comparing a family of 4 estimates

Analysis of Variance of Aligned Rank Transformed Data

Table Type: Repeated Measures Analysis of Variance Table (Type I)
Model: Repeated Measures (aov)
Response: art(variable)

	Error Df	Df.res	F value	Pr(>F)
1 cond	anm:c	1	16	34.631	2.3047e-05 ***
2 cond:freq	anm::	3	48	13.074	2.2956e-06 ***

Signif. codes: 0 '***' 0.001 '**' 0.01 '*' 0.05 '.' 0.1 ' ' 1

Bonferroni post-hoc comparison

delta	theta	beta	gamma
0.01538086	0.05145264	0.0033569336	0.0001220703

Power active periods PFC

two-way anova
Analysis of Variance of Aligned Rank Transformed Data

Table Type: Repeated Measures Analysis of Variance Table (Type I)
Model: Repeated Measures (aov)
Response: art(variable)

	Error Df	Df.res	F value	Pr(>F)
1 cond	anm:c	1	16	19.642	0.00041858 ***
2 cond:freq	anm::	3	48	13.957	1.1375e-06 ***

Signif. codes: 0 '***' 0.001 '**' 0.01 '*' 0.05 '.' 0.1 ' ' 1

Bonferroni post-hoc comparison

delta	theta	beta	gamma
0.28564453	0.35461426	1.0000000000	1.0000000000

Figure 2E

Log firing rate full signal PFC

one-way anova
Analysis of Variance of Aligned Rank Transformed Data

Analysis of Variance of Aligned Rank Transformed Data

Table Type: Repeated Measures Analysis of Variance Table (Type I)
Model: Repeated Measures (aov)
Response: art(variable)

	Error Df	Df.res	F value	Pr(>F)
1 cond	anm:c	1	16	21.758	0.00025899 ***
2 cond:freq	anm::	3	48	17.300	9.4437e-08 ***

Signif. codes: 0 '***' 0.001 '**' 0.01 '*' 0.05 '.' 0.1 ' ' 1

Bonferroni post-hoc comparison

delta	theta	beta	gamma
0.31872559	0.04394531	0.0006103516	0.0003051758

Power active periods HP

two-way anova
Analysis of Variance of Aligned Rank Transformed Data

Table Type: Repeated Measures Analysis of Variance Table (Type I)
Model: Repeated Measures (aov)
Response: art(variable)

	Error Df	Df.res	F value	Pr(>F)
1 cond	anm:c	1	16	2.8510	0.1107108
2 cond:freq	anm::	3	48	5.6962	0.0020285 **

Signif. codes: 0 '***' 0.001 '**' 0.01 '*' 0.05 '.' 0.1 ' ' 1

Bonferroni post-hoc comparison

delta	theta	beta	gamma
0.12207031	1.00000000	1.0000000000	0.4355468750

Figure 2E

Log firing rate full signal HP

one-way anova
Analysis of Variance of Aligned Rank Transformed Data

Table Type: Repeated Measures Analysis of Variance Table (Type I)
Model: Repeated Measures (aov)
Response: art(variable)

	Error Df	Df.res	F value	Pr(>F)
1 time anm:t	3	48	5.0897	0.0038626 **

Signif. codes: 0 '***' 0.001 '**' 0.01 '*' 0.05 '.' 0.1 ' ' 1

contrast	estimate	SE	df	t.ratio	p.value
1 - 2	2.735294	3.186585	48	0.858	0.8261
1 - 3	10.441176	3.186585	48	3.277	0.0102
1 - 4	9.411765	3.186585	48	2.954	0.0242
2 - 3	7.705882	3.186585	48	2.418	0.0872
2 - 4	6.676471	3.186585	48	2.095	0.1693
3 - 4	-1.029412	3.186585	48	-0.323	0.9882

P value adjustment: tukey method for comparing a family of 4 estimates

Table Type: Repeated Measures Analysis of Variance Table (Type I)
Model: Repeated Measures (aov)
Response: art(variable)

	Error Df	Df.res	F value	Pr(>F)
1 time anm:t	3	48	21.092	7.4021e-09 ***

Signif. codes: 0 '***' 0.001 '**' 0.01 '*' 0.05 '.' 0.1 ' ' 1

contrast	estimate	SE	df	t.ratio	p.value
1 - 2	4.911765	3.228287	48	1.521	0.4329
1 - 3	14.352941	3.228287	48	4.446	0.0003
1 - 4	23.676471	3.228287	48	7.334	<.0001
2 - 3	9.441176	3.228287	48	2.925	0.0261
2 - 4	18.764706	3.228287	48	5.813	<.0001
3 - 4	9.323529	3.228287	48	2.888	0.0286

P value adjustment: tukey method for comparing a family of 4 estimates

Log firing rate active periods PFC

one-way anova
Analysis of Variance of Aligned Rank Transformed Data

Table Type: Repeated Measures Analysis of Variance Table (Type I)
Model: Repeated Measures (aov)
Response: art(variable)

	Error Df	Df.res	F value	Pr(>F)
1 time anm:t	3	48	11.305	9.9724e-06 ***

Signif. codes: 0 '***' 0.001 '**' 0.01 '*' 0.05 '.' 0.1 ' ' 1

contrast	estimate	SE	df	t.ratio	p.value
1 - 2	-4.000000	3.69339	48	-1.083	0.7015
1 - 3	-7.588235	3.69339	48	-2.055	0.1829
1 - 4	-20.294118	3.69339	48	-5.495	<.0001
2 - 3	-3.588235	3.69339	48	-0.972	0.7662
2 - 4	-16.294118	3.69339	48	-4.412	0.0003
3 - 4	-12.705882	3.69339	48	-3.440	0.0064

Log firing rate active periods HP

one-way anova
Analysis of Variance of Aligned Rank Transformed Data

Table Type: Repeated Measures Analysis of Variance Table (Type I)
Model: Repeated Measures (aov)
Response: art(variable)

	Error Df	Df.res	F value	Pr(>F)
1 time anm:t	3	48	2.6759	0.057595 .

Signif. codes: 0 '***' 0.001 '**' 0.01 '*' 0.05 '.' 0.1 ' ' 1

contrast	estimate	SE	df	t.ratio	p.value
1 - 2	-0.8235294	3.42545	48	-0.240	0.9950
1 - 3	-6.4705882	3.42545	48	-1.889	0.2463
1 - 4	-7.8823529	3.42545	48	-2.301	0.1120
2 - 3	-5.6470588	3.42545	48	-1.649	0.3619
2 - 4	-7.0588235	3.42545	48	-2.061	0.1807
3 - 4	-1.4117647	3.42545	48	-0.412	0.9761

P value adjustment: tukey method for comparing a family of 4 estimates

P value adjustment: tukey method for comparing a family of 4 estimates

Figure S1A

Imaginary coherence PFC-HP

two-way anova
Analysis of Variance of Aligned Rank Transformed Data

Table Type: Repeated Measures Analysis of Variance Table (Type I)
Model: Repeated Measures (aov)
Response: art(variable)

	Error Df	Df.res	F value	Pr(>F)
1 cond	anm:c	1	18	0.274684	0.60660
2 cond:freq	anm::	3	54	0.098025	0.96078

Signif. codes: 0 '***' 0.001 '**' 0.01 '*' 0.05 '.' 0.1 ' ' 1

two-way anova

Bonferroni post-hoc comparison

delta theta beta gamma
1.000000e+00 1.000000e+00 1.000000e+00 1.000000e+00

Figure S1A

Imaginary coherence LEC-OB

two-way anova
Analysis of Variance of Aligned Rank Transformed Data

Table Type: Repeated Measures Analysis of Variance Table (Type I)
Model: Repeated Measures (aov)
Response: art(variable)

	Error Df	Df.res	F value	Pr(>F)
1 cond	anm:c	1	20	0.55076	0.466636
2 cond:freq	anm::	3	60	2.20480	0.096781 .

Signif. codes: 0 '***' 0.001 '**' 0.01 '*' 0.05 '.' 0.1 ' ' 1

two-way anova

Bonferroni post-hoc comparison

delta theta beta gamma
0.81166840 1.000000e+00 1.000000e+00 0.9159431458

Figure S1C

PPC PFC

two-way anova
Analysis of Variance of Aligned Rank Transformed Data

Table Type: Repeated Measures Analysis of Variance Table (Type I)
Model: Repeated Measures (aov)
Response: art(variable)

	Error Df	Df.res	F value	Pr(>F)
1 cond	anm:c	1	18	2.5610	0.126930
2 cond:freq	anm::	3	54	2.3506	0.082532 .

Signif. codes: 0 '***' 0.001 '**' 0.01 '*' 0.05 '.' 0.1 ' ' 1

Bonferroni post-hoc comparison

delta theta beta gamma

Figure S1C

PPC HP

two-way anova
Analysis of Variance of Aligned Rank Transformed Data

Table Type: Repeated Measures Analysis of Variance Table (Type I)
Model: Repeated Measures (aov)
Response: art(variable)

	Error Df	Df.res	F value	Pr(>F)
1 cond	anm:c	1	18	0.76678	0.39275
2 cond:freq	anm::	3	54	1.11065	0.35286

Signif. codes: 0 '***' 0.001 '**' 0.01 '*' 0.05 '.' 0.1 ' ' 1

Bonferroni post-hoc comparison

delta theta beta gamma

Figure S1C

PPC LEC

two-way anova
Analysis of Variance of Aligned Rank Transformed Data

Table Type: Repeated Measures Analysis of Variance Table (Type I)
Model: Repeated Measures (aov)
Response: art(variable)

	Error Df	Df.res	F value	Pr(>F)
1 cond	anm:c	1	20	2.2892	0.145922
2 cond:freq	anm::	3	60	2.8296	0.045918 *

Signif. codes: 0 '***' 0.001 '**' 0.01 '*' 0.05 '.' 0.1 ' ' 1

Bonferroni post-hoc comparison

delta theta beta gamma

Figure S1C

PPC OB

two-way anova
Analysis of Variance of Aligned Rank Transformed Data

Table Type: Repeated Measures Analysis of Variance Table (Type I)
Model: Repeated Measures (aov)
Response: art(ppcOB)

	Error Df	Df.res	F value	Pr(>F)
1 cond_ppcOB	an_OB:_OB	1	11	1.70329	0.2185
2 cond_ppcOB:freq_ppcOB	a_OB:_OB:	3	33	0.49268	0.6898

Signif. codes: 0 '***' 0.001 '**' 0.01 '*' 0.05 '.' 0.1 ' ' 1

Bonferroni post-hoc comparison

delta theta beta gamma

1.000000e+00 6.751709e-01
1.000000e+00 1.000000e+00

Figure S1D

1/f slope PFC

one-way anova
Analysis of Variance of Aligned Rank Transformed Data

Table Type: Repeated Measures Analysis of Variance Table (Type I)
Model: Repeated Measures (aov)
Response: art(variable)

	Error Df	Df.res	F value	Pr(>F)
1 time anm:t	3	54	0.18187	0.90826

Signif. codes: 0 '***' 0.001 '**' 0.01 '*' 0.05 '.' 0.1 ' ' 1

	contrast	estimate	SE	df	t.ratio	p.value
1	2 - 2	-3.0000000	7.083249	54	-0.424	0.9742
2	1 - 3	-5.1578947	7.083249	54	-0.728	0.8854
3	1 - 4	-3.3157895	7.083249	54	-0.468	0.9657
4	2 - 3	-2.1578947	7.083249	54	-0.305	0.9901
5	2 - 4	-0.3157895	7.083249	54	-0.045	1.0000
6	3 - 4	1.8421053	7.083249	54	0.260	0.9938

P value adjustment: tukey method for comparing a family of 4 estimates

Figure S1F

Sample entropy PFC

two-way anova
Analysis of Variance of Aligned Rank Transformed Data

Table Type: Repeated Measures Analysis of Variance Table (Type I)
Model: Repeated Measures (aov)
Response: art(variable)

	Error Df	Df.res	F value	Pr(>F)
1 cond	anm:c 1	18	0.043354	0.83740
2 cond:freq	anm:: 3	54	0.721699	0.54341

1.000000e+00 2.408295e-01
1.000000e+00 1.000000e+00

Figure S1D

1/f slope HP

one-way anova
Analysis of Variance of Aligned Rank Transformed Data

Table Type: Repeated Measures Analysis of Variance Table (Type I)
Model: Repeated Measures (aov)
Response: art(variable)

	Error Df	Df.res	F value	Pr(>F)
1 time anm:t	3	54	0.59431	0.62144

Signif. codes: 0 '***' 0.001 '**' 0.01 '*' 0.05 '.' 0.1 ' ' 1

	contrast	estimate	SE	df	t.ratio	p.value
1	2 - 2	3.684211	7.330003	54	0.503	0.9581
2	1 - 3	9.263158	7.330003	54	1.264	0.5897
3	1 - 4	1.894737	7.330003	54	0.258	0.9939
4	2 - 3	5.578947	7.330003	54	0.761	0.8715
5	2 - 4	-1.789474	7.330003	54	-0.244	0.9948
6	3 - 4	-7.368421	7.330003	54	-1.005	0.7470

P value adjustment: tukey method for comparing a family of 4 estimates

Figure S1F

Sample entropy HP

two-way anova
Analysis of Variance of Aligned Rank Transformed Data

Table Type: Repeated Measures Analysis of Variance Table (Type I)
Model: Repeated Measures (aov)
Response: art(variable)

	Error Df	Df.res	F value	Pr(>F)
1 cond	anm:c 1	18	0.051911	0.82234
2 cond:freq	anm:: 3	54	1.105389	0.35498

0.23802948 1.000000e+00
1.000000e+00 1.0000000000

Figure S1D

1/f slope LEC

one-way anova
Analysis of Variance of Aligned Rank Transformed Data

Table Type: Repeated Measures Analysis of Variance Table (Type I)
Model: Repeated Measures (aov)
Response: art(variable)

	Error Df	Df.res	F value	Pr(>F)
1 time anm:t	3	60	0.2308	0.87458

Signif. codes: 0 '***' 0.001 '**' 0.01 '*' 0.05 '.' 0.1 ' ' 1

	contrast	estimate	SE	df	t.ratio	p.value
1	2 - 2	3.8095238	6.694838	60	0.569	0.9409
2	1 - 3	-1.3333333	6.694838	60	-0.199	0.9972
3	1 - 4	-0.4761905	6.694838	60	-0.071	0.9999
4	2 - 3	-5.1428571	6.694838	60	-0.768	0.8685
5	2 - 4	-4.2857143	6.694838	60	-0.640	0.9186
6	3 - 4	0.8571429	6.694838	60	0.128	0.9992

P value adjustment: tukey method for comparing a family of 4 estimates

Figure S1F

Sample entropy LEC

two-way anova
Analysis of Variance of Aligned Rank Transformed Data

Table Type: Repeated Measures Analysis of Variance Table (Type I)
Model: Repeated Measures (aov)
Response: art(variable)

	Error Df	Df.res	F value	Pr(>F)
1 cond	anm:c 1	20	0.4563	0.50709
2 cond:freq	anm:: 3	60	1.4887	0.22671

1.00000000 1.000000e+00
1.000000e+00 0.1367187500

Figure S1D

1/f slope OB

one-way anova
Analysis of Variance of Aligned Rank Transformed Data

Table Type: Repeated Measures Analysis of Variance Table (Type I)
Model: Repeated Measures (aov)
Response: art(variable)

	Error Df	Df.res	F value	Pr(>F)
1 time anm:t	3	60	0.3423	0.79481

Signif. codes: 0 '***' 0.001 '**' 0.01 '*' 0.05 '.' 0.1 ' ' 1

	contrast	estimate	SE	df	t.ratio	p.value
1	2 - 2	-0.7142857	6.768396	60	-0.106	0.9996
2	1 - 3	-3.4761905	6.768396	60	-0.514	0.9555
3	1 - 4	3.3333333	6.768396	60	0.492	0.9605
4	2 - 3	-2.7619048	6.768396	60	-0.408	0.9768
5	2 - 4	4.0476190	6.768396	60	0.598	0.9323
6	3 - 4	6.8095238	6.768396	60	1.006	0.7465

P value adjustment: tukey method for comparing a family of 4 estimates

Figure S1F

entropy OB

two-way anova
Analysis of Variance of Aligned Rank Transformed Data

Table Type: Repeated Measures Analysis of Variance Table (Type I)
Model: Repeated Measures (aov)
Response: art(variable)

	Error Df	Df.res	F value	Pr(>F)
1 cond	anm:c 1	20	0.092223	0.76451
2 cond:freq	anm:: 3	60	0.134148	0.93933

Signif. codes: 0 ‘***’ 0.001 ‘**’ 0.01 ‘*’ 0.05 ‘.’ 0.1 ‘ ’ 1

Bonferroni post-hoc comparison

delta theta beta gamma
1.000000e+00 1.000000e+00 1.000000e+00 1.000000e+00

Signif. codes: 0 ‘***’ 0.001 ‘**’ 0.01 ‘*’ 0.05 ‘.’ 0.1 ‘ ’ 1

Bonferroni post-hoc comparison

delta theta beta gamma
1.000000e+00 5.787506e-01 1.000000e+00 1.000000e+00

Signif. codes: 0 ‘***’ 0.001 ‘**’ 0.01 ‘*’ 0.05 ‘.’ 0.1 ‘ ’ 1

Bonferroni post-hoc comparison

delta theta beta gamma
1.00000000 1.000000e+00 1.000000e+00 1.0000000000

Signif. codes: 0 ‘***’ 0.001 ‘**’ 0.01 ‘*’ 0.05 ‘.’ 0.1 ‘ ’ 1

Bonferroni post-hoc comparison

delta theta beta gamma
1.00000000 1.000000e+00 1.000000e+00 1.0000000000

Figure S2C

Power full signal PFC

two-way anova
Analysis of Variance of
Aligned Rank Transformed
Data

Table Type: Repeated Measures Analysis of Variance Table
(Type I)
Model: Repeated Measures
(aov)
Response: art(variable)

Error Df Df.res F value
Pr(>F)
1 cond anm:c 1 9
28.661 0.00046016 ***
2 cond:freq anm:: 3 27
12.890 2.0587e-05 ***

Signif. codes: 0 ‘***’ 0.001
‘**’ 0.01 ‘*’ 0.05 ‘.’ 0.1 ‘ ’ 1

Bonferroni post-hoc
comparison

delta theta beta gamma
0.03710938 0.3222656
0.001953125 0.001953125

PLOS BIOLOGY

RESEARCH ARTICLE

Anesthetics fragment hippocampal network activity, alter spine dynamics, and affect memory consolidation

Wei Yang[1☯], **Mattia Chini**[2☯], **Jastyn A. Pöpplau**[2], **Andrey Formozov**[1], **Alexander Dieter**[1], **Patrick Piechocinski**[1], **Cynthia Rais**[1], **Fabio Morellini**[3], **Olaf Sporns**[4,5], **Ileana L. Hanganu-Opatz**[2], **J. Simon Wiegert**[1]*

1 Research Group Synaptic Wiring and Information Processing, Center for Molecular Neurobiology Hamburg, University Medical Center Hamburg-Eppendorf, Hamburg, Germany, **2** Institute of Developmental Neurophysiology, Center for Molecular Neurobiology Hamburg, University Medical Center Hamburg-Eppendorf, Hamburg, Germany, **3** Research Group Behavioral Biology, Center for Molecular Neurobiology Hamburg, University Medical Center Hamburg-Eppendorf, Hamburg, Germany, **4** Department of Psychological and Brain Sciences, Indiana University, Bloomington, Indiana, United States of America, **5** Indiana University Network Science Institute, Indiana University, Bloomington, Indiana, United States of America

☯ These authors contributed equally to this work.
* simon.wiegert@zmnh.uni-hamburg.de

Citation: Yang W, Chini M, Pöpplau JA, Formozov A, Dieter A, Piechocinski P, et al. (2021) Anesthetics fragment hippocampal network activity, alter spine dynamics, and affect memory consolidation. PLoS Biol 19(4): e3001146. https://doi.org/10.1371/journal.pbio.3001146

Academic Editor: Jozsef Csicsvari, Institute of Science and Technology Austria, AUSTRIA

Received: June 29, 2020

Accepted: February 15, 2021

Published: April 1, 2021

Peer Review History: PLOS recognizes the benefits of transparency in the peer review process; therefore, we enable the publication of all of the content of peer review and author responses alongside final, published articles. The editorial history of this article is available here: https://doi.org/10.1371/journal.pbio.3001146

Data Availability Statement: The code generated during this study is available at https://github.com/mchini/Yang_Chini_et_al The datasets underlying the figures are available at: https://github.com/

Abstract

General anesthesia is characterized by reversible loss of consciousness accompanied by transient amnesia. Yet, long-term memory impairment is an undesirable side effect. How different types of general anesthetics (GAs) affect the hippocampus, a brain region central to memory formation and consolidation, is poorly understood. Using extracellular recordings, chronic 2-photon imaging, and behavioral analysis, we monitor the effects of isoflurane (Iso), medetomidine/midazolam/fentanyl (MMF), and ketamine/xylazine (Keta/Xyl) on network activity and structural spine dynamics in the hippocampal CA1 area of adult mice. GAs robustly reduced spiking activity, decorrelated cellular ensembles, albeit with distinct activity signatures, and altered spine dynamics. CA1 network activity under all 3 anesthetics was different to natural sleep. Iso anesthesia most closely resembled unperturbed activity during wakefulness and sleep, and network alterations recovered more readily than with Keta/Xyl and MMF. Correspondingly, memory consolidation was impaired after exposure to Keta/Xyl and MMF, but not Iso. Thus, different anesthetics distinctly alter hippocampal network dynamics, synaptic connectivity, and memory consolidation, with implications for GA strategy appraisal in animal research and clinical settings.

Introduction

General anesthesia is a drug-induced, reversible behavioral condition encompassing unconsciousness, amnesia, sedation, immobility, and analgesia [1,2]. Together, these aspects represent a state where surgery can be tolerated without the requirement for further drugs [2]. The

mchini/Yang_Chini_et_al/tree/master/Stats_Dataset_(R)/datasets The calcium imaging and electrophysiology data sets generated during this study are available at https://gin.g-node.org/SW_lab/Anesthesia_CA1.

Funding: This work was funded by the Deutsche Forschungsgemeinschaft (DFG, SPP1926, FOR2419/P6, SFB936/B8 to J.S.W., SPP 1665/Ha 4466/10-1/Ha4466/12-1, SFB 936/B5 to I.L.H.-O., SFB 936/B7 to F.M.), the European Research Council (ERC2016-StG-714762 to J.S.W., ERC-2015-CoG 681577 to I.L.H.-O.), the German Academic Exchange Service (DAAD, STG/19/5744091 to A.F.), and the Chinese Scholarship Council (CSC 201606210129 to W.Y.). The funders had no role in study design, data collection and analysis, decision to publish, or preparation of the manuscript.

Competing interests: The authors have declared that no competing interests exist.

Abbreviations: AMPAR, α-amino-3-hydroxy-5-methyl-4-isoxazolepropionic acid receptor; AP, affinity propagation; APC, affinity propagation clustering; dCA1, CA1 area of the dorsal hippocampus; E/I, excitation/inhibition; EMG, electromyography; FAB, flumazenil/atipamezole/buprenorphine; FOV, field of view; GA, general anesthetic; GABAR, γ-aminobutyric acid receptor; ID, identity; Iso, isoflurane; Keta/Xyl, ketamine/xylazine; LFP, local field potential; MMF, medetomidine/midazolam/fentanyl; NMDAR, N-methyl-D-aspartate receptor; NREM, non-rapid eye movement; PAC, phase-amplitude coupling; PCA, principal component analysis; PPC, pairwise phase consistency; REM, rapid eye movement; ROI, region of interest; S.L.M., stratum lacunosum moleculare; S.O., stratum oriens; S.R., stratum radiatum; STTC, spike time tiling coefficient; SUA, single-unit activity; tSNE, t-distributed stochastic neighbor embedding.

behavioral effects of general anesthetics (GAs) are dose dependent. At clinical (i.e., highest) dosage, they should induce unconsciousness, even though experimental evidence of this phenomenon is challenging to collect (in the absence of a verifiable consciousness theory). At lower doses, some GAs cause unresponsiveness and loss of working memory, phenomena that have both been hypothesized to potentially confound the apparent loss of consciousness [3,4]. At much lower doses still, GAs cause profound retrograde amnesia. When general anesthesia fails to induce such behavioral effects, intraoperative awareness ensues, a condition that is associated with long-term adverse health consequences [5]. While loss of memory is required during anesthesia administration, so that no memories of the surgical procedure are formed [1,6], long-term impairment of retrograde or anterograde memories is not desired. Although general anesthesia is generally considered a safe procedure, growing literature points to the possibility of long-term negative effects on the central nervous system [7]. This is particularly true for specific categories of patients, such as the elderly, infants, and children [7]. Among the observed side effects, the most common are postoperative cognitive dysfunction syndromes, including postoperative delirium and postoperative cognitive decline. Postoperative cognitive disturbances are positively correlated with the duration of anesthesia, and a single exposure to GAs can cause retrograde and anterograde memory deficits that persist for days to weeks in rodent models [8]. These aspects point to a generalized action of GAs on the memory system.

Given that amnesia is a fundamental part of general anesthesia and that the hippocampus controls memory formation and consolidation, it is important to understand how anesthetics affect hippocampal function and how this compares to sleep—a naturally occurring state of unconsciousness. Together with the subiculum, the CA1 area constitutes the main hippocampal output region. CA1 pyramidal cells receive excitatory synaptic input mainly from CA3 (in stratum oriens [S.O.] and stratum radiatum [S.R.]) and layer 3 of entorhinal cortex (in stratum lacunosum moleculare [S.L.M.]), relaying information about the internal state of the animal and sensory inputs from the external environment, respectively [9]. Inputs along these pathways are processed in an integrative manner in CA1 [10]. Thus, CA1 pyramidal cells have been suggested to be a site of sensory integration, with synaptic spines as a possible location of memory storage [11–14]. Moreover, dynamic modulation of spine stability has been linked to synaptic plasticity [15–18]. Synaptic plasticity, in turn, underlies learning and memory formation [19], suggesting that spine turnover in the hippocampus directly reflects these processes [20,21]. Considering the low concentrations of anesthetics required to induce amnesia, these compounds are thought of being particularly effective on the hippocampus. One possible explanation of this sensitivity is the fact that a class of γ-aminobutyric acid receptors (GABARs), which is strongly modulated by some anesthetics, is predominantly expressed in the hippocampus [22,23]. Other anesthetics, such as ketamine, inhibit N-methyl-D-aspartate receptors (NMDARs) in a use-dependent manner and therefore may be particularly effective in inhibiting synaptic plasticity, required for the formation of episodic-like memories [24]. However, a systematic investigation of the effects of anesthetics on the hippocampus, bridging synaptic, network, and behavioral levels, is still lacking.

Here, using extracellular electrophysiological recordings and chronic 2-photon calcium and spine imaging in vivo in combination with behavioral analysis, we systematically assessed how CA1 network dynamics, synaptic structure, and memory performance are affected by 3 commonly used combinations of GAs: isoflurane (Iso), medetomidine/midazolam/fentanyl (MMF), and ketamine/xylazine (Keta/Xyl). We further measured CA1 network dynamics during wakefulness and natural sleep. Unlike sleep, all 3 GAs strongly reduced overall neuronal spiking compared to wakefulness. Moreover, opposite to what has been found in the neocortex [25–27], they decorrelated network activity, leading to a fragmented network state. However, the induced patterns of activity were highly distinct between the 3 different anesthetic

conditions and recovered to the preanesthetic status with disparate rates. Testing the effect of repeated anesthesia on spine dynamics revealed that Keta/Xyl, the condition which most strongly affected calcium activity, significantly reduced spine turnover, leading to an overall (over)stabilization of hippocampal synapses. In contrast, Iso and MMF mildly increased spine turnover. Finally, we show that the 2 anesthetic conditions which induce the strongest reduction and fragmentation of CA1 network activity, Keta/Xyl and MMF, negatively influenced hippocampus-dependent memory consolidation. On the other hand, Iso, which most closely resembled unperturbed sleep and wakefulness, did not impair memory consolidation, even when maintained over time periods matching the longer recovery phase of Keta/Xyl or MMF. Thus, different anesthetics, despite inducing a similar physiological state, strongly differ in their effects on synaptic stability, hippocampal network activity, and memory consolidation.

Results

Iso, Keta/Xyl, and MMF induce distinct patterns of network activity

Iso, Keta/Xyl, and MMF have distinct molecular targets and modes of action in the brain. We therefore hypothesized that electrical activity in the hippocampus might be uniquely altered by the 3 anesthesia strategies. To test this hypothesis, we investigated local field potentials (LFPs) and firing of individual neurons (single-unit activity, SUA) extracellularly recorded in the CA1 area of the dorsal hippocampus (dCA1) during wakefulness, followed by 45 minutes of anesthesia and 45 minutes of recovery (Fig 1A, S1A Fig). We found that the anesthetics differently affected population activity, inducing characteristic modulation of various frequency bands (Fig 1B). During wakefulness, LFP power in CA1 was highest in the theta (4 to 12 Hz) and low-gamma (40 to 60 Hz) frequency bands (S1B Fig). Exposure to 2% to 2.5% Iso led to a strong reduction of LFP power >4 Hz within the first 2 minutes, which was accompanied by complete loss of mobility of the animal (Fig 1C, S1B and S1C Fig). Similarly, MMF injection promptly decreased LFP power in the same frequency bands. In contrast, Keta/Xyl increased power across all frequencies during the first 10 minutes after injection, the most prominent effect being observed for activity at 5 to 30 Hz. This is consistent with previous reports, finding enhanced theta and low-gamma power in CA1 of rats under ketamine anesthesia [28]. The initial LFP power increase was followed by a gradual, significant decrease of 30 to 100 Hz activity (Fig 1C, S1B and S1C Fig).

It is widely accepted that, in the neocortex, GAs favor slow oscillations at the expense of faster ones [29]. To determine whether this is also the case in the hippocampus, we next asked how the investigated anesthetics affect slow network oscillations. Consistent with previous reports [30–32], Keta/Xyl strongly enhanced LFP power at 0.5 to 4 Hz throughout the entire recording period (Fig 1C and 1D, S1C Fig), but suppressed frequencies lower than 0.5 Hz. In contrast, Iso strongly augmented LFP power below 0.5 Hz, peaking at 0.1 to 0.2 Hz (Fig 1C and 1D, S1C Fig), whereas MMF induced no significant increase in the low-frequency regime. However, similar to Keta/Xyl, a significant reduction was present below 0.5 Hz, which persisted throughout the entire recording period (Fig 1C and 1D). Analysis of the power-law decay exponent (1/f slope) of the LFP power spectrum facilitates detection of noncanonical changes in LFP power, including aperiodic (non-oscillatory) components [33]. The 1/f slope has been hypothesized to track excitation/inhibition (E/I) balance [34,35] and is reduced in the cortex under anesthesia [36,37], indicating a shift toward inhibition. Considering the robust effects on LFP power that we reported, we reasoned that the 1/f slope might also be altered. Indeed, all anesthetics significantly decreased the 1/f slope, albeit with a different temporal profile. While the effect of Iso occurred within a few minutes, MMF and Keta/Xyl operated on a longer timescale (Fig 1E). Moreover, periods of activity were consistently and

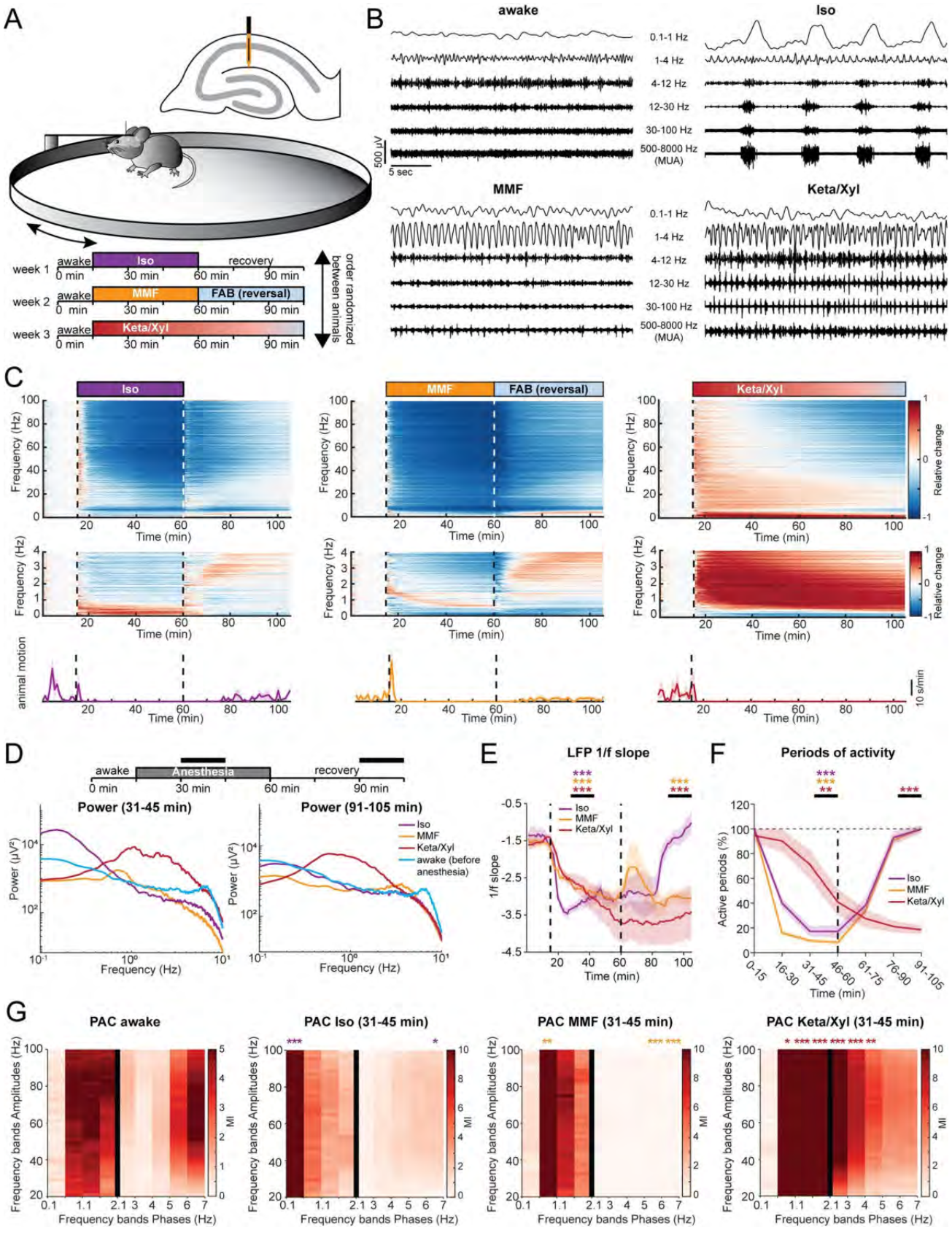
A
week 1
awake
Iso
recovery
0 min
30 min
60 min
90 min
week 2
MMF
FAB (reversal)
week 3
Keta/Xyl
order randomized between animals
B
awake
Iso
MMF
Keta/Xyl
0.1-1 Hz
1-4 Hz
4-12 Hz
12-30 Hz
30-100 Hz
500-8000 Hz (MUA)
500 µV
5 sec
C
Frequency (Hz)
Time (min)
Relative change
animal motion
10 s/min
D
Power (31-45 min)
Power (91-105 min)
Power (µV²)
Frequency (Hz)
awake (before anesthesia)
E
LFP 1/f slope
1/f slope
F
Periods of activity
Active periods (%)
0-15
16-30
31-45
46-60
61-75
76-90
91-105
G
PAC awake
PAC Iso (31-45 min)
PAC MMF (31-45 min)
PAC Keta/Xyl (31-45 min)
Frequency bands Amplitudes (Hz)
Frequency bands Phases (Hz)
MI

Fig 1. LFP recordings in dorsal CA1 during wakefulness and anesthesia reveal distinct and complex alterations by Iso, Keta/Xyl, and MMF. (A) Experimental setup. Extracellular electrical recordings in dorsal CA1 were performed in 4 head-fixed mice for 105 minutes, continuously. Each animal was recorded under all anesthetics as indicated in the scheme. Order of anesthetics was pseudo-randomized. **(B)** Characteristic LFP recordings during wakefulness and under 3 different anesthetics. **(C)** Color-coded heat maps depicting relative change (upper and middle panels) for LFP power and motion profiles (lower panels) for the 3 different anesthetic conditions. Upper panels display LFP power for 0–100 Hz frequency range, lower panels for 0–4 Hz. **(D)** Line plot displaying LFP power spectra for the 2 time periods indicated by horizontal black bars. For comparison, the 15-minute spectrum of the awake period before anesthesia induction is plotted in both graphs. Statistical differences are indicated in S1C Fig. **(E)** Line plot displaying the power-law decay exponent (1/f) of the LFP power spectrum for the 30–50 Hz range. Lines display mean ± SEM. **(F)** Line plot displaying the fraction of active periods compared to the preanesthetic wakeful state, in 15-minute bins throughout the entire recording duration. Lines display mean ± SEM. **(G)** Heat map displaying PAC for preanesthetic wakeful state (left) and for the indicated time periods during anesthesia. Different bin sizes (0.5 Hz and 1 Hz, separated by vertical black line) are used to resolve low- and high-frequency PAC. Vertical dashed lines in (C) and (E) indicate time points of anesthesia induction (Iso, MMF, and Keta/Xyl) and reversal (Iso and MMF only). Vertical dashed line in (F) indicates time point of anesthesia reversal (Iso and MMF only). Asterisks in (E) and (F) indicate significance of time periods indicated by black horizontal line compared to 15-minute period before anesthesia. Anesthetic conditions are color coded. Asterisks in (G) indicate significant differences compared to the corresponding frequency band during wakefulness. * $p < 0.05$, ** $p < 0.01$, *** $p < 0.001$, $n = 4$ mice. For full report of statistics, see S1 Table. All datasets of this figure can be found under https://github.com/mchini/Yang_Chini_et_al/tree/master/Stats_Dataset_(R)/datasets/Figure1_S1. FAB, flumazenil/atipamezole/buprenorphine; Iso, isoflurane; Keta/Xyl, ketamine/xylazine; LFP, local field potential; MMF, medetomidine/midazolam/fentanyl; PAC, phase-amplitude coupling.

https://doi.org/10.1371/journal.pbio.3001146.g001

strongly reduced immediately under Iso and MMF, but delayed by 30 minutes under Keta/Xyl (Fig 1F). These results indicate that all anesthetics shift the LFP to lower frequencies and tilt the E/I balance toward inhibition, albeit with different temporal profiles.

In contrast to Keta/Xyl anesthesia, Iso and MMF anesthesia can be efficiently antagonized. Removing the face mask is sufficient to antagonize Iso anesthesia, while antagonization of MMF anesthesia requires injection of a wake-up cocktail (flumazenil/atipamezole/buprenorphine, FAB) [38,39]. Moreover, 20 to 30 minutes after Iso withdrawal, animals regained motility and periods of silence in the LFP receded (Fig 1C and 1F). However, in contrast to post-Iso, LFP power did not fully recover after FAB, remaining significantly reduced at frequencies below 0.5 and above 30 Hz for the entire 45 minutes postanesthesia recording period (Fig 1C and 1D). In contrast, elevated LFP power in the 0.5 to 4 Hz band and reduction in active periods remained significant throughout the entire recording in the presence of Keta/Xyl. In line with these results, the 1/f slope promptly reverted to values similar to baseline after Iso discontinuation. In contrast, the recovery was only transitory and partial after MMF antagonization, and virtually absent for Keta/Xyl (Fig 1E), indicating that the E/I balance recovered only after Iso within 45 minutes.

Cross-frequency coupling between theta and gamma oscillations has been suggested to underlie information transfer in the hippocampus [40]. Given the strong decrease of theta power in the presence of Iso and MMF, we reasoned the phase modulation of the gamma rhythm could also be altered. To test this, we used phase-amplitude coupling (PAC) to measure whether the phase of slow LFP oscillations modulated the amplitude of the signal at a higher frequency. In line with previous results [41,42], a significant coupling between theta and gamma frequency bands, as well as between frequencies in the 1 to 2 Hz range and gamma, was present in the awake state (Fig 1G). Moreover, anesthesia strongly altered PAC. In accordance with the LFP power analysis, the coupling reached a maximum strength between the dominant slow-frequency oscillations induced by the various anesthetics (<0.5 Hz for Iso, approximately 1 Hz for MMF, and 0.5 to 4 Hz for Keta/Xyl) and gamma (Fig 1G). For all anesthetics, the range of phase-modulated amplitudes was wide, suggesting that the modulating phase corresponds to the identified slow-wave activity.

Taken together, these data show that all 3 GAs differently and persistently modulated the network oscillations in dCA1, a full recovery of activity being detected within 45 minutes only for Iso.

Delayed recovery of neuronal spiking patterns after anesthesia

While the LFP provides information about general network states in the hippocampus, it is influenced by long-range activity and highly active regions in the vicinity of CA1 [43]. To assess the effects of GAs on CA1 neurons, we analyzed the spiking of individual units (56 to 72 units per animal, $n = 4$ mice) before, during, and after each of the anesthetic conditions. All anesthetics significantly and rapidly (<1 minute) decreased spiking activity in CA1 neurons (Fig 2A and 2B, S2 Fig), with MMF leading to the most potent suppression, followed by Iso and Keta/Xyl. These alterations were generally present in all layers of CA1 (S2C Fig). Although the bulk spike rate was strongly reduced, the number of active neurons (see Methods) was only mildly affected (Fig 2C), reaching a significant reduction only with MMF. This observation suggests that anesthesia broadly reduces neuronal activity and does not modulate only a discrete subpopulation of neurons. Both firing rate and the number of active neurons recovered within 45 minutes after reversal for MMF and Iso (Fig 2A–2C, S2 Fig). As previously reported for non-rapid eye movement (NREM) sleep [44], we found a negative correlation between the anesthesia-induced reduction of firing rate and the firing rate in wakefulness (S2B Fig).

To investigate whether the rhythmicity of single neuron firing was affected similarly to the LFP, we analyzed the spectral properties of 1-ms binned SUA firing (i.e., power of SUA spike trains; for details, see Methods). In the presence of Iso, SUA power was consistently increased in the range between 0 and 0.5 Hz (Fig 2A and 2D, S2 Fig), in line with the strong modulation of LFP at 0.1 to 0.2 Hz. Of note, this effect did not vanish after Iso removal, suggesting that Iso has a long-lasting impact on firing rhythmicity. In contrast, and in line with its effects on the LFP, MMF generally reduced, albeit less strongly, SUA power, including the low frequencies. A significant reduction of SUA power was still present 45 minutes after antagonization in the 0 to 0.5 Hz band. Keta/Xyl, on the other hand, only showed a tendency toward reduced SUA power in the frequency band below 0.5 Hz, but increased SUA power significantly in the range between 0.5 and 4 Hz, consistent with its effect on the LFP (Fig 2D). This modulation was present throughout the entire recording. At higher frequencies, Iso led to a peak in the theta frequency range, similar to wakefulness (Fig 2E), yet it reduced the SUA power in the beta/gamma range. Keta/Xyl and MMF caused an overall reduction in SUA power at frequencies >5 Hz (Fig 2E). Thus, GAs differentially impair spiking rhythmicity. These changes appeared to follow similar dynamics than those in the LFP.

To confirm the synchrony between spikes and low-frequency oscillations, we calculated their pairwise phase consistency (PPC) [45]. When compared to pre-anesthesia, PPC values for the 0.1 to 0.5 Hz frequency band were augmented by Iso. Keta/Xyl increased coupling of spikes to the LFP between 0.5 and 1 Hz, whereas MMF showed a weak, but significant increase of coupling at frequencies below 1 Hz (Fig 2F).

Similar to the LFP, the SUA firing rate nearly fully recovered during the 45 minutes post-Iso (Fig 2A and 2B, S2 Fig), with even a slight, but significant increase at the end of the recording period. In contrast, after FAB-induced MMF reversal, CA1 spiking activity remained slightly reduced, reflecting the lack of LFP recovery. For Keta/Xyl, SUA remained suppressed during the entire recording period (Fig 2B). Strikingly, SUA power did not fully recover for any of the tested anesthetics (Fig 2E).

Taken together, we show that all investigated GAs caused a persistent and robust reduction of CA1 firing. Moreover, spiking during anesthesia was phase-locked to the GA-induced slow network oscillations.

Iso, Keta/Xyl, and MMF reduce the number, amplitude, and duration of calcium transients

To monitor the population dynamics of CA1 neurons in the presence of different anesthetics, we imaged the same field of view (FOV) using the genetically encoded indicator GCaMP6f

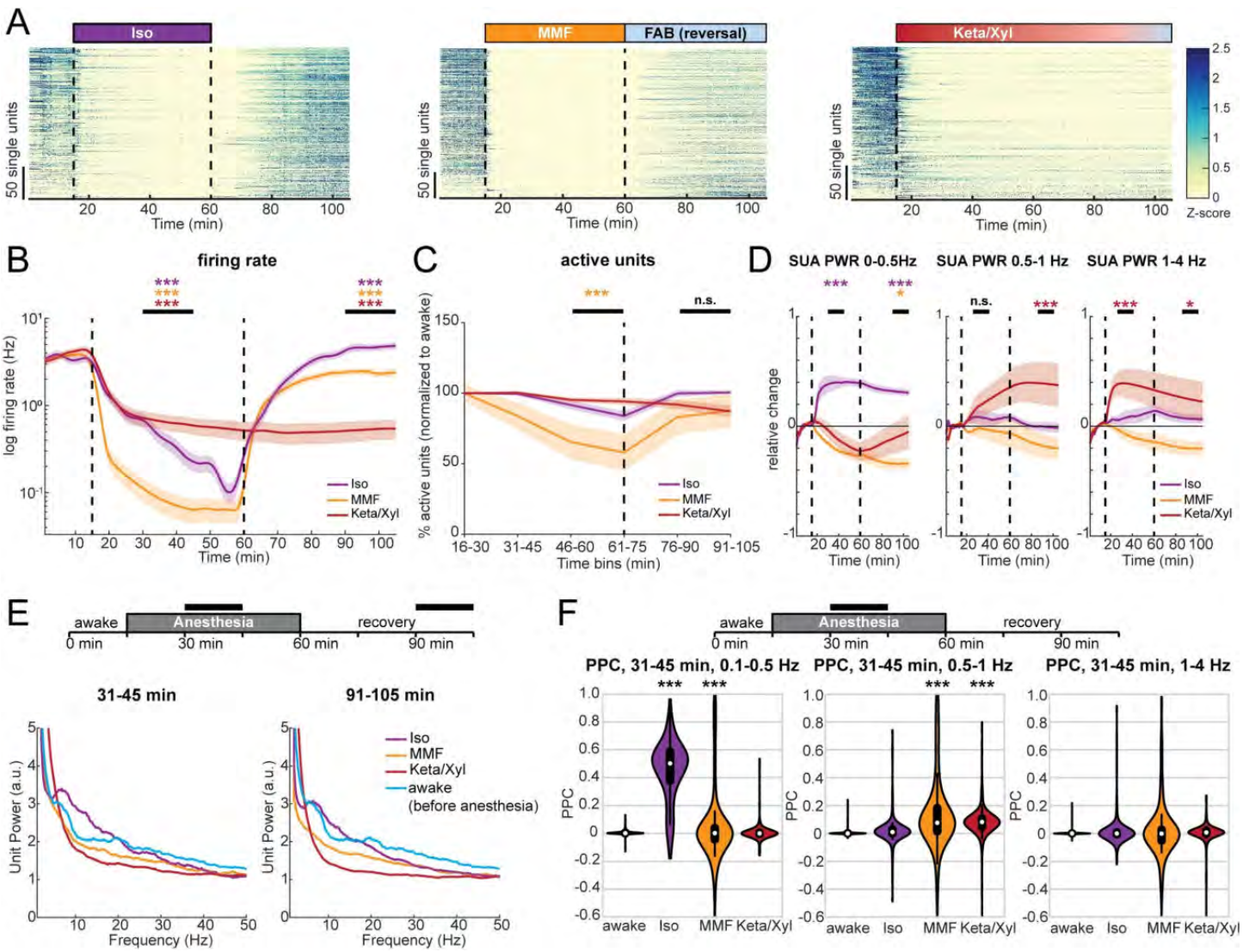

Fig 2. SUA in dorsal CA1 is strongly reduced during anesthesia and remains significantly altered long after its termination. **(A)** Raster plots of z-scored SUA for the 3 different anesthetic strategies in 4 mice. Units are sorted according to initial activity during wakefulness. **(B)** Line plot of SUA firing rate before, during, and after anesthesia induction. **(C)** Line plot displaying the fraction of active units compared to the preanesthetic wakeful state, for all 3 anesthetics in 15-minute bins throughout the entire recording duration. **(D)** Relative change of population firing rate power in the 0–0.5, 0.5–1, and 1–4 Hz frequency band. **(E)** Line plot displaying the normalized power spectra of population firing rate for the 2 time periods indicated by horizontal black bars. For comparison, the 15-minute spectrum for preanesthetic wakeful state is plotted in both graphs. **(F)** PPC at low frequencies in the same frequency bands as (D), for the indicated time points during anesthesia. White dots indicate median, and vertical thick and thin lines indicate first to third quartile and interquartile range, respectively. Colored lines in (B)–(D) display mean ± SEM. Vertical dashed lines in panels (A), (B), and (D) indicate time points of anesthesia induction (Iso, MMF, and Keta/Xyl) and reversal (Iso and MMF only). The vertical dashed line in (C) indicates the time point of anesthesia reversal (Iso and MMF only). Asterisks in (B)–(D) indicate significance of periods indicated by black horizontal line compared to period before anesthesia. Anesthetic conditions are color coded. Asterisks in (F) indicate significant differences to wakefulness. * $p < 0.05$, ** $p < 0.01$, *** $p < 0.001$, $n = 4$ mice. For full report of statistics, see S1 Table. All datasets of this figure can be found under https://github.com/mchini/Yang_Chini_et_al/tree/master/Stats_Dataset_(R)/datasets/Figure2_S2. FAB, flumazenil/atipamezole/buprenorphine; Iso, isoflurane; Keta/Xyl, ketamine/xylazine; MMF, medetomidine/midazolam/fentanyl; PPC, pairwise phase consistency; SUA, single-unit activity; SUA PWR, power of SUA spike trains.

https://doi.org/10.1371/journal.pbio.3001146.g002

[46] and systematically compared the activity of identified neurons during quiet wakefulness and in the presence of different anesthetics (Fig 3A).

First, we considered all active neurons in each condition and analyzed the average rate (i.e., the number of transients), amplitude, and duration (i.e., the decay constant) of calcium transients across all imaging sessions in 7 mice. In line with the results of SUA analysis (see

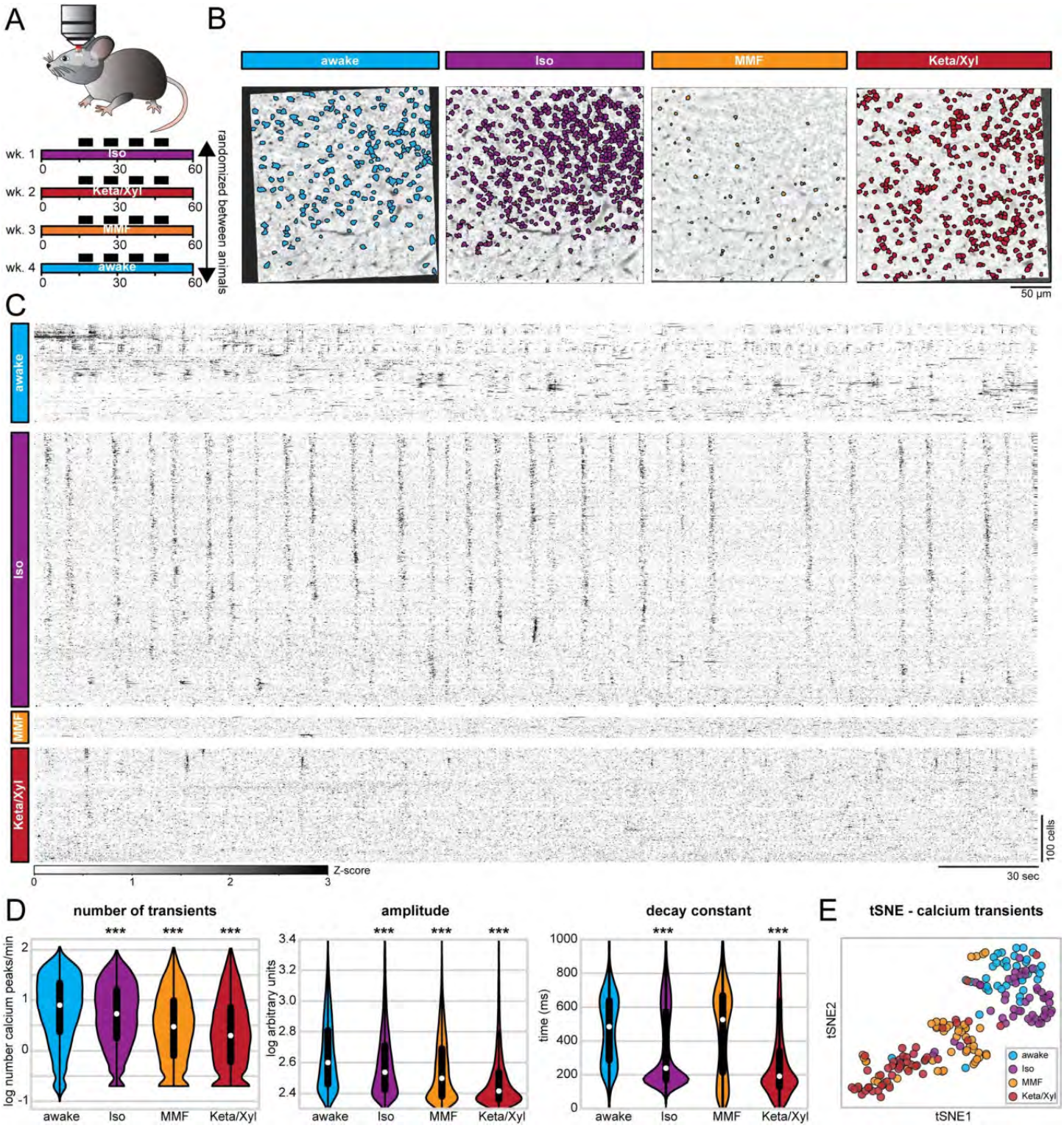

Fig 3. Repeated calcium imaging in dorsal CA1 reveals distinct activity profiles for Iso, MMF, and Keta/Xyl. (A) Experimental strategy for chronic calcium imaging of cellular activity in dorsal CA1. For each condition, 7 mice were imaged 4 times for 5 minutes, as indicated by black fields in the scheme. The order of imaging conditions was pseudo-randomized. **(B)** Time-averaged, 2-photon images of the same FOV in CA1 aligned to the Iso condition. ROIs of automatically extracted, active neurons are overlaid for each condition. **(C)** Raster plots of z-scored calcium transients in the same animal under different conditions. Traces are sorted by similarity. **(D)** Violin plots quantifying the number (left), amplitude (middle), and decay (right) of detected calcium transients. White dots indicate median, and vertical thick and thin lines indicate first to third quartile and interquartile range, respectively. **(E)** tSNE plot summarizing the average calcium transients properties. Each data point represents 1 recording

session. Asterisks in (D) indicate significant differences to wakefulness. *** $p < 0.001$. Note, to facilitate readability, only differences to wakefulness are indicated. For full report of statistics, see S1 Table. All datasets of this figure can be found under https://github.com/mchini/Yang_Chini_et_al/tree/master/Stats_Dataset_(R)/datasets/Figure3_S3. FOV, field of view; Iso, isoflurane; Keta/Xyl, ketamine/xylazine; MMF, medetomidine/midazolam/fentanyl; ROI, region of interest; tSNE, t-distributed stochastic neighbor embedding.

https://doi.org/10.1371/journal.pbio.3001146.g003

Fig 2C), a large number of CA1 pyramidal neurons were active in the presence of all 3 GAs. Using extraction parameters that restricted the number of region of interests (ROIs) but maximized signal quality (see Methods), we obtained a median of 311 (min-max of 16 to 817) active neurons per FOV, for a total of one hundred and eighty-nine 5-minute recordings. All GAs significantly altered calcium dynamics in CA1 neurons, reducing the activity (Fig 3C and 3D), as previously shown for neuronal spiking (Fig 2B). Also in line with the effect on SUA (S2B Fig), the magnitude of the anesthesia-induced reduction of calcium transients was negatively correlated with the wakefulness calcium transients rate (S6D Fig). However, each condition could be characterized by a specific signature in their calcium dynamics. Iso yielded only a mild decrease of rate and amplitude, but a strong reduction of duration of calcium transients (Fig 3D). Consistent with effects on LFP and SUA, calcium transients showed a spectral peak between 0.1 and 0.2 Hz (S4 Fig). In contrast to Iso, MMF did not significantly affect the duration of transients but reduced their rate and amplitude when compared to wakefulness. Keta/Xyl anesthesia had the strongest effect on calcium transients, leading to a reduction of all 3 parameters compared to wakefulness (Fig 3D). Unlike for electrophysiological recordings, no spectral peak was present in calcium transients, most likely due to the strong suppression of calcium activity by Keta/Xyl. Considering all parameters, the 4 groups tended to segregate into clusters, one consisting mostly of recordings under Keta/Xyl and another one consisting of awake and Iso recordings. Most recordings under MMF clustered between these 2 groups (Fig 3E). Importantly, these findings were robust to changes in the signal extraction pipeline. Varying the threshold for calcium transient detection across a wide range of values did not affect the reported effects on rate and height of transients (S3B Fig). Further, conducting the same analysis on neuronal activity metrics that are independent of calcium transients detection (integral and standard deviation) or on dF/F calcium signals also yielded analogous results (S3C–S3E Fig).

Iso, Keta/Xyl, and MMF distinctly modulate cellular calcium dynamics in individual neurons

One possible explanation for the distinct modes of calcium activity could be that each anesthetic condition recruits a unique set of neurons characterized by particular spiking properties. We tested this possibility by analyzing calcium transients in neurons that were active during all conditions (Fig 4A, S5 and S6 Figs). To obtain a sufficient number of active neurons, we extracted calcium transients using a lower quality threshold, accepting more neurons per recording (see Methods). In this manner, we obtained a median of 783 neurons per recording (min-max of 156 to 1,641). While this shifted the overall distribution of calcium parameters to lower values, the relative ratios between the 4 conditions remained the same, and the differences between anesthesia groups were preserved (S3F and S3G Fig). Also when considering only neurons that were active in all 4 conditions, rate as well as amplitude of calcium peaks were generally reduced under anesthesia, being lowest in the Keta/Xyl condition (Fig 4B and 4C). Compared to the whole dataset, differences in decay constant were less pronounced. The median decay constant strongly decreased for awake and MMF conditions, while it increased for Iso and Keta/Xyl. These results indicate that discrepancies between conditions generally decreased when considering only neurons active under all conditions.

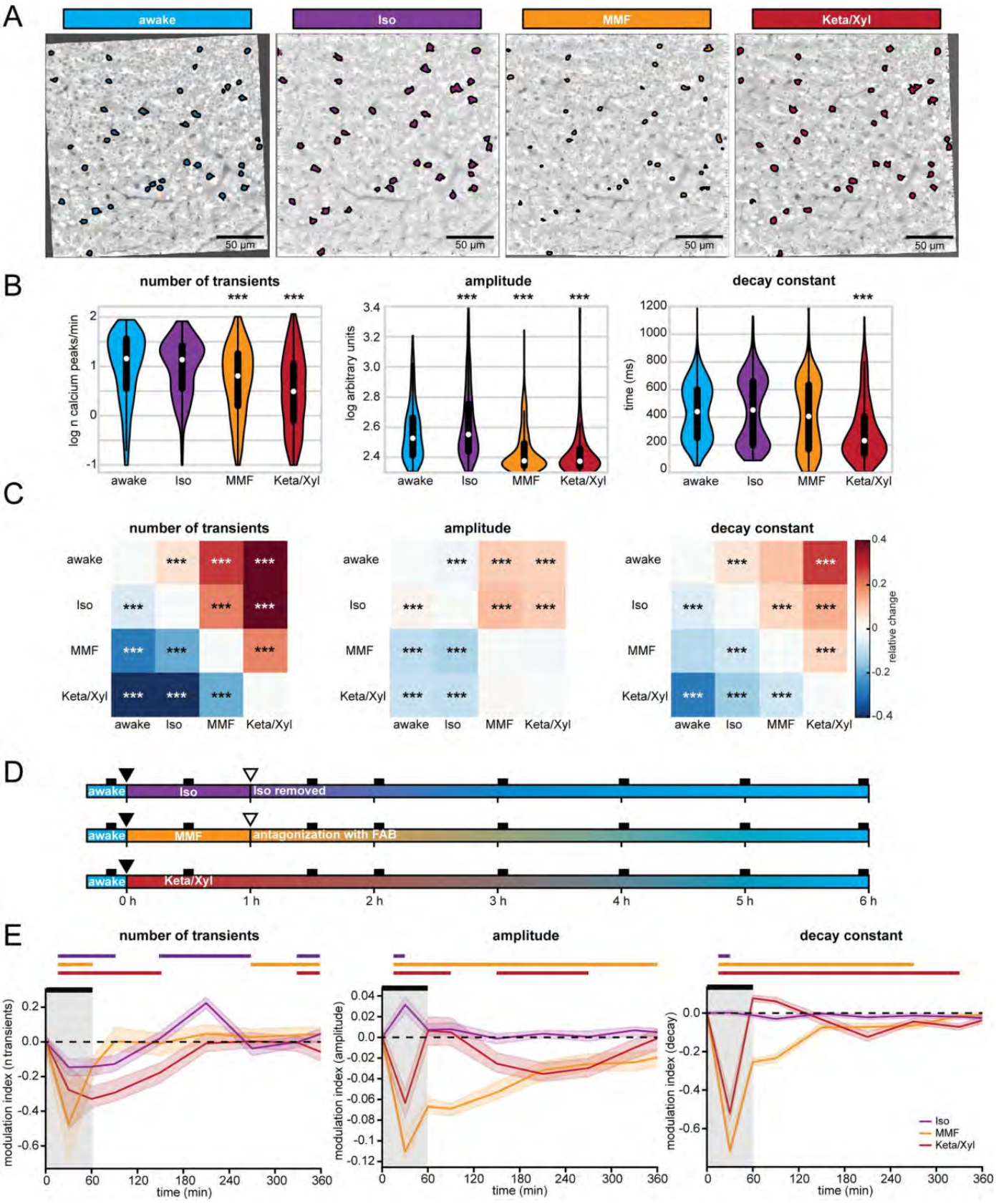
A
awake
Iso
MMF
Keta/Xyl
50 µm
B
number of transients
log n calcium peaks/min
amplitude
log arbitrary units
decay constant
time (ms)
awake
Iso
MMF
Keta/Xyl
C
number of transients
amplitude
decay constant
relative change
D
awake
Iso
Iso removed
MMF
antagonization with FAB
Keta/Xyl
0 h
1 h
2 h
3 h
4 h
5 h
6 h
E
number of transients
amplitude
decay constant
modulation index (n transients)
modulation index (amplitude)
modulation index (decay)
time (min)
Iso
MMF
Keta/Xyl

Fig 4. Calcium activity profiles in neurons active during all conditions are similar between wakefulness and Iso. (A) Two-photon time-averaged images of the same FOV in CA1, aligned to the Iso condition (same images as in Fig 3). ROIs show neurons active in each condition, allowing direct comparison of calcium transients in the same cells under different conditions. **(B)** Violin plots quantifying the number (left), amplitude (middle), and decay (right) of detected calcium transients. White dots indicate median, and vertical thick and thin lines indicate first to third quartile and interquartile range, respectively. **(C)** Heat maps displaying the relative change in the number (left), amplitude (middle), and decay (right) of calcium transients between neurons active in pairs of conditions (see also S6C Fig). **(D)** Schematic representation of long-term calcium imaging experiments to assess recovery from anesthesia. Black rectangles indicate imaging time points (up to 10 minutes duration each). Filled and open triangles indicate the start and end of the anesthesia period. **(E)** Line diagrams showing the relative change of the median number of calcium transients (left), their amplitude (middle), and decay constant (right) during anesthesia and recovery relative to the awake state before anesthesia induction. The black bar indicates the anesthesia period. Shaded, colored lines indicate 95% confidence interval. Note, Keta/Xyl anesthesia could not be terminated. The horizontal, colored lines indicate significant difference ($p < 0.05$) to awake time point (t = 0) for the respective condition. Asterisks in (B) and (C) indicate significant differences to wakefulness. *** $p < 0.001$. Note, to facilitate readability, only differences to wakefulness are indicated. For full report of statistics, see S1 Table. All datasets of this figure can be found under https://github.com/mchini/Yang_Chini_et_al/tree/master/Stats_Dataset_(R)/datasets/Figure4_S6. FOV, field of view; Iso, isoflurane; Keta/Xyl, ketamine/xylazine; MMF, medetomidine/midazolam/fentanyl; ROI, region of interest.

https://doi.org/10.1371/journal.pbio.3001146.g004

The relatively low number of neurons active in all 4 conditions (335 neurons) limited the statistical analysis. Therefore, we compared neurons that were active in any 2 combinations of conditions (S6C Fig). This analysis further corroborated the similarity of neurons active during wakefulness and Iso anesthesia (Fig 4C, S6C Fig). Rate, amplitude, and duration of calcium transients were most similar between wakefulness and Iso compared to the other GAs. In contrast, neurons active during wakefulness and either Keta/Xyl or MMF showed decreased rate, amplitude, and duration under anesthesia, with Keta/Xyl causing the strongest phenotype (S6C Fig). Overall, this indicates that anesthetics influence the firing properties of hippocampal neurons. However, the magnitude and direction of these effects vary considerably. On the one hand, Iso anesthesia has the mildest effect, and it most likely arises from distinct neuronal populations being active in the 2 conditions (wakefulness versus Iso anesthesia), as the firing properties of cells that are active in both are barely affected (Fig 4B and 4C). On the other hand, the strong effects of MMF and Keta/Xyl on all calcium parameters in the same cells indicate that different anesthetics directly alter the firing properties of individual neurons. Thus, alterations in firing properties of neuronal populations (e.g., SUA, Fig 2B and 2D) are not solely explainable by different subpopulations of neurons being active between awake and anesthesia.

Population activity recovers with different temporal dynamics after Iso, Keta/Xyl, and MMF

The LFP recordings showed that network activity remained altered for 1.5 hours after Keta/Xyl injection, but also after antagonization of MMF, while most aspects returned to preanesthetic conditions during 45 minutes after Iso removal. To assess network effects of the different anesthetics on a longer timescale, we used repeated calcium imaging during 6 hours after anesthesia onset and 5 hours after Iso termination and MMF antagonization (Fig 4D). In line with our previous results, the number of calcium transients was strongly reduced 30 minutes after MMF or Keta/Xyl injection, while the reduction had a lower magnitude for Iso. Similarly, MMF and Keta/Xyl most strongly reduced the amplitude and duration of calcium transients, while Iso mildly increased amplitude without affecting the decay constant (Fig 4E).

Confirming the dynamics monitored by LFP recordings in vivo, recovery from Iso anesthesia was fast, and only the rate of transients mildly changed during the hours after removing the mask. In contrast, after Keta/Xyl injection, amplitude and duration of transients were altered throughout the following 6 hours, while the reduction of the calcium transients rate was not reverted until up to 4 hours later. Recovery to the preanesthetic state was even slower after MMF/FAB. Despite antagonization of MMF anesthesia with FAB, calcium transients remained disturbed for up to 6 hours. Thus, the different anesthetics not only induce unique alterations of CA1 network dynamics, but also show different recovery profiles (S6E Fig).

Anesthesia decorrelates hippocampal activity

Calcium imaging studies in the visual cortex of ketamine-anesthetized rats [27] and Iso-anesthetized mice [25] showed that anesthesia increases the overall pairwise correlations between firing neurons and, consequently, induces more structured patterns of activity. While neocortical L2/3 cells typically show a high degree of local interconnectivity [47], this is not the case for CA1, where pyramidal cells receive their main excitatory input from CA3 and entorhinal cortex and send their efferents to subiculum and extrahippocampal areas [9]. Another difference between neocortex and hippocampal CA1 area is that the neocortex receives strong direct input from primary thalamus, which is a major source for slow oscillations during anesthesia-induced unconsciousness and sleep [1,48,49]. In comparison to neocortex, hippocampus shows different patterns of activity, including sharp waves, which are generated intrinsically in the hippocampus, likely originating in CA3 [50]. To investigate whether these differences cause a different impact of anesthesia on the population activity in CA1 when compared to the neocortex, we analyzed the dynamical structure of population activity using both calcium imaging and SUA of extracellular recordings in vivo. First, we analyzed Fisher-corrected Pearson pairwise correlation between neuropil-corrected raw fluorescence traces. We found that both correlation and anticorrelation were highest in animals during quiet wakefulness (Fig 5A and 5B). In particular, the awake condition had a higher proportion of correlation coefficients both in the first as well as in the fourth quartile of the entire distribution and, accordingly, higher absolute correlation values (Fig 5B, S7A Fig). Similar to the firing properties (SUA, Fig 2), Iso induced the milder changes, whereas Keta/Xyl caused the strongest phenotype. This relationship was preserved in neurons active during all conditions (S7B Fig), indicating that anesthesia generally reduces correlated activity between neurons and that this effect is not attributable to the activity of particular neuronal subpopulations. Moreover, these effects were not influenced by the distance between the pair of neurons whose correlation was quantified (Fig 5C). These findings highlight the major differences between the anesthesia-induced effects on neuronal coupling in hippocampal CA1 and neocortex. In accordance with the anatomy of CA1, the correlation between pairs of neurons was only mildly affected by the distance between them, with or without anesthesia. Not only were neurons less highly correlated to each other under anesthesia, but also their coupling to the whole population activity [51] was reduced as well. The proportion of neurons with population coupling in the fourth quartile of the entire distribution was highest for awake and most strongly reduced under Keta/Xyl and MMF, while Iso showed only mild effects (Fig 5D).

To further relate the calcium imaging data to extracellular recordings of neuronal firing, we carried out an analogous analysis on SUA. To avoid the confounding effect of firing rate, we quantified the correlation between pairs of neurons using the spike time tiling coefficient (STTC) [52], a measure that is largely insensitive to variations of the firing rate (see Methods). To be consistent with the calcium data, we quantified correlations within 1 second, a timescale of the same magnitude as the decay constant used to extract calcium signals (700 ms). This analysis confirmed that all anesthetics decorrelated neuronal activity (Fig 5E). This effect was still present, albeit less pronounced, using an integration window of 10 ms, which is closer to the duration of action potentials (S7C Fig). Overall, the decorrelation was milder under Iso anesthesia and stronger under Keta/Xyl and MMF. Thus, all 3 GAs decorrelated calcium transients and spiking activity in the CA1 area, with MMF and Keta/Xyl inducing the most prominent effects.

Anesthesia fragments temporal and spatial structure of hippocampal activity

The decorrelation of neuronal activity during anesthesia suggests that GAs might impact the spatial and temporal organization of CA1 neuronal ensembles (see Fig 5A). To test this

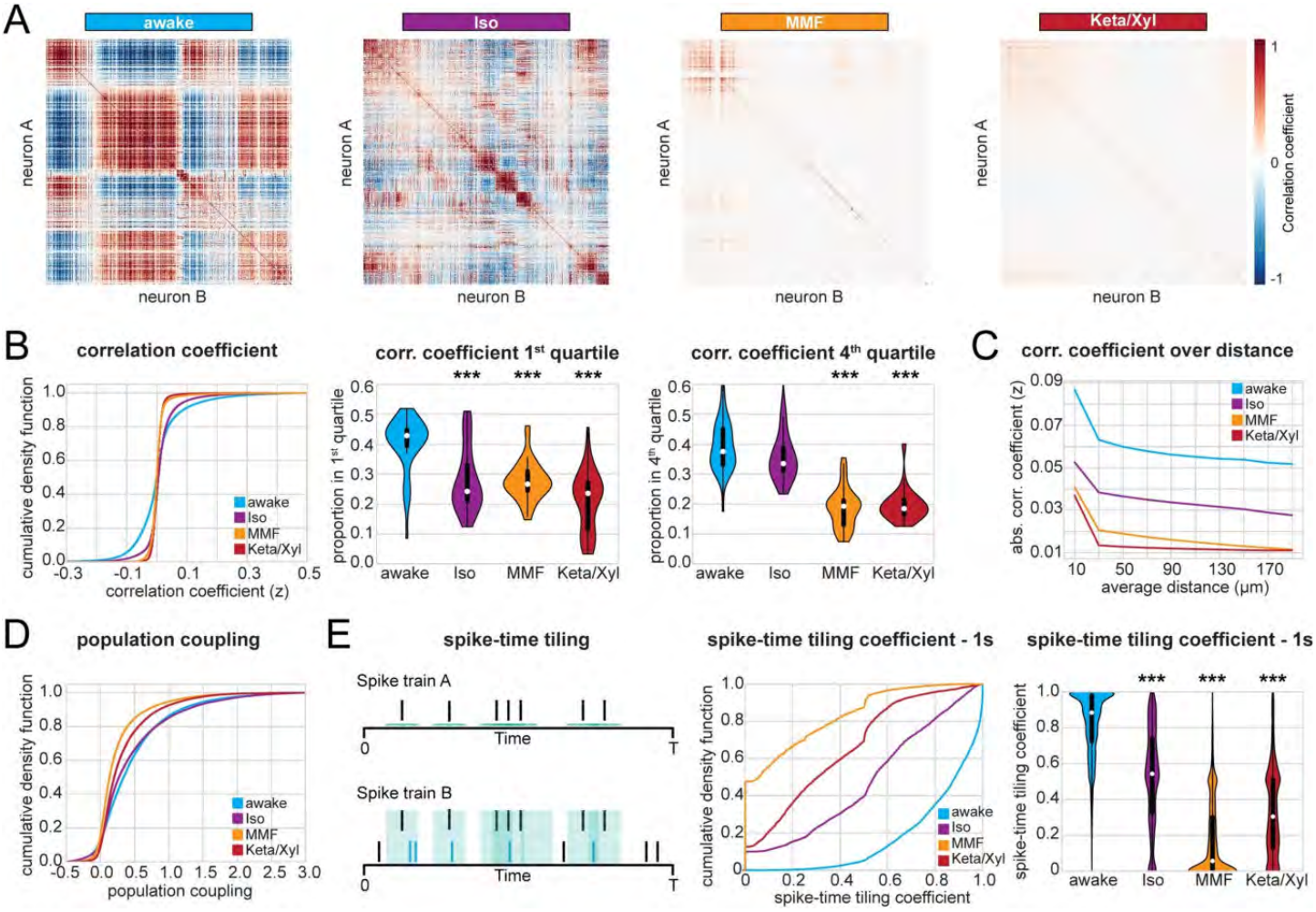

Fig 5. Correlation analysis of CA1 calcium activity and SUA shows decorrelation under anesthesia. **(A)** Heat maps displaying representative correlation matrices of calcium activity between pairs of neurons during wakefulness and the 3 different anesthetic conditions in the same animal. Matrices are sorted by similarity. **(B)** Left: Line plot displaying cumulative distribution of Fisher-corrected Pearson correlation coefficients between pairs of neurons (calcium imaging). Center: violin plot displaying the proportion of pairs found in the first (most negative) and fourth (most positive) quartile of the distribution. **(C)** Line plot displaying the absolute pairwise correlation coefficients over distance (calcium imaging, 25-micrometer bins). **(D)** Line plot displaying the cumulative distribution of population coupling (calcium imaging). **(E)** Quantification of correlation between pairs of extracellularly recorded single units using the STTC. Left: Schematic illustration of the STTC quantification. Center: cumulative distribution of the STTC with a 1,000-ms integration window. Right: violin plot quantifying the STTC. In violin plots, white dots indicate median, and vertical thick and thin lines indicate first to third quartile and interquartile range, respectively. Asterisks in (B) and (E) indicate significant differences to wakefulness. *** $p < 0.001$. Note, only differences to wakefulness are indicated. For comparison between conditions, see S1 Table. All datasets of this figure can be found under https://github.com/mchini/Yang_Chini_et_al/tree/master/Stats_Dataset_(R)/datasets/Figure5_S7. Iso, isoflurane; Keta/Xyl, ketamine/xylazine; MMF, medetomidine/midazolam/fentanyl; STTC, spike time tiling coefficient; SUA, single-unit activity.

https://doi.org/10.1371/journal.pbio.3001146.g005

hypothesis, we analyzed the same number of active neurons for each condition, since a different number of neurons in each condition potentially influences the number and size of detected clusters. First, we monitored the impact of GAs on the temporal structure of CA1 activity. We defined the number of clusters identified by principal component analysis (PCA) as the number of components that were needed to explain 90% of the variance. Moreover, we assessed the power-law slope of variance explained over the first 100 components (Fig 6A). Both methods led to a larger number of clusters and a flatter power-law slope for anesthesia when compared to wakefulness (Fig 6A). Further corroborating these findings, both t-distributed stochastic neighbor embedding (tSNE) dimensionality reduction and affinity propagation

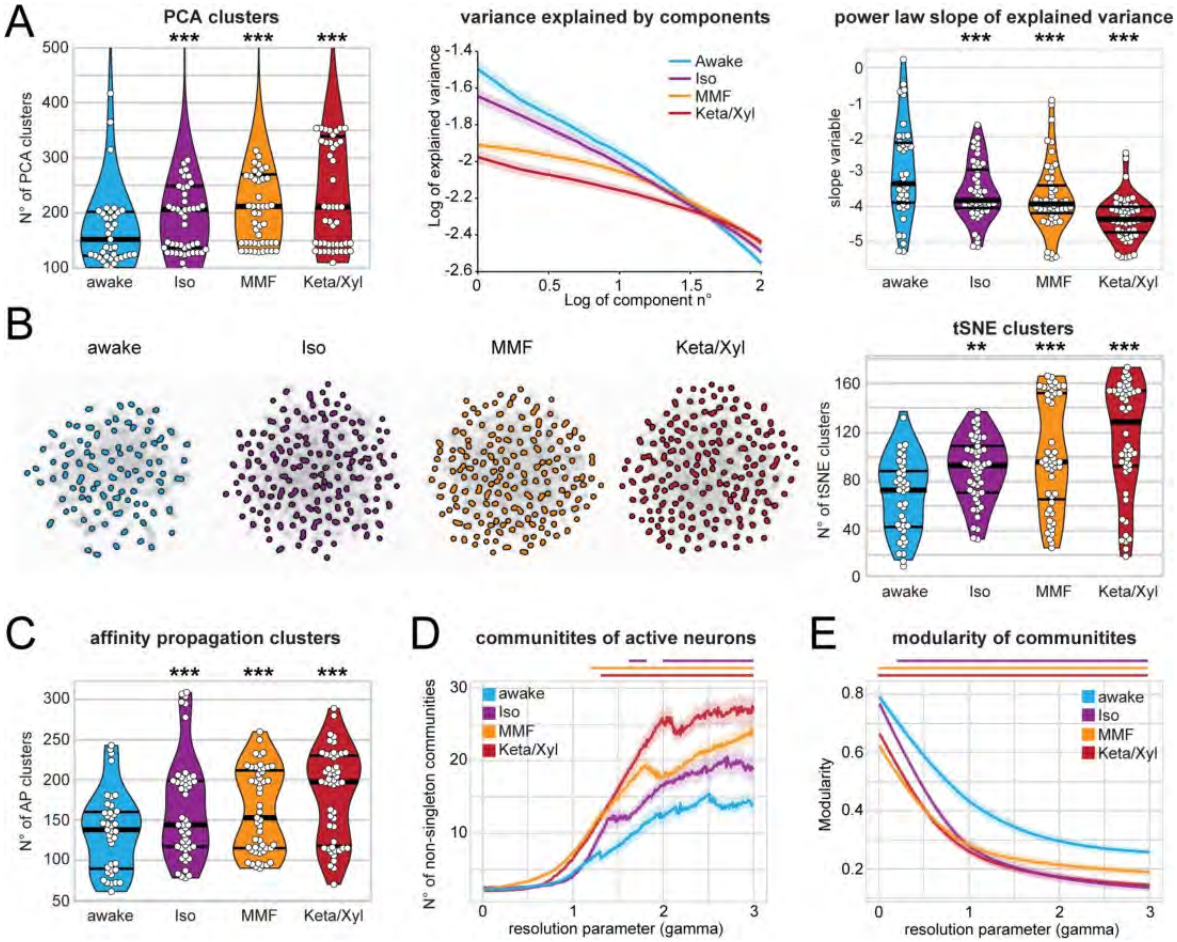

Fig 6. Calcium activity in CA1 is temporally and spatially fragmented during anesthesia. (A) Left: violin plot quantifying the number of PCA clusters during wakefulness or anesthesia, as indicated. Middle: log-log line plot displaying the variance explained by the first 100 components for each condition. Right: violin plot quantifying the power-law slope of the variance explained by the first 100 components for each condition. **(B)** Left: tSNE plots of network events recorded in the same animal under the 4 indicated conditions. Right: Violin plot quantifying the number of tSNE clusters obtained from calcium recordings during the 4 different treatments. **(C)** Violin plot quantifying the number of clusters obtained by AP from calcium recordings during the 4 different treatments. **(D)** and **(E)** Line plots quantifying the number of detected communities and the modularity of the detected communities with the resolution parameter gamma ranging from 0 to 3. Horizontal lines in violin plots indicate median and first to third quartile. Asterisks in (A)–(C) indicate significant differences to wakefulness. ** $p < 0.01$, *** $p < 0.001$. Horizontal lines above plots in (D) and (E) indicate significant difference to wakefulness. Anesthetic conditions are color coded. Note, only differences to wakefulness are indicated. For comparison between conditions, see S1 Table. All datasets of this figure can be found under https://github.com/mchini/Yang_Chini_et_al/tree/master/Stats_Dataset_(R)/datasets/Figure6_S8. AP, affinity propagation; Iso, isoflurane; Keta/Xyl, ketamine/xylazine; MMF, medetomidine/midazolam/fentanyl; PCA, principal component analysis; tSNE, t-distributed stochastic neighbor embedding.

https://doi.org/10.1371/journal.pbio.3001146.g006

(AP) clustering (see Methods) also revealed a larger number of clusters for anesthesia compared to wakefulness (Fig 6B and 6C). These observations indicate that activity is less structured under anesthesia. In line with previous results, Iso had the weakest effect, whereas Keta/Xyl consistently induced the most pronounced phenotype. Analysis of the deconvolved calcium traces led to comparable results (S8A and S8B Fig). These findings support the idea that GAs fragment the hippocampal network into a more diverse repertoire of microstates.

Second, we tested whether anesthesia disrupted the spatial structure of hippocampal activity, employing a modularity maximization approach [53,54] designed to detect internally densely connected communities (modules). To allow detection of modules at varying sizes, we carried out our analysis while varying a resolution parameter (gamma) and thus focusing on

different spatial scales. Using this approach, we showed that GAs increase the number of detected communities over a wide range of resolution parameter values (Fig 6D). Moreover, the modularity of these communities was lower than in wakefulness (Fig 6E). These results indicate that anesthesia results in a more fractured network with, on average, smaller and less coherent communities. A multiresolution approach [55] followed by the selection of partitions based on hierarchical consensus clustering yielded similar results (S8C Fig). Among GAs, Iso induced the mildest phenotype, whereas Keta/Xyl had the most prominent effects. Thus, GAs not only decorrelate hippocampal activity, but also consistently fragment both its temporal and spatial structure.

Network alterations during sleep are less pronounced compared to anesthesia

Altered CA1 activity under anesthesia may affect synaptic function and memory processing. A naturally occurring form of unconsciousness is sleep, which is required for network processes involved in memory consolidation [49,56]. To decide whether the network perturbations described above resemble those naturally occurring during sleep, we first monitored CA1 activity by recording the LFP and spiking together with animal motion and the neck-muscle electromyography (EMG) in head-fixed mice (S9A Fig). We classified the signal into 30-second long epochs of wake, rapid eye movement (REM) and NREM sleep. Further, a certain fraction of epochs, which we labeled as "uncertain," could not be reliably classified into any of the previous 3 categories (see Methods for details). Given that the behavioral attribution of these epochs is uncertain and difficult to interpret, we excluded them from further analysis. The animals spent most of their sleeping time in the NREM phase, with only short periods of intermittent REM sleep (Fig 7A and 7I). The LFP showed enhanced theta power during REM phases, while the power at low frequencies was broadly increased during NREM sleep (Fig 7B and 7C). Compared to anesthesia (Fig 1), these changes in the LFP both during REM and NREM phases were modest. Along the same line, the 1/f slope during NREM and REM sleep slightly decreased, indicating a small reduction of the E/I balance that had a significantly lower magnitude than the perturbation induced by GAs (Fig 7D). Furthermore, the SUA rate was slightly reduced only in REM sleep (Fig 7E and 7F), in contrast to all anesthetics, that strongly suppressed firing (Fig 2). As previously reported [44], and similarly to the effect of GAs, we detected a small but significant negative correlation between the NREM-induced reduction of firing rate and the wakefulness firing rate, whereas the effect failed to reach statistical significance for REM sleep alone (Fig 7G). Moreover, NREM sleep induced a small reduction of pairwise correlation between pairs of neurons, as measured by the STTC with an integration window of 1 second.

To additionally investigate the effect of sleep on hippocampal activity, we used the above-mentioned recordings to train a machine learning algorithm to classify wakefulness, NREM, and REM sleep from eye videography images alone (S9 Fig) [57] (see Methods for details). In line with previous results, we were able to reliably distinguish wakefulness and NREM sleep (4-fold cross-validation accuracy >85%), whereas REM classification was less precise (4-fold cross-validation accuracy approximately 30%). This classifier was then used to predict the physiological state of mice from which we recorded calcium transients in CA1 neurons. In the calcium imaging dataset, sleep was dominated by the NREM phase, and only 17 minutes of REM sleep could be detected in a total of 864 minutes (Fig 7I and 7J). Given the limited amount of detected REM sleep, its effects on hippocampal calcium activity should be interpreted with caution. As reported for LFP data, NREM only mildly reduced the rate of calcium transients, whereas REM sleep induced a small increase. In contrast, both NREM and REM

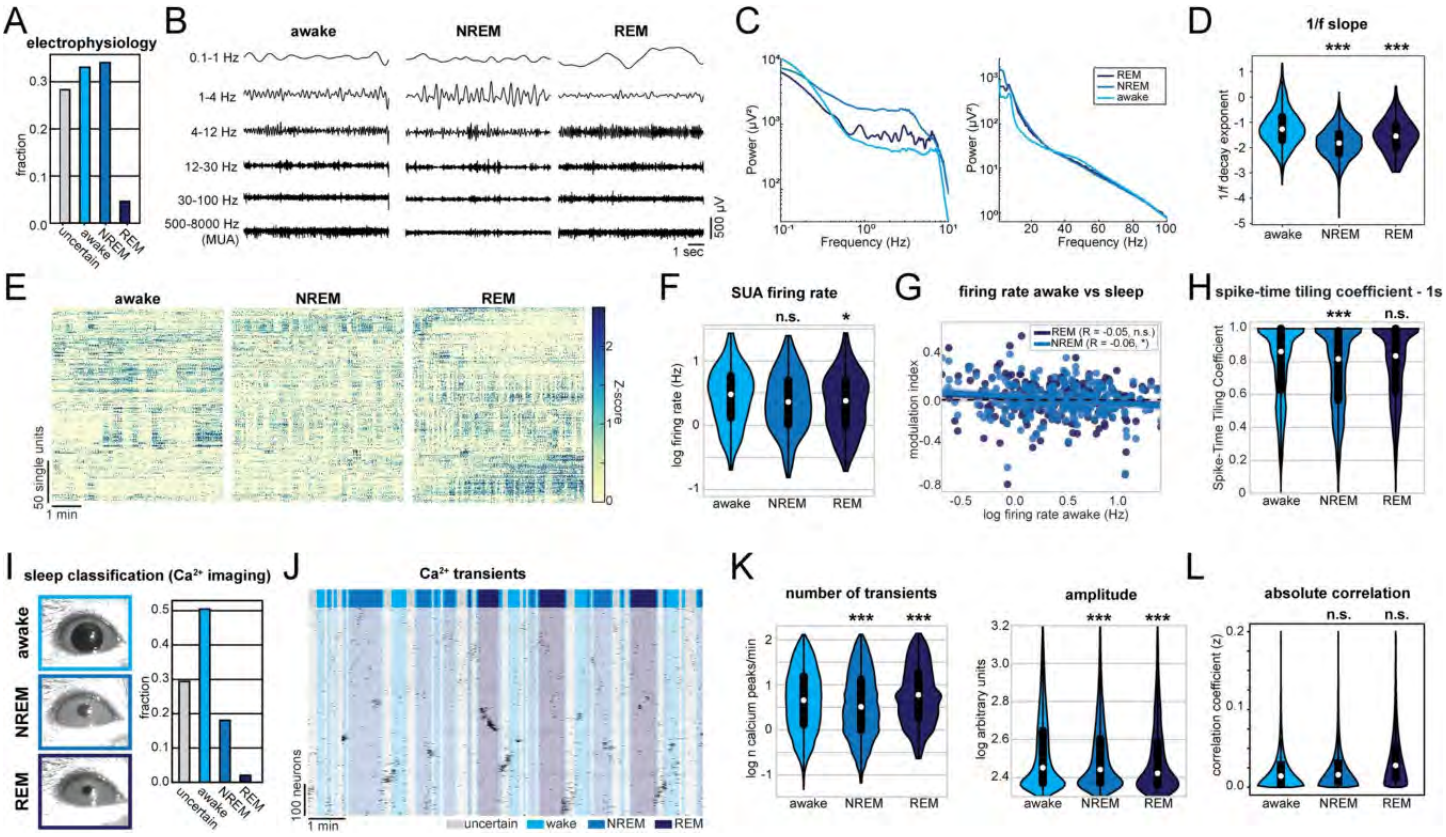

Fig 7. Sleep alters CA1 activity in a similar way to anesthesia but with a lower magnitude. **(A)** Classification of activity states during electrical recordings. **(B)** Characteristic LFP recordings during wakefulness, NREM, and REM sleep. **(C)** Line plot displaying LFP power spectra for the indicated activity states. **(D)** Violin plot displaying the power-law decay exponent (1/f) of the LFP power spectrum. **(E)** Raster plots of z-scored SUA for the 3 different activity states in 4 mice. Units are sorted according to initial activity during wakefulness. **(F)** Violin plot showing SUA firing rate. **(G)** Scatter plot showing modulation of SUA firing rate during NREM (light blue) and REM sleep (dark blue) with respect to activity during wakefulness. **(H)** Violin plot quantifying the STTC. **(I)** Classification of activity states during CA1 calcium imaging based on eye videography. **(J)** Raster plots of z-scored calcium transients in an example recording of 1 animal transiting between wakefulness and sleep. Traces are sorted by similarity. **(K)** Violin plots quantifying the number (left) and amplitude (right) of detected calcium transients. **(L)** Violin plots quantifying absolute pairwise correlation of all recorded neurons. White dots indicate median, and vertical thick and thin lines indicate first to third quartile and interquartile range, respectively. * $p < 0.05$, ** $p < 0.01$, *** $p < 0.001$ w.r.t. to wake state, $n = 3–7$ mice. For full report of statistics, see S1 Table. All datasets of this figure can be found under https://github.com/mchini/Yang_Chini_et_al/tree/master/Stats_Dataset_(R)/datasets/Figure7_S9. LFP, local field potential; NREM, non-rapid eye movement; REM, rapid eye movement; STTC, spike time tiling coefficient; SUA, single-unit activity.

https://doi.org/10.1371/journal.pbio.3001146.g007

sleep caused a small reduction in transient amplitude (Fig 7K). Further, we did not detect an effect of the sleep state on absolute pairwise correlations (Fig 7L).

In conclusion, sleep and GAs similarly affect the CA1 activity. However, the magnitude of effects was much smaller for sleep than for GAs. Both NREM and REM states were more similar to wakefulness than to the anesthetic state. Compared to the 3 different anesthetics, sleep had the closest resemblance to Iso. Thus, among the 3 different anesthetics, network alterations under Iso deviate the least from natural states such as wakefulness and sleep.

Repeated anesthesia alters spine dynamics in CA1

The impact of Iso, MMF, and Keta/Xyl on CA1 activity might alter spine dynamics at CA1 pyramidal neurons. This issue is of critical relevance, since GAs disrupt activity patterns during development [58] also involving alteration of synaptic connectivity [59–61], but less is known about the impact of GAs on hippocampal synaptic structure during adulthood. So far, spine dynamics in hippocampus were only investigated under anesthesia, lacking comparison

to the wake state. Moreover, the reported turnover rates varied strongly between studies [21,62,63]. Thus, it is unknown how repeated anesthesia in itself affects spine stability.

We repeatedly imaged the same basal, oblique, and tuft dendritic segments of CA1 pyramidal neurons under all 4 conditions (5 times per condition, every 4 days), interrupted by a

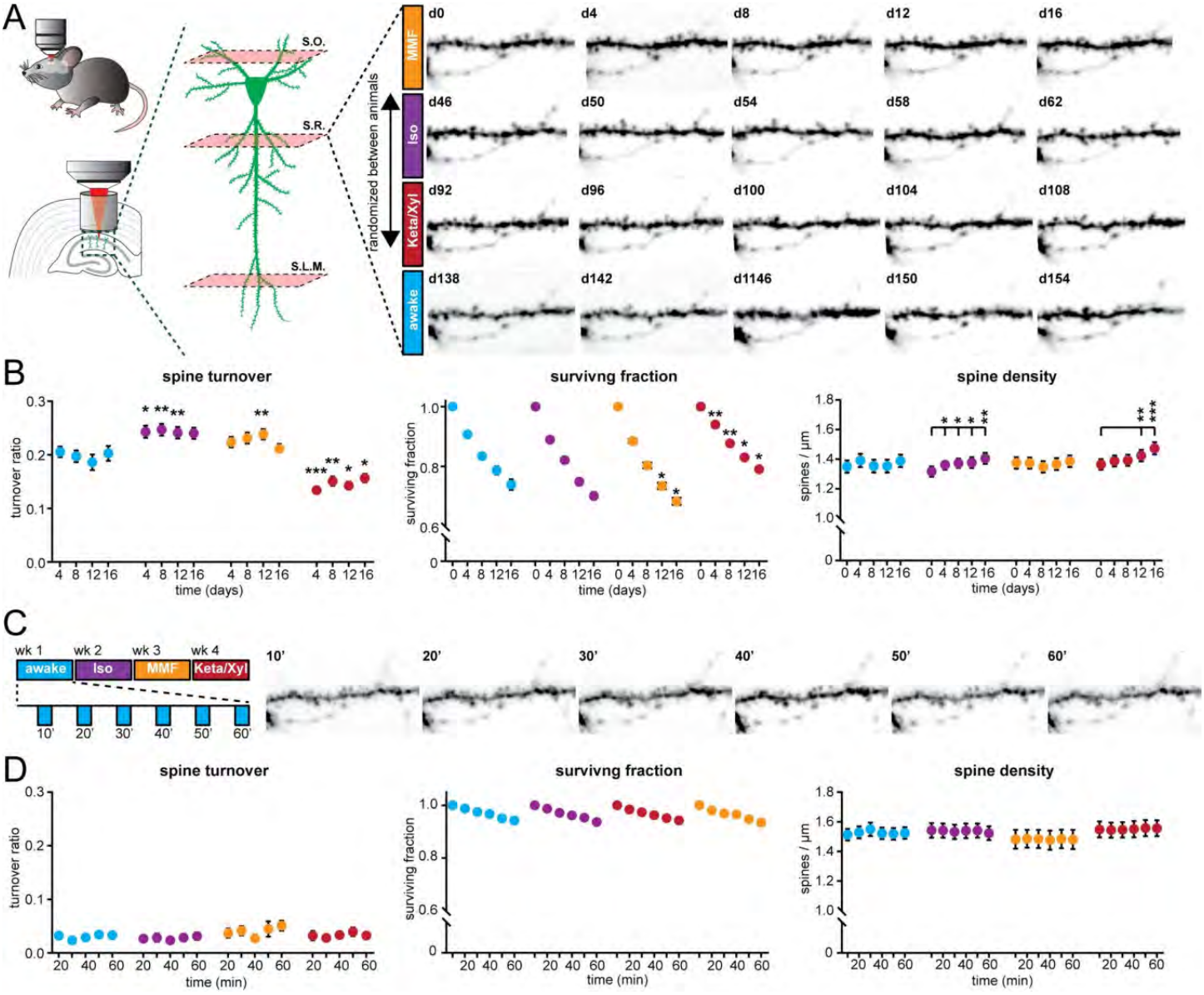

Fig 8. Spine turnover at CA1 pyramidal neurons is distinctly altered by repeated application of Iso, MMF, and Keta/Xyl. (A) Left: Schematic illustration of in vivo spine imaging strategy. In each animal, spines were imaged on basal dendrites located in S.O., oblique dendrites in S.R., and tuft dendrites in S.L.M. Right: Example showing an oblique dendrite in S.R. imaged chronically during all conditions. The order of anesthetic treatments was pseudo-randomized between mice (see S10A Fig). **(B)** Dot plots showing quantification of spine turnover (left), spine survival (middle), and spine density (right) under the 4 indicated treatments. Note that spines were imaged on the same dendrites across all conditions. Dots indicate mean ± SEM. Asterisks indicate significant differences to wakefulness in the left and middle panel. In the right panel, asterisks denote significant changes within each treatment compared to day 0. * $p < 0.05$, ** $p < 0.01$, *** $p < 0.001$. **(C)** Imaging of acute spine dynamics during 4 different conditions. Left: schematic of the experimental timeline. Right: example of dendrite imaged during wakefulness in 10-minute intervals (same dendrite as in A). **(D)** Dot plots showing quantification of acute spine turnover (left), spine survival (center), and spine density (right) under the 4 indicated treatments. Dots indicate mean ± SEM. For full report of statistics, see S1 Table. All datasets of this figure can be found under https://github.com/mchini/Yang_Chini_et_al/tree/master/Stats_Dataset_(R)/datasets/Figure8_S10. Iso, isoflurane; Keta/Xyl, ketamine/xylazine; MMF, medetomidine/midazolam/fentanyl; S.L.M., stratum lacunosum moleculare; S.O., stratum oriens; S.R., stratum radiatum.

https://doi.org/10.1371/journal.pbio.3001146.g008

30-day recovery period between conditions (Fig 8A, S10A Fig). To rule out time effects, we pseudo-randomized the order of anesthetics (S10A Fig). During wakefulness, without any anesthesia in between, the turnover ratio of spines on all dendrites was on average 18.6% to 20.5% per 4 days. This turnover ratio was stable and did not change systematically over successive imaging sessions (Fig 8B). Notably, all anesthetics affected spine turnover. Both MMF and Iso anesthesia mildly increased the turnover ratio compared to wakefulness (21.1% to 23.8% for MMF and 24.0% to 24.7% for Iso). Iso did not alter the surviving fraction of spines. Together with the significant increase in spine density over time (Fig 8B), these results indicate that the elevated turnover ratio was due to a rise in the gained fraction of spines (S10B Fig). In contrast, MMF led to a slight increase in the fraction of lost spines (S10B Fig) and correspondingly, slightly decreased the surviving fraction compared to wakefulness. Spine density did not change over time. Keta/Xyl anesthesia showed the strongest effect on spine turnover (13.4% to 15.7%), which was opposite to MMF and Iso, and therefore significantly lower, rather than higher, compared to the awake condition (Fig 8B). This lower turnover ratio was accompanied by a higher surviving fraction and an increase in density with time (Fig 8B). Consistently, the fraction of lost spines was most strongly reduced (S10B Fig). Thus, Keta/Xyl anesthesia resulted in marked stabilization of existing spines and a reduction in the formation of new spines, indicative of a significant effect on structural plasticity. These effects were present on basal dendrites of S.O., oblique dendrites in S.R., and tuft dendrites in S.L.M., albeit with different magnitude. Under Keta/Xyl, the strongest impact on spine density was present in S.L.M., while turnover was most strongly reduced in S.O. Also, the increased spine turnover seen under Iso and MMF was most pronounced in S.O. (S10D Fig).

To rule out that the age of the animal-influenced spine dynamics in the awake condition, we measured spine turnover in a group of age-matched animals to the first anesthesia group (S10A and S10C Fig). Moreover, to rule out that the chronic imaging procedure per se and anesthesia in general had a long-lasting effect on the awake-imaging condition, we added another awake-imaging control group with naïve, age-matched animals to the awake-imaging time point in the experimental group (S10A and S10C Fig). In all 3 groups, spine turnover was indistinguishable, indicating that neither age nor previous imaging under anesthesia impacted spine dynamics in the awake-imaging group (S10C Fig).

Next, we asked whether the modulation of spine turnover by GAs was due to acute remodeling of spines during the time of anesthesia. Alternatively, spine turnover might be driven by long-lasting changes in network activity imposed by the slow reversal of all GAs. To capture fast events such as filopodia formation, we acquired image stacks every 10 minutes (Fig 8C). Spine turnover, survival, or density were not significantly altered during the 1 hour of imaging (Fig 8D). Thus, spines were stable during the 1 hour irrespective of the treatment. While mature spines typically show low elimination/formation rates over 1 hour, filopodia are more dynamic [64–66]. Unlike other reports that observed an acute selective formation of filopodia under Keta/Xyl, but not Iso [67], we did not detect any acute effects of GAs on filopodia turnover of CA1 pyramidal cell dendrites. Thus, chronic exposure to all GAs consistently impacted spine dynamics, whereas acute effects were lacking. Keta/Xyl caused a strong decrease in spine turnover, accompanied by a higher surviving fraction and an increased density over time.

Episodic memory consolidation is impaired by MMF and Keta/Xyl, but not by Iso

Episodic memory formation and consolidation require hippocampal activity. Newly learned experiences are thought of being consolidated via replay events that co-occur with low-

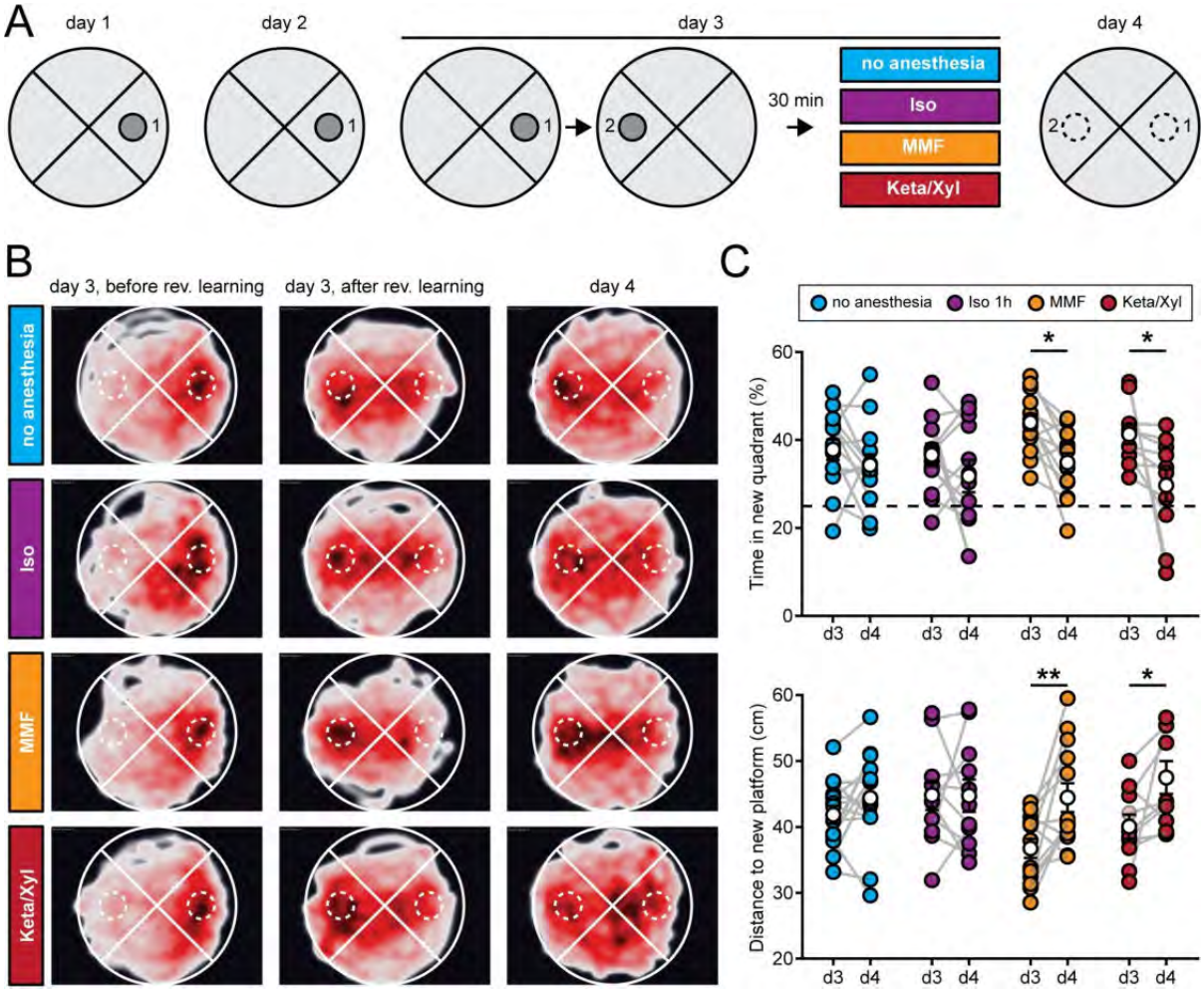

Fig 9. Episodic memory consolidation is impaired by MMF and Keta/Xyl, but not by Iso. (A) Experimental design to test episodic-like memory in a Morris water maze. On days 1 and 2, animals were trained to find the platform in position 1. Reversal learning was performed on day 3 where animals had to learn that the platform was moved to position 2. The training was followed 30 minutes later by a 1-hour period of one of the 4 indicated treatments per group. On day 4, consolidation of the memory for the platform in position 2 was tested. **(B)** Heat maps showing trajectories of all mice during the first probe trial before reversal learning on day 3 (left column), after reversal learning on day 3 (middle column), and after treatment on day 4 (right column). The position of the target zone is indicated by dashed circles. **(C)** Scatter plots showing quantification of time spent in the new target quadrant (top) and distance to the new platform (bottom) after reversal learning on day 3 and on day 4. Filled, colored circles indicate individual animals, and white circles indicate mean ± SEM. Asterisks in (C) indicate significant differences between days. * $p < 0.05$, ** $p < 0.01$. For full report of statistics, see S1 Table. All datasets of this figure can be found under https://github.com/mchini/Yang_Chini_et_al/tree/master/Stats_Dataset_(R)/datasets/Figure9_S11. Iso, isoflurane; Keta/Xyl, ketamine/xylazine; MMF, medetomidine/midazolam/fentanyl.

https://doi.org/10.1371/journal.pbio.3001146.g009

frequency oscillations [49,68–70]. In the hippocampus, these low-frequency events typically occur as sharp waves [50] during sleep, but also during awake resting behavior [70]. The above results from electrophysiological recordings and imaging showed that GAs strongly altered network oscillations in the CA1 area, in the case of MMF and Keta/Xyl, also long after anesthesia discontinuation. Spine turnover of CA1 pyramidal neurons was also affected, especially after Keta/Xyl administration. Therefore, we tested whether inducing anesthesia shortly after the acquisition of a new episodic memory affected its consolidation (Fig 9A). In line with previous experiments, we restricted Iso and MMF anesthesia to 1 hour, while Keta/Xyl anesthesia was left to recede spontaneously. We assessed episodic-like memory with a water maze

protocol for reversal learning, when the hidden platform was moved to the quadrant opposite the initial target location (Fig 9A). Specifically, we tested the effects of the different anesthetics on the consolidation of the memory of the new platform location. We compared the performance of the mice during the probe trial done on day 3 immediately after the reversal learning protocol (and 30 minutes before anesthesia), with the performance during the probe trial on day 4, 24 hours after anesthesia. During the probe trial on day 3, animals of all 4 groups spent significantly more time in the new target quadrant compared to chance (25%), indicating that they learned the new platform position successfully (Fig 9B and 9C).

On day 4, control animals that did not undergo anesthesia showed the same performance as on day 3, suggesting that they had retained the memory of the new platform location (Fig 9B and 9C). However, animals that were anesthetized with Keta/Xyl or MMF spent significantly less time in the new target quadrant and showed a significantly larger mean distance to the target platform position compared to the probe trial on day 3. In the Iso group, no significant difference compared to day 3 was detectable (Fig 9B and 9C, S11A Fig). The impairment of memory consolidation was not explained by the longer duration of recovery after Keta/Xyl or MMF compared to Iso, because anesthesia for up to 4 hours with Iso had no disruptive effect (S11B and S11C Fig). Thus, it is not the duration of the induced unconsciousness but rather the type of anesthetic that likely explains the impaired memory consolidation. Notably, the effects were relatively mild, and the decrease in performance on day 4 was not significantly different between treatment groups. In summary, consistent with long-lasting effects on CA1 network activity, Keta/Xyl and MMF impaired episodic-like memory consolidation. In contrast, Iso, which overall caused a weaker disturbance of neuronal population activity and a faster recovery profile, did not significantly affect memory consolidation.

Discussion

We investigated and systematically compared the intra- and postanesthetic effects of different commonly used anesthetic strategies on the mouse hippocampus across multiple levels of analysis. Despite sharing some common traits, brain and cellular network states differ substantially under the influence of various types of anesthetics [30,71,72]. Indeed, at the neuronal level, compared with awake state and natural sleep, all 3 anesthetics showed robustly reduced spiking activity in single neurons, reduced power in the high oscillation frequency band, and decorrelated cellular population activity. However, the induced network states in CA1 were highly distinct between the 3 different conditions, with Iso leading to prominent network oscillations at around 0.1 Hz, which timed the spiking activity of single units and neuronal calcium transients. Keta/Xyl caused pronounced oscillations between 0.5 and 4 Hz and the strongest reduction in calcium dynamics. MMF, in contrast, most strongly reduced LFP and SUA and impaired population dynamics for many hours as assessed with calcium imaging. Differences were also present in the long-term effects on spine dynamics, with Keta/Xyl stabilizing spines, leading to reduced turnover and increased density. MMF, on the other hand, mildly increased spine dynamics. Keta/Xyl cannot be antagonized, and therefore, changes of the CA1 network mediated by this anesthetic were present hours after the injection, in agreement with long-lasting overall changes of global animal physiology [38]. More unexpectedly, and in contrast to overall effects on physiology [38], CA1 network dynamics were still disturbed for at least 6 hours after antagonization of MMF anesthesia. These long-lasting alterations were associated with impairment of episodic memory consolidation after exposure to Keta/Xyl or MMF, but not Iso. Thus, despite fulfilling the same hallmarks of general anesthesia, different GAs distinctly alter hippocampal network dynamics, synaptic connectivity, and memory consolidation.

Iso, MMF, and Keta/Xyl have different molecular targets and distinctly modulate functional and structural features of CA1

The GAs used here represent 3 different strategies based on the large repertoire of currently available anesthetics. Iso represents the class of halogenated diethyl ether analogues, which are volatile and therefore administered via inhalation. Fentanyl, in combination with the analgesic medetomidine and the sedative midazolam (MMF), represents an anesthetic approach based on the injection of a combination of drugs with sedative, analgesic, and anxiolytic properties. In the clinic, propofol can be used instead of midazolam. Finally, ketamine is used both as an anesthetic and, at a lower dosage, as a treatment against depression. For anesthesia, it is generally combined with xylazine, which acts as a sedative, analgesic, and muscle relaxant. All 3 strategies differ markedly in their molecular targets. Consequently, they uniquely modulate general animal physiology [38] and brain activity [72]. Iso is a potent GABA and glycine receptor agonist. Moreover, it activates 2-pore potassium channels and acts as α-amino-3-hydroxy-5-methyl-4-isoxazolepropionic acid receptor (AMPAR) inhibitor [4]. Similar to Iso, midazolam, the hypnotic component of the MMF mix, mainly acts as a GABAR agonist with little effect on NMDARs. In contrast, ketamine is a potent, use-dependent NMDAR blocker with less pronounced effects on potassium channels, GABA, glycine, and other glutamate receptors such as AMPA or kainite receptors [4]. Moreover, while most anesthetics reduce the activity of thalamic nuclei, ketamine increases thalamic drive [73], leading to enhanced rather than reduced oscillations in mid-to-high frequency bands such as theta and gamma [28,74]. In accordance with this, our study reveals major differences in the action of the different anesthetics on functional and structural features of CA1. With both electrical recordings and calcium imaging, we report a robust reduction of neuronal spiking and pairwise neuronal correlation. Notably, effects on electrical activity and calcium activity were well in line for both Iso and MMF, despite the different recording methods. However, we observed some divergence for Keta/Xyl.

Comparison of electrophysiological recordings and calcium imaging

Generally, differences in electrophysiological recordings and calcium imaging data may stem from the location where the signal is detected. In the calcium imaging experiments, the signal was sampled in a horizontal plane located inside and parallel to stratum pyramidale of CA1. In this configuration, somatic, action potential-driven calcium transients mainly from pyramidal neurons dominate the signal. Due to the kinetics and calcium-binding properties of GCaMP6f, action potentials can only be resolved below approximately 5 Hz and are reported nonlinearly [46,75]. Moreover, expression of the calcium indicator itself influences the detected signals. Low expression levels may bias the detection toward the most active neurons, while strong overexpression of calcium indicators may alter cellular physiology and distort calcium dynamics [76]. In contrast, electrical recordings do not rely on exogenously expressed activity reporters, but require physical insertion of electrodes into the tissue. The electrodes on linear probes are arranged orthogonally to the strata of CA1 and parallel to the dendrites of CA1 cells. Thus, synaptic potentials mainly constitute the LFP across all layers, and spikes are picked up from both pyramidal cells (in stratum pyramidale) and GABAergic neurons in all layers. Moreover, the first method samples neurons that spatially distribute over a large area. In contrast, the second one is biased toward large, active neurons that are in close proximity of the electrode.

More specifically, under Keta/Xyl, the overall firing rate of single units showed the smallest reduction of all 3 anesthetics. At the same time, imaging revealed the most substantial reduction in rate, amplitude, and duration of calcium transients (compare Figs 2B and 3D). One reason for this discrepancy may be the inhibitory action of ketamine on NMDARs. CA1

pyramidal cells display large, NMDAR-driven dendritic plateau potentials and calcium spikes [77]. Moreover, ketamine likely inhibits L-type voltage-gated calcium channels [78] and reduces burst firing [79], leading to calcium transients with reduced amplitude and a faster decay constant. In contrast, ketamine has little influence on sodium spikes and AMPAR-mediated synaptic potentials, which are detected in electrical recordings as SUA and LFP, respectively. In accordance with electrical recordings, calcium transients showed increased power at 0.1 to 0.2 Hz under Iso. However, we did not detect a clear peak at 1 to 4 Hz in the presence of Keta/Xyl, as seen in LFP and SUA, probably due to its strongly dampening effect on calcium transients. The (low-pass) filtering of neuronal activity imposed by calcium indicators might also play a role [75].

Notably, the differences between electrical recordings and calcium imaging under Keta/Xyl are relevant. Calcium is a second messenger central to neuronal plasticity and metabolism [80,81]. NMDARs are a major source for activity-dependent calcium entry into the cell, involved in regulating synaptic plasticity, metabolism, and pathology [82]. The present findings suggest that Keta/Xyl has a particularly strong effect on neuronal calcium activity, uncoupling action potential firing from associated cytosolic calcium transients, leading to reduced intracellular calcium signaling. In contrast, calcium transients under MMF and Iso anesthesia closely matched the electrical activity profile of neurons. Therefore, aside from overall effects on network activity, Keta/Xyl may selectively alter neuronal plasticity by suppressing NMDAR-dependent postsynaptic calcium signals.

In contrast to neocortex, GAs decorrelate neuronal activity in CA1

All anesthetics decorrelated neuronal activity in CA1, leading to an overall fragmented network state with an increased number of temporal and spatial clusters. This is in contrast with what has been reported from studies on GAs and cortical activity both at adulthood [25–27] and during development [58]. This discrepancy may arise from different ways of analyzing the data. In the present study, all active neurons were identified for each imaging session. Thus, a breakdown of the network results in a larger number of clusters containing less neurons per cluster. In contrast, if a defined population of neurons is followed over time [26], fragmentation of the network may lead to less clusters, since not all neurons remain active during anesthesia. Another reason for the different observations in hippocampus and neocortex may be the distinct architecture of CA1 compared to L2/3 of the neocortex, the latter showing a high degree of local excitatory interconnectivity [47]. In CA1, this is not the case. Pyramidal cells receive their main excitatory input from CA3 and entorhinal cortex and send their efferents to subiculum and extrahippocampal areas without making local connections among each other [9]. Afferent activity originating in various sources and converging in CA1, may arrive out of phase under anesthesia, leading to desynchronized firing of CA1 pyramidal cells. Such a phenomenon has been proposed as a candidate mechanism underlying desynchronization of neuronal firing in basal ganglia under conditions of slow oscillations (slow-wave sleep) and high synchrony in the neocortex [83]. Notably, the pairwise correlation was not entirely independent of the distance between neurons. Synchronization of pyramidal neurons via local, GABAergic interneurons may be another factor that increases spatial correlations. Both in the neocortex and hippocampus, various types of GABAergic interneurons, such as basket or bistratified cells, locally connect to and synchronize pyramidal neurons [84].

Coordinated neuronal network dynamics, including pairwise correlation of calcium transients and single units, population coupling, clustering in the temporal and spatial domain were consistently impaired most strongly with Keta/Xyl and MMF. Iso, both in electrophysiological as well as calcium recordings, showed the mildest effects and permitted hippocampal activity patterns that most closely resembled wakefulness and NREM/REM sleep. Iso and

MMF, in contrast to Keta/Xyl, are thought to be immediately reversible [38]. However, especially MMF showed significant disruption of network dynamics long after reversal both in electrical recordings and with calcium imaging. Antagonization of MMF failed to fully recover calcium dynamics within the following 5 hours. Such long-lasting alterations might interfere with hippocampal function shortly after antagonization of MMF and must be considered when performing whole-cell recordings in freely moving animals [85–87].

Since all anesthetics had a much longer effect on network activity than we expected, we asked whether this is reflected in long-term effects of these different types of anesthetics on spine dynamics of CA1 pyramidal neurons. Recent studies investigating spine dynamics at CA1 pyramidal neurons came to incongruent conclusions reporting spine turnover ranging from 3% [63] over 12% [21] to approximately 80% [62] over 4 days. However, all studies used either Iso- [21] or Keta/Xyl-based [62,63] anesthesia during the repeated imaging sessions. Thus, to what extent anesthesia itself influences spine dynamics is not clear.

Iso, MMF, and Keta/Xyl distinctly alter spine dynamics in CA1

More generally, various effects of general anesthesia on spine dynamics were reported, depending on the brain region, preparation, age of the animal, and anesthetic strategy. For example, enhanced synaptogenesis has been reported with different types of anesthetics on cortical and hippocampal neurons during development [59,60]. In contrast, one study indicated that spine dynamics were not altered on cortical neurons of adult mice with Keta/Xyl or Iso [67], while another study demonstrated an increase in spine density in somatosensory cortex with ketamine [88]. Also, fentanyl-mediated, concentration-dependent bidirectional modulations of spine dynamics were reported in hippocampal cultures [89].

To systematically compare spine dynamics in CA1 in vivo under different anesthetic treatments, we imaged spines at basal, oblique, and tuft dendrites in a large set of dendrites. We found small, but robust chronic effects of repeated anesthesia. These alterations were present in all strata of CA1, consistent with a layer-independent reduction of SUA during anesthesia. Keta/Xyl decreased spine turnover, leading to a mild increase in spine density over time by stabilizing existing spines. This observation agrees with recent studies that showed a stabilizing effect of ketamine in the somatosensory cortex, resulting in increased spine density [88]. Thus, repeated anesthetic doses of Keta/Xyl may limit overall synaptic plasticity and thus spine turnover. It was further shown that sub-anesthetic, antidepressant doses of ketamine enhance spine density in the prefrontal cortex [90,91], similar to our study of CA1 neurons. Iso and MMF had contrasting effects on spine dynamics compared to Keta/Xyl, mildly enhancing spine turnover, which might be explained by their different pharmacology compared to ketamine, as pointed out above. A second aspect that distinguishes Keta/Xyl from Iso and MMF is its irreversibility, which might lead to longer-lasting alterations of synaptic transmission and E/I ratios leading to differential spine dynamics. This idea is supported by the observation that during the anesthesia period itself, spine turnover was not altered, suggesting that long-lasting and repeated disturbances are required to leave a mark in synaptic connectivity.

MMF and Keta/Xyl, but not Iso, retrogradely affect episodic-like memory formation

Sleep is a natural form of unconsciousness and is required for memory consolidation, including hippocampus-dependent memories [49,56]. Recent work suggested that sleep- and anesthesia-promoting circuits differ [92,93] while others identified circuit elements shared between sleep and general anesthesia [94], especially during development [58]. Therefore, we asked how the diverse alterations of CA1 network dynamics imposed by the different

anesthetics impact memory consolidation. In our study, Iso resembled most closely network states during wakefulness and natural sleep, while Keta/Xyl and MMF caused strong, lasting alterations of LFP, SUA, and calcium dynamics.

Notably, a single dose of anesthesia with Keta/Xyl and MMF, but not Iso, disrupted memory consolidation using a water maze assay in adult mice. Retrograde amnesia appeared to be more sensitive to the magnitude than the duration of CA1 network disturbance imposed by the various anesthetics. Keta/Xyl and MMF most strongly decorrelated CA1 network activity and reverted only slowly. Extending the duration of Iso anesthesia up to 4 hours, to match the slow recovery after MMF and Keta/Xyl, did not affect memory consolidation. This observation indicates that the slow recovery of network activity after Keta/Xyl and MMF alone cannot explain anesthesia-mediated disruptions of memory consolidation. Instead, specific aspects of the different anesthetics may selectively impact hippocampus-dependent memory formation. For example, ketamine is an NMDAR blocker that has been shown to be necessary for the long-term stabilization of place fields in CA1 [95], encoding of temporal information of episodes [96], and formation of episodic-like memory [97]. Notably, maintenance of Iso anesthesia over much longer time periods eventually also disrupts cognitive performance, suggesting that aside from drug-specific effects, loss of consciousness for extended durations may generally affect synaptic function and memory consolidation [98].

Our results appear at odds with a report [99], where a single, 1-hour treatment with Iso caused deficits in the formation of contextual fear memory, object recognition memory, and performance in the Morris water maze in the following 48 hours. However, this study investigated memory acquisition after anesthesia (i.e., anterograde amnesia), while our study asked whether anesthesia affects the consolidation of a memory formed shortly before the treatment (i.e., retrograde amnesia).

Changes in synaptic connections are considered essential for memory formation and storage [11–14]. Despite a small effect on spine dynamics, the strong and lasting disturbance of hippocampal network activity in CA1 (and most likely other brain areas) by Keta/Xyl and MMF was sufficient to interfere with memory consolidation. The chronic alterations of spine turnover, especially by Keta/Xyl, may therefore indicate that repeated anesthesia can impact long-lasting hippocampus-dependent memories.

To establish a direct link between spine dynamics, network disruptions, and memory, future studies are required that investigate both spine turnover and changes in population coupling at hippocampal neurons causally involved in memory formation and maintenance.

Taken together, we report a novel effect of anesthesia on brain dynamics, namely fragmentation of network activity in hippocampus. We consistently observe this phenomenon across multiple levels of analysis. This unique response compared to the cortex may underlie its high sensitivity to anesthesia, including its central role in amnesia. The extent, duration, and reversibility of network fragmentation depend on the GA used. Therefore, this study may help guide the choice of an appropriate anesthetic strategy, dependent on experimental requirements and constraints, especially in the neurosciences. More generally, our findings might also have relevance for the clinic. Postoperative delirium, a condition that involves memory loss, is still an unresolved mystery. Minimizing the disturbance of hippocampal function may be one building block to overcome this undesired condition.

Methods

Experimental models and methods

Mice. Adult (3 to 9 months of age) C57BL/6J mice and transgenic Thy1-GFP-M mice of both sexes were used in this study. They were housed and bred in pathogen-free conditions at

the University Medical Center Hamburg-Eppendorf. The light/dark cycle was 12/12 hours, and the humidity and temperature were kept constant (40% relative humidity; 22˚C). Food and water were available ad libitum. All procedures were performed in compliance with German law according and the guidelines of Directive 2010/63/EU. Protocols were approved by the Behörde für Gesundheit und Verbraucherschutz of the City of Hamburg under the license numbers 09/15, 32/17, N18/015, and N19/121.

Hippocampal recording window surgery and in vivo electrophysiology. Chronic multisite extracellular recordings were performed in dorsal CA1 during the dark phase of the dark/light cycle, except for sleep recordings, which were done during the light period. The adapter for head fixation was implanted at least 4 days before recordings. Mice were anesthetized via intraperitoneal injection of MMF and placed on a heating blanket to maintain the body temperature. Eyes were covered with eye ointment (Vidisic, Bausch + Lomb, Berlin, Germany) to prevent drying. Prior to surgery, the depth of anesthesia and analgesia was evaluated with a toe pinch to test the paw withdrawal reflex. Subsequently, mice were fixed in a stereotactic frame, the fur was removed with a fine trimmer, and the skin of the head was disinfected with Betaisodona. After removing the skin, 0.5% bupivacaine/1% lidocaine was locally applied to cutting edges. A metal headpost (Neurotar, Helsinki, Finland) was attached to the skull with dental cement (Super Bond C&B, Sun Medical, Moriyama, Japan), and a craniotomy was performed above the to the dorsal CA1 area (−2.0 mm AP, ± 1.3 mm ML relative to Bregma) which was subsequently protected by a customized synthetic window filled with Kwik-Cast sealant (World Precision Instruments, Friedberg, Germany). After recovery from anesthesia, mice were returned to their home cage and were provided with Meloxicam mixed into soft food for 3 days. After recovery from the surgery, mice were accustomed to head fixation and trained to move in the Mobile HomeCage system (Neurotar). For recordings, craniotomies were reopened by removal of the Kwik-Cast sealant, and multisite electrodes (NeuroNexus, Michigan, United States of America) were inserted into the dorsal CA1 (one-shank, A1x16 recording sites, 50-μm spacing, 1.6-mm deep). A silver wire served as ground and reference in the craniotomy between skull and brain tissue. Extracellular signals were band-pass filtered (0.1 to 8,000 Hz) and digitized (32 kHz) with a multichannel extracellular amplifier (Digital Lynx SX; Neuralynx, Bozeman, Montana, USA). The same animals were recorded weekly under different anesthesia. After 15 minutes of non-anesthetized recording, mice received a subcutaneous injection of Keta/Xyl, MMF, or inhalation of Iso in a pseudo-randomized order. The following drug combinations were administered: 2.0% Iso in 100% O_2; 130 mg/kg ketamine, 10 mg/kg xylazine s.c.; 5.0 mg/kg midazolam, 0.2 mg/kg medetomidine and 0.05 mg/kg fentanyl s.c.; and for complete reversal of anesthesia, 0.5 mg/kg flumazenil, 2.5 mg/kg atipamezole, and 0.1 mg/kg buprenorphine s.c. Recordings were conducted for 1.5 hours. After recordings, the craniotomy was closed, and mice were returned to their home cage. Electrode position was confirmed in brain slices postmortem.

EMG recordings. EMG electrodes for sleep state classification were implanted during hippocampal recording window surgery. Two gold plates (approximately 3-mm diameter) soldered to epoxy lacquered wires and attached to a connector were inserted into the right and left nuchal muscles and fixed with dental cement (Super Bond C&B, Sun Medical). For EMG recordings, a cable was attached to the implanted connector and directly digitized (32 kHz) and band-pass filtered (8 to 8,000 Hz) through a customized break-out channel board with a multichannel amplifier (Digital Lynx SX; Neuralynx). EMG recordings were done at least for 1 hour and 45 minutes in non-anesthetized mice without disturbances. Mice were recorded 1 to 2 times.

Virus injection and hippocampal window surgery for in vivo calcium imaging. C57BL/6J wild-type mice were anesthetized via intraperitoneal injection of MMF and placed on a

heating blanket to maintain the body temperature. Eyes were covered with eye ointment (Vidisic, Bausch + Lomb) to prevent drying. Prior to surgery, the depth of anesthesia and analgesia was evaluated with a toe pinch to test the paw withdrawal reflex. Subsequently, mice were fixed in a stereotactic frame, the fur was removed with a fine trimmer, and the skin of the head was disinfected with Betaisodona. The skin was removed by a midline scalp incision (1 to 3 cm), the skull was cleaned using a bone scraper (Fine Science Tools, Heidelberg, Germany), and a small hole was drilled with a dental drill (Foredom, Bethel, Connecticut, USA) above the injection site. AAV2/7-syn-GCaMP6f was targeted unilaterally to the dorsal CA1 area (−2.0 mm AP, ±1.3 mm ML, −1.5 mm DV relative to Bregma). Moreover, 0.6 μl of virus suspension was injected. All injections were done at 100 $nl^{*}min^{-1}$ using a glass micropipette. After the injection, the pipette stayed in place for at least 5 minutes before it was withdrawn, and the scalp was closed with sutures. For complete reversal of anesthesia, mice received a subcutaneous dose of FAB. During the 2 days following surgery, animals were provided with Meloxicam mixed into soft food. Two weeks after virus injection, mice were anesthetized as described above to implant the hippocampal window. After fur removal, skin above the frontal and parietal bones of the skull was removed by 1 horizontal cut along basis of skull and 2 rostral cuts. The skull was cleaned after removal of the periosteum, roughened with a bone scraper, and covered with a thin layer of cyanoacrylate glue (Pattex, Düsseldorf, Germany). After polymerization a 3-mm circle was marked on the right parietal bone (anteroposterior, −2.2 mm; mediolateral, +1.8 mm relative to bregma) with a biopsy punch, and the bone was removed with a dental drill (Foredom). The dura and somatosensory cortex above the hippocampus were carefully aspirated until the white matter tracts of the corpus callosum became visible. The craniotomy was washed with sterile PBS, and a custom-built imaging window was inserted over the dCA1. The window consisted of a hollow glass cylinder (diameter: 3 mm, wall thickness: 0.1 mm, and height: 1.8 mm) glued to a No. 1 coverslip (diameter: 3 mm and thickness: 0.17 mm) on the bottom and to a stainless-steel rim on the top with UV-curable glass glue (Norland NOA61, Cranbury, New Jersey, USA). The steel rim and a head holder plate (Luigs & Neumann, Ratingen, Germany) were fixed to the skull with cyanoacrylate gel (Pattex). After polymerization, cranial window and head holder plate were covered with dental cement (Super Bond C&B, Sun Medical) to provide strong bonding to the skull bone. Following the surgery, animals were provided with Meloxicam mixed into soft food for 3 days. The position of the hippocampal window was confirmed in brain slices postmortem.

Two-photon calcium imaging in anesthetized and awake mice. The same animals were sequentially imaged under Keta/Xyl, MMF, or Iso in a pseudo-randomized order during the dark phase of the dark/light cycle (for details, see above). After losing the righting reflex, generally 5 to 10 minutes after application of the anesthetics, the animals were positioned on a heating pad to maintain body temperature at approximately 37˚C during anesthesia. The intensity of anesthesia and evaluation of the different stages of anesthesia were assessed by recording the presence or absence of distinct reflex responses: righting reflex, palpebral reflex, and toe pinch reflex. Between each imaging session, mice were allowed to recover for 1 week.

Anesthetized mice were head-fixed under the microscope on a heated blanket to maintain body temperature. Eyes were covered with eye ointment (Vidisic, Bausch + Lomb) to prevent drying. The window was centered under the 2-photon microscope (MOM scope, Sutter Instrument, Novato, California, USA modified by Rapp Optoelectronics, Wedel, Germany), and GCaMP6f expression was verified in the hippocampus using epi fluorescence. Images were acquired with a 16× water immersion objective (Nikon CFI75 LWD 16X W, 0.80 NA, 3.0 mm WD, Nikon, Amsterdam, the Netherlands). For awake imaging, we used a linear treadmill, which allowed imaging during quiet and running states. Moreover, 5-minute time-lapse images were acquired every 10 minutes for a period of 50 minutes. Only quiet periods were

considered for analysis in this study. Image acquisition was carried out with a Ti:Sa laser (Chameleon Vision-S, Coherent, Dieburg, Germany) tuned to 980 nm to excite GCaMP6f. Single planes (512 × 512 pixels) were acquired at 30 Hz with a resonant galvanometric scanner at 29 to 60 mW (980 nm) using ScanImage 2017b (Vidrio Technologies, Leesburg, Virginia, USA). Emitted photons were detected by a pair of photomultiplier tubes (H7422P-40, Hamamatsu, Herrsching am Ammersee, Germany). A 560 DXCR dichroic mirror and a 525/50 emission filter (Chroma Technology, Bellows Falls, Vermont, USA) was used to detect green fluorescence. Excitation light was blocked by short-pass filters (ET700SP-2P, Chroma Technology). For the repetitive imaging, the position of the FOV was registered in the first imaging session with the help of vascular landmarks and cell bodies of CA1 pyramidal neurons. This allowed for subsequent retrieval of the FOV for each mouse.

Calcium imaging experiments to measure recovery from anesthesia were done in 5 additional animals. They were trained to maintain immobile on the treadmill for extended periods. We ensured to measure the same FOV and to maintain overall stability of fluorescence intensity for every recording in each imaging session for a given animal. The time-lapse recordings were extended to up to a maximum of 10 minutes per time point to have a higher probability of capturing motionless periods continuously, in awake and recovery states. Iso was applied for 60 minutes. FAB was injected 60 minutes after the application of MMF. Keta/Xyl was not antagonized. Imaging of calcium activity was performed before, 0.5, 1.5, 2, 3, 4, 5, and 6 hours after induction of anesthesia. For Iso and MMF, the 1.5-hour time point represented the first imaging session after reversal. Untreated control animals were imaged every hour for the same amount of time.

To habituate mice to sleep under head fixation, we used a linear treadmill, which allowed the mice to move at will. Through the first 4 sessions, mice were kept head-fixed for 15 to 30 minutes. In 10 following sessions, the fixation period was extended up to 4 hours with increasing intervals of 30 minutes. The state of the mouse was continuously monitored with a USB camera, and the running speed was recorded with custom-written scripts in the MATLAB. After habituation to 4-hour head fixation, sleep imaging sessions were recorded, which were synchronized with recordings of the pupil and running speed. Sleep imaging was performed during the light phase of the dark/light cycle.

Two-photon spine imaging in anesthetized and awake mice. Three to 4 weeks after window implantation, chronic spine imaging started in Tg(Thy1-EGFP)MJrs/J mice with the first of a total of 4 imaging series (see S10A Fig). Each imaging series was done under one of the 3 anesthetic conditions (Iso, Keta/Xyl, and MMF; see above for details) or during wakefulness. Within 1 series, mice were imaged 5 times every 4 days. Afterwards, mice were allowed to recover for 3 to 4 weeks until the next imaging series under a different anesthetic condition was started. Thus, each experiment lasted approximately 5 months. To avoid time-dependent effects, anesthetic conditions were pseudo-randomized (see S10A Fig). For imaging sessions under anesthesia, mice were head-fixed under the microscope on a heated blanket to maintain body temperature. Eyes were covered with eye ointment (Vidisic, Bausch + Lomb) to prevent drying. The window was centered under the 2-photon microscope (MOM scope, Sutter Instrument, modified by Rapp Optoelectronics), and GFP expression was verified in the hippocampus using epi-fluorescence. Image acquisition was carried out with a Ti:Sa laser (Chameleon Vision-S, Coherent) tuned to 980 nm to excite GFP. Images were acquired with a 40× water immersion objective (Nikon CFI APO NIR 40X W, 0.80 NA, 3.5 mm WD). Single planes (512 × 512 pixels) were acquired at 30 Hz with a resonant scanner at 10 to 60 mW (980 nm) using ScanImage 2017b. Before the first imaging session, we registered the FOVs with the help of vascular landmarks and cell bodies of CA1 pyramidal neurons and selected several regions for longitudinal monitoring across the duration of the time-lapse experiment. Each of these

regions contained between 1 and 2 dendritic segments visibly expressing GFP. The imaging sessions lasted for max 60 minutes, and mice were placed back to their home cages where they woke up.

Morris water maze. We designed a protocol for reversal learning in the spatial version of the water maze to assess the possible effects of the different anesthetics on episodic-like memory in mice [100,101]. The water maze consisted of a circular tank (145 cm in diameter) circled by dark curtains and walls. The water was made opaque by the addition of nontoxic white paint such that the white platform (14-cm diameter, 9-cm high, and 1 cm below the water surface) was not visible. Four landmarks (35 × 35 cm) differing in shape and gray gradient were positioned on the wall of the maze. Four white spotlights on the floor around the swimming pool provided homogeneous indirect illumination of 60 lux on the water surface. Mice were first familiarized for 1 day to swim and climb onto a platform (diameter of 10 cm) placed in a small rectangular maze (42.5 × 26.5 cm and 15.5-cm high). During familiarization, the position of the platform was unpredictable since its location was randomized, and training was performed in darkness. After familiarization, mice underwent 3 learning days, during which they had to learn the location of a hidden platform. The starting position and the side of the maze from which mice were taken out of the maze were randomized. On day 1, mice underwent 4 learning trials (maximum duration of 90 seconds, intertrial interval of 10 minutes). After staying on the platform for 15 seconds, mice were returned to their home cage and warmed up under red light. On day 2, mice underwent 2 training trials before they performed a 60-second long probe trial to assess their searching strategy. Afterwards, 1 additional training trial was used to reconsolidate the memory of the platform position, and mice were distributed into 4 groups with a similar distribution of performance. On day 3, the long-term memory of the platform position was tested with a 45-second long probe trial, followed by another training trial with the platform in place to avoid extinction. Then mice underwent 4 reversal learning trials with the platform located in the quadrant opposite the one in which the platform was during the previous training trials. To assess whether the mice learned the new platform position, mice underwent a 60-second long probe trial followed by 1 more training trial to consolidate the memory of the new location. One hour after the last reversal learning trial, mice were anesthetized to analyze the effects of the anesthesia on the consolidation of the memory of the new platform position. Mice were assigned to 4 groups with an equal average performance during the probe trial on day 2. Each group was subjected to different conditions: 1-hour Iso anesthesia, 1-hour MMF anesthesia and Keta/Xyl anesthesia (which was not antagonized), and 1 group was left untreated. On day 4, mice underwent a 60-second long probe trial to evaluate their searching strategies, namely the "episodic-like memory" of the reversal learning trials performed 1 hour before having been anesthetized on day 3 (see Fig 9A).

Quantification and statistical analysis

Electrophysiology. In vivo electrophysiology data were analyzed with custom-written scripts in the MATLAB environment available at https://github.com/mchini/HanganuOpatzToolbox. We selected the recording site in the pyramidal layer of CA1. Data were band-pass filtered (1 to 100 Hz or 0.1 to 100 Hz for low-frequency LFP analysis) using a third-order Butterworth forward and backward filter to preserve phase information before down-sampling to analyze LFP.

Detection of active periods. Active periods were detected with an adapted version of an algorithm for ripple detection (https://github.com/buzsakilab/buzcode/blob/master/detectors/detectEvents/bz_FindRipples.m). Briefly, active periods were detected on the band-pass filtered (4 to 20 Hz) normalized squared signal using both absolute and relative thresholds. We

first passed the signal through a boxcar filter and then performed hysteresis thresholding: We first detected events whose absolute or relative power exceeded the higher threshold and considered as belonging to the same event all data points that were below the lower (absolute or relative) threshold. Absolute thresholds were set to 7 and 15 μV, relative thresholds to 1 and 2. Periods were merged if having an inter-period interval shorter than 900 ms and discarded if lasted less than 500 ms. Percentage of active periods was calculated for 15-minute bins. Time stamps were preserved for further analysis.

Power spectral density. Power spectral density was calculated on 30-second long windows of 0.1 to 100 Hz filtered signal using Welch's method with a signal overlap of 15 seconds.

Relative change. Relative change was calculated as (value anesthesia − value pre-anesthetized) / (value anesthesia + value pre-anesthetized).

Power-law decay exponent of the LFP power spectrum. The 1/f slope was computed as in [36]. We used robust linear regression (MATLAB function *robustfit.m*) on the log10 of the LFP power spectrum in the 30 to 50 Hz frequency range.

Phase-amplitude coupling (PAC). PAC was calculated on 0.1 to 100 Hz filtered full signal using the PAC toolbox based on relative change measure [102]. Range of phase vector was set to 0.1 to 8 Hz, and range of amplitude vector was set to 20 to 100 Hz. Significant coupling was calculated in comparison to a shuffled dataset. Nonsignificant values were rejected.

Single unit analysis. SUA was detected and clustered using klusta [103] and manually curated using phy (https://github.com/cortex-lab).

Active units. The recording was divided into 15-minute bins. Single units were considered to be active in the time interval if they fired at least 5 times.

Pairwise phase consistency. PPC was computed as previously described [104]. Briefly, the phase in the band of interest was extracted as mentioned above, and the mean of the cosine of the absolute angular distance (dot product) among all single unit pairs of phases was calculated.

Unit power. SUA spike trains of each recording were summed in a population vector, and power spectral density was calculated on 30-second long windows using Welch's method with a signal overlap of 15 seconds. The resulting power spectra were normalized by the firing rate in that window.

STTC was computed as previously described [52]. Briefly, we quantified the proportion (P_A) of spikes of spike train A that fall within ±Δt of a spike from spike train B. To this value, we subtract the proportion of time that occurs within ±Δt of spikes from spike train B (T_B). This is then divided by 1 minus the product of these 2 values. The same is then applied after inverting spike train A and B, and the mean between the 2 values is kept.

$$STTC = \frac{1}{2}\left(\frac{P_A - T_B}{1 - P_A T_B} + \frac{P_B - T_A}{1 - P_B T_A}\right)$$

Importantly, this coefficient has several desirable properties. It is bounded between −1 and 1. It is symmetric with respect to the 2 spike trains. Computing it over different timescales is readily done by controlling the value of the parameter "Δt." Lastly, and most importantly, traditionally used methods of assessing correlations between pairs of spike trains show an inverse correlation between their value and firing rate, due to the fact that spiking is sparse with respect to the sampling frequency, and therefore quiescent period in both spike trains artificially increase the correlation. This is not the case for the STTC [52]. Given that there are large differences in the average firing rate of our conditions, we chose STTC analysis over pure correlation analysis to circumvent this major bias. On the flipside, STTC cannot be straightforwardly applied to negative correlations, which were therefore not investigated in SUA data.

Calcium imaging data. In vivo calcium imaging data were analyzed with custom-written scripts in the Python and MATLAB environment available at https://github.com/mchini/Yang_Chini_et_al.

Alignment of multiple recordings. To track the activity of the same set of neurons in different anesthetic conditions and during wakefulness, we acquired 2-photon time series of a defined FOV for each animal and each condition across multiple weeks. Over such long time periods, the FOV was susceptible to geometrical transformations from 1 recording to another and thus, any 2 time series were never perfectly aligned. This problem scaled with time that passed between recordings. However, optimal image alignment is critical for the successful identification and calcium analysis of the same neurons across time [105,106].

To address this problem, we developed an approach based on the pystackreg package, a Python implementation of the ImageJ extension TurboReg/StackReg [107]. The source code that reproduces the procedure described in this section is available on github (https://pypi.org/project/pystackreg/). The *pystackreg* package is capable of using different combinations of geometrical transformations for the alignment. We considered rigid body (translation + rotation + scaling) and affine (translation + rotation + scaling + shearing) transformation methods, which we applied to mean and enhanced mean intensity images generated by Suite2p during the registration of each single recording. We performed the alignment using all 4 combinations (2 transformations × 2 types of images) choosing the one with the best performance according to the following procedure. Squared difference between the central part of a reference and aligned image served as a distance function *d* to quantify the alignment (since the signal is not always present on the borders of the image, they were truncated):

$$d = \sum_{i,j}^{\substack{Trunc.\\ images}} (x_{i,j}^{ref} - x_{i,j}^{aligned})^2,$$

where $x_{i,j}^{ref}$ and $x_{i,j}^{aligned}$ are intensities of the pixel with coordinates *i,j* of the reference and aligned images. The combination with the smallest score was chosen for the final transformation. In some rare cases, the algorithm of the alignment did not converge for a given transformation method and image type (mean or enhanced mean), crumbling the aligned image in a way that most of the FOV remained empty. This combination may have the smallest distance function *d* and may be falsely identified as the best one. To overcome this issue, an additional criterion was applied, which requires the central part of the aligned picture to contain more than 90% of the non-empty pixels. The overall performance of the algorithm was verified by visual inspection. An example of the alignment of 2 recordings is shown in S5 Fig.

In case of relatively small distortions across recordings, for example, when consecutive acquisitions were done within 1 imaging session, registration can alternatively be performed simultaneously with ROI detection in Suite2p by concatenating those TIFF stacks. In this approach, every ROI is automatically labeled with the same identity (ID) number across all recordings.

Identification of the same neurons across different recordings and unique neuron ID assignment. After the alignment procedure, we set out to identify neurons which were active across multiple recordings (and thus, multiple conditions). To achieve this, we developed an algorithm similar to the one described in Sheintuch and colleagues [106].

The algorithm processes in series all recordings for a given animal and assigns unique ID numbers to each ROIs of every recording. Since the recordings under Iso anesthesia had the largest number of active neurons, we chose the first recording of this condition as reference.

We assigned IDs that ranged from 1 to the total amount of neurons to all the ROIs of this recording. For every other recording of each mouse, neuron ID assignment consisted of (1) comparison of the properties (details below) of each ROI with each ROI that had already been processed; (2a) if the properties of the ROI matched the properties of an ROI from a previously analyzed recording, the ROI received the same neuron ID; and (2b) if no match was found, a new (in sequential order) neuron ID was assigned to the ROI. In order to be identified as representing the same neuron in 2 different recordings, 2 ROIs had to respect the following criteria: The distance between their centroids had to be below 3 μm, and the overlap between their pixels had to be above 70%. An example of the identification of unique neuron pairs in 2 recordings is presented in S6A Fig. The thresholds were chosen based on the distribution of the distances between centroids and percentage of the overlaps. An example for a single mouse is graphically illustrated in S6B Fig. Both properties have a clearly bimodal distribution (similar to [106]) with cutoffs close to the chosen thresholds.

Signal extraction and analysis. Signal extraction, correlation, and spectral analysis for calcium signal was performed using Python (Python Software Foundation, New Hampshire, USA) in the Spyder (Pierre Raybaut, The Spyder Development Team) development environment. Calcium imaging data were analyzed with the Suite2p toolbox [108] using the parameters given in Table 1.

The same analytical pipeline was applied to both the raw fluorescence traces as well as the deconvolved ("spikes") signal, as extracted by the Suite2p toolbox. Generally, the raw fluorescence signal was preferred over the deconvolved one given that its extraction is more straightforward and relies on less assumptions. However, while the reported effects varied in magnitude depending on which of the 2 signals was considered, the same results were obtained on both datasets. The effects were entirely consistent. For raw signal analysis of each neuron, previous to any further step, we subtracted 0.7 of the corresponding neuropil fluorescence trace.

The number and height of calcium transients properties were calculated with the scipy function *find_peaks* on the raw calcium traces with the following parameters: height = 200, distance = 10, and prominence = 200. The decay was computed on the 10 best isolated transients of each neuron, using the *OASIS* toolbox (https://github.com/j-friedrich/OASIS). We used the *deconvolve* function with the following parameters: penalty = 0 and optimize_g = 10. Traces with an estimated decay over 2 seconds were considered cases of failed extraction and removed from further analysis.

The choice of the parameter values for transient detection is somewhat arbitrary. Similarly, it is debatable whether and how the calcium traces should best be normalized. Therefore, we tested the robustness of our findings by systematically varying signal extraction choices. We first varied the height and prominence threshold across a wide range of values (50 to 700 arbitrary units). We further computed transients features on normalized ΔF/F calcium traces. To normalize calcium signals, we used the baseline value as extracted by the *deconvolve* function. Also, in this case, we varied the height and prominence threshold across a wide range of values (0.5 to 3 arbitrary units). Finally, we computed 2 measures of neuronal activity that are independent of calcium transients detection: the average of the trace integral and its standard deviation, with and without normalization. Across all of these scenarios, the reported effects were robustly consistent.

Correlations were computed both as Pearson (numpy function *corrcoeff*) and Spearman (custom-written function) coefficient on the z-scored signal. To both sets of coefficients, the Fisher correction (the inverse of the hyperbolic tangent function, numpy function *arctanh*) was applied. For power analysis, we first created a population activity vector by summing all the single neuron z-scored signals and then estimated the power spectral density by applying

Table 1. Parameters used in Suite2p for calcium imaging data analysis.

Parameter	Variable	Value
Sampling rate, frames per second	fs	30
Registration		
Subsampled frames for finding reference image	nimg_init	2,000
Number of frames per batch	batch_size	200
Maximum allowed registration shift, as a fraction of frame max (width and height)	maxregshift	0.1
Precision of subpixel registration (1/subpixel steps)	subpixel	10
Smoothing	smooth_sigma	1.15
Bad frames to be excluded	th_badframes	100.0
Nonrigid registration		
Use nonrigid registration	nonrigid	True
Block size to register (** keep this a multiple of 2 **)	block_size	[128,128]
If any nonrigid block is below this threshold, it gets smoothed until above this threshold. 1.0 results in no smoothing	snr_thresh	2.0
Maximum pixel shift allowed for nonrigid, relative to rigid	maxregshiftNR	10
Cell detection		
Run ROI extraction	roidetect	True
Run sparse_mode	sparse_mode	False
Diameter for filtering and extracting	diameter	12.0
Keep ROIs fully connected (set to 0 for dendrites)	connected	True
Maximum number of binned frames for cell detection	nbinned	5,000
Maximum number of iterations to do cell detection	max_iterations	20
Adjust the automatically determined threshold by this scalar multiplier	threshold_scaling	1.0 or 0.1
Cells with more overlap than this get removed during triage, before refinement	max_overlap	0.75
Running mean subtraction with window of size "high_pass"	high_pass	100
ROI extraction		
Number of pixels to keep between ROI and neuropil donut	inner_neuropil_radius	2
Minimum number of pixels in the neuropil	min_neuropil_pixels	100
Pixels that are overlapping are thrown out (False) or added to both ROIs (True)	allow_overlap	True
Deconvolution		
Deconvolution time constant, seconds	tau	0.7

ROI, region of interest.

https://doi.org/10.1371/journal.pbio.3001146.t001

the Welch method (sampling frequency = 30 Hz, number of points for fast Fourier transformation = 1,024, and no overlap, window length = 1 second).

For analysis of recovery from anesthesia, all recordings of the imaging session for a given animal were concatenated in Suite2p. As a consequence, each recording in the imaging session has the same set of reconstructed neurons. A time window of 5,000 frames was used for the analysis to ensure continuous motionless periods. To track the neuronal activity changes, the number of fluorescence peaks, their amplitude, and the characteristic decay constant of the transients were considered. Each imaging session's threshold was chosen to match the median activity in the pre-anesthesia (awake) state across all animals. To assess the relative changes of these parameters induced by anesthesia and their subsequent recovery over time, the parameters were normalized to their median value at the pre-anesthesia (awake) state. Notably, we focused our analysis on neurons that maintained some detectable activity during anesthesia, and neurons with no detected peaks were excluded from the distributions. Additionally, we applied the cut $decay\ constant > 1/30$ [s] (where 30 frames per second is an acquisition rate) to remove the traces where the OASIS algorithm considered a single noise peak to be a calcium transient.

Complexity analysis was performed in the MATLAB (MathWorks) environment. For complexity analysis, we limited the number of neurons to the minimum (N_{min}) present in any recording of any condition for each single mouse (median = 265, min = 156, and max = 1068). The resulting matrix therefore had the $T_{rec}xN_{min}$ dimensions, where T_{rec} represents the time vector for the recording, with a length of 5 minutes and a sampling rate of 30 Hz. For recordings that had a number of neurons larger than N_{min} for that mouse, we randomly sampled $n = N_{min}$ neurons and repeated the analysis 5 times. For every extracted parameter, we then considered the median value over the 5 repetitions. For further analysis, the signal was down-sampled from the original sampling frequency of 30 Hz to 10 Hz (100-ms bins). The same analytical pipeline was then applied to both the raw fluorescence traces, as well as the deconvolved signal.

tSNE clustering. tSNE clustering was performed similar to [26]. Briefly, in a range between 5 and 45, the perplexity value that minimized the reconstruction error was selected. The number of PCA components used for this step was limited to 30. For the raw fluorescence signal, Euclidian distance was used, whereas for the deconvolved signal, we opted for cosine distance, as it is better suited to a sparse signal. We computed the probability distribution of the resulting embedded matrix ($2xT_{rec}$), that was then convolved with a 2D Gaussian window (standard deviation was set to be equal to 1/40 of the total maximum value). To evaluate the number of clusters in the distribution, we then applied a series of standard steps in image analysis: background subtraction with the rolling ball method, smoothing with a median filter, thresholding, watershedding to avoid undersegmentation, and extended minima transformation. Finally, the exterior boundaries of the objects were automatically traced and counted. This gave the number of clusters.

Affinity propagation clustering (APC). APC was performed using a MATLAB toolbox [https://www.psi.toronto.edu/index.php?q=affinity%20propagation] and similarly to [26]. We first obtained a distance map, which was computed as 1 minus the pairwise cosine distance between observations of the $T_{rec}xN_{min}$ matrix. This distance matrix was then fed to the AP algorithm with the input preference set equal to the median of the distance matrix.

Principal component analysis (PCA) clustering and variance explained. Standard PCA was applied to the $T_{rec}xN_{min}$ matrix. The number of clusters was computed as the number of components that was needed to cumulatively explain 90% of the variance of the input matrix. Further, we computed the loglog decay coefficient of number of components versus variance explained.

Community detection. To detect communities, we used the Louvain algorithm from the Brain Connectivity Toolbox (https://sites.google.com/site/bctnet/), a modularity maximization procedure widely used in studies examining brain networks [109]. This approach aims at subdividing the network into partitions that are more internally dense than would be expected by chance [53]. As input to the algorithm, we used Fisher-transformed correlation matrices obtained from calcium imaging time series. Matrices were not thresholded, and both positive and negative correlations were taken into account to determine optimal modular partitions. The algorithm was evaluated while varying the resolution parameter gamma between 0 and 3, in steps of 0.1. For the multiresolution approach and hierarchical consensus clustering, data were analyzed using code available at https://github.com/LJeub/HierarchicalConsensus and according to the procedure described in [55]. The number of communities detected by the finest level partition of the consensus hierarchy was used for further analysis. While neurons in the awake condition tended to be spatially closer to each other than for the other conditions (S8E Fig), this is unlikely to have influenced the results of the analysis, as the difference was minimal, and there was no correlation between median distance in a recording and the number of detected communities (S8F Fig).

Sleep scoring. Sleep scoring was carried out in 2 steps. We first used electrophysiological features (see below) to classify the behavioral state of the electrophysiological recordings. Then, using this dataset as ground truth, we extracted pupil/eyelid features that we used to extend our classification to the calcium imaging recordings.

Electrophysiological recordings. We divided the signal in 30-s epochs with a 50% overlap and used a rule-based approach similar to that applied in [57,110]. NREM sleep epochs were defined as epochs having LFP power in the delta band (1 to 4 Hz) higher than the 70th percentile, EMG broadband (30 to 300 Hz) power lower than the median, and no movement. REM sleep epochs were defined as epochs having a ratio between theta (6 to 12 Hz) and delta LFP power higher than the 70th percentile, EMG broadband power lower than the 25th percentile, and no movement. Finally, wakefulness epochs were defined as epochs having EMG broadband power that exceeded the 80th percentile or with mouse movement. Given that this rule-based approach left approximately 49% of the epochs as unclassified, we extended this classification with a machine learning approach using the scikit-learn toolbox [111]. Using the classified epochs as the labeled dataset, we trained a K-nearest neighbors classifier (number of neighbors = 20, weights = distance, algorithm = auto, leaf size = 5, p = 2, and scoring = f1 macro) to which we fed the following quantile-transformed (quantiles = 20) features: LFP power in the delta and theta band, ratio between LFP delta and theta power, and EMG broadband power and average movement. After training, the algorithm was asked to predict the unclassified epochs. Predictions that were done with a probability estimate above 99% were kept, and the others were left as unclassified. This adjunction to the rule-based approach allowed us to lower the percentage of unclassified (uncertain) epochs to approximately 28%.

Pupil and eyelid analysis. During electrophysiological recordings, the eye of the mouse was recorded with a monochrome, infrared sensitive camera (UI-3360CP-NIR-GL Rev. 2, iDS imaging, Germany, objective: LMZ45T3 2/3" 18 to 108 mm/F2.5 manual macro zoom lens, Kowa, Germany) under red light. Videos were captured with the uEye Cockpit software (iDS imaging) with a framerate of 30 Hz. Pupil, EMG, and electrophysiological recordings were synchronized with a customized light/digital pulse shutter. During calcium imaging, eye recordings were done with an infrared sensitive camera (DMK 33UX249; The Imaging Source, Germany) equipped with a macro objective (TMN 1.0/50; The Imaging Source) at a frame rate of 10 Hz. Contours of the mouse eye were tracked using the deep neural network-based software module DeepLabCut [112] and subsequently processed in MATLAB. We trained a neural network (residual neural network, 152 layers, and 200,000 iterations) to detect the upper, lower, left, and right edges of the pupil and eyelid, respectively, in images down-sampled to 256 pixels on the shorter edge (n = 1,038 frames for videos from electrophysiology and n = 2,255 frames for videos from calcium imaging). Besides the position of each tracked point, DeepLabCut provides a value quantifying the certainty about the determined position (which is low in the case of occluded objects, e.g., the pupil during an eyeblink). Samples with a certainty <0.5 were linearly interpolated from the last point before to the first point after the respective samples which had a certainty of >0.5 (0.24/0.56% of total pupil samples and 0.11/0.12% of total eyelid samples acquired during electrophysiology and calcium imaging experiments, respectively). We then calculated the pupil diameter (as the maximum distance between 2 opposing points of the pupil), as well as its center of mass, and the opening of the eye (as the distance between the top and the bottom eyelid). Finally, blinks were removed from the eye-opening data by linearly interpolating regions which exceed the moving median minus 3 times moving median absolute deviation (sliding window = 30 seconds).

Calcium imaging recordings. Using the expanded classification of the electrophysiology dataset, we extracted the following pupil/eyelid features: maximum and minimum pupil diameter, standard deviation of the pupil diameter, pupil area, pupil motion, and eyelid distance.

We then tested the extent to which it was possible to correctly predict the behavioral state on these features alone, similarly to Yüzgec and colleagues. To this aim, we quantile-transformed these features (quantiles = [50, 100, 500]), and passed them to a K-nearest neighbors classifier with similar hyper-parameters as the previous one (number of neighbors = [5, 10], weights = uniform, algorithm = auto, leaf size = 1, p = 2, scoring = f1 macro). Hyper-parameter tuning was done using GridSearchCV. We then iteratively (n = 100) tested the prediction accuracy on 25% of the dataset, yielding good average accuracy for wakefulness (approximately 86%) and NREM sleep (approximately 90%). On the contrary, most REM sleep was mostly classified as NREM (approximately 62%), and the accuracy for this category was significantly lower (approximately 27%). Finally, we retrained the classifier on the entire dataset of pupil/eyelid electrophysiological features and used it to predict the behavioral state of the calcium imaging dataset.

Two-photon spine image processing. In each animal, at least 1 GFP-expressing CA1 pyramidal neuron was selected, and 1 to 3 dendrites of 20- to 50-μm length of each of the following types were analyzed: basal dendrites, oblique dendrites emerging from the apical trunk, and tuft dendrites. Motion artifacts were corrected with a custom-modified Lucas–Kanade-based alignment algorithm written in MATLAB. Spines that laterally emanated from the dendrite were counted by manually scrolling through the z-stacks of subsequent imaging time points of the same dendritic element, by an expert examiner blinded to the experimental condition. Protrusions from the dendrite that reached a threshold of 0.2 μm were scored as dendritic spines regardless of shape. If spine neck positions differed 0.5 μm on the subsequent images, the spine was scored as a new spine. Spines were scored as lost if they fell below the threshold of 0.2 μm. Spine density was calculated as the number of spines per μm. The turnover ratio was calculated for every time point by dividing the sum of gained and lost spines by the number of present spines. The survival fraction of spines was calculated as the percentage of remaining spines compared with the first imaging time point.

Statistical analysis. Statistical analyses were performed using R Statistical Software (Foundation for Statistical Computing, Vienna, Austria) or GraphPad Prism 9.0 (graphpad.com). All R scripts and datasets are available on GitHub https://github.com/mchini/Yang_Chini_et_al/tree/master/Stats_Dataset_(R)). Nested data were analyzed with linear mixed-effect models to account for the commonly ignored increased false positive rate inherent in nested design [113]. We used "mouse," "recording," "neuron" (calcium imaging), and "single unit" (electrophysiology) as random effects, according to the specific experimental design. Parameter estimation was done using the lmer function implemented in the *lme4* R package [114]. Model selection was performed according to experimental design. Significance and summary tables for lmer model fits were evaluated with the *lmerTest* R package [115], using the Satterthwaite's degrees of freedom method. Post hoc analysis with Tukey multiple comparison correction was carried out using the *emmeans* R package. All statistical analyses can be found at https://github.com/mchini/Yang_Chini_et_al/tree/master/Stats_Dataset_(R)/stats summary.xlsx.

Supporting information

S1 Fig. LFP recordings in dorsal CA1 during wakefulness and anesthesia. (A) Histology images showing the position of the recording electrode in the dorsal hippocampus. Left: Bright-field image merged with fluorescence image of DiI staining. The position of the electrode is indicated by white line drawing. Right: Close-up of dorsal hippocampus showing nuclear DAPI-staining in blue and DiI label from recording electrode position in magenta. **(B)** Heat map displaying raw LFP power in the 0–100 Hz frequency band for the 3 different

anesthetic strategies. **(C)** Average LFP power over time in different frequency bands. Vertical dashed lines in all panels indicate time points of anesthesia induction (Iso, MMF, and Keta/Xyl) and reversal (Iso and MMF only). Lines display mean ± SEM. Asterisks indicate significance of time periods indicated by black horizontal line compared to 15-minute period before anesthesia. Anesthetic conditions are color coded. * $p < 0.05$, ** $p < 0.01$, *** $p < 0.001$. For full report of statistics, see S1 Table. All datasets of this figure can be found under https://github.com/mchini/Yang_Chini_et_al/tree/master/Stats_Dataset_(R)/datasets/Figure1_S1. Iso, isoflurane; Keta/Xyl, ketamine/xylazine; LFP, local field potential; MMF, medetomidine/midazolam/fentanyl.
(TIF)

S2 Fig. SUA in dorsal CA1 during wakefulness and anesthesia. (A) Raster plots of z-scored SUA during indicated time periods (black horizontal bars) for the 3 different anesthetic strategies. Units are sorted according to initial activity during wakefulness. Same data as in Fig 2A. **(B)** Scatter plot showing modulation of unit activity during anesthesia with respect to firing rate during wakefulness. *** $p < 0.001$. **(C)** Violin plot showing modulation of unit activity during anesthesia with respect to CA1 anatomical layers. For full report of statistics, see S1 Table. All datasets of this figure can be found under https://github.com/mchini/Yang_Chini_et_al/tree/master/Stats_Dataset_(R)/datasets/Figure2_S2. SUA, single-unit activity.
(TIF)

S3 Fig. Anesthesia-induced changes in calcium activity profiles are insensitive to the choice of signal extraction parameters. (A) Histology images showing the position of the imaging window above the dorsal hippocampus. Left: Bright-field image merged with fluorescence. GCaMP6f expression is shown in green. Right: magnified view of the hippocampus. **(B)** Line plot of the number (left) and amplitude (right) of detected calcium transients across varying threshold values used for transient detection. **(C)** Violin plots quantifying the integral (left) and standard deviation (right) of calcium traces. White dots indicate median, and vertical thick and thin lines indicate first to third quartile and interquartile range, respectively. **(D)** and **(E)** As (B, C), for dF/F calcium transients and traces. **(F)** Violin plots quantifying the number (left), amplitude (middle), and decay (right) of calcium transients extracted with the *threshold_scaling* variable set to 0.1 instead of 1. **(G)** tSNE plot summarizing the average calcium transients properties. Each data point represents 1 recording session. Asterisks in (C, E, F) indicate significant differences to wakefulness. *** $p < 0.001$. Note, to facilitate readability, only differences to wakefulness are indicated. For full report of statistics, see S1 Table. All datasets of this figure can be found under https://github.com/mchini/Yang_Chini_et_al/tree/master/Stats_Dataset_(R)/datasets/Figure3_S3. tSNE, t-distributed stochastic neighbor embedding.
(TIF)

S4 Fig. Oscillations of calcium transients are distinctly altered by Iso, MMF, and Keta/Xyl. Line plot displaying the spectrograms for population activity power, for raw calcium transients (left) and deconvolved spikes (right) during wakefulness and 3 different anesthetic conditions. All datasets of this figure can be found under https://github.com/mchini/Yang_Chini_et_al/tree/master/Stats_Dataset_(R)/datasets/Figure3_S3. Iso, isoflurane; Keta/Xyl, ketamine/xylazine; MMF, medetomidine/midazolam/fentanyl.
(TIF)

S5 Fig. Alignment and ROI matching of imaging sessions. Enhanced mean intensity images are shown to demonstrate the alignment procedure between a recording in Iso **(A)** and one during wakefulness **(B)**. **(C)** Mean intensity image of the awake recording aligned to the

anesthesia condition. **(D)** Overlaid, enhanced mean intensity images before and after **(E)** the alignment algorithm was applied. **(F)** ROIs of active neurons during wakefulness (pink), Iso anesthesia (cyan), and their overlap (black). **(G–I)** Magnified views of a randomly selected sections from panels (D)–(F). Iso, isoflurane; ROI, region of interest.
(TIF)

S6 Fig. ID assignment and comparison of calcium transients in identified neurons between pairs of conditions. **(A)** Time-averaged 2-photon images of the same FOV in CA1 from an "awake" (top left) and an Iso (top right) imaging session aligned to the Iso condition (same images as in Figs 3 and 4). ROIs of active neurons were automatically extracted with a lower quality threshold, accepting more neurons per recording (see Methods). Lower left: geometrical overlay of the 2 images with overlapping ROIs. Lower right: ROIs of identified neurons active in both conditions. **(B)** Kernel density plot and probability density functions for distances between centroids and area overlap for pairs of closest ROIs from the 2 different recordings. A clear bimodal distribution in both parameters is appreciable. Values in the lower right corner indicate highly matched neurons that were considered active in both conditions. **(C)** Kernel density plot and probability density functions for the number (top row), amplitude (middle row), and decay (bottom row) of detected calcium transients for each pair of conditions. From left to right: Iso vs. awake, MMF vs. awake, Keta/Xyl vs. awake, Iso vs. MMF, Iso vs. Keta/Xyl, and MMF vs. Keta/Xyl. Asterisks indicate significant differences between pairs of conditions. Asterisks are always on the side of the unity line with higher values. *** $p < 0.001$. **(D)** Scatter plot showing modulation of calcium transients during anesthesia with respect to calcium activity during wakefulness. *** $p < 0.001$. **(E)** Recovery of CA1 pyramidal neurons from anesthesia. The dots at the beginning of each trajectory represent median values of 2 principal components (PC1 and PC2) calculated on the number, height, and decay of the calcium transients during anesthesia (see Fig 4E). The arrowheads represent the state 6 hours later. Blue dots correspond to awake states in the control group. Every trajectory connects anesthesia and postanesthesia (recovery) states during the following 6 hours for a given animal. The trajectories were obtained using third-degree B-splines. All datasets of this figure can be found under https://github.com/mchini/Yang_Chini_et_al/tree/master/Stats_Dataset_(R)/datasets/Figure4_S6. FOV, field of view; ID, identification; Iso, isoflurane; Keta/Xyl, ketamine/xylazine; MMF, medetomidine/midazolam/fentanyl; ROI, region of interest.
(TIF)

S7 Fig. Additional correlation analysis. **(A)** Violin plots quantifying absolute pairwise correlation of all neurons recorded during calcium imaging shown in Fig 5. **(B)** Decorrelation of calcium activity during anesthesia is sustained also in neurons active during all conditions. Left: Line plot displaying cumulative distribution of Fisher-corrected Pearson correlation coefficients between the same pairs of neurons, which were active in each condition. Right: Violin plots quantifying absolute pairwise correlation coefficients. In violin plots, white dots indicate median, and vertical thick and thin lines indicate first to third quartile and interquartile range, respectively. **(C)** Quantification of correlation between pairs of extracellularly recorded single units using the STTC with shorter integration window. Left: Schematic illustration the quantification of the STTC. Middle: cumulative distribution of the STTC with a 10-ms integration window. Right: violin plot quantifying the tiling coefficient. In all violin plots, white dots indicate median, and vertical thick and thin lines indicate first to third quartile and interquartile range, respectively. Asterisks indicate significant differences to wakefulness. * $p < 0.05$, *** $p < 0.001$. Note, only differences to wakefulness are indicated. For comparison between conditions, see S1 Table. All datasets of this figure can be found under https://github.com/mchini/Yang_Chini_et_al/tree/master/Stats_Dataset_(R)/datasets/Figure5_S7. STTC, spike time tiling

coefficient.
(TIF)

S8 Fig. Clustering analysis of deconvolved calcium imaging data. (A) Violin plot quantifying the number of tSNE clusters obtained from deconvolved calcium recordings (i.e., "spikes") during wakefulness, Iso, MMF, and Keta/Xyl anesthesia. **(B)** Violin plot quantifying the number of clusters obtained by AP from deconvolved calcium recordings (i.e., "spikes") during the 4 different conditions. **(C)** Violin plot quantifying the number of communities obtained by MRCC for the 4 different conditions. **(D)** Line plot quantifying maximum community cluster size normalized by the total number of neurons across the resolution parameter gamma ranging from 0 to 3. **(E)** Cumulative distribution of the distance between neurons randomly selected for the spatial cluster analysis showing no difference between conditions. **(F)** Scatter plot displaying absence of a relationship between the median distance of neurons and the number of detected communities. Horizontal lines in violin plots indicate median and first to third quartile. Asterisks in (A)–(C) indicate significant differences to wakefulness. * $p < 0.05$, ** $p < 0.01$, *** $p < 0.001$. Horizontal lines above plots in (D) and (E) indicate significant difference to wakefulness. Anesthetic conditions are color coded. Note, only differences to wakefulness are indicated. For comparison between conditions, see S1 Table. All datasets of this figure can be found under https://github.com/mchini/Yang_Chini_et_al/tree/master/Stats_Dataset_(R)/datasets/Figure6_S8. APC, affinity propagation clustering; Iso, isoflurane; Keta/Xyl, ketamine/xylazine; MMF, medetomidine/midazolam/fentanyl; MRCC, multiresolution consensus clustering; tSNE, t-distributed stochastic neighbor embedding.
(TIF)

S9 Fig. Sleep scoring. Sleep scoring was carried out in 2 steps. We first used electrophysiological features to classify the behavioral state of the electrophysiological recordings. Then, using this dataset as ground truth, we extracted pupil/eyelid features that we used to expand our classification to the calcium imaging recordings. **(A)** Wake, NREM and REM sleep epochs were classified based on animal motion, neck muscle EMG broad power, MUA, and several LFP features. **(B)** Using the electrophysiology-based classification, the following pupil/eyelid features were extracted to classify sleep: maximum and minimum pupil diameter, standard deviation of pupil diameter, pupil area, pupil motion, and eyelid distance. **(C)** Confusion matrix and prediction accuracy for the classification of sleep periods based on eye imaging alone. **(D)** Probability distribution of pupil diameter for predicted wake, NREM, and REM periods in the calcium imaging dataset. **(E)** Classification of activity states in individual mice during electrical recordings (left) and calcium imaging (right). Note that different animals were used for electrophysiology and calcium imaging. All datasets of this figure can be found under https://github.com/mchini/Yang_Chini_et_al/tree/master/Stats_Dataset_(R)/datasets/Figure7_S9. EMG, electromyography; LFP, local field potential; MUA, multi-unit activity; NREM, non-rapid eye movement; REM, rapid eye movement.
(TIF)

S10 Fig. Chronic spine imaging. (A) Experimental scheme for chronic spine turnover measurements. Spine imaging was performed in a pseudo-randomized order for the different anesthetics followed by imaging during wakefulness. Each colored box indicates 1 imaging session. For each condition, imaging was done 5 times every 4 days, followed by a 1-month break. To control for long-term effects of anesthesia and age on the awake condition, we performed imaging only during wakefulness in additional mice as indicated. **(B)** Dot plots showing quantification of overall gain and loss of spines during chronic imaging under the 4 different treatments. Dots indicate mean ± SEM. **(C)** Dot plots showing quantification of spine turnover

(left), spine survival (middle), and spine density (right) during wakefulness after anesthetic treatments (same data as "awake" in Fig 7B) and wakeful imaging in the 2 control groups ("awake early" and "awake late"). Dots indicate mean ± SEM. **(D)** Dot plots showing quantification of spine turnover (left column), spine survival (middle column), and spine density (right column) separately for basal (top row), oblique (middle row), and tuft dendrites (bottom row). Same data as in Fig 8B. Asterisks indicate significant differences to wakefulness. * $p < 0.05$, ** $p < 0.01$. For full report of statistics, see S1 Table. All datasets of this figure can be found under https://github.com/mchini/Yang_Chini_et_al/tree/master/Stats_Dataset_(R)/datasets/Figure8_S10.
(TIF)

S11 Fig. Comparison of the effect of Iso, MMF, and Keta/Xyl on episodic memory consolidation. (A) Scatter plots showing quantification of change in the time spent in the new target quadrant (left) and distance to the new platform (right) on day 4 after 1 hour of indicated anesthesia or no treatment compared to day 3. **(B)** Scatter plots showing quantification of time spent in the new target quadrant (left) and distance to the new platform (right) after reversal learning on day 3 and on day 4 after 1, 2, and 4 hours of Iso anesthesia. Filled, colored circles indicate individual animals. White circles indicate mean ± SEM. **(C)** Scatter plots showing quantification of change in the time spent in the new target quadrant (left) and distance to the new platform (right) on day 4 after 1, 2, and 4 hours of Iso anesthesia compared to day 3. Asterisks indicate significant deviation from 0. * $p < 0.05$, ** $p < 0.01$. Note, significant differences between groups were not evident. For full report of statistics, see S1 Table. All datasets of this figure can be found under https://github.com/mchini/Yang_Chini_et_al/tree/master/Stats_Dataset_(R)/datasets/Figure9_S11. Iso, isoflurane; Keta/Xyl, ketamine/xylazine; MMF, medetomidine/midazolam/fentanyl.
(TIF)

S1 Table. Statistics summary.
(XLSX)

Acknowledgments

We thank Stefan Schillemeit and Kathrin Sauter for technical assistance and Thomas G. Oertner and Amit Marmelshtein for critical feedback on the manuscript.

Author Contributions

Conceptualization: Wei Yang, Mattia Chini, Jastyn A. Pöpplau, Fabio Morellini, Olaf Sporns, Ileana L. Hanganu-Opatz, J. Simon Wiegert.

Data curation: Wei Yang, Mattia Chini, Jastyn A. Pöpplau, Andrey Formozov, Alexander Dieter.

Formal analysis: Wei Yang, Mattia Chini, Jastyn A. Pöpplau, Andrey Formozov, Alexander Dieter, Patrick Piechocinski, Cynthia Rais, Fabio Morellini, Olaf Sporns, J. Simon Wiegert.

Funding acquisition: Wei Yang, Andrey Formozov, Ileana L. Hanganu-Opatz, J. Simon Wiegert.

Investigation: Wei Yang, Jastyn A. Pöpplau, J. Simon Wiegert.

Methodology: Wei Yang, Mattia Chini, Jastyn A. Pöpplau, Andrey Formozov, Alexander Dieter, Fabio Morellini, Olaf Sporns, J. Simon Wiegert.

Project administration: J. Simon Wiegert.

Resources: Ileana L. Hanganu-Opatz, J. Simon Wiegert.

Software: Mattia Chini, Andrey Formozov, Alexander Dieter, Olaf Sporns.

Supervision: Ileana L. Hanganu-Opatz, J. Simon Wiegert.

Writing – original draft: Wei Yang, Mattia Chini, J. Simon Wiegert.

Writing – review & editing: Wei Yang, Mattia Chini, Ileana L. Hanganu-Opatz, J. Simon Wiegert.

References

1. Rudolph U, Antkowiak B. Molecular and neuronal substrates for general anaesthetics. Nat Rev Neurosci. 2004; 5(9):709–20. Epub 2004/08/24. https://doi.org/10.1038/nrn1496 PMID: 15322529.
2. Urban BW, Bleckwenn M. Concepts and correlations relevant to general anaesthesia. Br J Anaesth. 2002; 89(1):3–16. Epub 2002/08/14. https://doi.org/10.1093/bja/aef164 PMID: 12173238.
3. Sanders RD, Tononi G, Laureys S, Sleigh JW. Unresponsiveness not equal unconsciousness. Anesthesiology. 2012; 116(4):946–59. Epub 2012/02/09. https://doi.org/10.1097/ALN.0b013e318249d0a7 PMID: 22314293; PubMed Central PMCID: PMC3311716.
4. Alkire MT, Hudetz AG, Tononi G. Consciousness and anesthesia. Science. 2008; 322(5903):876–80. Epub 2008/11/08. https://doi.org/10.1126/science.1149213 PMID: 18988836; PubMed Central PMCID: PMC2743249.
5. Mashour GA, Orser BA, Avidan MS. Intraoperative awareness: from neurobiology to clinical practice. Anesthesiology. 2011; 114(5):1218–33. Epub 2011/04/06. https://doi.org/10.1097/ALN.0b013e31820fc9b6 PMID: 21464699.
6. Antognini JF, Carstens E. In vivo characterization of clinical anaesthesia and its components. Br J Anaesth. 2002; 89(1):156–66. Epub 2002/08/14. https://doi.org/10.1093/bja/aef156 PMID: 12173227.
7. Vutskits L, Xie Z. Lasting impact of general anaesthesia on the brain: mechanisms and relevance. Nat Rev Neurosci 2016; 17(11):705–17. Epub 2016/10/19. https://doi.org/10.1038/nrn.2016.128 PMID: 27752068.
8. Zurek AA, Yu J, Wang DS, Haffey SC, Bridgwater EM, Penna A, et al. Sustained increase in alpha5-GABAA receptor function impairs memory after anesthesia. J Clin Invest. 2014; 124(12):5437–41. Epub 2014/11/05. https://doi.org/10.1172/JCI76669 PMID: 25365226; PubMed Central PMCID: PMC4348961.
9. Neves G, Cooke SF, Bliss TV. Synaptic plasticity, memory and the hippocampus: a neural network approach to causality. Nat Rev Neurosci. 2008; 9(1):65–75. Epub 2007/12/21. https://doi.org/10.1038/nrn2303 PMID: 18094707.
10. Larkum M. A cellular mechanism for cortical associations: an organizing principle for the cerebral cortex. Trends Neurosci. 2012. Epub 2013/01/01. https://doi.org/10.1016/j.tins.2012.11.006 PMID: 23273272.
11. Segal M. Dendritic spines and long-term plasticity. Nat Rev Neurosci. 2005; 6(4):277–84. Epub 2005/04/02. https://doi.org/10.1038/nrn1649 PMID: 15803159.
12. Kasai H, Fukuda M, Watanabe S, Hayashi-Takagi A, Noguchi J. Structural dynamics of dendritic spines in memory and cognition. Trends Neurosci. 2010; 33(3):121–9. Epub 2010/02/09. https://doi.org/10.1016/j.tins.2010.01.001 PMID: 20138375.
13. Frey U, Morris RG. Synaptic tagging and long-term potentiation. Nature. 1997; 385(6616):533–6. https://doi.org/10.1038/385533a0 PMID: 9020359.
14. Yang G, Pan F, Gan WB. Stably maintained dendritic spines are associated with lifelong memories. Nature. 2009; 462(7275):920–4. Epub 2009/12/01. https://doi.org/10.1038/nature08577 PMID: 19946265.
15. Wiegert JS, Pulin M, Gee CE, Oertner TG. The fate of hippocampal synapses depends on the sequence of plasticity-inducing events. Elife. 2018; 7. Epub 2018/10/13. https://doi.org/10.7554/eLife.39151 PMID: 30311904; PubMed Central PMCID: PMC6205809.
16. Wiegert JS, Oertner TG. Long-term depression triggers the selective elimination of weakly integrated synapses. Proc Natl Acad Sci U S A. 2013; 110(47):E4510–9. Epub 2013/11/06. https://doi.org/10.1073/pnas.1315926110 PMID: 24191047; PubMed Central PMCID: PMC3839749.

17. De Roo M, Klauser P, Muller D. LTP promotes a selective long-term stabilization and clustering of dendritic spines. PLoS Biol. 2008; 6(9):e219. Epub 2008/09/16. https://doi.org/10.1371/journal.pbio.0060219 PMID: 18788894; PubMed Central PMCID: PMC2531136.

18. Nagerl UV, Eberhorn N, Cambridge SB, Bonhoeffer T. Bidirectional activity-dependent morphological plasticity in hippocampal neurons. Neuron. 2004; 44(5):759–67. Epub 2004/12/02. https://doi.org/10.1016/j.neuron.2004.11.016 PMID: 15572108.

19. Whitlock JR, Heynen AJ, Shuler MG, Bear MF. Learning induces long-term potentiation in the hippocampus. Science. 2006; 313(5790):1093–7. https://doi.org/10.1126/science.1128134 PMID: 16931756.

20. Schmid LC, Mittag M, Poll S, Steffen J, Wagner J, Geis HR, et al. Dysfunction of Somatostatin-Positive Interneurons Associated with Memory Deficits in an Alzheimer's Disease Model. Neuron. 2016; 92 (1):114–25. https://doi.org/10.1016/j.neuron.2016.08.034 PMID: 27641495.

21. Attardo A, Fitzgerald JE, Schnitzer MJ. Impermanence of dendritic spines in live adult CA1 hippocampus. Nature. 2015; 523(7562):592–6. Epub 2015/06/23. https://doi.org/10.1038/nature14467 PMID: 26098371; PubMed Central PMCID: PMC4648621.

22. Sur C, Fresu L, Howell O, McKernan RM, Atack JR. Autoradiographic localization of alpha5 subunit-containing GABAA receptors in rat brain. Brain Res. 1999; 822(1–2):265–70. Epub 1999/03/20. https://doi.org/10.1016/s0006-8993(99)01152-x PMID: 10082908.

23. Bonin RP, Orser BA. GABA(A) receptor subtypes underlying general anesthesia. Pharmacol Biochem Behav. 2008; 90(1):105–12. Epub 2008/01/19. https://doi.org/10.1016/j.pbb.2007.12.011 PMID: 18201756.

24. Chrobak JJ, Hinman JR, Sabolek HR. Revealing past memories: proactive interference and ketamine-induced memory deficits. J Neurosci. 2008; 28(17):4512–20. Epub 2008/04/25. https://doi.org/10.1523/JNEUROSCI.0742-07.2008 PMID: 18434529; PubMed Central PMCID: PMC6670951.

25. Goltstein PM, Montijn JS, Pennartz CM. Effects of isoflurane anesthesia on ensemble patterns of Ca2 + activity in mouse v1: reduced direction selectivity independent of increased correlations in cellular activity. PLoS ONE. 2015; 10(2):e0118277. Epub 2015/02/24. https://doi.org/10.1371/journal.pone.0118277 PMID: 25706867; PubMed Central PMCID: PMC4338011.

26. Wenzel M, Han S, Smith EH, Hoel E, Greger B, House PA, et al. Reduced Repertoire of Cortical Microstates and Neuronal Ensembles in Medically Induced Loss of Consciousness. Cell Syst. 2019; 8 (5):467–74 e4. Epub 2019/05/06. https://doi.org/10.1016/j.cels.2019.03.007 PMID: 31054810; PubMed Central PMCID: PMC6544156.

27. Greenberg DS, Houweling AR, Kerr JN. Population imaging of ongoing neuronal activity in the visual cortex of awake rats. Nat Neurosci. 2008; 11(7):749–51. Epub 2008/06/17. https://doi.org/10.1038/nn.2140 PMID: 18552841.

28. Soltesz I, Deschenes M. Low- and high-frequency membrane potential oscillations during theta activity in CA1 and CA3 pyramidal neurons of the rat hippocampus under ketamine-xylazine anesthesia. J Neurophysiol. 1993; 70(1):97–116. Epub 1993/07/01. https://doi.org/10.1152/jn.1993.70.1.97 PMID: 8395591.

29. Purdon PL, Sampson A, Pavone KJ, Brown EN. Clinical Electroencephalography for Anesthesiologists: Part I: Background and Basic Signatures. Anesthesiology. 2015; 123(4):937–60. Epub 2015/08/15. https://doi.org/10.1097/ALN.0000000000000841 PMID: 26275092; PubMed Central PMCID: PMC4573341.

30. Steriade M, Nunez A, Amzica F. A novel slow (< 1 Hz) oscillation of neocortical neurons in vivo: depolarizing and hyperpolarizing components. J Neurosci. 1993; 13(8):3252–65. Epub 1993/08/01. https://doi.org/10.1523/JNEUROSCI.13-08-03252.1993 PMID: 8340806; PubMed Central PMCID: PMC6576541.

31. Collins DR, Pelletier JG, Pare D. Slow and fast (gamma) neuronal oscillations in the perirhinal cortex and lateral amygdala. J Neurophysiol. 2001; 85(4):1661–72. Epub 2001/04/05. https://doi.org/10.1152/jn.2001.85.4.1661 PMID: 11287489.

32. Contreras D, Steriade M. Cellular basis of EEG slow rhythms: a study of dynamic corticothalamic relationships. J Neurosci. 1995; 15(1 Pt 2):604–22. Epub 1995/01/01. https://doi.org/10.1523/JNEUROSCI.15-01-00604.1995 PMID: 7823167; PubMed Central PMCID: PMC6578315.

33. Donoghue T, Haller M, Peterson EJ, Varma P, Sebastian P, Gao R, et al. Parameterizing neural power spectra into periodic and aperiodic components. Nat Neurosci. 2020; 23(12):1655–65. https://doi.org/10.1038/s41593-020-00744-x PMID: 33230329

34. Trakoshis S, Martínez-Cañada P, Rocchi F, Canella C, You W, Chakrabarti B, et al. Intrinsic excitation-inhibition imbalance affects medial prefrontal cortex differently in autistic men versus women. Elife. 2020; 9. https://doi.org/10.7554/eLife.55684 PMID: 32746967

35. Lombardi F, Herrmann HJ, De Arcangelis L. Balance of excitation and inhibition determines 1/f power spectrum in neuronal networks. Chaos. 2017; 27(4):047402. https://doi.org/10.1063/1.4979043 PMID: 28456161

36. Gao R, Peterson EJ, Voytek B. Inferring synaptic excitation/inhibition balance from field potentials. Neuroimage. 2017; 158:70–8. Epub 2017/07/06. https://doi.org/10.1016/j.neuroimage.2017.06.078 PMID: 28676297.

37. Colombo MA, Napolitani M, Boly M, Gosseries O, Casarotto S, Rosanova M, et al. The spectral exponent of the resting EEG indexes the presence of consciousness during unresponsiveness induced by propofol, xenon, and ketamine. Neuroimage. 2019; 189:631–44. https://doi.org/10.1016/j.neuroimage.2019.01.024 PMID: 30639334

38. Albrecht M, Henke J, Tacke S, Markert M, Guth B. Effects of isoflurane, ketamine-xylazine and a combination of medetomidine, midazolam and fentanyl on physiological variables continuously measured by telemetry in Wistar rats. BMC Vet Res. 2014; 10:198. Epub 2014/08/26. https://doi.org/10.1186/s12917-014-0198-3 PMID: 25149627; PubMed Central PMCID: PMC4363998.

39. Fleischmann T, Jirkof P, Henke J, Arras M, Cesarovic N. Injection anaesthesia with fentanyl-midazolam-medetomidine in adult female mice: importance of antagonization and perioperative care. Lab Anim. 2016; 50(4):264–74. Epub 2016/02/11. https://doi.org/10.1177/0023677216631458 PMID: 26860578.

40. Canolty RT, Knight RT. The functional role of cross-frequency coupling. Trends Cogn Sci. 2010; 14 (11):506–15. Epub 2010/10/12. https://doi.org/10.1016/j.tics.2010.09.001 PMID: 20932795; PubMed Central PMCID: PMC3359652.

41. Schomburg EW, Fernandez-Ruiz A, Mizuseki K, Berenyi A, Anastassiou CA, Koch C, et al. Theta phase segregation of input-specific gamma patterns in entorhinal-hippocampal networks. Neuron. 2014; 84(2):470–85. Epub 2014/09/30. https://doi.org/10.1016/j.neuron.2014.08.051 PMID: 25263753; PubMed Central PMCID: PMC4253689.

42. Scheffer-Teixeira R, Belchior H, Caixeta FV, Souza BC, Ribeiro S, Tort AB. Theta phase modulates multiple layer-specific oscillations in the CA1 region. Cereb Cortex. 2012; 22(10):2404–14. Epub 2011/11/15. https://doi.org/10.1093/cercor/bhr319 PMID: 22079925.

43. Buzsaki G, Anastassiou CA, Koch C. The origin of extracellular fields and currents—EEG, ECoG, LFP and spikes. Nat Rev Neurosci. 2012; 13(6):407–20. Epub 2012/05/19. https://doi.org/10.1038/nrn3241 PMID: 22595786; PubMed Central PMCID: PMC4907333.

44. Watson BO, Levenstein D, Greene JP, Gelinas JN, Buzsaki G. Network Homeostasis and State Dynamics of Neocortical Sleep. Neuron. 2016; 90(4):839–52. Epub 2016/05/03. https://doi.org/10.1016/j.neuron.2016.03.036 PMID: 27133462; PubMed Central PMCID: PMC4873379.

45. Vinck M, Battaglia FP, Womelsdorf T, Pennartz C. Improved measures of phase-coupling between spikes and the Local Field Potential. J Comput Neurosci. 2012; 33(1):53–75. Epub 2011/12/22. https://doi.org/10.1007/s10827-011-0374-4 PMID: 22187161; PubMed Central PMCID: PMC3394239.

46. Chen TW, Wardill TJ, Sun Y, Pulver SR, Renninger SL, Baohan A, et al. Ultrasensitive fluorescent proteins for imaging neuronal activity. Nature. 2013; 499(7458):295–300. Epub 2013/07/23. https://doi.org/10.1038/nature12354 PMID: 23868258; PubMed Central PMCID: PMC3777791.

47. Harris KD, Mrsic-Flogel TD. Cortical connectivity and sensory coding. Nature. 2013; 503(7474):51–8. Epub 2013/11/10. https://doi.org/10.1038/nature12654 PMID: 24201278.

48. Franks NP. General anaesthesia: from molecular targets to neuronal pathways of sleep and arousal. Nat Rev Neurosci. 2008; 9(5):370–86. Epub 2008/04/22. https://doi.org/10.1038/nrn2372 PMID: 18425091.

49. Klinzing JG, Niethard N, Born J. Mechanisms of systems memory consolidation during sleep. Nat Neurosci. 2019; 22(10):1598–610. Epub 2019/08/28. https://doi.org/10.1038/s41593-019-0467-3 PMID: 31451802.

50. Buzsaki G. Hippocampal sharp waves: their origin and significance. Brain Res. 1986; 398(2):242–52. Epub 1986/11/29. https://doi.org/10.1016/0006-8993(86)91483-6 PMID: 3026567.

51. Okun M, Steinmetz N, Cossell L, Iacaruso MF, Ko H, Bartho P, et al. Diverse coupling of neurons to populations in sensory cortex. Nature. 2015; 521(7553):511–5. Epub 2015/04/08. https://doi.org/10.1038/nature14273 PMID: 25849776; PubMed Central PMCID: PMC4449271.

52. Cutts CS, Eglen SJ. Detecting pairwise correlations in spike trains: an objective comparison of methods and application to the study of retinal waves. J Neurosci. 2014; 34(43):14288–303. Epub 2014/10/24. https://doi.org/10.1523/JNEUROSCI.2767-14.2014 PMID: 25339742; PubMed Central PMCID: PMC4205553.

53. Sporns O, Betzel RF. Modular Brain Networks. Annu Rev Psychol. 2016; 67:613–40. Epub 2015/09/24. https://doi.org/10.1146/annurev-psych-122414-033634 PMID: 26393868; PubMed Central PMCID: PMC4782188.

54. Newman ME, Girvan M. Finding and evaluating community structure in networks. Phys Rev E Stat Nonlinear Soft Matter Phys. 2004; 69(2 Pt 2):026113. Epub 2004/03/05. https://doi.org/10.1103/PhysRevE.69.026113 PMID: 14995526.

55. Jeub LGS, Sporns O, Fortunato S. Multiresolution Consensus Clustering in Networks. Sci Rep. 2018; 8. ARTN 325910.1038/s41598-018-21352-7 WOS:000425380900042. https://doi.org/10.1038/s41598-018-21352-7 PMID: 29459635

56. Diekelmann S, Born J. The memory function of sleep. Nat Rev Neurosci. 2010; 11(2):114–26. Epub 2010/01/05. https://doi.org/10.1038/nrn2762 PMID: 20046194.

57. Yüzgec O, Prsa M, Zimmermann R, Huber D. Pupil Size Coupling to Cortical States Protects the Stability of Deep Sleep via Parasympathetic Modulation. Curr Biol. 2018; 28(3):392–400 e3. Epub 2018/01/24. https://doi.org/10.1016/j.cub.2017.12.049 PMID: 29358069; PubMed Central PMCID: PMC5807087.

58. Chini M, Gretenkord S, Kostka JK, Popplau JA, Cornelissen L, Berde CB, et al. Neural Correlates of Anesthesia in Newborn Mice and Humans. Frontiers Neural Circuits. 2019; 13:38. Epub 2019/06/14. https://doi.org/10.3389/fncir.2019.00038 PMID: 31191258; PubMed Central PMCID: PMC6538977.

59. Briner A, De Roo M, Dayer A, Muller D, Habre W, Vutskits L. Volatile anesthetics rapidly increase dendritic spine density in the rat medial prefrontal cortex during synaptogenesis. Anesthesiology. 2010; 112(3):546–56. Epub 2010/02/04. https://doi.org/10.1097/ALN.0b013e3181cd7942 PMID: 20124985.

60. De Roo M, Klauser P, Briner A, Nikonenko I, Mendez P, Dayer A, et al. Anesthetics rapidly promote synaptogenesis during a critical period of brain development. PLoS ONE. 2009; 4(9):e7043. Epub 2009/09/17. https://doi.org/10.1371/journal.pone.0007043 PMID: 19756154; PubMed Central PMCID: PMC2738943.

61. Briner A, Nikonenko I, De Roo M, Dayer A, Muller D, Vutskits L. Developmental Stage-dependent persistent impact of propofol anesthesia on dendritic spines in the rat medial prefrontal cortex. Anesthesiology. 2011; 115(2):282–93. Epub 2011/06/28. https://doi.org/10.1097/ALN.0b013e318221fbbd PMID: 21701379.

62. Pfeiffer T, Poll S, Bancelin S, Angibaud J, Inavalli VK, Keppler K, et al. Chronic 2P-STED imaging reveals high turnover of dendritic spines in the hippocampus in vivo. Elife. 2018; 7. Epub 2018/06/23. https://doi.org/10.7554/eLife.34700 PMID: 29932052; PubMed Central PMCID: PMC6014725.

63. Gu L, Kleiber S, Schmid L, Nebeling F, Chamoun M, Steffen J, et al. Long-term in vivo imaging of dendritic spines in the hippocampus reveals structural plasticity. J Neurosci. 2014; 34(42):13948–53. Epub 2014/10/17. https://doi.org/10.1523/JNEUROSCI.1464-14.2014 PMID: 25319691; PubMed Central PMCID: PMC6705298.

64. Portera-Cailliau C, Pan DT, Yuste R. Activity-regulated dynamic behavior of early dendritic protrusions: evidence for different types of dendritic filopodia. J Neurosci. 2003; 23(18):7129–42. Epub 2003/08/09. https://doi.org/10.1523/JNEUROSCI.23-18-07129.2003 PMID: 12904473; PubMed Central PMCID: PMC6740658.

65. Lendvai B, Stern EA, Chen B, Svoboda K. Experience-dependent plasticity of dendritic spines in the developing rat barrel cortex in vivo. Nature. 2000; 404(6780):876–81. Epub 2000/04/29. https://doi.org/10.1038/35009107 PMID: 10786794.

66. Dailey ME, Smith SJ. The dynamics of dendritic structure in developing hippocampal slices. J Neurosci. 1996; 16(9):2983–94. Epub 1996/05/01. https://doi.org/10.1523/JNEUROSCI.16-09-02983.1996 PMID: 8622128; PubMed Central PMCID: PMC6579052.

67. Yang G, Chang PC, Bekker A, Blanck TJ, Gan WB. Transient effects of anesthetics on dendritic spines and filopodia in the living mouse cortex. Anesthesiology. 2011; 115(4):718–26. Epub 2011/07/20. https://doi.org/10.1097/ALN.0b013e318229a660 PMID: 21768874; PubMed Central PMCID: PMC3815535.

68. Moscovitch M, Cabeza R, Winocur G, Nadel L. Episodic Memory and Beyond: The Hippocampus and Neocortex in Transformation. Annu Rev Psychol. 2016; 67:105–34. Epub 2016/01/05. https://doi.org/10.1146/annurev-psych-113011-143733 PMID: 26726963.

69. Nadel L, Moscovitch M. Memory consolidation, retrograde amnesia and the hippocampal complex. Curr Opin Neurobiol. 1997; 7(2):217–27. Epub 1997/04/01. https://doi.org/10.1016/s0959-4388(97)80010-4 PMID: 9142752.

70. O'Neill J, Pleydell-Bouverie B, Dupret D, Csicsvari J. Play it again: reactivation of waking experience and memory. Trends Neurosci. 2010; 33(5):220–9. Epub 2010/03/09. https://doi.org/10.1016/j.tins.2010.01.006 PMID: 20207025.

71. Clark DL, Rosner BS. Neurophysiologic effects of general anesthetics. I. The electroencephalogram and sensory evoked responses in man. Anesthesiology. 1973; 38(6):564–82. Epub 1973/06/01. PMID: 4145825.

72. Sarasso S, Boly M, Napolitani M, Gosseries O, Charland-Verville V, Casarotto S, et al. Consciousness and Complexity during Unresponsiveness Induced by Propofol, Xenon, and Ketamine. Curr Biol. 2015; 25(23):3099–105. Epub 2016/01/12. https://doi.org/10.1016/j.cub.2015.10.014 PMID: 26752078.

73. Langsjo JW, Maksimow A, Salmi E, Kaisti K, Aalto S, Oikonen V, et al. S-ketamine anesthesia increases cerebral blood flow in excess of the metabolic needs in humans. Anesthesiology. 2005; 103 (2):258–68. Epub 2005/07/30. https://doi.org/10.1097/00000542-200508000-00008 PMID: 16052107.

74. Lee U, Ku S, Noh G, Baek S, Choi B, Mashour GA. Disruption of frontal-parietal communication by ketamine, propofol, and sevoflurane. Anesthesiology. 2013; 118(6):1264–75. Epub 2013/05/23. https://doi.org/10.1097/ALN.0b013e31829103f5 PMID: 23695090; PubMed Central PMCID: PMC4346246.

75. Wei Z, Lin B-J, Chen T-W, Daie K, Svoboda K. Druckmann S. A comparison of neuronal population dynamics measured with calcium imaging and electrophysiology. PLoS Comput Biol. 2020; 16(9): e1008198. https://doi.org/10.1371/journal.pcbi.1008198 PMID: 32931495

76. Steinmetz NA, Buetfering C, Lecoq J, Lee CR, Peters AJ, Jacobs EAK, et al. Aberrant Cortical Activity in Multiple GCaMP6-Expressing Transgenic Mouse Lines. eNeuro. 2017; 4(5). https://doi.org/10.1523/ENEURO.0207-17.2017 PMID: 28932809; PubMed Central PMCID: PMC5604087.

77. Katz Y, Menon V, Nicholson DA, Geinisman Y, Kath WL, Spruston N. Synapse distribution suggests a two-stage model of dendritic integration in CA1 pyramidal neurons. Neuron. 2009; 63(2):171–7. Epub 2009/07/31. S0896-6273(09)00510-8 [pii] 10.1016/j.neuron.2009.06.023 https://doi.org/10.1016/j.neuron.2009.06.023 PMID: 19640476.

78. Yamakage M, Hirshman CA, Croxton TL. Inhibitory effects of thiopental, ketamine, and propofol on voltage-dependent Ca2+ channels in porcine tracheal smooth muscle cells. Anesthesiology. 1995; 83 (6):1274–82. Epub 1995/12/01. https://doi.org/10.1097/00000542-199512000-00018 PMID: 8533920.

79. Yang Y, Cui Y, Sang K, Dong Y, Ni Z, Ma S, et al. Ketamine blocks bursting in the lateral habenula to rapidly relieve depression. Nature. 2018; 554(7692):317–22. Epub 2018/02/16. https://doi.org/10.1038/nature25509 PMID: 29446381.

80. West AE, Griffith EC, Greenberg ME. Regulation of transcription factors by neuronal activity. Nat Rev Neurosci. 2002; 3(12):921–31. https://doi.org/10.1038/nrn987 PMID: 12461549.

81. Wiegert JS, Bading H. Activity-dependent calcium signaling and ERK-MAP kinases in neurons: a link to structural plasticity of the nucleus and gene transcription regulation. Cell Calcium. 2011; 49(5):296–305. Epub 2010/12/18. https://doi.org/10.1016/j.ceca.2010.11.009 PMID: 21163523.

82. Hardingham GE, Bading H. Synaptic versus extrasynaptic NMDA receptor signalling: implications for neurodegenerative disorders. Nat Rev Neurosci. 2010. Epub 2010/09/16. nrn2911 [pii] 10.1038/nrn2911 https://doi.org/10.1038/nrn2911 PMID: 20842175.

83. Mizrahi-Kliger AD, Kaplan A, Israel Z, Bergman H. Desynchronization of slow oscillations in the basal ganglia during natural sleep. Proc Natl Acad Sci U S A. 2018; 115(18):E4274–E83. Epub 2018/04/19. https://doi.org/10.1073/pnas.1720795115 PMID: 29666271; PubMed Central PMCID: PMC5939089.

84. Klausberger T, Somogyi P. Neuronal diversity and temporal dynamics: the unity of hippocampal circuit operations. Science. 2008; 321(5885):53–7. Epub 2008/07/05. https://doi.org/10.1126/science.1149381 PMID: 18599766.

85. Lee D, Shtengel G, Osborne JE, Lee AK. Anesthetized- and awake-patched whole-cell recordings in freely moving rats using UV-cured collar-based electrode stabilization. Nat Protoc. 2014; 9(12):2784–95. Epub 2014/11/07. https://doi.org/10.1038/nprot.2014.190 PMID: 25375992.

86. Lee AK, Manns ID, Sakmann B, Brecht M. Whole-cell recordings in freely moving rats. Neuron. 2006; 51(4):399–407. Epub 2006/08/16. https://doi.org/10.1016/j.neuron.2006.07.004 PMID: 16908406.

87. Epsztein J, Brecht M, Lee AK. Intracellular determinants of hippocampal CA1 place and silent cell activity in a novel environment. Neuron. 2011; 70(1):109–20. Epub 2011/04/13. https://doi.org/10.1016/j.neuron.2011.03.006 PMID: 21482360; PubMed Central PMCID: PMC3221010.

88. Pryazhnikov E, Mugantseva E, Casarotto P, Kolikova J, Fred SM, Toptunov D, et al. Longitudinal two-photon imaging in somatosensory cortex of behaving mice reveals dendritic spine formation enhancement by subchronic administration of low-dose ketamine. Sci Rep. 2018; 8(1):6464. Epub 2018/04/25. https://doi.org/10.1038/s41598-018-24933-8 PMID: 29691465; PubMed Central PMCID: PMC5915413.

89. Lin H, Higgins P, Loh HH, Law PY, Liao D. Bidirectional effects of fentanyl on dendritic spines and AMPA receptors depend upon the internalization of mu opioid receptors. Neuropsychopharmacology.

2009; 34(9):2097–111. Epub 2009/03/20. https://doi.org/10.1038/npp.2009.34 PMID: 19295508; PubMed Central PMCID: PMC2731771.

90. Li N, Lee B, Liu RJ, Banasr M, Dwyer JM, Iwata M, et al. mTOR-dependent synapse formation underlies the rapid antidepressant effects of NMDA antagonists. Science. 2010; 329(5994):959–64. Epub 2010/08/21. https://doi.org/10.1126/science.1190287 PMID: 20724638; PubMed Central PMCID: PMC3116441.

91. Phoumthipphavong V, Barthas F, Hassett S, Kwan AC. Longitudinal Effects of Ketamine on Dendritic Architecture In Vivo in the Mouse Medial Frontal Cortex. eNeuro. 2016; 3(2). Epub 2016/04/12. https://doi.org/10.1523/ENEURO.0133-15.2016 PMID: 27066532; PubMed Central PMCID: PMC4819286.

92. Eikermann M, Akeju O, Chamberlin NL. Sleep and Anesthesia: The Shared Circuit Hypothesis Has Been Put to Bed. Curr Biol. 2020; 30(5):R219–R21. Epub 2020/03/11. https://doi.org/10.1016/j.cub.2020.01.057 PMID: 32155424.

93. Vanini G, Bassana M, Mast M, Mondino A, Cerda I, Phyle M, et al. Activation of Preoptic GABAergic or Glutamatergic Neurons Modulates Sleep-Wake Architecture, but Not Anesthetic State Transitions. Curr Biol. 2020; 30(5):779–87 e4. Epub 2020/02/23. https://doi.org/10.1016/j.cub.2019.12.063 PMID: 32084397; PubMed Central PMCID: PMC7156032.

94. Jiang-Xie LF, Yin L, Zhao S, Prevosto V, Han BX, Dzirasa K, et al. A Common Neuroendocrine Substrate for Diverse General Anesthetics and Sleep. Neuron. 2019; 102(5):1053–65 e4. Epub 2019/04/23. https://doi.org/10.1016/j.neuron.2019.03.033 PMID: 31006556; PubMed Central PMCID: PMC6554048.

95. Kentros C, Hargreaves E, Hawkins RD, Kandel ER, Shapiro M, Muller RV. Abolition of long-term stability of new hippocampal place cell maps by NMDA receptor blockade. Science. 1998; 280(5372):2121–6. Epub 1998/06/26. https://doi.org/10.1126/science.280.5372.2121 PMID: 9641919.

96. Hayashi Y. NMDA Receptor-Dependent Dynamics of Hippocampal Place Cell Ensembles. J Neurosci. 2019; 39(26):5173–82. Epub 2019/04/25. https://doi.org/10.1523/JNEUROSCI.0243-19.2019 PMID: 31015340; PubMed Central PMCID: PMC6595956.

97. de Souza I, Meurer Y, Tavares PM, Pugliane KC, Lima RH, Silva RH, et al. Episodic-like memory impairment induced by sub-anaesthetic doses of ketamine. Behav Brain Res. 2019; 359:165–71. Epub 2018/10/26. https://doi.org/10.1016/j.bbr.2018.10.031 PMID: 30359643.

98. Wenzel M, Leunig A, Han S, Peterka DS, Yuste R. Prolonged anesthesia alters brain synaptic architecture. Proc Natl Acad Sci U S A. 2021; 118(7):e2023676118. https://doi.org/10.1073/pnas.2023676118 PMID: 33568534

99. Zurek AA, Bridgwater EM, Orser BA. Inhibition of alpha5 gamma-Aminobutyric acid type A receptors restores recognition memory after general anesthesia. Anesth Analg. 2012; 114(4):845–55. Epub 2012/03/03. https://doi.org/10.1213/ANE.0b013e31824720da PMID: 22383672.

100. Chen G, Chen KS, Knox J, Inglis J, Bernard A, Martin SJ, et al. A learning deficit related to age and beta-amyloid plaques in a mouse model of Alzheimer's disease. Nature. 2000; 408(6815):975–9. Epub 2001/01/05. https://doi.org/10.1038/35050103 PMID: 11140684.

101. Morellini F. Spatial memory tasks in rodents: what do they model? Cell Tissue Res. 2013; 354(1):273–86. Epub 2013/06/25. https://doi.org/10.1007/s00441-013-1668-9 PMID: 23793547.

102. Onslow AC, Bogacz R, Jones MW. Quantifying phase-amplitude coupling in neuronal network oscillations. Prog Biophys Mol Biol. 2011; 105(1–2):49–57. Epub 2010/09/28. https://doi.org/10.1016/j.pbiomolbio.2010.09.007 PMID: 20869387.

103. Rossant C, Kadir SN, Goodman DFM, Schulman J, Hunter MLD, Saleem AB, et al. Spike sorting for large, dense electrode arrays. Nat Neurosci. 2016; 19(4):634–41. Epub 2016/03/15. https://doi.org/10.1038/nn.4268 PMID: 26974951; PubMed Central PMCID: PMC4817237.

104. Vinck M, van Wingerden M, Womelsdorf T, Fries P, Pennartz CM. The pairwise phase consistency: a bias-free measure of rhythmic neuronal synchronization. Neuroimage. 2010; 51(1):112–22. Epub 2010/02/02. https://doi.org/10.1016/j.neuroimage.2010.01.073 PMID: 20114076.

105. Rose T, Jaepel J, Hubener M, Bonhoeffer T. Cell-specific restoration of stimulus preference after monocular deprivation in the visual cortex. Science. 2016; 352(6291):1319–22. Epub 2016/06/11. https://doi.org/10.1126/science.aad3358 PMID: 27284193.

106. Sheintuch L, Rubin A, Brande-Eilat N, Geva N, Sadeh N, Pinchasof O, et al. Tracking the Same Neurons across Multiple Days in Ca(2+) Imaging Data. Cell Rep. 2017; 21(4):1102–15. https://doi.org/10.1016/j.celrep.2017.10.013 PMID: 29069591; PubMed Central PMCID: PMC5670033.

107. Thevenaz P, Ruttimann UE, Unser M. A pyramid approach to subpixel registration based on intensity. IEEE Trans Image Process. 1998; 7(1):27–41. Epub 2008/02/13. https://doi.org/10.1109/83.650848 PMID: 18267377.

108. Pachitariu M, Stringer C, Dipoppa M, Schröder S, Rossi LF, Dalgleish H, et al. Suite2p: beyond 10,000 neurons with standard two-photon microscopy. bioRxiv. 2017:061507. https://doi.org/10.1101/061507

109. Rubinov M, Sporns O. Complex network measures of brain connectivity: Uses and interpretations. Neuroimage. 2010; 52(3):1059–69. WOS:000280181800027. https://doi.org/10.1016/j.neuroimage.2009.10.003 PMID: 19819337

110. Mizuseki K, Sirota A, Pastalkova E, Buzsaki G. Theta oscillations provide temporal windows for local circuit computation in the entorhinal-hippocampal loop. Neuron. 2009; 64(2):267–80. Epub 2009/10/31. https://doi.org/10.1016/j.neuron.2009.08.037 PMID: 19874793; PubMed Central PMCID: PMC2771122.

111. Pedregosa F, Varoquaux G, Gramfort A, Michel V, Thirion B, Grisel O, et al. Scikit-learn: Machine Learning in Python. J Mach Learn Res. 2011; 12:2825–30. WOS:000298103200003.

112. Mathis A, Mamidanna P, Cury KM, Abe T, Murthy VN, Mathis MW, et al. DeepLabCut: markerless pose estimation of user-defined body parts with deep learning. Nat Neurosci. 2018; 21(9):1281–9. Epub 2018/08/22. https://doi.org/10.1038/s41593-018-0209-y PMID: 30127430.

113. Aarts E, Verhage M, Veenvliet JV, Dolan CV, van der Sluis S. A solution to dependency: using multi-level analysis to accommodate nested data. Nat Neurosci. 2014; 17(4):491–6. Epub 2014/03/29. https://doi.org/10.1038/nn.3648 PMID: 24671065.

114. Bates D, Machler M, Bolker BM, Walker SC. Fitting Linear Mixed-Effects Models Using lme4. J Stat Softw. 2015; 67(1):1–48. WOS:000365981400001.

115. Kuznetsova A, Brockhoff PB, Christensen RHB. lmerTest Package: Tests in Linear Mixed Effects Models. J Stat Softw. 2017; 82(13):1–26. WOS:000417711600001.

S1 Fig. LFP recordings in dorsal CA1 during wakefulness and anesthesia.

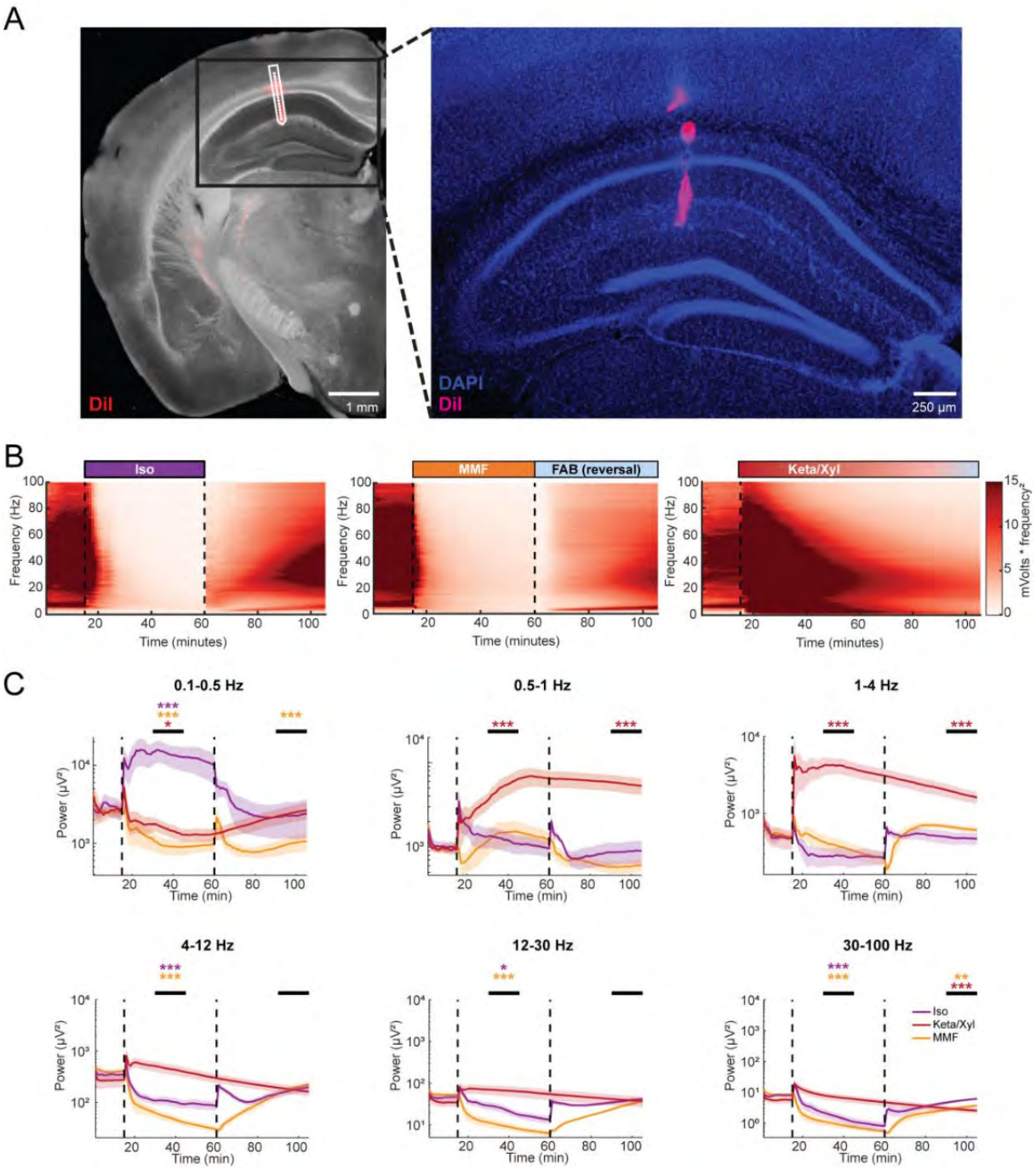

S2 Fig. SUA in dorsal CA1 during wakefulness and anesthesia.

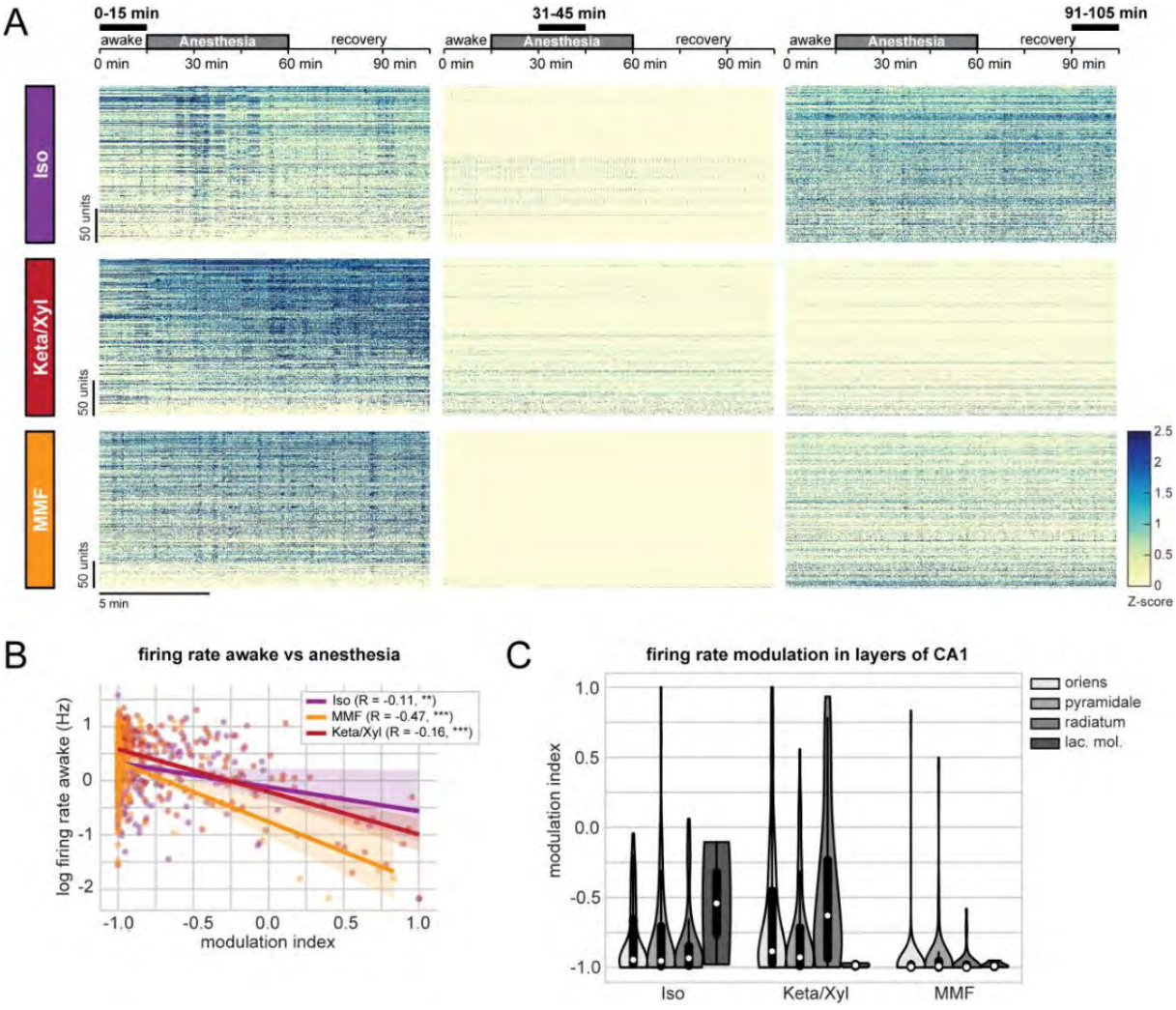

S3 Fig. Anesthesia-induced changes in calcium activity profiles are insensitive to the choice of signal extraction parameters.

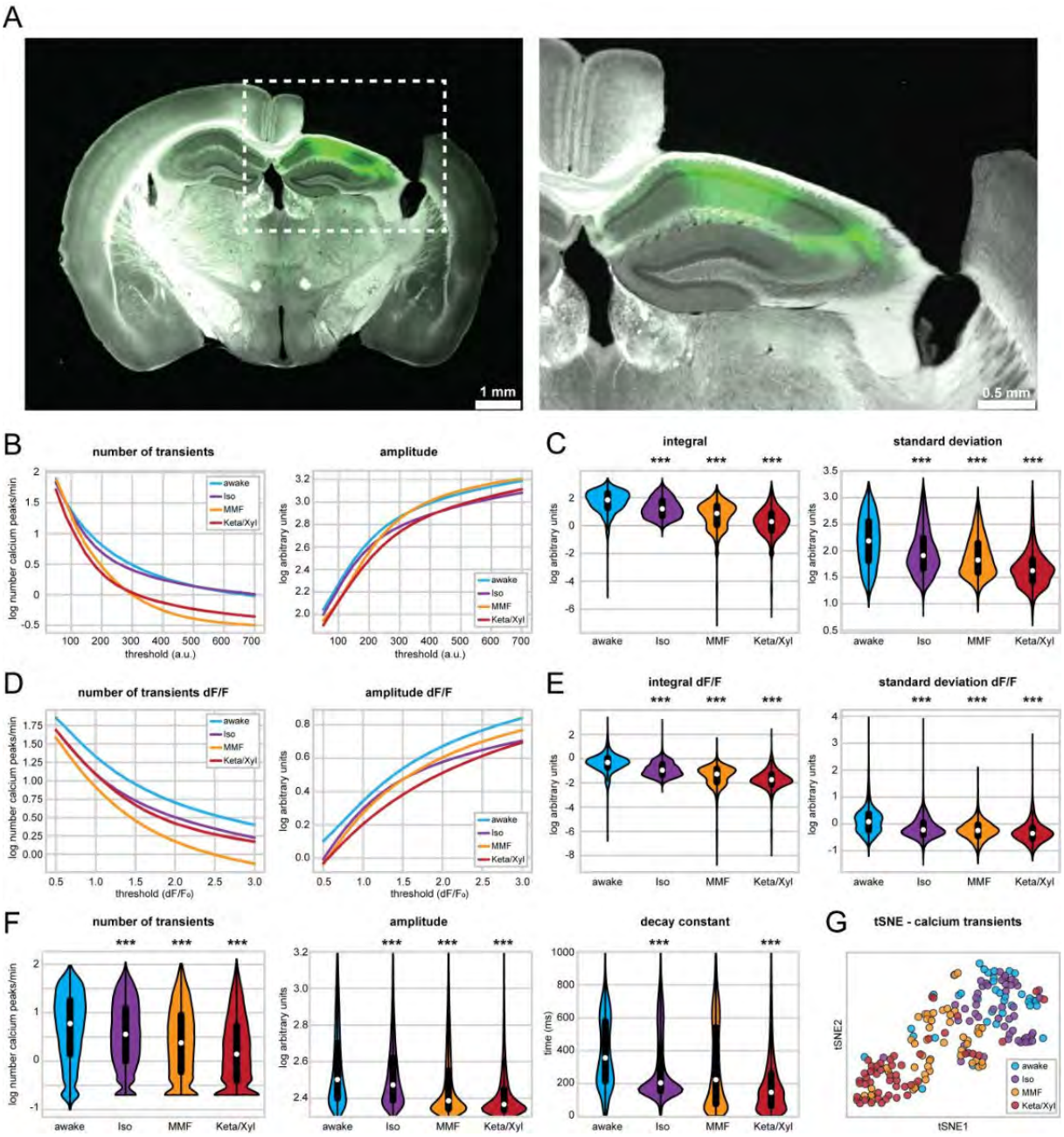

S4 Fig. Oscillations of calcium transients are distinctly altered by Iso, MMF, and Keta/Xyl.

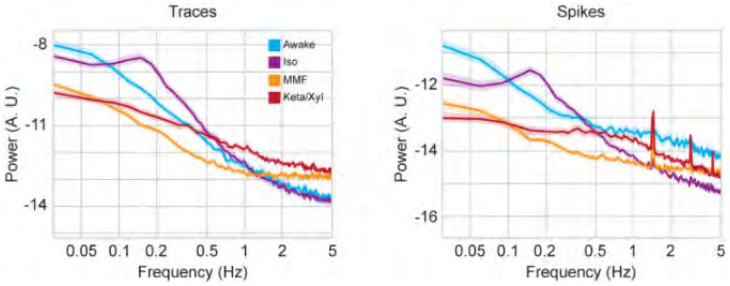

S5 Fig. **Alignment and ROI matching of imaging sessions.**

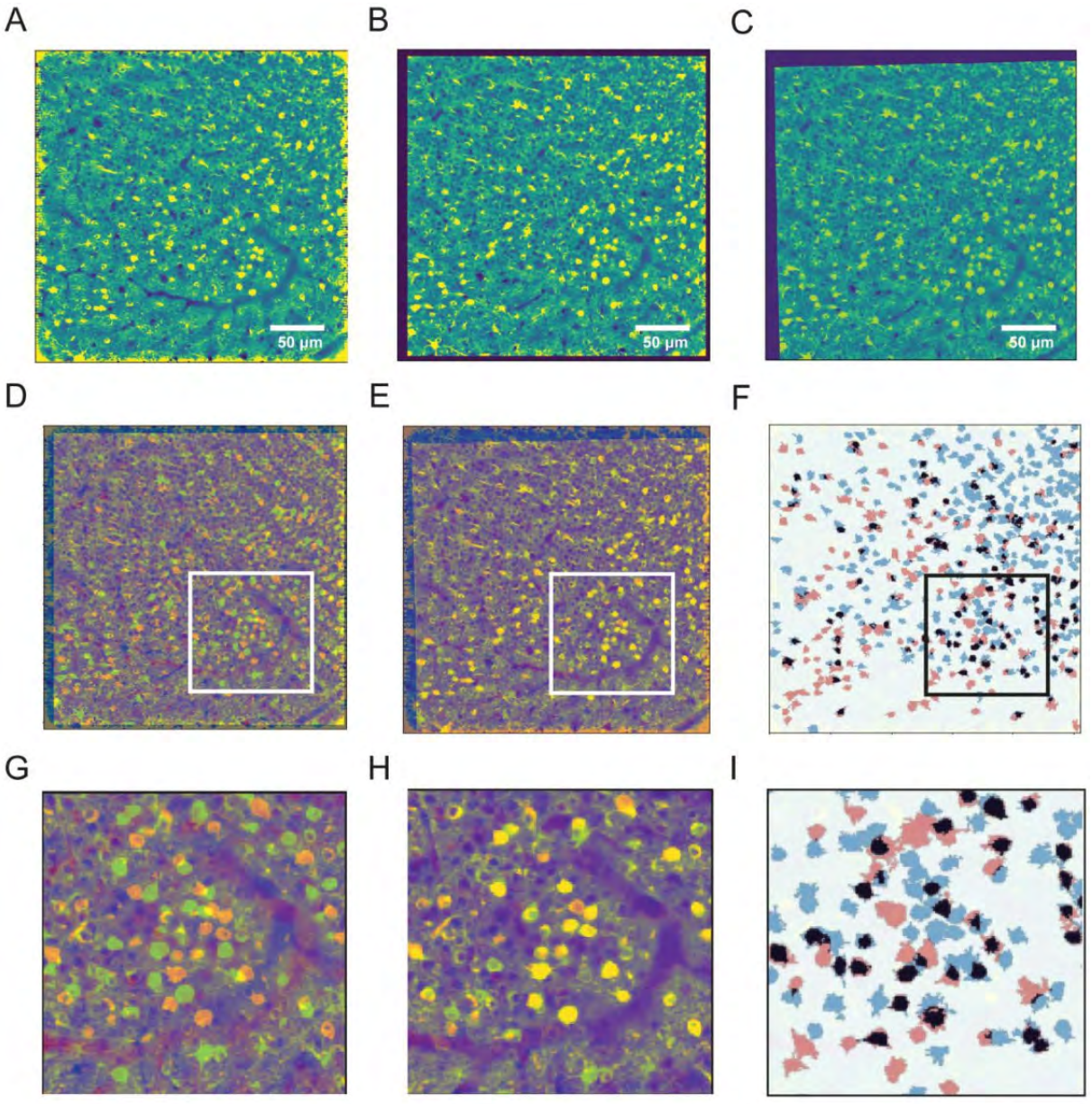

S6 Fig. ID assignment and comparison of calcium transients in identified neurons between pairs of conditions.

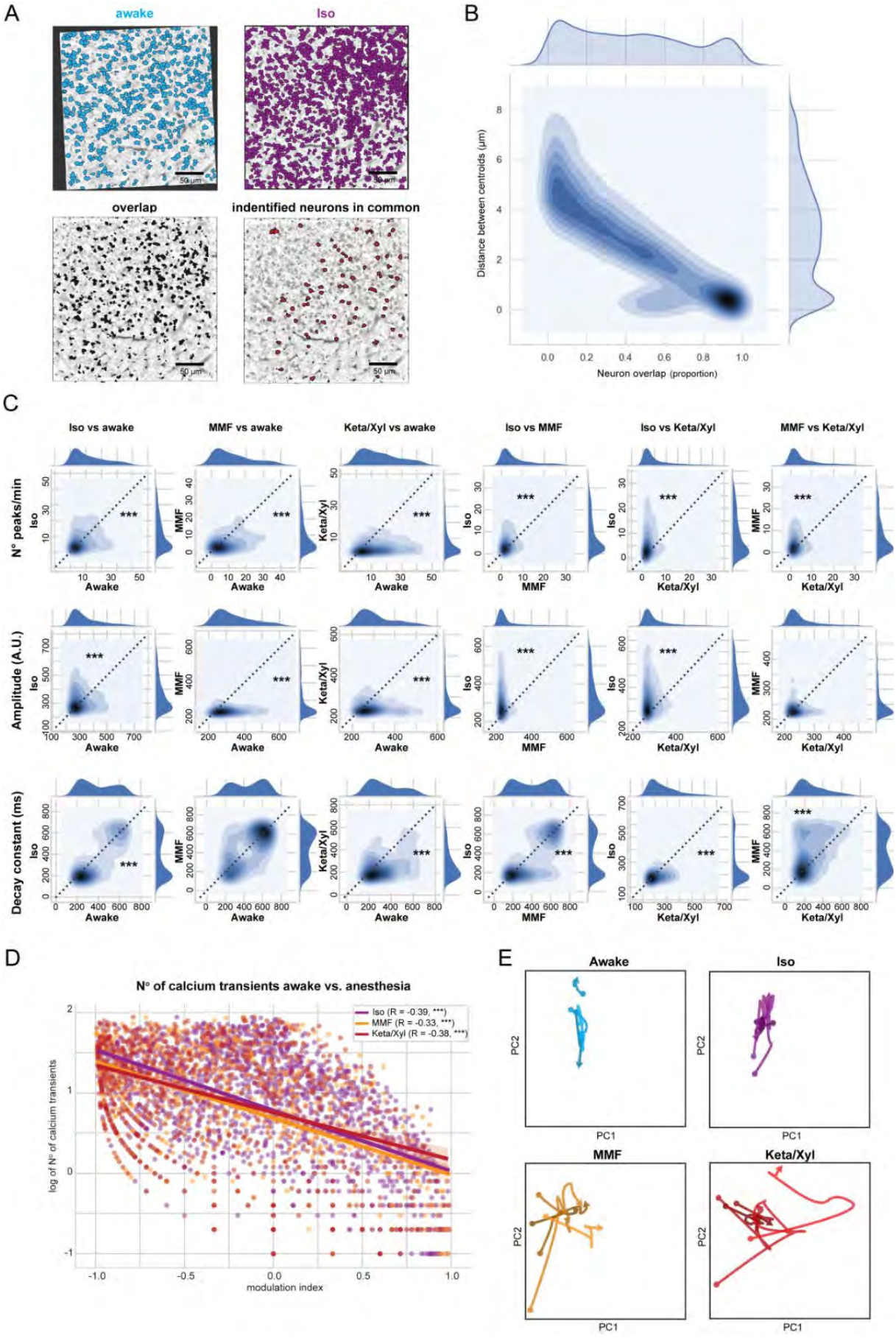

S7 Fig. Additional correlation analysis.

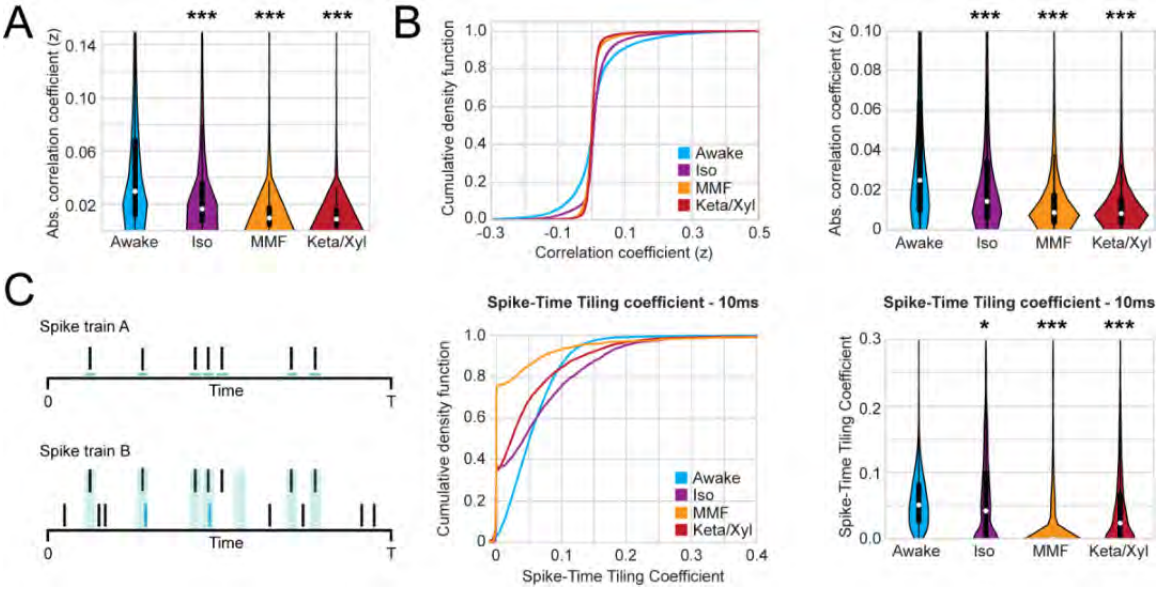

S8 Fig. Clustering analysis of deconvolved calcium imaging data.

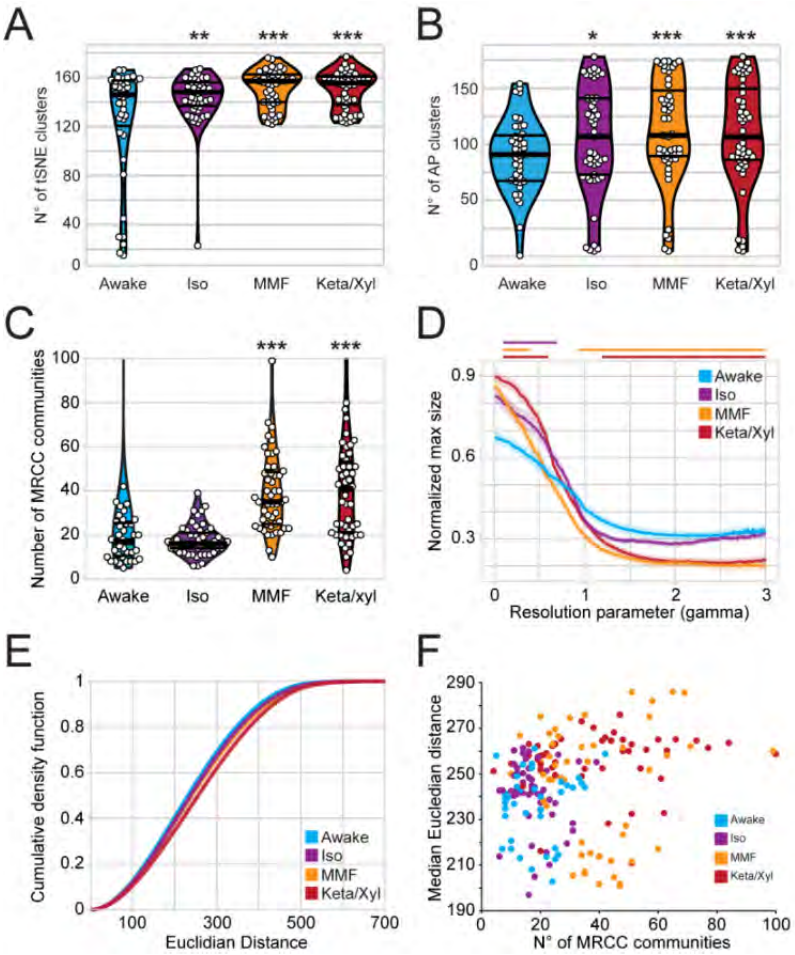

S9 Fig. Sleep scoring.

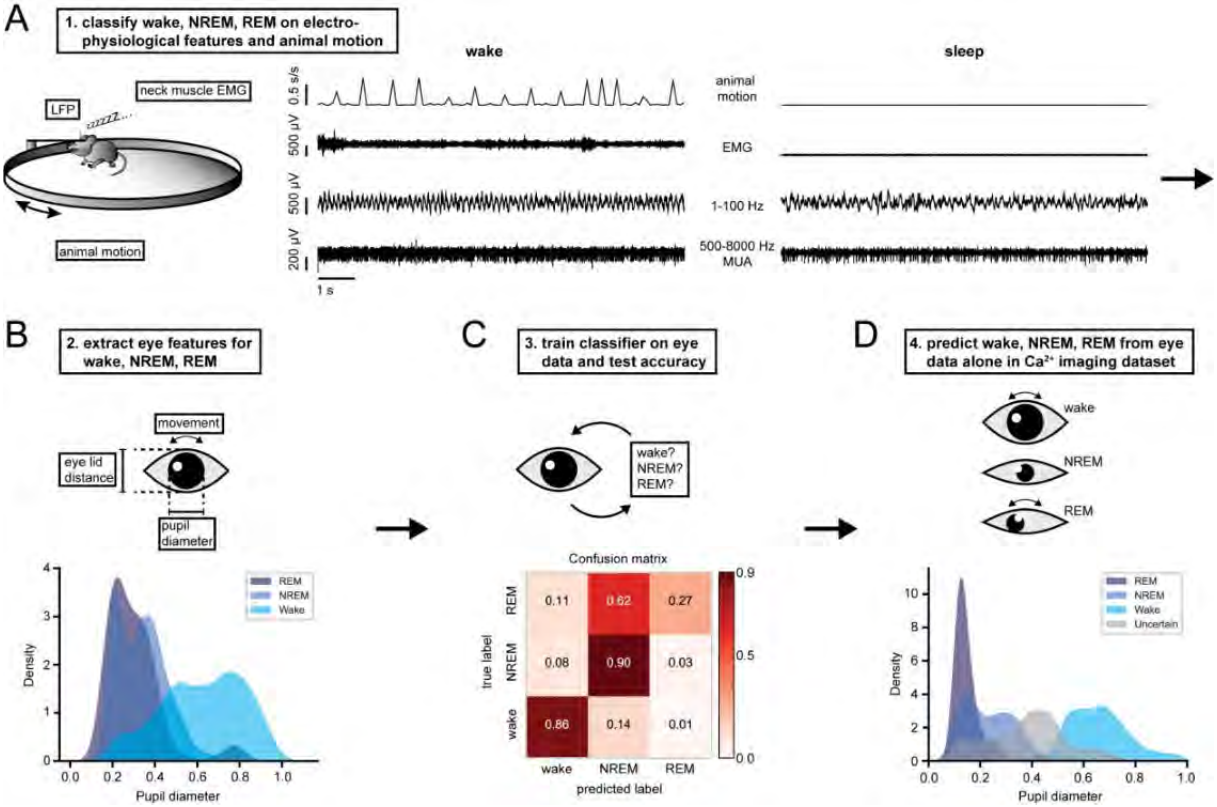

S10 Fig. Chronic spine imaging.

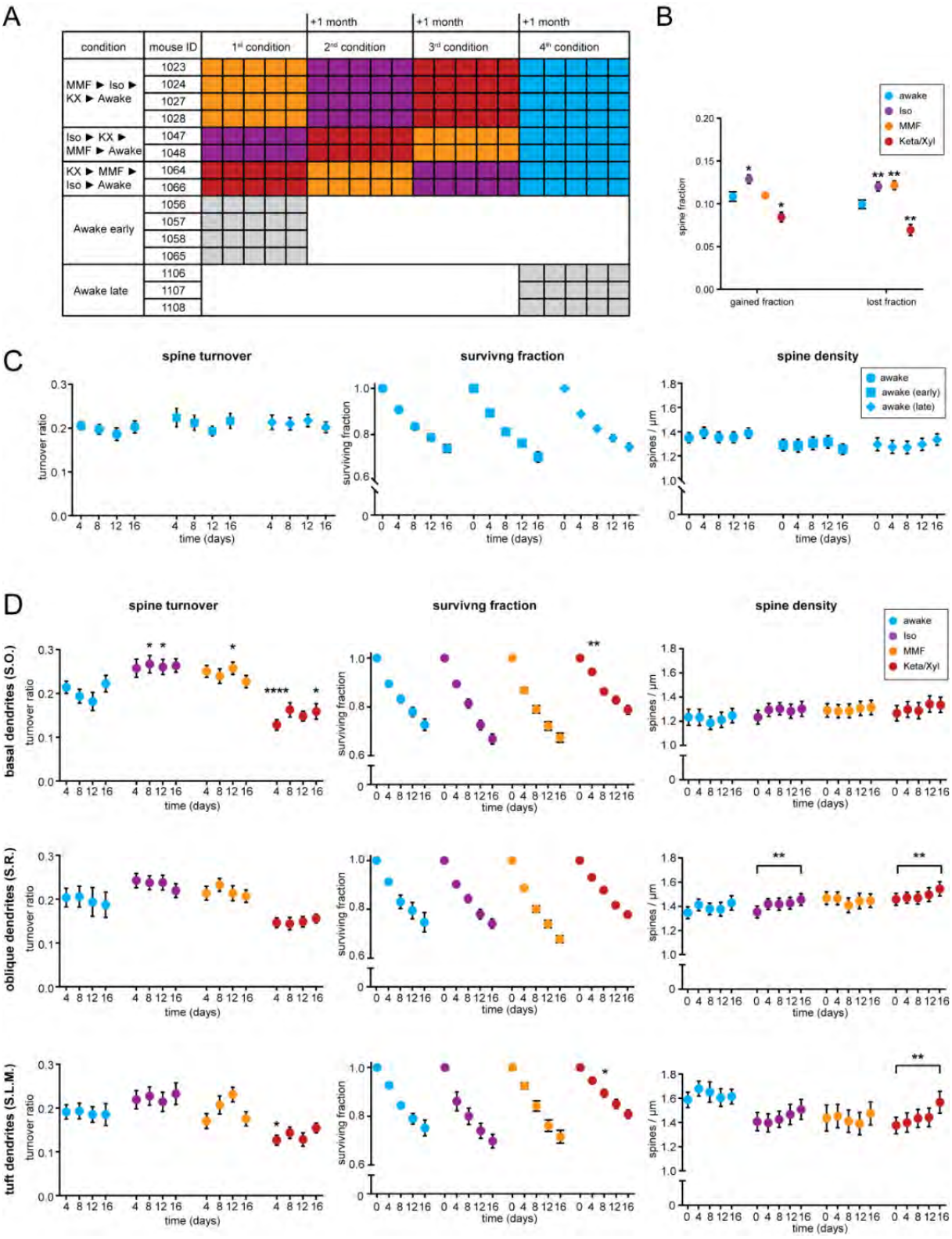

S11 Fig. Comparison of the effect of Iso, MMF, and Keta/Xyl on episodic memory consolidation.

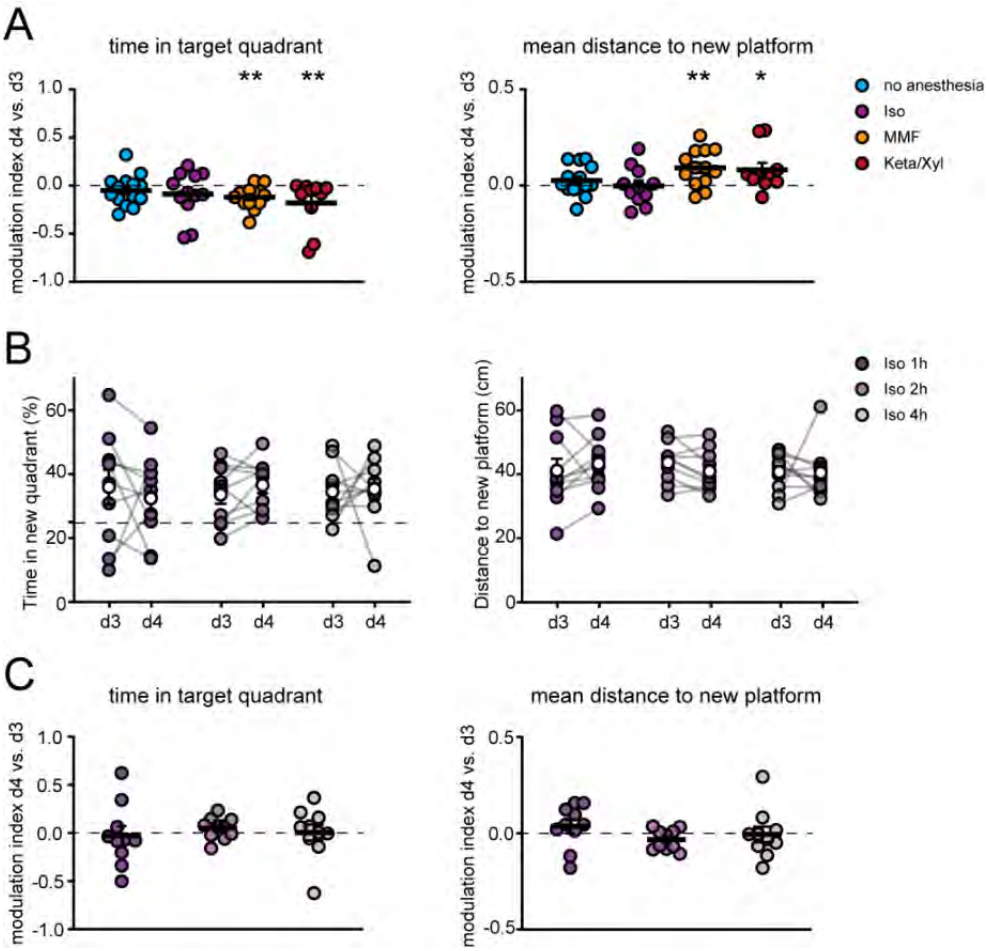

RESEARCH ARTICLE

Gamma activity accelerates during prefrontal development

Sebastian H Bitzenhofer†*, Jastyn A Pöpplau, Ileana Hanganu-Opatz*

Institute of Developmental Neurophysiology, Center for Molecular Neurobiology, University Medical Center Hamburg-Eppendorf, Hamburg, Germany

Abstract Gamma oscillations are a prominent activity pattern in the cerebral cortex. While gamma rhythms have been extensively studied in the adult prefrontal cortex in the context of cognitive (dys)functions, little is known about their development. We addressed this issue by using extracellular recordings and optogenetic stimulations in mice across postnatal development. We show that fast rhythmic activity in the prefrontal cortex becomes prominent during the second postnatal week. While initially at about 15 Hz, fast oscillatory activity progressively accelerates with age and stabilizes within gamma frequency range (30–80 Hz) during the fourth postnatal week. Activation of layer 2/3 pyramidal neurons drives fast oscillations throughout development, yet the acceleration of their frequency follows similar temporal dynamics as the maturation of fast-spiking interneurons. These findings uncover the development of prefrontal gamma activity and provide a framework to examine the origin of abnormal gamma activity in neurodevelopmental disorders.

***For correspondence:**
sbitzenhofer@ucsd.edu (SHB);
ileana.hanganu-opatz@zmnh.uni-hamburg.de (IH-O)

Present address: †Center for Neural Circuits and Behavior, Department of Neurosciences, University of California, San Diego, United States

Competing interests: The authors declare that no competing interests exist.

Funding: See page 15

Received: 10 March 2020
Accepted: 06 November 2020
Published: 18 November 2020

Reviewing editor: Martin Vinck, Ernst Strüngmann Institute (ESI) for Neuroscience in Cooperation with Max Planck Society, Germany

Introduction

Synchronization of neuronal activity in fast oscillatory rhythms is a commonly observed feature in the adult cerebral cortex. While its exact functions are still a matter of debate, oscillatory activity in gamma frequency range has been proposed to organize neuronal ensembles and to shape information processing in cortical networks (***Singer, 2018***; ***Cardin, 2016***; ***Sohal, 2016***). Gamma activity emerges from reciprocal interactions between excitatory and inhibitory neurons. In the visual cortex, fast inhibitory feedback via soma-targeting parvalbumin (PV)-expressing inhibitory interneurons leads to fast gamma activity (30–80 Hz) (***Cardin et al., 2009***; ***Chen et al., 2017***), whereas dendrite-targeting somatostatin (SOM)-expressing inhibitory interneurons contribute to beta/low gamma activity (20–40 Hz) (***Chen et al., 2017***; ***Veit et al., 2017***). A fine-tuned balance between excitatory drive and inhibitory feedback is mandatory for circuit function underlying cognitive performance. Interneuronal dysfunction and ensuing abnormal gamma activity in the medial prefrontal cortex (mPFC) have been linked to impaired cognitive flexibility (***Cho et al., 2015***). Moreover, imbalance between excitation and inhibition in cortical networks and resulting gamma disruption have been proposed to cause cognitive disabilities in autism and schizophrenia (***Cho et al., 2015***; ***Cao et al., 2018***; ***Rojas and Wilson, 2014***).

Despite substantial literature linking cognitive abilities and disabilities to gamma oscillations in the adult mPFC, the ontogeny of prefrontal gamma activity is poorly understood. This knowledge gap is even more striking considering that abnormal patterns of fast oscillatory activity have been described at early postnatal age in autism and schizophrenia mouse models (***Chini et al., 2020***; ***Richter et al., 2019***; ***Hartung et al., 2016***). Knowing the time course of prefrontal gamma maturation is essential for understanding the developmental aspects of mental disorders.

To this end, we performed an in-depth investigation of the developmental profile of gamma activity in the mouse mPFC from postnatal day (P) five until P40. We show that pronounced fast oscillatory activity emerges toward the end of the second postnatal week and increases in frequency and amplitude with age. While activation of layer 2/3 pyramidal neurons (L2/3 PYRs) drives fast

oscillatory activity throughout development, the acceleration of its frequency follows the same dynamics as the maturation of inhibitory feedback and fast-spiking (FS) interneurons.

Results

Fast oscillatory activity in the prefrontal cortex accelerates during development

Extracellular recordings in the mPFC of anesthetized and non-anesthetized P5-40 mice revealed that oscillatory activity at fast frequencies (>12 Hz) can be detected at the beginning of the second postnatal week. The temporal dynamics of these fast oscillations are similar in the two states, yet their magnitude is higher in non-anesthetized mice, as previously described (***Chini et al., 2019***). The magnitude of fast oscillations increases with age (Mann-Kendall trend test, $p=3.93\times10^{-22}$, n = 114 recordings, tau-b 0.625) and can be detected as distinct peaks in power spectra at the end of the second postnatal week (***Figure 1a,b***). The peak frequency of these oscillations gradually increases with age (Mann-Kendall trend test, $p=2.73\times10^{-8}$, n = 114 recordings, tau-b 0.361), starting at ~ 20 Hz at P12 and reaching the characteristic gamma frequency of 50–60 Hz at P25 (***Figure 1b–d***). Both, peak strength and peak frequency, do not change after P25. A linear regression model of peak frequency and peak amplitude shows significant correlation with age (n = 114, df = 111, $R^2 = 0.542$, $p=5.48\times10^{-20}$; ANOVA: peak frequency $F(1,111)=17.8$, $p=4.86\times10^{-5}$, peak amplitude $F(1,111)=74.4$, $p=5.05\times10^{-14}$).

FS interneuron maturation resembles the time course of gamma development

FS PV-expressing interneurons have been identified as key elements for the generation of oscillatory activity in gamma frequency range in the adult cortex (***Cardin et al., 2009***). To assess whether the developmental gamma dynamics relate to FS PV-expressing interneuron maturation, we performed immunohistochemistry and single unit analysis in P5-40 mice.

First, immunostainings showed that PV expression in the mPFC starts at the end of the second postnatal week, increases until P25 and stabilizes afterwards (Mann-Kendall trend test, $p=1.29\times10^{-7}$, n = 38 mice, tau-b 0.623) (***Figure 2a***). These dynamics over age follow a similar trend as the changes in peak power and peak frequency of the fast oscillations described above. In

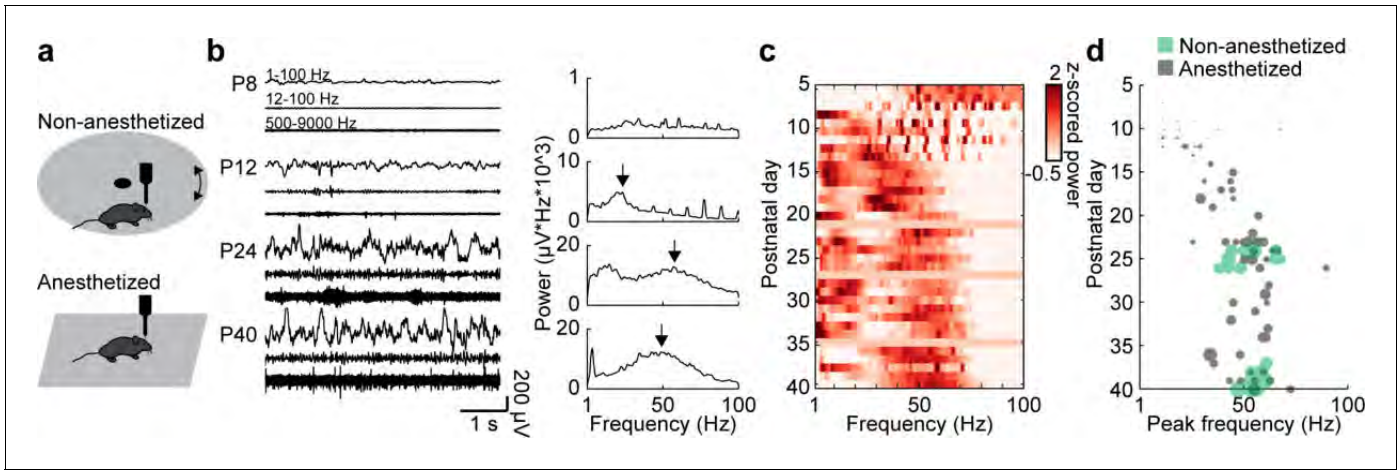

Figure 1. Development of gamma activity in the mouse mPFC. (**a**) Schematic of extracellular recordings in the mPFC of anesthetized and non-anesthetized P5-40 mice. (**b**) Characteristic examples of extracellular recordings of local field potentials (LFP) and multi-unit activity (MUA) at different ages after band-pass filtering (left) and the corresponding power spectra (right). (**c**) Z-scored average power spectra of spontaneous oscillatory activity for P5-40 mice (n = 114 recordings from 100 mice). (**d**) Scatter plot displaying peak frequencies of fast oscillations (12–100 Hz) during postnatal development of anesthetized (gray, n = 80 recordings/mice) and non-anesthetized mice (green, n = 34 recordings from 20 mice). Marker size displays peak strength. (See ***Supplementary file 1*** for a summary of experimental conditions. See ***Supplementary file 2*** for statistics.).

The online version of this article includes the following source data for figure 1:

Source data 1. Source data for ***Figure 1b***.

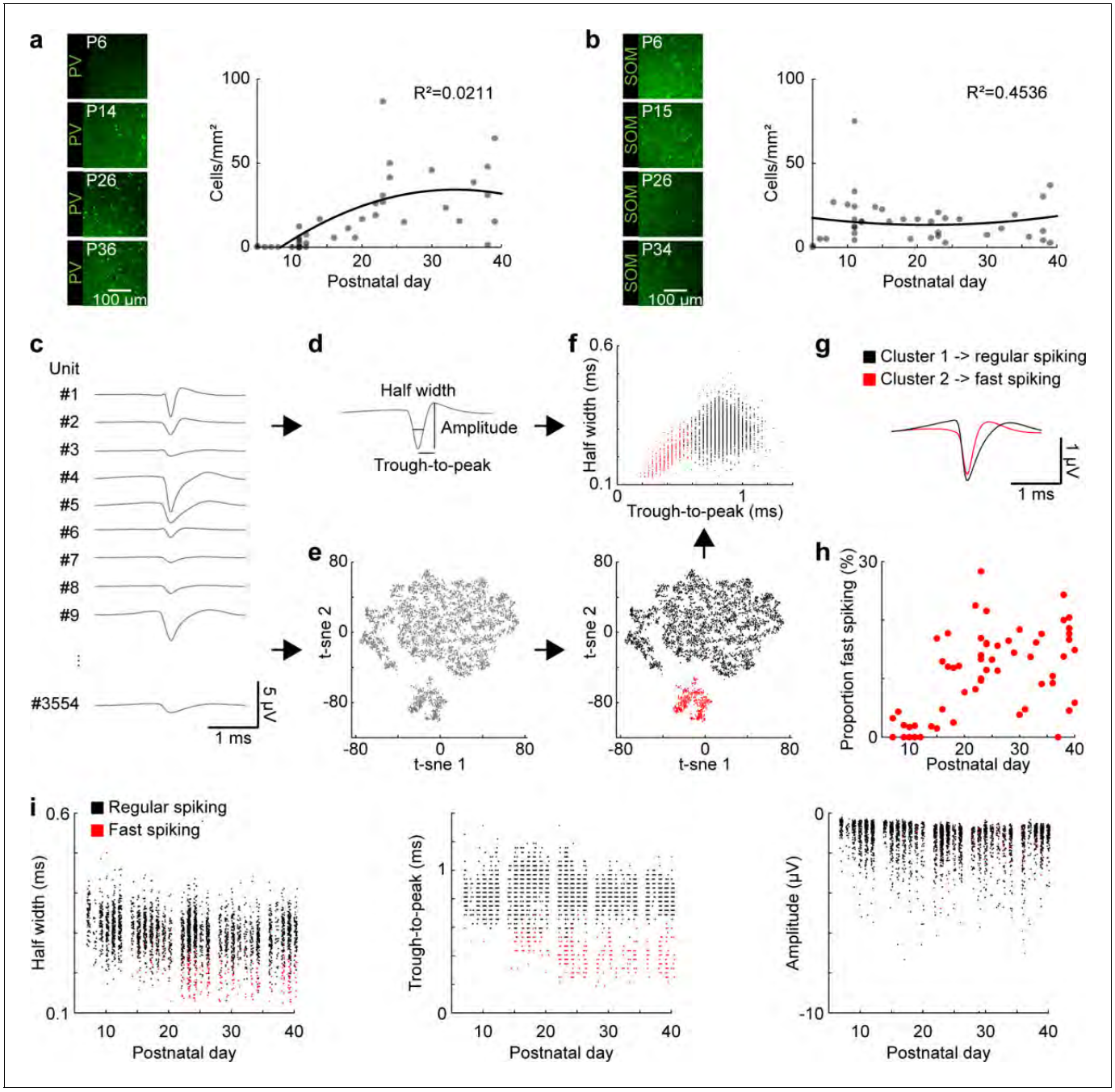

Figure 2. Development of FS interneurons in the mouse mPFC. (**a**) Left, examples of PV immunostaining in the mPFC at different ages. Right, scatter plot displaying the density of PV-immunopositive neurons in the mPFC of P5-40 mice (n = 38 mice). (**b**) Same as (**a**) for SOM-immunopositive neurons (n = 39 mice). (**c**) Example mean waveforms of extracellular recorded single units from P5-40 mice. (**d**) Schematic showing features classically used to distinguish RS and FS units in adult mice. (**e**) Left, scatter plot showing the first two components of a t-sne dimensionality reduction on the mean waveforms for all units recorded from P5-40 mice (n = 3554 units from 66 recordings/mice). Right, same as left with the first two clusters obtained by hierarchical clustering labeled in black and red. (**f**) Scatter plot of half width and trough-to-peak time for cluster 1 (black) and 2 (red). (**g**) Mean waveform for cluster 1 (black) and 2 (red). (**h**) Scatter plot showing the proportion of FS units for P5-40 mice. (**i**) Scatter plots showing classic spike shape features for P5-40 for cluster 1 (RS, black) and 2 (FS, red). (See ***Supplementary file 1*** for a summary of experimental conditions. See ***Supplementary file 2*** for statistics).

The online version of this article includes the following source data and figure supplement(s) for figure 2:

Source data 1. Source data for ***Figure 2a,b***.
Source data 2. Source data for ***Figure 2f***.
Source data 3. Source data for ***Figure 2g***.

Figure 2 continued on next page

Figure 2 continued

Source data 4. Source data for ***Figure 2h***.
Source data 5. Source data for ***Figure 2i***.
Figure supplement 1. t-sne dimensionality reduction.
Figure supplement 1—source data 1. Source data for ***Figure 2—figure supplement 1b–d***.

contrast, the number of SOM positive neurons does not significantly vary along postnatal development (Mann-Kendall trend test, p=0.99, n = 39 mice, tau-b −0.003) (***Figure 2b***).

Second, to directly assess the functional maturation of FS putatively PV-expressing neurons, we used bilateral extracellular recordings and identified single unit activity (SUA). The classically used action potential features to distinguish adult FS and regular-spiking (RS) neurons (i.e. trough to peak time and half width) cannot be applied during early development, because of a strong overlap of these features. Therefore, we developed an algorithm to classify RS and FS units using dimensionality reduction with t-Distributed Stochastic Neighbor Embedding (t-sne) on the mean waveforms of all units recorded across development, followed by hierarchical clustering based on pairwise Euclidean distance (***Figure 2c–e***). This approach resulted in an unbiased detection of FS units across age (***Figure 2f,g***). Of note, a more detailed analysis revealed that the dimensionality reduction based on mean waveforms correlates with features like trough to peak and half width, but is less affected by age, cortical layer, and amplitude (***Figure 2—figure supplement 1***). The classification of units with this method revealed that FS units start to be detected at the end of the second postnatal week. Their number gradually increased until P25 (Mann-Kendall trend test, $p=1.44\times10^{-7}$, n = 66 recordings, tau-b 0.458) (***Figure 2h***). A comparison of the classical features across age showed that trough-to-peak duration (Mann-Kendall trend test, RS, $p=4.57\times10^{-5}$, n = 3172 units, tau-b −0.051; FS, $p=9.23\times10^{-11}$, n = 382 units, tau-b −0.236), half width (Mann-Kendall trend test, RS, $p=1.61\times10^{-28}$, n = 3172 units, tau-b −0.134; FS, $p=5.17\times10^{-17}$, n = 382 units, tau-b −0.295), and negative amplitude (Mann-Kendall trend test, RS, $p=4.45\times10^{-22}$, n = 3172 units, tau-b −0.117; FS, $p=3.82\times10^{-6}$, n = 382 units, tau-b −0.163) of RS and FS units gradually decreased from the end of the second

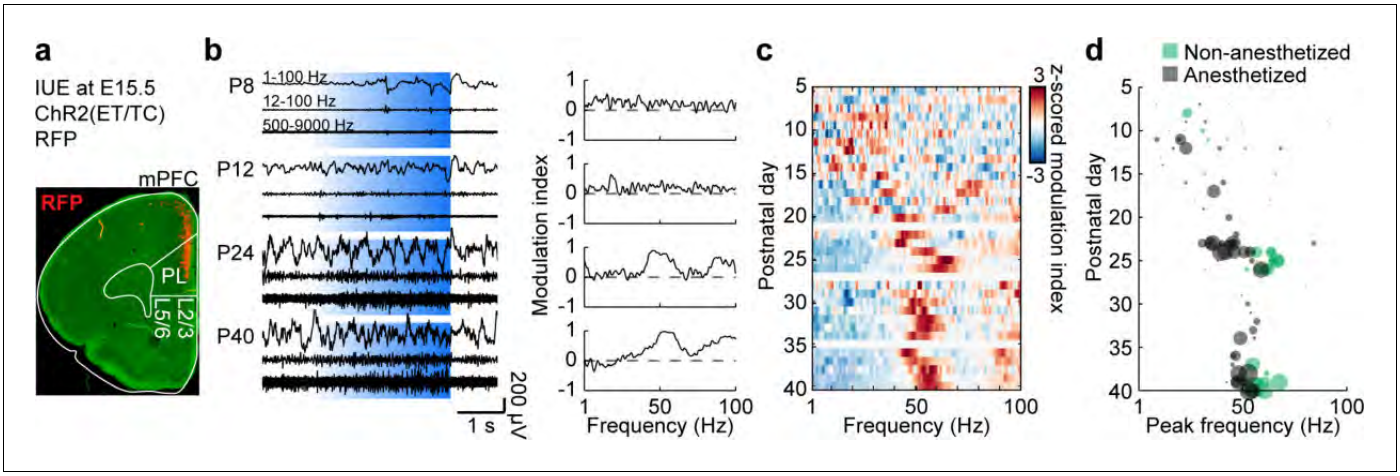

Figure 3. Development of L2/3 PYR-driven gamma in the mPFC. (**a**) ChR2(ET/TC)−2A-RFP-expression in L2/3 PYRs in mPFC after IUE at E15.5 in a coronal slice of a P10 mouse. (**b**) Characteristic examples of extracellular recordings of LFP and MUA during ramp light stimulations (473 nm, 3 s) of prefrontal L2/3 PYRs at different ages (left) and the corresponding MI of power spectra (right). (**c**) Z-scored average MI of power spectra for P5-40 mice (n = 115 recordings from 101 mice). (**d**) Scatter plot displaying stimulus induced peak frequencies during postnatal development for anesthetized (gray, n = 80 recordings/mice) and non-anesthetized mice (green, n = 35 recordings from 21 mice). Marker size displays peak strength. (See ***Supplementary file 1*** for a summary of experimental conditions. See ***Supplementary file 2*** for statistics).
The online version of this article includes the following source data and figure supplement(s) for figure 3:

Source data 1. Source data for ***Figure 3d***.
Figure supplement 1. Control stimulations of L2/3 PYRs in the mPFC.
Figure supplement 1—source data 1. Source data for ***Figure 3—figure supplement 1c***.

postnatal week until P25. However, the most prominent changes were detected for through-to-peak duration and half width of FS units (***Figure 2i***). A linear regression model of single unit features shows significant correlation with age (n = 52, df = 44, R^2 = 0.550, p=2.31×10^{-7}; see ***Supplementary file 2*** for details). These results are consistent with a detailed description of the physiological development of prefrontal PV-expressing interneurons performed in brain slices (***Miyamae et al., 2017***).

Thus, in line with the immunohistochemical examination, the analysis of single units showed that FS putatively PV-positive interneurons show similar dynamics of maturation as fast oscillations recorded in the mPFC of P5-40 mice.

Activation of L2/3 pyramidal neurons drives fast oscillations with similar acceleration across development as spontaneous activity

Besides FS interneurons, L2/3 PYRs in mPFC have been found to induce fast oscillations in the mPFC of P8-10 mice. Their non-rhythmic activation (but not activation of L5/6PYRs) drives oscillatory activity peaking within 15–20 Hz range (***Bitzenhofer et al., 2017a***; ***Bitzenhofer et al., 2017b***), similar to the peak frequency of spontaneous network activity at this age. To test if L2/3 PYRs-driven activity also accelerates with age, we optogenetically manipulated these neurons in P5-40 mice. Stable expression of the light-sensitive channelrhodopsin two derivate E123T T159C (ChR2(ET/TC)) restricted to about 25% of PYR in L2/3 of the mPFC was achieved by in utero electroporation (IUE) at embryonic day (E) 15.5 (***Figure 3a***). Optogenetic stimulation with ramps of steadily increasing light power (473 nm, 3 s, 30 repetitions) were performed during extracellular recordings in the mPFC. As previously shown, this type of stimulation activates the network without forcing a specific rhythm (***Bitzenhofer et al., 2017a***).

Similar to spontaneous activity, activating L2/3 PYRs induced oscillatory activity with a gradually increasing frequency during development (***Figure 3b–d***). Consistent peaks in the modulation index (MI) of power spectra were detected at 15–20 Hz at the beginning of the second postnatal week and increased in frequency (Mann-Kendall trend test, p=7.69×10^{-6}, n = 115 recordings, tau-b 0.288) and amplitude (Mann-Kendall trend test, p=1.04×10^{-9}, n = 115 recordings, tau-b 0.392) until reaching stable values within 50–60 Hz at P25. A linear regression model of peak frequency and peak amplitude shows significant correlation with age (n = 115, df = 112, R^2 = 0.364, p=3.72×10^{-12}; ANOVA: peak frequency F(1,112)=13.9, p=2.95×10^{-4}, peak amplitude F(1,112)=43.8, p=1.26×10^{-9}). Control stimulations with light that does not activate ChR2(ET/TC) (594 nm, 3 s, 30 repetitions) did not induce activity and led to the detection of unspecific peak frequencies (Mann-Kendall trend test, p=0.09, n = 111 recordings, tau-b 0.111) and low amplitudes (Mann-Kendall trend test, p=0.74, n = 111 recordings, tau-b 0.022) (***Figure 3—figure supplement 1***).

Peak frequency and amplitude of activity induced by ramp light stimulation are significantly correlated with peak frequency and amplitude of spontaneous activity at the level of individual recordings (peak frequency n = 114, df = 112, R^2 = 0.16, p=6.00×10^{-6}; peak amplitude n = 114, df = 112, R^2 = 0.206, p=2.30×10^{-7}). Thus, L2/3 PYR-driven activity in the mPFC follows the same developmental dynamics as spontaneous activity indicating the importance of L2/3 PYRs for gamma maturation.

The rhythmicity of pyramidal cell and interneuron firing follows similar development as accelerating gamma activity in mPFC

To assess the contribution of distinct cell types to the emergence of gamma during postnatal development, we compared the firing of RS units, mainly corresponding to PYRs, and FS units, mainly corresponding to PV-expressing interneurons, during ramp light stimulations of L2/3 PYRs in P5-40 mice (***Figure 4a,b***, ***Figure 4—figure supplement 1***).

The average firing rate of RS and FS units in the stimulated hemisphere in the mPFC increased in response to ramp stimulation (***Figure 4c***). While ramp-induced firing rate changes averaged for RS units (Mann-Kendall trend test, p=0.07, n = 7 age groups, tau-b 0.619) became more prominent at older age, the average firing rate changes were stable for FS units (Mann-Kendall trend test, p=0.88, n = 7 age groups, tau-b 0.047) (***Figure 4d***). At the level of individual units, most RS units showed positive modulation of their firing rates in response to stimulation at P5-10, whereas at older age the proportion of positively modulated units decreased (Mann-Kendall trend test, p=1.52×10^{-14},

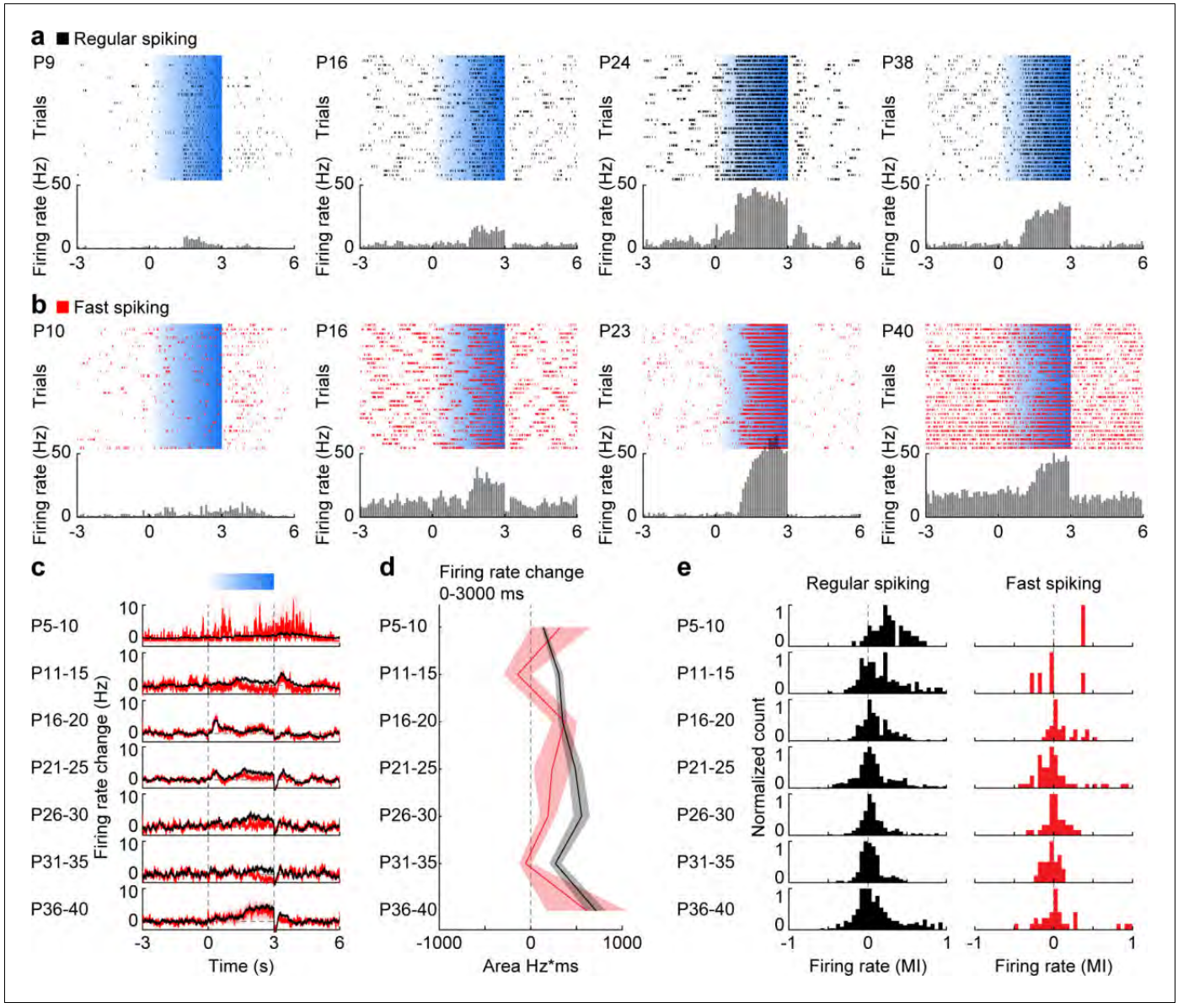

Figure 4. Development of RS and FS unit activity during L2/3 PYR-driven gamma in the mPFC. (**a**) Raster plots and peri-stimulus time histograms for activated RS example units in response to ramp light stimulation (3 s, 473 nm, 30 repetitions) of prefrontal PYRs at different ages. (**b**) Same as (**a**) for FS units. (**c**) Average firing rate change of RS (black, n = 1824 units from 66 recordings/mice) and FS (red, n = 226 units from 66 recordings/mice) units in response to ramp light stimulation of prefrontal L2/3 PYRs for different age groups. (**d**) Line plot displaying the average firing rate changes of RS and FS units during ramp light stimulation for different age groups. (**e**) Histograms of the MI of firing rates in response to ramp light stimulation for RS and FS units. (Average data is displayed as mean ± sem. See ***Supplementary file 1*** for a summary of experimental conditions. See ***Supplementary file 2*** for statistics.).

The online version of this article includes the following source data and figure supplement(s) for figure 4:

Source data 1. Source data for ***Figure 4d***.

Figure supplement 1. RS and FS unit activity during L2/3 PYR-driven gamma in the mPFC.

n = 1821 units, tau-b −0.123) (***Figure 4e***). In contrast, individual FS units showed both positive and negative modulation of activity throughout development (Mann-Kendall trend test, p=0.91, n = 225 units, tau-b −0.005), yet the low number of FS units at young age precluded clear conclusions. Thus, during early postnatal development most RS units are activated by ramp light stimulations but only moderately increase their firing rate. During late postnatal development some RS units strongly increase their firing rate, whereas others reduce their firing rate.

Next, we tested whether RS and FS units engage in rhythmic activity and calculated autocorrelations and spike-triggered LFP power of individual units. While no clear peaks of rhythmicity were found during spontaneous activity before stimulations (***Figure 5—figure supplement 1***), autocorrelations showed that a subset of RS and FS units fire rhythmically in response to ramp light stimulation of prefrontal L2/3 PYRs (***Figure 5a***). The power of autocorrelations revealed that prominent rhythmic firing starts at about P15 and increases in frequency before it stabilizes at about P25 (***Figure 5b***). A multifactorial ANOVA shows significant effects for age group ($F(6,153093) = 25.4$, $p=2.21\times10^{-30}$) and frequency ($F(99,153093) = 492.7$, $p=0.000$), but not between RS and FS units ($F(1,153093) = 1.56$, $p=0.211$). Next, we calculated the power of averaged spike-triggered LFPs to

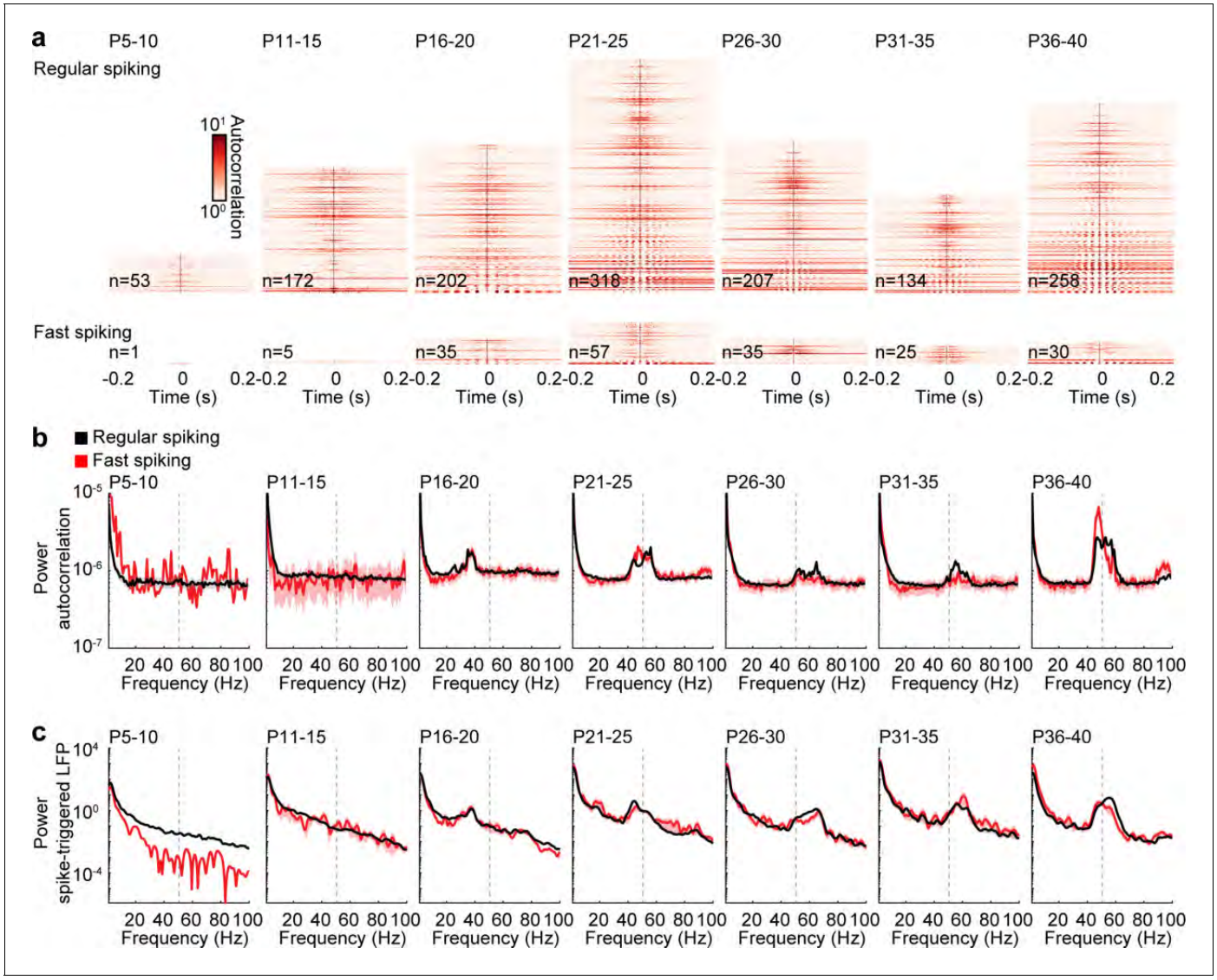

Figure 5. Rhythmicity of RS and FS units across age. (**a**) Color-coded autocorrelations of prefrontal RS (top) and FS (bottom) units during ramp light stimulation (3 s, 473 nm) for different age groups. Each row represents one unit (only units firing > 1 Hz are included). (**b**) Average autocorrelation power of RS (black) and FS (red) units during ramp light stimulation for different age groups. (**c**) Average power of mean spike-triggered LFP of RS (black) and FS (red) units during ramp light stimulation for different age groups. (Average data is displayed as mean ± sem. See ***Supplementary file 1*** for a summary of experimental conditions. See ***Supplementary file 2*** for statistics.).

The online version of this article includes the following figure supplement(s) for figure 5:

Figure supplement 1. Rhythmicity of RS and FS units during spontaneous activity.

Figure supplement 2. Additional measures for rhythmicity of RS and FS units.

Figure supplement 3. Crosscorrelations of RS and FS units during spontaneous activity.

examine the interaction of single unit rhythmicity with oscillatory LFP activity. The development of spike-triggered LFP power is consistent with the development of single unit autocorrelation power (multifactorial ANOVA: unit type F(1,814825) = 277.2, $p=3.12\times10^{-62}$, age group F (6,814825) = 847.4, p=0.000, frequency F(400, 814825)=614.5, p=0.000), indicating that single unit rhythmicity of local neurons is reflected in the prefrontal LFP. Consistent results were obtained for inter-spike intervals and pairwise phase consistency (***Figure 5—figure supplement 2***), as well as crosscorrelations between simultaneously recorded unit pairs (***Figure 5—figure supplement 3***). RS units show higher values at lower instantaneous frequencies for inter-spike intervals than FS units, suggesting that they tend to skip cycles of induced gamma activity (***Figure 5—figure supplement 2d***). Overall, the dynamics of RS and FS rhythmicity are similar to the development of spontaneous and stimulated gamma activity, indicating close interactions between RS and FS units during fast oscillations.

Inhibitory feedback maturation resembles the dynamics of gamma development

Stimulation of prefrontal L2/3 PYRs with short light pulses (3 ms, 473 nm) at different frequencies was used to test the maximal firing frequencies of RS and FS units in P5-40 mice. Pulse stimulations induced a short increase of firing for both RS and FS units (***Figure 6a***). Confirming previous results (***Bitzenhofer et al., 2017a***), RS units did not follow high stimulation frequencies in mice younger than P11 and showed strong attenuation in the response to repetitive pulses. With ongoing development, this attenuation at high stimulation frequencies became less prominent for RS and FS units (***Figure 6b***), yet the low number of FS units at young age precluded clear conclusions. Inter-spike intervals of individual units revealed several peaks at fractions of the stimulation frequency for RS and FS, especially at higher stimulation frequencies (***Figure 6—figure supplement 1***). These data suggest that individual units do not fire in response to every light pulse in the pulse train but skip some pulses.

To assess the development of inhibitory feedback, we examined the firing rate changes of RS and FS units from P5-40 mice in response to individual 3 ms-long light pulses. The firing rate of RS and FS units transiently increased after pulse stimulation (***Figure 6c***). This effect significantly increased with age for RS units (Mann-Kendall trend test, p=0.04, n = 7 age groups, tau-b 0.714), but not for FS units (Mann-Kendall trend test, p=0.07, n = 7 age groups, tau-b 0.619) (***Figure 6d***). Next, we analyzed the delays of light-induced firing peaks for the two populations of units. The similar delays observed for RS and FS units suggest that the majority of RS units are non-transfected neurons, that are indirectly activated. The initial peak of increased firing was followed by reduced firing rates for RS and FS units only during late postnatal development (***Figure 6e,f***). The magnitude and duration of this firing depression gradually augmented with age and reached significance for RS units (Mann-Kendall trend test, RS, $p=6.9\times10^{-3}$, n = 7 age groups, tau-b −0.905; FS, p=0.07, n = 7 age groups, tau-b −0.619). Thus, the inhibitory feedback in response to L2/3 PYR firing in the mPFC increases with age.

FS characteristics and rhythmicity of single units relate to the frequency of fast oscillatory activity

We used stepwise linear regression models to identify the most important correlations of single unit measures with gamma activity across development at the level of individual mice. The models included the following predictor variables (average values for each mouse): (i) proportion of FS units, action potential half width, trough-to-peak, and amplitude for RS and FS units (see ***Figure 2***), (ii) firing rate change, peak power of autocorrelation, and peak power of spike-triggered LFP for RS and FS units during ramp light stimulation (see ***Figure 5***), and (iii) firing rate change for RS and FS units 0–10 ms and 10–50 ms after pulse stimulation (see ***Figure 6***). Stepwise linear regression to predict the peak frequency during ramp light stimulation identified action potential half width of FS units, as well as peak power of autocorrelation of RS and FS units as best predictor variables (n = 42, df = 38, R^2 = 0.136, p=0.036; see ***Supplementary file 2*** for detailed statistics). Stepwise linear regression to predict the peak amplitude during ramp light stimulation identified firing rate change of RS units during ramp light stimulation, peak power of spike-triggered LFP for RS units, as well as RS firing rate change 0–10 ms after pulse stimulation and FS firing rate change 10–50 ms after pulse

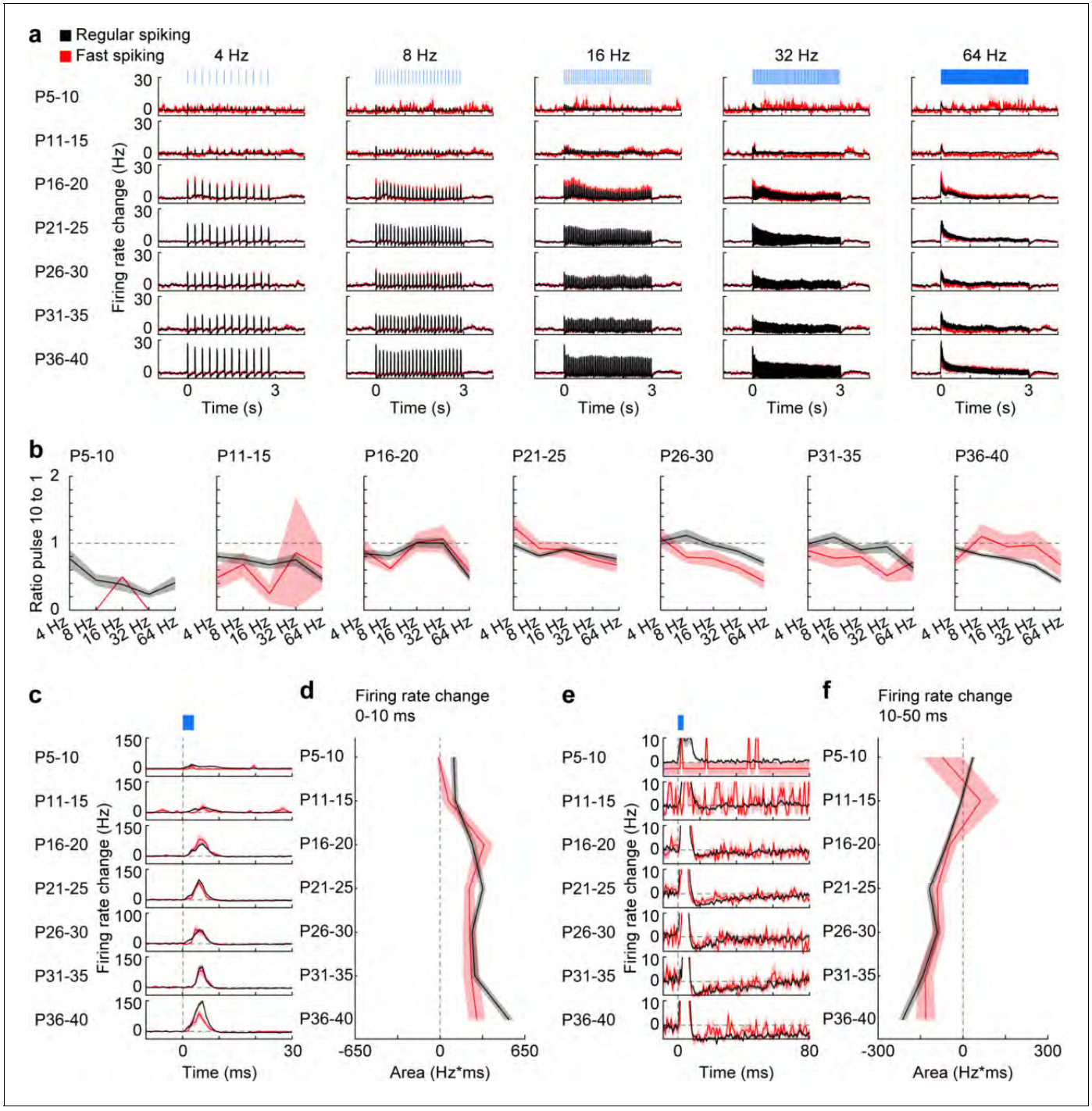

Figure 6. Firing of RS and FS units in response to pulse light stimulation. (**a**) Firing rate changes of prefrontal RS (black, n = 1824 units from 66 recordings/mice) and FS (red, n = 226 units from 66 recordings/mice) units in response to repetitive pulse light stimulation (3 ms, 473 nm) of 4, 8, 16, 32, and 64 Hz averaged for different age groups. (**b**) Line plots displaying the ratio of firing rate change in response to the 10^{th} versus the 1^{st} pulse for different frequencies and age groups (multifactorial ANOVA: unit type F(1,7698) = 0.39, p=0.530, age group F(6, 7698)=18.7, $p=1.00\times10^{-21}$, stimulation frequency F(4, 7698)=36.0, $p=6.29\times10^{-30}$). (**c**) Firing rate changes of RS and FS units in response to pulse light stimulation (3 ms, 473 nm) of L2/3 PYRs averaged for different age groups. (**d**) Line plot displaying the average firing rate change of RS and FS units 0–10 ms after pulse light stimulation for different age groups. (**e**) Same as (**c**) displayed at longer time scale. (**f**) Same as (**d**) for 10–50 ms after pulse start. (Average data is displayed as mean ± sem. See ***Supplementary file 1*** for a summary of experimental conditions. See ***Supplementary file 2*** for statistics).
The online version of this article includes the following source data and figure supplement(s) for figure 6:

Source data 1. Source data for ***Figure 6b***.

Figure 6 continued on next page

Figure 6 continued

Source data 2. Source data for ***Figure 6d***.
Source data 3. Source data for ***Figure 6f***.
Figure supplement 1. Inter-spike intervals of RS and FS units during pulse light stimulation.

stimulation as best predictor variables (n = 48, df = 43, R^2 = 0.716, p=4.35×10^{-12}; see ***Supplementary file 2*** for detailed statistics).

Thus, peak amplitude during ramp light stimulation is correlated with firing rate changes in response to ramp and pulse stimulations, indicating the importance of stimulation efficacy for peak amplitude. On the other hand, FS characteristics and rhythmicity of single units show the strongest correlation with the peak frequency of LFP power.

Discussion

Gamma oscillations (30–80 Hz) result from a fine-tuned interplay between excitation and inhibition in the adult brain (***Atallah and Scanziani, 2009***). For example, in sensory cortices, they arise through inhibitory feedback from PV-expressing interneurons (***Cardin et al., 2009***; ***Chen et al., 2017***). Specifically, fast synaptic inhibition of the perisomatic region of pyramidal neurons by PV-expressing interneurons is critical for the generation of gamma oscillations (***Cardin, 2016***). Suppressing PV-expressing interneurons in the adult mPFC reduces the power in gamma frequency and impairs interhemispheric synchronization and cognitive abilities (***Cho et al., 2015***; ***Cho et al., 2020***). SOM-expressing interneurons contribute to oscillatory activity at the lower end of the gamma frequency range (20–40 Hz) (***Chen et al., 2017***; ***Veit et al., 2017***). In contrast, the mechanisms controlling the emergence of gamma activity during development are still poorly understood. Here, we reveal that the fast oscillatory activity in the mouse mPFC emerges during the second postnatal week and increases in frequency and amplitude before it stabilizes in gamma frequency range (30–80 Hz) during the fourth postnatal week. Further, we show that the functional maturation of FS PV-expressing interneurons and single unit rhythmicity of RS and FS units are best correlated with the accelerating gamma activity in the LFP. While activation of L2/3 PYR drives fast oscillatory activity throughout development, the acceleration toward higher frequencies relates to the maturation of inhibitory feedback and of FS interneurons. The time course of the maturation of FS units, putatively PV-expressing interneurons, is consistent with a recent characterization of PV-expressing interneuron physiology in the mPFC in vitro (***Miyamae et al., 2017***). These results suggest that the interplay between excitatory and inhibitory neurons is not only critical for the generation of adult gamma activity but also for its emergence during postnatal development.

The L2/3 PYRs-driven oscillatory activity was strongly correlated with spontaneously occurring fast frequency oscillations. However, broader peaks in power spectra for spontaneous activity indicate that the stimulation-induced activity might not cover the full diversity of spontaneous gamma activity. The broadness of spontaneous activity gamma power might also explain the absence of clear locking and rhythmicity of single units in the absence of prefrontal stimulation or task-induced activation of the mPFC.

Starting with the first electroencephalographic recordings, adult brain rhythms have been defined according to their frequencies and related to a specific state or task (***Buzsáki and Draguhn, 2004***). These 'classical' frequency bands (i.e. delta, theta, alpha, beta, gamma) are largely preserved between different mammalian species (***Buzsáki and Draguhn, 2004***; ***Buzsáki et al., 2013***). However, how they emerge during development is still largely unknown. Synchronization of cortical areas in fast oscillatory rhythms starts during the first postnatal week (***Brockmann et al., 2011***). These low-amplitude patterns are detected in the rodent mPFC as early as P5,1–2 days later compared to primary sensory cortices (S1, V1) (***Minlebaev et al., 2011***; ***Yang et al., 2013***; ***Dupont et al., 2006***; ***Shen and Colonnese, 2016***; ***Yang et al., 2009***). However, this neonatal fast activity has a relative low frequency (around 20 Hz) (***Brockmann et al., 2011***; ***Yang et al., 2009***). It is organized in infrequent short bursts and its detection is hampered by the lack of a clear peak in LFP power spectra. We previously showed that in the developing mPFC the detection of prominent fast oscillations with frequencies above 12 Hz coincides with the switch from discontinuous to continuous activity (***Brockmann et al., 2011***). These oscillations are initially within 15-20 Hz frequency range that was

classically defined as beta range. The present results indicate that these rhythms progressively increase their frequency and amplitude with age until they stabilize in gamma frequency range at 50–60 Hz during the fourth postnatal week. A similar increase in gamma frequency has been previously described after eye opening in the visual cortex (**Hoy and Niell, 2015**). Therefore, identification of oscillatory patterns in developing circuits according to 'classical' frequency bands established for adults should be avoided.

Adult gamma activity in the cerebral cortex relies on FS PV-expressing interneurons (**Cardin et al., 2009**). To test whether this mechanism underlies the fast rhythms in the developing brain, we developed an unbiased approach to detect FS units corresponding to putatively PV-expressing interneurons. Since PV expression and FS characteristics do not completely overlap (**Ma et al., 2006**; **Onorato et al., 2020**), the method has the same drawback as that typically used for the distinction of adult RS and FS and cannot identify RS interneurons. For this, clustering of prefrontal neurons from mice of all investigated ages was performed based on a dimensionality reduction of their mean waveforms and not on pre-defined waveform features. To validate this approach, we compared the results to pre-defined waveform features typically used to identify FS units and found that they largely agree for adult mice. We demonstrate that FS units are detected in the mPFC during the second postnatal week and progressively mature until the fourth postnatal week, consistent with PV interneuron maturation (**Okaty et al., 2009**). The similar dynamics of FS interneuron maturation and acceleration of fast oscillatory activity, as well as the correlation of FS characteristics with induced fast oscillation frequencies across age supports the hypothesis that FS interneurons are key elements for prefrontal gamma development. In the absence of FS interneurons at early age, inhibitory feedback from SOM neurons – important for slow gamma activity in the adult cortex (**Veit et al., 2017**) – might contribute to early oscillatory activity at frequencies within 12–20 Hz range.

While we only found minor age-dependent changes in the extracellular waveforms of RS units, an in-depth investigation of prefrontal PYRs during development had identified prominent changes in their dendritic arborization, passive and active membrane properties, as well as excitatory and inhibitory inputs (**Kroon et al., 2019**). These changes, even though not detected with extracellular recordings, most likely contribute to the maturation of pyramidal-interneuronal interactions and finally, of gamma activity. Indeed, we found that the maturation of inhibitory feedback in response to prefrontal L2/3 PYRs stimulation follows the same dynamics as the development of gamma oscillations. Furthermore, rhythmicity of single RS and FS units were identified as good predictors for the frequencies of oscillatory activity.

GABAergic transmission in the rodent cortex matures during postnatal development, reaching an adult-like state toward the end of the fourth postnatal week (**Le Magueresse and Monyer, 2013**; **Butt et al., 2017**; **Lim et al., 2018**). Shortly after birth, GABA acts depolarizing due to high intracellular chloride in immature neurons expressing low levels of the chloride cotransporter KCC2 relative to NKCC1 (**Rivera et al., 1999**; **Lim et al., 2018**). However, this depolarization is not sufficient to trigger action potential firing and results in shunting inhibition (**Kirmse et al., 2018**). The switch of GABA action from depolarizing to hyperpolarizing has been reported to occur during the second postnatal week (**Ben-Ari et al., 2012**), coinciding with the emergence of gamma band oscillations. Moreover, the composition of $GABA_A$-receptor subunits changes during postnatal development, causing a progressive decrease of decay-time constants of inhibitory postsynaptic currents (IPSCs) until they reach adult-like kinetics in the fourth postnatal week (**Okaty et al., 2009**; **Bosman et al., 2005**; **Laurie et al., 1992**). Simulations of neuronal networks proposed that increasing IPSCs kinetics in FS interneurons results in increasing gamma frequency (**Doischer et al., 2008**). The gradual increase of prefrontal gamma frequency from the second to the fourth postnatal week provides experimental evidence for this hypothesis.

In-depth understanding of the dynamics and mechanisms of gamma activity in the developing cortex appears relevant for neurodevelopmental disorders, such as schizophrenia and autism. Both, in patients and disease mouse models, gamma oscillations have been reported to be altered, likely to reflect abnormal pyramidal-interneuronal interactions (**Cho et al., 2015**; **Cao et al., 2018**; **Rojas and Wilson, 2014**). These dysfunction seems to emerge already during development (**Chini et al., 2020**; **Richter et al., 2019**; **Hartung et al., 2016**). Elucidating the developmental dynamics of cortical gamma activity might uncover the timeline of disease-related deficits.

Materials and methods

Key resources table

Reagent type (species) or resource	Designation	Source or reference	Identifiers	Additional information
Antibody	Rabbit polyclonal-anti-parvalbumin	Abcam	ab11427	(1:500)
Antibody	Rabbit polyclonal-anti-somatostatin	Santa Cruz	sc13099	(1:250)
Antibody	Goat-anti-rabbit secondary antibody, Alexa Fluor 488	Invitrogen-Thermo Fisher	A11008	(1:500)
Chemical compound, drug	Isoflurane	Abbott	B506	
Chemical compound, drug	Urethane	Fluka analytical	94300	
Strain, strain background (mouse, both genders)	C57Bl/6J	Universitä tsklinikum Hamburg-Eppendorf –Animal facility	C57Bl/6J	https://www.jax.org/strain/008199
Recombinant DNA reagent	pAAV-CAG-ChR2(E123T/T159C)−2AtDimer2	Provided by T. G. Oertner	pAAV-CAG-ChR2(E123T/T159C)−2AtDimer2	http://www.oertner.com/
Software, algorithm	Matlab R2018b	MathWorks	Matlab R2018b	https://www.mathworks.com/
Software, algorithm	Kilosort2	MouseLand		https://github.com/MouseLand/Kilosort2
Software, algorithm	ImageJ	ImageJ		https://imagej.nih.gov/ij/
Other	Arduino Uno SMD	Arduino	A000073	
Other	Digital Lynx 4SX	Neuralynx	Digital Lynx 4SX	http://neuralynx.com/
Other	Diode laser (473 nm)	Omicron	LuxX 473–100	
Other	Electroporation device	BEX	CUY21EX	
Other	Electroporation tweezer-type paddles	Protech	CUY650-P5	
Other	Recording electrode (one-shank, 16 channels)	Neuronexus	A1 × 16 5 mm	
Other	Recording electrode (four-shank, 16 channels)	Neuronexus	A4 × 4 5 mm	

Animals

All experiments were performed in compliance with the German laws and the guidelines of the European Community for the use of animals in research and were approved by the local ethical committee (G132/12, G17/015, N18/015). Timed-pregnant mice from the animal facility of the University Medical Center Hamburg-Eppendorf were housed individually at a 12 hr light/12 hr dark cycle and were given access to water and food ad libitum. The day of vaginal plug detection was considered embryonic day (E) 0.5, the day of birth was considered postnatal day (P) 0. Experiments were carried out on C57Bl/6J mice of both sexes.

In utero electroporation (IUE)

Pregnant mice (C57Bl6/J, The Jackson Laboratory, ME, USA) received additional wet food daily, supplemented with 2–4 drops Metacam (0.5 mg/ml, Boehringer-Ingelheim, Germany) one day before until two days after in IUE. At E15.5, pregnant mice were injected subcutaneously with buprenorphine (0.05 mg/kg body weight) 30 min before surgery. Surgery was performed under isoflurane anesthesia (induction 5%, maintenance 3.5%) on a heating blanket. Eyes were covered with eye ointment and pain reflexes and breathing were monitored to assess anesthesia depth. Uterine horns were exposed and moistened with warm sterile PBS. 0.75–1.25 µl of opsin- and fluorophore-encoding plasmid (pAAV-CAG-ChR2(E123T/T159C)−2A-tDimer2, 1.25 µg/µl) purified with NucleoBond (Macherey-Nagel, Germany) in sterile PBS with 0.1% fast green dye was injected in the right lateral ventricle of each embryo using pulled borosilicate glass capillaries. Electroporation tweezer paddles of 5 mm diameter were oriented at a rough 20˚ leftward angle from the midline of the head and a rough 10˚ downward angle from the anterior to posterior axis to transfect precursor cells of medial prefrontal layer 2/3 PYRs neurons with five electroporation pulses (35 V, 50 ms, 950 ms interval, CU21EX, BEX, Japan). Uterine horns were placed back into the abdominal cavity. Abdominal cavity was filled with warm sterile PBS and abdominal muscles and skin were sutured with absorbable and non-absorbable suture thread, respectively. After recovery from anesthesia, mice were returned to their home cage, placed half on a heating blanket for two days after surgery. Fluorophore expression was assessed at P2 in the pups with a portable fluorescence flashlight (Nightsea, MA, USA) through the intact skin and skull and confirmed in brain slices postmortem.

Electrophysiology

Acute head-fixed recordings

Multi-site extracellular recordings were performed unilaterally or bilaterally in the mPFC of non-anesthetized or anesthetized P5-40 mice. Mice were on a heating blanket during the entire procedure. Under isoflurane anesthesia (induction: 5%; maintenance: 2.5%), a craniotomy was performed above the mPFC (0.5 mm anterior to bregma, 0.1–0.5 mm lateral to the midline). Pups were head-fixed into a stereotaxic apparatus using two plastic bars mounted on the nasal and occipital bones with dental cement. Multi-site electrodes (NeuroNexus, MI, USA) were inserted into the mPFC (four-shank, A4 × 4 recording sites, 100 µm spacing, 125 µm shank distance, 1.8–2.0 mm deep). A silver wire was inserted into the cerebellum and served as ground and reference. For non-anesthetized and anesthetized recordings, pups were allowed to recover for 30 min prior to recordings. For anesthetized recordings, urethane (1 mg/g body weight) was injected intraperitoneally prior to the surgery.

Acute head-fixed recordings with chronically implanted head-fixation adapters

Multisite extracellular recordings were performed unilaterally in the mPFC of P23-25 and P38-40 mice. The adapter for head fixation was implanted at least 5 days before recordings. Under isoflurane anesthesia (5% induction, 2.5% maintenance), a metal head-post (Luigs and Neumann, Germany) was attached to the skull with dental cement and a craniotomy was performed above the mPFC (0.5–2.0 mm anterior to bregma, 0.1–0.5 mm right to the midline) and protected by a customized synthetic window. A silver wire was implanted between skull and brain tissue above the cerebellum and served as ground and reference. 0.5% bupivacaine/1% lidocaine was locally applied to cutting edges. After recovery from anesthesia, mice were returned to their home cage. After recovery from the surgery, mice were accustomed to head-fixation and trained to run on a custom-made spinning

disc. For non-anesthetized recordings, craniotomies were uncovered and multi-site electrodes (NeuroNexus, MI, USA) were inserted into the mPFC (one-shank, A1 × 16 recording sites, 100 µm spacing, 2.0 mm deep).

Extracellular signals were band-pass filtered (0.1–9000 Hz) and digitized (32 kHz) with a multichannel extracellular amplifier (Digital Lynx SX; Neuralynx, Bozeman, MO, USA). Electrode position was confirmed in brain slices postmortem.

Optogenetic stimulation

Ramp (linearly increasing light power) light stimulation and pulsed (short pulses of 3 ms) light stimulation at different frequencies was performed using an Arduino uno (Arduino, Italy) controlled laser system (473 nm / 594 nm wavelength, Omicron, Austria) coupled to a 50 µm (four- shank electrodes) or 105 µm (one-shank electrodes) diameter light fiber (Thorlabs, NJ, USA) glued to the multisite electrodes, ending 200 µm above the top recording site. Each type of stimulation was repeated 30 times. At the beginning of each recording, laser power was adjusted to reliably trigger neuronal spiking in response to light pulses of 3 ms duration.

Histology

Mice (P5-40) were anesthetized with 10% ketamine (aniMedica, Germanry)/2% xylazine (WDT, Germany) in 0.9% NaCl (10 µg/g body weight, intraperitoneal) and transcardially perfused with 4% paraformaldehyde (Histofix, Carl Roth, Germany). Brains were removed and postfixed in 4% paraformaldehyde for 24 hr. Brains were sectioned coronally with a vibratom at 50 µm for immunohistochemistry.

Immunohistochemistry

Free-floating slices were permeabilized and blocked with PBS containing 0.8% Triton X-100 (Sigma-Aldrich, MO, USA), 5% normal bovine serum (Jackson Immuno Research, PA, USA) and 0.05% sodium azide. Slices were incubated over night with primary antibody rabbit-anti-parvalbumin (1:500, #ab11427, Abcam, UK) or rabbit-anti-somatostatin (1:250, #sc13099, Santa Cruz, CA, USA), followed by 2 hr incubation with secondary antibody goat-anti-rabbit Alexa Fluor 488 (1:500, #A11008, Invitrogen-Thermo Fisher, MA, USA). Sections were transferred to glass slides and covered with Fluoromount (Sigma-Aldrich, MO, USA).

Cell quantification

Images of immunofluorescence in the right mPFC were acquired with a confocal microscope (DM IRBE, Leica, Germany) using a 10x objective (numerical aperture 0.3). Immunopositive cells were automatically quantified with custom-written algorithms in ImageJ environment. The region of interest (ROI) was manually defined over L2/3 of the mPFC. Image contrast was enhanced before applying a median filter. Local background was subtracted to reduce background noise and images were binarized and segmented using the watershed function. Counting was done after detecting the neurons with the extended maxima function of the MorphoLibJ plugin.

Data analysis

Electrophysiological data were analyzed with custom-written algorithms in Matlab environment. Data were band-pass filtered (500–9000 Hz for spike analysis or 1–100 Hz for local field potentials (LFP)) using a third-order Butterworth filter forward and backward to preserve phase information before down-sampling to analyze LFP. Each type of optogenetic stimulation (ramps or pulses at different frequencies) was repeated 30 times for each recording. Each recording contributes a single data point for ***Figures 1*** and ***3***. Most mice were recorded once. Only mice with chronically implanted head fixation were recorded more than one time (13 recordings from six mice at P24-26 and 12 recordings from five mice at P37-40), but all recordings were with acutely inserted electrodes. All mice for single unit analysis were recorded only once. (See ***Supplementary file 1*** for a summary of experimental conditions.)

Power spectral density

For power spectral density analysis, 2 s-long windows of LFP signal were concatenated and the power was calculated using Welch's method with non-overlapping windows. Spectra were multiplied with squared frequency.

Modulation index

For optogenetic stimulations, MI was calculated as (value stimulation - value pre- stimulation) / (value stimulation + value pre-stimulation).

Peak frequency and strength

Peak frequency and peak strength were calculated for the most prominent peak in the spectrum defined by the product of peak amplitude, peak half width and peak prominence.

Single unit analysis

Spikes were detected and sorted with Kilosort2 in Matlab. t-sne dimensionality reduction was applied on mean waveforms of all units. Hierarchical clustering was performed to identify FS and RS units for all ages simultaneously. Autocorrelations of single units with a minimum firing rate of 1 Hz were calculated before and during optogenetic ramp stimulation. Power spectral densities of mean autocorrelations were calculated per unit. Crosscorrelations of simultaneously recorded RS-RS, FS-FS, and RS-FS unit pairs were calculated during optogenetic ramp stimulation. Power of the mean spike-triggered LFP, pairwise phase consistency (***Vinck et al., 2010***), coefficient of variation, C_{V2} (***Holt et al., 1996***), and inter-spike intervals were calculated for individual units before and during optogenetic ramp stimulation.

Statistics

No statistical measures were used to estimate sample size since effect size was unknown. Data were tested for consistent trends across age with the non-parametric Mann-Kendall trend test. Mann-Kendall coefficient tau-b adjusting for ties is reported. Multifactorial ANOVAs were used to compare main effects. Linear regression models were used to test for significant links of averaged single unit and LFP activity measures with age per recording. Stepwise linear regression was used to identify significant links from averaged single unit activity measures (proportion FS units, as well as half width, trough to peak, amplitude, rate change for ramp light stimulation, autocorrelation peak during ramp light stimulation, spike-triggered LFP peak frequency during ramp stimulation, and rate change early (0–10 ms) and late (10–50 ms) after pulse stimulation for RS and FS units) with LFP activity (ramp light-induced frequency peak and amplitude). See ***Supplementary file 2*** for detailed statistics.

Acknowledgements

We thank M Chini for helpful discussions and comments on the manuscript as well as A Marquardt, P Putthoff, A Dahlmann, and K Titze for excellent technical assistance. This work was funded by grants from the European Research Council (ERC-2015-CoG 681577 to ILH-O) and the German Research Foundation (Ha 4466/10–1, Ha4466/11-1, Ha4466/12-1, SPP 1665, SFB 936 B5 to ILH-O).

Additional information

Funding

Funder	Grant reference number	Author
H2020 European Research Council	ERC-2015-CoG 681577	Ileana Hanganu-Opatz
Deutsche Forschungsgemeinschaft	Ha4466/10-1	Ileana Hanganu-Opatz
Deutsche Forschungsgemeinschaft	Ha4466/11-1	Ileana Hanganu-Opatz

Deutsche Forschungsgemeinschaft	Ha4466/12-1	Ileana Hanganu-Opatz
Deutsche Forschungsgemeinschaft	SPP 1665	Ileana Hanganu-Opatz
Deutsche Forschungsgemeinschaft	SFB 936 B5	Ileana Hanganu-Opatz

The funders had no role in study design, data collection and interpretation, or the decision to submit the work for publication.

Author contributions

Sebastian H Bitzenhofer, Conceptualization, Data curation, Software, Formal analysis, Supervision, Investigation, Visualization, Methodology, Writing - original draft, Writing - review and editing; Jastyn A Pöpplau, Data curation, Formal analysis, Investigation, Methodology, Writing - review and editing; Ileana Hanganu-Opatz, Conceptualization, Supervision, Funding acquisition, Project administration, Writing - review and editing

Author ORCIDs

Sebastian H Bitzenhofer https://orcid.org/0000-0003-0736-6251
Jastyn A Pöpplau https://orcid.org/0000-0002-4350-3164
Ileana Hanganu-Opatz https://orcid.org/0000-0002-4787-1765

Ethics

Animal experimentation: All experiments were performed in compliance with the German laws and the guidelines of the European Community for the use of animals in research and were approved by the local ethical committee (G132/12, G17/015, N18/015).

Decision letter and Author response

Decision letter https://doi.org/10.7554/eLife.56795.sa1
Author response https://doi.org/10.7554/eLife.56795.sa2

Additional files

Supplementary files

- Supplementary file 1. Recording summary. Table summarizing the recordings for each experimental condition.
- Supplementary file 2. Detailed statistical results. Table summarizing the statistical results.
- Transparent reporting form

Data availability

The authors declare that all data and code supporting the findings of this study are included in the manuscript. LFP and SUA data for all recordings is available at the following open-access repository: https://doi.org/10.12751/g-node.heyl6r.

The following dataset was generated:

Author(s)	Year	Dataset title	Dataset URL	Database and Identifier
Bitzenhofer SB, Pöpplau A, Hanganu-Opatz IL	2020	Ephys data associated with the paper *Gamma activity accelerates during prefrontal development*	https://doi.org/10.12751/g-node.heyl6r	g-node, 10.12751/g-node.heyl6r

References

Atallah BV, Scanziani M. 2009. Instantaneous modulation of gamma oscillation frequency by balancing excitation with inhibition. *Neuron* **62**:566–577. DOI: https://doi.org/10.1016/j.neuron.2009.04.027, PMID: 19477157

Ben-Ari Y, Khalilov I, Kahle KT, Cherubini E. 2012. The GABA excitatory/inhibitory shift in brain maturation and neurological disorders. *The Neuroscientist* **18**:467–486. DOI: https://doi.org/10.1177/1073858412438697, PMID: 22547529

Bitzenhofer SH, Ahlbeck J, Wolff A, Wiegert JS, Gee CE, Oertner TG, Hanganu-Opatz IL. 2017a. Layer-specific optogenetic activation of pyramidal neurons causes beta-gamma entrainment of neonatal networks. *Nature Communications* **8**:14563. DOI: https://doi.org/10.1038/ncomms14563, PMID: 28216627

Bitzenhofer SH, Ahlbeck J, Hanganu-Opatz IL. 2017b. Methodological approach for optogenetic manipulation of neonatal neuronal networks. *Frontiers in Cellular Neuroscience* **11**:239. DOI: https://doi.org/10.3389/fncel.2017.00239, PMID: 28848399

Bosman LW, Heinen K, Spijker S, Brussaard AB. 2005. Mice lacking the major adult GABAA receptor subtype have normal number of synapses, but retain juvenile IPSC kinetics until adulthood. *Journal of Neurophysiology* **94**:338–346. DOI: https://doi.org/10.1152/jn.00084.2005, PMID: 15758057

Brockmann MD, Pöschel B, Cichon N, Hanganu-Opatz IL. 2011. Coupled oscillations mediate directed interactions between prefrontal cortex and Hippocampus of the neonatal rat. *Neuron* **71**:332–347. DOI: https://doi.org/10.1016/j.neuron.2011.05.041, PMID: 21791291

Butt SJ, Stacey JA, Teramoto Y, Vagnoni C. 2017. A role for GABAergic interneuron diversity in circuit development and plasticity of the neonatal cerebral cortex. *Current Opinion in Neurobiology* **43**:149–155. DOI: https://doi.org/10.1016/j.conb.2017.03.011, PMID: 28399421

Buzsáki G, Logothetis N, Singer W. 2013. Scaling Brain Size, Keeping Timing: Evolutionary Preservation of Brain Rhythms. *Neuron* **80**:751–764. DOI: https://doi.org/10.1016/j.neuron.2013.10.002

Buzsáki G, Draguhn A. 2004. Neuronal oscillations in cortical networks. *Science* **304**:1926–1929. DOI: https://doi.org/10.1126/science.1099745, PMID: 15218136

Cao W, Lin S, Xia QQ, Du YL, Yang Q, Zhang MY, Lu YQ, Xu J, Duan SM, Xia J, Feng G, Xu J, Luo JH. 2018. Gamma oscillation dysfunction in mPFC leads to social deficits in neuroligin 3 R451C knockin mice. *Neuron* **97**:1253–1260. DOI: https://doi.org/10.1016/j.neuron.2018.02.001, PMID: 29503190

Cardin JA, Carlén M, Meletis K, Knoblich U, Zhang F, Deisseroth K, Tsai LH, Moore CI. 2009. Driving fast-spiking cells induces gamma rhythm and controls sensory responses. *Nature* **459**:663–667. DOI: https://doi.org/10.1038/nature08002, PMID: 19396156

Cardin JA. 2016. Snapshots of the brain in action: local circuit operations through the Lens of γ oscillations. *Journal of Neuroscience* **36**:10496–10504. DOI: https://doi.org/10.1523/JNEUROSCI.1021-16.2016, PMID: 27733601

Chen G, Zhang Y, Li X, Zhao X, Ye Q, Lin Y, Tao HW, Rasch MJ, Zhang X. 2017. Distinct inhibitory circuits orchestrate cortical beta and gamma band oscillations. *Neuron* **96**:1403–1418. DOI: https://doi.org/10.1016/j.neuron.2017.11.033, PMID: 29268099

Chini M, Gretenkord S, Kostka JK, Pöpplau JA, Cornelissen L, Berde CB, Hanganu-Opatz IL, Bitzenhofer SH. 2019. Neural correlates of anesthesia in newborn mice and humans. *Frontiers in Neural Circuits* **13**:00038. DOI: https://doi.org/10.3389/fncir.2019.00038

Chini M, Pöpplau JA, Lindemann C, Carol-Perdiguer L, Hnida M, Oberländer V, Xu X, Ahlbeck J, Bitzenhofer SH, Mulert C, Hanganu-Opatz IL. 2020. Resolving and rescuing developmental miswiring in a mouse model of cognitive impairment. *Neuron* **105**:60–74. DOI: https://doi.org/10.1016/j.neuron.2019.09.042, PMID: 31733940

Cho KK, Hoch R, Lee AT, Patel T, Rubenstein JL, Sohal VS. 2015. Gamma rhythms link prefrontal interneuron dysfunction with cognitive inflexibility in Dlx5/6+/− mice. *Neuron* **85**:1332–1343. DOI: https://doi.org/10.1016/j.neuron.2015.02.019, PMID: 25754826

Cho KKA, Davidson TJ, Bouvier G, Marshall JD, Schnitzer MJ, Sohal VS. 2020. Cross-hemispheric gamma synchrony between prefrontal parvalbumin interneurons supports behavioral adaptation during rule shift learning. *Nature Neuroscience* **23**:892–902. DOI: https://doi.org/10.1038/s41593-020-0647-1, PMID: 32451483

Doischer D, Hosp JA, Yanagawa Y, Obata K, Jonas P, Vida I, Bartos M. 2008. Postnatal differentiation of basket cells from slow to fast signaling devices. *Journal of Neuroscience* **28**:12956–12968. DOI: https://doi.org/10.1523/JNEUROSCI.2890-08.2008, PMID: 19036989

Dupont E, Hanganu IL, Kilb W, Hirsch S, Luhmann HJ. 2006. Rapid developmental switch in the mechanisms driving early cortical columnar networks. *Nature* **439**:79–83. DOI: https://doi.org/10.1038/nature04264, PMID: 16327778

Hartung H, Cichon N, De Feo V, Riemann S, Schildt S, Lindemann C, Mulert C, Gogos JA, Hanganu-Opatz IL. 2016. From Shortage to Surge: A Developmental Switch in Hippocampal–Prefrontal Coupling in a Gene–Environment Model of Neuropsychiatric Disorders. *Cerebral Cortex* **26**:4265–4281. DOI: https://doi.org/10.1093/cercor/bhw274

Holt GR, Softky WR, Koch C. 1996. Comparison of discharge variability visual cortex neurons . *Journal of Neurophysiology* **75**:1806–1814. DOI: https://doi.org/10.1152/jn.1996.75.5.1806

Hoy JL, Niell CM. 2015. Layer-specific refinement of visual cortex function after eye opening in the awake mouse. *Journal of Neuroscience* **35**:3370–3383. DOI: https://doi.org/10.1523/JNEUROSCI.3174-14.2015, PMID: 25716837

Kirmse K, Hübner CA, Isbrandt D, Witte OW, Holthoff K. 2018. GABAergic transmission during brain development: multiple effects at multiple stages. *The Neuroscientist* **24**:36–53. DOI: https://doi.org/10.1177/1073858417701382, PMID: 28378628

Kroon T, van Hugte E, van Linge L, Mansvelder HD, Meredith RM. 2019. Early postnatal development of pyramidal neurons across layers of the mouse medial prefrontal cortex. *Scientific Reports* **9**:5037. DOI: https://doi.org/10.1038/s41598-019-41661-9, PMID: 30911152

Laurie DJ, Wisden W, Seeburg PH. 1992. The distribution of thirteen GABAA receptor subunit mRNAs in the rat brain. III. embryonic and postnatal development. *The Journal of Neuroscience* **12**:4151–4172. DOI: https://doi.org/10.1523/JNEUROSCI.12-11-04151.1992

Le Magueresse C, Monyer H. 2013. GABAergic interneurons shape the functional maturation of the cortex. *Neuron* **77**:388–405. DOI: https://doi.org/10.1016/j.neuron.2013.01.011, PMID: 23395369

Lim L, Mi D, Llorca A, Marín O. 2018. Development and functional diversification of cortical interneurons. *Neuron* **100**:294–313. DOI: https://doi.org/10.1016/j.neuron.2018.10.009, PMID: 30359598

Ma Y, Hu H, Berrebi AS, Mathers PH, Agmon A. 2006. Distinct Subtypes of Somatostatin-Containing Neocortical Interneurons Revealed in Transgenic Mice. *Journal of Neuroscience* **26**:5069–5082. DOI: https://doi.org/10.1523/JNEUROSCI.0661-06.2006

Minlebaev M, Colonnese M, Tsintsadze T, Sirota A, Khazipov R. 2011. Early γ oscillations synchronize developing thalamus and cortex. *Science* **334**:226–229. DOI: https://doi.org/10.1126/science.1210574, PMID: 21998388

Miyamae T, Chen K, Lewis DA, Gonzalez-Burgos G. 2017. Distinct physiological maturation of Parvalbumin-Positive neuron subtypes in mouse prefrontal cortex. *The Journal of Neuroscience* **37**:4883–4902. DOI: https://doi.org/10.1523/JNEUROSCI.3325-16.2017, PMID: 28408413

Okaty BW, Miller MN, Sugino K, Hempel CM, Nelson SB. 2009. Transcriptional and electrophysiological maturation of neocortical fast-spiking GABAergic interneurons. *Journal of Neuroscience* **29**:7040–7052. DOI: https://doi.org/10.1523/JNEUROSCI.0105-09.2009, PMID: 19474331

Onorato I, Neuenschwander S, Hoy J, Lima B, Rocha K-S, Broggini AC, Uran C, Spyropoulos G, Klon-Lipok J, Womelsdorf T, Fries P, Niell C, Singer W, Vinck M. 2020. A Distinct Class of Bursting Neurons with Strong Gamma Synchronization and Stimulus Selectivity in Monkey V1. *Neuron* **105**:180–197. DOI: https://doi.org/10.1016/j.neuron.2019.09.039

Richter M, Murtaza N, Scharrenberg R, White SH, Johanns O, Walker S, Yuen RKC, Schwanke B, Bedürftig B, Henis M, Scharf S, Kraus V, Dörk R, Hellmann J, Lindenmaier Z, Ellegood J, Hartung H, Kwan V, Sedlacik J, Fiehler J, et al. 2019. Altered TAOK2 activity causes autism-related neurodevelopmental and cognitive abnormalities through RhoA signaling. *Molecular Psychiatry* **24**:1329–1350. DOI: https://doi.org/10.1038/s41380-018-0025-5

Rivera C, Voipio J, Payne JA, Ruusuvuori E, Lahtinen H, Lamsa K, Pirvola U, Saarma M, Kaila K. 1999. The K+/Cl- co-transporter KCC2 renders GABA hyperpolarizing during neuronal maturation. *Nature* **397**:251–255. DOI: https://doi.org/10.1038/16697, PMID: 9930699

Rojas DC, Wilson LB. 2014. γ-band abnormalities as markers of autism spectrum disorders. *Biomarkers in Medicine* **8**:353–368. DOI: https://doi.org/10.2217/bmm.14.15

Shen J, Colonnese MT. 2016. Development of Activity in the Mouse Visual Cortex. *Journal of Neuroscience* **36**:12259–12275. DOI: https://doi.org/10.1523/JNEUROSCI.1903-16.2016

Singer W. 2018. Neuronal oscillations: unavoidable and useful? *European Journal of Neuroscience* **48**:2389–2398. DOI: https://doi.org/10.1111/ejn.13796, PMID: 29247490

Sohal VS. 2016. How close are we to understanding what (if anything) γ oscillations do in cortical circuits? *Journal of Neuroscience* **36**:10489–10495. DOI: https://doi.org/10.1523/JNEUROSCI.0990-16.2016, PMID: 27733600

Veit J, Hakim R, Jadi MP, Sejnowski TJ, Adesnik H. 2017. Cortical gamma band synchronization through somatostatin interneurons. *Nature Neuroscience* **20**:951–959. DOI: https://doi.org/10.1038/nn.4562, PMID: 28481348

Vinck M, van Wingerden M, Womelsdorf T, Fries P, Pennartz CM. 2010. The pairwise phase consistency: a bias-free measure of rhythmic neuronal synchronization. *NeuroImage* **51**:112–122. DOI: https://doi.org/10.1016/j.neuroimage.2010.01.073, PMID: 20114076

Yang JW, Hanganu-Opatz IL, Sun JJ, Luhmann HJ. 2009. Three patterns of oscillatory activity differentially synchronize developing neocortical networks in vivo. *Journal of Neuroscience* **29**:9011–9025. DOI: https://doi.org/10.1523/JNEUROSCI.5646-08.2009, PMID: 19605639

Yang JW, An S, Sun JJ, Reyes-Puerta V, Kindler J, Berger T, Kilb W, Luhmann HJ. 2013. Thalamic network oscillations synchronize ontogenetic columns in the newborn rat barrel cortex. *Cerebral Cortex* **23**:1299–1316. DOI: https://doi.org/10.1093/cercor/bhs103, PMID: 22593243

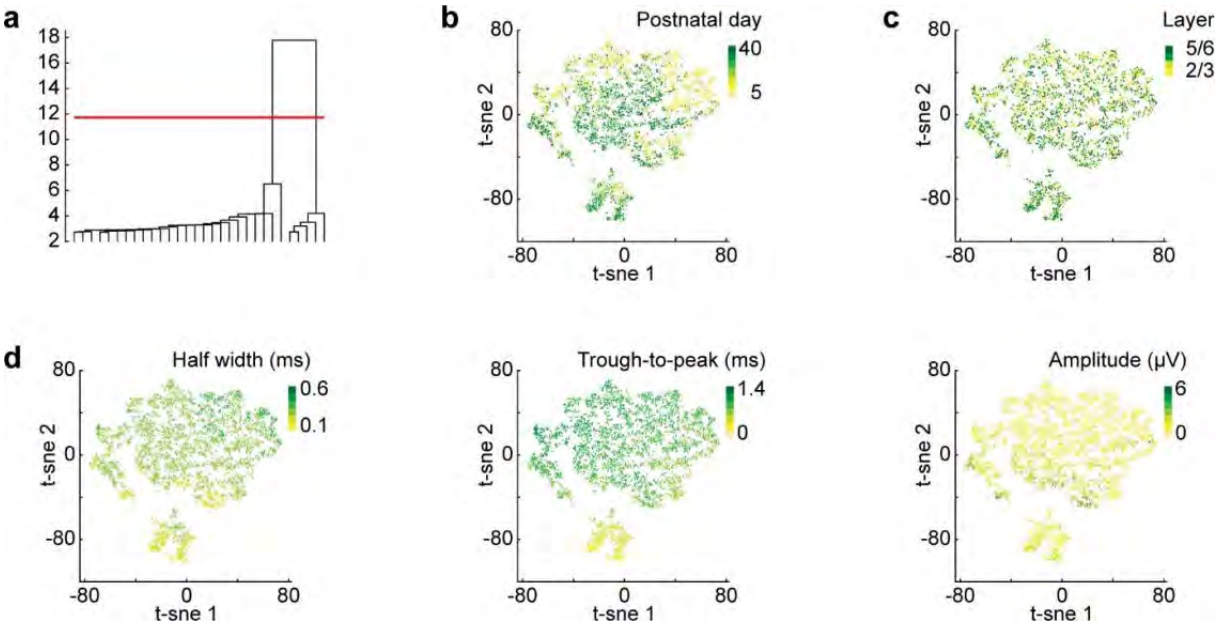

Figure 2 – figure supplement 1. t-sne dimensionality reduction.

(**a**) Dendrogram of binary hierarchical clustering after t-sne dimensionality reduction. The height of the lines represents the distance between subclusters. (**b**) Scatter plot showing the first two components of a t-sne dimensionality reduction on the mean waveforms for all units recorded from P5-40 (n = 3554 units from 66 recordings/mice) color coded by age. (**c**) Same as (**b**) color coded by mPFC layer. (**d**) Same as (**b**) color coded by values of classic spike shape features (half width, trough to peak time, amplitude).

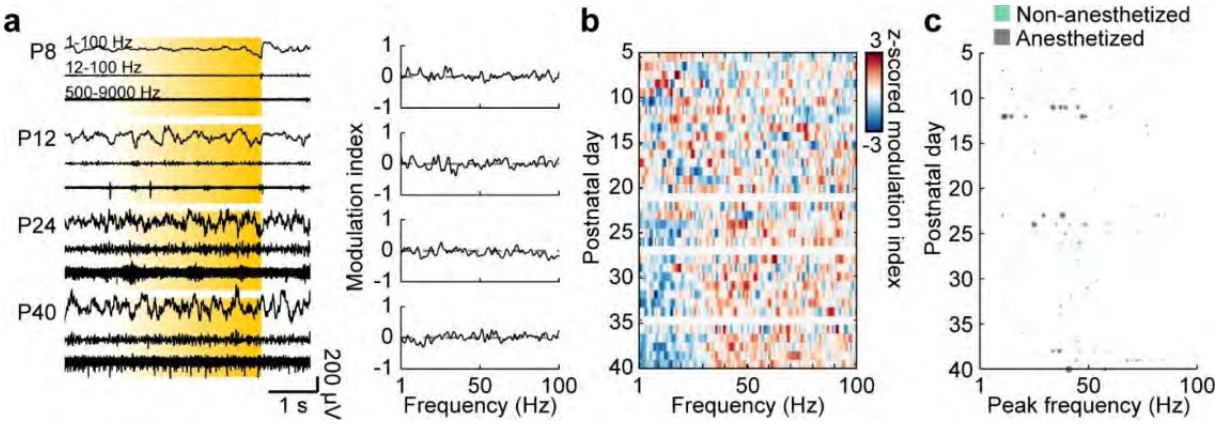

Figure 3 – figure supplement 1. Control stimulations of L2/3 PYRs in the mPFC.

(**a**) Characteristic examples of extracellular recordings of LFP and MUA during control ramp light stimulations (594 nm, 3 s) of mPFC L2/3 PYR at different ages (left) and the corresponding MI of power spectra (right). (**b**) Z-scored average MI of power spectra for P5-40 mice (n = 111 recordings from 97 mice). (c) Scatter plot displaying stimulus induced peak frequencies across age for anesthetized (gray, n = 76 recordings/mice) and non-anesthetized mice (green, n = 35 recordings from 21 mice). Marker size displays peak strength. (See Supplementary file 1 for a summary of experimental conditions. See Supplementary file 2 for statistics).

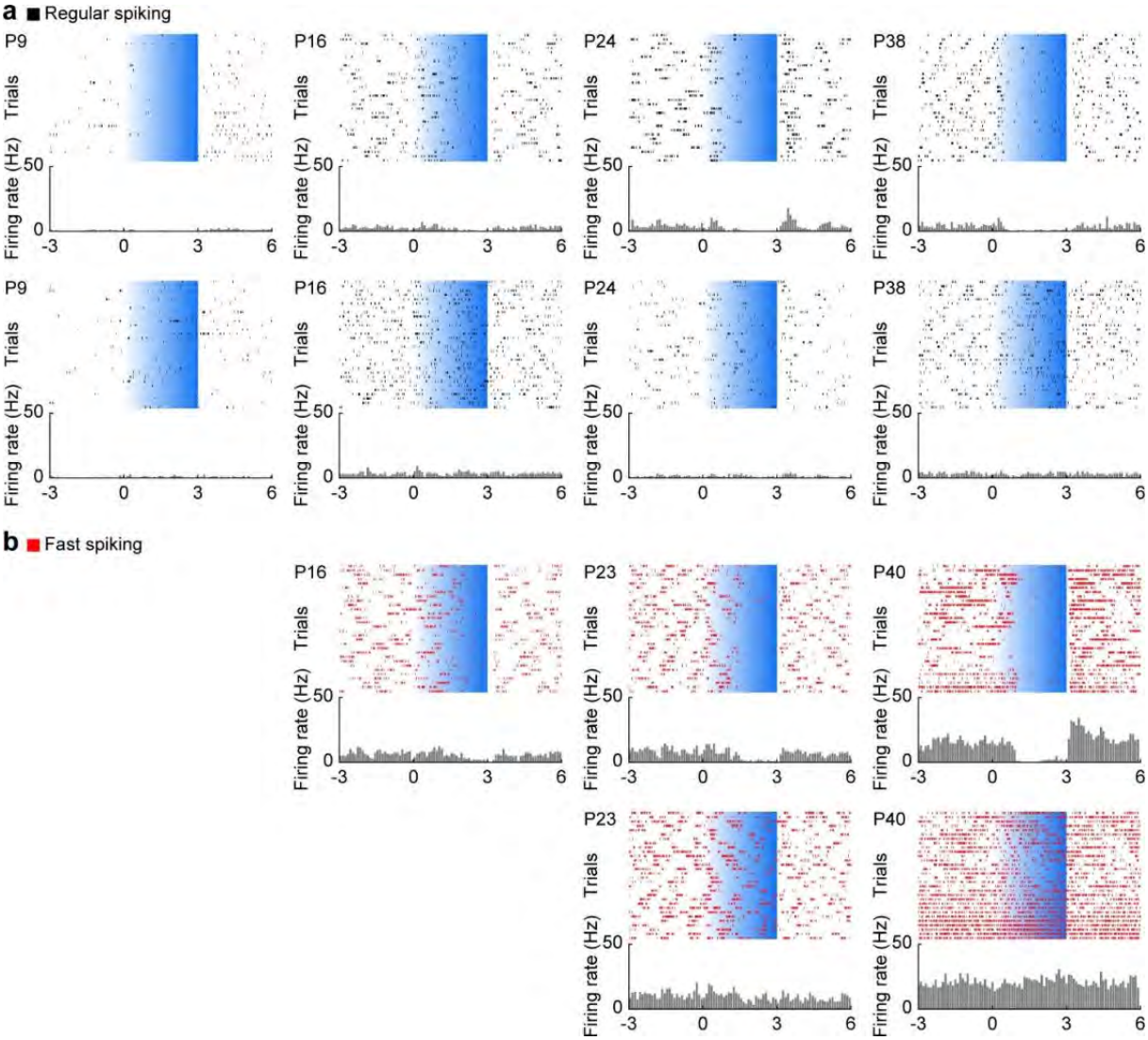

Figure 4 – figure supplement 1. RS and FS unit activity during L2/3 PYR-driven gamma in the mPFC.

(**a**) Raster plots and peri-stimulus time histograms for inactivated (top) and unaffected (bottom) RS example units in response to ramp light stimulation (3 s, 473 nm) of prefrontal L2/3 PYRs at different ages. The displayed example units were recorded simultaneously with the examples shown in Figure 4a. (**b**) Same as (**a**) for FS units. These example units were recorded simultaneously with the examples shown in Figure 4b.

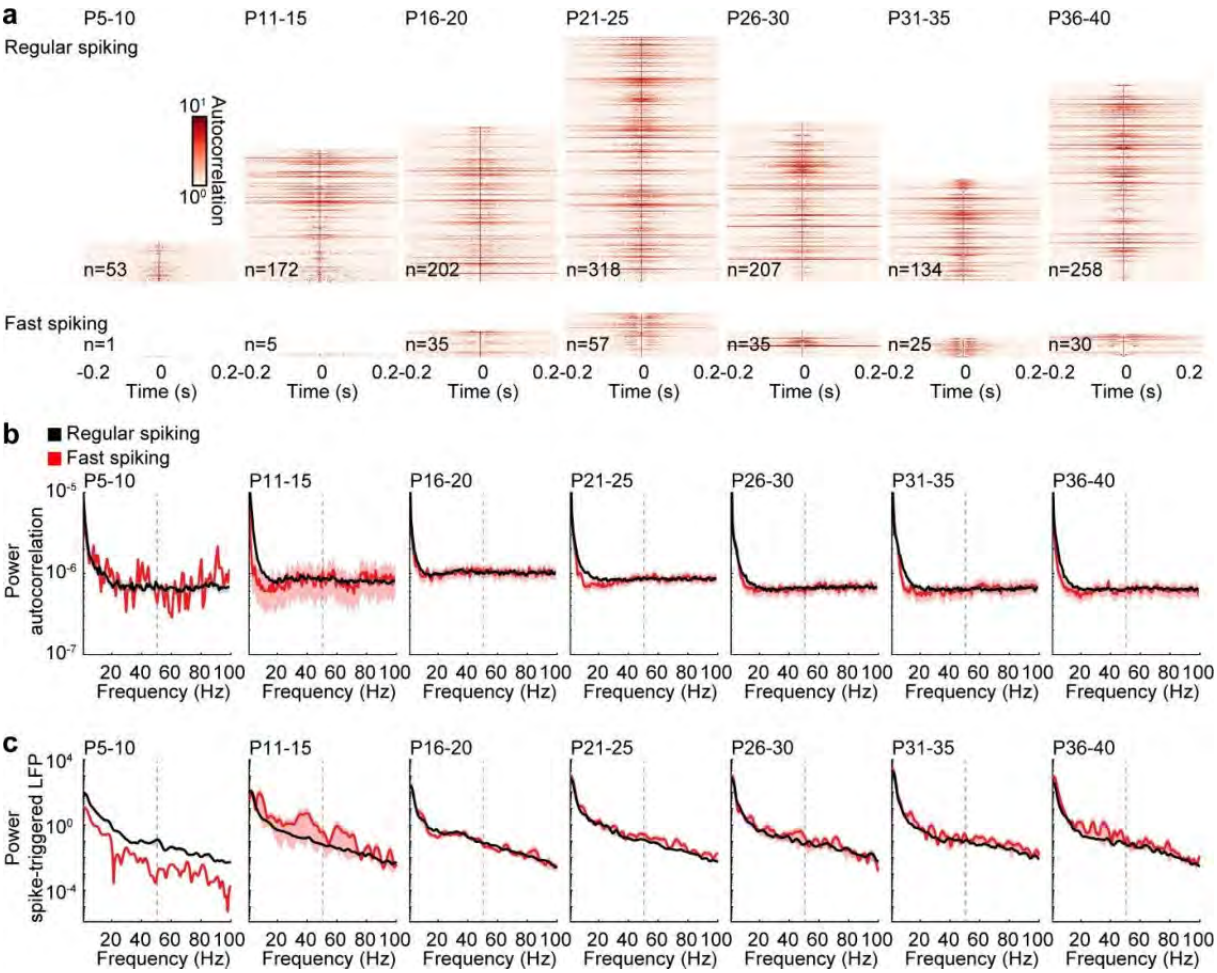

Figure 5 – figure supplement 1. Rhythmicity of RS and FS units during spontaneous activity.

(**a**) Color-coded autocorrelations of prefrontal RS (top) and FS (bottom) units during spontaneous activity for different age groups. Each row represents one unit (only units firing > 1 Hz included). (**b**) Average autocorrelation power of RS (black) and FS (red) units during spontaneous activity for different age groups (multifactorial ANOVA: unit type $F(1,153093) = 1.88$, $p=0.169$, age group $F(6, 153093)=41.8$, $p=2.53\times10^{-51}$, frequency $F(99, 153093)=663.5$, $p=0.000$). (**c**) Average power of mean spike-triggered LFP of RS (black) and FS (red) units during spontaneous activity for different age groups (multifactorial ANOVA: unit type $F(1,805201) = 248.426$, $p=5.83\times10^{-56}$, age group $F(6, 805201)=1413.2$, $p=0.000$, frequency $F(400, 805201)=747.0$, $p=0.000$). (Average data is displayed as mean ± sem. See Supplementary file 1 for a summary of experimental conditions. See Supplementary file 2 for statistics).

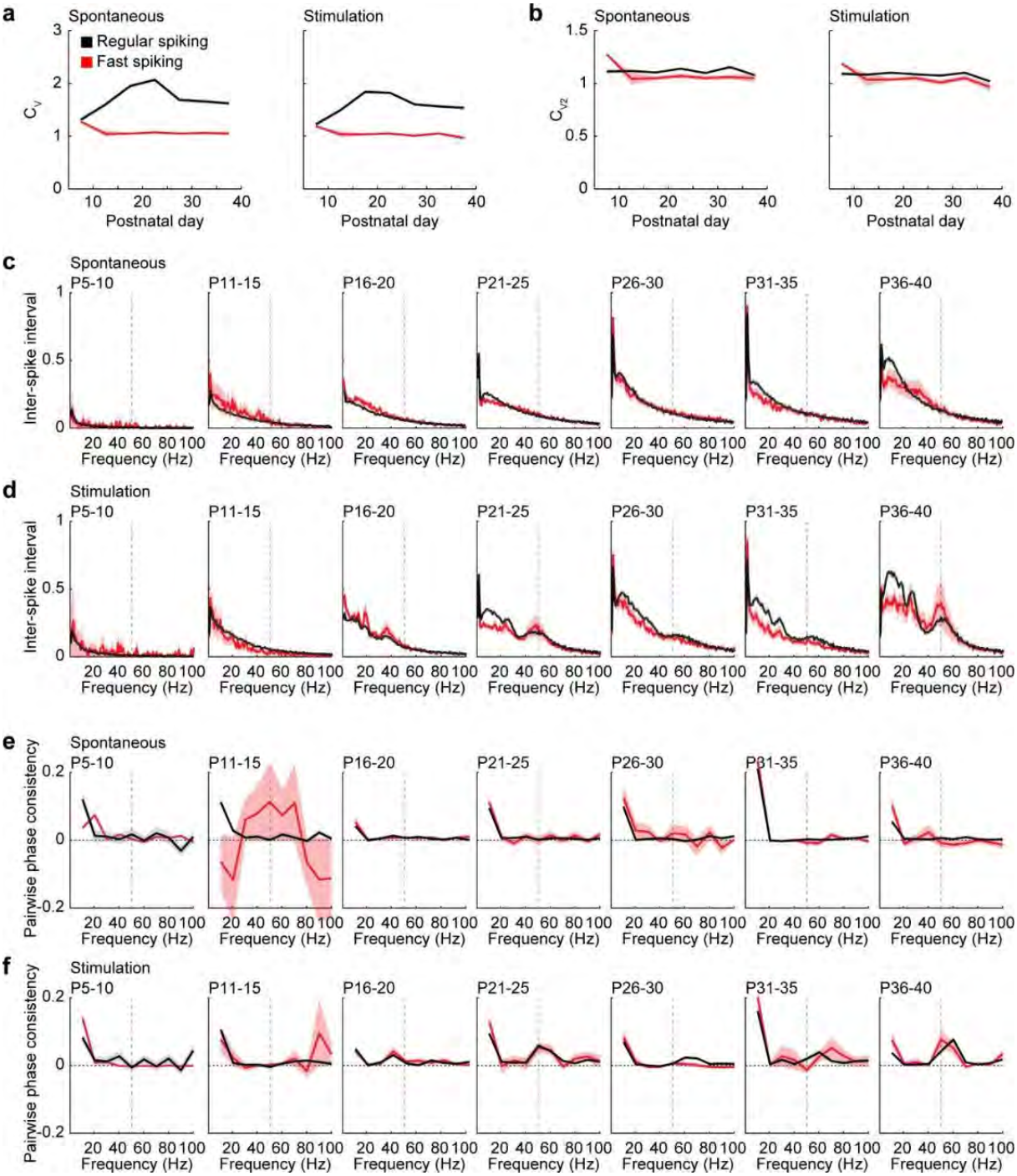

Figure 5 – figure supplement 2. Additional measures for rhythmicity of RS and FS units.

(**a**) Average variability of spiking measured as coefficient of variation (C_V) of inter-spike intervals of RS (black) and FS (red) units during spontaneous activity (Mann-Kendall trend test, RS p=0.763, n = 7 age groups, tau-b 0.142; FS p=0.880, n = 7 age groups, tau-b 0.047) and ramp light stimulation (Mann-Kendall trend test, RS p=0.880, n = 7 age groups, tau-b 0.047; FS p=0.367, n = 7 age groups, tau-b −0.333) for different age groups. (**b**). Average variability of spiking measured as C_{V2} of adjacent inter-spike intervals of RS (black) and FS (red) units during spontaneous activity (Mann-Kendall trend test, RS p=0.763, n = 7 age groups, tau-b −0.142; FS p=0.880, n = 7 age groups, tau-b 0.047) and ramp light stimulation (Mann-Kendall trend test, RS p=0.367, n = 7 age groups, tau-b −0.333; FS p=0.367, n = 7 age groups, tau-b −0.333) for different age groups. (**c**) Average inter-spike intervals (shown as instantaneous frequency) of RS (black) and FS (red) units during spontaneous activity for different age groups (multifactorial ANOVA: unit type F(1,204893) = 5.24, p=0.022, age group F(6, 204893)=3519.8, p=0.000, frequency F(99, 204893)=583.2, p=0.000). (**d**) Same as (**c**) for RS and FS

units during ramp light stimulation (multifactorial ANOVA: unit type $F(1,204893) = 146.6$, $p=9.64\times10^{-34}$, age group $F(6, 204893)=2745.0$, $p=0.000$, frequency $F(99, 204893)=447.1$, $p=0.000$). (**e**) Average pairwise phase consistency of RS (black) and FS (red) units during spontaneous activity for different age groups (multifactorial ANOVA: unit type $F(1, 20262)=1.14$, $p=0.283$, age group $F(6, 20262)=6.83$, $p=2.93\times10^{-7}$, frequency $F(9, 20262)=164.0$, $p=2.67\times10^{-301}$). (**f**) Same as (**e**) for RS and FS units during ramp light stimulation (multifactorial ANOVA: unit type $F(1,20385) = 3.61$, $p=0.057$, age group $F(6, 20385)=13.5$, $p=1.90\times10^{-15}$, frequency $F(9, 20385)=124.8$, $p=8.13\times10^{-230}$). (Average data is displayed as mean ± sem. See Supplementary file 1 for a summary of experimental conditions. See Supplementary file 2 for statistics).

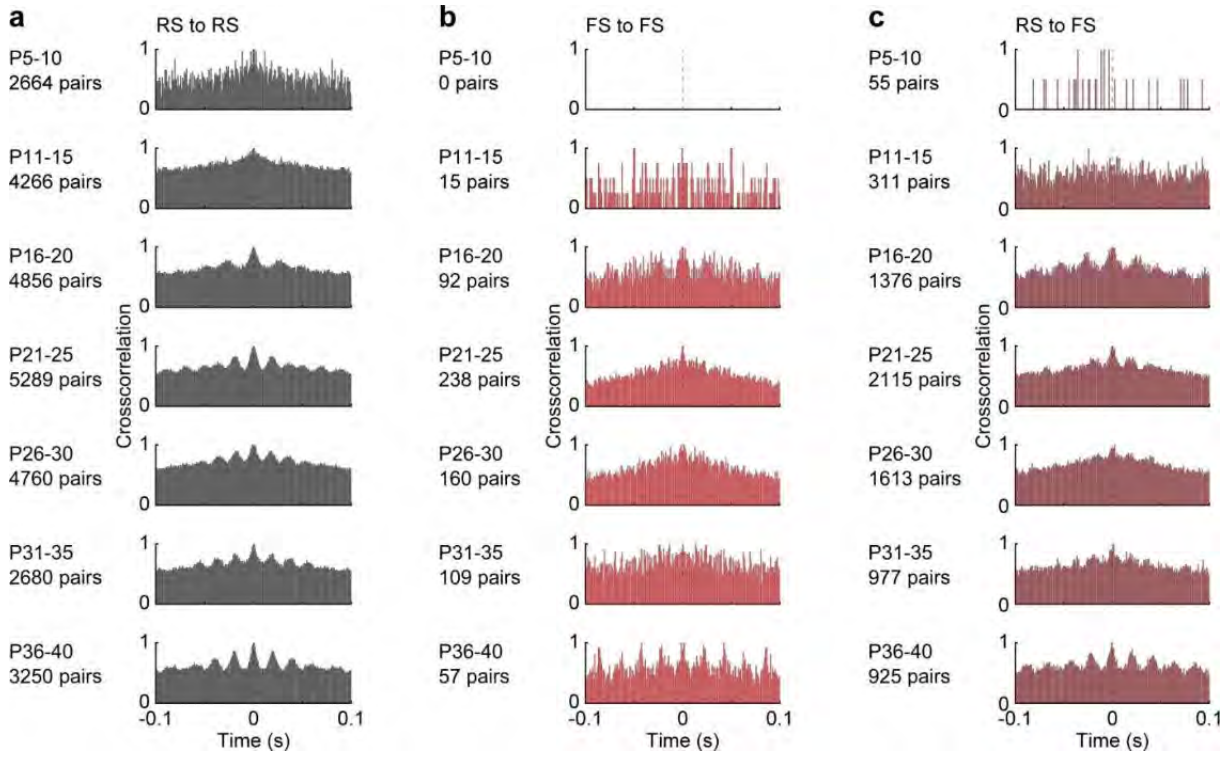

Figure 5 – figure supplement 3. Crosscorrelations of RS and FS units during spontaneous activity.

(**a**) Average crosscorrelation histograms of all simultaneously recorded RS unit pairs during ramp light stimulation for different age groups. (**b**) Same as (**a**) for FS unit pairs. (**c**) Same as (**a**) for RS-FS unit pairs (See Supplementary file 1 for a summary of experimental conditions).

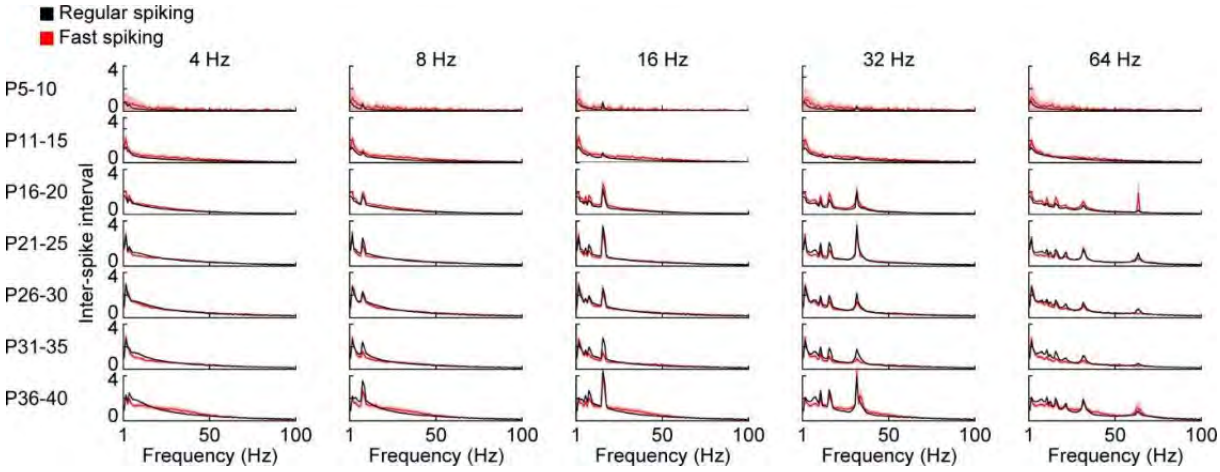

Figure 6 – figure supplement 1. Inter-spike intervals of RS and FS units during pulse light stimulation.

Inter-spike intervals of prefrontal RS (black, n = 1824 units from 66 recordings/mice) and FS (red, n = 226 units from 66 recordings/mice) units in response to repetitive ramp light stimulation of L2/3 PYRs (3 ms, 473 nm) of 4, 8, 16, 32, and 64 Hz averaged for different age groups. (Average data is displayed as mean ± sem. See Supplementary file 1 for a summary of experimental conditions).

Article

Neuron

Resolving and Rescuing Developmental Miswiring in a Mouse Model of Cognitive Impairment

Graphical Abstract

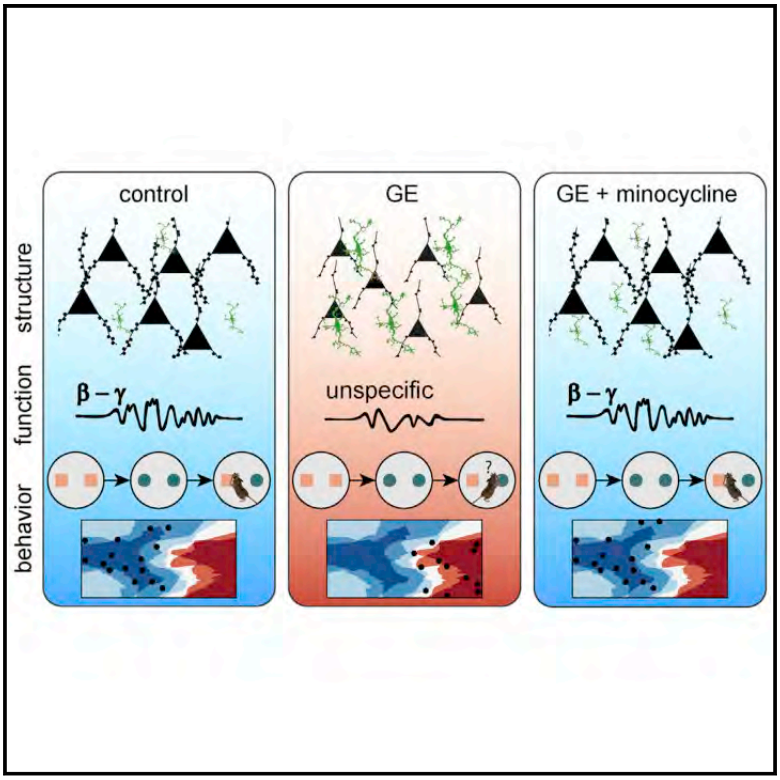

Authors

Mattia Chini, Jastyn A. Pöpplau, Christoph Lindemann, ..., Sebastian H. Bitzenhofer, Christoph Mulert, Ileana L. Hanganu-Opatz

Correspondence

hangop@zmnh.uni-hamburg.de

In Brief

In a mouse model of mental disorders, Chini et al. dissect an early-emerging prefrontal network dysfunction that subsequently gives rise to cognitive deficits. They show that this deficiency can be rescued by minocycline administration, thus identifying a potential biomarker amenable for future therapies.

Highlights

- Mice mimicking the etiology of mental illness have dysregulated prefrontal network
- Weaker beta activation of prefrontal circuits results from superficial layers deficits
- Rescue of microglial function restores developing prefrontal function and behavior
- Early prefrontal dysfunction relates to later-emerging cognitive performance

Chini et al., 2020, Neuron *105*, 60–74
January 8, 2020
https://doi.org/10.1016/j.neuron.2019.09.042

CellPress

CellPress

Neuron
Article

Resolving and Rescuing Developmental Miswiring in a Mouse Model of Cognitive Impairment

Mattia Chini,[1] Jastyn A. Pöpplau,[1] Christoph Lindemann,[1] Laura Carol-Perdiguer,[1] Marilena Hnida,[1] Victoria Oberländer,[1,3] Xiaxia Xu,[1] Joachim Ahlbeck,[1,4] Sebastian H. Bitzenhofer,[1,5] Christoph Mulert,[2,6] and Ileana L. Hanganu-Opatz[1,7,*]

[1]Developmental Neurophysiology, Institute of Neuroanatomy, University Medical Center Hamburg-Eppendorf, 20246 Hamburg, Germany
[2]Psychiatry Neuroimaging Branch (PNB), Department of Psychiatry and Psychotherapy, University Medical Center Hamburg-Eppendorf, 20246 Hamburg, Germany
[3]Present address: Department of Neuroscience, University of Helsinki, Helsinki 00014, Finland
[4]Present address: Department of Neurophysiology and Pathophysiology, University Medical Center Hamburg-Eppendorf, 20246 Hamburg, Germany
[5]Present address: Center for Neural Circuits and Behavior, Department of Neurosciences, University of California, San Diego, La Jolla, CA 92093, USA
[6]Present address: Centre for Psychiatry and Psychotherapy, Justus Liebig University, Giessen, Germany
[7]Lead Contact
*Correspondence: hangop@zmnh.uni-hamburg.de
https://doi.org/10.1016/j.neuron.2019.09.042

SUMMARY

Cognitive deficits, core features of mental illness, largely result from dysfunction of prefrontal networks. This dysfunction emerges during early development, before a detectable behavioral readout, yet the cellular elements controlling the abnormal maturation are still unknown. Here, we address this open question by combining *in vivo* electrophysiology, optogenetics, neuroanatomy, and behavioral assays during development in mice mimicking the dual genetic-environmental etiology of psychiatric disorders. We report that pyramidal neurons in superficial layers of the prefrontal cortex are key elements causing disorganized oscillatory entrainment of local circuits in beta-gamma frequencies. Their abnormal firing rate and timing relate to sparser dendritic arborization and lower spine density. Administration of minocycline during the first postnatal week, potentially acting via microglial cells, rescues the neuronal deficits and restores pre-juvenile cognitive abilities. Elucidation of the cellular substrate of developmental miswiring causing later cognitive deficits opens new perspectives for identification of neurobiological targets amenable to therapies.

INTRODUCTION

Cortical function relies on the precise wiring and activation of diverse populations of pyramidal cells and interneurons that are entrained in oscillatory rhythms. Although recent studies have revealed several assembling rules of cortical microcircuits in the adult brain (Harris and Shepherd, 2015), their ontogeny is still poorly understood. Given the uniqueness of the developing brain in its spatial and temporal organization of coordinated activity (Brockmann et al., 2011; Khazipov et al., 2004), the depolarizing action of GABA (Kirmse et al., 2015) and the formation of transient connectivity patterns (Marques-Smith et al., 2016), the functional coupling within immature microcircuits is likely to bear equally unique traits. Elucidating the features of such immature networks is of paramount importance in the context of neurodevelopmental disorders, as their early disruption is thought to underlie the later emergence of devastating symptoms that characterize these diseases (Marín, 2016).

We started to elucidate the mechanisms of functional coupling within the developing brain and have shown that pyramidal neurons in the superficial layers of the prefrontal cortex (PFC) play a fundamental role in generating beta/low-gamma oscillations in the neonatal mouse (Bitzenhofer et al., 2017). At adulthood, coordinated activity in gamma-frequency band is instrumental to cognitive processing (Bosman et al., 2014) and relates to the pathophysiology of psychiatric disorders (Cho et al., 2015; Uhlhaas and Singer, 2015). Disturbed gamma activity has been observed long before the onset of psychosis in high-risk humans (Leicht et al., 2016) and during neonatal development in animal models (Hartung et al., 2016). However, the circuit dysfunction underlying such abnormalities is still unknown.

To address this knowledge gap, we interrogate the developing prefrontal network in a mouse model mimicking both the genetic (mutation of the intracellular hub of developmental processes Disrupted-In-Schizophrenia 1 [DISC1] gene; Brandon and Sawa, 2011) and the environmental (challenge by maternal immune activation [MIA]) background that has been related to mental illness (dual-hit genetic-environmental [GE] mice). At adult age, these mice mimic, to a large extent, the network dysfunction as well as memory and attention deficits identified in human psychiatric disorders (Abazyan et al., 2010). The impairment of prefrontal-hippocampal circuits underlying

poorer cognitive performance emerges early in life only when both risk factors converge and is absent in neonatal mice challenged with the genetic or environmental stressor alone (Hartung et al., 2016). To elucidate the mechanisms of developmental dysfunction, we focus on neonatal age (end of 1st–beginning of 2nd postnatal week) of rodents that roughly corresponds to the second/third trimester of human pregnancy, a period of high vulnerability for mental disorders (Selemon and Zecevic, 2015). We combine *in vivo* and *in vitro* electrophysiology with optogenetics, pharmacology, behavioral testing, and confocal microscopy-based structural investigations of the prelimbic subdivision (PL) of the prefrontal cortex. We show that pyramidal neurons in superficial layers exhibit major morphological, synaptic, and functional deficits and lack the ability to organize the beta-gamma entrainment of local prelimbic circuits in neonatal dual-hit GE mice, while deep layers neurons are largely unaffected. Transient administration of minocycline, potentially modulating microglia inflammatory response (Kobayashi et al., 2013), rescues electrophysiological and structural deficits, as well as cognitive abilities at juvenile age. Moreover, we propose that early disruption of prefrontal networks might be predictive of memory impairment at juvenile age.

RESULTS

Layer- and Frequency-Specific Dysfunction of Local Circuits in the Prelimbic Cortex of Dual-Hit GE Mice

To get first insights into the source of prelimbic dysfunction in dual-hit GE mice, we performed extracellular recordings of the local field potential (LFP) and multiple-unit activity (MUA) over prelimbic layers using four-shank 16 site electrodes in lightly anesthetized (Chini et al., 2019) postnatal day (P) 8–10 control (n = 38 pups from 13 litters) and GE mice (n = 18 pups from 6 litters). This developmental stage corresponds to the initiation of hippocampus-driven entrainment of prelimbic circuitry (Ahlbeck et al., 2018; Brockmann et al., 2011). The exact position of recording sites covering superficial and deep layers was confirmed by the reconstruction of electrode tracks *post mortem* (Figure 1A). In line with our previous findings (Bitzenhofer et al., 2015; Brockmann et al., 2011; Cichon et al., 2014; Hartung et al., 2016), the first patterns of network activity in the neonatal PL of all investigated control and dual-hit GE mice were discontinuous, i.e., spindle-shaped oscillations switching between theta and beta-gamma frequency components alternated with long periods of network silence (Figure 1B). The firing of prelimbic neurons was strongly timed by the oscillatory rhythms. As previously reported (Chini et al., 2019), the patterns of network oscillations and neuronal firing in the PL were similar in urethane-anesthetized and non-anesthetized neonatal pups, yet the magnitude of activity decreased in the presence of anesthesia (Figure S1). The similarities might be due to the ability of urethane to mimic sleep conditions (Clement et al., 2008), the dominant behavioral state of neonatal mice (Cirelli and Tononi, 2015). Although dual-hit GE mice have been reported to have profoundly altered network activity and neuronal firing at neonatal age when compared with controls (Hartung et al., 2016), it is still unclear whether the dysfunction equally affects the local prelimbic circuits. To address this question, we first monitored the layer-specific differences between oscillatory patterns of control and dual-hit GE mice. Major differences in the occurrence, duration, and broadband power of oscillatory events were detected when comparing the two groups of mice (Figures 1C, 1D, and S2A–S2E; Table S1). However, these detected differences were similar across layers. This might be due, on the one hand, to a layer-unspecific overall damping of entrainment in dual-hit GE mice and, on the other hand, to non-specific conduction synchrony within a rather small tissue volume (300- to 400-μm radius). To discriminate between the two sources, in a second step, we investigated the layer-specific firing rate and timing by oscillatory phase, which are not contaminated by non-specific volume conduction. The firing of neurons in prelimbic superficial layers in GE mice (log −2.1 ± 0.1 spikes/s) was significantly ($p < 10^{-7}$) reduced when compared to controls (0.61 ± 0.04 spikes/s; Figure 1E). In contrast, neurons in deep layers similarly fired in control (−0.95 ± 0.05 spikes/s) and GE mice (−1.3 ± 0.2 spikes/s). The timing of neuronal firing in relation to beta (12–30 Hz) and gamma (30–100 Hz) frequency was also disturbed and lost its precision in superficial layers ($p < 1 \times 10^{-4}$ and p = 0.021, respectively), but not deep-layer neurons of GE mice when compared to controls (Figures 1F–1H). The timing of spiking by theta oscillations in both superficial and deep layers was similar in control and dual-hit GE mice (Figure S2E). To verify that our results were not biased by anesthesia, we recorded a set of non-anesthetized P8–P10 control (n = 16) and GE (n = 18) mice and confirmed that GE mice have reduced broadband LFP power. The decreased MUA and single-unit activity (SUA) firing rates were limited to neurons in superficial layers (Figures S1G–S1L). In contrast to the significant perturbation of prelimbic activity in neonatal dual-hit GE mice, the oscillatory and firing patterns of one-hit genetic (G) (i.e., only DISC1) or environmental (E) (i.e., only MIA) mice were similar to those of control pups (Figures S2F–S2H). Furthermore, the layer-specific dysfunction seems to be characteristic to the investigated developmental stage P8–P10. In mice of 4–6 days of age, a time window in which neurons are still migrating (Ignacio et al., 1995), deficits are present, yet the layer specificity is lacking (Figures S2I–S2K). On the other hand, in line with our previous data (Hartung et al., 2016), the properties of prelimbic network oscillations were similar in control and dual-hit GE mice at pre-juvenile age (P20–P23; Figures S2L–S2N).

These results demonstrate abnormal beta-gamma band oscillations and entrainment of superficial layers of PL in dual-hit GE mice during this defined developmental period (P8–P10).

Beta-Gamma Band Dysfunction of Prelimbic Circuits in Dual-Hit GE Mice Results from Abnormal Activation of Superficial Layers Pyramidal Neurons

In developing circuits, beta-gamma band oscillatory activity has been recently shown to require the activation of pyramidal neurons in superficial ($PYRs_{SUP}$), but not deep, layers ($PYRs_{DEEP}$) of PL (Bitzenhofer et al., 2017). Therefore, the weaker beta-gamma entrainment of prelimbic circuits and coupling of neuronal firing to fast oscillations identified in GE mice might result from dysfunction of $PYRs_{SUP}$. To test this hypothesis, we monitored the effects of light activation of prelimbic neurons

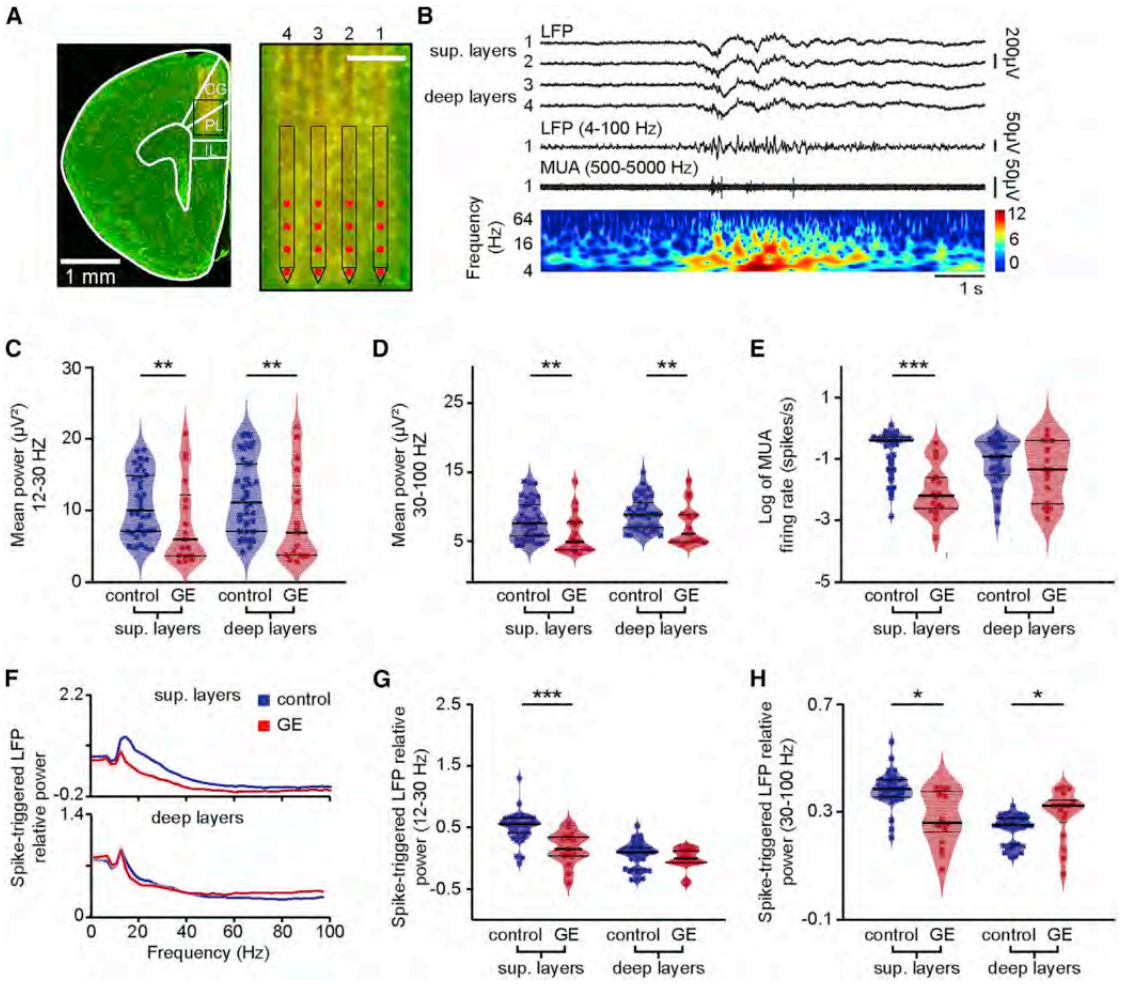

Figure 1. Abnormal Patterns of Discontinuous Oscillatory Activity and Neuronal Firing over the Layers of Prelimbic Cortex of Neonatal Dual-Hit GE Mice

(A) Digital photomontage reconstructing the position of a 4-shank DiI-labeled recording electrode in the PL of a Nissl-stained 100-µm-thick coronal section (green) from a P9 mouse. Inset, the position of recording sites (red) over the prelimbic layers is displayed at higher magnification. Scale bar, 200 µm.

(B) Characteristic discontinuous oscillatory activity recorded in superficial and deep layers of PL before (top) and after band pass (4–100 Hz) filtering (middle; recording site 1 in superficial layers) and the corresponding MUA after band pass (500–5,000 Hz) filtering (bottom; recording site 1 in superficial layers). Color-coded frequency plot shows the wavelet of the LFP (recording site 1) at identical timescale.

(C) Violin plot displaying the power in beta frequency band of oscillations in superficial and deep layers of the prelimbic cortex of control (blue; n = 38) and GE (red; n = 18) mice.

(D and E) Same as (C) for the power in gamma frequency band (D) and MUA firing rate (E).

(F) Plots of frequency-dependent relative power of spike-triggered LFP in superficial (top) and deep layers (bottom) of control (blue) and GE (red) mice.

(G) Violin plot displaying the relative power of spike-triggered LFP in beta band for superficial and deep layers of control (blue; n = 38) and GE (red; n = 18) mice.

(H) Same as (G) for the LFP in gamma band.

For (C)–(E), (G), and (H), data are presented as median with 25th and 75th percentile, and single data points are shown as asterisks. The shaded area represents the probability distribution of the variable. *p < 0.05, **p < 0.01, and ***p < 0.001; analysis of covariance (ANCOVA) with age as covariate (C–E) and Yuen's bootstrap test (G and H) with 20% level of trimming for the mean.

that were transfected with light-sensitive proteins and the red fluorescent protein tDimer2. Using our recently established protocol for optogenetic manipulation of developing circuits (Bitzenhofer et al., 2017), we achieved cell-type-, layer-, and area-specific transfection of neurons by *in utero* electroporation (IUE) (Figures S3A and S3B). Constructs coding for the double mutant channelrhodopsin E123 T159 (ChR2(ET/TC)) were transfected by IUE at embryonic day (E) 15.5 and E12.5 for selective targeting of superficial and deep layers, respectively (Figures S3C and S3D). Staining for NeuN showed that a similar fraction of neurons was transfected in control (34.7% ± 0.8%; n = 13 pups) and GE mice (32.0% ± 0.7%; n = 8 pups). The pyramidal-like shape and orientation of primary dendrites confirmed that the expression constructs were exclusively integrated into cell lineages of pyramidal neurons. Omission of ChR2(ET/TC) from the expression construct (i.e., opsin-free) yielded similar

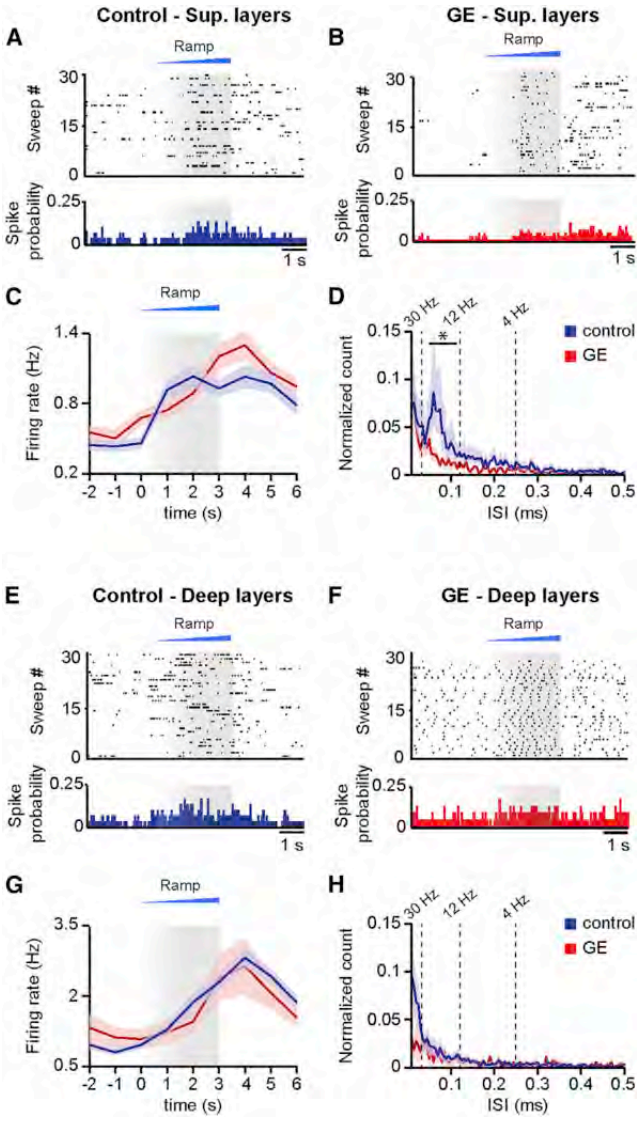

Figure 2. Firing Patterns after Optogenetic Activation of $PYRs_{SUP}$ and $PYRs_{DEEP}$ in Control and Dual-Hit GE Mice *In Vivo*

(A) Representative raster plot and corresponding spike probability histogram displaying the firing of a $PYRs_{SUP}$ from a control mouse in response to 30 sweeps of ramp stimulation (473 nm; 3 s).

(B) Same as (A) for transfected $PYRs_{SUP}$ from GE mice.

(C) Line plot displaying the mean MUA firing rate in transfected $PYRs_{SUP}$ of control (blue; n = 43 recording sites from 13 pups) and GE (red; n = 40 recording sites from 10 mice) mice in response to ramp illumination.

(D) Same as (C) for inter-spike interval within 10- to 500-ms range normalized to all ISIs.

(E–H) Same as (A)–(D) for transfected $PYRs_{DEEP}$ from control (n = 116 recording sites from 13 pups) and GE mice (n = 27 recording sites from n = 6 pups). Data are presented as mean ± SEM. *p < 0.05; linear mixed-effect model with animal as a random effect.

expression rates and distribution of tDimer2-positive neurons. Moreover, the success rate of transfection by IUE was similar in control and dual-hit GE mice in the presence and absence of opsin (Figure S3E).

The transfection procedure by IUE had no major effects on the overall development of animals (Figures S3F–S3K). Although IUE caused significant reduction of litter size in both control and GE mice (non-electroporated: 8.3 ± 1.1 pups/litter; IUE: 4.6 ± 1.3 pups/litter; p = 0.03), all investigated pups had similar body length, tail length, and weight during the early postnatal period. Vibrissa placing, surface righting, and cliff aversion reflexes were also not affected by IUE or transfection of neurons with opsins (Figures S3I–S3K).

First, we assessed the efficiency of light stimulation in inducing action potentials (APs) in prelimbic neurons of control and dual-hit GE mice *in vitro*. For this, whole-cell patch-clamp recordings were performed from tDimer2-positive $PYRs_{SUP}$ (n = 42) and $PYRs_{DEEP}$ (n = 38) in coronal slices containing the PL from P8–P10 mice after IUE at E15.5 and E12.5, respectively. In line with the previously reported "inside-out" pattern of cortical maturation and, correspondingly, the more mature profile of neurons in deep versus superficial layers, $PYRs_{SUP}$ and $PYRs_{DEEP}$ in control mice significantly differed in some of their passive and active membrane properties (Bitzenhofer et al., 2017). However, in dual-hit GE mice, the resting membrane potential of $PYRs_{SUP}$ (−53.2 ± 0.37 mV) was more positive when compared with controls (−63.2 ± 0.3 mV; $p = 2 \times 10^{-4}$), and the maximum amplitude of action potentials decreased (44.8 ± 0.80 mV versus 29.2 ± 0.36 mV in controls; p = 0.018). These alterations of intrinsic neuronal properties might point to the immaturity of $PYRs_{SUP}$ in GE mice, even though membrane resistance, membrane time constant, and action potential half-width were not significantly different across conditions (Figures S4A–S4E). The passive and active properties of ChR2(ET/TC)-transfected neurons were similar to those previously reported for age-matched mice (Bitzenhofer et al., 2017). Pulsed light stimulation (3 ms, 473 nm, 5.2 mW/mm^2) depolarized transfected fluorescently labeled neurons and led to robust firing in all pups. The probability of triggering APs by pulsed light stimuli decreased with increasing stimulation frequency, yet it differed in its dynamics in control versus GE mice. Whereas $PYRs_{SUP}$ of control mice were able to reliably follow light stimulations up to 16 Hz, in GE mice, they had a significant firing drop already between 8 and 16 Hz (Figures S4E and S4F). Light stimulation of $PYRs_{DEEP}$ showed a similar decrease of firing probability with augmenting stimulation frequency in control and GE mice.

To elucidate the consequences of abnormal intrinsic firing preference for oscillatory network entrainment, we monitored the effects of light activation of either $PYRs_{SUP}$ or $PYRs_{DEEP}$ *in vivo*. In controls, activation of $PYRs_{SUP}$ selectively drove the neonatal prelimbic networks in beta-gamma frequency range, whereas activation of $PYRs_{DEEP}$ caused non-specific network activation. We reasoned that, if $PYRs_{SUP}$ are indeed the cause of the previously demonstrated disruption of beta-gamma activity in the PL of GE mice, then their light stimulation *in vivo* should not be able to selectively induce oscillations in this range.

Ramp light stimulation increased the neuronal firing of ChR2(ET/TC)-transfected $PYRs_{SUP}$ and $PYRs_{DEEP}$ in control and GE mice ($p < 10^{-4}$ for all conditions), but not of neurons transfected with opsin-free constructs (Figures 2A–2H and S5).

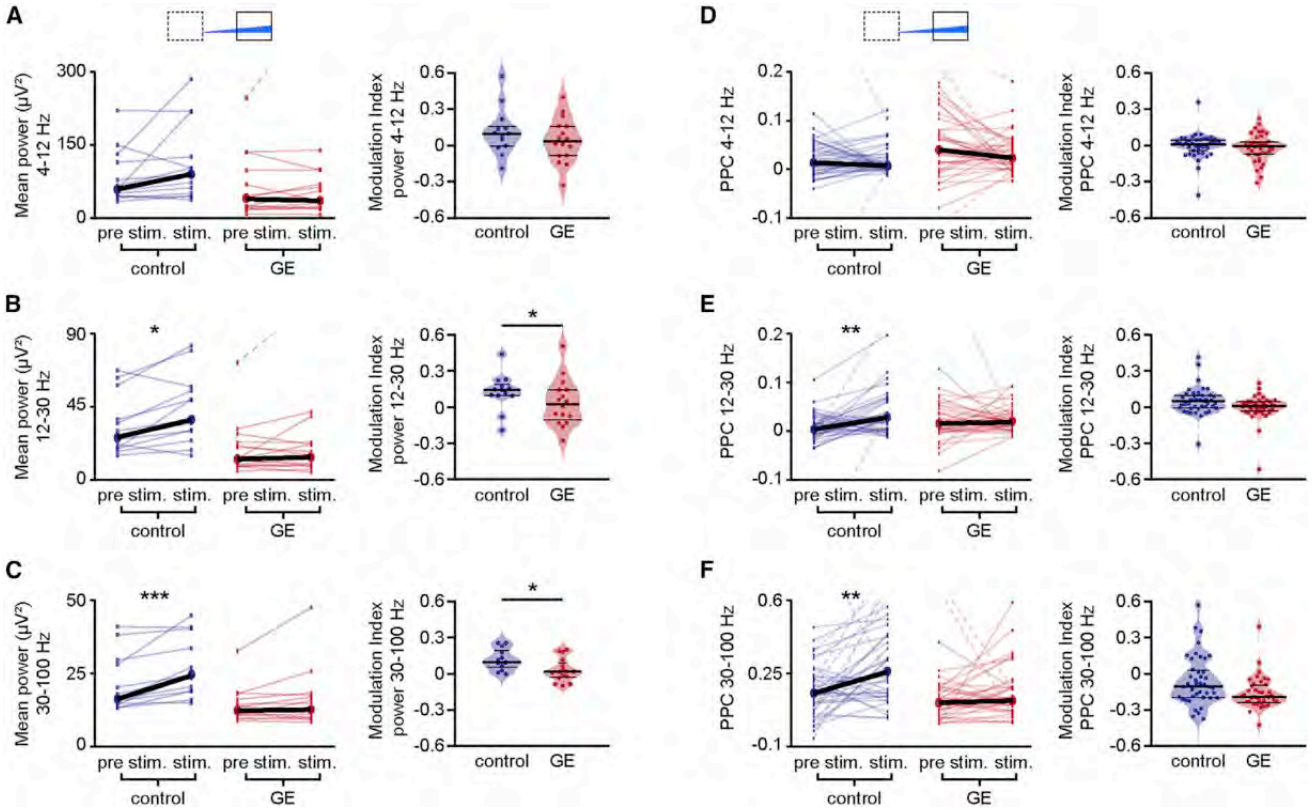

Figure 3. Network Activity after Optogenetic Activation of $PYRs_{SUP}$ in Control and Dual-Hit GE Mice *In Vivo*

(A) Left: scatterplot displaying the LFP power in the theta (4–12 Hz) frequency band for control (blue; n = 13) and GE (red; n = 16) mice before (pre stim.; 1.5 s) and during the second half (stim.; 1.5 s) of ramp stimulation. Right: violin plot displaying the stimulation modulation index of light-induced LFP power in the theta frequency band for control and GE mice is shown.

(B and C) Same as (A) for beta (12–30 Hz) and gamma (30–100) frequency bands.

(D–F) Same as (A)–(C) for pairwise phase consistency (PPC) of $PYRs_{SUP}$ in control (n = 43 recording sites from 13 pups) and GE (n = 40 recording sites from 10 pups) mice.

In scatterplots (A–F), data are presented as median, and individual values are displayed as thin dots and lines. In violin plots (A–F), data are presented as median with 25th and 75th percentile, and single data points are shown as asterisks. *p < 0.05, **p < 0.01, and ***p < 0.001; Yuen's bootstrap test (A–F) with 20% level of trimming for the mean and linear mixed-effect model with animal as a random effect (D–F).

The light-induced augmentation of firing was similar in the two groups of mice (p = 0.46 and p = 0.24 for $PYRs_{SUP}$ and $PYRs_{DEEP}$, respectively). The spike discharge initiated once the power exceeded a certain threshold. For some neurons, the firing decreased toward the end of the ramp stimulations, indicating that, similar to the *in vitro* conditions, their membrane potential reached a depolarizing plateau, preventing further spiking. However, for the majority of neurons, the firing rate after stimulus remained higher than before the stimulus (Figures 2C and 2G), suggesting that global network activation had been induced by light stimulation in the developing circuits. Major differences in the firing of prelimbic neurons from control and GE mice were detected. Although $PYRs_{SUP}$ in controls had a preferred inter-spike interval of ~60 ms, equivalent to a population firing at 16.7 Hz (Figures 2A and 2D), a coordinated frequency-tuned discharge pattern was absent in GE mice upon ramp stimulation of $PYRs_{SUP}$ (condition effect, $p = 4 \times 10^{-5}$; p < 0.05 in the 15- to 20-Hz range with the exception of p = 0.059 at 16.7 Hz; Figures 2B and 2D). In contrast, the firing dynamics of $PYRs_{DEEP}$ was similar in control and GE mice (condition effect p = 0.11) and showed no frequency-specific concentration of firing during ramp stimulation (Figures 2E–2H).

To causally prove the contribution of abnormal firing of $PYRs_{SUP}$ to the weaker beta-gamma band entrainment previously identified in the PL of dual-hit GE mice, we tested the effects of ramp stimulations on the discontinuous network oscillations. When compared with pulsed stimulations, ramp stimulations have the advantage of not inducing power contamination by repetitive and fast large-amplitude voltage deflections resulting from simultaneous opening of light-activated channels and to trigger more physiological and not artificially synchronous firing patterns (Bitzenhofer et al., 2017). In control mice, the LFP power in beta- and gamma-frequency range significantly increased during ramp stimulation of $PYRs_{SUP}$ (p = 0.02 and p = 0.002, respectively), whereas the theta-band activity remained unaffected (p = 0.26). In contrast, $PYRs_{SUP}$ in GE mice lost their ability to boost neonatal prelimbic oscillations in a frequency-specific manner, because ramp

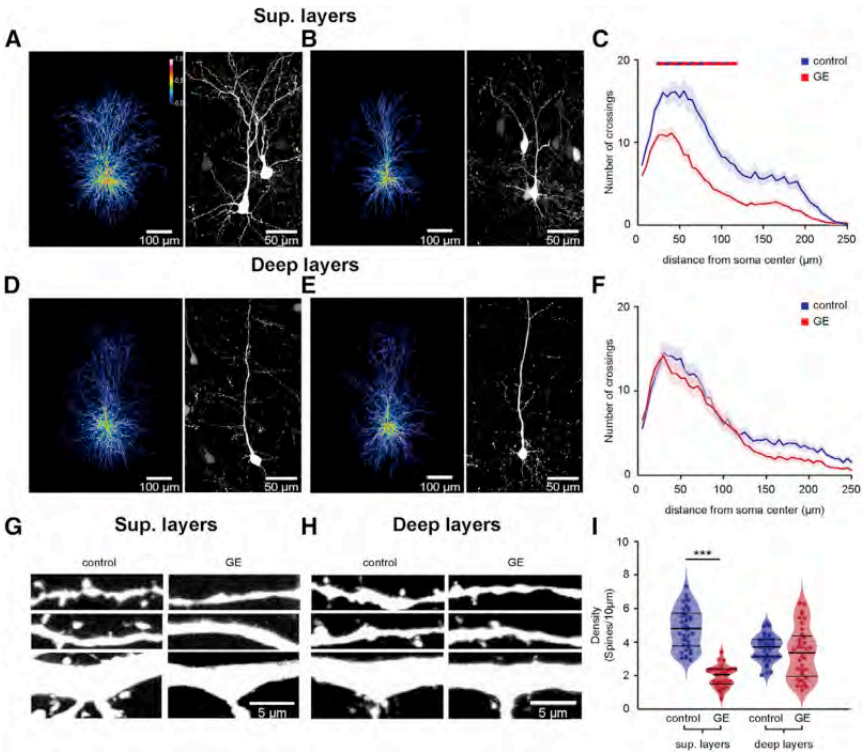

Figure 4. Simplified Dendritic Arborization and Reduced Spine Density in $PYRs_{SUP}$ of Dual-Hit GE Mice

(A) Left: heatmap displaying an overlay of all traced dendrites of transfected $PYRs_{SUP}$ in control mice. Right: photograph of a representative $PYRs_{SUP}$ in a P10 mouse is shown.

(B) Same as (A) for a P10 dual-hit GE mouse.

(C) Graph displaying the average number of dendritic intersections within a 250-µm radius from the soma center of $PYRs_{SUP}$ in control (blue; n = 21 neurons from 3 pups) and GE (red; n = 21 neurons from 3 pups) mice. Blue/red bar indicates significant difference between control and GE mice.

(D–F) Same as (A)–(C) for $PYRs_{DEEP}$ from control (blue; n = 21 neurons from 3 pups) and GE (red; n = 21 neurons from 3 pups) mice.

(G) Photograph displays representative basal (top), secondary apical (middle), and proximal oblique and apical (bottom) dendrites of a $PYRs_{SUP}$ from a P10 control mouse (left) and a P10 GE mouse (right).

(H) Same as (G) for $PYRs_{DEEP}$.

(I) Violin plot displaying the average spine density on dendrites from $PYRs_{SUP}$ of control (blue; n = 39 dendrites from 13 neurons) and GE (red; n = 30 dendrites from 10 neurons) mice.

In (C) and (F), data are presented as mean ± SEM. In (I), data are presented as median with 25th and 75th percentile, and single data points are displayed as asterisks. *p < 0.05, **p < 0.01, and ***p < 0.001; linear mixed-effect model with animal (C and F) and neuron (I) as random effects.

stimulations did not affect the LFP power (p = 0.49, p = 0.57, and p = 0.44 for theta-, beta-, and gamma-frequency band, respectively; Figure 3A). Moreover, stimulation of $PYRs_{SUP}$ differently modulated power in beta- and gamma-frequency band between control and GE mice (p = 0.03 and p = 0.03, respectively). Not only the light-induced inter-spike interval and power of network oscillations were disrupted in GE mice, but also the timing of firing by the oscillatory phase was impaired. To quantify this relationship, we used pairwise phase consistency (PPC), a measure of synchrony that is not biased by firing rates (Vinck et al., 2010). In control mice, stimulation increased the PPC for beta (p = 0.008) and gamma oscillations (p = 0.003), but not for theta (p = 0.24). In contrast, the PPC for theta (p = 0.09), beta (p = 0.86), and gamma oscillations (p = 0.37) during stimulation of $PYRs_{SUP}$ in GE mice did not change (Figures 3D–3F), indicating that the synchronization of spikes relative to the phase of these oscillations was not affected by light activations of $PYRs_{SUP}$. However, due to high variability, no difference in PPC modulation between the two mouse groups achieved statistical significance (Figures 3D–3F).

In line with the frequency-unspecific augmentation of firing rate after light activation of $PYRs_{DEEP}$ in control mice, the LFP power in all frequency bands increased during stimulation and remained at a high level even after it. In GE mice, optogenetic stimulation did not augment the power. No differences in power modulation between the two mouse groups were detected (Figure S6).

Thus, the reduced beta-gamma activity in the PL of neonatal dual-hit GE mice relates to the dysfunction of firing dynamics of $PYRs_{SUP}$.

Pyramidal Neurons in the Superficial Layers of PL in Neonatal Dual-Hit GE Mice Show Major Morphological and Synaptic Deficits

The selective dysfunction of $PYRs_{SUP}$ and the corresponding abnormal network activity in GE mice might relate to abnormal morphology and connectivity of these neurons at neonatal age. To test this hypothesis, we undertook a detailed histological examination of the cytoarchitecture of tDimer-labeled pyramidal neurons in superficial and deep layers of P10 control and GE mice. $PYRs_{SUP}$, but not $PYRs_{DEEP}$, of GE mice showed a significant reduction in the soma size when compared to neurons of controls (n = 21 neurons for every condition; p = 0.039 for $PYRs_{SUP}$ and p = 0.95 for $PYRs_{DEEP}$; Figure S7A). The complexity of dendritic branching was assessed by Sholl analysis of three-dimensionally reconstructed $PYRs_{SUP}$ and $PYRs_{DEEP}$. When compared to controls, $PYRs_{SUP}$ of GE mice had major reduction in dendritic branching (condition effect $p < 1 \times 10^{-9}$; Figures 4A–4C). These deficits were particularly prominent within a radius of 20–115 µm from the cell soma center (p < 0.05 for all pairwise comparisons). In accordance with our electrophysiological results, we found no significant differences in the complexity of dendritic arborization for $PYRs_{DEEP}$ of GE and control mice (condition effect p = 0.56; Figures 4D–4F). Accordingly, the total dendritic branch length was reduced in

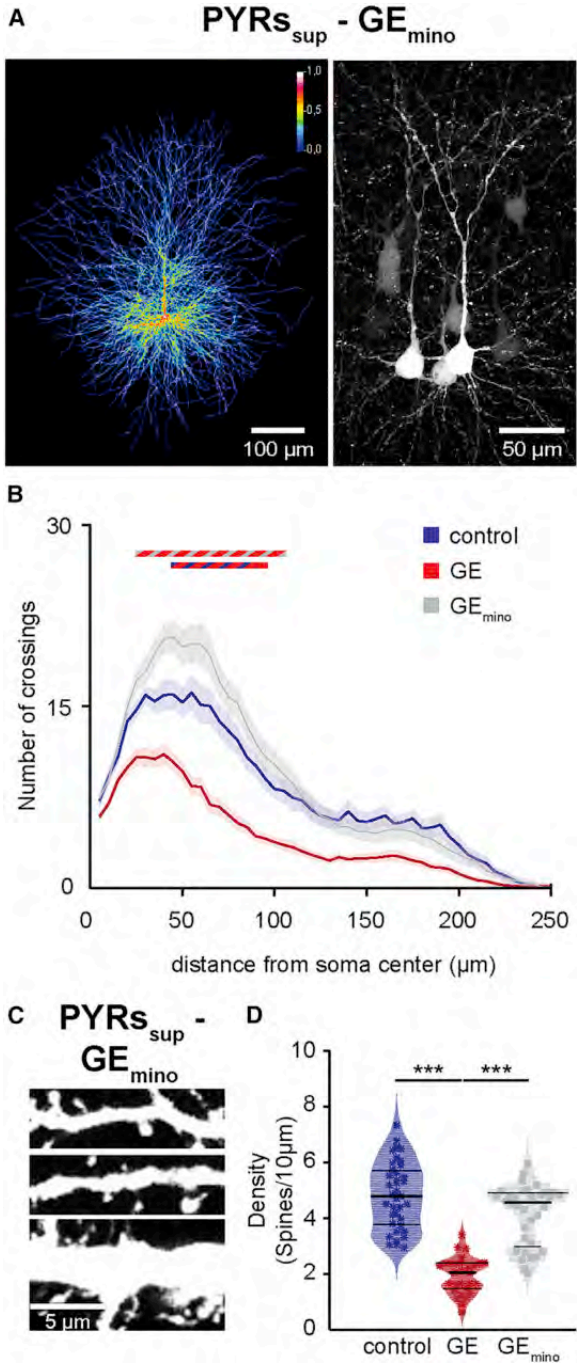

Figure 5. Minocycline Treatment Rescues the Abnormal Structure of $PYRs_{SUP}$ in GE Mice

(A) Left: heatmap displaying an overlay of all traced dendrites of transfected $PYRs_{SUP}$ in GE_{mino} mice. Right: photograph of a representative PYR_{SUP} in a P10 GE_{mino} mouse is shown.

(B) Graph displaying the average number of dendritic intersections within a 250-µm radius from the soma center of $PYRs_{SUP}$ in control (blue; n = 21 neurons from 3 pups), GE (red; n = 21 neurons from 3 pups), and GE_{mino} (gray; n = 21 neurons from 3 pups) mice. Blue/red and gray/red bars indicate significant difference between control and GE mice and GE and GE_{mino} mice, respectively.

(C) Photograph displays representative basal (top), secondary apical (middle), and proximal oblique and apical (bottom) dendrites of a PYR_{SUP} from a P10 GE_{mino} mouse.

(D) Violin plot displaying the average spine density on dendrites from $PYRs_{SUP}$ of control (blue; n = 39 dendrites from 13 neurons), GE (red; n = 30 dendrites from 10 neurons), and GE_{mino} (gray; n = 36 dendrites from 12 neurons) mice.

In (B), data are presented as mean ± SEM. In (D), data are presented as median with 25th and 75th percentile, and single data points are displayed as asterisks. ***p < 0.001; linear mixed-effect model with animal (B) and neuron (D) as random effects.

$PYRs_{SUP}$, but not $PYRs_{DEEP}$, of GE mice (n = 21 neurons for every condition; p = 0.024 for $PYRs_{SUP}$ and p = 0.37 for $PYRs_{DEEP}$; Figure S7B).

Next, we examined the spine density along the dendrites of $PYRs_{SUP}$ and $PYRs_{DEEP}$, whose dendritic morphology we had previously analyzed. $PYRs_{SUP}$ of GE mice (n = 10 neurons) had significantly lower density when compared to controls (n = 13 neurons; condition effect $p = 7 \times 10^{-4}$), whereas the values were comparable for $PYRs_{DEEP}$ of control (n = 9 neurons) and GE mice (n = 9 neurons; condition effect p = 0.75; Figures 4G–4I). The magnitude of density reduction was similar for different types of dendrites (apical and proximal oblique dendrites, secondary apical dendrites, and basal dendrites; condition effect $p = 7 \times 10^{-4}$, $p = 5 \times 10^{-4}$, and p = 0.001, respectively; Figures S7C–S7E). In line with the network dysfunction, the prominent morphological/structural deficits seem to be largely confined to neonatal age. $PYRs_{SUP}$ of pre-juvenile (P21) GE mice had a normal dendritic arborization (n = 28 neurons; condition effect p = 0.99) and spine density (n = 16 neurons; condition effect p = 0.3). Only soma size and total dendritic path length were slightly decreased, yet not at significance level (n = 28 neurons; p = 0.088 and p = 0.055, respectively; Figures S7F–S7J).

The simplified dendritic arborization and the decreased spine density of $PYRs_{SUP}$, but not $PYRs_{DEEP}$, further confirm the layer-specific dysfunction in neonatal dual-hit GE mice.

Transient Minocycline Administration Rescues Prelimbic Deficits in Dual-Hit GE Mice

We next set out to determine whether the morphological and functional deficits of $PYRs_{SUP}$ in the PL of GE mice could be rescued during early development. Minocycline is a tetracycline antibiotic that exerts a variety of functions and has anti-inflammatory properties (Garrido-Mesa et al., 2013). Minocycline has recently shown promising results as an adjunct drug to treat depression (Emadi-Kouchak et al., 2016), bipolar disorder (Savitz et al., 2018), and schizophrenia (Zhang et al., 2018) and even to delay or prevent the incidence of schizophrenia (Sellgren et al., 2019). However, in the absence of mechanistic insights, its therapeutic potential remains controversial (Deakin et al., 2018; Kishimoto et al., 2018).

We administered minocycline from P1 to P8 by adding it to the drinking water of the dam (Dansie et al., 2013; Luzi et al., 2009) and analyzed the morphological, functional, and behavioral consequences in P8–P10 pups. First, Sholl analysis of three-dimensionally reconstructed tDimer-positive $PYRs_{SUP}$ (n = 21 neurons) from GE_{mino} mice showed that the complexity of dendritic branching was fully restored after treatment, being

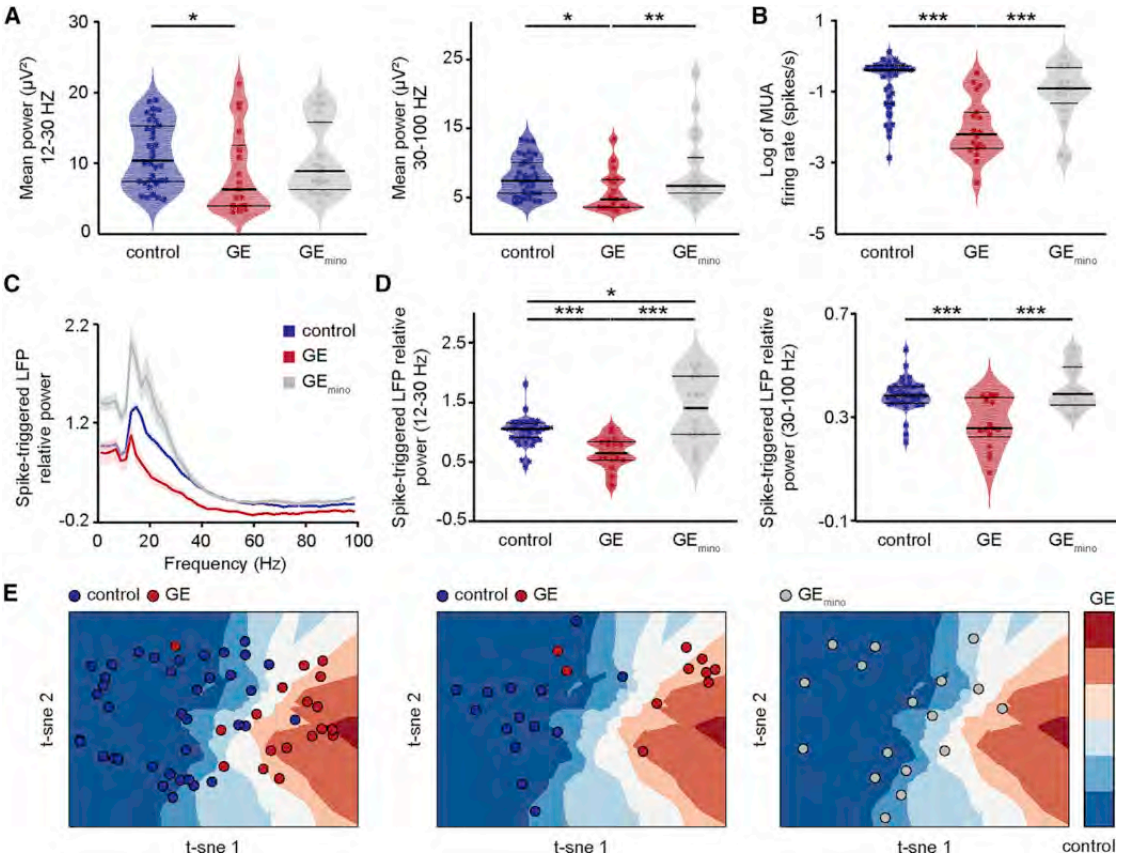

Figure 6. Minocycline Treatment Rescues Electrophysiological Core Dysfunctions in Dual-Hit GE Mice

(A) Violin plot displaying the beta (left) and gamma (right) band power of oscillations in superficial layers of the PL of control (blue; n = 38), GE (red; n = 18), and GE_{mino} (gray; n = 18) mice.

(B) Same as (A) for MUA firing rate.

(C) Plots of frequency-dependent relative power of spike-triggered LFP in superficial layers (top) of control (blue), GE (red), and GE_{mino} (gray) mice.

(D) Violin plot displaying the relative power of spike-triggered LFP in beta (left) and gamma (right) band for superficial layers of control (blue; n = 38), GE (red; n = 18), and GE_{mino} (gray; n = 18) mice.

(E) t-Distributed stochastic neighbor embedding (T-SNE) plot of superficial layers electrophysiological features of control (blue dots) and GE (red dots) mice in the training/cross-validation (left) and test (middle) set and GE_{mino} (gray dots; right).

The background represents an approximation of the decision space of the classifier. *p < 0.05, **p < 0.01, and ***p < 0.001; ANCOVA with age as covariate (A and B) and Yuen's bootstrap test (D) with 20% level of trimming for the mean.

similar to that of controls (condition effect p = 0.77; p > 0.05 for all pairwise comparisons; Figures 5A and 5B). Minocycline treatment rescued the synaptic deficits too. $PYRs_{SUP}$ from GE_{mino} mice (n = 12 neurons) had a similar spine density as those from control mice (condition effect p = 0.78) that was significantly increased when compared to GE mice (condition effect p = 5×10^{-5}; Figures 5C and 5D). The effect was similar across the different types of dendrites that were analyzed.

Second, we assessed the properties of prelimbic network oscillations and neuronal firing in GE_{mino} mice and compared them with those from control and GE mice. The power in beta and gamma band of prelimbic oscillations recorded in superficial layers was similar in control and minocycline-treated GE mice (p = 0.90 and p = 0.31, respectively; Figures 6A and 6B; Table S1). Similarly, the prelimbic firing rate and timing by oscillatory phase were rescued (Figures 6C and 6D). The firing rate of neurons in superficial layers was similar for controls (log values −0.61 ± 0.04) and GE_{mino} mice (log values −0.9 ± 0.1; p = 0.59). The timing of prelimbic firing in superficial layers of GE_{mino} mice, as measured by spike-triggered LFP power, was rescued (gamma band; p = 0.48) or even slightly increased (beta band; p = 0.026) when compared to controls (Figure 6D). In contrast to the profound changes observed in superficial layers after minocycline treatment, the network activity and neuronal firing in deep layers of PL from GE_{mino} mice remained largely unaffected (Figures S8A–S8F). Moreover, the neuronal and network properties in control mice ($control_{mino}$ n = 12) did not change after minocycline administration. Theta, beta, and gamma power of prelimbic oscillations as well as firing rate and spike-triggered relative LFP power in superficial layers were similar in controls and $control_{mino}$ (p = 0.68, p = 0.95, p = 0.36, p = 0.16, p = 0.1, and p = 0.06, respectively). The activity in deep layers was also largely unaffected, with only gamma power being significantly increased (p = 0.006; Figures S8G–S8L).

These data indicate that the abnormal firing and network coupling patterns in the PL of dual-hit GE mice are rescued by administration of minocycline during a defined developmental period.

Electrophysiological Features of Prelimbic Superficial Layers Are Sufficient to Distinguish Control from GE Mice

To test the robustness of conclusions above, we developed a machine-learning classification algorithm (k-nearest neighbors classification), to which we asked to predict whether mice belonged to the control or the GE group (Figure 6E). As input features, we used only the electrophysiological features characterized for neonatal PL: LFP power in beta- and gamma-frequency bands and firing rates of neurons in superficial layers and their spike-triggered LFP power in beta- and gamma-frequency bands. We first used 3-fold cross-validation and iteratively (n = 500) split the dataset of mice (n = 56 mice) into a training (n = 38 mice) and a cross-validation (n = 18) set. The training set was used to tune the algorithm hyper-parameters (further using 3-fold cross-validation), whereas the assessment of the prediction quality was carried out on the cross-validation set. By these means, we were able to obtain a median classification accuracy of 83% on the cross-validation set, thereby showing that superficial-layers-derived features are valid predictors for this classification task (Figure 6E, left). To confirm the robustness and generalizability of our findings, we tested the predictions of the pre-trained k-nearest neighbors classifier on an entirely new dataset (n = 24; test dataset), to which it had not been exposed during the training phase. On the test dataset, the machine-learning classification achieved high classification accuracy (median 80%; Figure 6E, middle). Moreover, when we asked the algorithm to predict to which class GE_{mino} mice belonged to, on average, all but one of them (94%) were classified as belonging to the control group (Figure 6E, right). These data show that superficial-layers-derived electrophysiological features are strong and robust predictors for distinguishing control and GE mice and further confirm the efficacy of the minocycline-administration rescue.

Transient Minocycline Treatment Rescues Abnormal Microglia Function in Dual-Hit GE Mice

Minocycline has been shown to block the stress-induced inflammatory responses of microglia (Kobayashi et al., 2013) and to reduce microglia overpruning in schizophrenic-patients-derived induced microglia-like cells (Sellgren et al., 2019). Therefore, their modulation might represent a possible mechanism explaining the observed minocycline effects. Microglia are key players during early brain development and have been reported to control synapse formation (Miyamoto et al., 2016) and to sculpt the developing circuits by engulfing and remodeling synapses in an activity-dependent manner (Schafer et al., 2012; Weinhard et al., 2018). Transient perturbations in the development of microglia, such as those induced by maternal immune activation (MIA), have far-reaching effects on adult neuronal function and behavior (Shin Yim et al., 2017) that have been linked to mental illness.

In accordance with this stream of evidence, microglia in the PL of neonatal GE mice are profoundly perturbed. When compared with controls, not only was microglia number significantly augmented (+47%; $p < 1 \times 10^{-5}$), but also morphological features, such as area and cell spread, were likewise significantly increased by 29% (n = 1,250 cells for control; n = 1,173 cells for GE mice; $p < 1 \times 10^{-6}$) and 25% ($p < 1 \times 10^{-13}$), respectively (Figures 7A–7D). Moreover, microglia cell perimeter and roundness, but not eccentricity, were also substantially changed in dual-hit GE mice (Figures 7E–7G). These deficits were observed throughout the entire prelimbic cortex and had no layer specificity. Although minocycline-treated GE (GE_{mino}) mice had no reduction in the number of microglial cells (−13%; p = 0.17), microglia showed a reduced area (−35%; n = 1,614 cells; p = 0.015) and cell spread (−11%; $p = 8 \times 10^{-4}$) when compared to GE mice (Figures 7A–7D).

To get insights into the mechanisms that enable microglia to control neuronal function in developing PL, we quantified microglia phagocytosis of pre-synaptic terminals, identified as VGLUT-1-positive puncta. Quantitative analysis revealed that, in GE mice (n = 52 cells), both the number as well as the volume of engulfed VGLUT-1-positive puncta were increased in comparison to control (n = 54 cells; p = 0.006 and p = 0.006, respectively) and, to a less amount, to GE_{mino} (n = 56 cells; p = 0.084 and p = 0.084, respectively) mice. In contrast, there was no difference between controls and GE_{mino} mice (p = 0.287 and p = 0.296, respectively; Figures 7H–7K). High-definition morphological analysis confirmed that GE mice have over all prelimbic layers microglia cells with larger distal volume (condition effect p = 0.019) in comparison to GE_{mino} (p = 0.008) and, to a lesser extent, to controls (p = 0.072).

These data confirm that minocycline has an effect on microglia cells and that it partially restores the phenotype of these cells in GE mice. Although minocycline is a pleiotropic drug, part of its effect on GE mice might therefore be mediated by microglia modulation.

Dysfunction of Prelimbic Superficial Layers and Its Rescue Relates to Later Cognitive Performance

Previous investigations showed that compromised function of PFC in neonatal dual-hit GE mice has behavioral impact on later cognitive abilities. In line with these results, we monitored the novelty detection and recognition memory, which have been shown to rely on functional communication within prefrontal-hippocampal networks. Novel object recognition (NOR) and recency recognition (RR) are based on the innate preference of mice to explore novel or less familiar objects over more familiar ones (Figures 8A and 8C). Therefore, their testing requires no prior training or deprivation and can be achieved shortly after full maturation of sensory and motor abilities (i.e., P17 to P18). All three groups of mice, control, GE, and GE_{mino} were tested using a custom-design arena and objects of different size, color, and texture. We quantified the relative amount of time spent interacting with the novel/less recent object when compared to the familiar/more recent one (discrimination ratio), as well as the relative duration of single interactions with the two objects. During the familiarization trial of NOR test, all mice (P17 to P18) spent equal time investigating the two objects in the arena.

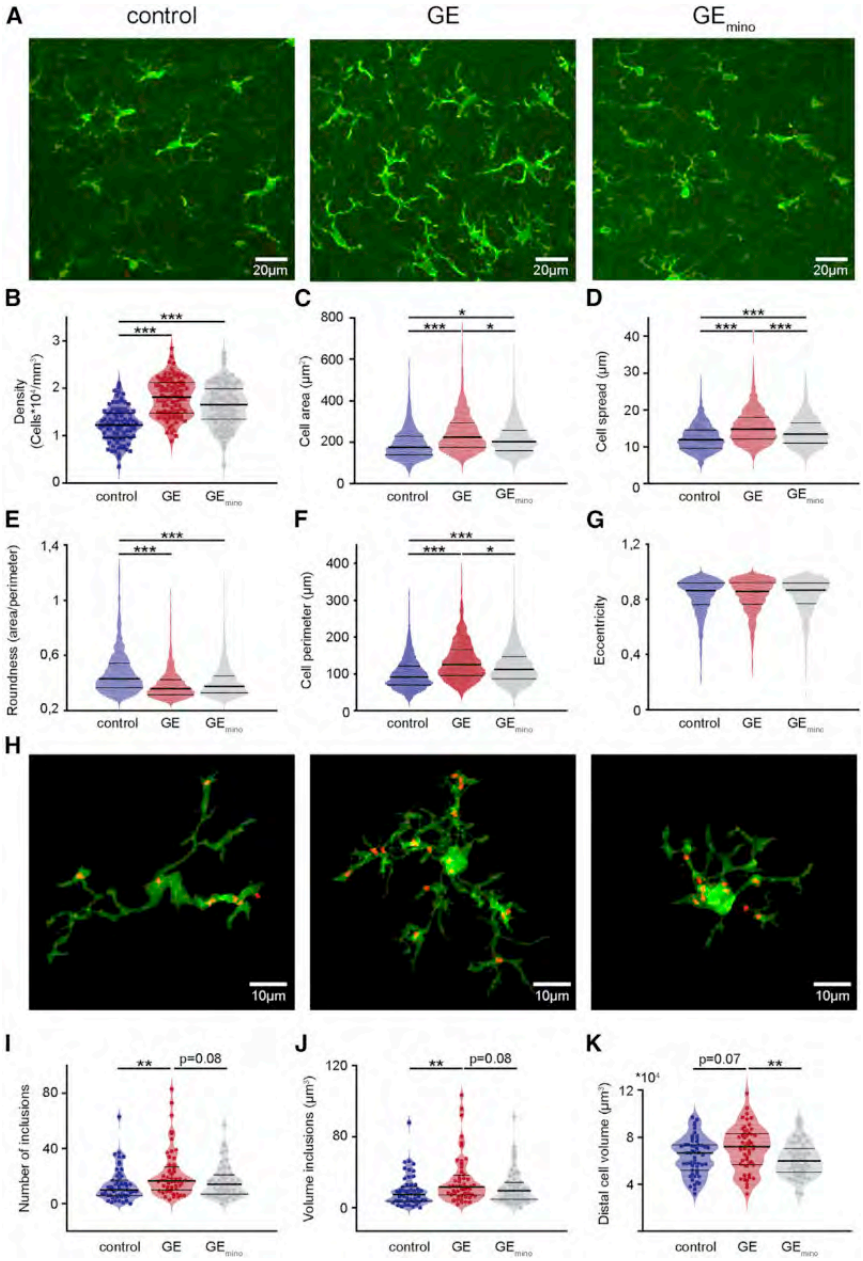

Figure 7. Altered Microglial Cell Morphology and Phagocytic Activity in Dual-Hit GE Mice Are Partially Restored by Minocycline Treatment

(A) Photographs of Iba-1-stained microglial cells in the PL of a P10 control mouse (left), of a P10 GE mouse (center), and of a P10 GE_{mino} mouse (right).

(B) Violin plot displaying the average density of Iba-1-stained cells in the PL of control (blue; n = 64 images from 4 pups), GE (red; n = 64 images from 4 pups), and GE_{mino} mice (gray; n = 64 images from 4 pups).

(C–G) Same as (B) for cell area (C), cell spread (D), roundness (E), perimeter (F), and eccentricity (G). For (C)–(G), n = 1,250, 1,738, and 1,614 cells, respectively, from 12 sections of 4 pups for all three conditions.

(H) Photographs of Iba-1-stained microglial cells and phagocyted VGLUT-1 puncta in the PL of a P8 control mouse (left), of a P8 GE mouse (center), and of a P8 GE_{mino} mouse (right).

(I) Violin plot displaying the number of inclusions per microglia cell in the PL of control (blue; n = 53 cells from 4 pups), GE (red; n = 52 cells from 4 pups), and GE_{mino} mice (gray; n = 55 cells from 4 pups).

(J and K) Same as (I) for the volume of inclusions per microglia cell (J) and the distal volume of microglia cells (K). Data are presented as median with 25^{th} and 75^{th} percentile.

In (B) and (I)–(K), single data points are displayed as asterisks, whereas in (C)–(G), single data points are omitted due to their high number. *p < 0.05, **p < 0.01, and ***p < 0.001; linear mixed-effect model with animal as a random effect (B–G) and robust, bootstrapped ANOVA with 20% level of trimming for the mean (I–K).

During the testing phase, GE mice (n = 15) showed poorer recognition abilities as mirrored by the lower discrimination ratio index and single interaction time when compared with control (n = 15) and GE_{mino} mice (n = 16; Figure 8B). Despite this trend, the differences did not reach significance levels, most likely due to high inter-animal variability reported for NOR test. During RR task, mice (P19–P22) had to process temporal information by recognizing the object with which they most recently interacted. GE mice had a significantly poorer discrimination ratio (condition effect p = 0.013) when compared to both control ($p < 10^{-4}$) and GE_{mino} mice (p = 0.038; Figure 8D). The exploratory and anxiety behavior was similar for all three groups of mice, indicating that the poor performance of GE mice does not result from lower motor abilities or fear to approach the objects. Taking into account the similarity of behavioral performance in control and GE_{mino} mice, we suggest that the recognition abilities of pre-juvenile GE mice are rescued after transient treatment with minocycline during early postnatal development. Importantly, the timing of minocycline administration is crucial for the rescue. When we administered minocycline from P9 to P16 to GE mice (GE_{mino}late; n = 16), the RR deficits persisted, the discrimination ratio being significantly decreased when compared to controls (n = 14; p = 0.03; Figure S9A). Moreover, when we considered the entire behavioral dataset, we found that GE_{mino}late mice have a RR deficit even when compared to GE_{mino} mice (p = 0.037) and are not significantly different from untreated GE mice (p = 0.85).

To confirm the link between prefrontal dysfunction throughout development and behavioral performance at pre-juvenile age, we resorted to a machine-learning classification algorithm with different inputs (discrimination ratios and single interaction time for the two tasks) but a similar architecture (k-nearest neighbors classification) to the one discussed above (Figure 7E). As

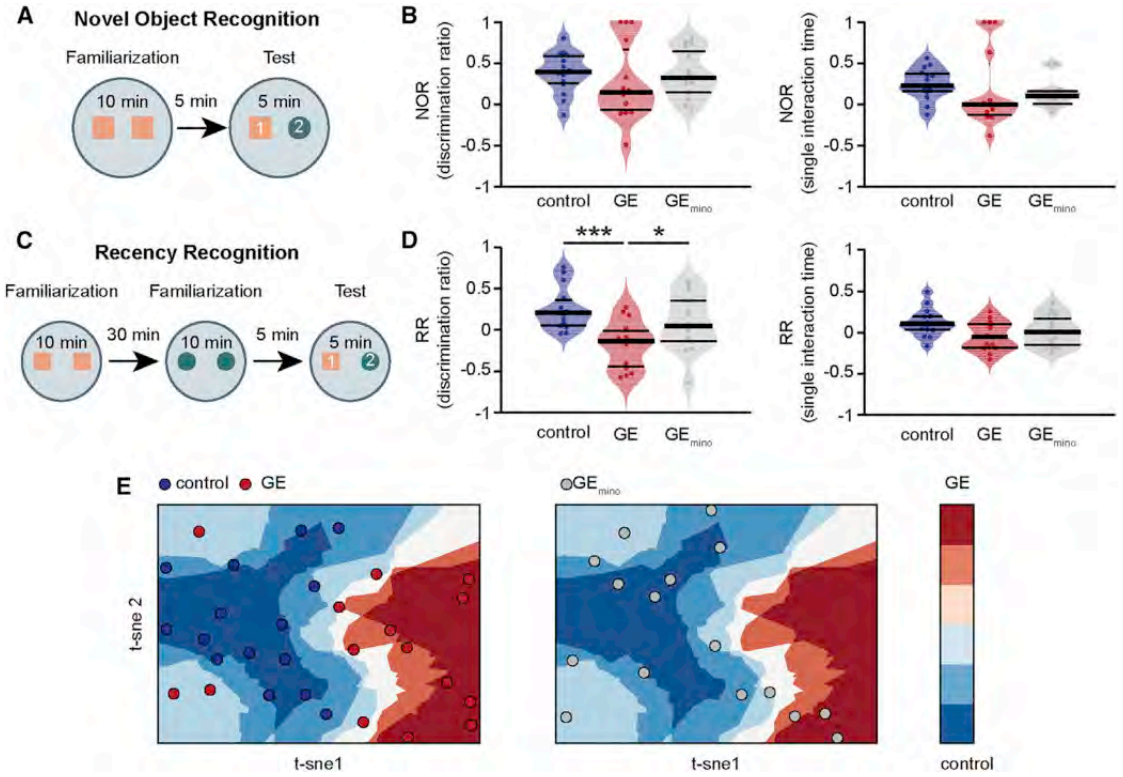

Figure 8. Minocycline Treatment Rescues Behavioral Deficits in Dual-Hit GE Mice

(A) Schematic diagram of the experimental protocol for NOR.

(B) Violin plot displaying NOR discrimination ratio (middle) and single interaction time (right) of control (blue; n = 15), GE (red; n = 15), and GE_{mino} (gray; n = 16) mice.

(C and D) Same as (A) and (B) for RR.

(E) T-SNE plot of behavioral features of control (blue dots) and GE (red dots) mice in the training/cross-validation set (left) and GE_{mino} (gray dots; right).

In (B) and (D), data are presented as median with 25th and 75th percentile, and single data points are shown as asterisks. *p < 0.05 and ***p < 0.001; robust, bootstrapped ANOVA with 20% level of trimming for the mean (B and D).

before, we iteratively (n = 500) used 3-fold cross-validation (n = 20 mice in the training set and n = 10 in the cross-validation set) to tune the algorithm hyper-parameters (training set) and assess its accuracy (cross-validation set). By these means, we were able to obtain a median classification accuracy of 83% on the cross-validation set. When we asked the algorithm to predict to which class GE_{mino} mice belonged to, 75% of them were classified as belonging to the control group (Figure 8E). These data show that, on a group level, early disruption of prefrontal networks is predictive of later impaired cognition. Accordingly, early rescue of such deficits is associated with restored cognitive development.

DISCUSSION

Although neurodevelopmental miswiring has been postulated to result in major functional and behavioral deficits at adulthood, the mechanisms of early impairment are still largely unresolved. A major consequence of this knowledge gap is the poor understanding of disease pathophysiology that hampers the development of tailored therapies for mental illness. Toward the aim of elucidating the substrate of developmental dysfunction, the present study uncovers layer- and cell-type-specific deficits in the PL of neonatal mice reproducing the gene-environment interactions involved in the pathogenesis of psychiatric disorders. We show that, in dual-hit GE mice, (1) the lower entrainment of neonatal prefrontal circuits in beta-gamma oscillations relates to structural and functional deficits of superficial layers pyramidal neurons; (2) minocycline administration during the first postnatal week restores the morphology, synaptic function, and firing and oscillatory patterns in local prefrontal circuits; and (3) at group level, early prefrontal network activity is predictive of pre-juvenile cognitive abilities. These findings highlight the major contribution of glutamatergic dysfunction to the abnormal refinement of circuits during development and support the hypothesis that such deficits emerge already at neonatal age. Moreover, the results demonstrate the efficacy of minocycline in preventing the emergence of developmental circuit dysfunction with relevance for cognitive disabilities. A limitation of the current study is that major conclusions rely on investigations at group level. Future longitudinal recordings across entire postnatal development, which are still currently technically demanding, will prove whether these conclusions hold also on an individual level.

Wiring of Prefrontal Circuits at Neonatal Age: Checkpoint of Cognitive Maturation

Anatomical investigations revealed that, although the PFC develops according to a similar time schedule as other neocortical areas, some maturation events (e.g., volumetric decline and growth and pruning of afferents and efferents) are protracted (van Eden et al., 1990). Correspondingly, the prefrontal patterns of coordinated activity share the general spatial and temporal organization of early neocortical oscillations (Hanganu-Opatz, 2010), yet they emerge later and have a frequency-specific structure. In rodents, the discontinuous oscillatory activity of PFC appears 1 to 2 days later than in the hippocampus and 2 to 3 days later than in primary visual and somatosensory cortices (Brockmann et al., 2011). The neonatal oscillations are detectable and have similar organization in both urethane-anesthetized and non-anesthetized rats and mice, yet their magnitude decreased under anesthesia, as shown by the present and previous studies (Chini et al., 2019).

The present findings show that frequency-specific communication within local prefrontal circuits emerges very early. Such precise interactions might represent the pre-requisite for functional entrainment of adult networks and cognitive performance. Abundant literature highlighted the link between theta-band hippocampal activation and fast oscillatory entrainment of prefrontal circuits during various cognitive tasks at adulthood (Sirota et al., 2008). Currently, only few attempts have been made to directly prove the role of timed interactions during development for the later emergence of network function and adult behavior. Recently, the key role of vasoactive intestinal peptide (VIP) and cholecystokinine (CCK)-positive interneurons for cortical circuit development has been demonstrated (Batista-Brito et al., 2017; Del Pino et al., 2017). In the same line, our findings identify pyramidal neurons in superficial layers as generators of early activity, facilitating the coupling within local neocortical circuits and glutamatergic communication between upper and deeper layers (Anastasiades and Butt, 2012), whose early function later impacts cognitive abilities. Identification of key cellular elements controlling circuit development opens new perspectives for the interrogation of long-term network effects.

Mechanisms of Abnormal Wiring in Prefrontal Circuits of Neonatal Dual-Hit GE Mice

The pathogenesis of cognitive dysfunction in major psychiatric disorders has been reported to involve interactions between a large number of susceptibility genes and environmental factors that might act at diverse stages of development (van Os et al., 2008). In the present study, we combine the abnormally translocated DISC1 gene with viral infection causing maternal immune activation (Meyer et al., 2005). This dual hit has a clear link to human pathology (Ayhan et al., 2009). Although each of the factors (i.e., either genetic or environmental) leads to structural, functional, and cognitive deficits of weak to moderate magnitude, it is only their combination that has been found to produce a neurobehavioral phenotype at adulthood that resembles aspects of mental illness. For example, the prefrontal-hippocampal networks accounting for mnemonic and executive abilities at adult age show major developmental deficits when both hits co-occur (abnormal DISC1 and maternal immune activation), whereas single-hit models show a largely normal network development (Hartung et al., 2016). In dual-hit GE mice, the patterns of coordinated activity in PFC and hippocampus appeared disorganized, and the long-range coupling between them was weaker at neonatal age.

Although these data demonstrate the developmental origin of dysfunction in dual-hit GE mice, they do not mechanistically explain the network and behavioral deficits. These deficits might result from either abnormal maturation of local prefrontal networks, a weaker theta activity in hippocampus, or sparser connectivity between the two areas. The present results fill the knowledge gap and identify the pyramidal neurons of superficial layers as key players of developmental miswiring, whereas pyramidal neurons in deeper cortical layers are indistinguishable in their structure and function in controls and dual-hit GE mice. The disorganized patterns of oscillatory activity in the PL result from superficial layers neurons that lost their timed firing and cannot generate the entrainment of local circuits in beta-low gamma frequencies. In turn, the neuronal spiking is controlled by the inputs that these neurons receive. Taking into account the oversimplified dendritic arborization and reduced number of spines, it is likely that pyramidal neurons in superficial layers of PL from dual-hit GE mice receive fewer inputs, which are randomly timed. The cell-type- and layer-dependent structural abnormalities in PFC (e.g., decreased dendritic spine density) have also been detected in other mouse models of schizophrenia (Koukouli et al., 2017) and in schizophrenia patients, in which it has been related to abnormalities in the excitatory transmission (Kolluri et al., 2005). Despite the integrity of pyramidal neurons in deep layers both at morphological and functional level, the local prefrontal circuitry relying on dense vertical and horizontal interactions between upper and deeper layers is compromised in dual-hit GE mice. Therefore, the theta hippocampal drive targeting deep layers pyramidal neurons cannot optimally entrain the PFC. Although some properties of oscillatory activity and neuronal firing over prefrontal layers are similar in P8–P10 GE mice and P4–P6 control mice, the overall properties of activity patterns suggest that the neonatal dysfunction is not solely the result of a delayed maturation caused by abnormal DISC1 and environmental stressors.

The selective structural deficits and dysfunction of pyramidal neurons in prefrontal superficial layers was prevented by minocycline administration during the first, but not the second, postnatal week. Minocycline is a pleiotropic drug that, among having other functions, is a potent inhibitor of microglial activation (Dean et al., 2012). Altered number of activated microglia has been found in the brain of MIA offspring (Borrell et al., 2002). Resulting from maternal infection, the stimulation of cytokine pathways (Meyer et al., 2005) and microglia overpruning of synapses (Neniskyte and Gross, 2017) have been proposed to interfere with developmental processes, such as neuronal proliferation, differentiation, and synaptogenesis (Neniskyte and Gross, 2017). A similar mechanism, microglia excessively engulfing the synaptic terminals, might represent the mechanism underlying the deficits reported here for dual-hit GE mice. During the first postnatal week, these MIA-induced

deficits alone seem to have no functional readout, because neonatal one-hit environmental mice (i.e., MIA offspring) have largely normal firing and network activity patterns (Hartung et al., 2016). Solely the combination with genetic risk factors, such as mutant DISC1, causes early circuit miswiring, as reported in the present study. DISC1 has a key role in neuronal proliferation and migration as well as in development and maintenance of synapses. However, the phenotypes in the mouse models of mutated DISC1 are rather modest (Brandon and Sawa, 2011). They become potentiated by the synergistic combination with MIA. This could be due to the fact that mutated DISC1 might modulate the basal or polyI:C-induced cytokine production by interfering with glycogen synthase kinase-3 (Beurel et al., 2010). Alternatively, DISC1 might confer neuronal vulnerability, making pyramidal neurons more susceptible to environmental stressors.

Minocycline has been found to be neuroprotective in numerous pathologies (Hinwood et al., 2013). In particular, its use alone or as adjunctive therapy to antipsychotics improved the behavioral and cognitive performance of schizophrenia patients (De Picker et al., 2017; Miyaoka et al., 2008). Although the mode of action of minocycline in the adult brain has been well characterized, only few studies focused on its preventive potential during development, before the onset of disease symptoms. Recently, minocycline use during adolescence was associated with a reduction in the incidence of psychosis, most likely by reducing microglia-mediated synapse uptake (Sellgren et al., 2019). In mice, when administrated during the course of peripubertal stress exposure, minocycline has been found to prevent the emergence of multiple behavioral abnormalities relevant to human cognitive dysfunction (Giovanoli et al., 2016), yet the mechanisms underlying the behavioral rescue are largely unknown. Here, we show that, already during neonatal development, minocycline is effective in preventing prelimbic structural, functional, and behavioral deficits. One possible mechanism of these effects is its action on microglia. However, the pathways that selectively link pyramidal neurons in superficial layers of PFC with the anti-inflammatory action of minocycline remain to be investigated in detail and in a more mechanistic manner. Of note, superficial layers neurons are thought of being more dependent on microglia activity than those of deep layers (Neniskyte and Gross, 2017). This might contribute to the layer-specific differences that we identified in the present study.

Because the efficacy of minocycline fades if it is administered at a later point of development, the question arises why the PFC during the investigated time window (i.e., P8–P10) is particularly sensitive to perturbations. Future studies need to address the role of hippocampal projections that drive the initial beta-gamma entrainment of prefrontal circuits (Brockmann et al., 2011; Ahlbeck et al., 2018) as well as of neuromodulators, such as dopamine with D1 receptors first appearing at this age (Leslie et al., 1991).

Relevance for Human Mental Illness

The relevance of animal models for human mental disorders has often been questioned, because they do not fulfill the validity criteria used for other pathologies. Optimally, animal models recapitulate etiologic processes (i.e., construct validity) or symptom features (i.e., face validity). In case of mental disorders, such as schizophrenia, bipolar disorder, or depression, the available mouse models have either excellent construct validity (e.g., models mimicking the genetic background) but limited face validity or vice versa (e.g., models of hippocampal damage or pharmacological models). Dual-hit models mimic both genetic and environmental risk factors and recapitulate some of the structural and circuit deficits observed in patients. For example, lower spine density in upper layers of PFC as well as dysfunctional prefrontal gamma-band oscillations, which have been reported here, have also been described for schizophrenia patients (Senkowski and Gallinat, 2015). Similarly, microglia abnormalities and resulting synaptic deficits have been related to several brain pathologies (Neniskyte and Gross, 2017). Therefore, we propose that dual-hit GE mice recapitulate both the etiology (construct validity) as well as the general rules of neuronal, glial, and circuit dysfunction (face validity) that relate to cognitive impairment in mental disorders. They appear highly instrumental for the identification of cellular key players of disease that, for ethical and technical reasons, are not accessible in humans of comparable age. This brings us closer to one of the major goals of circuit psychiatry that is the identification of key neurobiological targets amenable to tailored therapies (Gordon, 2016) that not only treat but also prevent disease-related cognitive and behavioral deficits.

STAR★METHODS

Detailed methods are provided in the online version of this paper and include the following:

- KEY RESOURCES TABLE
- LEAD CONTACT AND MATERIALS AVAILABILITY
- EXPERIMENTAL MODEL AND SUBJECT DETAILS
  - Mice
  - Minocycline administration
- METHOD DETAILS
  - In utero electroporation
  - Developmental milestones
  - Behavioral experiments
  - In vitro electrophysiology and optogenetics
  - In vivo electrophysiology and optogenetics
  - Histology
- QUANTIFICATION AND STATISTICAL ANALYSIS
  - Image analysis
  - In vitro electrophysiology
  - In vivo electrophysiology
  - K-nearest neighbors classifiers
  - Statistical analysis
- DATA AND CODE AVAILABILITY

SUPPLEMENTAL INFORMATION

Supplemental Information can be found online at https://doi.org/10.1016/j.neuron.2019.09.042.

ACKNOWLEDGMENTS

We thank Dr. Joseph Gogos for providing the DISC1 mice, Drs. S. Wiegert and T. Oertner for providing opsin derivates, and A. Marquardt, A. Dahlmann, I. Ohmert, and K. Titze for excellent technical assistance. This work was funded by grants from the European Research Council (ERC-2015-CoG 681577 to I.L.H.-O.) and the German Research Foundation (Ha4466/10-1, Ha4466/11-1, Ha4466/12-1, SPP 1665, and SFB 936 B5 to I.L.H.-O. and C6 to C.M.). I.L.H.-O. is a founding member of the FENS Kavli Network of Excellence.

AUTHOR CONTRIBUTIONS

I.L.H.-O. conceived the study. M.C. and I.L.H.-O. designed the experiments. M.C., J.A.P., C.L., L.C.-P., M.H., V.O., J.A., and S.H.B. carried out experiments. M.C. and X.X. analyzed the data. M.C., C.M., and I.L.H.-O. interpreted the data. M.C. and I.L.H.-O. wrote the article. All authors discussed and commented on the manuscript.

DECLARATION OF INTERESTS

The authors declare no competing interests.

Received: March 28, 2019
Revised: August 14, 2019
Accepted: September 24, 2019
Published: November 13, 2019

REFERENCES

Aarts, E., Verhage, M., Veenvliet, J.V., Dolan, C.V., and van der Sluis, S. (2014). A solution to dependency: using multilevel analysis to accommodate nested data. Nat. Neurosci. *17*, 491–496.

Abazyan, B., Nomura, J., Kannan, G., Ishizuka, K., Tamashiro, K.L., Nucifora, F., Pogorelov, V., Ladenheim, B., Yang, C., Krasnova, I.N., et al. (2010). Prenatal interaction of mutant DISC1 and immune activation produces adult psychopathology. Biol. Psychiatry *68*, 1172–1181.

Ahlbeck, J., Song, L., Chini, M., Bitzenhofer, S.H., and Hanganu-Opatz, I.L. (2018). Glutamatergic drive along the septo-temporal axis of hippocampus boosts prelimbic oscillations in the neonatal mouse. eLife *7*, e33158.

Anastasiades, P.G., and Butt, S.J. (2012). A role for silent synapses in the development of the pathway from layer 2/3 to 5 pyramidal cells in the neocortex. J. Neurosci. *32*, 13085–13099.

Ayhan, Y., Sawa, A., Ross, C.A., and Pletnikov, M.V. (2009). Animal models of gene-environment interactions in schizophrenia. Behav. Brain Res. *204*, 274–281.

Batista-Brito, R., Vinck, M., Ferguson, K.A., Chang, J.T., Laubender, D., Lur, G., Mossner, J.M., Hernandez, V.G., Ramakrishnan, C., Deisseroth, K., et al. (2017). Developmental dysfunction of VIP interneurons impairs cortical circuits. Neuron *95*, 884–895.e9.

Bellesi, M., de Vivo, L., Chini, M., Gilli, F., Tononi, G., and Cirelli, C. (2017). Sleep loss promotes astrocytic phagocytosis and microglial activation in mouse cerebral cortex. J. Neurosci. *37*, 5263–5273.

Beurel, E., Michalek, S.M., and Jope, R.S. (2010). Innate and adaptive immune responses regulated by glycogen synthase kinase-3 (GSK3). Trends Immunol. *31*, 24–31.

Bitzenhofer, S.H., Sieben, K., Siebert, K.D., Spehr, M., and Hanganu-Opatz, I.L. (2015). Oscillatory activity in developing prefrontal networks results from theta-gamma-modulated synaptic inputs. Cell Rep. *11*, 486–497.

Bitzenhofer, S.H., Ahlbeck, J., Wolff, A., Wiegert, J.S., Gee, C.E., Oertner, T.G., and Hanganu-Opatz, I.L. (2017). Layer-specific optogenetic activation of pyramidal neurons causes beta-gamma entrainment of neonatal networks. Nat. Commun. *8*, 14563.

Borrell, J., Vela, J.M., Arévalo-Martin, A., Molina-Holgado, E., and Guaza, C. (2002). Prenatal immune challenge disrupts sensorimotor gating in adult rats. Implications for the etiopathogenesis of schizophrenia. Neuropsychopharmacology *26*, 204–215.

Bosman, C.A., Lansink, C.S., and Pennartz, C.M. (2014). Functions of gamma-band synchronization in cognition: from single circuits to functional diversity across cortical and subcortical systems. Eur. J. Neurosci. *39*, 1982–1999.

Brandon, N.J., and Sawa, A. (2011). Linking neurodevelopmental and synaptic theories of mental illness through DISC1. Nat. Rev. Neurosci. *12*, 707–722.

Brockmann, M.D., Pöschel, B., Cichon, N., and Hanganu-Opatz, I.L. (2011). Coupled oscillations mediate directed interactions between prefrontal cortex and hippocampus of the neonatal rat. Neuron *71*, 332–347.

Chini, M., Gretenkord, S., Kostka, J.K., Pöpplau, J.A., Cornelissen, L., Berde, C.B., Hanganu-Opatz, I.L., and Bitzenhofer, S.H. (2019). Neural correlates of anesthesia in newborn mice and humans. Front. Neural Circuits *13*, 38.

Cho, K.K., Hoch, R., Lee, A.T., Patel, T., Rubenstein, J.L., and Sohal, V.S. (2015). Gamma rhythms link prefrontal interneuron dysfunction with cognitive inflexibility in Dlx5/6(+/-) mice. Neuron *85*, 1332–1343.

Cichon, N.B., Denker, M., Grün, S., and Hanganu-Opatz, I.L. (2014). Unsupervised classification of neocortical activity patterns in neonatal and pre-juvenile rodents. Front. Neural Circuits *8*, 50.

Cirelli, C., and Tononi, G. (2015). Cortical development, electroencephalogram rhythms, and the sleep/wake cycle. Biol. Psychiatry *77*, 1071–1078.

Clement, E.A., Richard, A., Thwaites, M., Ailon, J., Peters, S., and Dickson, C.T. (2008). Cyclic and sleep-like spontaneous alternations of brain state under urethane anaesthesia. PLoS ONE *3*, e2004.

Dansie, L.E., Phommahaxay, K., Okusanya, A.G., Uwadia, J., Huang, M., Rotschafer, S.E., Razak, K.A., Ethell, D.W., and Ethell, I.M. (2013). Long-lasting effects of minocycline on behavior in young but not adult Fragile X mice. Neuroscience *246*, 186–198.

De Picker, L.J., Morrens, M., Chance, S.A., and Boche, D. (2017). Microglia and brain plasticity in acute psychosis and schizophrenia illness course: a meta-review. Front. Psychiatry *8*, 238.

Deakin, B., Suckling, J., Barnes, T.R.E., Byrne, K., Chaudhry, I.B., Dazzan, P., Drake, R.J., Giordano, A., Husain, N., Jones, P.B., et al.; BeneMin Study team (2018). The benefit of minocycline on negative symptoms of schizophrenia in patients with recent-onset psychosis (BeneMin): a randomised, double-blind, placebo-controlled trial. Lancet Psychiatry *5*, 885–894.

Dean, O.M., Data-Franco, J., Giorlando, F., and Berk, M. (2012). Minocycline: therapeutic potential in psychiatry. CNS Drugs *26*, 391–401.

Del Pino, I., Brotons-Mas, J.R., Marques-Smith, A., Marighetto, A., Frick, A., Marín, O., and Rico, B. (2017). Abnormal wiring of CCK^{+} basket cells disrupts spatial information coding. Nat. Neurosci. *20*, 784–792.

Emadi-Kouchak, H., Mohammadinejad, P., Asadollahi-Amin, A., Rasoulinejad, M., Zeinoddini, A., Yalda, A., and Akhondzadeh, S. (2016). Therapeutic effects of minocycline on mild-to-moderate depression in HIV patients: a double-blind, placebo-controlled, randomized trial. Int. Clin. Psychopharmacol. *31*, 20–26.

Garrido-Mesa, N., Zarzuelo, A., and Gálvez, J. (2013). Minocycline: far beyond an antibiotic. Br. J. Pharmacol. *169*, 337–352.

Giovanoli, S., Weber-Stadlbauer, U., Schedlowski, M., Meyer, U., and Engler, H. (2016). Prenatal immune activation causes hippocampal synaptic deficits in the absence of overt microglia anomalies. Brain Behav. Immun. *55*, 25–38.

Gordon, J.A. (2016). On being a circuit psychiatrist. Nat. Neurosci. *19*, 1385–1386.

Hanganu-Opatz, I.L. (2010). Between molecules and experience: role of early patterns of coordinated activity for the development of cortical maps and sensory abilities. Brain Res. Brain Res. Rev. *64*, 160–176.

Harris, K.D., and Shepherd, G.M. (2015). The neocortical circuit: themes and variations. Nat. Neurosci. *18*, 170–181.

Hartung, H., Cichon, N., De Feo, V., Riemann, S., Schildt, S., Lindemann, C., Mulert, C., Gogos, J.A., and Hanganu-Opatz, I.L. (2016). From shortage to surge: a developmental switch in hippocampal-prefrontal coupling in a

gene-environment model of neuropsychiatric disorders. Cereb. Cortex *26*, 4265–4281.

Hinwood, M., Tynan, R.J., Charnley, J.L., Beynon, S.B., Day, T.A., and Walker, F.R. (2013). Chronic stress induced remodeling of the prefrontal cortex: structural re-organization of microglia and the inhibitory effect of minocycline. Cereb. Cortex *23*, 1784–1797.

Ignacio, M.P.D., Kimm, E.J., Kageyama, G.H., Yu, J., and Robertson, R.T. (1995). Postnatal migration of neurons and formation of laminae in rat cerebral cortex. Anat. Embryol. (Berl.) *191*, 89–100.

Khazipov, R., Sirota, A., Leinekugel, X., Holmes, G.L., Ben-Ari, Y., and Buzsáki, G. (2004). Early motor activity drives spindle bursts in the developing somatosensory cortex. Nature *432*, 758–761.

Kirmse, K., Kummer, M., Kovalchuk, Y., Witte, O.W., Garaschuk, O., and Holthoff, K. (2015). GABA depolarizes immature neurons and inhibits network activity in the neonatal neocortex in vivo. Nat. Commun. *6*, 7750.

Kishimoto, T., Horigome, T., and Takamiya, A. (2018). Minocycline as a treatment for schizophrenia: is the discussion truly finished? Lancet Psychiatry *5*, 856–857.

Kobayashi, K., Imagama, S., Ohgomori, T., Hirano, K., Uchimura, K., Sakamoto, K., Hirakawa, A., Takeuchi, H., Suzumura, A., Ishiguro, N., and Kadomatsu, K. (2013). Minocycline selectively inhibits M1 polarization of microglia. Cell Death Dis. *4*, e525.

Kolluri, N., Sun, Z., Sampson, A.R., and Lewis, D.A. (2005). Lamina-specific reductions in dendritic spine density in the prefrontal cortex of subjects with schizophrenia. Am. J. Psychiatry *162*, 1200–1202.

Koukouli, F., Rooy, M., Tziotis, D., Sailor, K.A., O'Neill, H.C., Levenga, J., Witte, M., Nilges, M., Changeux, J.P., Hoeffer, C.A., et al. (2017). Nicotine reverses hypofrontality in animal models of addiction and schizophrenia. Nat. Med. *23*, 347–354.

Leicht, G., Vauth, S., Polomac, N., Andreou, C., Rauh, J., Mußmann, M., Karow, A., and Mulert, C. (2016). EEG-informed fMRI reveals a disturbed gamma-band-specific network in subjects at high risk for psychosis. Schizophr. Bull. *42*, 239–249.

Leslie, C.A., Robertson, M.W., Cutler, A.J., and Bennett, J.P., Jr. (1991). Postnatal development of D1 dopamine receptors in the medial prefrontal cortex, striatum and nucleus accumbens of normal and neonatal 6-hydroxydopamine treated rats: a quantitative autoradiographic analysis. Brain Res. Dev. Brain Res. *62*, 109–114.

Luzi, P., Abraham, R.M., Rafi, M.A., Curtis, M., Hooper, D.C., and Wenger, D.A. (2009). Effects of treatments on inflammatory and apoptotic markers in the CNS of mice with globoid cell leukodystrophy. Brain Res. *1300*, 146–158.

Marín, O. (2016). Developmental timing and critical windows for the treatment of psychiatric disorders. Nat. Med. *22*, 1229–1238.

Marques-Smith, A., Lyngholm, D., Kaufmann, A.K., Stacey, J.A., Hoerder-Suabedissen, A., Becker, E.B., Wilson, M.C., Molnár, Z., and Butt, S.J. (2016). A transient translaminar GABAergic interneuron circuit connects thalamocortical recipient layers in neonatal somatosensory cortex. Neuron *89*, 536–549.

Meyer, U., Feldon, J., Schedlowski, M., and Yee, B.K. (2005). Towards an immuno-precipitated neurodevelopmental animal model of schizophrenia. Neurosci. Biobehav. Rev. *29*, 913–947.

Miyamoto, A., Wake, H., Ishikawa, A.W., Eto, K., Shibata, K., Murakoshi, H., Koizumi, S., Moorhouse, A.J., Yoshimura, Y., and Nabekura, J. (2016). Microglia contact induces synapse formation in developing somatosensory cortex. Nat. Commun. *7*, 12540.

Miyaoka, T., Yasukawa, R., Yasuda, H., Hayashida, M., Inagaki, T., and Horiguchi, J. (2008). Minocycline as adjunctive therapy for schizophrenia: an open-label study. Clin. Neuropharmacol. *31*, 287–292.

Neniskyte, U., and Gross, C.T. (2017). Errant gardeners: glial-cell-dependent synaptic pruning and neurodevelopmental disorders. Nat. Rev. Neurosci. *18*, 658–670.

Rossant, C., Kadir, S.N., Goodman, D.F.M., Schulman, J., Hunter, M.L.D., Saleem, A.B., Grosmark, A., Belluscio, M., Denfield, G.H., Ecker, A.S., et al. (2016). Spike sorting for large, dense electrode arrays. Nat. Neurosci. *19*, 634–641.

Savitz, J.B., Teague, T.K., Misaki, M., Macaluso, M., Wurfel, B.E., Meyer, M., Drevets, D., Yates, W., Gleason, O., Drevets, W.C., and Preskorn, S.H. (2018). Treatment of bipolar depression with minocycline and/or aspirin: an adaptive, 2×2 double-blind, randomized, placebo-controlled, phase IIA clinical trial. Transl. Psychiatry *8*, 27.

Schafer, D.P., Lehrman, E.K., Kautzman, A.G., Koyama, R., Mardinly, A.R., Yamasaki, R., Ransohoff, R.M., Greenberg, M.E., Barres, B.A., and Stevens, B. (2012). Microglia sculpt postnatal neural circuits in an activity and complement-dependent manner. Neuron *74*, 691–705.

Selemon, L.D., and Zecevic, N. (2015). Schizophrenia: a tale of two critical periods for prefrontal cortical development. Transl. Psychiatry *5*, e623.

Sellgren, C.M., Gracias, J., Watmuff, B., Biag, J.D., Thanos, J.M., Whittredge, P.B., Fu, T., Worringer, K., Brown, H.E., Wang, J., et al. (2019). Increased synapse elimination by microglia in schizophrenia patient-derived models of synaptic pruning. Nat. Neurosci. *22*, 374–385.

Senkowski, D., and Gallinat, J. (2015). Dysfunctional prefrontal gamma-band oscillations reflect working memory and other cognitive deficits in schizophrenia. Biol. Psychiatry *77*, 1010–1019.

Shin Yim, Y., Park, A., Berrios, J., Lafourcade, M., Pascual, L.M., Soares, N., Yeon Kim, J., Kim, S., Kim, H., Waisman, A., et al. (2017). Reversing behavioural abnormalities in mice exposed to maternal inflammation. Nature *549*, 482–487.

Sirota, A., Montgomery, S., Fujisawa, S., Isomura, Y., Zugaro, M., and Buzsáki, G. (2008). Entrainment of neocortical neurons and gamma oscillations by the hippocampal theta rhythm. Neuron *60*, 683–697.

Uhlhaas, P.J., and Singer, W. (2015). Oscillations and neuronal dynamics in schizophrenia: the search for basic symptoms and translational opportunities. Biol. Psychiatry *77*, 1001–1009.

van Eden, C.G., Kros, J.M., and Uylings, H.B. (1990). The development of the rat prefrontal cortex. Its size and development of connections with thalamus, spinal cord and other cortical areas. Prog. Brain Res. *85*, 169–183.

van Os, J., Rutten, B.P., and Poulton, R. (2008). Gene-environment interactions in schizophrenia: review of epidemiological findings and future directions. Schizophr. Bull. *34*, 1066–1082.

Vinck, M., van Wingerden, M., Womelsdorf, T., Fries, P., and Pennartz, C.M. (2010). The pairwise phase consistency: a bias-free measure of rhythmic neuronal synchronization. Neuroimage *51*, 112–122.

Weinhard, L., di Bartolomei, G., Bolasco, G., Machado, P., Schieber, N.L., Neniskyte, U., Exiga, M., Vadisiute, A., Raggioli, A., Schertel, A., et al. (2018). Microglia remodel synapses by presynaptic trogocytosis and spine head filopodia induction. Nat. Commun. *9*, 1228.

Zhang, L., Zheng, H., Wu, R., Zhu, F., Kosten, T.R., Zhang, X.Y., and Zhao, J. (2018). Minocycline adjunctive treatment to risperidone for negative symptoms in schizophrenia: association with pro-inflammatory cytokine levels. Prog. Neuropsychopharmacol. Biol. Psychiatry *85*, 69–76.

STAR★METHODS

KEY RESOURCES TABLE

REAGENT or RESOURCE	SOURCE	IDENTIFIER
Antibodies		
mouse monoclonal Alexa Fluor-488 conjugated antibody against NeuN	Merck Millipore	Cat# MAB377X; RRID: AB_2149209
rabbit polyclonal primary antibody against GABA	Sigma-Aldrich	Cat#A2052; RRID: AB_477652
Alexa Fluor-488 goat anti-rabbit IgG secondary antibody	Merck Millipore	Cat# A-11008; RRID: AB_143165
rabbit monoclonal primary antibody against IBA-1	Wako	Cat# 019-19741; RRID: AB_839504
Deposited Data		
LFP and SUA data for all the non-anesthetized mice	This paper	https://gin.g-node.org/mchini/Resolving_and_rescuing_developmental_miswiring_in_a_mouse_model_of_cognitive_impairment
Chemicals, Peptides, and Recombinant Proteins		
Isoflurane	Abbott	B506
Urethane	Fluka analytical	94300
Minocycline	Sigma-Aldrich	M9511
Experimental Models: Organisms/Strains		
Mouse: C57BL/6J	Universitätsklinikum Hamburg-Eppendorf – Animal facility	N/A
Mouse: Disc1Tm1Kara /C57BL/6J	J. Gogos Lab	N/A
Recombinant DNA		
pAAV-CAG-ChR2(E123T/T159C)-2AtDimer2	T. G. Oertner Lab	http://www.oertner.com/
pAAV-CAG-tDimer2	T. G. Oertner Lab	http://www.oertner.com/
Software and Algorithms		
MATLAB R2016a	MathWorks	https://www.mathworks.com
Offline Sorter	Plexon	http://plexon.com/
ImageJ 2.0.0	ImageJ	https://imagej.nih.gov/ij/
R Statistical Software 3.5.1	RStudio	https://rstudio.com
Cheetah 6	Neuralynx	https://neuralynx.com/
Anaconda 1.9.6	Anaconda	https://www.anaconda.com
Spyder 3.3.2	Spyder	https://www.spyder-ide.org
Video Mot2	TSE Systems	https://www.tse-systems.com/product-details/videomot
Other		
Arduino Uno SMD	Arduino	A000073
Digital Lynx 4SX	Neuralynx	https://neuralynx.com/
Diode laser (473 nm)	Omicron	LuxX 473-100
Electroporation device	BEX	CUY21EX
Electroporation tweezer-type paddles	Protech	CUY650-P5
Recording electrode (1 shank, 16 channels)	Neuronexus	A1x16-3mm-703-A16
Recording optrode (1 shank, 16 channels)	Neuronexus	A1x16-5mm-703-OA16LP
Recording electrode (4 shanks, 16 channels)	Neuronexus	A4x4-3mm-100-125-703
Recording tetrode (4 shanks, 16 channels)	Neuronexus	A4x4-3mm-100-125-703-OA16LP

LEAD CONTACT AND MATERIALS AVAILABILITY

Further information and requests for resources and reagents should be directed to and will be fulfilled by the Lead Contact,Ileana L. Hanganu-Opatz (hangop@zmnh.uni-hamburg.de).

This study did not generate new unique reagents.

EXPERIMENTAL MODEL AND SUBJECT DETAILS

Mice

Experiments were performed in compliance with German laws and the guidelines of the European Community for the use of animals in research, and were approved by the local ethical committee (111/12, 132/12). Experiments were carried out on C57BL/6J mice of both sexes, at the age of P8–10. Heterozygous mutant DISC1 pups carrying a Disc1 allele (Disc1Tm1Kara) on a C57Bl6/J background and C57Bl6/J, whose dams were injected i.v. at embryonic day (E) 9 with the viral mimetic poly I:C (5 mg/kg) were used as dual-hit genetic-environmental model (dual-hit GE) (Hartung et al., 2016). Pups born from homozygous Disc1Tm1Kara dams and wild-type males and pups born from wild-type dams and homozygous Disc1Tm1Kara males were pooled together, as no difference between the two groups was found. Genotypes were assessed using genomic DNA (tail biopsies) and following primer sequences: forward primer 5′-TAGCCACTCTCATTGTCAGC-3′ and reverse primer 5′-CCTCATCCCTTCCACTCAGC-3′. Non-treated wild-type mice and the offspring of dams injected at E9 with saline (0.9%) were used as controls and combined together, as no difference between the two groups was found. For single-hit experiments, the offspring of wild-type E9 poly I:C injected dams (single-hit E) and heterozygous mutant Disc1Tm1Kara pups of E) saline injected dams (single-hit G) were used. Timed-pregnant mice from the animal facility of the University Medical Center Hamburg-Eppendorf, of both aforementioned conditions, were housed individually at a 12 h light/12 h dark cycle, and were given access to water and food *ad libitum*. The day of vaginal plug detection was considered as E0.5, while the day of birth as P0. In accordance with the three Rs guidelines of the European Community for the use of animals in research, we re-analyzed part of the mice used for one of our previous publications (Bitzenhofer et al., 2017).

Minocycline administration

Minocycline was administered to neonatal mice from either P1 to P8 or from P9 to P16 by adding it to the drinking water of the dam, which then passed it on to the offspring via lactation (Dansie et al., 2013). In line with previous studies (Dansie et al., 2013), the daily dosage of minocycline was 30 mg/kg body weight. To cover the taste of the antibiotic, sucrose was added to the solution. No difference in liquid intake was observed between dams receiving water and dams receiving water supplemented with minocycline. This administration route has been shown to result in detectable concentrations of the drug in the breast milk of the lactating dam (Luzi et al., 2009).

METHOD DETAILS

In utero electroporation

Additional wet food supplemented with 2-4 drops of Metacam (meloxicam; 0.5 mg ml−1; Boehringer-Ingelheim, Germany) was administered from one day before until two days after surgery. At E12.5 or E15.5 randomly assigned pregnant mice received a subcutaneous injection of buprenorphine (0.05 mg/kg body weight) at least 30 min before surgery. Surgery was performed on a heated surface; pain reflexes (toe and tail pinch) and breathing were monitored throughout. Under isoflurane anesthesia (induction: 5%; maintenance: 3.5%), the eyes of the dam were covered with eye ointment to prevent damage, before the uterine horns were exposed and moistened with warm sterile PBS (37 °C). Solution containing 1.25 μg/μl DNA (pAAV-CAG-ChR2(E123T/T159C)-2AtDimer2 or pAAV-CAG-tDimer2)) and 0.1% fast green dye at a volume of 0.75–1.25 μl were injected into the right lateral ventricle of individual embryos using pulled borosilicate glass capillaries with a sharp, long tip. Plasmid DNA was purified with NucleoBond (Macherey-Nagel, Germany). 2A encodes for a ribosomal skip sentence, splitting the fluorescent protein tDimer2 from the opsin during gene translation. Each embryo within the uterus was placed between the electroporation tweezer-type paddles (3 mm diameter for E12.5; 5 mm diameter for E14.5-15.5; Protech, TX, USA) that were roughly oriented at a 20° leftward angle from the midline and a 10° angle downward from anterior to posterior. By these means, neural precursor cells from the subventricular zone, which radially migrate into the medial PFC, were transfected. Electrode pulses (35 V, 50 ms) were applied five times at intervals of 950 ms controlled by an electroporator (CU21EX; BEX, Japan). Uterine horns were placed back into the abdominal cavity after electroporation, which was filled with warm sterile PBS (37 °C). Abdominal muscles and skin were sutured individually with absorbable and non-absorbable suture thread, respectively. After recovery, pregnant mice were returned to their home cages, which were half placed on a heating blanket for two days after surgery. Opsin expression was assessed with a portable fluorescent flashlight (Nightsea, MA, USA) through the intact skull and skin at P2–3 and confirmed post mortem by fluorescence microscopy in brain slices. Pups without expression in the PFC were excluded from the analysis.

Developmental milestones

Mouse pups were tested for their somatic development and reflexes at P2, P5 and P8. Weight, body and tail length were assessed. Surface righting reflex was quantified as time (max 30 s) until the pup turned over with all four feet on the ground after being placed on its back. Cliff aversion reflex was quantified as time (max 30 s) until the pup withdrew after snout and forepaws were positioned over an elevated edge. Vibrissa placing was rated positive if the pup turned its head after gently touching the whiskers with a toothpick.

Behavioral experiments

The behavioral experiments were carried out in pre-juvenile mice that did not experience IUE, using previously established experimental protocols. Briefly, all behavioral tests were conducted in a circular white arena, the size of which (D: 34 cm, H: 30 cm) maximized exploratory behavior, while minimizing incidental contact with testing objects. The objects used for testing of novelty recognition were five differently shaped, and colored, easy to clean items that were provided with magnets to fix them to the bottom of the arena. Object sizes (H: 3 cm, diameter: 1.5–3 cm) were smaller than twice the size of the mouse and did not resemble living stimuli (no eye spots, predator shape). The objects were positioned at 10 cm from the borders and 8 cm from the center of the arena. After every trial, the objects and arena were cleaned with 0.1% acetic acid to remove all odors. A black and white CCD camera (VIDEOR TECHNICAL E. Hartig GmbH) was mounted 100 cm above the arena and connected to a PC via PCI interface serving as frame grabber for video tracking software (Video Mot2 software, TSE Systems GmbH).

Exploratory Behavior in the Open Field

Pre-juvenile mice (P16-17) were allowed to freely explore the testing arena for 10 min. The floor area of the arena was digitally subdivided in 8 zones (4 center zones and 4 border zones) using the zone monitor mode of the VideoMot 2 analysis software (VideoMot 2, TSE Systems GmbH). The time spent by pups in center and border zones as well as the running distance and velocity were quantified. Mice that did not exit the center area for >1 min (n = 2) were excluded from further analysis.

Novelty Recognition Paradigms

All protocols for assessing item recognition memory in pre-juvenile mice consisted of familiarization and testing trials. During the familiarization trial, each mouse was placed into the arena containing two identical objects. The mice were released against the center of the opposite wall with the back to the objects. After 10 min of free exploration of objects, the mice were returned to a temporary holding cage. In the novel object recognition (NOR) task, tested in P17-P18 mice, the familiarization trial was followed 5 min later by a test trial in which one object used in the familiarization and one new object were placed in the arena at the same positions as during the familiarization trials. The mice were allowed to investigate the familiar and the novel object, with different shape and color, for 5 min. Object interaction during the first five minutes and the length of single interaction with the objects were analyzed and compared between the groups. In the recency recognition (RR) task, tested at P19–22, mice experienced two 10 min familiarization trials with two different sets of identical objects that were separated by a delay of 30 min. The second familiarization trial was followed after 5 min by a test trial in which one object used in the first and one object used in the second more recent familiarization trial were placed in the arena in the same positions as during the familiarization trials. Object interaction during the first five minutes and the length of single interaction with the objects were analyzed and compared between the groups. All trials were video-tracked using the Video Mot2 analysis software. The object recognition module of the software was used and a 3-point tracking method identified the head, the rear end and the center of gravity of the mouse. Digitally, a square zone was created around each object and every entry of the head point into this area was considered as object interaction. Climbing or sitting on the object, defined as having both head and center of gravity points within the square zone, were not counted as interactions. Data were imported and analyzed offline using custom-written tools in MATLAB software (MathWorks). Discrimination ratios were calculated as (Time spent interacting with novel object – time spent interacting with less recent object) / (Time spent interacting with novel object + time spent interacting with less recent object). Single interaction time ratios were analogously calculated.

In vitro electrophysiology and optogenetics

As previously described (Bitzenhofer et al., 2017), whole-cell patch-clamp recordings were performed from t-Dimer expressing superficial and deep layers prelimbic neurons in brain slices of P8–10 mice after IUE at E15.5 and E12.5, respectively. Briefly, pups were decapitated, brains were removed and immediately sectioned coronally at 300 μm in ice-cold oxygenated high sucrose-based artificial cerebral spinal fluid (ACSF) (in mM: 228 sucrose, 2.5 KCl, 1 NaH2PO4, 26.2 NaHCO3, 11 glucose, 7 MgSO4; 320 mOsm). Slices were incubated in oxygenated ACSF (in mM: 119 NaCl, 2.5 KCl, 1 NaH2PO4, 26.2 NaHCO3, 11 glucose, 1.3 MgSO4; 320 mOsm) at 37 °C for 45 min before cooling to room temperature and superfused with oxygenated ACSF in the recording chamber. tDimer2-positive neurons were patched under optical control using pulled borosilicate glass capillaries (tip resistance of 4-7 MΩ) filled with pipette solution (in mM: 130 K-gluconate, 10 HEPES, 0.5 EGTA, 4 Mg-ATP, 0.3 Na-GTP, 8 NaCl; 285 mOsm, pH 7.4). Recordings were controlled with the Ephus software in the MATLAB environment (MathWorks, MA, USA). Capacitance artifacts and series resistance were minimized using the built-in circuitry of the patch-clamp amplifier (Axopatch 200B; Molecular devices, CA, USA). Responses of neurons to hyper- and depolarizing current injections, as well as blue light pulses (473 nm, 5.2 mW/mm^2) were digitized at 5 kHz in current-clamp mode.

In vivo electrophysiology and optogenetics

Surgery

Multisite extracellular recordings were performed in the PL of P8–10 mice. For recordings in non-anesthetized state, 0.5% bupivacain / 1% lidocaine was locally applied on the neck muscles. For recordings in anesthetized state, mice were injected i.p. with urethane (1 mg/g body weight; Sigma-Aldrich) before surgery. For both groups, the surgery was performed under isoflurane anesthesia (induction: 5%; maintenance: 1.5%). The head of the pup was fixed into a stereotaxic apparatus using two plastic bars mounted on the nasal and occipital bones with dental cement. The bone above the PFC (0.5 mm anterior to bregma, 0.1 mm right to the midline for superficial layers, 0.5 mm for deep layers) was carefully removed by drilling a hole of < 0.5 mm in diameter. Before recordings, mice were allowed to recover for 10–20 min on a heating blanket.

One- or four-shank multisite optoelectrodes (NeuroNexus, MI, USA) were inserted 2.4 or 1.9 mm (respectively) deep into PFC, perpendicular to the skull surface. One-shank optoelectrodes contained 1 × 16 recordings sites (0.4-0.8 MΩ impedance, 100 μm spacing) aligned with an optical fiber (105 μm diameter) ending 200 μm above the top recording site. Four-shank optoelectrodes contained 4 × 4 recording sites (0.4-0.8 MΩ impedance, 100 μm spacing, 125 μm intershank spacing) aligned with optical fibers (50 μm diameter) ending 200 μm above the top recording sites. A silver wire was inserted into the cerebellum and served as ground and reference electrode. Before signal acquisition, a recovery period of 15 min after electrode insertion was provided.

Signal acquisition

Extracellular signals were band-pass filtered (0.1–9,000 Hz) and digitized (32 kHz) with a multichannel extracellular amplifier (Digital Lynx SX; Neuralynx, Bozeman, MO, USA) and the Cheetah acquisition software (Neuralynx). Spontaneous (i.e., not induced by light stimulation) activity was recorded for 15 min at the beginning of each recording session.

Light stimulation

Ramp (i.e., linearly increasing power) light stimulations were performed with an arduino uno (Arduino, Italy) controlled diode laser (473 nm; Omicron, Austria). Laser power was adjusted to trigger neuronal spiking in response to >25% of 3-ms-long light pulses at 16 Hz. Resulting light power was in the range of 20–40 mW/mm^2 at the fiber tip.

Post mortem assessment of electrode position

Wide field fluorescence images were acquired to reconstruct the recording electrode position in brain slices of electrophysiologically investigated pups and to localize tDimer2 expression in pups after IUE. Only pups with correct electrode and transfection position were considered for further analysis.

Histology

Perfusion

P8–10 mice were anesthetized with 10% ketamine (aniMedica, Germany) / 2% xylazine (WDT, Germany) in 0.9% NaCl solution (10 μg/g body weight, intraperitoneally (i.p.)) and transcardially perfused with Histofix (Carl Roth, Germany) containing 4% paraformaldehyde.

Immunohistochemistry

Brains were postfixed in Histofix for 24 h and sectioned coronally at 50 μm (immunohistochemistry) or 100 μm (Sholl and spine analysis). For anti-NeuN, anti-CamKII and anti-GABA stainings, free-floating slices were permeabilized and blocked with PBS containing 0.8% Triton X-100 (Sigma-Aldrich, MO, USA) and 5% normal bovine serum (Jackson Immuno Research, PA, USA). For IBA-1 and VGLUT1 stainings, slices were permeabilized and blocked with PBS containing 0.3% Triton X-100 and 3% normal bovine serum. Subsequently, slices were incubated overnight with mouse monoclonal Alexa Fluor-488-conjugated antibody against NeuN (1:100, MAB377X; Merck Millipore, MA, USA), rabbit polyclonal primary antibody against CaMKII (1:200, PA5-38239; Thermo Fisher Scientific, MA, USA), rabbit polyclonal primary antibody against GABA (1:1,000, no. A2052; Sigma-Aldrich), rabbit monoclonal primary antibody against IBA-1 (1:500, catalog #019-19741, Wako), or polyclonal guinea-pig antibody against VGLUT1 (1:1000, Synaptic Systems, Germany) followed by 2 h incubation with Alexa Fluor-488 goat anti-rabbit IgG secondary antibody (1:500, A11008; Merck Millipore), Alexa Fluor-568 donkey anti-rabbit (1:500, Life Technologies, CA, USA) or Alexa Fluor-488 goat anti-guinea pig (1:500, Molecular Probes, OR, USA). Finally, slices were transferred to glass slides and covered with Vecta-Shield (Vector Laboratories).

Imaging

Sections were examined with a confocal microscope (DM IRBE, Leica Microsystems, Zeiss LSN700 and Olympus FX-100). To quantify the t-Dimer overlap with NeuN, CaMKII and GABA, microscopic fields over PFC were acquired as 1024 × 1024 pixel images (pixel size, 1465 nm) using a 10X objective (numerical aperture, 0.3). The same settings were used to quantify the number of CaMKII positive neurons (n = 4 fields per section, 3 sections per mouse). For IBA-1, 20-images microscopic stacks (n = 8 stacks per section, 3 sections per mouse) were acquired as 512 × 512 pixel images (pixel size, 732 nm; Z-step, 1000 nm) using a 40X objective (numerical aperture, 1.25). For analysis of IBA-1^+-cells and VGLUT1 vesicle overlay, microscopic stacks (n = 5 stacks per sections, 3 sections per mouse) were acquired as 1024x1024 pixels images (pixel size, 103 nm; Z-step, 750 nm) using a 60X objective (numerical aperture, 1.35). Microscopic stacks used for Sholl and spine analysis were acquired as 2048 × 2048 pixel images (pixel size, 156 nm; Z-step, 1000 and 500 nm, respectively).

QUANTIFICATION AND STATISTICAL ANALYSIS

Image analysis

CaMKII$^+$ cells quantification

The number of CaMKII-positive neurons was semi-automatically assessed with a custom-written algorithm in the ImageJ environment. Briefly, a Region of Interest (ROI) was manually placed over either superficial or deep prefrontal layers. The image contrast was enhanced (*enhance contrast* function, 0.5% of saturated pixels) and a *median filter* was applied (radius = 1.5). To reduce background noise, we used the *subtract background* function, with a radius of 30 pixels. The image was then binarized (*convert to mask*) and segmented using the *watershed* function. To identify the neurons we used the *extended maxima* function of the MorphoLibJ plugin (dynamic = 30, connectivity = 4). We subtracted the regional maxima with the lowest intensity (i.e., the objects with bigger area) using *area opening* (pixel = 150) and counted the remaining objects (*analyze particles*).

Neuronal morphological analysis

Sholl analysis and spine density quantification were carried out in the ImageJ environment. For Sholl analysis, images were binarized (*auto threshold*) and dendrites were traced using the semi-automatical plugin *Simple Neurite Tracer*. The traced dendritic tree was analyzed with the plugin *Sholl Analysis*, after the geometric center was identified using the *blow/lasso tool*. For spine density quantification, we first traced the dendrite of interest (apical, basal, proximal oblique or secondary apical) and measured its length (*line*) and then manually counted the number of spines (*point picker*).

Iba-1$^+$-cells quantification

To quantify the number of Iba-1 stained cells we used a custom-written algorithm in ImageJ. The image stacks were collapsed to a maximum intensity Z-projection, and background noise was subtracted (*despeckle*). To facilitate automatic thresholding, the image was passed through a Gaussian filter (*Gaussian blur*, sigma = 2) before being binarized (*auto threshold* with the *triangle* method). The number of cells was counted using *analyze particles* (size >150 pixels).

Iba-1$^+$-cells morphological analysis

The morphology of microglial cells was assessed on maximum intensity Z-projections in the MATLAB environment, using previously reported criteria (Bellesi et al., 2017). Images (n = 64 for each group of mice) were automatically thresholded (*graythresh* and *im2bw* functions) and putative microglial cells were identified as objects between 200 and 1500 pixels (*bwareaopen*). Around the center of mass of each of the isolated cells, a region of interest (ROI) of 110x110 pixels was computed and visually examined. If the ROI contained a properly segmented microglia cells, its features (area, perimeter, eccentricity) were quantified (*regionprops*). ROIs in which the microglial cell touched the boundaries of the image or in which more than one cell was included were discarded. Further, cell spread (analogous to process length) was computed as the average distance between the center of mass and the ''extrema'' of the cell; roundness was defined as the ratio between 4*pi*area and the square of the perimeter of the cell. Only mice that did not experience IUE were used for this analysis.

Iba-1$^+$-cells and VGLUT1$^+$ puncta overlay

Overlay of Iba-1$^+$ cells and VGLUT1$^+$ puncta was assessed according to previously reported criteria (Bellesi et al., 2017). Briefly, background noise of VGLUT1 stacks was reduced in the ImageJ environment using the subtract background (rolling ball radius, 2 pixels) and despeckle functions. Stacks were passed through a maximum filter (radius, 2 pixels), thresholded (auto threshold) and segmented (watershed). Further processing was carried out in the MATLAB environment. Puncta were labeled (bwlabeln, connectivity = 8) and their volume was measured (histcounts). Puncta <100 pixel or >500 pixel were discarded. Microglia stacks were entirely processed in the MATLAB environment. Stacks were passed through a 3D hysteresis filter (hysteresis3d function; lower threshold = 0.1, upper threshold = 0.5, connectivity = 26) and a 3D median filter (ordfilt3D function). VGLUT1 positive puncta showing 100% overlap with the processed Iba1 signal were then quantified. VGLUT-1 puncta were considered to be phagocyted if they showed a 100% overlap in xyz with the imaged microglial cell. Microglia cells were also quantified in their distal cell volume (volume computed starting from 7 μm of distance from the center of mass of the cell).

In vitro electrophysiology

As previously described (Bitzenhofer et al., 2017), data were imported and analyzed offline using custom-written tools in the MATLAB environment (MathWorks). For *in vitro* data, all potentials were corrected for liquid junction potentials (−10 mV) for the gluconate-based electrode solution. The RMP was measured immediately after obtaining the whole-cell configuration. To assess input resistance, hyperpolarizing current pulses of 200 ms duration were applied. Active membrane properties and current–voltage relationships were determined by unsupervised analysis of responses to a series of 600 ms long hyper- and depolarizing current pulses. Amplitude of APs was measured from threshold to peak.

In vivo electrophysiology

In vivo data were analyzed with custom-written algorithms in the MATLAB environment. Data were processed as following: band-pass filtered (500–5,000 Hz) to analyze MUA and band-pass filtered (4-100 Hz) using a third-order Butterworth filter before down-sampling to 3.2 kHz to analyze LFP. All filtering procedures were performed in a phase preserving manner. In recordings of non-anesthetized mice, to reduce the influence of movement-related artifacts, the signal was processed according to the *common-average and rereference* method before power spectral analysis and spike detection.

Detection of oscillatory activity

The detection of discontinuous patterns of activity in the neonatal PL was performed using a modified version of the previously developed algorithm for unsupervised analysis of neonatal oscillations (Cichon et al., 2014). Briefly, deflections of the root mean square of band-pass filtered signals (1–100 Hz) exceeding a variance-depending threshold were considered as network oscillations. The threshold was determined by a Gaussian fit to the values ranging from 0 to the global maximum of the root-mean-square histogram. If two oscillations occurred within 200 ms of each other they were considered as one. Only oscillations lasting >1 s were included, and their occurrence, duration, and amplitude were computed.

Power spectral density

For power spectral density analysis, 1 s-long windows of network oscillations were concatenated and the power was calculated using Welch's method with non-overlapping windows. For optical stimulation, we compared the average power during the 1.5 s-long time window preceding the stimulation to the last 1.5 s-long time window of light-evoked activity.

Multi-unit activity

MUA was detected as the peak of negative deflections exceeding five times the standard deviation of the filtered signal and having a prominence larger than half the peak itself.

Single unit activity

SUA was detected and clustered using klusta (Rossant et al., 2016) and manually curated using phy (https://github.com/cortex-lab/phy). Data were imported and analyzed using custom-written tools in the MATLAB software (MathWorks).

Firing rate

The firing rate was computed by dividing the total number of spikes by the duration of the analyzed time window.

Inter-spike-interval

Inter-spike interval (ISI) was calculated at 2 ms resolution and was normalized to all the detected ISI. For plotting and statistics only the 10-500 ms range was considered.

Pairwise phase consistency

Pairwise phase consistency (PPC) was computed as previously described (Vinck et al., 2010). Briefly, the phase in the band of interest was extracted as mentioned above, and the mean of the cosine of the absolute angular distance (dot product) among all pairs of phases was calculated.

Spike-triggered LFP power

Spike-triggered LFP spectra were calculated as

$$(\mathrm{Power}_{\mathrm{spike}} - \mathrm{Power}_{\mathrm{baseline}})/\mathrm{Power}_{\mathrm{baseline}},$$

where the spike-triggered power spectrum ($\mathrm{Power}_{\mathrm{spike}}$) was calculated using Welch's method for a 200 ms-log time window centered on each spike, and the power spectrum of baseline LFP ($\mathrm{Power}_{\mathrm{baseline}}$) was averaged for two time windows, 100-300 ms and 200-400 ms before each spike.

K-nearest neighbors classifiers

Machine learning analyses were performed using Python (Python Software Foundation, Wolfeboro Falls, New Hampshire, USA) in the Spyder (Pierre Raybaut, The Spyder Development Team) development environment. Model training and performance evaluation were carried out using the scikit-learn toolbox. The set was iteratively (n = 500) divided in a training (2/3 of the set) and a cross-validation (1/3) set. Hyper-parameter of the model were tuned on the training set, which was further split using the standard 3-fold cross-validation split implemented by the function ''GridSearchCV,'' to which a ''pipeline'' object was passed. The ''pipeline'' object was built using the ''Pipeline'' function, and concatenating quantile transformation of the input features (''Quantile Transformer,'' tuning the number of quantiles), feature selection (''Select Percentile,'' using mutual information and tuning the percentage of features to select) and K-nearest neighbors classification (tuning the number of neighbors, the weight function to use for prediction, the algorithm used to compute the nearest neighbors, and the size of the leaf). Performance assessment was then computed on the cross-validation set (to which it had not been exposed during hyper-parameters tuning). Performance was stable across a wide range of parameters. To plot the classifier decision space, we used t-sne to reduce the feature space to two dimensions, while preserving the hyper-dimensional structure of the data. The decision space was then approximated by imposing a Voronoi tessellation on the 2d plot, using k-nearest regression on the t-sne coordinates of the predicted classes of the mice.

Statistical analysis

Statistical analyses were performed using R Statistical Software (Foundation for Statistical Computing, Vienna, Austria). Normally distributed, homoscedastic, having equal variance and non-nested data were tested for significant differences (*$p < 0.05$, **$p < 0.01$ and ***$p < 0.001$) using paired t test, unpaired t test, one-way repeated-measures ANOVA, or one-way ANCOVA with age as a covariate (only if age had a significant effect) and with Bonferroni-Tukey corrected post hoc analysis. Not normally distributed, heteroskedastic or not having equal variance data were tested with yuen's bootstrap test (n = 5000 repetitions), yuen's paired sample robust t test, or bootstrapped (n = 5000 repetitions) heteroscedastic one way ANOVA for trimmed means (yuenbt, yuend, t1waybt, mcppb20, glht, lsmeans functions of the WRS2, multcomp and lsmeans R package). A standard 20% level of trimming for the mean

was selected for these tests. Such tests were preferred to more traditional non-parametric tests in virtue of the (sometimes) high levels of unequal variance in our data. To account for the commonly ignored increased false positive rate inherent in nested design (Aarts et al., 2014), nested data were analyzed with linear mixed-effect models. Parameter estimation was done using the *lmer* function implemented in the lme4-R package. Model selection was performed using the Akaike Information Criterion (AIC) and/or the Bayesian information criterion (BIC), as differences between the two criteria were minimal. To test the significance of condition in our model, we performed a likelihood ratio test against a reduced model in which we removed condition (aov R function). Post hoc analysis with Tukey multiple comparison correction was carried out using the glhp function of the multcomp R package. For analysis of phagocytic activity of microglia cells, we used bootstrapped heteroscedastic one-way ANOVA for trimmed means instead of linear mixed-effect model in virtue of the highly non-normality of the data. No statistical measures were used to estimate sample size since effect size was unknown. Investigators were blinded to the group allocation when Sholl, spine analyses, microglia morphology, and engulfment were assessed. For other investigations, unsupervised analysis software was used to preclude investigator biases. Statistical parameters can be found in the main text and/or in the figure legends. More information about test used, its values, and its parameters are provided in Data S1.

DATA AND CODE AVAILABILITY

The authors declare that all data and code supporting the findings of this study are included in the manuscript and its Supplementary Information or are available from the corresponding authors on request. LFP and SUA data for all the non-anesthetized mice is available at the following open-access repository:

https://gin.g-node.org/mchini/Resolving_and_rescuing_developmental_miswiring_in_a_mouse_model_of_cognitive_impairment

Neuron, Volume *105*

Supplemental Information

Resolving and Rescuing Developmental Miswiring in a Mouse Model of Cognitive Impairment

Mattia Chini, Jastyn A. Pöpplau, Christoph Lindemann, Laura Carol-Perdiguer, Marilena Hnida, Victoria Oberländer, Xiaxia Xu, Joachim Ahlbeck, Sebastian H. Bitzenhofer, Christoph Mulert, and Ileana L. Hanganu-Opatz

Resolving and rescuing developmental miswiring in a mouse model of cognitive impairment

Mattia Chini[1], Jastyn A. Pöpplau[1], Christoph Lindemann[1], Laura Carol-Perdiguer[1], Marilena Hnida[1], Victoria Oberländer[1,†], Xiaxia Xu[1], Joachim Ahlbeck[1,††], Sebastian H. Bitzenhofer[1,†††], Christoph Mulert[2,§] & Ileana L. Hanganu-Opatz[1,3*]

Inventory of Supplemental Information

SUPPLEMENTARY INFORMATION

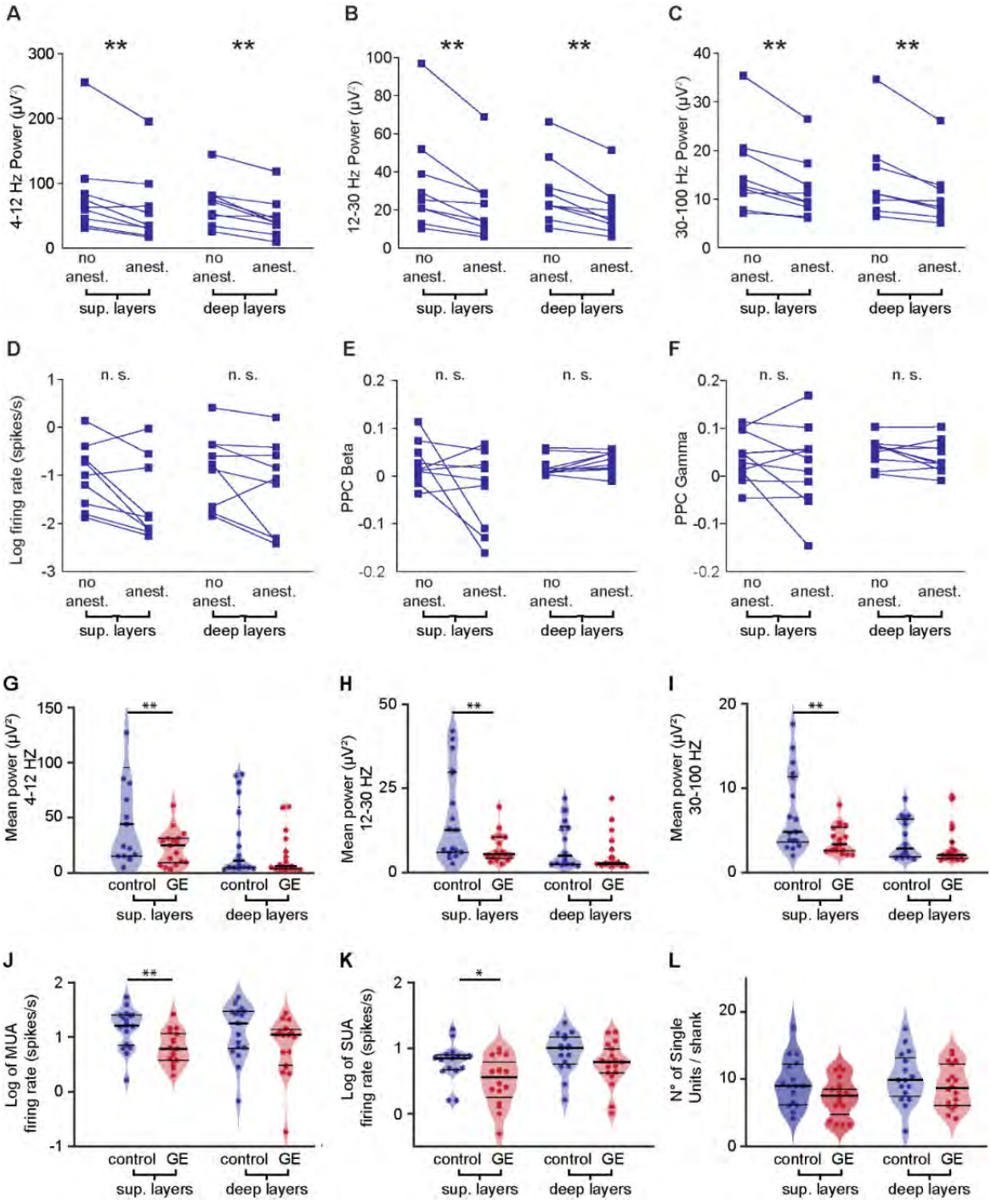

Figure S1. Related to Figure 1. Effect of urethane anesthesia on network oscillations and firing of neonatal control and GE mice. (A) Scatter plot displaying the oscillatory power in theta frequency band for superficial and deep layers of the prelimbic cortex before (left, n=9 mice) and after urethane anesthesia (right, n=9 mice). **(B-F)** Same as (A) for power in beta (B) and gamma (C) frequency bands, MUA firing rate (D), as well as pairwise phase consistency for beta (E) and gamma (F) oscillations. **(G)** Violin plot displaying the power for theta frequency band in superficial and deep layers of the prelimbic cortex of non-anesthetized control (blue, n=16) and GE (red, n=18) mice. **(H-L)** Same as (G) for power in beta (H) and gamma (I)

frequency bands, MUA (J) and SUA (K) firing rate, and number of single units per shank (L). In scatter plots (A-F), single data points are presented as squares. In violin plots (G-L), data is presented as median with 25th and 75th percentile and single data points are shown as asterisks. *P<0.05, **P<0.01 and ***P<0.001, Wilcoxon signed-rank test (A-F), ANCOVA with age as covariate (G-L), and yuen's bootstrap test (J-L) with 20% level of trimming for the mean.

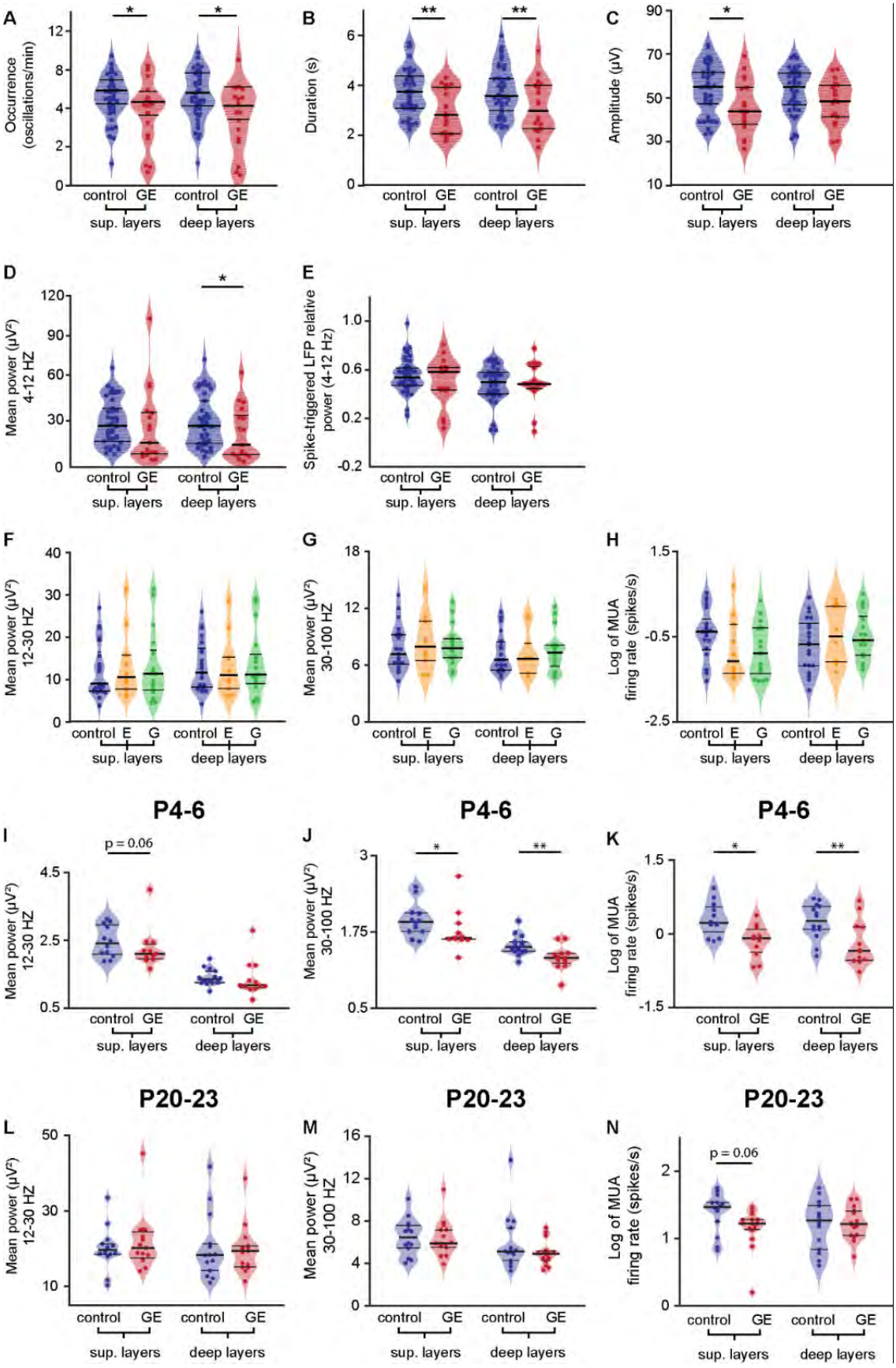
A
Occurrence (oscillations/min)
B
Duration (s)
C
Amplitude (µV)
D
Mean power (µV²) 4-12 HZ
E
Spike-triggered LFP relative power (4-12 Hz)
F
Mean power (µV²) 12-30 HZ
G
Mean power (µV²) 30-100 HZ
H
Log of MUA firing rate (spikes/s)
P4-6
I
p = 0.06
J
K
P20-23
L
M
N
p = 0.06
control GE
control E G
sup. layers
deep layers

Figure S2. Related to Figure 1. Properties of discontinuous oscillatory activity and neuronal firing over the layers of PL from neonatal one-hit and dual-hit GE mice as well as P4-6 and P20-23 control and dual-hit GE mice. (A) Violin plot displaying the occurrence of oscillations in prelimbic superficial and deep layers of control (blue, n=38) and GE (red, n=18) mice. **(B-E)** Same as (A) for oscillation duration (B), amplitude (C), power in theta frequency band (D), the relative power of spike-triggered LFP in theta band (E). **(F)** Violin plot displaying the mean power (12-30 Hz) of oscillations in prelimbic superficial and deep layers of control (blue, n=21), E (yellow, n=10) and G (green, n=17) neonatal mice. (**G,H**) Same as (F) for mean power (30-100 Hz) (G) and MUA firing rate (H). (**I**) Violin plot displaying the mean power (12-30 Hz) in prelimbic superficial and deep layers of control (blue, n=14) and GE (red, n=13) P4-6 mice. (**J,K**) Same as (I) for mean power (30-100 Hz) (J) and MUA firing rate (K). (**L**) Violin plot displaying the mean power (12-30 Hz) in prelimbic superficial and deep layers of control (blue, n=14) and GE (red, n=15) P20-23 mice. (**M,N**) Same as (L) for mean power (30-100 Hz) (M) and MUA firing rate (N). Data is presented as median with 25th and 75th percentile and single data points are shown as asterisks. The shaded area represents the probability distribution of the variable. *P<0.05, **P<0.01, ANCOVA with age as covariate (A-D, F-K), and yuen's bootstrap test (E, I-N) with 20% level of trimming for the mean.

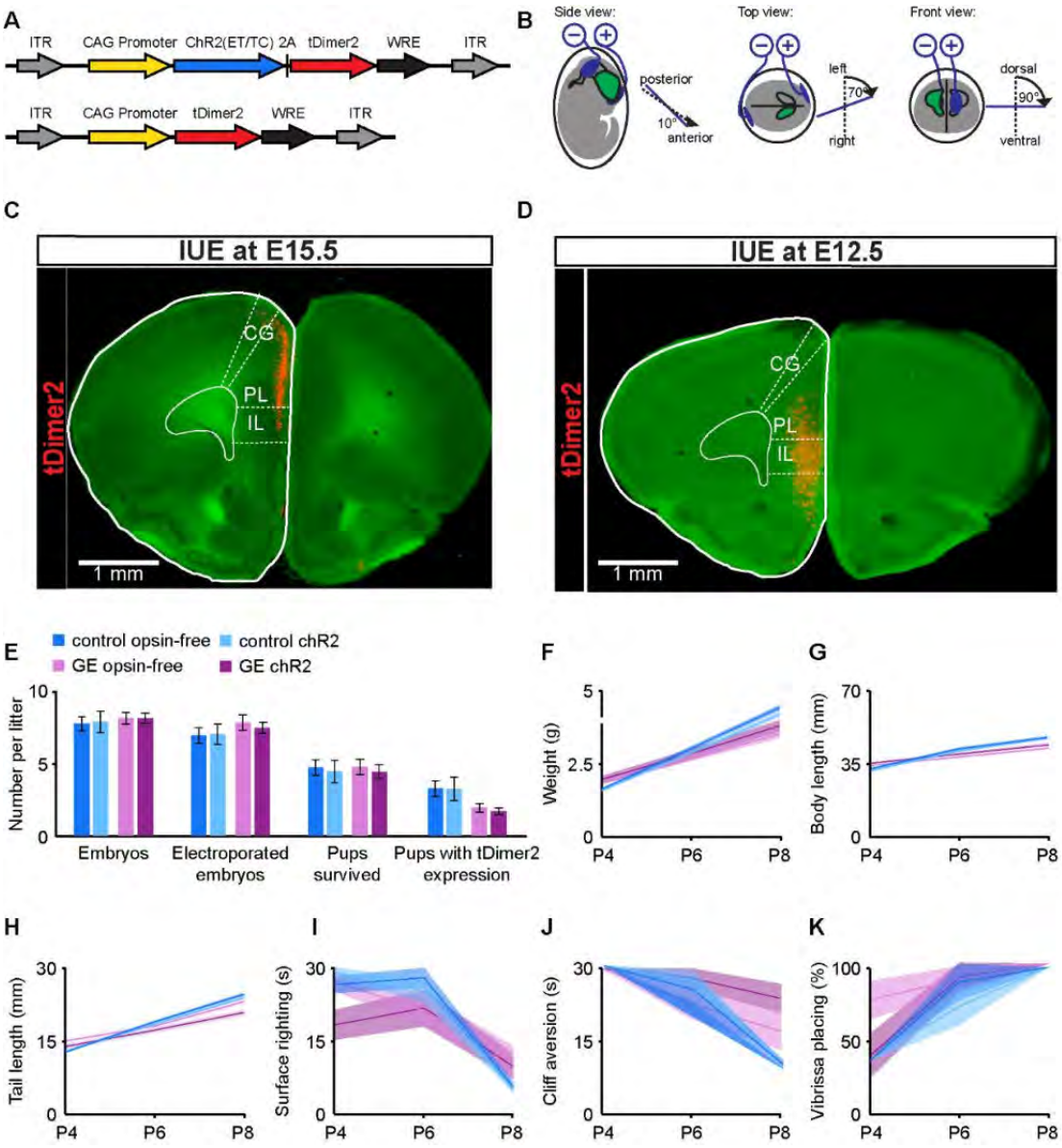

Figure S3. Related to Figures 2-5. Cell- and layer-specific transfection of neonatal prelimbic cortex by site-directed in utero electroporation. (a) Structure of the ChR2(ET/TC)-containing and opsin-free plasmids. **(B)** Schematic drawing illustrating the orientation of electrode paddles for specific targeting of $PYRs_{SUP}$ and $PYRs_{DEEP}$. **(C)** TDimer2-expressing cells (red) in a 50 µm-thick coronal section of a P10 mouse at the level of PFC after IUE at E15.5. Note that the transfection is restricted to neurons located in superficial layers. **(D)** Same as (C) after IUE at E12.5. Note that the transfection is mainly restricted to neurons located in deep layers. **(E)** Bar diagram displaying the mean number of embryos, electroporated embryos, surviving pups, and positively transfected pups when ChR2(ET/TC)-containing (control, dark blue, n=13 litters; GE, dark purple, n=10 litters) and opsin-free constructs (control, light blue, n=5 litters; GE, light purple, n=8 litters) were transfected by IUE at E15.5. **(F-H)** Line plots displaying the developmental profile of somatic growth: weight (F), body length (G), tail length (H) of P2-8 pups expressing ChR2(ET/TC) (control, dark blue, n=31; GE, dark purple, n=26) or opsin-free constructs (control, light blue, n=11; GE, light purple, n=7) in $PYRs_{SUP}$. **(I-K)** Line plots displaying the development profile of reflexes: surface righting (I), cliff aversion (J), and vibrissa placing (K) of P2-8 pups expressing ChR2(ET/TC)

(control, dark blue, n=31; GE, dark purple, n=26) or opsin-free constructs (control, light blue, n=11; GE, light purple, n=7) in $PYRs_{SUP}$. Data are displayed as mean ± SEM. *$p < 0.05$, one-way repeated-measures analysis of variance (ANOVA) with Bonferroni-corrected post hoc analysis.

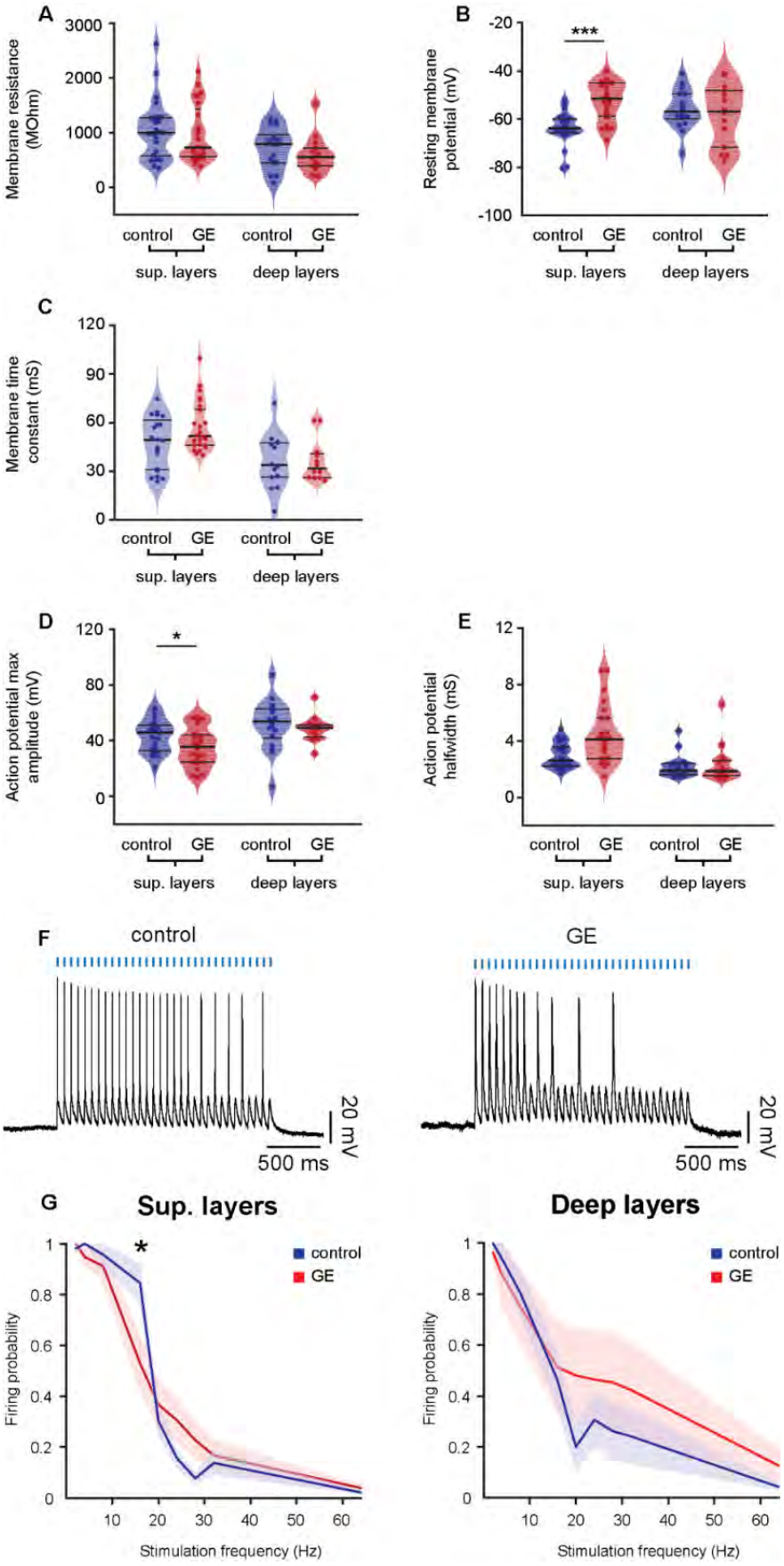

Figure S4. Related to Figures 2-3. Optogenetic activation of PYRs$_{SUP}$ and PYRs$_{DEEP}$ in control and dual-hit GE mice in vitro. (A) Violin plot displaying the membrane resistance for

$PYRs_{SUP}$ and $PYRs_{DEEP}$ of control (blue, n=25 and n=24, respectively) and GE mice (red, n=17 and n=14, respectively). **(B-E)** Same as (A) for resting membrane potential (B), membrane time constant (C), maximum light-triggered action potential amplitude (D), and light-triggered action potential half-width (E). **(F)** Representative voltage responses of a transfected $PYRs_{SUP}$ from a P9 control (left) and a P9 GE mouse (right) to repetitive trains of 3 ms-long light pulses at 16 Hz. **(G)** Graph displaying the mean firing probability of superficial (left) and deep layers (right) transfected control and GE neurons in response to repetitive light stimuli of different frequencies. In (G) data is presented as mean ± sem. In (A-E) data is presented as median with 25th and 75th percentile and single data points are shown as asterisks. The shaded area represents the probability distribution of the variable. *P<0.05, **P<0.01 and ***P<0.001, one-way repeated-measures analysis of variance (ANOVA) with Bonferroni-corrected post hoc analysis (F), and bootstrap yuen test with 20% level of trimming for the mean and 5000 bootstrap samples.

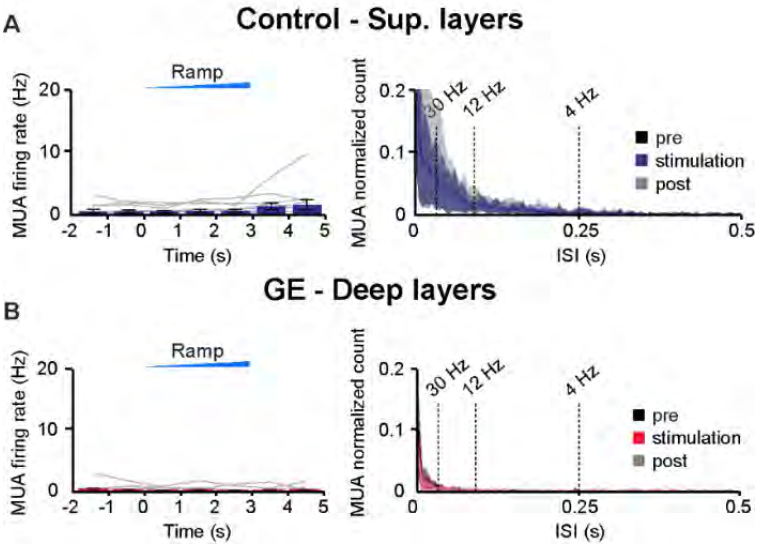

Figure S5. Related to Figure 2. In vivo spiking of PYRs$_{SUP}$ transfected by IUE with opsin-free constructs. (A) Left, bar diagram displaying the mean MUA firing rate in transfected PYRs$_{SUP}$ of control mice in response to ramp illumination. Right, occurrence rate of interspike intervals averaged for 3 s before light stimulation (pre, black), 3 s during ramp stimulation (stimulation, blue) and 3 s after light stimulation (post, grey, n=11 recording sites from 11 pups). **(B)** Same as (A) for PYRs$_{SUP}$ of GE mice (n=10 recording sites from 8 pups). Data is presented as mean ± s.e.m. P>0.05, one-way repeated-measures analysis of variance (ANOVA) with Bonferroni-corrected post hoc analysis.

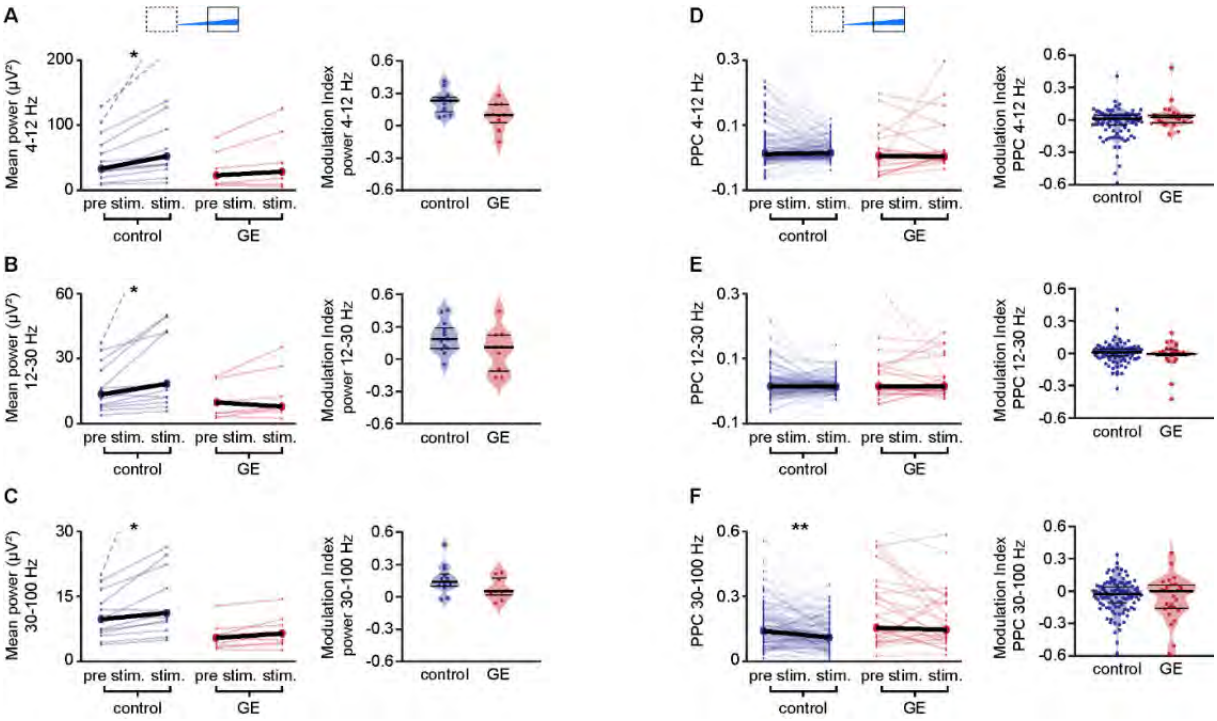

Figure S6. Related to Figure 3. Network activity after optogenetic activation of PYRs$_{DEEP}$ in control and dual-hit GE mice in vivo. (A) Left, scatter plot displaying the LFP power in the theta (4–12 Hz) frequency band for control (blue, n=13) and GE (red, n=9) mice before (pre stim., 1.5 s) and during the second half (stim., 1.5 s) of ramp stimulation. Right, violin plot displaying the stimulation modulation index of LFP power in the theta frequency band for control and GE mice. **(B,C)** Same as (A) for beta (12-30 Hz) and gamma (30-100) frequency bands. **(D-F)** Same as (A-C) for PPC of PYRs$_{DEEP}$ in control (n=116 recording sites from 13 pups) and GE (n=27 recording sites from 6 pups) mice. In scatter plots (A-F) data is presented as median, and individual values are displayed as thin dots and lines. In violin plots (A-F) data is presented as median with 25th and 75th percentile and single data points are shown as asterisks. The shaded area represents the probability distribution of the variable. *P<0.05, **P<0.01 and ***P<0.001, yuen's bootstrap test (A-F) with 20% level of trimming for the mean and linear mixed-effect model with animal as a random effect (D-F).

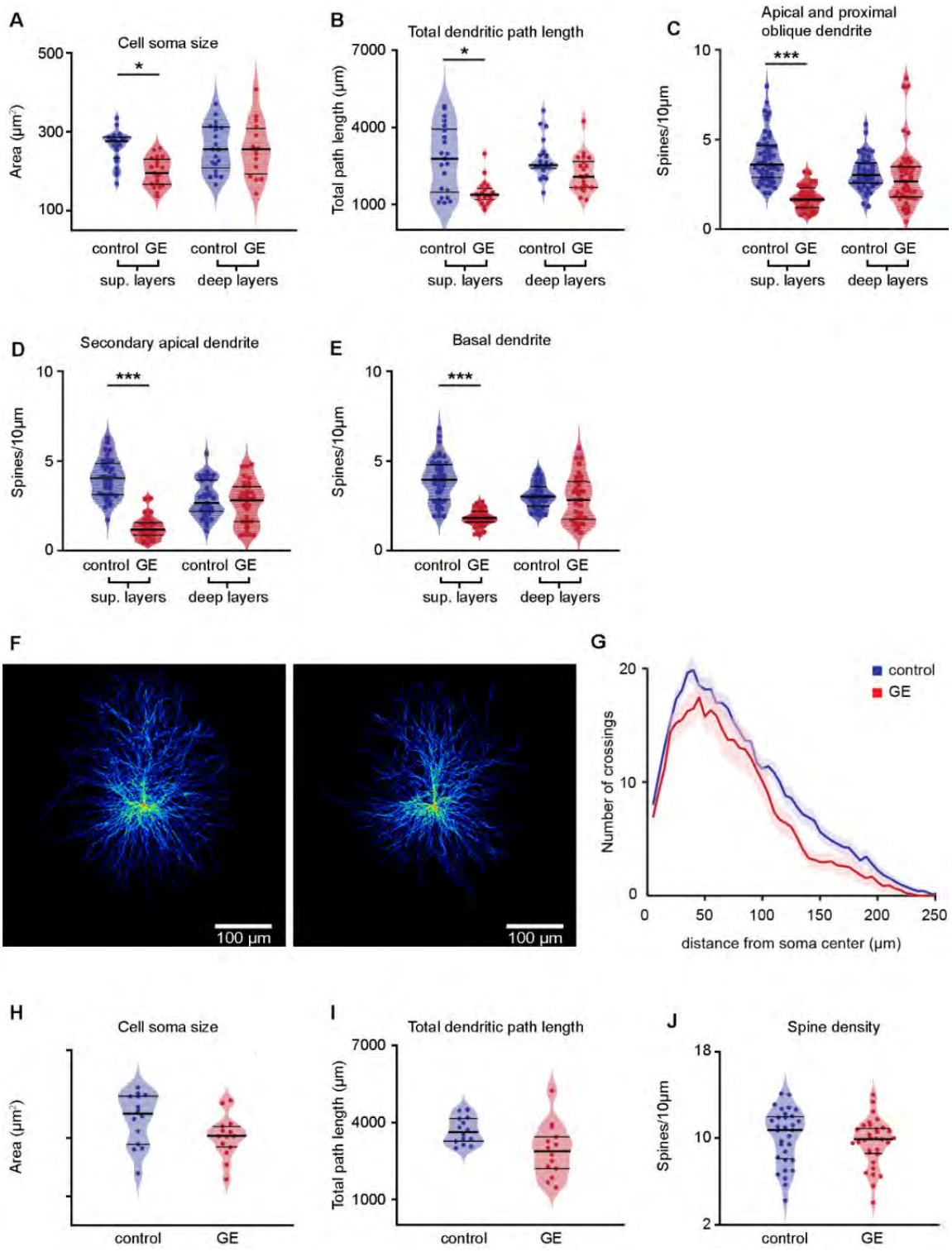

Figure S7. Related to Figure 4. Reduced soma size, dendritic path length and spine density in PYRs$_{SUP}$ of neonatal but not pre-juvenile dual-hit GE mice. (A) Left, violin plot displaying the average soma size from PYRs$_{SUP}$ of control (blue, n=21 neurons) and GE (red, n=21 neurons) mice. Right, same as left for PYRs$_{DEEP}$ from control (blue, n=21 neurons) and GE (red, n=15 neurons) mice. **(B)** Same as (A) for total dendritic path length. **(C)** Same as (A) for spine density on apical and proximal oblique dendrites from PYRs$_{SUP}$ of control (blue, n=53 dendrites from 13 neurons) and GE (red, n=35 dendrites from 10 neurons) mice. Right, same as left for PYRs$_{DEEP}$ from control (blue, n=43 dendrites from 12 neurons) and GE (red, n=44

dendrites from 12 neurons) mice. **(D,E)** same as (C) for secondary apical (B) and basal dendrites (C). **(F)** Heatmaps displaying an overlay of all traced dendrites of transfected $PYRs_{SUP}$ in pre-juvenile control (left) and GE (right) mice. **(G)** Graph displaying the average number of dendritic intersections within a 250 µm radius from the soma center of $PYRs_{SUP}$ in pre-juvenile control (blue, n=14 neurons from 2 pups) and GE (red, n=14 neurons from 2 pups) mice. **(H)** Violin plot displaying the average soma size from $PYRs_{SUP}$ of pre-juvenile control (blue, n=14 neurons) and GE (red, n=21 neurons) mice. (**I**) Same as (H) for total dendritic path length. (**J**) Violin plot displaying the average spine density on dendrites from $PYRs_{SUP}$ of pre-juvenile control (blue, n=24 dendrites from 8 neurons) and GE (red, n=24 dendrites from 8 neurons) mice. In (G) data is presented as mean ± s.e.m. In (A-E, H-J) data is presented as median with 25th and 75th percentile and single data points are shown as asterisks. The shaded area represents the probability distribution of the variable. ***P<0.001, linear mixed-effect model with animal as a random effect.

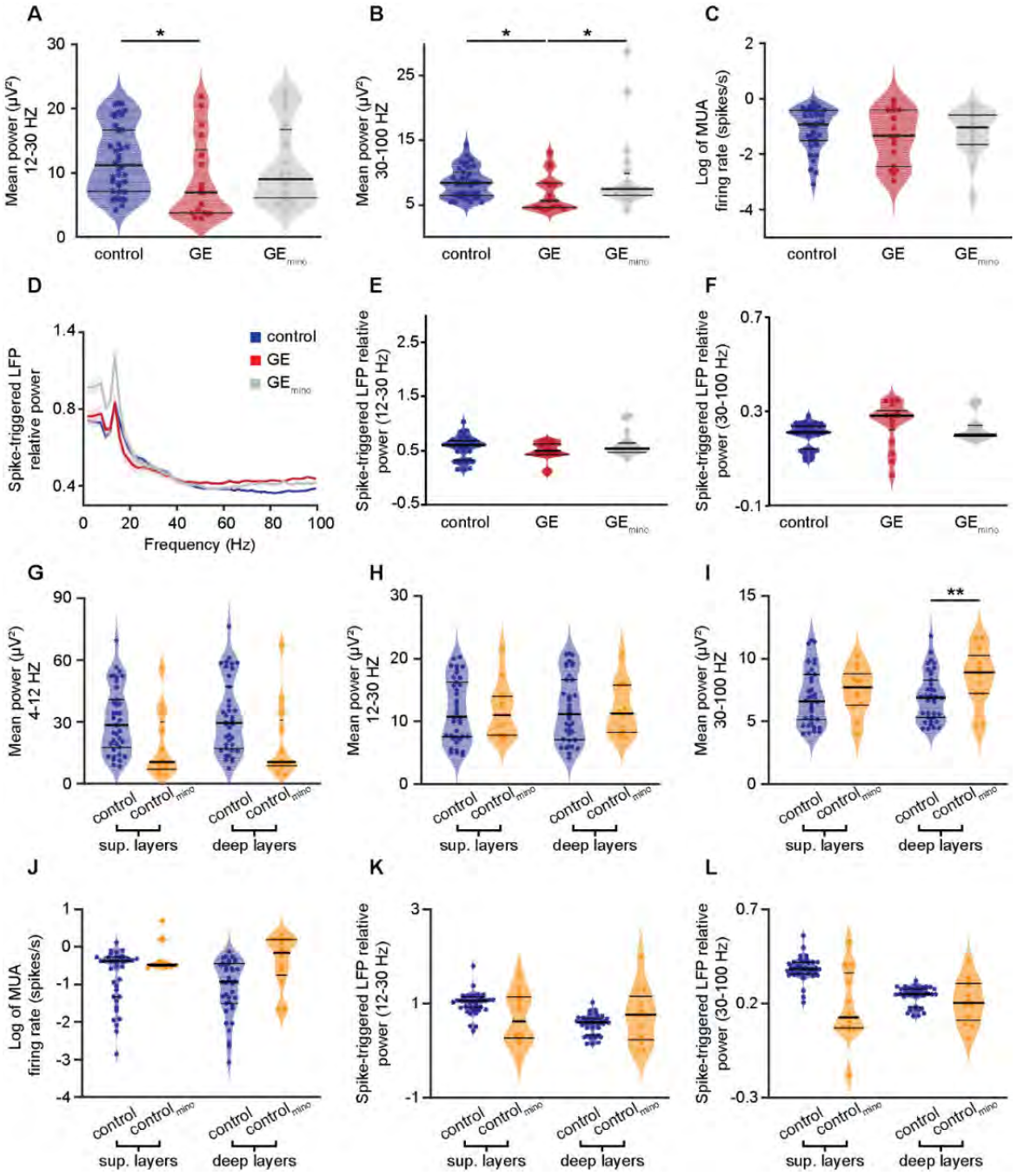

Figure S8. Related to Figure 5-6. Minocycline effect on neonatal control and dual-hit GE mice. (A) Violin plot displaying the power in beta frequency band of oscillations in deep layers of the PL of control (blue, n=38), GE (red, n=18), and GE_{mino} mice (gray, n=18). **(B-C)** Same as (A) for power in gamma (B) frequency bands and MUA firing rate (C). **(D)** Plots of frequency-dependent relative power of spike-triggered LFP in deep layers (top) of control (blue), GE (red), and GE_{mino} mice (gray). **(E)** Violin plot displaying the relative power of spike-triggered LFP in beta band for deep layers of control (blue, n=38), GE (red, n=18), and GE_{mino} mice (gray, n=18). **(F)** Same as (E) for the LFP in gamma band. **(G)** Violin plot displaying the power in theta frequency band of oscillations in superficial and deep layers of the prelimbic cortex of control (blue, n=38) and $control_{mino}$ (yellow, n=12) mice. **(H-L)** Same as (G) for the power in beta (H) and gamma (I) frequency band, MUA firing rate (J), relative power of spike-triggered LFP in beta (K) and gamma (L) band. In (D) data is presented as mean ± sem. In (A-C,E-L) data is presented as median with 25th and 75th percentile and single data points are shown as

asterisks. The shaded area represents the probability distribution of the variable. *P<0.05, **P<0.01, ANCOVA with age as covariate and 20% level of trimming for the mean (A-C), robust ANOVA with 20% level of trimming for the mean (E-F) with Bonferroni-Holm post-hoc analysis, and yuen's bootstrap test (G-L) with 20% level of trimming for the mean.

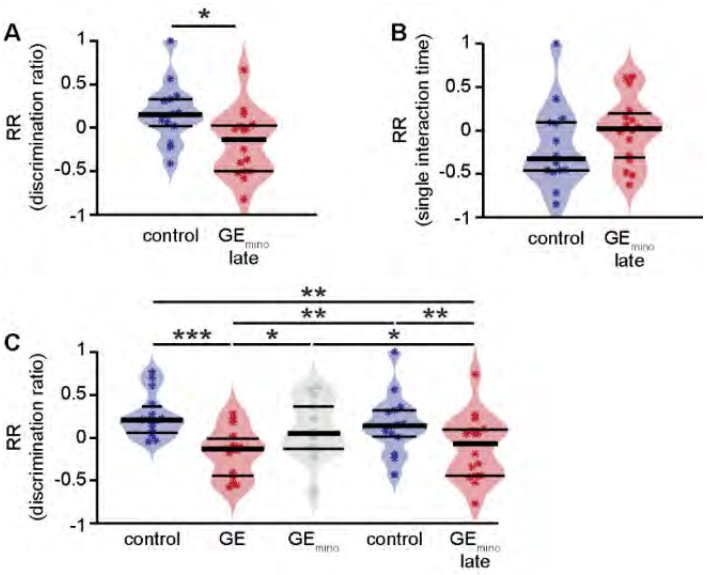

Figure S9. Related to Figure 8. Late minocycline treatment does not rescue behavioral deficits in dual-hit GE mice. (A) Violin plot displaying RR discrimination ratio of control (blue, n=14) and GE_{mino}late (red, n=15). **(B)** Same as (A) for single interaction time. **(C)** Same as (A) for control (blue, n=16), GE (red, n=15), GE_{mino} (gray, n=16), control (blue, n=14) and GE_{mino}late (red, n=15). Data is presented as median with 25th and 75th percentile and single data points are shown as asterisks. The shaded area represents the probability distribution of the variable. *P<0.05, robust, bootstrapped ANOVA with 20% level of trimming for the mean.

Data files S1. Related to Figures 1-8. Detailed statistical results.

	Superficial layers			*Deep layers*		
	Control	**GE**	**GE+mino**	**Control**	**GE**	**GE+mino**
Occurrence (oscillations/min)	6.6 ± 0.02	5.4 ± 0.2 *	6.7 ± 0.1	6.5 ± 0.05	5.2 ± 0.3 *	7 ± 0.1
Duration (s)	3.6 ± 0.1	3 ± 0.3 *	3.2 ± 0.03	3.7 ± 0.01	3 ± 0.26 *	3.2 ± 0.02
Amplitude (μV)	54.5 ± 1.1	45.7 ± 2.3 *	51.2 ± 0.4	54.3 ± 0.9	48.3 ± 1.6 *	49.8 ± 0.6
Theta power (μV^2)	28.9 ± 2.2	19.5 ± 4.4 **	23.6 ± 3.8	29.7 ± 2.5	19.3 ± 3.6 **	25.0 ± 4.8
Beta power (μV^2)	13.7 ± 0.7	7.0 ± 1.3 */°	10.2 ± 1.3	15.2 ± 0.7	6.9 ± 1.2 **	10.1 ± 1.4
Gamma power (μV^2)	6.6 ± 0.3	4.8 ± 0.4 **/°°	6.6 ± 0.7	6.7 ± 0.3	5.2 ± 0.5 **/°°	6.2 ± 0.5
Log firing rate (spikes/s)	-0.61 ± 0.04	-2-1 ± 0.1 ***/°°°	-0.9 ± 0.1	-0.95 ± 0.05	-1.3 ± 0.2	-0.96 ± 0.2
Spike triggered LFP relative power (4-12 Hz)	0.81 ± 0.02	0.89 ± 0.05 °°	1.3 ± 0.07 ^^	0.73 ± 0.03	0.67 ± 0.05 °	0.89 ± 0.05 ^
Spike triggered LFP relative power (12-30 Hz)	1.1 ± 0.03	0.64 ± 0.06 ***/°°	1.4 ± 0.17 ^	0.60 ± 0.04	0.50 ± 0.03	0.53 ± 0.03
Spike triggered LFP relative power (30-100 Hz)	0.38 ± 0.07	0.26 ± 0.03 ^/ */°	0.39 ± 0.02	0.25 ± 0.08	0.32 ± 0.02	0.24 ± 0.08

Table S1. Related to Figures 1, 6. Properties of oscillations in superficial and deep layers of PL in control, GE and GE_{mino} mice, as well as of their MUA firing and its timing to network oscillations. Asterisks (*) indicate significance level between control and GE mice. Circles (°) indicate significance level between GE and GE_{mino} mice. Carets (^) indicate significance level between control and GE_{mino} mice. ^/ */° $p<0.05$, ^^/ **/°° $p<0.005$, ^^^/ ***/°°° $p<0.001$.

Neuron

Article

A transient developmental increase in prefrontal activity alters network maturation and causes cognitive dysfunction in adult mice

Graphical Abstract

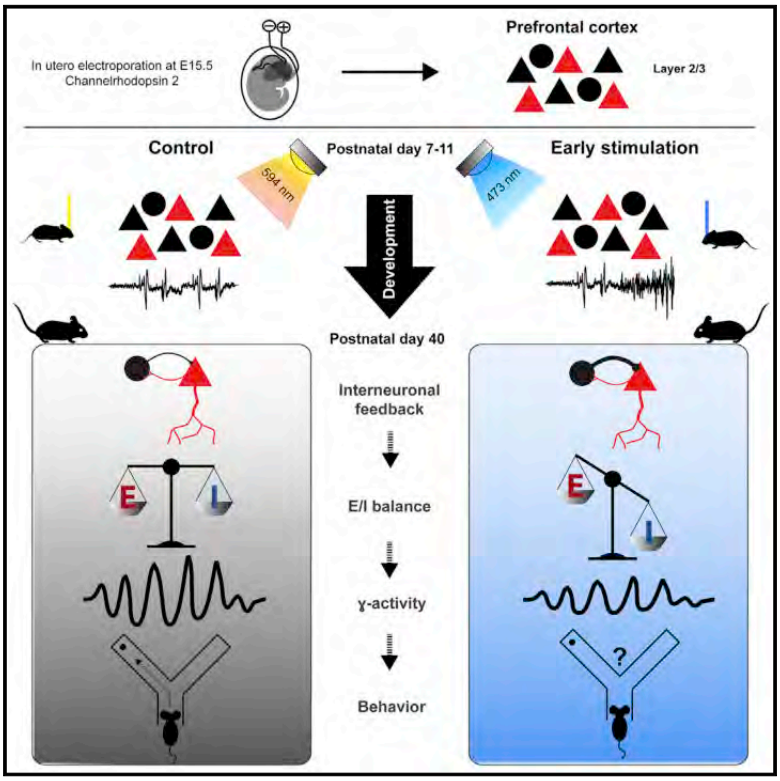

Highlights

- Increasing neonatal coordinated activity causes transient dendritic surge in mPFC
- Increasing neonatal activity disrupts gamma synchrony in adult prefrontal circuits
- Increasing neonatal activity causes excitation/inhibition imbalance in adult mPFC
- Increasing neonatal prefrontal activity disrupts adult cognitive abilities

Authors

Sebastian H. Bitzenhofer, Jastyn A. Pöpplau, Mattia Chini, Annette Marquardt, Ileana L. Hanganu-Opatz

Correspondence

sbitzenhofer@ucsd.edu (S.H.B.), hangop@zmnh.uni-hamburg.de (I.L.H.-O.)

In brief

Bitzenhofer et al. manipulate early activity in the prefrontal cortex of neonatal mice, resulting in disruption of coordinated patterns of electrical activity, excitation-inhibition imbalance, and impaired cognitive abilities at adult age. Thus, prefrontal activity during development is critical for adult network function and behavioral performance.

Bitzenhofer et al., 2021, Neuron *109*, 1350–1364
April 21, 2021
https://doi.org/10.1016/j.neuron.2021.02.011

CellPress

CellPress
OPEN ACCESS

Neuron

Article

A transient developmental increase in prefrontal activity alters network maturation and causes cognitive dysfunction in adult mice

Sebastian H. Bitzenhofer,[1,2,3,*] Jastyn A. Pöpplau,[1,2] Mattia Chini,[1] Annette Marquardt,[1] and Ileana L. Hanganu-Opatz[1,4,*]
[1]Institute of Developmental Neurophysiology, Center for Molecular Neurobiology, University Medical Center Hamburg-Eppendorf, 20251 Hamburg, Germany
[2]These authors contributed equally
[3]Present address: Center for Neural Circuits and Behavior, Department of Neurosciences, University of California, San Diego, La Jolla, CA 92093, USA
[4]Lead contact
*Correspondence: sbitzenhofer@ucsd.edu (S.H.B.), hangop@zmnh.uni-hamburg.de (I.L.H.-O.)
https://doi.org/10.1016/j.neuron.2021.02.011

SUMMARY

Disturbed neuronal activity in neuropsychiatric pathologies emerges during development and might cause multifold neuronal dysfunction by interfering with apoptosis, dendritic growth, and synapse formation. However, how altered electrical activity early in life affects neuronal function and behavior in adults is unknown. Here, we address this question by transiently increasing the coordinated activity of layer 2/3 pyramidal neurons in the medial prefrontal cortex of neonatal mice and monitoring long-term functional and behavioral consequences. We show that increased activity during early development causes premature maturation of pyramidal neurons and affects interneuronal density. Consequently, altered inhibitory feedback by fast-spiking interneurons and excitation/inhibition imbalance in prefrontal circuits of young adults result in weaker evoked synchronization of gamma frequency. These structural and functional changes ultimately lead to poorer mnemonic and social abilities. Thus, prefrontal activity during early development actively controls the cognitive performance of adults and might be critical for cognitive symptoms in neuropsychiatric diseases.

INTRODUCTION

The prefrontal cortex acts as a hub of cognitive processing indispensable for daily life (Frith and Dolan, 1996; Miller, 2000). Disruption of prefrontal cortex-dependent short-term memory and executive performance is a major burden with neuropsychiatric diseases such as schizophrenia and autism spectrum disorders (Baron-Cohen, 2004; van Os and Kapur, 2009; Stuchlik and Sumiyoshi, 2014). These diseases are associated with a large variety of genes and environmental risk factors that increase susceptibility (Clifton et al., 2019; Sahin and Sur, 2015). The absence of a clear understanding of their pathophysiology has resulted in primarily symptom-based treatments with low response rates (Marín, 2016). Many of the genes and risk factors associated with neuropsychiatric diseases regulate brain development, leading to the hypothesis that abnormal maturation causes impaired network function and, ultimately, poor cognitive abilities later in life (Geschwind, 2011; Hall et al., 2015; Marín, 2016; Schmitt et al., 2014). Indeed, rhythmic network activity of cortical and particularly prefrontal circuits is already compromised in prodromal patients (Leicht et al., 2016; Mikanmaa et al., 2019) and during early postnatal development in mouse models of schizophrenia and autism (Chini et al., 2020; Hartung et al., 2016a; Peixoto et al., 2016; Richter et al., 2019).

Neuronal activity regulates the development of cortical networks in many ways, from controlling neuronal differentiation, migration, and apoptosis to shaping establishment of sensory maps and local and large-scale networks (Blanquie et al., 2017; Katz and Shatz, 1996; Kirischuk et al., 2017; Kirkby et al., 2013). Early in life, activity in the prefrontal cortex is coordinated in oscillatory patterns, but, in line with delayed structural maturation and emergence of cognitive abilities, these patterns appear later than in other cortical areas (Brockmann et al., 2011; Chini and Hanganu-Opatz, 2020). Inputs from cortical and subcortical areas boost activation of local prefrontal circuits (Ahlbeck et al., 2018; Brockmann et al., 2011; Hartung et al., 2016b; Janiesch et al., 2011). Moreover, intracortical interactions lead to emergence of oscillatory activity at fast frequencies (Bitzenhofer et al., 2015, 2017a, 2020). However, whether early activity is necessary for maturation of prefrontal function and cognitive abilities is still unknown. Conversely, whether altered activity during development actively contributes to adult miswiring instead of simply reflecting pathological maturation remains to be elucidated.

To address these questions, we manipulated cortical activity during early development and monitored the long-term consequences for network activity and behavioral abilities. The manipulation was performed by transient light stimulation of a subset of pyramidal neurons (PYRs) in layer (L) 2/3 of the mouse medial prefrontal cortex (mPFC) from post-natal day 7 (P7) to P11, the developmental time window corresponding to the second/third trimester of gestation in humans (Workman et al., 2013). This light stimulation induces rhythmic activity in beta/low gamma frequency in the developing PFC (Bitzenhofer et al., 2017a). Throughout the neocortex, at the age of stimulation, migration of cortical neurons is largely finished, and activity-dependent formation of synaptic connections is fully in progress (Anastasiades and Butt, 2012; Van Eden and Uylings, 1985; Lim et al., 2018). We focused on this developmental period of cortical network formation, when mouse models of psychiatric diseases start to show altered prefrontal activity caused by L2/3 PYR dysfunction (Chini and Hanganu-Opatz, 2020; Chini et al., 2020). We demonstrate that the transient increase in prefrontal activity during early development is sufficient to disrupt prefrontal function and cognitive performance at adult age.

RESULTS

Stimulation of L2/3 PYRs induces coordinated activity in the neonatal mPFC

To uncover the role of early activity in adult prefrontal function, we first established a protocol to optically manipulate the activity of L2/3 PYRs from P7–P11, a developmental time window of high relevance for formation of synaptic contacts in the mPFC (Figure 1A). A subset of precursor cells of L2/3 PYRs in the prelimbic subdivision of the mPFC was transfected with channelrhodopsin 2 E123T/T159C (ChR2(ET/TC)) by *in utero* electroporation (IUE) at embryonic day 15.5 (E15.5) (STAR methods). As reported previously, the IUE protocol yields unilateral expression of ChR2(ET/TC) in 20%–30% of PYRs confined to L2/3 in the mPFC (Figure 1B; Bitzenhofer et al., 2017b).

Ramp stimulation of linearly increasing light power (473 nm, 3 s) was used to transcranially activate transfected L2/3 PYRs from P7–P11. In line with previous data (Bitzenhofer et al., 2017a), prefrontal network activity tended to organize itself rhythmically in the beta frequency range at 15–20 Hz upon ramp stimulation (Figures 1C and 1D). Control light stimulation (594 nm, ramp, 3 s) that did not activate ChR2(ET/TC) did not change the network activity in the mPFC. Transcranial ramp light stimulation was titrated in power and duration to reliably induce oscillatory bursts that resemble those occurring spontaneously in the neonatal mPFC (Figures 1E and S1; Brockmann et al., 2011; Lindemann et al., 2016). Transcranial ramp light stimulation transiently increased neuronal firing in a subset of neurons (20.6% of units activated significantly, 0.0% of units inactivated significantly) (Figures 1F and 1G). Control light stimulation (594 nm, ramp, 3 s) did not change the firing activity in the mPFC. The average firing rate increased during stimulation and continued to be increased significantly 2 s after stimulation before dropping back to pre-stimulation levels (Figure 1H). Induced firing was not random but peaked at 15–20 Hz for individual units, in line with the induced beta band network activity (Figure 1I).

A transient increase in prefrontal activity during neonatal development disrupts cognitive performance of young adults

To transiently increase neuronal firing and network activation in the developing mPFC, we performed a transcranial stimulation protocol, which induced fast oscillatory discharges, daily from P7–P11. This developmental period has been identified as being critical for altered prefrontal activity in a mouse model of neuropsychiatric diseases (Chini et al., 2020). On each of the 5 days of manipulation, mice received 180 transcranial ramp light stimulations (3 s long, 7-s intervals) at 594 nm (control) or 473 nm (early stimulation, ES) to activate ChR2(ET/TC)-transfected L2/3 PYRs in the mPFC.

Subsequently, we tested the behavioral abilities of control and ES mice, focusing on tasks that require prefrontal function. Data from mice of both sexes were pooled because their performance was comparable in all tasks (Table S2). Transient ES did not affect overall somatic and reflex development (Figure S2A). First we monitored recognition memory as a form of short-term memory that emerges at pre-juvenile age (P16–P22), as soon as sensory and motor abilities are fully mature (Le Roy et al., 2001). In contrast to control mice, ES mice were not able to distinguish a novel from a familiar object (novel object recognition [NOR]) as well as an object they interacted with more recently (recency recognition [RR]) (Figures S2C and S2E). However, because of the large variability of behavioral performance at juvenile age, group differences did not reach the significance threshold. The novel position of an object (object location recognition [OLR]) was distinguished by control and ES mice (Figure S2D). In contrast to NOR and RR, OLR depends more on the hippocampus (HP) than the mPFC (Barker and Warburton, 2011). Social interactions were impaired significantly in pre-juvenile ES mice. Their preference for interaction with the dam-containing container over an empty container was reduced significantly compared with control mice (Figure 2A).

Second, we tested the mPFC-dependent working memory of young adult (P36–P40) control and ES mice. We used an 8-arm radial maze test with 4 baited arms, a Y-maze test for spontaneous alternations, and a delayed non-match-to-sample task. ES mice showed working memory and reference memory deficits in the 8-arm radial maze test (Figures 2B, 2C, and S2F). Moreover, compared with controls, ES mice showed poorer performance during spontaneous alternation (Figures 2D and S2G) and in the delayed non-match-to-sample task (Figure 2E). The deficits identified in ES mice are not due to impaired motor abilities or enhanced anxiety because neither the behavior in an open field nor the interactions with objects and mazes were different between groups (Figures S2B, 2F, and 2G). Thus, transient elevation of prefrontal activity at neonatal age caused long-lasting impairment of mPFC-dependent short-term and working memory as well as social behavior.

A transient increase in neonatal prefrontal activity induces premature dendritic growth in L2/3 PYRs

To test whether impaired cognitive abilities of juvenile and adult ES mice resulted from permanent structural disruption of the mPFC after a transient increase in neonatal activity, we monitored the structural development of PYRs in control

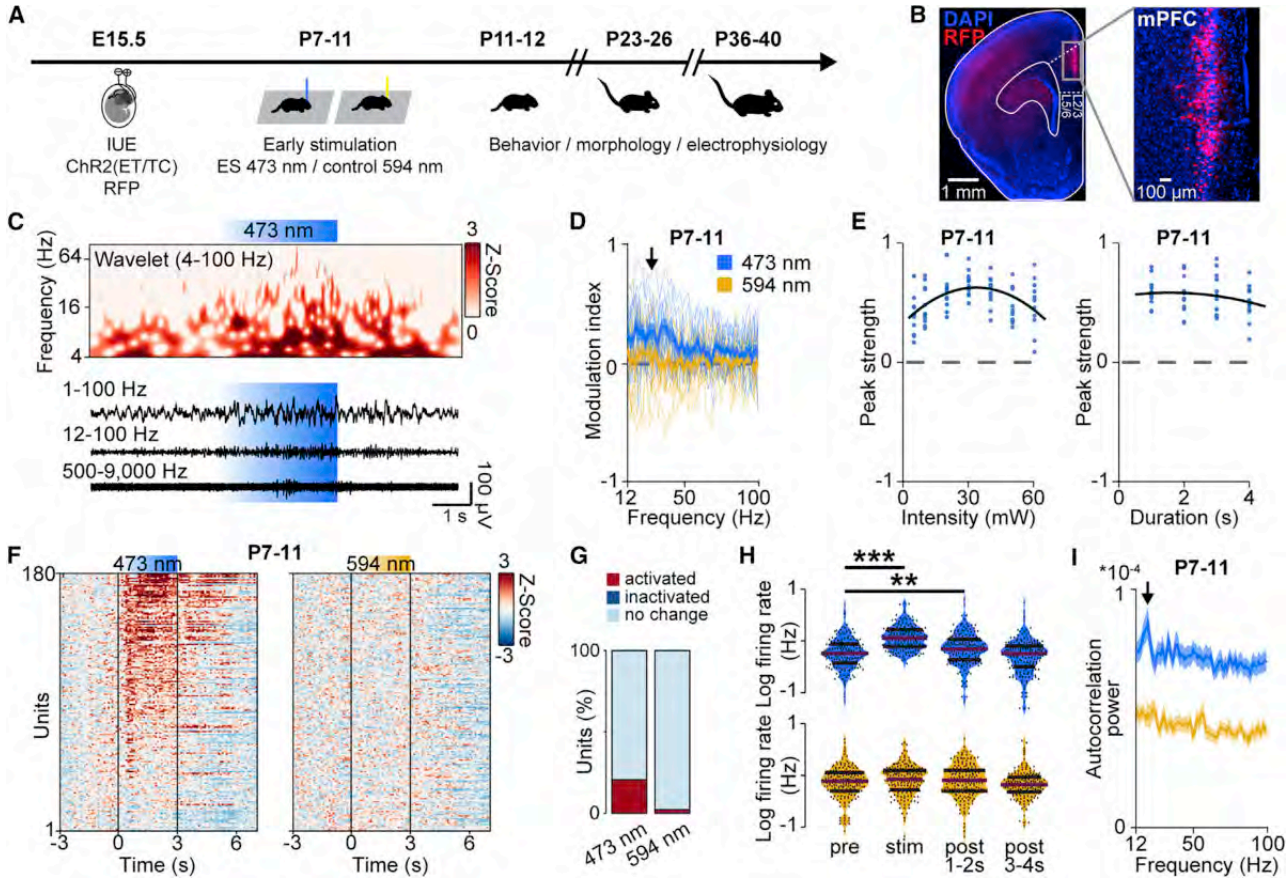

Figure 1. Light stimulation of L2/3 PYRs in the neonatal mPFC

(A) Schematic of the protocol for early light stimulation and long-lasting monitoring of structural, functional, and behavioral effects during development.

(B) Representative image showing ChR2(ET/TC)-2A-RFP expression in L2/3 PYRs after IUE at E15.5 in a DAPI-stained coronal slice, including the mPFC, from a P11 mouse. RFP, red fluorescent protein

(C) Representative extracellular recording with a corresponding wavelet spectrum at an identical timescale during transcranial ramp light stimulation (473 nm, 3 s) of L2/3 PYRs in the mPFC of a P10 mouse.

(D) Modulation index of local field potential (LFP) power in response to ramp light stimulation at 473 nm (blue) and 594 nm (yellow) averaged for P7–P11 mice (n = 13 mice).

(E) Peak strength for transcranial ramp light stimulation at different intensities and durations for P7–P11 mice (n = 11 mice).

(F) Firing rates of single units (n = 180 units from 13 mice) in response to transcranial ramp light stimulation *Z* scored to the pre-stimulation period at P7–P11.

(G) Percentage of significantly modulated units ($p < 0.01$) during ramp light stimulation.

(H) Average single-unit firing rate in response to ramp light stimulation at 473 nm and 594 nm averaged for P7–P11 mice (n = 180 units from 13 mice).

(I) Power of single-unit autocorrelations during ramp light stimulation at 473 nm and 594 nm averaged for P7–P11 mice (n = 180 units from 13 mice).

In (D) and (I), data are presented as mean ± SEM. In (H), data are presented as median with 25th and 75th percentiles; the shaded area represents the probability distribution of the variable. Asterisks (*$p < 0.05$, **$p < 0.01$, ***$p < 0.001$) indicate significant differences. See also Figure S1 and Table S1 for detailed statistics.

and ES mice. The density of Ca^{2+}/calmodulin-dependent protein kinase II (CaMKII)-positive neurons and ChR2(ET/TC)-transfected neurons in the prelimbic subdivision of the mPFC did not differ between control and ES mice at any of the investigated developmental time points (P11–P12, P23–P25, and P38–P40) (Figure S3). Investigation of the dendritic morphology of L2/3 PYRs after transient stimulation at P7–P11 revealed that, immediately after this time window, the dendritic arborization of these neurons was increased in ES compared with control mice (Figures 3A–3C). However, the exuberant arborization was transient, and from P23–P25 onward, the dendritic arbors of L2/3 PYRs in the mPFC of ES mice were similar to controls. A comparison across age revealed that the dendritic length increased with age for control (linear mixed effect model [LMEM]; P11–P12 to P23–P25, **$p = 0.002$; P11–P12 to P38–P40, ***$p = 0.0002$), but not for ES mice (LMEM; P11–P12 to P23–P25, $p = 0.79$; P11–P12 to P38–P40, $p = 0.07$).The dendritic length of L2/3 PYRs in ES mice at P11–P12 was comparable with that in control mice at P23–P25 (LMEM, $p = 0.33$). In-depth analysis of dendritic spines showed that the spine density was larger in P11–P12 ES mice (Figures 3D and 3E). These results suggest that increased activity in the neonatal mPFC relates to premature dendritic maturation of L2/3 PYRs.

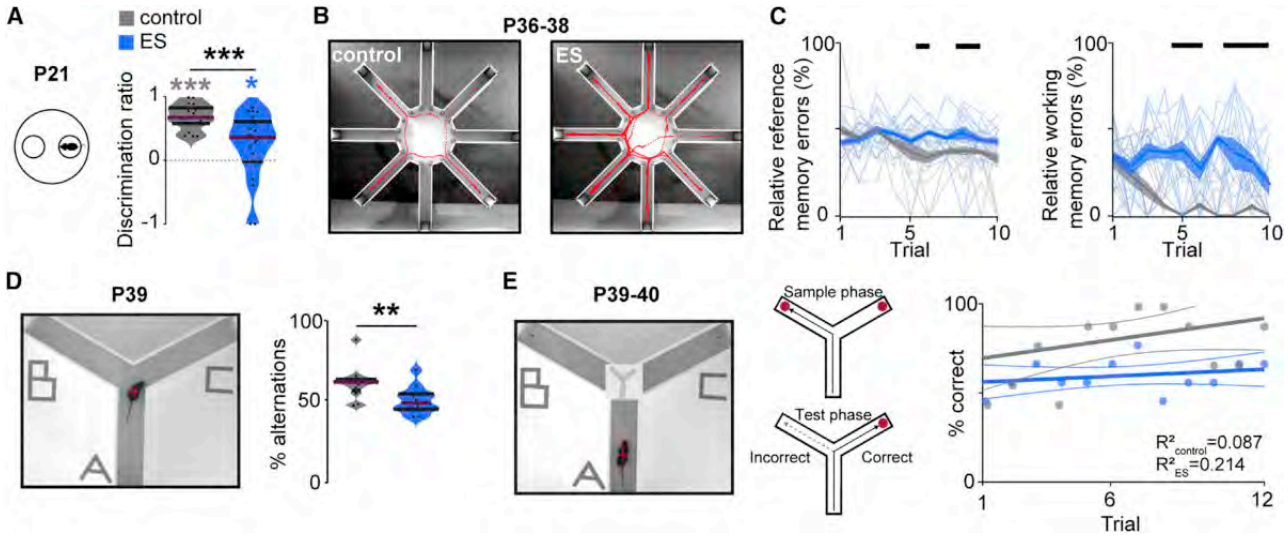

Figure 2. Transient ES impairs the cognitive abilities of juvenile and young adult mice

(A) Schematic of the maternal interaction task and violin plot displaying the discrimination ratio of interaction time with the mother versus empty bin for control (n = 19) and ES (n = 21) mice at P21 (Wilcoxon rank; control, $p < 0.001$; ES, $p = 0.045$; control ES, $p < 0.001$).

(B) Representative tracking of a control (left) and an ES mouse (right) in an 8-arm radial maze memory task with 4 baited arms at P36–P38.

(C) Plots displaying the relative reference (left) and working-memory errors (right) in the 8-arm radial maze memory task over 10 trials on 3 consecutive days for control (n = 12) and ES (n = 12) mice. (Kruskal-Wallis; relative reference memory errors, $p < 0.001$; relative working memory errors, $p < 0.001$).

(D) Photograph illustrating a spontaneous alternation task in a Y maze (left) and violin plot displaying the percentage of spontaneous alternations (right) for control (n = 12) and ES (n = 12) mice at P39. (Wilcoxon rank, $p = 0.006$).

(E) Photograph illustrating a delayed non-match-to-sample task in a Y maze (left) and dot plot displaying the percentage of correct choices over 12 consecutive trials (6 trials/day) (right) for control (n = 12) and ES (n = 12) mice at P39–P40.

In (A) and (D), data are presented as median with 25th and 75th percentiles; the shaded area represents the probability distribution of the variable. In (C), data are presented as median ± median absolute deviation (MAD). Black lines and asterisks (*$p < 0.05$, **$p < 0.01$, ***$p < 0.001$) indicate significant differences. See also Figure S2 and Tables S1 and S2 for detailed statistics.

A transient increase in neonatal prefrontal activity reduces gamma power and network synchrony in the adult mPFC

Transient alteration of neonatal activity might perturb the function of prefrontal circuits, ultimately leading to abnormal behavior. To test this hypothesis, we monitored spontaneous neuronal and network activity of the mPFC across development. We performed extracellular recordings from head-fixed control and ES mice immediately after transient ES (P11–P12) as well as at juvenile (P23–P26) and young adult (P38–P40) age (Figures 4A and 4B). With increasing age, spontaneous oscillatory activity in the mPFC of control and ES mice increased in power, and fast oscillations within 12–100 Hz became more prominent and faster (Figure 4C), consistent with the recently described acceleration of gamma activity during mPFC development (Bitzenhofer et al., 2020). At P11–P12, the power of these fast oscillations was higher in the mPFC of ES mice compared with control mice, potentially because of premature growth of L2/3 PYRs dendrites. At later stages of development, no differences were detected between control and ES mice. In contrast, the firing rates of single units were similar in control and ES mice during development, but, in adulthood, ES mice showed decreased firing in the mPFC (Figure 4D). Even though spontaneous (i.e., task/input-unrelated) activity is largely unaffected by the transient increase in activity at neonatal age, the mPFC might be engaged in tasks abnormally, reflecting disrupted processing and, ultimately, behavior. To test this hypothesis, we recorded prefrontal activity of control and ES mice during a social preference task when they could navigate freely in a mobile home cage at P38–P40 (Figure 4E). In contrast to controls, ES mice did not prefer interacting with another mouse over an object (Figures 4F and 4G). Although fast oscillations in the mPFC were similar for control and ES mice during periods of no interaction, gamma power quantified in the range of 40–80 Hz was reduced significantly for ES mice during interaction with another mouse (Figure 4H).

To corroborate the hypothesis that task/input-related mPFC activity is disturbed after transient ES, we used two additional approaches. The first approach relies on optogenetics to acutely stimulate ChR2(ET/TC)-transfected L2/3 PYRs in control and ES mice. Acute light stimulation (ramp, 473 nm, 3 s) triggered fast rhythmic activity with peak frequencies increasing from 15–20 Hz (beta frequency range) at P11–P12 to 50–60 Hz (gamma frequency range) at P23–P26 and P38–P40 in the mPFC of control and ES mice (Figure 5A), in line with the recently described acceleration of fast frequency oscillations during prefrontal development (Bitzenhofer et al., 2020). However, at P38–P40, the magnitude of light-induced gamma activity was significantly smaller in ES mice compared with controls.

The weaker prefrontal activation of fast oscillatory rhythms upon acute stimulation observed in young adult ES mice was replicated in a separate cohort of anesthetized head-fixed mice stimulated similarly from P7 to 11 (Figures S4A–S4C).

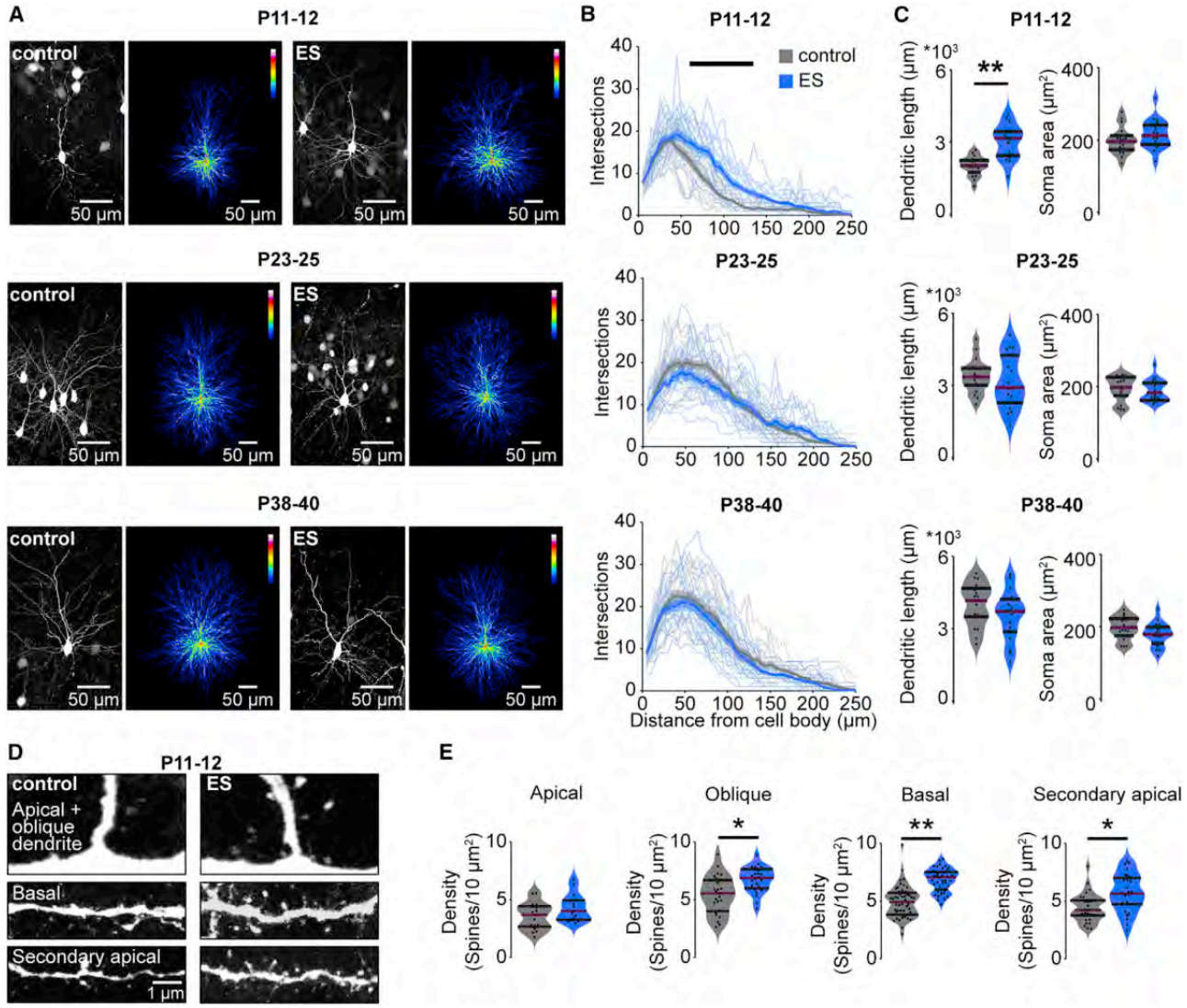

Figure 3. Transient ES induces premature dendritic growth in prefrontal L2/3 PYRs

(A) Representative photographs and corresponding average heatmaps of ChR2(ET/TC)-transfected L2/3 PYRs in the mPFC of P11–P12, P23–P25 and P38–P40 control (left) and ES mice (right).

(B) Line plots of dendritic intersections of L2/3 PYRs with concentric circles (0- to 250-µm radius) centered around the soma, averaged for control (18 cells of 3 mice/age group) and ES mice (18 cells of 3 mice/age group) at P11–P12, P23–P25, and P38–P40 (LMEM; P11–P12, $p < 0.001$; P23–P25, $p < 0.001$; P38–P40, $p < 0.001$).

(C) Violin plots displaying the dendritic length and soma area of L2/3 PYRs for control (18 cells from 3 mice/age group) and ES (18 cells from 3 mice/age group) mice for different age groups (LMEM; dendritic length: P11–P12, $p = 0.007$; P23–P25 $p = 0.631$; P38–P40, $p = 0.161$).

(D) Representative photographs of dendritic segments of ChR2(ET/TC)-transfected L2/3 PYRs in the mPFC of P11–P12 mice.

(E) Violin plots of dendritic spine density for control (124 dendrites, 17 cells, 3 mice) and ES mice (110 dendrites, 15 cells, 3 mice) at P11–P12 (LMEM; apical, $p = 0.106$; oblique, $p = 0.013$; basal, $p = 0.001$; secondary apical, $p = 0.016$).

In (B), data are presented as mean ± SEM. In (C) and (E), data are presented as median with 25th and 75th percentiles; the shaded area represents the probability distribution of the variable. Black lines and asterisks (*$p < 0.05$, **$p < 0.01$, ***$p < 0.001$) indicate significant differences. See Table S1 for detailed statistics. Black lines and asterisks (*$p < 0.05$, **$p < 0.01$, ***$p < 0.001$) indicate significant differences. See also Figure S3 and Table S1 for detailed statistics.

Furthermore, young adult ES mice had weaker synchrony within and between hemispheres during evoked activity. Coherence between L2/3 and L5/6 of the stimulated hemisphere and coherence between L2/3 across hemispheres was reduced in ES mice at P38–P40 but was normal at a younger age (Figures S4D and S4E).

We analyzed single-unit firing to assess the response of prefrontal neurons to acute light stimulation in control and ES mice across development. Calculation of autocorrelation for prefrontal units showed that, independent of age and group, neurons fire rhythmically in response to acute light stimulation (Figure 5B). Similar to network oscillations, the strength and frequency of the

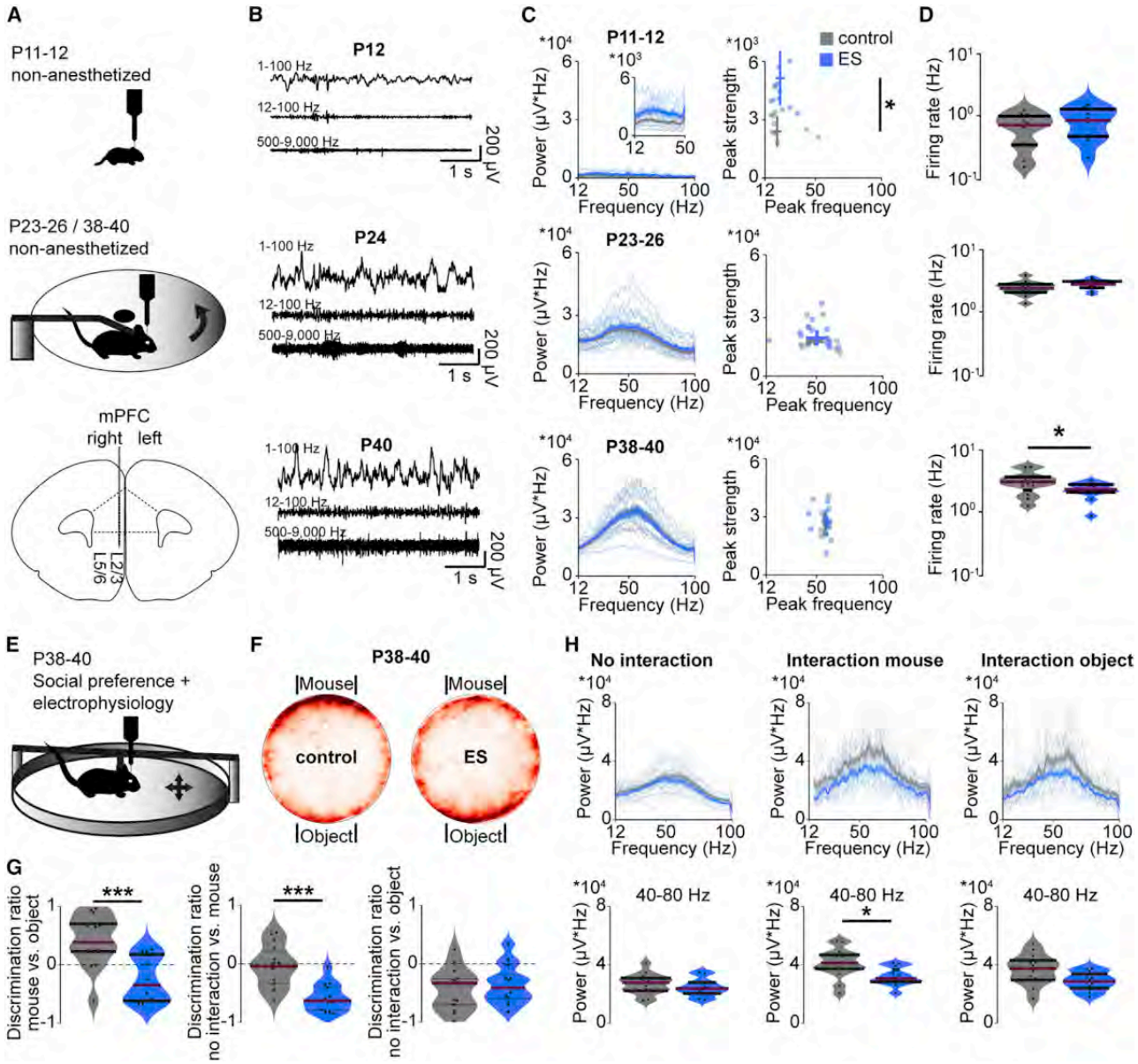

Figure 4. Transient ES has minor effects on spontaneous network activity but impairs task-related gamma oscillations in the mPFC

(A) Top: schematic illustrating the recording setups used for young mice with limited motor abilities (head fixed, no movement) and for juvenile and young adult mice (head fixed, moving freely on a spinning disk). Bottom: schematic of the recording configuration in the developing mPFC.

(B) Representative extracellular recordings in the mPFC at P12, P24, and P40.

(C) Left: average power spectra of spontaneous network activity in the mPFC of control and ES mice at P11–P12 (control, n = 11 recordings, 11 mice; ES, n = 10 recordings, 10 mice; inset at a different scale), P23–P26 (control, n = 13 recordings, 6 mice; ES, n = 14 recordings, 5 mice), and P38–P40 (control, n = 12 recordings, 5 mice; ES, n = 12 recordings, 5 mice). Right: scatterplots displaying peak strength and peak frequency of LFP power for control and ES mice (Wilcoxon rank, P11–P12, peak frequency p = 0.245, peak strength p = 0.015, LMEM, P23–P26, peak frequency p = 0.643, peak strength p = 0.665, P38–P40, peak frequency p = 0.856, peak strength p = 0.750).

(D) Violin plots displaying the firing rates of single units in the mPFC, averaged for control and ES mice at P11–P12, P23–P26, and P38–P40. (Wilcoxon rank, P11–P12 p = 0.275, LMEM, P23–P25 p = 0.072, P38–P40 p = 0.041).

(E) Schematic illustrating the setup used for *in vivo* extracellular recordings in P38–P40 mice during a social preference task in a mobile home cage.

(F) Heatmaps showing the preferred position of control (15 trials of 8 mice) and ES mice (13 trials of 7 mice) during a social preference task in a mobile home cage (15-min duration).

(G) Violin plots displaying the discrimination ratio of mouse versus object (LMEM, $p < 0.001$), no interaction versus mouse (LMEM, $p < 0.001$), and no interaction versus object (LMEM, p = 0.492) for control (15 trials of 8 mice) and ES mice (13 trials of 7 mice).

(H) Average power spectra of network activity in the mPFC (top) and power in the gamma frequency (bottom, 40–80 Hz) of control (14 recordings from 8 mice) and ES (12 recordings from 7 mice) mice at P38–P40 in the mobile home cage during no interaction (LMEM, p = 0.353), interaction with another mouse (LMEM, p = 0.019) and interaction with an object (LMEM, p = 0.052).

(legend continued on next page)

rhythmicity of neuronal firing increased with age, but the magnitude of the increase was lower for ES mice, reaching significance at P38–P40 (Figure 5C). To assess the effect of ES on synchrony within the prefrontal network during development, we calculated pairwise correlations of single units. During ramp light stimulation, pairwise correlations were reduced significantly at the third quartile in young adult ES mice compared with controls but comparable between groups at P11–P12 and P23–P26 (Figure S5). These data show that the synchrony of the highest correlated units in the mPFC is reduced in young adult ES mice.

The second approach relies on mPFC activation through stimulation of one of its major excitatory drives, the intermediate and ventral HP (Ahlbeck et al., 2018). Mice manipulated by transient ES of prefrontal L2/3 PYRs from P7–P11 were injected with a virus encoding for ChR2(H134R) in the intermediate HP at P22 (Figures 5D and 5E). Hippocampal activity was similar in control and ES mice at P38–P40. Acute light stimulation (473 nm, 3 s) of the intermediate HP at P38–P40 induced oscillatory activity in the HP that boosted gamma activity in the mPFC of control but not ES mice (Figures 5F–5H). Thus, the mPFC of ES mice lacks the ability to synchronize its activity in gamma frequency in response to incoming inputs, such as from the HP.

These data show that a normal level of coordinated activity during early development is critical for normal behavior and mPFC function at adulthood, but the specificity of the chosen age window (P7–P11) for stimulation remains to be tested. To address this question, we performed transient ES of L2/3 PYRs at a later developmental stage: P12–P16 (oES). Similar to stimulation from P7–P11, transcranial stimulation at P12–P16 induced fast rhythmic activity at about 20 Hz, detectable in the local field potential power and in the autocorrelation power of single units (Figures 6A–6C and S6). Of note, early transient stimulation induced activation (21.4%) as well as inactivation (19.3%) of single units (Figure S6C), reflecting maturation of the inhibitory network. As reported for stimulation at P7–P11, oES did not affect task non-related spontaneous activity in the mPFC at P38–P40 (Figure 6D). Differences between the output of ES at P7–P11 versus P12–P16 were detected when analyzing adult mPFC activation upon light stimulation. In contrast to transient ES at P7–P11, oES only mildly affected the peak frequency, but not the peak strength, of light-induced fast oscillatory activity or multi-unit activity (MUA) at P38–P40 (Figures 6E and 6F). Thus, we suggest that the outcome of manipulation of early activity depends on the time window of manipulation and propose that time windows of particular sensitivity, such as P7–P11, are present during mPFC development.

These results show that transiently increased activity during a defined time window at neonatal age diminishes task/input-related gamma band synchronization in the adult mPFC.

A transient increase in neonatal activity alters the excitation/inhibition balance in the adult mPFC

Network synchronization in the gamma frequency results from interactions between excitatory and inhibitory units (Atallah and Scanziani, 2009; Chen et al., 2017). To elucidate the mechanisms of abnormal network synchronization upon stimulation in ES mice, we analyzed the response of individual units in L2/3 of the mPFC to acute ramp light stimulation. At P11–P12, 25.3% of units in control mice and 20.3% of units in ES mice significantly increased their firing rate during ramp light stimulation. Only few units (control, 0.9%; ES, 3.4%) decreased their firing rates. In older mice, units with significantly increased (P23–P26: control 31.2%, ES 32.7%; P38–P40: control 33.7%, ES 25.5%) and decreased (P23–P26: control 27.0%, ES 23.6%; P38–P40: control 24.5%, ES 30.6%) firing rates were detected (Figures 7A and 7B). The ratio of activated versus inactivated neurons per mouse was similar across groups at P11–P12 and P23–P26 but reduced significantly in ES mice at P38–P40 compared with controls.

Decreased gamma synchrony and reduced activation versus inactivation in P38–P40 ES mice suggest that the transient increase in prefrontal activity at neonatal age causes long-term alterations of the balance between excitation and inhibition in the prefrontal circuitry. To test this hypothesis, we performed whole-cell patch-clamp recordings from non-transfected prefrontal L2/3 PYRs in coronal slices from control and ES mice (Figure 7C). During acute light stimulation of ChR2(ET/TC)-transfected L2/3 PYRs (473 nm, square pulse, 1 s), the ratio of excitatory postsynaptic currents (EPSCs) to inhibitory postsynaptic currents (IPSCs) in non-transfected L2/3 PYRs was shifted toward inhibition for P37–P40 ES mice compared with controls (Figure 7D). In contrast, the ratio was similar between groups at P23–P26. Basic active and passive membrane properties as well as spontaneous inputs were not affected in ES mice (Figure S7).

Stronger inhibition might result from altered interneuron functionality after a transient activity increase during neonatal age (Wong et al., 2018). To test this hypothesis, we performed immunohistochemical staining for parvalbumin (PV) and somatostatin (SOM) and quantified the distribution of these two distinct subsets of inhibitory interneurons in the mPFC of control and ES mice during development (Figure 8A). The density of SOM-positive neurons was reduced slightly in ES mice at P11–P12 and P38–P40, whereas the density of PV-positive neurons was increased significantly at P38–P40 (Figure 8B). This increase could also reflect an activity-dependent upregulation of PV expression (Caballero et al., 2020). In-depth morphological analysis showed increased dendritic arborization of PV-positive neurons in the L2/3 of the mPFC of P38–P40 ES mice (Figures 8C–8E). Thus, transient ES alters the maturation of PV interneurons.

Fast-spiking (FS) PV-expressing interneurons that mature toward the end of the developmental period are critical for generation of adult cortical gamma activity (Cardin et al., 2009; Chen et al., 2017; Gour et al., 2021). Therefore, the late-emerging decrease in gamma synchrony in adult ES mice may result from altered maturation of these neurons. To test this hypothesis, we distinguished regular-spiking (RS) and FS units in extracellular recordings from control and ES mice based on their spike

In (C) and (H) data are presented as mean ± SEM. In (D), (G), and (H), data are presented as median with 25th and 75th percentiles; the shaded area represents the probability distribution of the variable. Asterisks (*p < 0.05, **p < 0.01, ***p < 0.001) indicate significant differences. See Table S1 for detailed statistics.

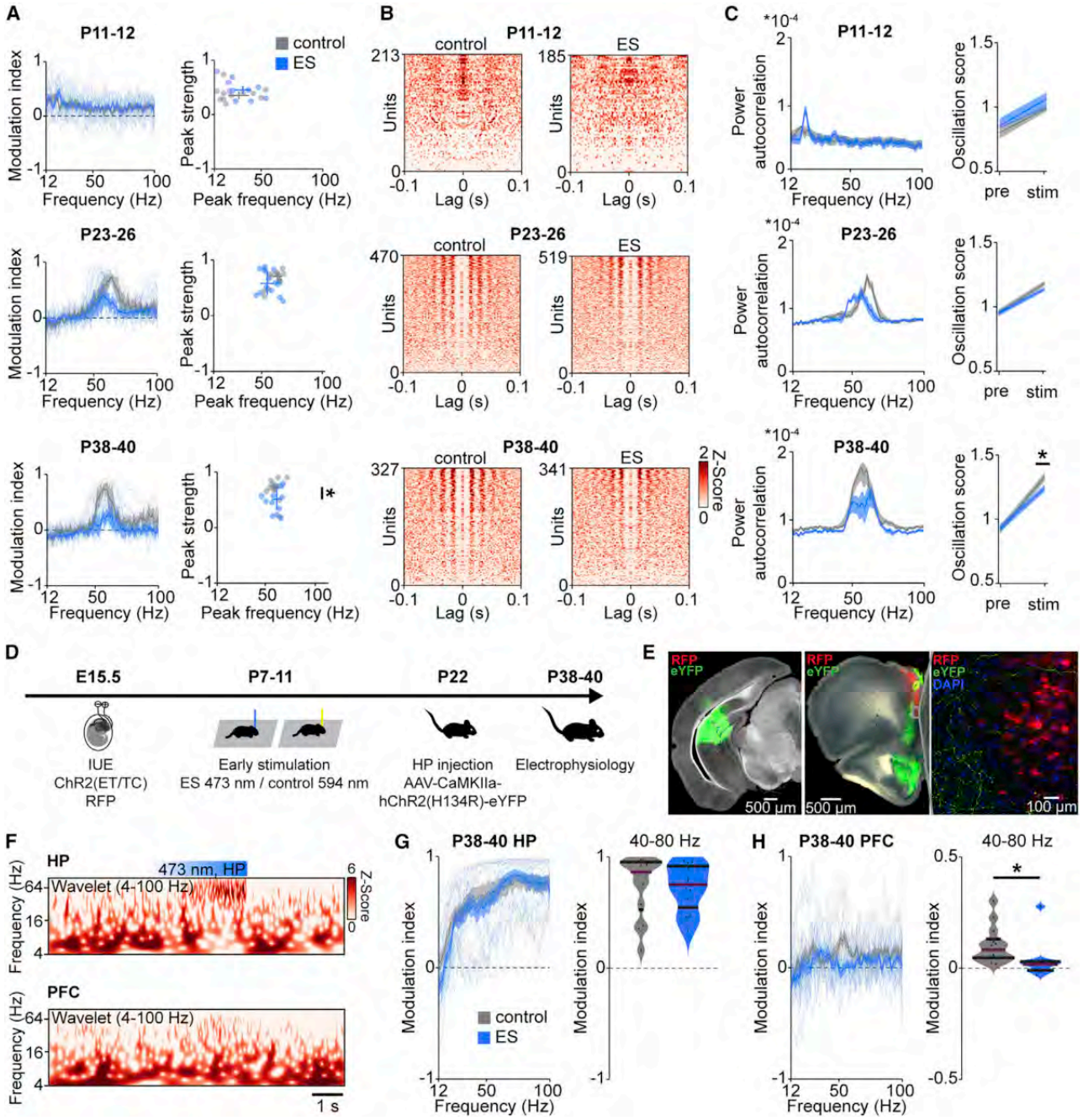

Figure 5. Transient ES decreases evoked network and neuronal gamma rhythmicity in the adult mPFC

(A) Left: modulation index of LFP power in response to acute ramp light stimulation (473 nm, 3 s) for control and ES mice at P11–P12 (control, n = 11 recordings, 11 mice; ES, n = 10 recordings, 10 mice), P23–P26 (control, n = 13 recordings, 6 mice; ES n = 14 recordings, 15 mice) and P38–P40 (control, n = 12 recordings, 5 mice; ES, n = 12 recordings, 5 mice). Right: scatterplots displaying the peak strength and peak frequency of the power modulation index for control and ES mice (Wilcoxon rank, P11–P12, peak frequency p = 0.307, peak strength p = 0.307, LMEM, P23–P26, peak frequency p = 0.136, peak strength p = 0.419, P38–P40, peak frequency p = 0.913, peak strength p = 0.043).

(B) *Z*-scored autocorrelograms of single units during acute ramp light stimulation, arranged by magnitude for control and ES mice at P11–P12 (control, n = 213 units, 11 mice; ES, n = 185 units, 10 mice), P23–P26 (control, n = 470 units, 6 mice; ES, n = 519 units, 5 mice), and P38–P40 (control, n = 327 units, 5 mice; ES, n = 341 units, 5 mice).

(C) Left: average power of single-unit autocorrelograms during acute ramp light stimulation for control and ES mice at different ages. Right: oscillation score of single units before (pre) and during (stim) acute ramp light stimulation (LMEM, oscillation score, P11–P12, pre p = 0.406, stim p = 0.156, P23–P26, pre p = 0.272, stim p = 0.478, P38–P40, pre p = 0.428, stim p = 0.030).

(D) Schematic of the protocol for early light stimulation and hippocampal ChR2 transfection.

(legend continued on next page)

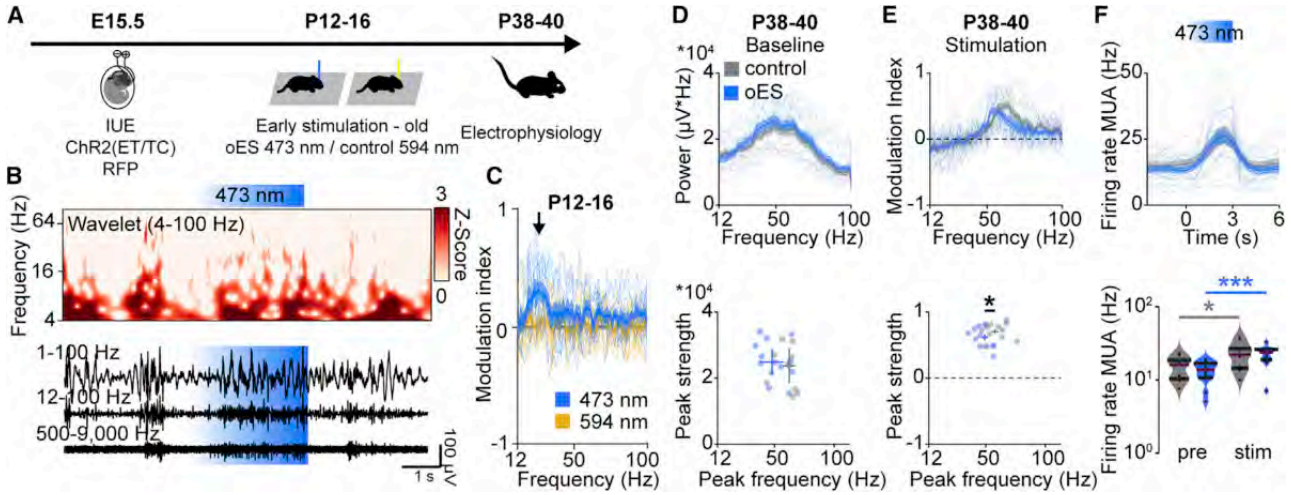

Figure 6. Transient ES at P12–P16 weakly affects activity in the adult mPFC

(A) Schematic of the protocol for early light stimulation at P12–P16.

(B) Representative extracellular recording with the corresponding wavelet spectrum at an identical timescale during transcranial ramp light stimulation (473 nm, 3 s) of L2/3 PYRs in the mPFC of a P16 mouse.

(C) Modulation index of LFP power in response to ramp light stimulation at 473 nm (blue) and 594 nm (yellow), averaged for P12–P16 mice (n = 8 mice).

(D) Top: average power spectra of spontaneous network activity in the mPFC of control and oES mice at P38–P40 (control, n = 11 recordings, 5 mice; oES n = 12 recordings, 6 mice). Bottom, scatterplot displaying peak strength and peak frequency of LFP power for control and oES mice. (LMEM, peak frequency p = 0.073, peak strength p = 0.250).

(E) Top: modulation index of LFP power in response to acute ramp light stimulation (473 nm, 3 s) for control and oES mice at P38–P40 (control, n = 11 recordings, 5 mice; oES, n = 12 recordings, 6 mice). Bottom: scatterplots displaying the peak strength and peak frequency of the power modulation index for control and oES mice (LMEM; peak frequency, p = 0.025; peak strength, p = 0.217).

(F) Top: MUA in response to acute ramp light stimulation (473 nm, 3 s) for control and oES mice at P38–P40 (control, n = 11 recordings, 5 mice; oES, n = 12 recordings, 6 mice). Bottom: MUA firing rate before (pre) and during (stim) acute ramp light stimulation for control and oES mice (LMEM; control pre versus stim, p = 0.018; control pre versus stim, p < 0.001; pre control versus oES, p = 0.364; stim control versus oES, p = 0.922).

In (C)–(F), top, data are presented as mean ± SEM. In (F), bottom, data are presented as median with 25th and 75th percentiles; the shaded area represents the probability distribution of the variable. Asterisks (*p < 0.05, **p < 0.01, ***p < 0.001) indicate significant differences. See also Figure S6 and Table S1 for detailed statistics.

waveform (Figures 8F and S8A). Moreover, we photo-tagged PV-expressing interneurons in the mPFC of PV-cre mice after viral transfection with cre-dependent ChR2(ET/TC) to confirm that FS units at P23–P26 and P38–P40 correspond to PV interneurons. We found that 84.9% of photo-tagged PV neurons fit our criteria for FS units (Figure S8E). The spontaneous firing rate of RS units is altered in ES mice at P23–P26 and P38–P40 compared with controls, whereas no changes were detected for FS units (Figures 8F and S8B). In contrast, evoked activity during acute ramp light stimulation was reduced for RS and FS units in ES mice at P38–P40 but normal earlier during development (Figures 8G and S8C). Reduced evoked activity of FS units seems to be in opposition with the increased numbers of PV-positive neurons in adult ES mice. However, the FS firing rate is mainly reduced during the late phase of the ramp, whereas the initial peak is not altered. Taking into account that PV neurons inhibit PYRs but also other PV neurons (Pfeffer et al., 2013), we hypothesized that FS putative PV neurons might provide more potent inhibition and thereby reduce RS and FS firing rates after initial activation in ES mice.

(E) Representative image showing ChR2(ET/TC)-2A-RFP expression in L2/3 PYRs after IUE at E15.5 and ChR2(H134R)-eYFP expression after hippocampal injection at P22 in a DAPI-stained coronal slice, including the mPFC from a P40 mouse. Note the hippocampal axons in the mPFC, visible at high exposure and magnification. eYFP, enhanced yellow fluorescent protein.

(F) Representative wavelet spectra of extracellular recordings in the HP and mPFC at identical timescales during ramp light stimulation (473 nm, 3 s) in the HP of a P39 mouse.

(G) Left: modulation index of hippocampal LFP power in response to hippocampal ramp light stimulation at 473 nm (blue), averaged for P38–P40 control (13 recordings from 6 mice) and ES mice (n = 12 recordings from 5 mice). Right: average modulation index of hippocampal LFP power in the gamma frequency (40–80 Hz) upon hippocampal ramp stimulation at P38–P40 (LMEM, p = 0.846).

(H) Left: modulation index of prefrontal LFP power in response to hippocampal ramp light stimulation at 473 nm (blue), averaged for P38–P40 control (13 recordings from 6 mice) and ES mice (n = 12 recordings from 5 mice). Right: average modulation index of prefontal LFP power in the gamma frequency (40–80 Hz) upon hippocampal ramp stimulation at P38–P40 (LMEM, p = 0.0328).

In (A); (C); (G), left; and (H), left, data are presented as mean ± SEM. In (G), right, and (H), right, data are presented as median with 25th and 75th percentiles; the shaded area represents the probability distribution of the variable. Asterisks (*p < 0.05, **p < 0.01, ***p < 0.001) indicate significant differences. See also Figures S4 and S5 and Table S1 for detailed statistics.

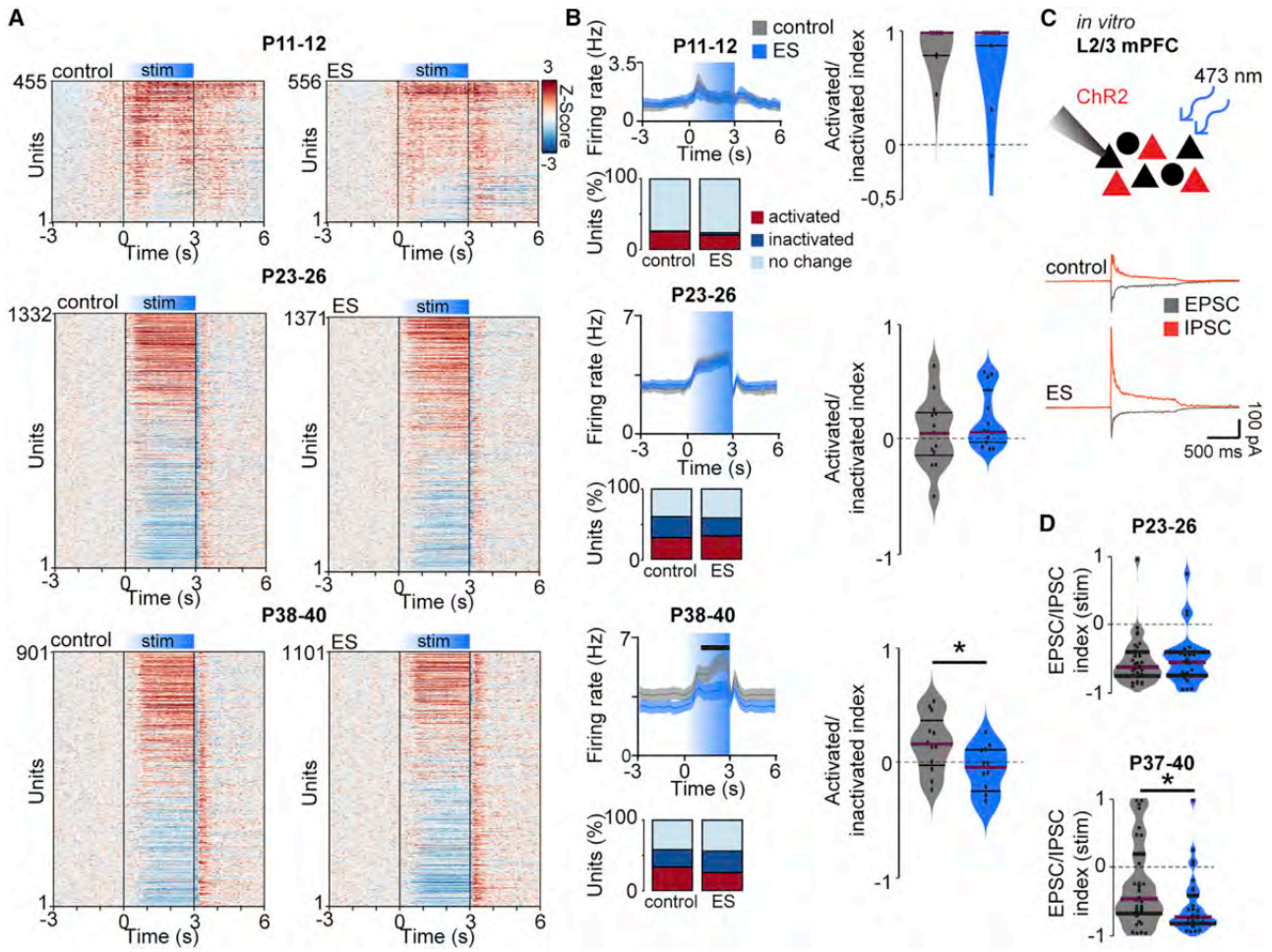

Figure 7. Transient ES alters the excitation/inhibition balance in the adult mPFC during acute light stimulation

(A) Single unit firing rates *Z* scored to pre-stimulation in response to acute ramp light stimulation (473 nm, 3 s) displayed for control (left) and ES mice (right) at P11–P12 (control, n = 455 units, 11 mice; ES, n = 556 units, 10 mice), P23–P26 (control, n = 1,332 units, 6 mice; ES, n = 1,371 units, 5 mice), and P38–P40 (control, n = 901 units, 5 mice; ES, n = 1,101 units, 5 mice).

(B) Line plots displaying average firing rates during acute light stimulation (top left), bar diagrams of the percentage of significantly activated and inactivated units ($p < 0.01$, bottom left), and violin plots showing the index of significantly activated versus inactivated units (right) for control and ES mice at P11–P12, P23–P26, and P38–P40 (P11–P12, LMEM, firing rate $p < 0.001$, Wilcoxon rank, activated/inactivated index $p = 0.982$, LMEM, P23–26, firing rate $p = 0.004$, activated/inactivated index $p = 0.317$, P38–P40, firing rate $p < 0.001$, activated/inactivated index $p = 0.033$).

(C) Schematic showing the protocol for *in vitro* whole-cell patch-clamp recordings from non-transfected L2/3 PYRs (black) during optogenetic stimulation of neighboring transfected cells (red) in the mPFC and representative examples.

(D) Violin plots displaying the EPSC/IPSC index during acute light stimulation (473 nm, square pulse, 1 s) for control and ES mice at P23–P26 (control, n = 35 neurons, 5 mice; ES, n = 30 neurons, 5 mice) and P37–P40 (control, n = 41 neurons, 6 mice; ES, n = 33 neurons, 4 mice) (LMEM; P23–P26, $p = 0.840$; P37–P40, $p = 0.030$).

In (B), left, data are presented as mean ± SEM. In (B), right, and (D), data are presented as median with 25th and 75th percentiles; the shaded area represents the probability distribution of the variable. Black lines and asterisks (*$p < 0.05$, **$p < 0.01$, ***$p < 0.001$) indicate significant differences. See also Figure S7 and Table S1 for detailed statistics.

Gamma synchronization in the adult cortex results from a temporally coordinated excitatory drive and inhibitory feedback (Atallah and Scanziani, 2009; Cardin et al., 2009). To investigate the timing of RS and FS firing, we performed acute stimulation with short light pulses of 3-ms duration. RS and FS units showed a pronounced peak in their firing rate for 5–10 ms in response to short light pulses (Figures 8H and S8D). The similar peak latency of RS and FS units indicates that the RS clusters contain a substantial number of non-transfected, indirectly activated units, in agreement with the sparse transfection achieved with IUE. FS units in control mice showed a second peak in their firing rate about 20 ms after the light pulse in P23–P26 and P37–P40 mice. The delay of 20 ms suggests a contribution of these units to gamma oscillations, which have a typical cycle duration of 20 ms at 50 Hz. This second peak was reduced significantly in ES mice at P23–P26 and P38–P40. Of note, similar to ramp-induced activity, the first peak was not affected in FS units, suggesting that FS units provide stronger inhibition after initial activation in ES mice.

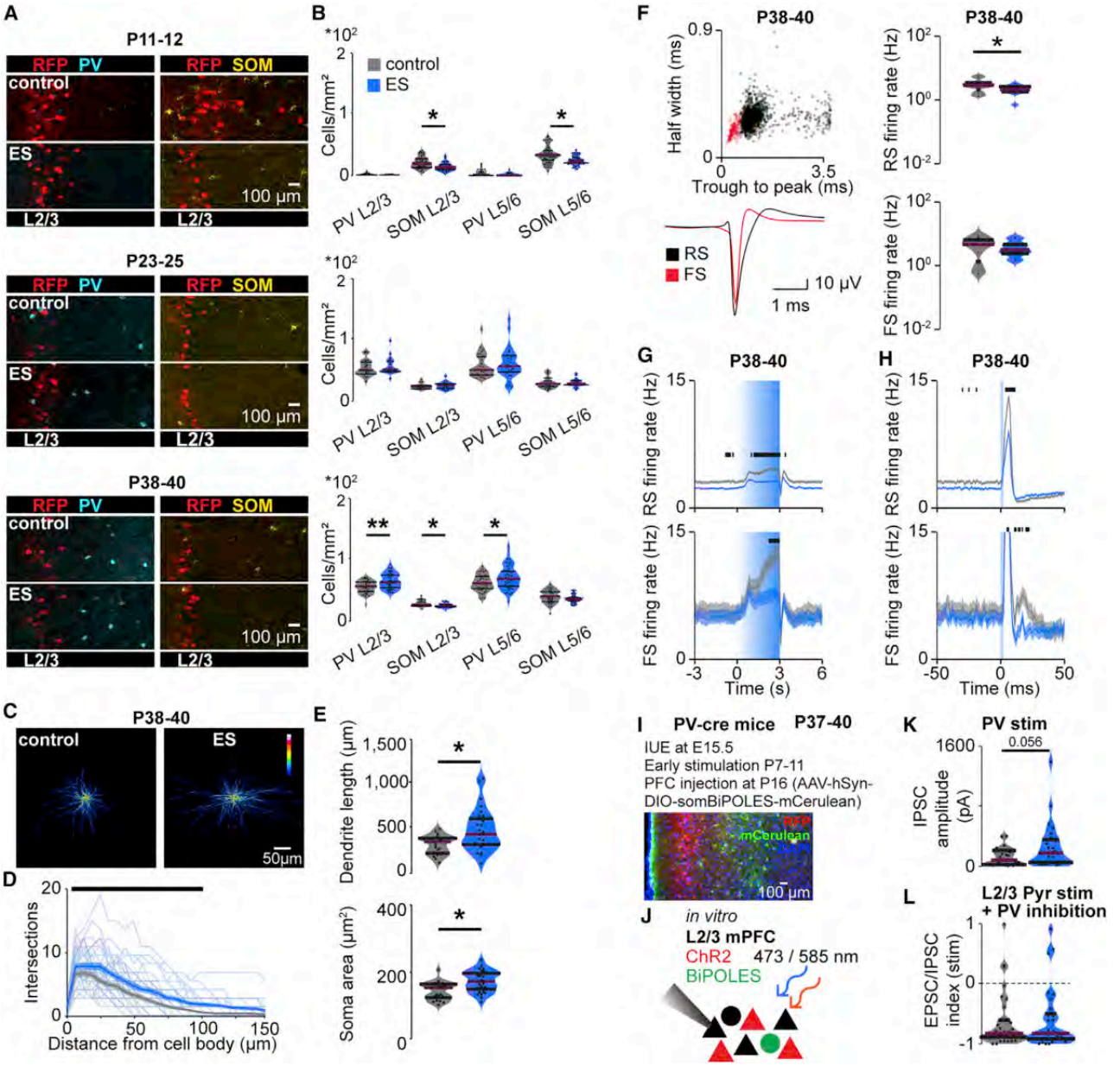

Figure 8. Transient ES alters inhibitory feedback from FS units in the mPFC

(A) Representative images showing PV and SOM immunostaining in the mPFC of control and ES mice at P11–P12, P23–P25, and P38–P40.

(B) Violin plots displaying the density of PV-positive and SOM-positive neurons in L2/3 and L5/6 of the mPFC of control and ES mice at P11–P12 (control: PV n = 54 slices, 12 mice; SOM n = 59 slices, 12 mice; ES: PV n = 38 slices, 9 mice; SOM n = 43 slices, 9 mice), P23–P25 (control: PV n = 25 slices, 5 mice; SOM n = 25 slices, 5 mice; ES: PV n = 27 slices, 6 mice; SOM n = 25 slices, 6 mice), and P38–P40 (control: PV n = 36 slices, 9 mice; SOM n = 36 slices, 9 mice; ES: PV n = 40 slices, 10 mice; SOM n = 43 slices, 11 mice) (LMEM, L2/3, P11–P12, PV p = 0.296, SOM p = 0.044, P23–P25, PV p = 0.403, SOM p = 0.390, P38–P40, PV p = 0.012, SOM p = 0.012).

(C) Average heatmaps of PV interneurons in the mPFC of P38–P40 control (left) and ES mice (right).

(D) Line plots of dendritic intersections of PV interneurons with concentric circles (0–150 µm radius) centered around the soma averaged for control (23 cells of 3 mice) and ES mice (28 cells of 3 mice) at P38–P40 (LMEM $p < 0.001$).

(E) Violin plots displaying the dendritic length and soma area of PV interneurons for control (23 cells of 3 mice) and ES mice (28 cells of 3 mice) at P38–P40 (LMEM; dendritic length, p = 0.016).

(F) Scatterplots displaying half-width and trough-to-peak duration (top left) and average waveforms for RS and FS units (bottom) as well as violin plots displaying average firing rates (right) for control and ES mice at P38–P40 (control, 814 RS and 84 FS units, 5 mice; ES, 992 RS and 104 FS units, 5 mice) (Wilcoxon rank, P38–P40, RS firing rate p = 0.040, FS firing rate p = 0.575).

(legend continued on next page)

To test this hypothesis, we performed transient ES of prefrontal L2/3 PYRs from P7–P11 in PV-cre mice, followed by viral transfection with a cre-dependent, bidirectional, dual-color optogenetic tool, BiPOLES (bidirectional pair of opsins for light-induced excitation and silencing) (Vierock et al., 2020), into the mPFC at P16 (Figure 8I). Red light (585 nm) activated PV neurons, whereas blue light (473 nm) activated L2/3 PYRs and inactivated PV neurons in the same mouse (Figure 8J). We performed whole-cell patch-clamp recordings from non-transfected prefrontal L2/3 PYRs in coronal slices, including the mPFC, of control and ES mice at P37–P40. Brief stimulation of PV interneurons (10-ms pulses, 585 nm) induced IPSCs in the recorded L2/3 PYRs of control and ES mice. The IPSCs had a slightly larger but not significant ($p = 0.056$) amplitude in ES mice, suggesting increased inhibition in ES compared with control mice (Figure 8K). Simultaneous activation of L2/3 PYRs and inhibition of PV neurons (1 s, 473 nm) removed the EPSC/IPSC imbalance in ES mice (compare Figure 8L with Figure 7D).

Thus, transiently increased activity at neonatal age alters the development of inhibitory feedback from FS interneurons and reduces evoked gamma synchronization of adult prefrontal circuits.

DISCUSSION

Seminal research identified electrical activity as a major contributor to development of the mammalian cerebral cortex. Early activity influences neuronal migration, differentiation, and apoptosis (Blanquie et al., 2017; Katz and Shatz, 1996; Kirkby et al., 2013) as well as establishment of synaptic connections (Clause et al., 2014; Huberman et al., 2006). In clinical settings, patterns of electroencephalographic activity of preterm infants provide prognostic value for neurodevelopmental outcome (Iyer et al., 2015). Several neuropsychiatric diseases have been proposed to be related to alterations in neuronal activity early in life (Marín, 2016; Robertson and Baron-Cohen, 2017). However, fundamental questions still need to be addressed. How does electrical activity during early development affect adult cortical function? Does altered prefrontal activity during early development contribute to cognitive deficits later in life? Here we address these questions and demonstrate that a transient increase in activity in the mouse mPFC during a short period of neonatal development critical for network formation causes long-lasting changes in inhibitory feedback and excitation/inhibition balance, leading to weaker evoked gamma band synchronization and, ultimately, poorer cognitive abilities.

To manipulate developmental activity, we optogenetically stimulated the mPFC, inducing discontinuous activity patterns with similar dynamics as ones occurring spontaneously. During early development, the mammalian cortex shows discontinuous activity, with neuronal discharges organized in oscillatory rhythms alternating with electrically silent periods (Hanganu et al., 2006; Khazipov et al., 2004). In the mPFC of neonatal mice, these 1- to 3 s-long oscillatory events with frequencies alternating between theta (4–12 Hz) and beta-low gamma (12–40 Hz) occur every 20–30 s (Bitzenhofer et al., 2015; Brockmann et al., 2011). The fast oscillations emerge as a result of L2/3 PYRs activation (Bitzenhofer et al., 2017a). Therefore, we used repeated ramp light stimulation (3 s duration, 6/min for 30 min per day) to activate L2/3 PYRs transfected with ChR2(ET/TC) by IUE and induced fast oscillatory discharges. At the age of transient ES (P7–P11), neurons have reached their final location in the cortical layers and are in the process of establishing synaptic connections (Van Eden and Uylings, 1985). Our stimulation protocol was designed to cause a modest increase in activity in the mPFC during this period critical for network formation. This type of stimulation not only augments the level of activity but coordinates the prefrontal networks in fast oscillatory rhythms evolving from beta to gamma frequencies with age (Bitzenhofer et al., 2020).

How does the transient increase in neuronal activity at neonatal age influence prefrontal development and, ultimately, behavior? The present data demonstrate that early manipulation triggers a cascade of structural and functional changes in the mPFC, leading to impairment of cognitive and social abilities. On the morphological level, increased neonatal activity induced premature growth of dendrites and spines in stimulated L2/3 PYRs. This is consistent with the activity-dependent growth of dendrites (Wayman et al., 2006) and reminiscent of the growth dynamics (i.e., initially excessive followed by arrested growth) during development in humans with autism spectrum disorders (Courchesne, 2004). Activity of PYRs from P5–P8 has been shown to regulate the survival of cortical interneurons (Denaxa et al., 2018; Wong et al., 2018). Accordingly, we found an increased number of PV-expressing interneurons in ES mice. In contrast to previous studies (Denaxa et al., 2018; Lim et al., 2018; Wong et al., 2018), this effect was specific for PV-expressing neurons, whereas the number of SOM-expressing neurons

(G) Average firing rate during acute ramp light stimulation (473 nm, 3 s) for control and ES mice at P38–P40. (LMEM, P38–P40, RS firing rate $p < 0.001$, FS firing rate $p < 0.001$).

(H) Average firing rate during acute pulse light stimulation (473 nm, 3 ms) for control and ES mice at P38–P40. (LMEM, P38–P40, RS firing rate $p < 0.001$, FS firing rate $p < 0.001$).

(I) Representative image of a P37 mouse showing L2/3 PYRs ChR2(ET/TC)-2A-RFP expression from IUE and BiPOLES-mCerulean expression in PV interneurons after viral injection at P16 into the mPFC.

(J) Schematic showing the protocol for *in vitro* whole-cell patch-clamp recordings from non-transfected L2/3 PYRs (black) during optogenetic stimulation of neighboring transfected PYRs (red) and/or PV interneurons (green) in the mPFC.

(K) Violin plot displaying IPSC amplitude in response to acute light stimulation of PV interneurons (595 nm, square pulse, 10 ms) for control and ES mice at P37–P40 (control, n = 32 neurons, 6 mice; ES, n = 31 neurons, 5 mice) (LMEM, $p = 0.056$).

(L) Violin plot displaying the EPSC/IPSC index during acute light stimulation of L2/3 PYRs and inhibition of PV interneurons (473 nm, square pulse, 1 s) for control and ES mice at P37–P40 (control, n = 35 neurons, 6 mice; ES: n = 30 neurons, 5 mice) (LMEM, $p = 0.785$).

In (B), (E), (F), (K), and (L), data are presented as median with 25^{th} and 75^{th} percentiles; the shaded area represents the probability distribution of the variable. In (D), (G), and (H), data are presented as mean ± SEM. Black lines and asterisks (*$p < 0.05$, **$p < 0.01$, ***$p < 0.001$) indicate significant differences. See also Figure S8 and Table S1 for detailed statistics.

was reduced. Several differences in experimental settings might explain this disparity. (1) Stimulation a few days later during developmental (P7–P11 versus P5–P8) is expected to have a stronger effect on late-maturing, PV-expressing interneurons (Lim et al., 2018). (2) Increased activity of a subset of PYRs (20%–30% of L2/3 PYRs versus all PYRs) might cause different activation of interneuron subtypes. (3) Optogenetic (versus chemogenetic) stimulation triggering fast oscillatory network activity might specifically engage PV-expressing interneurons.

Premature growth of dendrites and spines likely affects the connectivity of stimulated neurons. Together with altered interneuron numbers, these structural changes might have contributed to the shift in the excitation/inhibition balance in the mPFC of ES mice toward inhibition. In addition to the general increase in inhibition, the timing of FS, presumably PV-expressing interneurons was altered. In juvenile and adult control mice, brief activation of L2/3 PYRs induced a sharp peak in the firing rate of FS interneurons, followed by a second peak about 20 ms later. This second peak, supposedly critical for synchronization in the gamma frequency, was absent in ES mice. Accordingly, the transient increase of neuronal activity at neonatal age (but not later) led to impaired synchronization of the prefrontal network in the gamma frequency in young adults. This is consistent with the importance of PV-expressing FS interneurons for generation of cortical gamma activity (Atallah and Scanziani, 2009; Cardin et al., 2009). Late maturation of PV-expressing interneurons (Lim et al., 2018) and gamma activity in the mPFC (Bitzenhofer et al., 2020) most likely underlie the delayed onset of these physiological effects. These effects were only evident during evoked or task-related activity, whereas spontaneous activity in the mPFC was largely normal, reflecting the moderate effects of the stimulation protocol. This is consistent with alterations in evoked activity related to early emergence of sensory symptoms in humans with autism spectrum disorders (Robertson and Baron-Cohen, 2017).

Abnormal FS interneuron development impairs prefrontal gamma activity and cognitive flexibility in adults (Cho et al., 2015). Accordingly, a transient increase of neuronal activity at neonatal age ultimately resulted in impaired cognitive abilities in juvenile and young adult mice. Gamma activity in prefrontal L2/3 is particularly important for maintenance of information during working memory tasks (Bastos et al., 2018). This is consistent with the specific impairment of ES mice in short-term memory and working memory tasks as well as reduced social preference.

These data demonstrate that altered neuronal activity during early development induces structural and functional changes in the mPFC, ultimately resulting in impaired cognitive abilities. Even though cognitive symptoms are not the core deficits, they are a devastating burden in several neuropsychiatric diseases (Baron-Cohen, 2004; van Os and Kapur, 2009; Stuchlik and Sumiyoshi, 2014). An altered cortical excitation/inhibition balance and impaired gamma activity are critical for cognitive dysfunctions (Gallinat et al., 2004; Sohal and Rubenstein, 2019; Uhlhaas and Singer, 2010). Early prefrontal activity is reduced in mouse models of schizophrenia (Chini et al., 2020; Hartung et al., 2016a) and increased in mouse models of autism (Peixoto et al., 2016; Richter et al., 2019), but both show similar cognitive deficits, supporting the relevance of a balanced level of early activity. Thus, altered developmental activity of cortical circuits might actively contribute to cognitive symptoms in neuropsychiatric diseases (Chini and Hanganu-Opatz, 2020).

STAR★METHODS

Detailed methods are provided in the online version of this paper and include the following:

- KEY RESOURCES TABLE
- RESOURCE AVAILABILITY
  - Lead contact
  - Materials availability
  - Data and code availability
- EXPERIMENTAL MODEL AND SUBJECT DETAILS
- METHOD DETAILS
  - In utero electroporation
  - Transient early stimulation
  - Virus injections
  - Electrophysiology and optogenetics *in vivo*
  - Electrophysiology and optogenetics *in vitro*
  - Histology
  - Behavior
- QUANTIFICATION AND STATISTICAL ANALYSIS
  - Power spectral density
  - Imaginary coherence
  - Modulation index
  - Peak frequency and strength
  - Single unit analysis
  - EPSCs and IPSCs extraction
  - Statistics

SUPPLEMENTAL INFORMATION

Supplemental Information can be found online at https://doi.org/10.1016/j.neuron.2021.02.011.

ACKNOWLEDGMENTS

We thank Drs. T. Oertner and S. Wiegert for providing optogenetic tools; Dr. X. Xu for help with hippocampal injections; M. Hnida for help with early stimulation; and P. Putthoff, A. Dahlmann, and K. Titze for excellent technical assistance. This work was funded by grants from the European Research Council (ERC-2015-CoG 681577 to I.L.H.-O.) and the German Research Foundation (Ha 4466/10-1, Ha4466/11-1, Ha4466/12-1, SPP 1665, and SFB 936 B5 to I.L.H.-O.).

AUTHOR CONTRIBUTIONS

S.H.B., J.A.P., and I.L.H.-O. designed the experiments. S.H.B., J.A.P., M.C., and A.M. carried out the experiments. S.H.B., J.A.P., and M.C. analyzed the data. S.H.B., J.A.P., M.C., and I.L.H.-O. interpreted the data and wrote the manuscript. All authors discussed and commented on the manuscript.

DECLARATION OF INTERESTS

The authors declare no competing interests.

Received: May 11, 2020
Revised: January 6, 2021

Accepted: February 8, 2021
Published: March 5, 2021

REFERENCES

Ahlbeck, J., Song, L., Chini, M., Bitzenhofer, S.H., and Hanganu-Opatz, I.L. (2018). Glutamatergic drive along the septo-temporal axis of hippocampus boosts prelimbic oscillations in the neonatal mouse. eLife *7*, e33158.

Anastasiades, P.G., and Butt, S.J.B. (2012). A role for silent synapses in the development of the pathway from layer 2/3 to 5 pyramidal cells in the neocortex. J. Neurosci. *32*, 13085–13099.

Atallah, B.V., and Scanziani, M. (2009). Instantaneous modulation of gamma oscillation frequency by balancing excitation with inhibition. Neuron *62*, 566–577.

Barker, G.R.I., and Warburton, E.C. (2011). When is the hippocampus involved in recognition memory? J. Neurosci. *31*, 10721–10731.

Baron-Cohen, S. (2004). The cognitive neuroscience of autism. J. Neurol. Neurosurg. Psychiatry *75*, 945–948.

Bastos, A.M., Loonis, R., Kornblith, S., Lundqvist, M., and Miller, E.K. (2018). Laminar recordings in frontal cortex suggest distinct layers for maintenance and control of working memory. Proc. Natl. Acad. Sci. USA *115*, 1117–1122.

Berndt, A., Schoenenberger, P., Mattis, J., Tye, K.M., Deisseroth, K., Hegemann, P., and Oertner, T.G. (2011). High-efficiency channelrhodopsins for fast neuronal stimulation at low light levels. Proc. Natl. Acad. Sci. USA *108*, 7595–7600.

Bitzenhofer, S.H., Sieben, K., Siebert, K.D., Spehr, M., and Hanganu-Opatz, I.L. (2015). Oscillatory activity in developing prefrontal networks results from theta-gamma-modulated synaptic inputs. Cell Rep. *11*, 486–497.

Bitzenhofer, S.H., Ahlbeck, J., Wolff, A., Wiegert, J.S., Gee, C.E., Oertner, T.G., and Hanganu-Opatz, I.L. (2017a). Layer-specific optogenetic activation of pyramidal neurons causes beta-gamma entrainment of neonatal networks. Nat. Commun. *8*, 14563.

Bitzenhofer, S.H., Ahlbeck, J., and Hanganu-Opatz, I.L. (2017b). Methodological Approach for Optogenetic Manipulation of Neonatal Neuronal Networks. Front. Cell. Neurosci. *11*, 239.

Bitzenhofer, S.H., Pöpplau, J.A., and Hanganu-Opatz, I. (2020). Gamma activity accelerates during prefrontal development. eLife *9*, e56795.

Blanquie, O., Yang, J.-W., Kilb, W., Sharopov, S., Sinning, A., and Luhmann, H.J. (2017). Electrical activity controls area-specific expression of neuronal apoptosis in the mouse developing cerebral cortex. eLife *6*, e27696.

Brockmann, M.D., Pöschel, B., Cichon, N., and Hanganu-Opatz, I.L. (2011). Coupled oscillations mediate directed interactions between prefrontal cortex and hippocampus of the neonatal rat. Neuron *71*, 332–347.

Caballero, A., Flores-Barrera, E., Thomases, D.R., and Tseng, K.Y. (2020). Downregulation of parvalbumin expression in the prefrontal cortex during adolescence causes enduring prefrontal disinhibition in adulthood. Neuropsychopharmacology *45*, 1527–1535.

Cardin, J.A., Carlén, M., Meletis, K., Knoblich, U., Zhang, F., Deisseroth, K., Tsai, L.-H., and Moore, C.I. (2009). Driving fast-spiking cells induces gamma rhythm and controls sensory responses. Nature *459*, 663–667.

Chen, G., Zhang, Y., Li, X., Zhao, X., Ye, Q., Lin, Y., Tao, H.W., Rasch, M.J., and Zhang, X. (2017). Distinct Inhibitory Circuits Orchestrate Cortical beta and gamma Band Oscillations. Neuron *96*, 1403–1418.e6.

Chini, M., and Hanganu-Opatz, I.L. (2020). Prefrontal Cortex Development in Health and Disease: Lessons from Rodents and Humans. Trends Neurosci. *24*, S0166-2236(20)30250-2.

Chini, M., Pöpplau, J.A., Lindemann, C., Carol-Perdiguer, L., Hnida, M., Oberländer, V., Xu, X., Ahlbeck, J., Bitzenhofer, S.H., Mulert, C., and Hanganu-Opatz, I.L. (2020). Resolving and Rescuing Developmental Miswiring in a Mouse Model of Cognitive Impairment. Neuron *105*, 60–74.e7.

Cho, K.K.A., Hoch, R., Lee, A.T., Patel, T., Rubenstein, J.L.R., and Sohal, V.S. (2015). Gamma rhythms link prefrontal interneuron dysfunction with cognitive inflexibility in Dlx5/6(+/-) mice. Neuron *85*, 1332–1343.

Clause, A., Kim, G., Sonntag, M., Weisz, C.J.C., Vetter, D.E., Rűbsamen, R., and Kandler, K. (2014). The precise temporal pattern of prehearing spontaneous activity is necessary for tonotopic map refinement. Neuron *82*, 822–835.

Clifton, N.E., Hannon, E., Harwood, J.C., Di Florio, A., Thomas, K.L., Holmans, P.A., Walters, J.T.R., O'Donovan, M.C., Owen, M.J., Pocklington, A.J., and Hall, J. (2019). Dynamic expression of genes associated with schizophrenia and bipolar disorder across development. Transl. Psychiatry *9*, 74.

Courchesne, E. (2004). Brain development in autism: early overgrowth followed by premature arrest of growth. Ment. Retard. Dev. Disabil. Res. Rev. *10*, 106–111.

Denaxa, M., Neves, G., Rabinowitz, A., Kemlo, S., Liodis, P., Burrone, J., and Pachnis, V. (2018). Modulation of Apoptosis Controls Inhibitory Interneuron Number in the Cortex. Cell Rep. *22*, 1710–1721.

Friedrich, J., Zhou, P., and Paninski, L. (2017). Fast online deconvolution of calcium imaging data. PLoS Comput. Biol. *13*, e1005423.

Frith, C., and Dolan, R. (1996). The role of the prefrontal cortex in higher cognitive functions. Brain Res. Cogn. Brain Res. *5*, 175–181.

Gallinat, J., Winterer, G., Herrmann, C.S., and Senkowski, D. (2004). Reduced oscillatory gamma-band responses in unmedicated schizophrenic patients indicate impaired frontal network processing. Clin. Neurophysiol. *115*, 1863–1874.

Geschwind, D.H. (2011). Genetics of autism spectrum disorders. Trends Cogn. Sci. *15*, 409–416.

Gour, A., Boergens, K.M., Heike, N., Hua, Y., Laserstein, P., Song, K., and Helmstaedter, M. (2021). Postnatal connectomic development of inhibition in mouse barrel cortex. Science *371*, eabb4534.

Hall, J., Trent, S., Thomas, K.L., O'Donovan, M.C., and Owen, M.J. (2015). Genetic risk for schizophrenia: convergence on synaptic pathways involved in plasticity. Biol. Psychiatry *77*, 52–58.

Hanganu, I.L., Ben-Ari, Y., and Khazipov, R. (2006). Retinal waves trigger spindle bursts in the neonatal rat visual cortex. J. Neurosci. *26*, 6728–6736.

Hartung, H., Cichon, N., De Feo, V., Riemann, S., Schildt, S., Lindemann, C., Mulert, C., Gogos, J.A., and Hanganu-Opatz, I.L. (2016a). From Shortage to Surge: A Developmental Switch in Hippocampal-Prefrontal Coupling in a Gene-Environment Model of Neuropsychiatric Disorders. Cereb. Cortex *26*, 4265–4281.

Hartung, H., Brockmann, M.D., Pöschel, B., De Feo, V., and Hanganu-Opatz, I.L. (2016b). Thalamic and Entorhinal Network Activity Differently Modulates the Functional Development of Prefrontal-Hippocampal Interactions. J. Neurosci. *36*, 3676–3690.

Huberman, A.D., Speer, C.M., and Chapman, B. (2006). Spontaneous retinal activity mediates development of ocular dominance columns and binocular receptive fields in v1. Neuron *52*, 247–254.

Iyer, K.K., Roberts, J.A., Hellström-Westas, L., Wikström, S., Hansen Pupp, I., Ley, D., Vanhatalo, S., and Breakspear, M. (2015). Cortical burst dynamics predict clinical outcome early in extremely preterm infants. Brain *138*, 2206–2218.

Janiesch, P.C., Krüger, H.-S., Pöschel, B., and Hanganu-Opatz, I.L. (2011). Cholinergic control in developing prefrontal-hippocampal networks. J. Neurosci. *31*, 17955–17970.

Katz, L.C., and Shatz, C.J. (1996). Synaptic activity and the construction of cortical circuits. Science *274*, 1133–1138.

Khazipov, R., Sirota, A., Leinekugel, X., Holmes, G.L., Ben-Ari, Y., and Buzsáki, G. (2004). Early motor activity drives spindle bursts in the developing somatosensory cortex. Nature *432*, 758–761.

Kirischuk, S., Sinning, A., Blanquie, O., Yang, J.-W., Luhmann, H.J., and Kilb, W. (2017). Modulation of Neocortical Development by Early Neuronal Activity: Physiology and Pathophysiology. Front. Cell. Neurosci. *11*, 379.

Kirkby, L.A., Sack, G.S., Firl, A., and Feller, M.B. (2013). A role for correlated spontaneous activity in the assembly of neural circuits. Neuron *80*, 1129–1144.

Le Roy, I., Carlier, M., and Roubertoux, P.L. (2001). Sensory and motor development in mice: genes, environment and their interactions. Behav. Brain Res. *125*, 57–64.

Lee, J., Durand, R., Gradinaru, V., Zhang, F., Goshen, I., Kim, D.-S., Fenno, L.E., Ramakrishnan, C., and Deisseroth, K. (2010). Global and local fMRI signals driven by neurons defined optogenetically by type and wiring. Nature *465*, 788–792.

Leicht, G., Vauth, S., Polomac, N., Andreou, C., Rauh, J., Mußmann, M., Karow, A., and Mulert, C. (2016). EEG-Informed fMRI Reveals a Disturbed Gamma-Band-Specific Network in Subjects at High Risk for Psychosis. Schizophr. Bull. *42*, 239–249.

Lim, L., Mi, D., Llorca, A., and Marín, O. (2018). Development and functional diversification of cortical interneurons. Neuron *100*, 294–313.

Lindemann, C., Ahlbeck, J., Bitzenhofer, S.H., and Hanganu-Opatz, I.L. (2016). Spindle Activity Orchestrates Plasticity during Development and Sleep. Neural Plast. *2016*, 5787423.

Marín, O. (2016). Developmental timing and critical windows for the treatment of psychiatric disorders. Nat. Med. *22*, 1229–1238.

Mattis, J., Tye, K., Ferenczi, E., Ramakrishnan, C., O'Shea, D.J., Prakash, R., Gunaydin, L.A., Hyun, M., Fenno, L.E., Gradinaru, V., et al. (2011). Principles for applying optogenetic tools derived from direct comparative analysis of microbial opsins. Nat. Methods *9*, 159–172.

Mikanmaa, E., Grent-'t-Jong, T., Hua, L., Recasens, M., Thune, H., and Uhlhaas, P.J. (2019). Towards a neurodynamical understanding of the prodrome in schizophrenia. Neuroimage *190*, 144–153.

Miller, E.K. (2000). The prefrontal cortex and cognitive control. Nat. Rev. Neurosci. *1*, 59–65.

Peixoto, R.T., Wang, W., Croney, D.M., Kozorovitskiy, Y., and Sabatini, B.L. (2016). Early hyperactivity and precocious maturation of corticostriatal circuits in Shank3B(-/-) mice. Nat. Neurosci. *19*, 716–724.

Pennington, Z.T., Dong, Z., Feng, Y., Vetere, L.M., Page-Harley, L., Shuman, T., and Cai, D.J. (2019). ezTrack: An open-source video analysis pipeline for the investigation of animal behavior. Sci. Rep. *9*, 19979.

Pfeffer, C.K., Xue, M., He, M., Huang, Z.J., and Scanziani, M. (2013). Inhibition of inhibition in visual cortex: the logic of connections between molecularly distinct interneurons. Nat. Neurosci. *16*, 1068–1076.

Richter, M., Murtaza, N., Scharrenberg, R., White, S.H., Johanns, O., Walker, S., Yuen, R.K.C., Schwanke, B., Bedürftig, B., Henis, M., et al. (2019). Altered TAOK2 activity causes autism-related neurodevelopmental and cognitive abnormalities through RhoA signaling. Mol. Psychiatry *24*, 1329–1350.

Robertson, C.E., and Baron-Cohen, S. (2017). Sensory perception in autism. Nat. Rev. Neurosci. *18*, 671–684.

Rossant, C., Kadir, S.N., Goodman, D.F.M., Schulman, J., Hunter, M.L.D., Saleem, A.B., Grosmark, A., Belluscio, M., Denfield, G.H., Ecker, A.S., et al. (2016). Spike sorting for large, dense electrode arrays. Nat. Neurosci. *19*, 634–641.

Sahin, M., and Sur, M. (2015). Genes, circuits, and precision therapies for autism and related neurodevelopmental disorders. Science *350*, aab3897.

Schmitt, A., Malchow, B., Hasan, A., and Falkai, P. (2014). The impact of environmental factors in severe psychiatric disorders. Front. Neurosci. *8*, 19.

Sohal, V.S., and Rubenstein, J.L.R. (2019). Excitation-inhibition balance as a framework for investigating mechanisms in neuropsychiatric disorders. Mol. Psychiatry *24*, 1248–1257.

Stuchlik, A., and Sumiyoshi, T. (2014). Cognitive deficits in schizophrenia and other neuropsychiatric disorders: convergence of preclinical and clinical evidence. Front. Behav. Neurosci. *8*, 444.

Uhlhaas, P.J., and Singer, W. (2010). Abnormal neural oscillations and synchrony in schizophrenia. Nat. Rev. Neurosci. *11*, 100–113.

Van Eden, C.G., and Uylings, H.B.M. (1985). Postnatal volumetric development of the prefrontal cortex in the rat. J. Comp. Neurol. *241*, 268–274.

van Os, J., and Kapur, S. (2009). Schizophrenia. Lancet *374*, 635–645.

Vierock, J., Rodriguez-Rozada, S., Pieper, F., Dieter, A., Bergs, A., Zeitzschel, N., Ahlbeck, J., Sauter, K., Gottschalk, A., Engel, A.K., et al. (2020). BiPOLES: a tool for bidirectional dual-color optogenetic control of neurons. bioRxiv. https://doi.org/10.1101/2020.07.15.204347.

Wayman, G.A., Impey, S., Marks, D., Saneyoshi, T., Grant, W.F., Derkach, V., and Soderling, T.R. (2006). Activity-dependent dendritic arborization mediated by CaM-kinase I activation and enhanced CREB-dependent transcription of Wnt-2. Neuron *50*, 897–909.

Wong, F.K., Bercsenyi, K., Sreenivasan, V., Portalés, A., Fernández-Otero, M., and Marín, O. (2018). Pyramidal cell regulation of interneuron survival sculpts cortical networks. Nature *557*, 668–673.

Workman, A.D., Charvet, C.J., Clancy, B., Darlington, R.B., and Finlay, B.L. (2013). Modeling transformations of neurodevelopmental sequences across mammalian species. J. Neurosci. *33*, 7368–7383.

STAR★METHODS

KEY RESOURCES TABLE

REAGENT or RESOURCE	SOURCE	IDENTIFIER
Antibodies		
Alexa Fluor-488 goat anti-rabbit IgG secondaryantibody	Merck Millipore	Cat# A-11008; RRID: AB_143165
Rabbit polyclonal primary antibody against CamKII	Thermo Fisher Scientific	Cat# PA5-29648; RRID:AB_2547123
Rabbit monoclonal primary antibody against parvalbumin	Swant	Cat# 235; RRID:AB_10000343
Rabbit polyclonal primary antibody against somatostatin	Santa Cruz	Cat# sc-13099; RRID:AB_2195930
Deposited data		
Extracellular recording data and sorted single unit data	This paper	https://gin.g-node.org/Jastyn/Early_activity_is_critical_for_prefrontal_development
Chemicals, peptides, and recombinant proteins		
Urethane	Sigma-Aldrich	U2500
Isoflurane	Abbott	B506
Ketamine	Richter Pharma AG	Ketamidor
Xylazine	Bayer	Rompun
Experimental models: organisms/strains		
Mouse: C57BL/6J	Universitä tsklinikum Hamburg-Eppendorf – Animal facility	Mouse: C57BL/6J
Mouse: PV-Cre knock-in (B6.129P2-Pvalb$^{tm1(cre)Arbr}$/J)	Jackson Laboratory	Jax-mice: #008069
Recombinant DNA		
pAAV-CAG-ChR2(E123T/T159C)-2AtDimer2	Berndt et al., 2011	https://www.addgene.org/85399/
AAV9-Ef1alpha-DIO-hChR2(ET/TC)-eYFP	Mattis et al. 2011	https://www.addgene.org/35507/
AAV9-hSyn-DIO-SomBiPOLES-mCerulean	Vierock et al., 2020	Donated by Simon Wiegert
pAAV-CaMKIIa-hChR2(H134R)-eYFP	Lee et al., 2010	https://www.addgene.org/26969/
Software and algorithms		
MATLAB R2016a	MathWorks	https://www.mathworks.com
MATLAB R2019a	MathWorks	https://www.mathworks.com
ImageJ 2.0.0	ImageJ	https://imagej.nih.gov/ij/
R Statistical Software 3.5.1	RStudio	http://www.rstudio.com/
Cheetah 6	Neuralynx	https://neuralynx.com/
Anaconda 1.9.6	Anaconda	https://www.anaconda.com
Jupyter 6.0.0	Jupyter	https://jupyter.org/
Video Mot2	TSE Systems	https://www.tse-systems.com/product-details/videomot
uEye Cockpit	iDS Imaging	https://en.ids-imaging.com/ids-software-suite.html
Phy	https://github.com/cortex-lab	https://github.com/cortex-lab/phy
OASIS toolbox	https://github.com/zhoupc	https://github.com/zhoupc/OASIS_matlab
Other		
Arduino Uno SMD	Arduino	A000073
Digital Lynx 4SX	Neuralynx	https://neuralynx.com/

(*Continued on next page*)

Continued

REAGENT or RESOURCE	SOURCE	IDENTIFIER
Diode laser (473 nm)	Omicron	LuxX® 473-100
Diode laser (594 nm)	Omicron	SOLE® 594-100
Electroporation device	BEX	CUY21EX
Electroporation tweezer-type paddles	Protech	CUY650-P5
Recording optrode (1 shank, 16 channels)	Neuronexus	A1x16-5mm-100-703-OA16LP
Recording optrode (1 shank, 16 channels)	Neuronexus	A1x16-5mm-50-703-OA16LP
Recording optrode (4 shanks, 16 channels)	Neuronexus	A4x4-3mm-100-125-703-OA16LP
Confocal microscope	Zeiss	LSM 700
Confocal microscope	Leica	DM IRBE
Mobile HomeCage®	Neurotar	Mobile HomeCage Large® with tracking capability
Floating foam maze	Neurotar	Assembled foam sociability cage
Lightweight stainless-steel head plates	Neurotar	Model 3, round 6,2 mm opening
Headpost stand	Luigs & Neumann	200-200 500 1100
Head post - S (for mice)	Luigs & Neumann	200-100 500 2203

RESOURCE AVAILABILITY

Lead contact

Further information and requests for resources and reagents should be directed to and will be fulfilled by the Lead Contact, Ileana L. Hanganu-Opatz (hangop@zmnh.uni-hamburg.de).

Materials availability

The study did not generate new unique reagents.

Data and code availability

LFP and SUA data for all recordings are available at the following open-access repository: https://gin.g-node.org/Jastyn/Early_activity_is_critical_for_prefrontal_development. Further data and code supporting the findings of this study are available from the corresponding authors on request.

EXPERIMENTAL MODEL AND SUBJECT DETAILS

All experiments were performed in compliance with the German laws and the guidelines of the European Community for the use of animals in research and were approved by the local ethical committee (G132/12, G17/015, N18/015). Experiments were carried out on C57BL/6J and PV-cre (B6.129P2-*Pvalb*$^{tm1(cre)Arbr}$/J, #008069) mice of both sexes. Timed-pregnant mice from the animal facility of the University Medical Center Hamburg-Eppendorf were housed individually at a 12 h light/12 h dark cycle and were given access to water and food *ad libitum*. The day of vaginal plug detection was considered E0.5, the day of birth was considered P0.

METHOD DETAILS

In utero electroporation

Pregnant mice received additional wet food daily, supplemented with 2-4 drops Metacam (0.5 mg/ml, Boehringer-Ingelheim, Germany) one day before until two days after IUE. At E15.5, pregnant mice were injected subcutaneously with buprenorphine (0.05 mg/kg body weight) 30 min before surgery. Surgery was performed under isoflurane anesthesia (induction 5%, maintenance 3.5%) on a heating blanket. Eyes were covered with eye ointment and pain reflexes and breathing were monitored to assess anesthesia depth. Uterine horns were exposed and moistened with warm sterile phosphate-buffered saline (PBS). 0.75-1.25 μl of opsin- and fluorophore-encoding plasmid (pAAV-CAG-ChR2(E123T/T159C)-2A-tDimer2 (RFP), 1.25 μg/μl) purified with NucleoBond (Macherey-Nagel, Germany) in sterile PBS with 0.1% fast green dye was injected in the right lateral ventricle of each embryo using pulled borosilicate glass capillaries. Electroporation tweezer paddles of 5 mm diameter were oriented at a rough 20° leftward angle from the midline of the head and a rough 10° downward angle from the anterior to posterior axis to transfect precursor cells of medial prefrontal L2/3 PYRs with 5 electroporation pulses (35 V, 50 ms, 950 ms interval, CU21EX, BEX, Japan). Uterine horns were placed back into the abdominal cavity that was filled with warm sterile PBS. Abdominal muscles and skin were sutured with absorbable and non-absorbable suture thread, respectively. After recovery from

anesthesia, mice were returned to their home cage, placed half on a heating blanket for two days after surgery. Fluorophore expression in pups was detected at P2 with a portable fluorescence flashlight (Nightsea, MA, USA) through the intact skin and skull and confirmed in brain slices postmortem.

Transient early stimulation

A stimulation window was made at P7 for chronic transcranial optogenetic stimulation in mice transfected by in utero electroporation. Mice were placed on a heating blanket and anesthetized with isoflurane (5% induction, 2% maintenance). Breathing and pain reflexes were monitored to assess anesthesia depth. The skin above the skull was cut along the midline at the level of the mPFC and gently spread with forceps. The exposed skull was covered with transparent tissue adhesive (Surgibond, SMI, Belgium). Mice were returned to the dam in the home cage after recovery from anesthesia. From P7-11 mice were stimulated daily under isoflurane anesthesia (5% induction, 2% maintenance) with ramp stimulations of linearly increasing light power (473 nm wavelength, 3 s duration, 7 s interval, 180 repetitions, 30 min total duration). Light stimulation was performed using an Arduino uno (Arduino, Italy) controlled laser system (Omicron, Austria) coupled to a 200 μm diameter light fiber (Thorlabs, NJ, USA) positioned directly above the tissue adhesive window. Light power attenuation was set to 30 mW to reach 10 mW in the brain, adjusted for measured light attenuation by the tissue adhesive (~30%) and the thin skull at young age (~25%). Control animals were treated identical but stimulated with light of 594 nm wavelength that does not activate the expressed opsin ChR2(ET/TC). The same protocol was used for transient early stimulation at P12-16. At this age, the skull was etched and thinned before covering with transparent tissue adhesive.

Virus injections

Prefrontal cortex

At P12, virus encoding cre-dependent AAV9-Ef1alpha-DIO-hChR2(ET/TC)-eYFP was injected into the mPFC (0.5 mm anterior to bregma, 0.1-0.5 mm lateral to the midline, 1.6 mm deep) of PV-cre mice for opto-tagging experiments. At P16, virus encoding cre-dependent AAV9-hSyn-DIO-SomBiPOLES-mCerulean was injected into the mPFC (0.5 mm anterior to bregma, 0.1-0.5 mm lateral to the midline, 1.6 mm deep) of PV-cre mice for *in vitro* experiments.

Hippocampus

At P22, virus encoding pAAV-CaMKIIa-hChR2(H134R)-eYFP was injected into the intermediate HP (0.7 mm anterior to lambda, 2.3 mm lateral to the midline, 1.5 mm deep) of C57BL/6J mice for light stimulation.

Electrophysiology and optogenetics *in vivo*

Acute extracellular recordings

Multi-site extracellular recordings were performed unilaterally or bilaterally in the mPFC of non-anesthetized and anesthetized P7-40 mice. Under isoflurane anesthesia (induction: 5%; maintenance: 2.5%), a craniotomy was performed above the mPFC (0.5 mm anterior to bregma, 0.1-0.5 mm lateral to the midline). Mice were head-fixed into a stereotaxic apparatus using two plastic bars mounted on the nasal and occipital bones with dental cement. Multi-site electrodes (NeuroNexus, MI, USA) were inserted into the mPFC (four-shank, A4x4 recording sites, 100 μm spacing, 125 μm shank distance, 1.8-2.0 mm deep). A silver wire was inserted into the cerebellum and served as ground and reference. Pups were allowed to recover for 30 min prior to recordings. For recordings in anesthetized mice, urethane (1 mg/g body weight) was injected intraperitoneally prior to the surgery. Extracellular signals were band-pass filtered (0.1-9,000 Hz) and digitized (32 kHz) with a multichannel extracellular amplifier (Digital Lynx SX; Neuralynx, Bozeman, MO, USA). Electrode position was confirmed in brain slices postmortem.

Chronic extracellular recordings

Multi-site extracellular recordings were performed in the mPFC of P23-26 and P38-40 mice. Under isoflurane anesthesia (5% induction, 2.5% maintenance), a metal head-post for head fixation (Luigs and Neumann, Germany) was implanted at least 5 days before recordings. Above the mPFC (0.5-2.0 mm anterior to bregma, 0.1-0.5 mm right to the midline) and the intermediate HP (3.5 mm posterior to bregma, 3.5 mm lateral to the midline) a craniotomy was performed and protected by a customized synthetic window. A silver wire was implanted between skull and brain tissue above the cerebellum and served as ground and reference. 0.5% bupivacaine / 1% lidocaine was locally applied to cutting edges. After recovery from anesthesia, mice were returned to their home cage. Mice were allowed to recover from the surgery, accustomed to head-fixation and trained to run on a custom-made spinning disc. For recordings, craniotomies were uncovered and a multi-site electrode (NeuroNexus, MI, USA) was inserted into the mPFC (one-shank, A1x16 recording sites, 100 μm spacing, 2.0 mm deep) and, in some experiments, into the intermediate HP (one-shank, A1x16 recording sites, 50 μm spacing, 1.6 mm deep). Extracellular signals were band-pass filtered (0.1-9000 Hz) and digitized (32 kHz) with a multichannel extracellular amplifier (Digital Lynx SX; Neuralynx, Bozeman, MO, USA). Electrode position was confirmed in brain slices postmortem.

Acute light stimulation

Ramp (i.e., linearly increasing light power) light stimulation and 3 ms light pulses were performed using an Arduino uno (Arduino, Italy) controlled laser system (473 nm / 594 nm wavelength, Omicron, Austria) coupled to a 50 μm (4 shank electrodes) or 105 μm (1 shank electrodes) diameter light fiber (Thorlabs, NJ, USA) glued to the multisite electrodes, ending 200 μm above the top recording site. Acute ramp stimulations were repeated 30 times and acute pulse stimulations 360 times.

Photo-tagging

ChR2(ET/TC) expressing PV interneurons were stimulated with 3 ms light pulses at 473 nm wavelength. Firing rate increase at 2-6 ms after stimulation onset was compared to pre-stimulus firing rate for 720 single pulses to detect significantly activated units ($p < 0.001$ and MI > 0.2).

Electrophysiology and optogenetics *in vitro*

Patch-clamp recordings

Whole-cell patch-clamp recordings were performed from tDimer-negative L2/3 PYRs in the mPFC of P23-26 and P37-40 mice. Under anesthesia, mice were decapitated, brains were removed and sectioned coronally at 300 mm in ice-cold oxygenated high sucrose-based artificial cerebral spinal fluid (ACSF) (in mM: 228 sucrose, 2.5 KCl, 1 NaH2PO4, 26.2 NaHCO3, 11 glucose, 7 MgSO4; 310 mOsm). Slices were incubated in oxygenated ACSF (in mM: 119 NaCl, 2.5 KCl, 1 NaH2PO4, 26.2 NaHCO3, 11 glucose, 1.3 MgSO4; 310 mOsm) at 37°C for 45 min before cooling to room temperature. Slices were superfused with oxygenated ACSF in the recording chamber. Neurons were patched under optical control using pulled borosilicate glass capillaries (tip resistance of 3-7 MΩ) filled with pipette solution (in mM: 130 D-gluconic acid 49%–53%, 130 Cesium-OH 50%, 10 HEPES, 0.5 EGTA, 4 Mg-ATP, 0.3 Na2-GTP, 8 NaCl, 5 QX-314-Cl; 285 mOsm, pH 7.3). Data was acquired using PatchMaster (HEKA Elektronik, MA, USA). Capacitance artifacts and series resistance were minimized using the built-in circuitry of the patch-clamp amplifier (EPC 10; HEKA Elektronik, MA, USA). Responses of neurons were digitized at 10 kHz in voltage-clamp mode.

Light stimulation

Square light stimuli of 473 nm or 585 nm wavelength and 10 ms or 1 s duration were delivered with the pE-2 LED system (CoolLED, Andover, UK). Experiments were performed blind to the group identity (transient early stimulation at 473 nm or 585 nm) of mice.

Histology

P7-40 mice were anesthetized with 10% ketamine (aniMedica, Germanry) / 2% xylazine (WDT, Germany) in 0.9% NaCl (10 μg/g body weight, intraperitoneal) and transcardially perfused with 4% paraformaldehyde (Histofix, Carl Roth, Germany). Brains were removed and postfixed in 4% paraformaldehyde for 24 h. Brains were sectioned coronally with a vibratome at 50 μm for immunohistochemistry or 100 μm for examination of dendritic complexity and electrode reconstruction.

Immunohistochemistry

Free-floating slices were permeabilized and blocked with PBS containing 0.8% Triton X-100 (Sigma-Aldrich, MO, USA), 5% normal bovine serum (Jackson Immuno Research, PA, USA) and 0.05% sodium azide. Slices were incubated over night with primary antibody rabbit-anti-Ca^{2+}/calmodulin-dependent protein kinase II (1:200, #PA5-38239, Thermo Fisher, MA, USA; 1:500, #ab52476, Abcam, UK), rabbit-anti-parvalbumin (1:500, #ab11427, Abcam, UK) or rabbit-anti-somatostatin (1:250, #sc13099, Santa Cruz, CA, USA), followed by 2 h incubation with secondary antibody goat-anti-rabbit Alexa Fluor 488 (1:500, #A11008, Invitrogen-Thermo Fisher, MA, USA). Sections were transferred to glass slides and covered with Fluoromount (Sigma-Aldrich, MO, USA).

Cell quantification

Images of immunostainings and IUE-induced tDimer2 expression in the right mPFC were acquired on a confocal microscope (DM IRBE, Leica, Germany) using a 10x objective (numerical aperture 0.3). tDimer2-positive and immunopositive cells were automatically quantified with custom-written algorithms in ImageJ environment. The region of interest (ROI) was manually defined over L2/3 of the mPFC. Image contrast was enhanced before applying a median filter. Local background was subtracted to reduce background noise and images were binarized and segmented using the watershed function. Counting was done after detecting the neurons with the extended maxima function of the MorphoLibJ plugin. Experiments were performed blind to the group identity (transient early stimulation at 473 nm or 585 nm) of mice.

Dendritic complexity and spine quantification

Image stacks of tDimer2-positive PYRs or immune-positive PV neurons were acquired on a confocal microscope (LSN700, Zeiss, Germany) using a 40x objective. Stacks of 6 neurons per animal were acquired as 2048x2048 pixel images (voxel size 156*156*500 nm). Dendritic complexity was quantified by Sholl analysis in ImageJ environment. Images were binarized using auto threshold function and the dendrites were traced using the semi-automatic simple neurite tracer plugin. The geometric center was identified, and the traced dendritic tree was analyzed with the Sholl analysis plugin. Analysis was performed blind to the group identity (transient early stimulation at 473 nm or 585 nm) of mice. For spine quantification, spines on dendrite of interest (apical, basal, proximal oblique or secondary apical) were measured (line tool) and manually counted using the point picker tool in ImageJ environment.

Behavior

Mice were handled and adapted to the investigation room two days prior to behavioral examination. Arenas and objects were cleaned with 0.1% acetic acid before each trial. Animals were tracked online using video Mot2 software (Video Mot2, TSE Systems GmbH, Germany) or offline using the python-based tracking system ezTrack (Pennington et al., 2019).

Developmental milestones

Somatic and reflex development was examined every third day in P2-20 mice. Weight, body length, and tail length were measured. Grasping reflex was assessed by touching front paws with a toothpick. Vibrissa placing was measured as head movement in

response to gently touching the vibrissa with a toothpick. Auditory startle was assessed in response to finger snapping. The days of pinnae detachment and eye opening were monitored. Surface righting was measured as time to turn around after being positioned on the back (max 30 s). Cliff avoidance was measured as time until withdrawing after being positioned with forepaws and snout over an elevated edge (max 30 s). Bar holding was measured as time hanging on a toothpick grasped with the forepaws (max 10 s).

Open field

At P16, Mice were positioned in the center of a circular arena (34 cm in diameter) and allowed to explore for 10 min. Behavior was quantified as discrimination index of time spent in the center and the border of the arena ((time in surround - time in center) / (time in surround + time in center)), grooming time, average velocity and number of rearing, wall rearing and jumping.

Object recognition

Novel object recognition (NOR, P17), object location recognition (OLR, P18) and recency recognition (RR, P21) were performed in the same arena as the open field examination. Mouse center, tail and snout position were tracked automatically. Object interaction was defined as the snout being within < 1 cm distance from an object. For NOR, each mouse explored two identical objects for 10 min during the sample phase. After a delay period of 5 min in a break box, the mouse was placed back in the arena for the test phase, where one of the objects was replaced by a novel object. Behavior was quantified as discrimination index of time spent interacting with the novel and familiar object ((time novel object - time familiar object) / (time novel object + time familiar object)). OLR was performed similarly, but one object was relocated for the test phase instead of being exchanged. For RR, each mouse explored two identical objects during the first sample phase for 10 min, followed by a delay phase of 30 min, and a second sample phase of 10 min with two novel identical objects. After a second break of 5 min, the interaction time with an object of the first sample phase (old) and an object from the second sample phase (recent) was assessed during the test phase for 2 min. Behavior was quantified as discrimination index of time spent interacting with the novel and familiar object ((time old object – time recent object) / (time old object + time recent object)).

Maternal interaction

Maternal interaction was performed at P21 in the same arena as the open field examination. Two plastic containers were added to the arena, one empty and one containing the dam of the investigated mouse. Small holes in the containers allowed the mouse and the dam to interact. Behavior was quantified as discrimination index of time spent interacting with the empty container and the container containing the dam ((time dam container – time empty container) / (time dam container + time empty container)).

Spatial working memory

At P36-38, mice were positioned in the center of an elevated 8-arm radial maze. 4 arms contained a food pellet at the distal end (baited). On the first day, mice were allowed to examine the maze for 20 min or until all arms were visited. During the following 10 trials (2 trials on day 1 and 4 trials on day 2 and 3), mice were allowed to examine the maze until all baited arms were visited (for max 20 min) and arm entries were assessed. Visit of a non-baited arm was considered as reference memory error, repeated visit of the same arm in one trial as working memory error.

Spontaneous alteration

At P39, each mouse was positioned in the start arm of an elevated Y-maze. Visited arms during free exploration were monitored for 10 min. Percentage of alternations was calculated as (number of alternations / (entries - 2)). The test was used as habituation for delayed non-match-to-sample task.

Delayed non-match-to-sample task

At P39-40, mice were positioned in the start arm of an elevated Y-maze with access to the other arms containing a food pellet. After entering one arm, a central door was closed (sample choice). After the food pellet was consumed the mice were placed in the start arm for a second run (test choice) after a 30 s break. Each mouse performed 6 trials / day. Test choice was considered correct when visiting the arm not explored during sample phase.

Social preference

At P38-40, chronically implanted and trained mice were head fixed in the Mobile Home Cage system (Neurotar, Finland) for electrophysiological recordings during a social preference task. Two chambers attached to opposite sides of the mobile home cage contained a familiar or novel mouse and an object. Animals were free to move the mobile home cage for 20 min. After attaching a novel or familiar mouse and an object to the opposite sites of the home cage the recording was continued for 15 min and the position was monitored. Since no differences were found for interactions with a novel or a familiar mouse, the data were pooled. For power spectral density analysis, the first 6 s after interaction onset (mouse or object) of first 15 min of interaction were concatenated, and the power was calculated using Welch's method with non-overlapping windows. Spectra were multiplied with squared frequency.

QUANTIFICATION AND STATISTICAL ANALYSIS

Data from *in vivo* and *in vitro* recordings were analyzed with custom-written algorithms in MATLAB environment. *In vivo* data were band-pass filtered (500-9000 Hz for spike analysis or 1-100 Hz for LFP) using a third-order Butterworth filter forward and backward to preserve phase information before down-sampling to analyze LFP. For *in vitro* data, all potentials were corrected for liquid junction potentials (−10 mV). The resting membrane potential was measured immediately after obtaining the whole-cell configuration. To assess input resistance and membrane properties, 600 ms long hyperpolarizing current pulses were applied.

Power spectral density

For power spectral density analysis 2-6 s-long windows of LFP signal were concatenated and the power was calculated using Welch's method with non-overlapping windows. Spectra were multiplied with squared frequency.

Imaginary coherence

The imaginary part of complex coherence, which is insensitive to volume conduction, was calculated by taking the absolute value of the imaginary component of the normalized cross-spectrum.

Modulation index

For optogenetic stimulations, modulation index was calculated as (value stimulation - value pre stimulation) / (value stimulation + value pre stimulation).

Peak frequency and strength

Peak frequency and peak strength were calculated for the most prominent peak in the spectrum defined by the product of peak amplitude, peak half width and peak prominence.

Single unit analysis

Single unit activity (SUA) was detected and clustered using klusta (Rossant et al., 2016) and manually curated using phy (https://github.com/cortex-lab/phy). Modulation index of SUA firing rate was calculated on 3 s long windows pre- and during stimulation. Significance level was set at $p < 0.01$ and calculated using Wilcoxon signed rank test for zero median for single stimulation trials. Single unit autocorrelation histogram was calculated using 0.5 ms bins followed by frequency spectrum computation using discrete Fourier transform. Oscillation score was calculated by dividing peak magnitude of detected peak frequency by average spectrum magnitude for pre- and during stimulation periods. For pairwise neuronal correlation SUA spike trains were convolved using a Gaussian window with a standard deviation of 20 ms. Correlation of convolved spike trains was computed using Spearman's rho. Cumulative distribution functions from before and during stimulations were compared using the two-sample Kolmogorov-Smirnov test. RS and FS units were distinguished by manually setting a threshold based on spike half width and trough-to-peak duration (FS, P11-12 half width < 0.31 ms, trough to peak < 1.28 ms, P23-25 and P38-40 half width < 0.31 ms, trough to peak < 0.64 ms).

EPSCs and IPSCs extraction

Voltage-clamp traces were demeaned and detrended with a median filter (mdefilt1). Traces were then deconvolved using a double exponential kernel using the OASIS toolbox (https://github.com/zhoupc/OASIS_matlab; Friedrich et al., 2017). After manual optimization of two separate kernels for EPSCs and IPSCs, the software was run with the "foopsi" model and a regularization parameter "lambda" set at the value of 10^{-11}. The parameters "smin" and "b" were automatically optimized, separately for each trace. The deconvolved traces were then used to compute the integral of EPSCs and IPSCs for baseline and stimulation periods.

Statistics

Statistical analyses were performed in the MATLAB environment or in R Statistical Software (Foundation for Statistical Computing, Austria). Data were tested for significant differences ($*p < 0.05$, $**p < 0.01$ and $***p < 0.001$) using non-parametric Wilcoxon rank sum test for unpaired and Wilcoxon signed rank test for paired data or Kruskal-Wallis test with Bonferroni corrected post hoc analysis or Fisher's exact test for binary data analysis. Nested data were analyzed with linear mixed-effect models with animal as fixed effect and Turkey multi comparison correction for post hoc analysis. See Tables S1 and S2 for detailed statistics.

Neuron, Volume *109*

Supplemental information

A transient developmental increase in prefrontal activity alters network maturation and causes cognitive dysfunction in adult mice

Sebastian H. Bitzenhofer, Jastyn A. Pöpplau, Mattia Chini, Annette Marquardt, and Ileana L. Hanganu-Opatz

Supplementary Information

Transient developmental increase of prefrontal activity alters network maturation and causes cognitive dysfunction in adult mice

Sebastian H. Bitzenhofer[1,#,*,§], Jastyn A. Pöpplau[1,#], Mattia Chini[1], Annette Marquardt[1] & Ileana L. Hanganu-Opatz[1,+,*]

[1] Institute of Developmental Neurophysiology, Center for Molecular Neurobiology, University Medical Center Hamburg-Eppendorf, 20251 Hamburg, Germany
[#] These authors contributed equally
[§] Current address: Center for Neural Circuits and Behavior, Department of Neurosciences, University of California, San Diego, La Jolla, CA 92093, USA.
[+] Lead contact

* Corresponding authors: Ileana L. Hanganu-Opatz
hangop@zmnh.uni-hamburg.de
Falkenried 94, 20251 Hamburg, Germany

Sebastian Bitzenhofer
sbitzenhofer@ucsd.edu
9500 Gilman Dr., La Jolla, CA 92093, USA

Inventory of Supplementary Information page

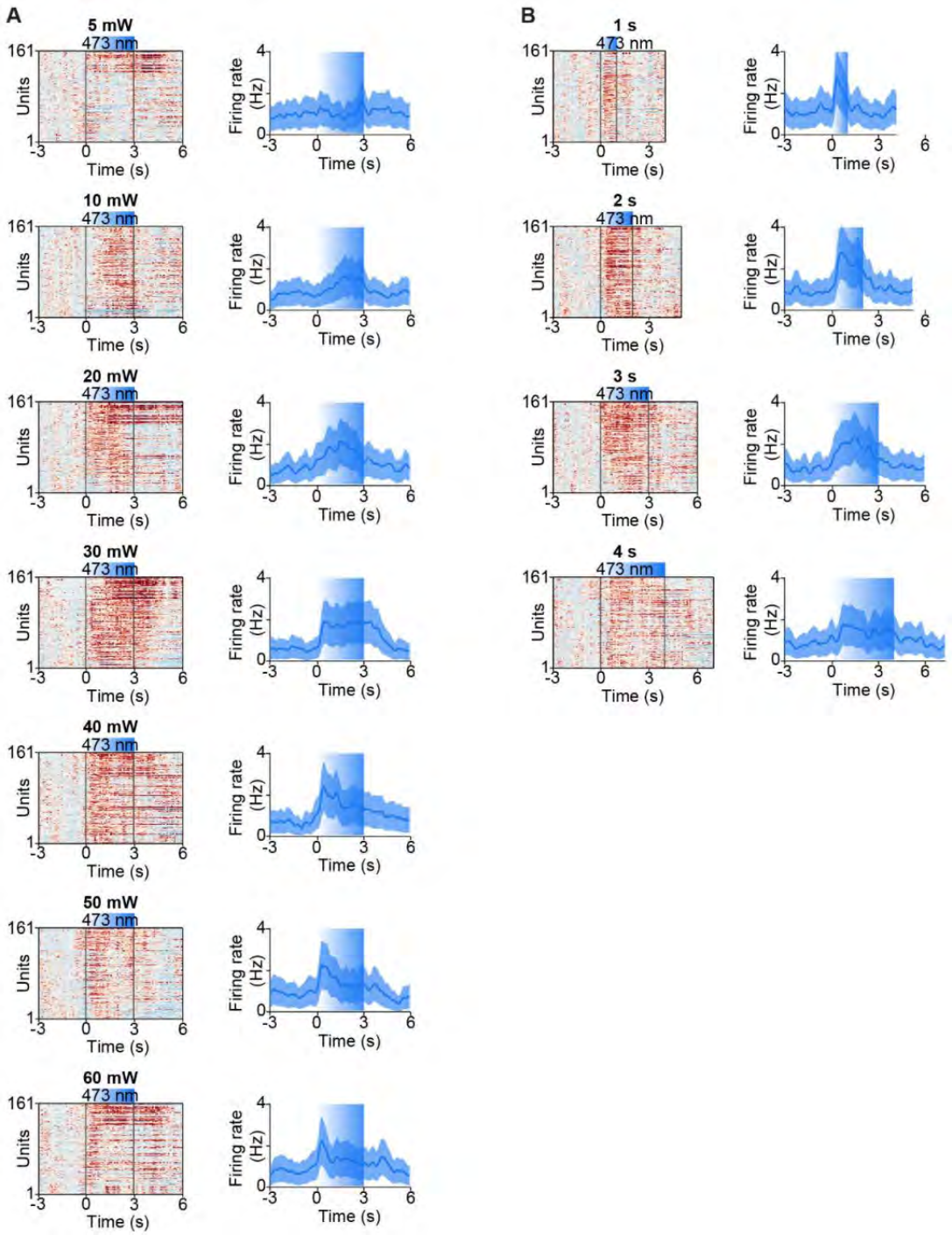

Figure S1. Related to Figure 1. Firing rates of L2/3 PYRs in the neonatal mPFC during light dose tests for transcranial stimulation.
(**A**) Firing rates of single units (n=161 units from 11 mice) in response to transcranial ramp light stimulation at P7-11 at different light intensities.
(**B**) Same as (A) for transcranial ramp light stimulation with different durations.
Data are presented as mean ± SEM.

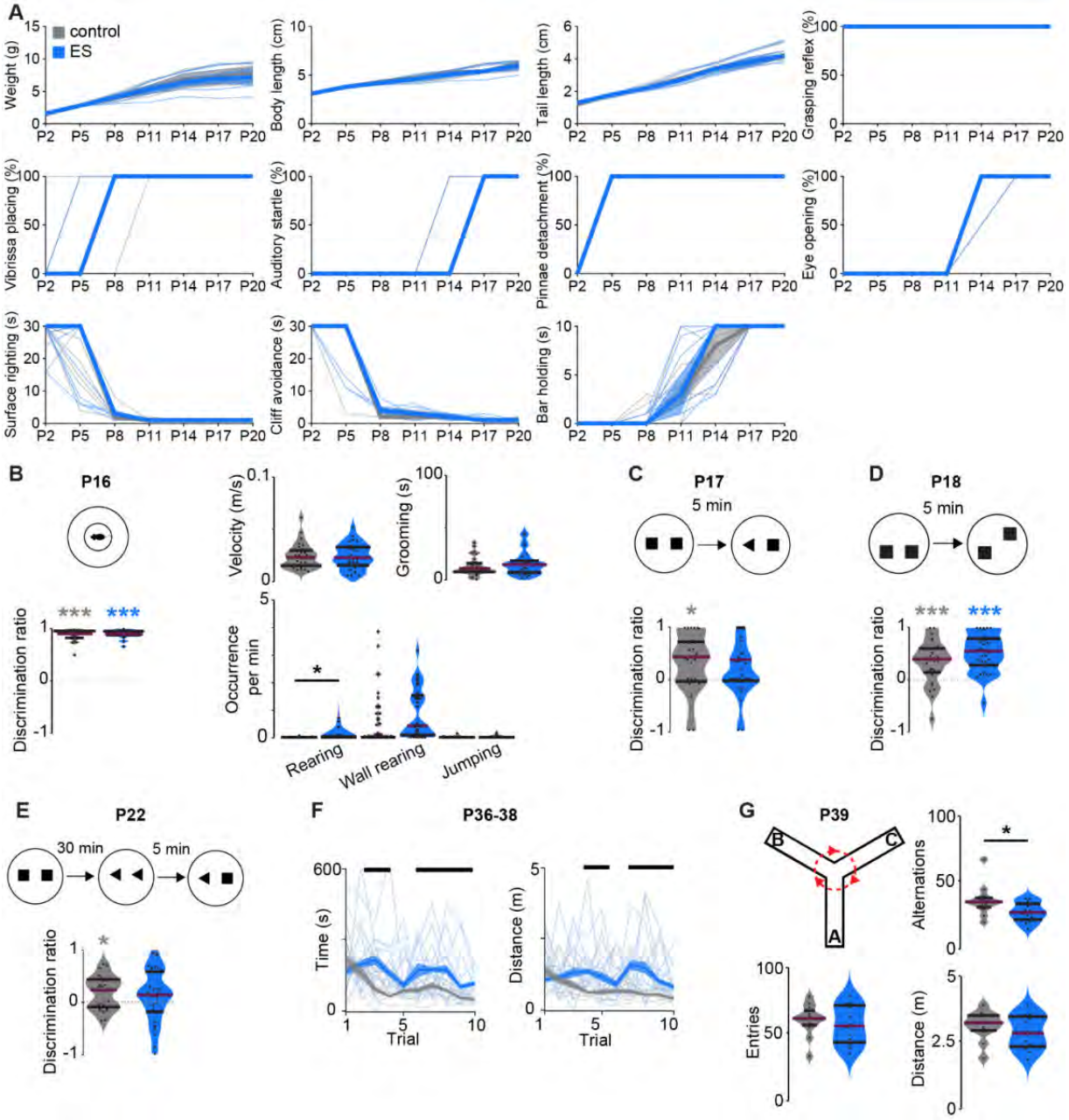

Figure S2. Related to Figure 2. Transient early stimulation impairs mPFC-dependent cognitive abilities but not reflex, motor and anxiety behavior of juvenile and young adult mice.

(**A**) Line plots displaying the age-dependence of developmental milestones for control (n=11) and ES (n=11) mice.

(**B**) Schematic of an open field task (top left) and violin plots displaying the discrimination ratio of time spend in border area vs. center area (bottom left), as well as the basic behavior (velocity, grooming, rearing, wall rearing, jumping) (right) for control (n=28) and ES (n=30) mice at P16. (Wilcoxon rank, discrimination ratio, control $p<0.001$, ES $p<0.001$, control-ES $p=0.809$).

(**C**) Schematic of NOR task and violin plot displaying the discrimination ratio of

interaction time with a novel vs. familiar object for control (n=28) and ES (n=30) mice at P17. (Wilcoxon rank, control p=0.018, ES p=0.157, control-ES p=0.177).
(**D**) Schematic of OLR task (top) and violin plot displaying the discrimination ratio of interaction time with an object in a novel vs. familiar location (bottom) for control (n=28) and ES (n=30) mice at P18. (Wilcoxon rank, control p<0.001, ES p<0.001, control-ES p=0.154).
(**E**) Schematic of RR task and violin plot displaying the discrimination ratio of interaction time with a less vs. more recent object for control (n=28) and ES (n=30) mice at P22. (Wilcoxon rank, control p=0.010, ES p=0.171, control-ES p=0.498).
(**F**) Line plots displaying time to completion and distance travelled for an 8-arm radial maze memory task over 10 trials on 3 consecutive days for control (n=12) and ES (n=12) mice at P36-38. (Kruskal-Wallis, time p<0.001).
(**G**) Schematic showing spontaneous alternation in a Y-maze as well as violin plots displaying quantified parameters (alternations, entries, distance) for control (n=12) and ES (n=12) mice at P39. (Wilcoxon rank, alternations, p=0.046).
Black lines and asterisks (* p<0.05, ** p<0.01, *** p<0.001) indicate significant differences. See Statistics table S1 for detailed statistics. For (A) data are presented as mean ± standard error of the mean (SEM). For (B-E), (G) data are presented as median with 25th and 75th percentile, shaded area represents the probability distribution of the variable. For (F) data are presented as median ± MAD.

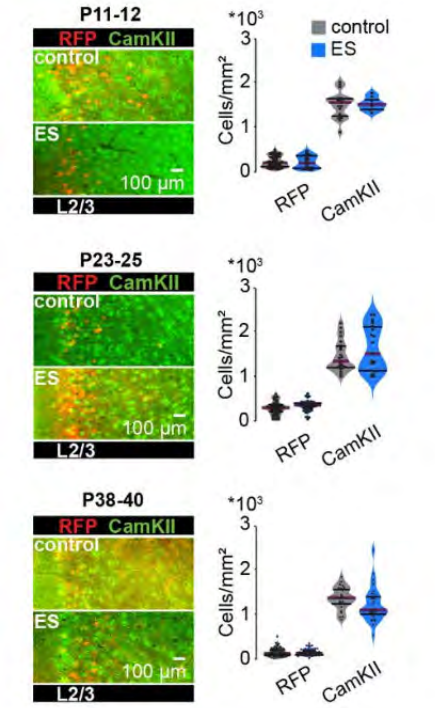

Figure S3. Related to Figure 3. Transient early stimulation does not alter the density of L2/3 PYRs.
Left, representative photographs displaying CaMKII immunostainings in the ChR2(ET/TC)-RFP-transfected mPFC of control and ES mice at P11-12 (control, RFP n=60 slices of 9 mice, CamKII n=19 slices of 6 mice; ES, RFP n=27 slices of 4 mice, CamKII n=9 slices of 2 mice), P23-25 (control, RFP n=47 slices of 5 mice, CamKII n=23 slices of 5 mice; ES, RFP n=43 slices of 5 mice, CamKII n=23 slices of 5 mice) and P38-40 (control, RFP n=65 slices of 5 mice, CamKII n=29 slices of 5 mice; ES, RFP n=62 slices of 5 mice, CamKII n=29 slices of 5 mice). Right, violin plots of RFP-expressing and CaMKII-positive neuronal density at different age groups. (LMEM, P11-12, RFP p=0.855, CamKII p=0.705, P23-25, RFP p=0.819, CamKII p=0.527, P38-40, RFP p=0.819, CamKII p=0.177).
Data are presented as median with 25th and 75th percentile, shaded area represents the probability distribution of the variable. See Statistics table S1 for detailed statistics.

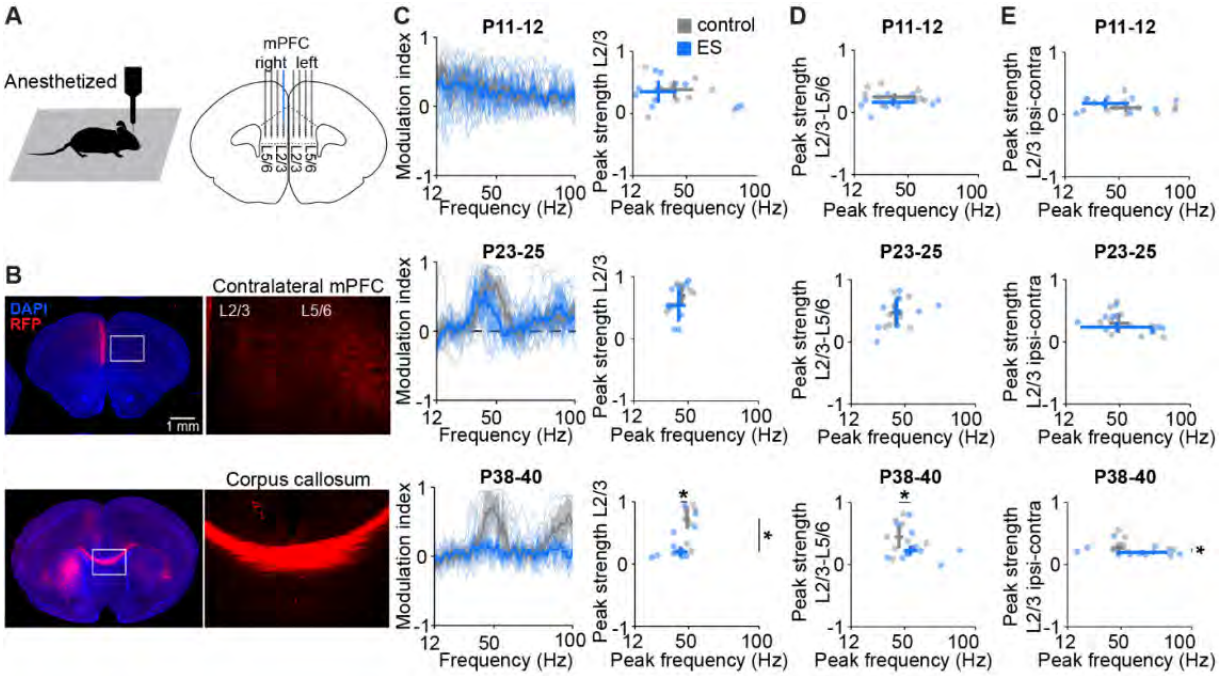

Figure S4. Related to Figure 5. Transient early stimulation impairs evoked intra- and interhemispheric synchrony in the adult mPFC.

(**A**) Schematic displaying bilateral multi-shank recordings in the mPFC of anesthetized mice.

(**B**) Representative photographs showing axonal projections of ChR2(ET/TC)-RFP-transfected L2/3 PYRs in coronal slices from a P10 mouse.

(**C**) Left, modulation index of LFP power in response to acute ramp light stimulation (473 nm, 3 s) for control and ES mice at P11-12 (control n=10 recordings, 10 mice, ES n=10 recordings, 10 mice), P23-25 (control n=10 recordings, 10 mice, ES n=11 recordings, 11 mice) and P38-40 (control n=9 recordings, 9 mice, ES n=12 recordings, 12 mice). Right, scatter plots displaying the peak strength and peak frequency of the power modulation index for control and ES mice. (Wilcoxon rank, P11-12, peak frequency p=0.520, peak strength p=0.909, P23-25, peak frequency p=0.290, peak strength p=0.459, P38-40, peak frequency p=0.039, peak strength p=0.025).

(**D**) Scatter plots displaying the peak strength and peak frequency of prefrontal L2/3-L5/6 coherence at different age. (Wilcoxon rank, P11-12, peak frequency p=1.000, peak strength p=0.053, P23-25, peak frequency p=0.943, peak strength p=0.915, P38-40, peak frequency p=0.042, peak strength p=0.069).

(**E**) Scatter plots displaying the peak strength and peak frequency of interhemispheric prefrontal L2/3-L2/3 coherence at different age. (Wilcoxon rank, P11-12, peak frequency p=0.212, peak strength p=0.623, P23-25, peak frequency p=0.832, peak strength p=0.915, P38-40, peak frequency p=0.270, peak strength p=0.036).

For (C, left) data are presented as mean ± SEM. For (C, right), (D), (E) data are presented as median ± MAD. Asterisks (* p<0.05, ** p<0.01, *** p<0.001) indicate significant differences. See Statistics table S1 for detailed statistics.

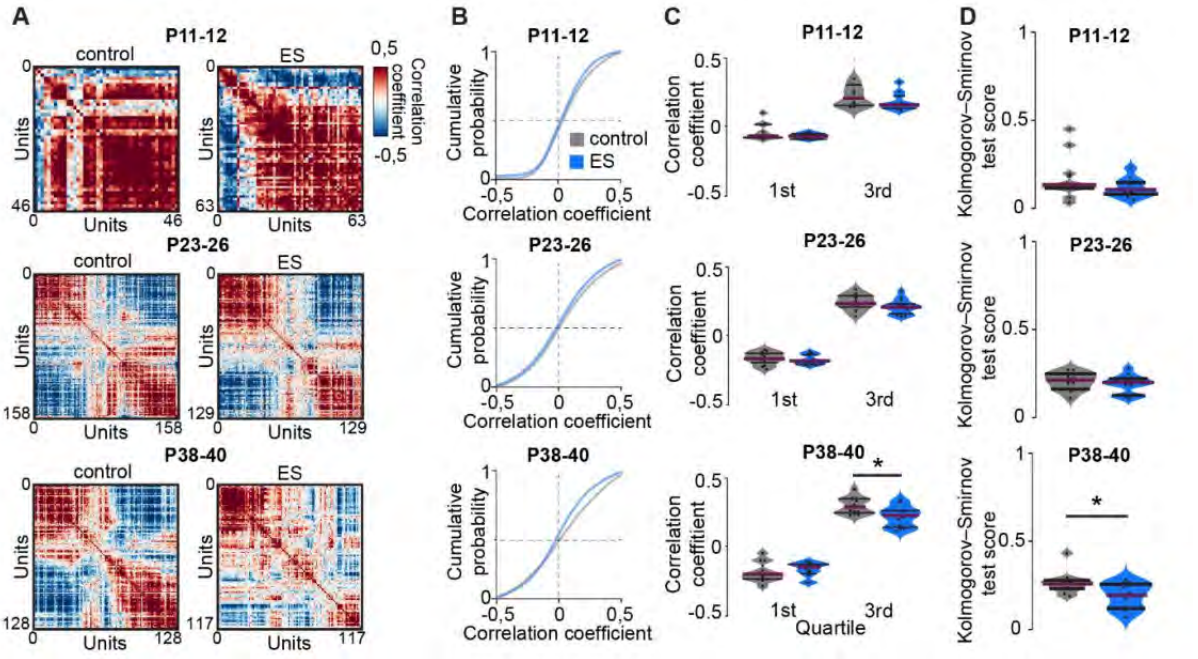

Figure S5. Related to Figure 5. Transient early stimulation reduces synchrony of highly correlated units in response to acute light stimulation in the adult mPFC.
(**A**) Representative pairwise correlations of L2/3 single units during acute ramp light stimulation (473 nm, 3 s) for a control (left) and ES mouse (right) at different developmental stages.
(**B**) Average cumulative density functions of pairwise correlations during acute ramp light stimulation for control and ES mice at P11-12 (control n=11 recordings, 11 mice, ES n=10 recordings, 10 mice), P23-26 (control n=13 recordings, 6 mice, ES n=14 recordings, 5 mice) and P38-40 (control n=12 recordings, 5 mice, ES n=12 recordings, 5 mice).
(**C**) Average intercept at 1st and 3rd quartile of correlation coefficients during acute ramp light stimulation for control and ES mice at different age. (Wilcoxon rank, P11-12, 1st quartile p=0.385, 3rd quartile p=0.162, LMEM, P23-26, 1st quartile p=0.470, 3rd quartile p=0.315, P38-40, 1st quartile p=0.537, 3rd quartile p=0.019).
(**D**) Kolmogorov-Smirnov test score of the distance between pre and stim cumulative density function of correlation coefficients for control and ES mice. (Wilcoxon rank, P11-12, p=0.418, LMEM, P23-26, p=0.631, P38-40, p=0.033).
For (C), (D) data are presented as median with 25th and 75th percentile, shaded area represents the probability distribution of the variable. Asterisks (* p<0.05, ** p<0.01, *** p<0.001) indicate significant differences. See Statistics table S1 for detailed statistics.

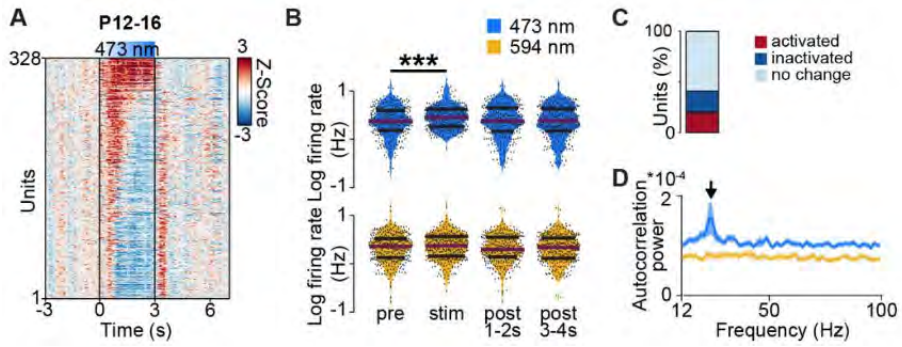

Figure S6. Related to Figure 6. Transcranial stimulation in the mPFC at P12-16.
(**A**) Firing rates of single units (n=328 units from 8 mice) in response to transcranial ramp light stimulation z-scored to pre-stimulation period at P12-16.
(**B**) Average single unit firing rate in response to ramp light stimulation at 473 nm and 594 nm averaged for P12-16 mice (n=328 units from 8 mice).
(**C**) Percent of significantly modulated units ($p<0.01$) during ramp light stimulation
(**D**) Power of single unit autocorrelations during ramp light stimulation at 473 nm and 594 nm averaged for P12-16 mice (n=328 units from 8 mice).
For (B) data are presented as median with 25th and 75th percentile, shaded area represents the probability distribution of the variable. For (D) data are presented as median ± median absolute deviation (MAD). Asterisks (* $p<0.05$, ** $p<0.01$, *** $p<0.001$) indicate significant differences. See Statistics table S1 for detailed statistics.

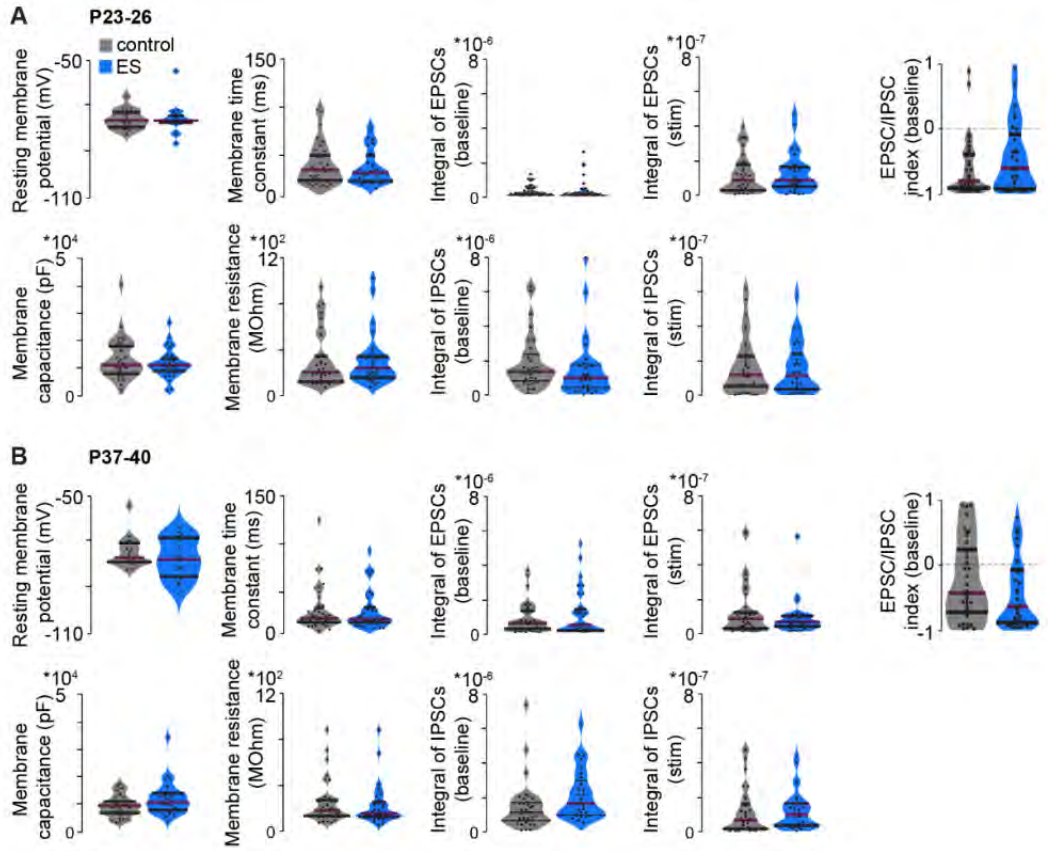

Figure S7. Related to Figure 7. Transient early stimulation does not alter the passive and active membrane properties of non-transfected L2/3 PYRs.
(**A**) Violin plots displaying passive and active membrane properties as well as properties of EPSCs and IPSCs induced by light stimulation in non-transfected L2/3 PYRs from control and ES mice at P23-26 (control n=35 neurons, 5 mice, ES n=30 neurons,5 mice). (LMEM, resting membrane potential p=0.545, membrane time constant p=0.426, EPSCs baseline p=0.743, EPSCs stim p=0.415 membrane capacitance p=0.218, membrane resistance p=0.564, IPSCs baseline p=0.234, IPSCs stim p=0.881, EPSC/IPSC index baseline p=0.218).
(**B**) Same as (A) for control and ES mice at P37-40 (control n=41 neurons, 6 mice, ES n=33 neurons, 4 mice). (LMEM, resting membrane potential p=0.526, membrane time constant p=0.907, EPSCs baseline p=0.339, EPSCs stim p=0.349 membrane capacitance p=0.304, membrane resistance p=0.436, IPSCs baseline p=0.332, IPSCs stim p=0.309, EPSC/IPSC index baseline p=0.402).
For (A), (B) data are presented as median with 25th and 75th percentile, shaded area represents the probability distribution of the variable. See Statistics table S1 for detailed statistics.

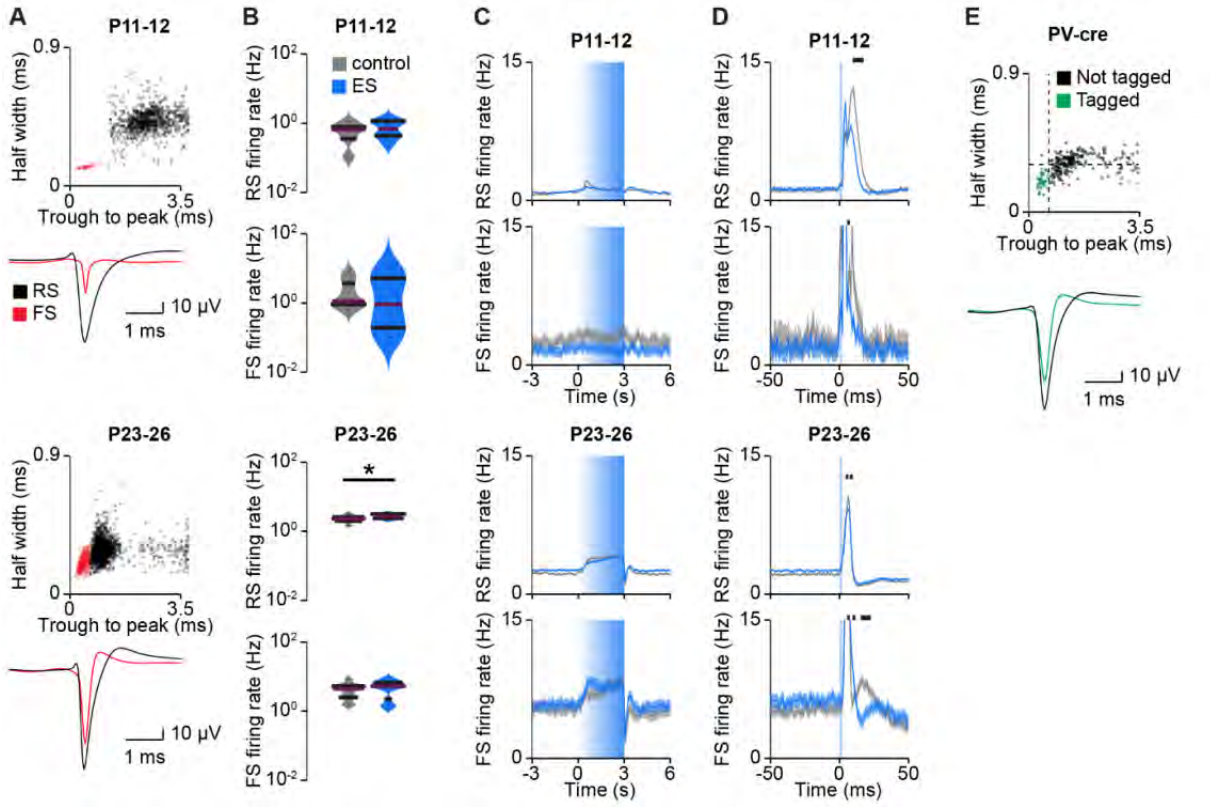

Figure S8. Related to Figure 8. Transient early stimulation alters inhibitory feedback in the mPFC.

(**A**) Scatter plots displaying half width and trough to peak duration (top) and average waveforms for RS and FS units (bottom) for control and ES mice at P11-12 (control 428 RS and 13 FS units, 11 mice, ES 475 RS and 22 FS units, 10 mice) and P23-26 (control 1140 RS and 185 FS units, 6 mice, ES 1220 RS and 141 FS units, 5 mice).

(**B**) Violin plots displaying spontaneous firing rate of RS and FS units for control and ES mice at P11-12 and P23-26. (Wilcoxon rank, P11-12, RS firing rate p=0.418, FS firing rate p=0.680, LMEM, P23-26, RS firing rate p=0.020, FS firing rate p=0.357).

(**C**) Average firing rate during acute ramp light stimulation (473 nm, 3 s) and percent of significantly modulated units for control and ES mice at P11-12 and P23-26. (LMEM, P11-12, RS firing rate p<0.001, FS firing rate p<0.001, P23-26, RS firing rate p<0.001, FS firing rate p<0.001).

(**D**) Average firing rate during acute pulse light stimulation (473 nm, 3 ms) for control and ES mice at P11-12 and P23-26. (LMEM, P11-12, RS firing rate p<0.001, FS firing rate p<0.001, P23-26, RS firing rate p<0.001, FS firing rate p<0.001).

(**E**) Scatter plots displaying half width and trough to peak duration (top) and average waveforms (bottom) for tagged (green) and not tagged (black) units of PV-cre mice expressing ChR2(ET/TC) in PV interneurons in the mPFC (3 mice P26, 5 mice P37-40).

For (B) data are presented as median with 25th and 75th percentile, shaded area represents the probability distribution of the variable. For (C), (D) data are presented as mean ± SEM. Black lines and asterisks (* p<0.05, ** p<0.01, *** p<0.001) indicate significant differences. See Statistics table S1 for detailed statistics.

Statistics table S2. Related to Figures 2 and S2. Statistics for comparison of male and female mice.

Behavioral test	Test	Groups	df	p-value
Open field Discrimination ratio	Linear mixed effect model (chi square)	control (28 mice (15 males, 13 females)) ES (30 mice (18 males, 12 females)) condition | sex	1	0.497 (χ^2=0.46)
Open field Velocity	Linear mixed effect model (chi square)	control (28 mice (15 males, 13 females)) ES (30 mice (18 males, 12 females)) condition | sex	1	1.000 (χ^2=0)
Open field Grooming	Linear mixed effect model (chi square)	control (28 mice (15 males, 13 females)) ES (30 mice (18 males, 12 females)) condition | sex	1	0.102 (χ^2=2.68)
Open field Rearing	Linear mixed effect model (chi square)	control (28 mice (15 males, 13 females)) ES (30 mice (18 males, 12 females)) condition | sex	1	0.101 (χ^2=2.67)
Open field Wall rearing	Linear mixed effect model (chi square)	control (28 mice (15 males, 13 females)) ES (30 mice (18 males, 12 females)) condition | sex	1	1.000 (χ^2=0)
Open field Jumping	Linear mixed effect model (chi square)	control (28 mice (15 males, 13 females)) ES (30 mice (18 males, 12 females)) condition | sex	1	1.000 (χ^2=0)
Novel object recognition Discrimination ratio	Linear mixed effect model (chi square)	control (28 mice (15 males, 13 females)) ES (30 mice (18 males, 12 females)) condition | sex	1	1.000 (χ^2=0)
Object location recognition Discrimination ratio	Linear mixed effect model (chi square)	control (28 mice (15 males, 13 females)) ES (30 mice (18 males, 12 females)) condition | sex	1	1.000 (χ^2=0)
Recency recognition Discrimination ratio	Linear mixed effect model (chi square)	control (28 mice (15 males, 13 females)) ES (30 mice (18 males, 12 females)) condition | sex	1	1.000 (χ^2=0)
Maternal interaction Discrimination ratio	Linear mixed effect model (chi square)	control (19 mice (9 males, 10 females)) ES (21 mice (9 males, 12 females)) condition | sex	1	1.000 (χ^2=0)
Spatial working memory Relative reference memory errors	Linear mixed effect model (chi square)	control (12 mice (8 males, 4 females)) ES (12 mice (8males, 4 females)) condition | sex	1	1.000 (χ^2=0)
Spatial working memory Relative working memory errors	Linear mixed effect model (chi square)	control (12 mice (8 males, 4 females)) ES (12 mice (8males, 4 females)) condition | sex	1	1.000 (χ^2=0)
Spatial working memory Time	Linear mixed effect model (chi square)	control (12 mice (8 males, 4 females)) ES (12 mice (8males, 4 females)) condition | sex	1	0.713 (χ^2=0.14)
Spatial working memory Reference memory errors	Linear mixed effect model (chi square)	control (12 mice (8 males, 4 females)) ES (12 mice (8males, 4 females)) condition | sex	1	1.000 (χ^2=0)

Spatial working memory Working memory errors	Linear mixed effect model (chi square)	control (12 mice (8 males, 4 females)) ES (12 mice (8males, 4 females)) condition | sex	1	1.000 (χ^2=0)
Spatial working memory Distance	Linear mixed effect model (chi square)	control (12 mice (8 males, 4 females)) ES (12 mice (8males, 4 females)) condition | sex	1	1.000 (χ^2=0)
Spatial working memory Time spent in baited arm	Linear mixed effect model (chi square)	control (12 mice (8 males, 4 females)) ES (12 mice (8males, 4 females)) condition | sex	1	0.262 (χ^2=1.26)
Spatial working memory Time spent in unbaited arm	Linear mixed effect model (chi square)	control (12 mice (8 males, 4 females)) ES (12 mice (8males, 4 females)) condition | sex	1	1.000 (χ^2=0)
Spontaneous alteration Entries	Linear mixed effect model (chi square)	control (12 mice (8 males, 4 females)) ES (12 mice (8males, 4 females)) condition | sex	1	1.000 (χ^2=0)
Spontaneous alteration Distance	Linear mixed effect model (chi square)	control (12 mice (8 males, 4 females)) ES (12 mice (8males, 4 females)) condition | sex	1	1.000 (χ^2=0)
Spontaneous alteration Alternations	Linear mixed effect model (chi square)	control (12 mice (8 males, 4 females)) ES (12 mice (8males, 4 females)) condition | sex	1	1.000 (χ^2=0)
Spontaneous alteration % alternations	Linear mixed effect model (chi square)	control (12 mice (8 males, 4 females)) ES (12 mice (8males, 4 females)) condition | sex	1	1.000 (χ^2=0)
Delayed non-match-to-sample task	Linear mixed effect model (chi square)	control (12 mice (8 males, 4 females)) ES (12 mice (8males, 4 females)) condition | sex	1	1.000 (χ^2=0)